UNIVERSIDADE FEDERAL DO RIO GRANDE DO SUL

INSTITUTO DE GEOCIÊNCIAS

PROGRAMA DE PÓS-GRADUAÇÃO EM GEOCIÊNCIAS

EVOLUÇÃO DE OFIOLITOS NEOPROTEROZÓICOS DO ESCUDO SUL-RIOGRANDENSE

KARINE DA ROSA ARENA

ORIENTADOR – Prof. Dr. Léo Afraneo Hartmann

Porto Alegre – 2017

UNIVERSIDADE FEDERAL DO RIO GRANDE DO SUL
INSTITUTO DE GEOCIÊNCIAS
PROGRAMA DE PÓS-GRADUAÇÃO EM GEOCIÊNCIAS

EVOLUÇÃO DE OFIOLITOS NEOPROTEROZÓICOS DO ESCUDO SUL-RIOGRANDENSE

KARINE DA ROSA ARENA

ORIENTADOR – Prof. Dr. Léo Afraneo Hartmann

BANCA EXAMINADORA
Prof. Dr. Miguel Ângelo Stipp Basei – Departamento de Mineralogia e Geotectônica, Universidade de São Paulo
Professor Dr. Farid Chemale Júnior – Departamento de Geologia, Universidade do Vale do Rio dos Sinos
Prof. Dr. Marcus Vinicius Dorneles Remus – Departamento de Mineralogia e Petrologia, Universidade Federal do Rio Grande do Sul

Tese de Doutorado apresentada como requisito parcial para a obtenção do Título de Doutor em Ciências

Porto Alegre – 2017

UNIVERSIDADE FEDERAL DO RIO GRANDE DO SUL

Reitor: Rui Vicente Oppermann

Vice-Reitor: Jane Fraga Tutikian

INSTITUTO DE GEOCIÊNCIAS

Diretor: André Sampaio Mexias

Vice-Diretor: Nelson Luiz Sambaqui Gruber

Arena, Karine da Rosa
Evolução de ofiolitos neoproterozóicos do Escudo Sul-Riograndense. / Karine da Rosa Arena. - Porto Alegre: IGEO/UFRGS, 2017.
[176 f.] il.

Tese (Doutorado).- Universidade Federal do Rio Grande do Sul. Programa de Pós-Graduação em Geocências. Instituto de Geociências. Porto Alegre, RS - BR, 2017.

Orientador(es): Léo Afraneo Hartmann

1. Ofiolitos. 2. Metassomatitos. 3. Escudo Sul-Rio-grandense. 4. Geocronologia e Geologia Isotópica. I. Título.
CDU 550.4

Catalogação na Publicação
Biblioteca Instituto de Geociências - UFRGS
Renata Cristina Grun CRB 10/1113

Universidade Federal do Rio Grande do Sul - Campus do Vale Av. Bento Gonçalves, 9500 - Porto Alegre RS - Brasil
CEP: 91501-970 / Caixa Postal: 15001.
Fone: +55 51 3308-6569
E-mail: bibgeo@ufrgs.br

AGRADECIMENTOS

Ao Programa de Pós-Graduação em Geociências da Universidade Federal do Rio Grande do Sul e projetos CNPq/FAPERGS coordenados por Léo Afraneo Hartmann, pelo apoio institucional e financeiro. Aos laboratórios da Universidade de São Paulo, Universidade Federal de Ouro Preto e Universidade Federal do Rio Grande do Sul, onde fiz as análises para elaboração dessa tese.

Agradeço ao meu orientador professor Léo Afraneo Hartmann pelas discussões geológicas que contribuiram para o amadurecimento do conhecimento. Pela orientação científica criteriosa e crítica ensinando a trilhar os caminhos da ciência. Que por fim aprendemos a trabalhar sem brigar muito nesses quase nove anos de convivência. Que me ensinou bastante sobre geologia e por quem tenho grande admiração e estima.

Agradeço ao pessoal de Ouro Preto pela acolhida, parceria, ajuda e suporte, no período em que estive por lá e posteriormente, principalmente Cristiano Lana, Lívia Teixeira, Ana Alkmim, Gláucia Queiroga, Marco de Castro, Anarda Simões, Fernanda Durães e as demais gurias da república Bem Q se Kiss.

Um agradecimento especial aos meus companheiros de pesquisa pelo tanto de tempo em que dividimos a “nossa salinha” compartilhando geologia e aprendizado, grandes amigos pra vida Juliana Pertille, Sandro Duarte e Thales Petry presentes em tantos momentos na salinha e fora dela. Grata também aos colegas da geologia pela parceria em campo Matheus Brückmann, Vitor Casagrande, Leonardo Mueller, Johnathan Gambeta. Gratidão aos amigos geólogos fiéis *forever* com quem pude dividir não só as dificuldades e alegrias das realizações acadêmicas mas também a vida: Adriano Reis, Dina Cabrita, Jaques Schmidt, Luciano Marquetto, Priscila Lourenzi, Renata Dillenburg e Saulo Borsatto.

Um profundo agradecimento à minha família, pelo carinho, paciência, incentivo e apoio incondicional (incluindo meus cuscos mais amados do mundo, que tornam a vida mais leve e cheia de amor). As amigas que estão comigo desde muito além Ana Paula Silva, Cristiani Vaz e Thais Recova. Agradeço ao Júlio Moraes que esteve presente de uma forma muito especial.

E como não há exagero mais belo que a gratidão: Imenso obrigada a vida e a geologia por tudo! Ho’oponopono!

“A tarefa não é tanto ver aquilo que ninguém viu, mas pensar o que ninguém ainda pensou sobre aquilo que todo mundo vê.”

Arthur Schopenhauer

RESUMO

O tempo de formação e acreção de crosta oceânica ao Orógeno Brasiliano são determinados, junto com a caracterização de litosfera oceânica. A dificuldade de datar ofiolitos é superada pela busca e descoberta de zircão em albititos e rochas metassomáticas contidas em serpentinitos. Foram selecionados três ofiolitos no terreno juvenil São Gabriel e um no cinturão de dobramentos e cavalgamento Porongos no sul do Escudo Brasileiro. Estudo isotópico de zircão e boro foi realizado. Análises U-Pb SHRIMP, Lu-Hf LA-ICP-MS e elementos-traço em zircão foram executadas na mesma região dos cristais. Análises isotópicas de boro foram realizadas em turmalinas de turmalinito. Microcopia eletrônica de varredura e análises químicas de rocha total também foram realizadas para classificar e interpretar o ambiente geológico dos ofiolitos. Estudos de zircão de albititos e metassomatitos levaram a idades Tonianas para os ofiolitos Cerro Mantiqueiras, Ibaré e Palma. Zircão dos albititos apresentam as idades mais antigas. No Cerro Mantiqueiras, duas idades Concordia distintas são de 923 ±3 Ma no núcleo e 786 ±13 Ma na borda com εHf = +8 a +13 e em Ibaré uma idade única de 892 ±3 Ma com εHf = +13 a +15. Análises de zircão de metassomatitos e rocha vulcanoclástica dos ofiolitos Ibaré e Palma indicam idades semelhantes, respectivamente 726 ±2 Ma e 722 ±3 Ma (metassomatitos) e 758 ±4 Ma (rocha vulcanoclástica). Outras três idades representativas registradas nos metassomatitos são 880 ±12, 836 ±6 e 780 ±5 Ma, interpretadas como sucessivos eventos de serpentinização. Composições isotópicas mantélicas de Hf em zircão dos metassomatitos variam de εHf = +12,1 a +1,4 e na rocha vulcanoclástica εHf = +11 a +6. O turmalinito maciço, imerso em serpentinito de Ibaré, apresenta composição química e isotópica homogênea (dravita) ($\delta^{11}B$ = +3 a +5 ‰) e origem em crosta oceânica alterada. O Granito Santa Rita resultou em idade de 585 ±2 Ma e εHf = -14 a -32. No ofiolito Capané, o zircão metassomático de rodingito *blackwall* contido em serpentinito exibe múltiplas idades U-Pb do Toniano ao Cryogeniano (793 ±0.9, 757 ±2, 715 ±2). Isótopos de Hf indicam zircão de manto depletado (εHf = +15,0 a +10,7) e elementos-traço de ambiente oceânico. Geoquímica de zircão se aproxima da derivação mantélica. Formação e acreção dos ofiolitos ocorreram no Toniano (923-722 Ma) no terreno São Gabriel. No Cinturão Porongos, a formação do ofiolito Capané ocorreu no Toniano-Cryogeniano (793-715 Ma) com início da acreção no Cryogeniano (650 Ma) durante a orogênese colisional. Esses dados registram, no Escudo Sul-Riograndense, o início da ampla tafrogenia no Toniano para ruptura de Rodinia e posterior reconstrução de Gondwana.

ABSTRACT

Timing of oceanic crust formation and accretion to the Brasiliano Orogen are determined, along with characterization of oceanic lithosphere. The difficulty of dating ophiolites is presently overcome by the search and finding of zircon in albitites and metasomatic rocks contained in serpentinite. Three ophiolites were selected from the juvenile São Gabriel terrane and one from Porongos fold and thrust belt, southern Brazilian Shield. Isotopic study of zircon and boron was performed. Zircon U-Pb SHRIMP, Lu-Hf LA-ICP-MS and trace element analyses were executed in the same region of the crystals. Boron isotopic analyses were conducted in tourmalines from tourmalinite. Scanning electron microscopy and whole-rock chemical analyses were done to classify and interpret the geological environment of ophiolites. Zircon studies of albitites and metasomatites yield Tonian ages for Cerro Mantiqueiras, Ibaré and Palma ophiolites. Zircon from albitites present the oldest ages. In Cerro Mantiqueiras, two distinct Concordia ages are 923 ±3 Ma in the cores and 786 ±13 Ma in the rims with εHf = +8 to +13; in Ibaré, a single age of 892 ±3 Ma with εHf = +13 to +15. Analyses of zircon from metasomatites and a volcanoclastic rock from Ibaré and Palma ophiolites indicate similar ages, respectively 726 ±2 Ma and 722 ±3 Ma (metasomatites) and 758 ±4 Ma (volcanoclastic rock). Other three representative ages recorded in the metasomatites are 880 ±12, 836 ±6 and 780 ±5 Ma, interpreted as successive serpentinization events. Mantle Hf isotope compositions of zircon in the metasomatites range from εHf = +12.1 to +1.4 and in the volcanoclastic rock εHf = +11 to +6. Massive tourmalinite enclosed in serpentinite in Ibaré has homogeneous chemical (dravite) and isotopic composition ($\delta^{11}B$ = +3 to +5‰), pointing to altered oceanic crust origin. The Santa Rita Granite resulted in age of 585 ±2 Ma and negative εHf (−14 to −32). In the Capané ofiolite, rodingite blackwall contained in serpentinite has metasomatic zircon that displays multiple U–Pb ages from Tonian to Cryogenian (793 ±0.9, 757 ±2, 715 ±2 Ma). Hf isotopes indicate zircon origin from a depleted mantle (εHf = +15 to +10.7) and trace elements point to oceanic environment. Zircon geochemistry is close to the mantle array. Ophiolite formation and accretion occurred in the Tonian (923-722 Ma) in São Gabriel terrane. In the Porongos belt, Capané ophiolite formation occurred in the Tonian-Cryogenian (793-715 Ma) with accretion starting in the Cryogenian (650 Ma) during collisional orogenesis. These data record, in the southern Brazilian Shield, the onset of intense taphrogeny in the Tonian for Rodinia break-up and later reconstruction of Gondwana.

Lista de Figuras

Lista de Tabelas

SUMÁRIO

Sobre a estrutura da tese:

Esta tese de Doutorado está estruturada contendo três artigos publicados e um artigo submetido a periódicos científicos internacionais. Consequentemente, sua organização compreende as seguintes partes principais:

1) Introdução sobre o tema e descrição do objeto da pesquisa de Doutorado, onde estão sumarizados os objetivos e uma descrição do estudo desenvolvido, do estado da arte sobre o tema, seguido de discussões integradoras sobre os resultados e interpretações.

2) O corpo principal da tese é formado por quatro artigos científicos elaborados pela autora durante o desenvolvimento da tese de Doutorado. Três artigos foram publicados e um submetido a periódicos internacionais.

1. Introdução

O estudo de zircões e turmalina de albititos e metassomatitos em serpentinitos causou um avanço na determinação do tempo de evolução dos ofiolitos e sua caracterização como litosfera oceânica. Ofiolitos têm sido amplamente utilizados na reconstrução de bacias oceânicas antigas e cinturões de montanhas. A presença de ofiolitos neoproterozóicos nos continentes torna esses fragmentos de manto e crosta oceânica mais significativa para a compreensão dos processos geotectônicos ativos no final do Pré-Cambriano. Em termos geotectônicos, o Orógeno Brasiliano representa uma unidade Neoproterozóica-Cambriana do Gondwana Oeste (Chemale Jr., 2000). O orógeno inclui cinturões móveis neoproterozóicos e rochas cambrianas, além do embasamento pré-Neoproterozóico retrabalhado durante a colisão. No Escudo Sul-Riograndense, o arcabouço geotectônico do Orógeno Brasiliano contém sucessões tectono-estratigráficas mistas. Rochas (950-535 Ma) de margens continentais rifteadas, restos de crosta oceânica imbricada e sucessões diacrônicas de arcos de ilhas acrescionados, além de bacias de antepaís (*foreland*), ocorrem associadas com remanescentes retrabalhados do embasamento.

Foram investigados três ofiolitos na porção oeste do escudo (terreno São Gabriel) e um ofiolito na porção centro-leste (Grupo Porongos). Essa tese apresenta isótopos U-Pb e Lu-Hf integrados com estudo de elementos-traço em zircão por SHIRIMP e LA-ICP-MS, análise química de rocha total e isótopos de boro de turmalina. Os estudos foram realizados em rochas metassomáticas, particularmente cloritito, turmalinito, rodingito *blackwall* de serpentinitos, além de albititos e também rocha vulcanoclástica, um metabasalto e um granito intrusivo, associadas aos ofiolitos. A serpentinização, rodingitização e cloritização são consequência de complexa interação de água do mar com a litosfera oceânica (Klein, 2009).

Esse é o primeiro estudo de datação direta de zircão formado em processos de serpentinização da crosta oceânica e manto e sua colocação no continente. Nesse contexto, os ofiolitos destacam-se como unidades fundamentais para a reconstrução da história geológica do Orógeno Brasiliano no Cinturão Dom Feliciano do Escudo Sul-Riograndense, que é parte do Escudo Brasileiro. O significado tectônico, as idades de formação e colocação dos ofiolitos e suas relações com as unidades adjacentes permanecem incertas e são abordados nesta tese. Os quatro ofiolitos selecionados no Escudo Sul-Riograndense são fragmentos de crosta oceânica e manto, formados durante a ruptura do Supercontinente Rodinia e aglomeração do Gondwana.

1.1 Problema científico

No Orógeno Brasiliano, foram descritos alguns ofiolitos e possíveis ofiolitos ao longo dos cinturões móveis neoproterozóicos (Figura 1, Tabela 1). No Cinturão Dom Feliciano (Santa Catarina, Rio Grande do Sul, Uruguai), conhecem-se apenas a idade do metabasalto do ofiolito Cerro Mantiqueiras (Leite et al., 1998) e algumas idades relacionadas aos arcos Passinho e São Gabriel (Babinski et al., 1996; Leite et al., 1998; Machado et al., 1990; Gubert et al., 2016). O Escudo Sul-Riograndense contém ofiolitos nas porções oeste, centro e leste. Na porção oeste, no terreno São Gabriel, o ofiolito Cerro Mantiqueiras (Leite, 1997) é uma associação de arco magmático juvenil de idade U-Pb = 879 ±14 Ma (arco Passinho), sendo constituído por harzburgito, serpentinito e seus produtos de transformação metassomática, além do metabasalto de idade U-Pb = 733 ±10 e 700 Ma. O ofiolito está encaixado em uma associação tonalito-trondhjemito-granodiorito de idade 750-700 Ma (Gnaisses Cambaí) metamorfizado na fácies anfibolito médio (Hartmann & Remus, 2000). Os ofiolitos Palma e Ibaré contêm serpentinito, xisto magnesiano e metassomatitos como cloritito, rodingito, turmalinito, além de albitito. Ambos ofiolitos estão associados a rochas metavulcano-sedimentares afetadas por metamorfismo de fácies xistos verdes. As rochas de Ibaré também foram recristalizadas por metamorfismo de contato pela intrusão do Granito Santa Rita (Chemale Jr., 1982; Naumann & Hartmann 1984; Naumann, 1985). Nessa associação, é conhecida a idade do Granito Jaguari como sendo 569 ±6 (Gastal et al., 2015).

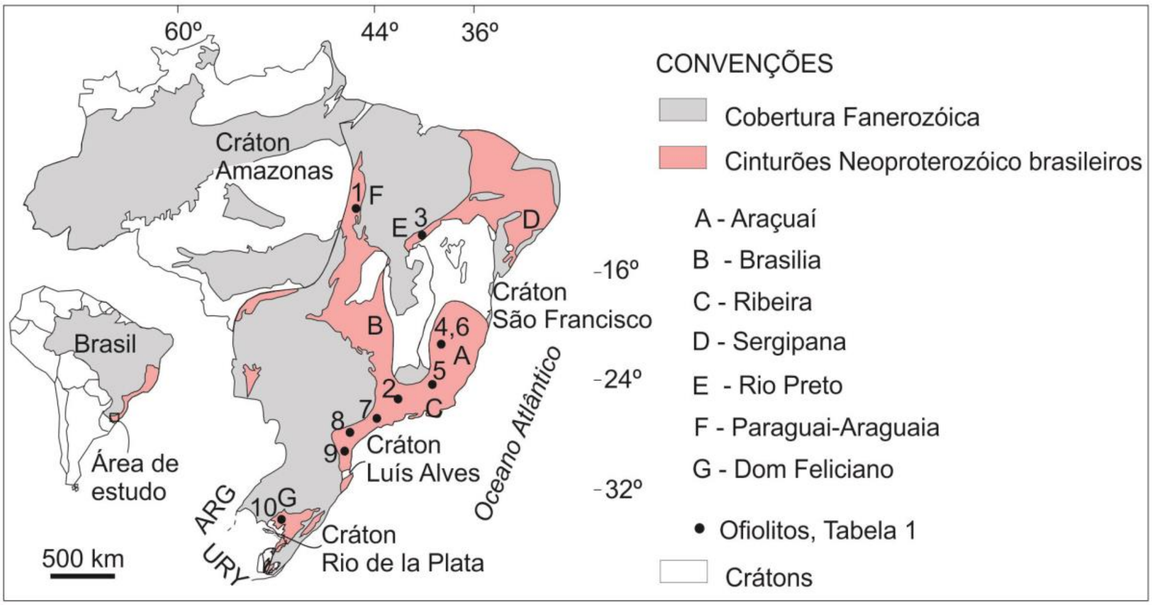

Figura 1. Distribuição dos ofiolitos neoproterozóicos no Brasil. Mapa extraído de Suita et al. (2004).

Na porção central do escudo, na região de Capané, as rochas ultramáficas estão contidas nos xistos do Grupo Porongos. As rochas vulcânicas associadas aos serpentinitos foram interpretadas por Marques et al. (1998, 2003) e Gollmann et al. (2008) como ambiente retro-arco (*backarc*). Rochas detríticas e riodacito no Cinturão Porongos, incluindo um xisto magnesiano na Antiforme Capané, mostram que as rochas são de origem continental e que o grupo é parte de um cinturão de dobramentos e cavalgamento (Pertille et al., 2015a, 2017). Na porção sudeste do escudo, na região de Arroio Grande, a presença de um complexo ofiolítico foi sugerida por Ramos (2014), com base em um conjunto de rochas metamáficas, meta-ultramáficas e metassedimentares, principalmente em virtude da associação geológica. O ofiolito Arroio Grande está associado aos granitos do Batólito Pelotas. Esse ofiolito foi sugerido como continuação, em território brasileiro, do Complexo La Tuna, encontrado no Uruguai (Ramos & Koester 2014).

Apesar de muitos estudos, os ofiolitos do Escudo Sul-Riograndense permanecem com idade, origem e ambiente de formação pouco conhecidos, sendo reconhecidas associações de rochas distintas e ambientes diversos. A ausência de dados robustos das rochas ultramáficas originou diferentes modelos para o escudo. Estudos integrados diretamente nas rochas ofiolíticas e rochas encaixantes se fazem necessários a fim de esclarecer a evolução tectônica dos ofiolitos no Orógeno Brasiliano. Os ofiolitos são primordiais para o entendimento das configurações geotectônicas dos supercontinentes Rodinia e Gondwana.

1.2 Objetivos e justificativa

Esta tese visa estabelecer por meio de estudos isotópicos e geoquímicos a época de formação da crosta oceânica e sua acresção ao Orógeno Brasiliano bem como as relações temporais com as margens tectônicas convergentes, em conjunto com a caracterização de litosfera oceânica. E contribuir na edificação da configuração geotectônica que controlou em grande parte a evolução Neoproterozóica do Cinturão Dom Feliciano no Escudo Sul-Riograndense.

A presença de numerosos corpos de rochas ultramáficas e paucidade de estudos geocronológicos dos ofiolitos e caracterização da listosfera oceânica tornaram importante o estudo do *blackwall* dos serpentinitos. Os metassomatitos apresentam potencial para datação direta da época de formação do ofiolito na crosta bem como a época de colocação e caracterização oceânica. Estudos dos ofiolitos são uma chave para o entendimento da evolução dos continentes.

Tabela1. Aspectos gerais e geocronológicos de ofiolitos neoproterozóicos brasileiros.

Faixa móvel	Complexo ofiolítico	Localização	Litologia	Idade (Ma)	Metamorfismo
Paraguai-Araguaia	Quatipuru	SE Pará	Serpentinito, gabro, harzburgito, piroxenito	757 ±49[1]	Xistos verdes
Brasília	Campos das Vertentes	S Minas Gerais	Serpentinito, dunito, harzburgito, piroxenito	604 ±16[2]	Eclogito (retro) Gr HP
Rio Preto	Faixa Rio Preto		Rocha máfica-ultramáfica	840[3]	Xistos verdes
Araçuaí	Ribeirão da Folha São José da Safira	NE Minas Gerais	Piroxenito, gabro, plagiogranito, basalto, xisto máfico	816[4]	Anfibolito
Araçuaí	Grupo Dom Silvério	Centro-leste MG	Anfibolito, xisto máfico	549[5]	Anfibolito
Araçuaí	Ribeirão da Folha	Minas Novas, MG	Plagiogranito	660 ±29[6]	Anfibolito
Ribeira	Complexo Pirapora do Bom Jesus	E São Paulo	Basalto, gabro	628 ±9[7]	Xistos verdes
Ribeira	Grupo São Roque-Açunguí		Basalto, gabro	619-608[8]	Xistos verdes
Ribeira	Suíte Piên	E Paraná-SC	Peridotito, gabro harzburgito, piroxenito	631 ±17[9]	Anfibolito
Dom Feliciano	Cerro Mantiqueiras	Terreno São Gabriel	Anfibolito	733 ±10[10]	Anf-xistos verdes

(1) Sm-Nd rocha total; Cordeiro & MC Cancless (1976); Goyareb (1989); Hieronymus et al. (1993); Kostchoubey & Hieronymus (1996); Kostchoubey et al. (1996); Teixeira (1996); Paixão & Nilson (2001, 2002); Paixão et al. 2002); CPRM (2004); (2) Almeida (1992); Trouw & Pankhurst (1993) em Ribeiro et al. (2003); (3) K-Ar anfibólio; Fuck et al. (1993); Brito Neves et al. (2000); (4) Sm-Nd rocha total; Pedrosa-Soares et al. (1998, 2001); Aracema (2000); Suita et al. (2003); (5) Sm-Nd minerais; Cunninham et al. (1997, 1998); Pedrosa-Soares et al. (2001); (6) U-Pb ICP; Queiroga et al. (2007); (7) U-Pb zircão, Tassinari et al. (2001); (8) Hackspacher et al. (2000); (9) U-Pb SHRIMP, Harara (1996, 2001); (10) U-Pb SHRIMP, Leite et al. (1998). Dados extraídos de Suita et al. (2004), com acréscimos.

1.3 Metamorfismo, metassomatismo e mobilidade do Zr

Metamorfismo é definido pela IUGS (Subcomissão sobre a Sistemática de Rochas Metamórficas) como um processo que envolve alterações no conteúdo mineral, composição e microestrutura de uma rocha, dominantemente no estado sólido. Este processo é principalmente devido a um ajuste da rocha para condições físicas que diferem daquelas em que a rocha originalmente foi formada e que também diferem das condições físicas que normalmente ocorrem na superfície da terra e na zona de diagênese. O processo pode coexistir com fusão parcial e pode também implicar alterações na composição química da massa de rocha.

A atual definição de metassomatismo, de acordo com a IUGS, é um processo metamórfico pelo qual a composição química da rocha ou a porção da rocha é alterada de uma forma difusa e que envolve a introdução e remoção de componentes químicos, como resultado da interação da rocha com fluídos aquosos. Durante o metassomatismo, a rocha permanece em estado sólido.

Portanto, metassomatismo e metamorfismo de rochas silicáticas estão normalmente interligados. No entanto, eles também podem ser mutuamente exclusivos. Por exemplo, pode ter metamorfismo isoquímico de tal modo que as características químicas e isotópicas do protólito sedimentar ou ígneo sejam retidas. Em contraste, na diagênese sedimentar, os fluídos da deposição de veios de minério ou depósitos de minério, alteração do fundo do mar e alteração de rocha em torno de nascentes de água quente ou fluídos meteóricos são dominados por processos metassomáticos que geralmente não são considerados metamórficos.

Transferência de massa assistida por fluído e subsequente re-equilíbrio mineral são as duas características definidoras do metassomatismo em rochas silicáticas e devem estar presentes para que ocorra o metamorfismo. Levando em conta a escala do tempo geológico, a quantidade de fluído requerida não necessita ser grande (consideravelmente menos do que 0,01% do volume total da rocha) e nem mesmo em fluxo contínuo. Mas o fluído deve ser capaz de fluir ativamente ao longo dos contatos de grãos e quimicamente reativos em relação aos minerais que encontram de tal forma que seja promovida eficiente transferência de massa (Harlov & Austrheim, 2013).

Evidência de metassomatismo durante processos tectono-metamórficos e orogênicos é abundante em todas as escalas. Em grande escala, os mais evidentes indicadores de transporte de grande quantidade de material dissolvido em fluído (o metassomatismo), são provavelmente alteração de rocha cristalina (por exemplo, rodingitização – Ague, 2003; Penniston-Dorland & Ferry, 2008).

Metassomatismo regional ocorre em muitos cinturões metamórficos do Proterozóico, sendo o Mount Isa Inlier (NE Austrália; Rubenach, 2013) um bom laboratório natural. Ele exibe heterogeneidade de tensão em todas as escalas que levaram a canalização de fluído, diversas rochas reativas, metamorfismo episódico e eventos intrusivos abrangendo, pelo menos, 250 Ma. Exemplos de metassomatismo generalizado no Mount Isa Inlier incluem alteração Na-Ca associada com rochas calcisilicáticas e albitização de xistos pelíticos e rochas metapsamíticas.

Metamorfismo e metassomatismo envolvem o re-equilíbrio de assembléias minerais, devido às mudanças de pressão, temperatura, e/ou ambiente químico. Ambos processos envolvem o transporte de material, mas em diferentes escalas de comprimento e, portanto, cada reação metamórfica é metassomática em uma escala local. Além dos sistemas geotérmicos de cadeias meso-oceânicas, exemplos de fluídos metassomáticos são salmouras de bacia sedimentar e fluídos magmáticos, assim como fluídos do manto e metamórficos.

Metassomatismo pode ser descrito como um processo de alteração que envolve simultaneamente reações e mudanças na composição de rocha total na presença de uma fase fluída com temperatura e pressão fixas ou variáveis. Mudanças metassomáticas são conduzidas por um desequilíbrio local (gradiente potencial químico) induzido pela interação da rocha pré-existente com fluídos quimicamente reativos (Goncalves et al., 2013). Fluídos proporcionam um mecanismo de transporte que é uma ordem de magnitude mais rápido do que a difusão de estado sólido e induz re-equilíbrio de fases principais através de dissolução e reprecipitação de produtos (Putnis & Austrheim, 2013).

No caso de metassomatismo, recristalização é um processo-chave que controla a petrologia e o registro isotópico de minerais. Pode ocorrer tanto sob a forma de neocristalização completa (por exemplo, em um veio) e como pseudomorfismo, dissolução, reprecipitação. A recristalização pode ser completa ou não, levantando a possibilidade de que relictos de um conjunto pré-metassomático podem ser preservados (Villa & Williams, 2013). Assembléias metassomáticas geralmente contêm misturas entre fases relíquiares e recém-formadas, cuja geocronologia é mais complexa que sistemas ideais simples, mas pode ser controlada. Eventos metassomáticos que alcançam recristalização completa da assembléia mineral fornecem idades precisas e fornecem isócronas com baixo MSWD (Villa & Williams, 2013).

Metassomatismo é um dos processos-chave na gênese e desenvolvimento de uma vasta gama de sistemas minerais. Metassomatismo está geralmente associado com a atividade de voláteis exsolvidos de magmas, que atuam tanto nas intrusões quanto nas rochas-protólito circundantes (Pirajno, 2013). Além disso, Zharikov et al. (2007) subdividiram os processos metassomáticos nos 4 tipos resumidos a seguir.

1) Metassomatismo de difusão: refere-se à difusão de um soluto por meio de um sistema de fluído estagnado. Isto ocorre porque a difusão de gradientes químicos entre a rocha e fluídos nos poros não requer o movimento de um fluído através da rocha.

2) Metassomatismo de infiltração: refere-se à transferência de material nos fluídos, que infiltram através das rochas hospedeiras. A força motriz é a pressão e um grande influxo de fluído tamponado externamente. Processos metassomáticos afetando

rochas ultramáficas, podem produzir rodingitos e listvenito, que em alguns casos podem conter mineralização de ouro.

3) Autometassomatismo: Na parte superior de intrusões ígneas durante a fase pós-magmática. Albitização é um exemplo clássico de autometassomatismo.

4) Metassomatismo-limite: É o que ocorre em resposta a atividade de gradiente de fluído no contato entre duas litologias diferentes. A geração de rodingitos e alteração *blackwall* estão relacionadas com metassomatismo-limite.

Metassomatismo de crosta oceânica e serpentinização associados levam a uma série de reações metassomáticas, uma das quais é a albitização e a formação de rochas peculiares conhecidas como rodingitos e cloritos. Em alguns casos, Au, Ag, e mineralização de Co, associados com rodingitos e serpentinitos carbonatados, têm sido relatados (Leblanc & Lbouabi, 1988).

Drásticas induções de transferências de fluído de massa metassomática estão limitadas a áreas de grande fluxo de fluído tais como zonas de fluxo hidrotermais ascendentes. Cloritização e sericitização são comuns nestas zonas de fluxo ascendentes. Metassomatismo por difusão é subordinada nas camadas da crosta (gabróica-dolerítica-basáltica), porque as diferenças de potencial químico entre as diferentes litologias são menores. Na crosta heterogênea (litologia mista máfica-ultramáfica), no entanto, difusão de transferências de massa entre litologias basálticas e peridotito é muito comum. Esses processos incluem, por exemplo, rodingitização de diques gabróicos no manto litosférico e esteatitização de serpentinitos em contato com intrusões gabróicas. A maioria destes processos ocorre sob condições de fácies xistos verdes, onde as diferenças nas atividades de sílica e prótons nos fluídos são mais pronunciadas (Bach et al., 2013).

Contatos máfico-ultramáficos hidratam em maiores extensões e em temperaturas mais elevadas do que as massas uniformes de rochas máficas ou ultramáficas. Por conseguinte, metassomatismo desempenha um papel fundamental na determinação das propriedades reológicas da litosfera oceânica ao longo dos centros de expansão oceânica lentos que, em termos de comprimento, constituem metade do sistema de dorsal meso-oceânica global.

Atividades com fluidos ácidos frequentemente considerados responsáveis pela transferência de Zr não são consistentes com serpentinização. Porém, a cristalização de zircão no *blackwall* é possível devido a uma diminuição do pH durante a formação de clorita. Redução local do pH do fluído ocorre relacionada à fixação de OH^- pela clorita (Saccocia et al., 1994). Com isso, durante processos de serpentinização, altamente alcalinos (pH 8-12), a mobilidade de Zr torna-se possível (Dubińska et al., 2004). Múltiplos eventos de alteração, com mais de um processo de serpentinização, foram registrados no presente estudo de tese. Como comparativo, mais de um evento de serpentinização foi descrito, por exemplo, por Ali et al. (2010) em ofiolito da China com idades entre 422-290 Ma cuja serpentinização iniciou no oceano e terminou durante a subducção e colocação. Adicionalmente, Dubińska et al. (2004) sugeriram que a serpentinização de peridotito começou na cadeia meso-oceânica e continuou durante o transporte dos tectonitos do manto em direção à zona de subducção.

1.4 Ofiolitos - definições e conceitos

O entendimento de definições e conceitos de ofiolitos permite a compreensão de sua forma de ocorrência e ambientes relacionados. Os ofiolitos em sistemas orogênicos são o registro de zonas de sutura entre terrenos acrescionados e placas colididas. As unidades litológicas e a geologia regional fornecem informações significativas sobre a incorporação dos ofiolitos nesses sistemas (Dilek, 2003a). Os ofiolitos ocorrem como rochas máficas-ultramáficas (remanescentes de crosta oceânica e manto superior) associadas com rochas metamórficas, sedimentares e ígneas de idades semelhantes e podem representar remanescentes de diferentes estágios de evolução do ciclo de Wilson. Não há um modelo único de formação de ofiolitos, pois podem desenvolver-se em diferentes configurações tectônicas (da cadeia meso-oceânica à zona de subducção) antes de serem incorporados aos continentes durante fechamento de oceanos (Coleman, 1977; Dilek, 2003b; Dilek & Furnes, 2014).

Na definição da Conferência Penrose (Anonymous, 1972), um ofiolito era descrito como uma assembéia de rochas máficas-ultramáficas composta da base para o topo por peridotitos tectonizados, peridotitos cumuláticos, piroxenitos sobrepostos por gabros em camadas, diques basálticos foliados, uma sequência vulcânica e uma cobertura sedimentar. Porém, de acordo com Dilek & Furnes (2011) um ofiolito pode estar incompleto, metamorfizado ou tectonicamente desmembrado. Para os autores a definição de Penrose é restritiva e não reflete a heterogeneidade de ocorrência de ofiolitos. Pearce (2008) e Dilek & Furnes (2011) classificaram os ofiolitos com base em assinatura geoquímica levando em consideração a tectônica regional. Os ofiolitos foram divididos em tipos relacionados à subducção (de zona de suprasubducção e de arco vulcânico) e não relacionados à subducção (do tipo margem continental, cadeia meso-oceânica e os do tipo pluma). Alguns fatores tais como local de formação (próximo à pluma ou fossa), propagação do oceano, composição do manto e disponibilidade de fluídos, controlam as variações dos ofiolitos como, por exemplo, assinatura geoquímica (Dilek & Furnes, 2014).

Ofiolitos são encontrados ao longo de zonas de sutura em cinturões orogênicos (Figura 2) tipo colisional (Alpino-Himalaia, Apalache-Caledoniano, Herciniano-Uraliano) e acrescionário (Andino, Pan-Africano e Brasiliano) que marcam limites principais entre terrenos acrescidos ou placas amalgamadas.

1.5 Sistemas orogênicos globais e ofiolitos selecionados

Uma síntese de ofiolitos em cinturões orogênicos globais é aqui referida e foi utilizada como base para o entendimento de processos relacionados desde sua geração até sua incorporação. Ofiolitos são amplamente estudados em orógenos Paleozóicos-Mesozóicos nos Himalaias, Europa, América do Norte, Ásia (do Neoproterozóico ao Mesozóico) e Andes (do Paleozóico ao Recente). Nos orógenos Neoproterozóicos, estudos têm sido realizados principalmente no Cinturão Pan-Africano, também Cadomiano e Brasiliano, com poucos registros no sul da China e pobremente documentados no sul da Índia (Figura 2, Tabela 2). Os cinturões orogênicos paleozóicos-mesozóicos são caracterizados por evolução orogênica em processo prolongado de abertura e fechamento de oceanos. Durante processo evolutivo envolveram acumulação de arcos de ilhas, ofiolitos, subducção, acresção e colisão representando diferentes tipos (ex.: rifte, MORB, ZSS - Tabela 2) e história tectônica que demonstram uma evolução do ciclo de Wilson (Dewey & Kidd, 1974; Dilek et al., 1990; Khain et al., 2002; Kovalenko et al., 2004; Ramos et al., 2000; Pushkov, 2009; Kroner & Romer, 2013).

Nos orógenos neoproterozóicos, a orogenia Pan-Africana (~750–650 Ma, Ali et al., 2010) contém rochas remascentes de ofiolitos (870-690 Ma, Stern et al., 2004). São conhecidos numerosos ofiolitos e fragmentos ofiolíticos no nordeste da África, em particular ao longo do escudo Árabe-Nubiano. Foram propostos vários cenários tectono-magmáticos para esses ofiolitos, incluindo bacias de *backarc*, *forearc*, ZSS e MORB (Abd El-Rahman et al., 2009; Stern et al., 2004). Ofiolitos no escudo Árabe-Nubiano têm sido datados em zircões de plagiogranitos e gabros. Por exemplo, no NW-central da Arábia o ofiolito Thurwah (Sutura Bir Umq) de idade 870 Ma, no NW da Arábia, o ofiolito Jabal Ess (sutura Yanbu) de idade 780 Ma e no NW da Àfrica o ofiolito Tasriwine de idade 762 Ma (Figura 2, Tabela 2) marcam a orogenia Pan-Africana. A orogenia Cadomiana no SE europeu (cinturão alpino-mediterrâneo) é contemporânea à Pan-Africana (750-520 Ma) representando estágios finais e também contém ofiolitos (Neubauer, 2002; Kounov et al., 2012; Garfunkel, 2015).

O Orógeno Brasiliano é comparável em extensão e tempo (950-500 Ma) ao Orógeno Pan-Africano (Stern et al., 2004) e representa o mais expressivo e importante conjunto de eventos tectônico-magmáticos de formação de unidades litológicas supracrustais ocorrido na América do Sul. Os ofiolitos no Brasil representam restos de crosta oceânica Neoproterozóica contidos nos Cinturões Dom Feliciano (sul do Brasil e Uruguai), Ribeira e Araçuaí. Seus homólogos africanos incluem os Cinturões Gariep, Damara, Congo e Kaoko (Goscombe et al., 2005; Basei et al., 2005, 2008; Philipp et al., 2016 e referências neles contidas). Alguns estudos geocronológicos em rochas máficas-ultramáficas foram realizados em ofiolitos e possíveis corpos de ofiolitos (Figura 1, Tabela 1) porém são poucos os dados de idade e ambiente de formação de ofiolitos no Orógeno Brasiliano. Muitos estudos têm sido realizados em rochas sin-pós colisionais, mas carecem estudos geocronológicos robustos nas rochas pré-colisionais relacionadas aos processos de abertura e colisões de crátons.

Os ofiolitos no Escudo Sul-Riograndense estão contidos no terreno São Gabriel e Grupo Porongos. A nomenclatura de terreno Tijucas é substuída pela caracterização como cinturão de dobramento e cavalgamento (Pertille et al., 2017). O escudo está inserido na porção sul da Província Mantiqueira (Figura 1) (Almeida et al., 1981), que corresponde ao sistema brasiliano sudeste estendendo-se do sul da Bahia até o Uruguai. O Cinturão Dom Feliciano é a extensão sul do Orógeno Brasiliano Neoproterozóico e é formado pelo terreno São Gabriel, Cinturão Porongos, Batólito Pelotas-Aiguá e associações de antepaís (Bacia do Camaquã) com rochas Arqueanas e Paleoproterozóicas do embasamento intercaladas (Remus et al., 1999; Chemale Jr., 2000; Paim et al., 2000; Philipp et al., 2002; Basei et al., 2008, 2011; Hartmann et al., 2008; Pertille et al., 2017). Os ofiolitos contêm serpentinitos e metassomatitos e estão associados com rochas vulcano-sedimentares e granitóides contidos no embasamento formados por rochas Arqueanas-Paleoproterozóicas que constituem o Cráton Rio de la Plata (Figura 3). Revisão do cráton foi feita por Santos et al. (2017).

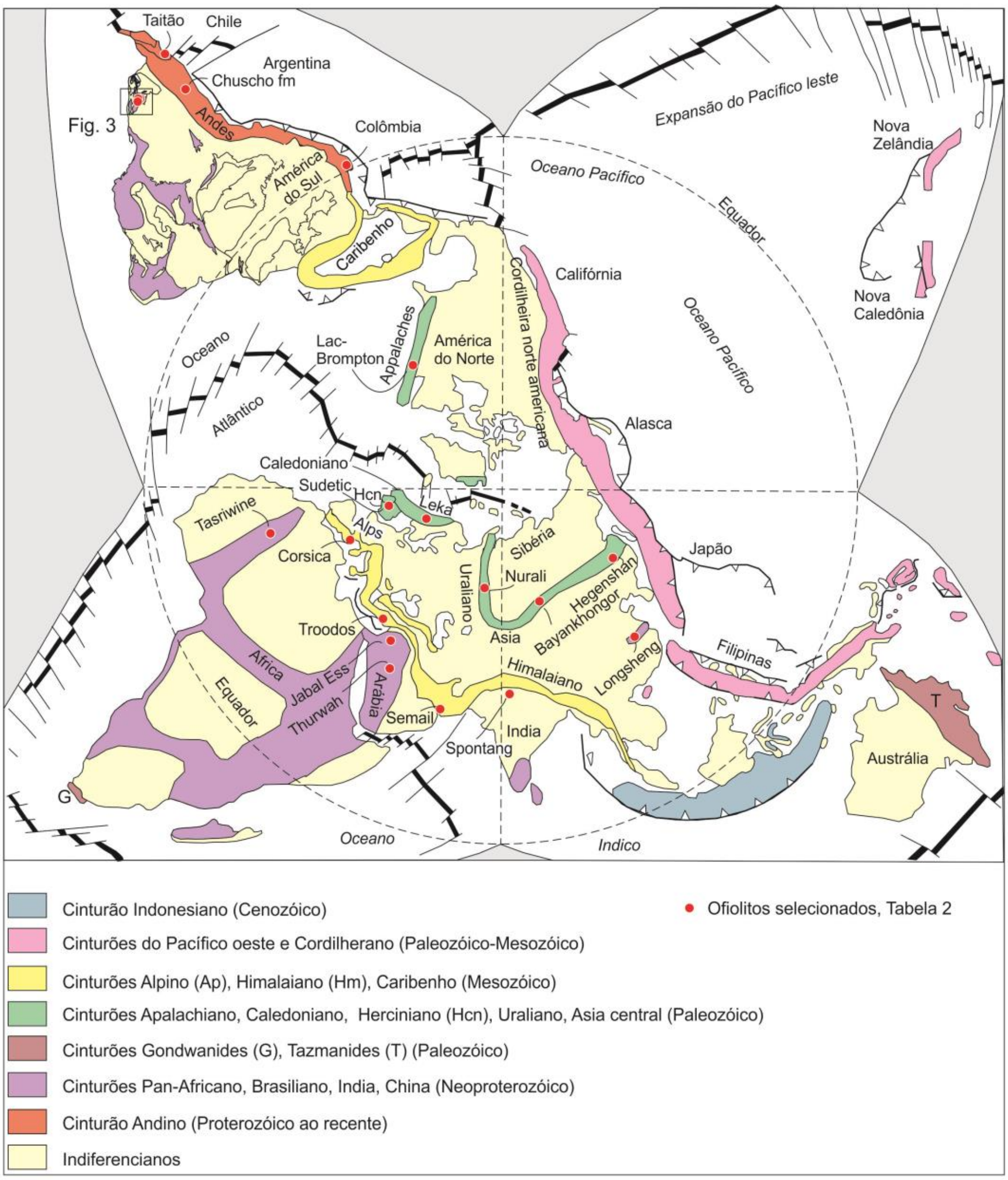

Figura 2. Distribuição global dos cinturões orogênicos e ofiolitos selecionados (Dilek, 2003b; Furnes et al., 2014).

1.6 Contexto geológico dos ofiolitos estudados

O terreno São Gabriel situa-se ao norte do terreno Taquarembó, ambos limitados ao norte e a oeste com a província vulcânica Paraná e separados pelo lineamento de Ibaré. O limite a leste é com os granitos e metamorfitos de Caçapava do Sul separados, pelo lineamento de Caçapava. O terreno é juvenil de idade Neoproterozóica (ver tabela 1 do artigo 1) formado pelas rochas do Gnaisses Cambaí, Granitóides Imbicuí, rochas do Supercomplexo Vacacaí (Chemale Jr., 2000), ofiolitos e granitos pós-colisionais. Os Gnaisses Cambaí (Leite, 1997) são constituídos por associações TTG de ambiente de arco de ilha; os Granitos Imbicuí sinorogênicos correspondem à Suíte Lagoa da Meia Lua e Suíte Sanga do Jobim (Saalmann et al., 2010; Hartmann et al., 2011).

Tabela 2. Aspectos selecionados de ofiolitos dos cinturões orogênicos.

Ofiolitos	Cinturão orogênico	Localização	Idade (Ma)	Litologia	Ambiente tectônico
Taitão	Andino	Chile Sul	≤10[1]	Basalto	MORB, ZSS
Amaime	Andino	Colômbia	125[2]	Basalto	ZSS
Chuscho fm	Andino	Argentina	454[3]	Basalto	Rifte, MORB
Troodos	Himalaiano	Chipre	92[4]	Basalto, gabro, harzburgito, dunito	ZSS, início de subducção
Semail	Himalaiano	Oman	96-94[5]	Gabro, tonalito, trondhjemito	MORB, ZSS
Spontang	Himalaiano	Índia	177-65[6]	Basalto, gabro, plagiogranito, vulcano-sedim.	MORB
Corsica	Alpino	Corsica	160[7]	Basalto, plagiogranito	Rift inicial, MORB
Sudetic	Herciniano	SW Polônia	420-400[8]	Gabro, rodingito	MORB, ZSS
Bayankhongor	Ásia Central	Mongólia	655-636[9]	Rodingito,gabro, anortosito, plagiogranito	MORB
Hegenshan	Ásia Central	China	400-350[10]	Basalto, gabro, serpentinito	Arco de ilha de bacia marginal
			354-333[11] 142-125[11]	Lherzolito, harzburgito	Ascenção de manto, amb. subcontinental
Nurali	Uraliano	Rússia	483-468[12]	Basalto, gabro, peridotito	Arco Intraoceânico ou marg. continental
Lac-Brompton	Appalachiano	Canadá (Quebec)	480[13]	Gabro, boninito, harsburgito, peridotito	Bacia de ante-arco
Leka	Caledoniano	Noruega	497[14]	Basalto, gabro, plagiogranito, peridotito	Intraoceânico, subducção
Tasriwine	Pan-Africano	NW África	762[15]	Plagiogranito	ZSS
Jabal Ess	Pan-Africano	NW Arábia	780[16]	Gabro	Retroarco
Thurwah	Pan-Africano	NW-C Arábia	870[16]	Gabro	Intra-arco
Longsheng	Jiangnan	SE China	869-867[17]	Gabro, diabásio	MORB

(1) = Le Moigne et al. (1996), Guivel et al. (1999), Lagabrielle et al. (2000), (2) = Aspden et al. (1987); (3) = Fauqué & Villar (2003); (4) = Rautenschlein et al. (1985), Pearce & Robinson et al. (2010); (5) = Rioux et al. (2013); (6) = Pedersen et al. (2010), Corfield et al. (2001); (7) = Saccani et al. (2008); (8) = Oliver et al. (1993), Dubińska et al. (2004); (9) = Jian et al. (2010); (10) = Robinson et al. (1999); (11) = Jian et al. (2012); (12) = Gaggero et al. (1997); (13) = De Souza et al. (2008); (14) = Furnes et al. (1988), Furnes et al. (1992); (15) = Samson et al. (2004); (16) = Pallister et al. (1988); (17) = Yao et al. (2016). (amb) = ambiente; (marg) = margem; (ZSS) = zona de suprasubducção.

O Supercomplexo Vacacaí é formado pelos Complexos Passo Feio (Bitencourt, 1983; Remus et al., 2000), Cambaizinho (Remus, 1990; Lena et al., 2014) Bossoroca-Palma (Chemale Jr., 1982; Zarpelon, 1986; Saalmann et al., 2005a, b; Gubert et al., 2016; Vedana et al., 2017) e Ibaré (Nauman, 1985). O Vacacaí inclui rochas máficas-ultramáficas com xistos magnesiano e serpentinito; rochas metasedimentares, metagabro, anifibolito e lentes de mármores; rochas vulcanoclásticas ácidas a básicas e chert (Chemale Jr., 2000). As associações de rochas máficas-ultramáficas representam lascas de ofiolitos.

O ofiolito Cerro Mantiqueiras está localizado 15 km a SW da cidade de Lavras do Sul, distando 330 km de Porto Alegre. As rochas máficas-ultramáficas estão contidas nos Gnaisses Cambaí e Granitóides Imbicuí, em associação com a Formação Maricá (Bacia do Camaquã) e o Granito Lavras (Leite, 1997). O ofiolito Cerro Mantiqueiras (Jost & Hartmann, 1984) está representado por um corpo ultramáfico metamorfizado e deformado, encaixado em gnaisses graníticos de fácies anfibolito. Possui uma associação de harzburgitos, serpentinitos, xistos magnesianos miloníticos e anfibolitos estruturados ao longo de um cinturão aproximadamente E-W com pelo menos 9 km de comprimento e 0,1 a 1,0 km de largura. Os xistos magnesianos estão concentrados principalmente nas bordas e são em grande proporção monominerálicos, caracterizando metassomatismo (Leite, 1997; Hartmann & Chemale Jr., 2003). O ofiolito compreende três unidades: ultramáfica, vulcânica máfica e xisto magnesiano.

A unidade ultramáfica ocorre como lentes alongadas E-W que ocupam principalmente as partes mais internas do ofiolito. No lado leste e no extremo oeste a unidade aflora como pods pequenos e delgados, alongados e elípticos envolta pela unidade xisto milonítico que por sua vez é circundada pela unidade vulcânica máfica. A unidade vulcânica máfica aflora principalmente na porção leste do ofiolito, como corpos descontínuos. A unidade de xisto magnesiano ocorre predominantemente ao longo da extremidade norte do ofiolito com exposições menores no lado leste e oeste onde englobam pequenos pods harzburgíticos. Os contatos entre as unidades ultramáfica e xisto magnesiano são de caráter transicional. Os harzburgitos da unidade ultramáfica são progressivamente transformados em xisto magnesiano. Essa transformação é vista em nível de afloramentos pelo desaparecimento de porfiroclastos de olivina e ortopiroxênio em tremolitito. Já o contato entre a unidade ultramáfica e a unidade vulcânica máfica, embora geralmente encoberto, parece ser abrupto (Leite, 1997).

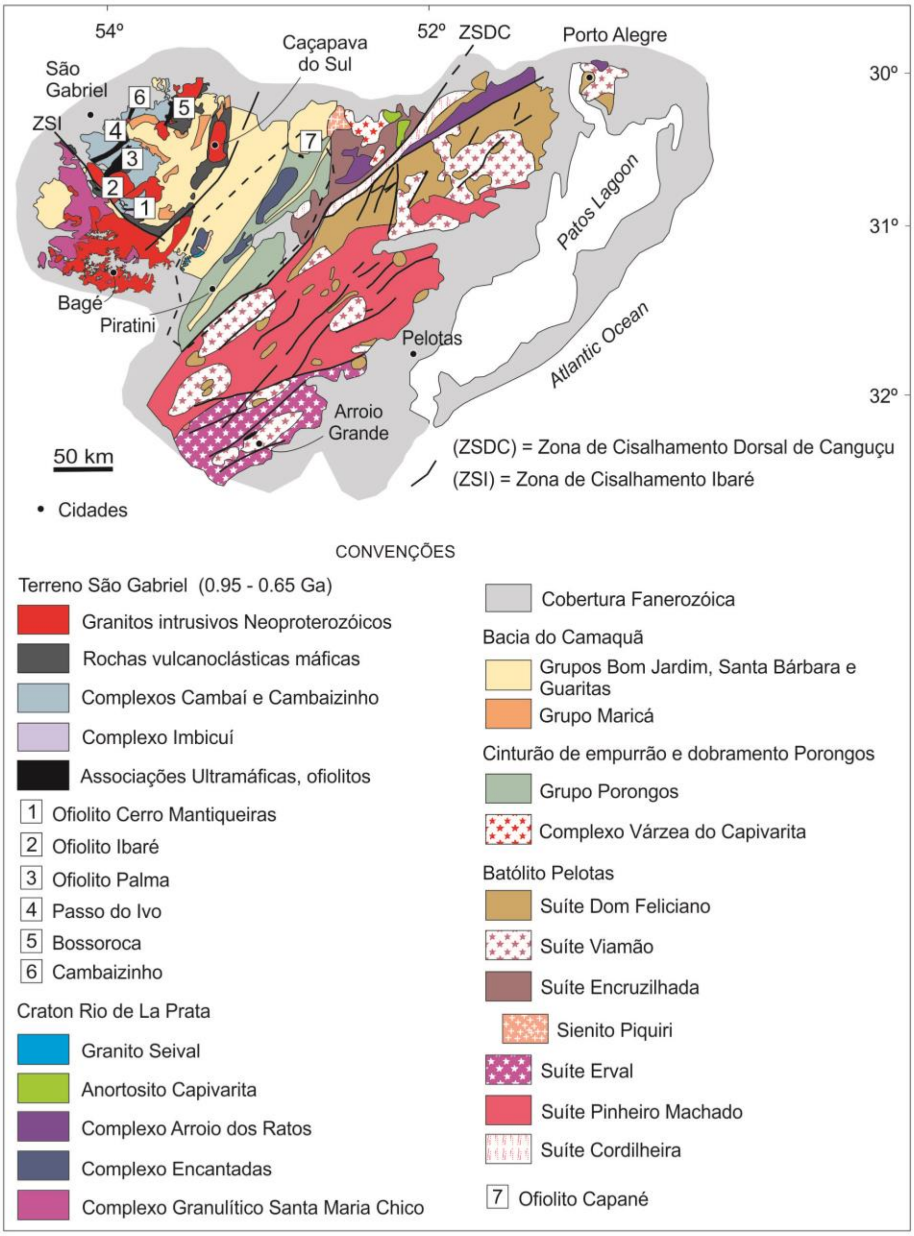

Figura 3. Mapa geológico do Cinturão Dom Feliciano com a localização dos ofiolitos e embasamento (Chemale Jr., 2000; Philipp et al., 2002; Hartmann et al., 2007; Laux et al., 2012; Camozzato et al., 2014; Pertille et al., 2017).

O ofiolito inclui harzburgitos, serpentinitos, cromititos e raro albitito. Os serpentinitos ocorrem associados com harzburgitos, como corpo serpentinítico fino e foliado, estreito e anastomosado e como massas difusas muito finas ao longo de várias ocorrências de harzburgitos. Cromititos (Leite, 1997) formam camadas maciças, pretas de até 3 cm x 20 cm, descontínuas e como bandas disseminadas e inclusos em ortopiroxênio. Os albititos (estudados nessa tese) tem ocorrência mais restrita, como pequenos blocos de até 50 cm; apresentam cor branca e também estão imersos no serpentinito.

O ofiolito Ibaré foi inicialmente caracterizado por duas unidades ultramáficas separadas geograficamente (Naumann, 1985) e constituídas por serpentinitos, xistos magnesianos e intercalações de rochas vulcanoclásticas. Imersos no corpo de serpentinito, afloram cloritito, rodingito e turmalinito, como evidência de intenso metassomatismo e também albitito. Seguindo o critério de distinção de ocorrências ultrabásicas ou ultramáficas, Naumann (1985) propôs a subdivisão do Complexo Ibaré em duas unidades definidas como Sequência Bela Vista (rochas metavulcano-sedimentares) e Sequência Corticeira (rochas ultramáficas). A unidade Corticeira engloba ocorrências com predomínio de rochas ultramáficas posicionadas próximo ao contato com o Monzogranito Santa Rita. As rochas ultramáficas dessa unidade são presentemente caracterizadas como ofiolito Ibaré (artigo 2). O ofiolito Ibaré apresenta aproximadamente 1000 m de área em direção aproximada leste-oeste. O ofiolito caracteriza-se pela intercalação de bandas e “boudins” de rodingitos, cloritito, turmalinito, xisto magnesiano e albitito subordinado a um corpo maior constituído por serpentinito. A presença de turmalinito restringe-se ao extremo noroeste do ofiolito. O limite sul-sudeste é definido por contatos com rochas vulcanoclásticas da unidade Bela Vista. Ao norte limita com o Granito Santa Rita e a sudoeste com o Granito Jaguarí. De oeste para sudeste ocorre o recobrimento local do ofiolito por sedimentos da Formação Rio Bonito (Naumann, 1985) e a leste-sudeste ocorrem rochas do embasamento.

O ofiolito Palma, localizado na borda oeste do Escudo Sul-Riograndense nas cabeceiras do Rio Vacacaí, estende-se desde 5 km ao sul da Vila Palma até aproximadamente 20 km para nordeste, com estrutura e alinhamento nordeste. É formado por rocha meta-sedimentar, meta-ígnea vulcânica ácida-intermediária, básica e rocha ultramáfica metamorfizada que ocorrem em toda sua extensão (Garcia & Hartmann, 1981). Szubert et al. (1977) consideraram todo o conjunto como uma mélange com imbricações tectônicas, devido ao seu alto grau de deformação que coloca rochas com afinidades diferentes justapostas lado a lado, na forma de pequenos corpos alongados. A região da Palma (Garcia, 1980; Chemale Jr., 1982) foi descrita como uma associação máfica-ultramáfica com peridotitos, serpentinitos e xistos magnesianos, em meio a rochas metasedimentares e metavulcânicas básicas e ácidas. Chemale Jr. (1982) dividiu o Complexo Palma em duas sequências: (1) Cerro da Cruz constituída por metaultramafitos, metabasitos, metapelitos e quartzitos, metavulcânicas de composição ácida e intermediária, mármores e rochas cálcio-silicáticas, (2) Pontas do Salso, constituída por rochas cálciosilicáticas e por sedimentos pelíticos e arcoseanos metamorfizados na fácies anfibolito. As rochas metaígneas constituem granitos, metadacitos, metandesitos, metabasaltos, metagabros, metaultrabásicas e lamprófiros (Garcia, 1980; Chemale Jr., 1982).

O ofiolito Palma está limitado por rochas gnáissicas e graníticas Cambaí e Imbicuí nas bordas oeste e norte, ao leste pelas rochas vulcano-sedimentares do Complexo Palma (Pontas do Salso - Vedana et al., 2017) e ao sul faz contato com o Granito Jaguari. Os afloramentos de rocha raramente são contínuos, sendo geralmente encobertos com camadas de solo com vegetação rasteira o que dificulta a observação de suas relações. A variação litológica lateral é bastante grande, em poucos metros podem-se observar mais de dois tipos de litologias distintas. Apesar da proximidade dos ofiolitos Ibaré e Palma, Garcia & Hartmann (1981) preferiram uma designação individual para as ocorrências principalmente em função da descontinuidade espacial.

À leste do terreno São Gabriel estão situados o Grupo Porongos e o Batólito Pelotas (680-550 Ma). O ofiolito Capané está localizado na região da Antiforme Capané e ocorre imbricado no Grupo Porongos (parte do cinturão de empurrão e cavalgamento Porongos). O Cinturão Porongos compreende (Pertille et al., 2015a; 2017) fragmentos das rochas do Batólito Pelotas (rochas graníticas relacionadas aos estágios colisionais e pós-colisionais do Ciclo Brasiliano); o Grupo Porongos (rochas metassimentares: metapelito, xisto e lente fina de quartzito); rochas metavulcânicas intermediária-félsicas, subordinados mármore, metaconglomerado, lentes de quartzito e rochas ultramáficas, serpentinitos e xistos magnesianos (Jost & Bitencourt, 1980; Porcher & Fernandes, 1990; Remus et al., 1991; Marques et al., 2003; Gollmann et al., 2008) cujo grau de metamorfismo varia de facies xistos verdes a anfibolito médio (Jost & Bitencourt, 1980; Porcher & Fernandes, 1990; Remus et al., 1991; Marques et al.,1998; 2003) e a Bacia do Camaquã, considerada uma bacia tipo molassa (Paim et al., 2000). A sequência supracrustal do Cinturão Porongos sobrepõe o embasamento pré-Brasiliano (Encantadas) incluindo quartzitos da Formação Santana (Hartmann et al., 2004; Pertille et al., 2015b). Dobras em escala regional do Cinturão Porongos geraram as quatro antiformes (Jost e Bitencourt, 1980) nomeados de norte para sul, Capané (10 × 20 km), Serra dos Pedrosa (5 × 30 km), Santana da Boa Vista (7 × 20 km), e Godinho (3 × 4 km). A antiforme Capané está localizada na parte norte do Grupo Porongos e é composta por xisto detrítico com lentes de serpentinito, xisto magnesiano, cloritito, rodingito (estudado nessa tese) e cromitito podiforme (Jost & Hartmann 1979; Marques et al., 2003).

Alguns modelos evolutivos foram sugeridos para o Cinturão Dom Feliciano, formado durante o Neoproterozóico-Paleozóico devido à aglutinação dos crátons

Kalahari e Rio de la Plata (Fernandes et al., 1992; Chemale et al., 1995; Basei et al., 2005). No terreno São Gabriel, Leite (1997) sugeriu uma evolução a partir de formação de dois arcos sucessivos, devido às idades com diferença de 150 Ma entre os granitóides ao norte do ofiolito Cerro Mantiqueiras (Evento São Gabriel = 750-700Ma) e os dioritos ao sul (Evento Passinho = 906-860 Ma). O ofiolito Cerro Mantiqueiras seria parte da sutura entre os dois arcos com possível incorporação entre 850 e 750 Ma.

Chemale Jr. (2000) sugeriu para as rochas do Complexo Palma origem de prisma acrescionário com ofiolitos, rochas de arco de margem passiva ou de *backarc* e dividiu a evolução do Cinturão Dom Feliciano em quatro fases. Uma primeira fase entre 900-800 Ma teria formado o oceano Charrua com o arco intra-oceânico Passinho e uma zona de fraqueza intraplaca (pluma mantélica na região dos cinturões Gariep e Damara) no cráton Kalahari; a segunda fase entre 800-700 Ma em uma configuração de margem ativa convergente a oeste (acresção Palma sob microcontinente Encantadas, formado na zona de fraqueza da primeira fase) e outra divergente a leste (rifte da bacia Gariep com formação de oceano em ~700 Ma); a terceira fase entre 700-650 Ma com o aumento do sistema *backarc* Gariep teve a geração do oceano Adamastor, cujo registro de rifteamento está documentado em sequências vulcânica-plutônicas de idade 750 Ma nos Cinturões Gariep e Damara; a fase quatro entre 650-540 Ma, o proto-oceano Adamastor teria iniciado processo de subducção com mergulho para oeste e subducção da placa Kalahari sob a microplaca Encantadas com formação do arco magmático Dom feliciano com a granitogênese do Batólito Pelotas entre 650-550 Ma. E o fechamento do oceano por processo transpressivo com deformações de empurrões e transcorrentes entre 650-540 Ma e os últimos episódios deformacionais relacionados à intrusão dos granitos sintranscorrentes (ex.: Granito Capané e Granito Caçapava) além das zonas de cisalhamento tardias.

Nos Complexos Palma e Bossoroca, Saalmann et al. (2005a) sugeriram uma relação estratigráfica entre as rochas máficas-ultramáficas e vulcano-sedimentares devido à semelhança geoquímica isotópica entre as rochas ultramáficas de ambos. Os autores consideraram as rochas máficas-ultramáficas como sendo a base e as rochas vulcano-sedimentares o topo de uma mesma sequência, que foram denominados Formações Campestre (topo) e Cerro do Ouro (base). Rochas máficas-ultramáficas incluindo um anfibolito e um clorita xisto do Complexo Bossoroca apresentaram idade modelo Nd entre 1188-850 Ma e εNd(t) de +5,66 a +2,53. Dois gnaisses tonalíticos foram analisados, um na região da Palma com idade modelo Nd

= 894 Ma e εNd(750)= +4,3 e outro na região da Sanga do Jobim com idade modelo Nd = 723 Ma e εNd(700)= +6,3 ambos dos Gnaisses Cambaí. Três filitos foram analisados, um na região da Palma e dois na região da Bossoroca com idades modelo entre Nd = 904-770 Ma e εNd(700) de +6,3 a +4,7. Baseados na similaridade Sm-Nd, Saalmann et al. (2005a) sugeriram correlação genética entre as rochas vulcânicas da Formação Campestre e as rochas intrusivas dos Gnaisses Cambaí. Segundo os autores, as rochas cálcioalcalinas do Cambaí (Chemale et al., 1995; Babinski et al., 1996; Leite et al., 1998; Hartmann et al., 2000) e sua contraparte vulcânica (Formação Campestre) teriam formado em um ambiente de zona de subducção.

Saalmann et al. (2005a) sugeriram a evolução em três fases. A primeira fase de 900-800 Ma com a formação do arco intra-oceânico Passinho (Leite et al., 1998) devido à subducção para leste com subsequente subducção (segunda fase) entre 850-700 Ma para oeste subductando sob a recém-formada margem continental ativa (Cráton Rio de la Plata + arco Passinho). Segundo os autores, partes das rochas do grupo Palma inferior (Cerro do Ouro) de fonte juvenil de 0,75-1,0 Ga e assinatura isotópica Sm-Nd citados acima são devido à deposição em região de *forearc*. O vulcanismo da Formação Campestre representa as partes vulcânicas do arco magmático Cambaí e as rochas vulcanoclásticas e metassedimentares depositadas em uma região de *backarc* com maior entrada de partes expostas do arco. Na terceira e fase final sugerida em ~700 Ma, ocorreu a colisão de Cráton Rio de la Plata com a margem passiva Porongos-Encantadas.

No Complexo Cambaizinho, Lena et al. (2014) estudaram zircões detríticos com idades U-Pb e asinatura isotópica de ^{18}O. A partir de três grupos de idades distintos, os autores consideraram uma evolução progressiva para o terreno São Gabriel. As idades entre 840-750 Ma e ^{18}O = 3,2 e 5,5 ‰ foram interpretadas como origem mantélica com alguma alteração hidrotermal de fonte crustal e relacionadas com o arco intra-oceânico Passinho (879 Ma). Seguido pelo desenvolvimento de uma margem convergente continental em 750-690 Ma na borda leste do Cráton Rio de la Plata, fornecendo sedimentos com zircões que exibem assinatura isotópica predominantemente continental. O período final na evolução do terreno entre 690-650 Ma representa acresção final dos sistemas de arcos ao Cráton Rio de la Plata.

No Cinturão Porongos foi proposto modelo de deposição em ambiente de retroarco (Fernandes et al., 1992, 1995a, b). Devido à presença de serpentinitos associados com rochas vulcânicas básicas, Marques et al. (1998, 2003) e Gollmann et al. (2008) propuseram que a região do Capané foi originada em ambiente de retroarco sendo as rochas máficas-ultramáficas parte basal de um ofiolito. Saalmann et al. (2006) propuseram três possíveis origens para o Cinturão Porongos: (1) em bacia de *backarc* ensiálica a oeste do Cinturão Dom Feliciano, assumido como arco magmático; (2) em uma bacia de *backarc* ensiálica a leste do arco magmático localizado no bloco São Gabriel; ou (3) em uma configuração de rifte associada a um ambiente de margem passiva.

Rochas com idade entre 802-767 Ma e afinidade de arco magmático continental foram registradas no leste do Cinturão Dom Feliciano, na região de Piratini, xenólitos máficos (Gnaisses Piratini), na região de Porto Alegre (Ortognaisse Chácara das Pedras), no Complexo Várzea do Capivarita (ortognaisse) e no Uruguai na região de Rocha (ortognaisse Cerro Bori) (Silva et al., 2005; Koester et al., 2016; Lenz et al., 2013; Martil et al., 2017). Algumas idades de cristalização em torno de 780 Ma foram obtidas no Porongos. Chemale Jr. (2000) obteve idade de 773 ±8 em um meta-andesito na Antiforme do Godinho. Porém as rochas vulcânicas e vulcanoclásticas do Grupo Porongos apresentaram valores εNd de -9,6 a -12,5 com idade modelo Nd entre 2,2 a 2,0 Ga e os autores sugeriram retrabalhamento crustal para idades de 780-770 Ma. Idade de 783 ±6 Ma (Porcher et al., 1999) em metariolito da Antiforme Capané e idade semelhante de 789 ±7 Ma (Saalmann et al., 2011) foi obtida em metariolito na Antiforme Serra dos Pedrosa. Basei et al. (2000) sugeriram a idade de 780 Ma como clímax metamórfico que levou à anatexia de nível sedimentar profundo resultando no vulcanismo. Como em campo, as rochas metavulcânicas são intercaladas com a rochas metassedimentares Saalmann et al. (2011) sugeriram para as idades de cristalização de ~780 Ma que a deposição e o magmatismo seriam contemporâneos no Grupo Porongos.

Análise Sm-Nd rocha total em rochas metavulcânicas mostraram εNd = -21,7 a -6,8 e em metassedimentares εNd = -17,9 a -6,2 e idade modelo Nd entre 1734 e 2710 Ma (Saalmann et al., 2006), sugerindo origem crustal. Na antiforme Capané, Sm-Nd rocha total em rochas metavulcânicas demostraram idade modelo Nd entre 2,59 e 0,9 Ga com εNd entre -22,3 e -1,5 (Gollmann et al., 2008). Adicionalmente, estudos recentes de Pertille et al. (2015a, b, 2017) demonstraram que o Porongos foi derivado de fontes misturadas (3200-550 Ma) incluindo riodacito com idades entre 773-809 Ma, idade modelo Hf de 2,5-1,3 Ga, assinatura εHf = -34 a -4 e $\delta^{18}O \geq 5,3$ ‰, característicos de magma crustal. Idades entre 2200-620 Ma também foram obtidas por Basei et al. (2008). A idade máxima de deposição da paleobacia Porongos foi estabelecida em 650-570 Ma (Pertille et al. 2015a). Os autores interpretaram que a evolução do Escudo Sul-Riograndense incluiu a formação de uma cadeia de montanhas (Batólito Pelotas) que causou subsidência flexural na bacia e em consequência seu preenchimento e deformação. Uma tríade orogênica sugerida com o Batólito Pelotas, o Cinturão Porongos e Bacia do Camaquã de evolução contemporânea (650-550 Ma). Mais recentemente, Silveira (2017) sugeriu uma divisão para o Porongos em duas sequências. Sequência Porongos I inclui rochas do Arqueano ao Toniano, sendo a idade do vulcanismo riolítico considerada a máxima deposicional com deposição em uma bacia de margem do Encantadas (750-700 Ma). A Sequência Porongos II inclui as unidades mais jovens pertencentes a uma bacia distinta relacionada à deposição sin-orogênica no Ediacarano.

Embora existam registros bem preservados de paleoceano(s) no terreno São Gabriel e no Grupo Porongos, ainda falta estudos sobre sua extensão, idade e relações das rochas com as encaixantes.

1.7 Análise Integradora

A dificuldade de datar ofiolitos foi superada pelo encontro de zircões em albititos, cloritos, turmalinito e rodingito *blackwall*, e também turmalinito, imersos em serpentinitos originados na litosfera/crosta oceânica. A caracterização isotópica e química de minerais e rochas possibilitou a classificação como litosfera oceânica. Os ofiolitos estão associados com rochas vulcano-sedimentares de arcos intra-oceânicos, continental, granitóides e rochas do embasamento que constituem o Cráton Rio de la Plata.

Este trabalho apresenta estudo de integração combinada de isótopos U-Pb-Hf e elementos-traço em zircão, geoquímica de rocha total e geoquímica elemental de clorita, elemental e isotópica de boro em turmalina. Os resultados levaram à datação direta de rocha oceânica e do processo de alteração do serpentinito na crosta oceânica e sua colocação no Escudo Sul-Riograndense.

Foram obtidos isótopos de U-Pb-Hf e elementos-traço em zircão no albitito do ofiolito Cerro Mantiqueiras, no cloritito do ofiolito Palma, no albitito, cloritito e turmalinito do ofiolito Ibaré, no Granito Santa Rita e em uma rocha vulcanoclástica de Ibaré e no rodingito *blackwall* do ofiolito Capané. Química de rocha total foram realizadas no anfibolito do Cerro Mantiqueiras, em rochas vulcanoclásticas de Ibaré e de um serpentinito e rodingito *blackwall* do ofiolito Capané para contribuir na interpretação do ambiente geotectônico desses ofiolitos. Análises química e isotópica de boro em turmalinas do turmalinito de Ibaré reforçaram o ambiente de formação do ofiolito.

No ofiolito Cerro Mantiqueiras, são conhecidas as idades dos Gnaisses Cambaí, granitóides Imbicuí e do anfibolito. O anfibolito tem granulometria média-grossa com porções mais ricas em anfibólios e outras mais ricas em feldspatos (o que reflete maior enriquecimento em SiO_2 em análise química, por exemplo amostra CM21 (ver apêndice P do artigo 2). O anfibolito foi datado em 733 ±10 Ma com idade metamórfica de ~700 Ma por Leite et al. (1998). Na presente tese, em estudos de albitito (artigo 1) foram obtidas idade magmática U-Pb = 923 ±3 Ma para núcleo de zircões e idade metamórfica de 786 ±13 Ma para bordas e εHf(t) = +13 e +8. A idade mais jovem do ofiolito Cerro Mantiqueiras é de 786 ±13 Ma (Figura 4), idade metamórfica do albitito oceânico (923 Ma) e interpretada como metamorfismo ocorrido possivelmente durante a acresção no continente (artigo 1).

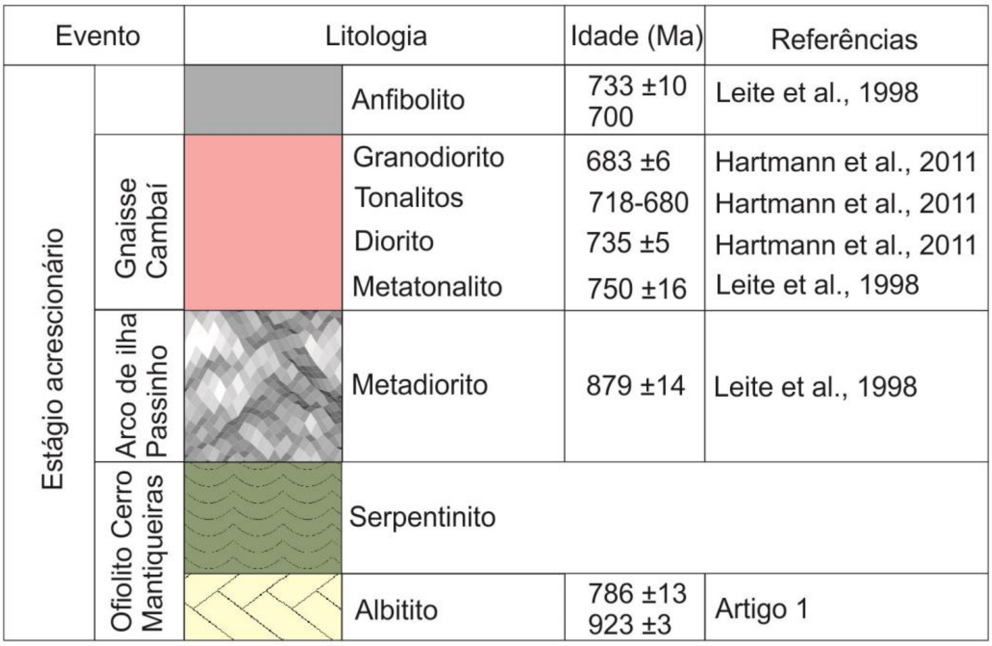

Evento		Litologia	Idade (Ma)	Referências
Estágio acrescionário		Anfibolito	733 ±10 700	Leite et al., 1998
	Gnaisse Cambaí	Granodiorito	683 ±6	Hartmann et al., 2011
		Tonalitos	718-680	Hartmann et al., 2011
		Diorito	735 ±5	Hartmann et al., 2011
		Metatonalito	750 ±16	Leite et al., 1998
	Arco de ilha Passinho	Metadiorito	879 ±14	Leite et al., 1998
	Ofiolito Cerro Mantiqueiras	Serpentinito		
		Albitito	786 ±13 923 ±3	Artigo 1

Figura 4. Principais eventos tectônicos associados ao ofiolito Cerro Mantiqueras.

O evento metamórfico de idade ~700 Ma registrado no anfibolito não foi reconhecido nos zircões do albitito. A textura recristalizada do albitito pode ter sido causadas por outros eventos metamórficos entre 786-700 Ma pois os zircões não registram tal baixa temperatura de recristalização tardia. Análises químicas de rocha total do anfibolito classificou-o como formado em ambiente de subducção (artigo 2). Rochas ígneas dos Gnaisses Cambaí (750-680 Ma) e do anfibolito (733-700 Ma) são mais jovens do que o ofiolito Cerro Mantiqueiras (923-786 Ma). O ofiolito foi obductado no arco Passinho (879 ±14 Ma; Leite et al., 1998), sugerindo que a região formou em um processo prolongado de geração de ofiolitos, arcos de ilhas, colocação e zona de subducção.

Nas unidades relacionadas aos ofiolitos Ibaré e Palma, algumas idades já são conhecidas (Figura 5). No arco São Gabriel, idades U-Pb em zircão são conhecidas na Bossoroca (Machado et al., 1990; Remus et al., 1999; Gubert et al., 2016). Também tem a idade modelo Nd, citada acima, do anfibolito na Bossoroca (Saalmann et al., 2005a), assim como a idade do Granito Jaguari (Gastal et al., 2015). Nas rochas máficas-ultramáficas da Palma, idades modelo Sm-Nd rocha total foram estabelecidas em 1350-650 Ma para xisto magnesiano e serpentinito (Saalmann et al., 2005a) mas a idade dos ofiolitos permanecia desconhecida.

Os resultados sugerem que os ofiolitos Ibaré e Palma são parte da mesma sutura. Os ofiolitos também formaram na cadeia oceânica conforme registro de albitito (892 ±3 Ma; artigo 1), cloritito e turmalinito (880 ±12 Ma; artigo 2). Nos zircões de idades entre 780-722 Ma, a heterogeneidade da razão $^{176}Hf/^{177}Hf$ e εHf entre +12,1 e +1,4 sugere que alguns domínios de zircões foram ligeiramente contaminados por componente crustal. Essa contaminação pode estar relacionada a crosta antiga ou manto litosférico contaminados no MORB. Dados isotópicos de boro em turmalinas do turmalinito de Ibaré mostram assinatura $\delta^{11}B$ = +3,5 a +5,2‰ indicando que ele formou em uma crosta oceânica, mas não fresca e sim alterada (artigo 4) sem interferência de zona de subducção.

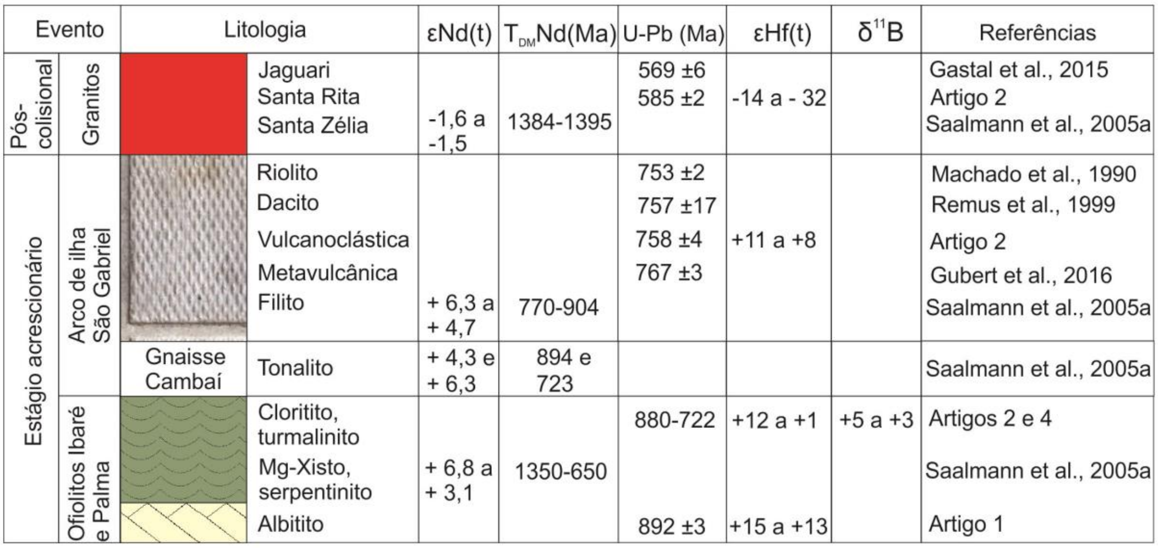

Evento		Litologia		εNd(t)	T_{DM}Nd(Ma)	U-Pb (Ma)	εHf(t)	$\delta^{11}B$	Referências
Pós-colisional	Granitos	🟥	Jaguari Santa Rita Santa Zélia	-1,6 a -1,5	1384-1395	569 ±6 585 ±2	-14 a - 32		Gastal et al., 2015 Artigo 2 Saalmann et al., 2005a
Estágio acrescionário	Arco de ilha São Gabriel	▨	Riolito Dacito Vulcanoclástica Metavulcânica Filito	+ 6,3 a + 4,7	770-904	753 ±2 757 ±17 758 ±4 767 ±3	+11 a +8		Machado et al., 1990 Remus et al., 1999 Artigo 2 Gubert et al., 2016 Saalmann et al., 2005a
		Gnaisse Cambaí	Tonalito	+ 4,3 e + 6,3	894 e 723				Saalmann et al., 2005a
	Ofiolitos Ibaré e Palma	🟩	Cloritito, turmalinito			880-722	+12 a +1	+5 a +3	Artigos 2 e 4
		🟩	Mg-Xisto, serpentinito	+ 6,8 a + 3,1	1350-650				Saalmann et al., 2005a
		🟨	Albitito			892 ±3	+15 a +13		Artigo 1

Figura 5. Principais eventos tectônicos associados aos ofiolitos Ibaré e Palma.

Análise geoquímica de rocha total de 18 amostras vulcanoclásticas do ofiolito Ibaré e 13 amostras de metabasaltos do ofiolito Cerro Mantiqueiras mostraram que estão relacionados com início de subducção (ver apêndices O e P, figura 13 do artigo 2). As vulcanoclásticas do ofiolito Ibaré têm assinaturas típicas de MORB e os metabasaltos do ofiolito Cerro Mantiqueiras tem assinatura transicional entre MORB e arco de ilha toleítico. De acordo com Pearce (2014), a tendência distinta ao longo do tempo é de razões semelhantes a MORB no início da subducção para arco de ilha toleítico com o aumento da influência de subducção. Isso sugere que as rochas vulcanoclásticas podem representar as rochas do próprio arco (conforme assinatura Hf, artigo 2), cujas rochas do Cambaí (750-700 Ma) poderiam ser parte desse arco e o anfibolito (733-700 Ma) do Cerro Mantiqueiras parte desse sistema de arco-subducção-acresção.

No Cinturão Porongos (Figura 6), as idades de 802-767 Ma sugeridas para um arco magmático continental e as idades vulcânicas de cristalização de ~780 Ma estão condizentes com a idade obtida para o ofiolito Capané (793-715 Ma; artigo 3). Essas idades sugerem um ambiente geotectônico correlato para formação dessas rochas. As idades do ofiolito Capané também sugerem que os eventos foram contemporâneos aos associados com os ofiolitos do terreno São Gabriel.

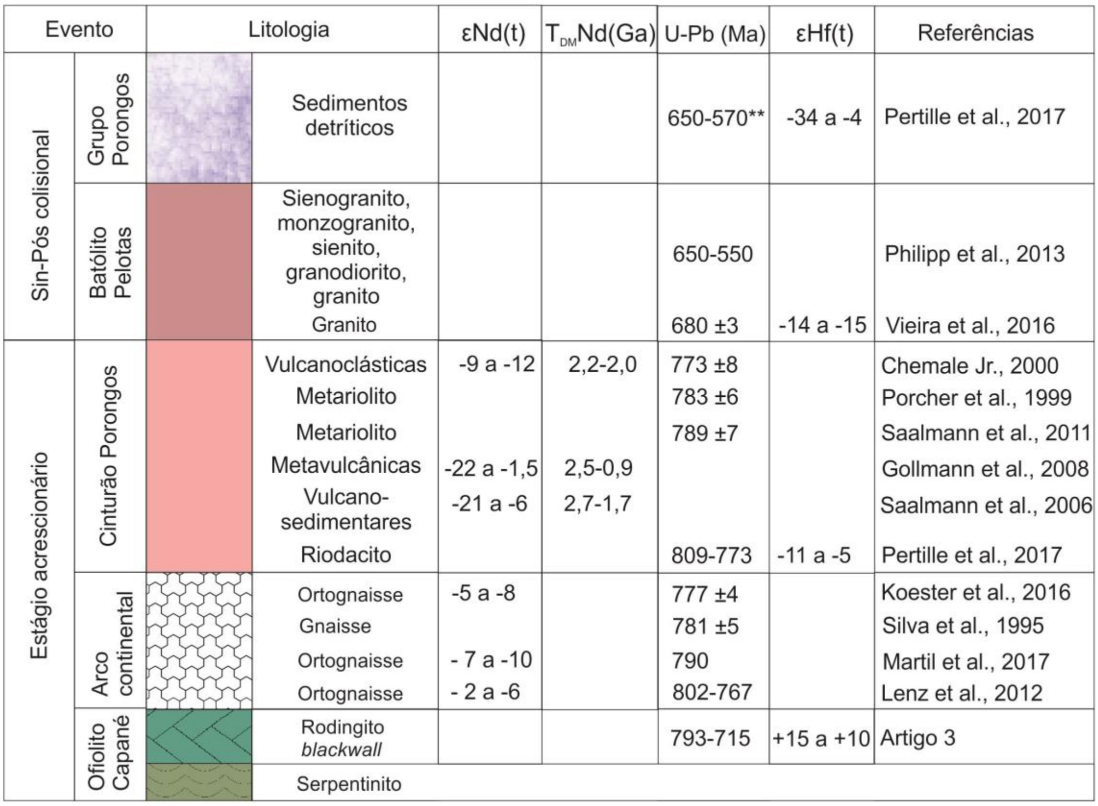

Evento		Litologia		εNd(t)	T_{DM}Nd(Ga)	U-Pb (Ma)	εHf(t)	Referências
Sin-Pós colisional	Grupo Porongos		Sedimentos detríticos			650-570**	-34 a -4	Pertille et al., 2017
	Batólito Pelotas		Sienogranito, monzogranito, sienito, granodiorito, granito			650-550		Philipp et al., 2013
			Granito			680 ±3	-14 a -15	Vieira et al., 2016
Estágio acrescionário	Cinturão Porongos		Vulcanoclásticas	-9 a -12	2,2-2,0	773 ±8		Chemale Jr., 2000
			Metariolito			783 ±6		Porcher et al., 1999
			Metariolito			789 ±7		Saalmann et al., 2011
			Metavulcânicas	-22 a -1,5	2,5-0,9			Gollmann et al., 2008
			Vulcano-sedimentares	-21 a -6	2,7-1,7			Saalmann et al., 2006
			Riodacito			809-773	-11 a -5	Pertille et al., 2017
	Arco continental		Ortognaisse	-5 a -8		777 ±4		Koester et al., 2016
			Gnaisse			781 ±5		Silva et al., 1995
			Ortognaisse	- 7 a -10		790		Martil et al., 2017
			Ortognaisse	- 2 a -6		802-767		Lenz et al., 2012
	Ofiolito Capané		Rodingito *blackwall*			793-715	+15 a +10	Artigo 3
			Serpentinito					

Figura 6. Principais eventos tectônicos associados ao ofiolito Capané. (**) = idade máxima de deposição.

O ofiolito Capané representa um pedaço do manto litosférico (εHf = +15,0 a + 10,7) sem interferência ou alteração de fonte crustal. Uma sugestão de possível fonte para formação das rochas (~800 Ma) contemporâneas do Cinturão Porongos é que as rochas vulcano-sedimentares são parte de vulcanismo relacionado ao arco magmático de idade semelhante (Figura 6). Para o ofiolito Capané são sugeridas duas hipóteses de posicionamento no manto. Ou o ofiolito estava posicionado na cunha do manto e não foi contaminado pela crosta continental, ou estiva posicionado na litosfera do manto antes da zona de subducção e não relacionado a ela (Figura 7b; artigo 3). O modelo de empurrão e cavalgamento para o Grupo Porongos de Pertille et al. (2015a, b, 17) foi adotado nessa tese. O ofiolito Capané foi jogado para dentro do continente (Figura 7c; artigo 3), impulsionado junto com as rochas do Cinturão Porongos por empurrões e cavalgamentos durante a colisão final (650-550 Ma) e representa o fechamento do Oceano Adamastor.

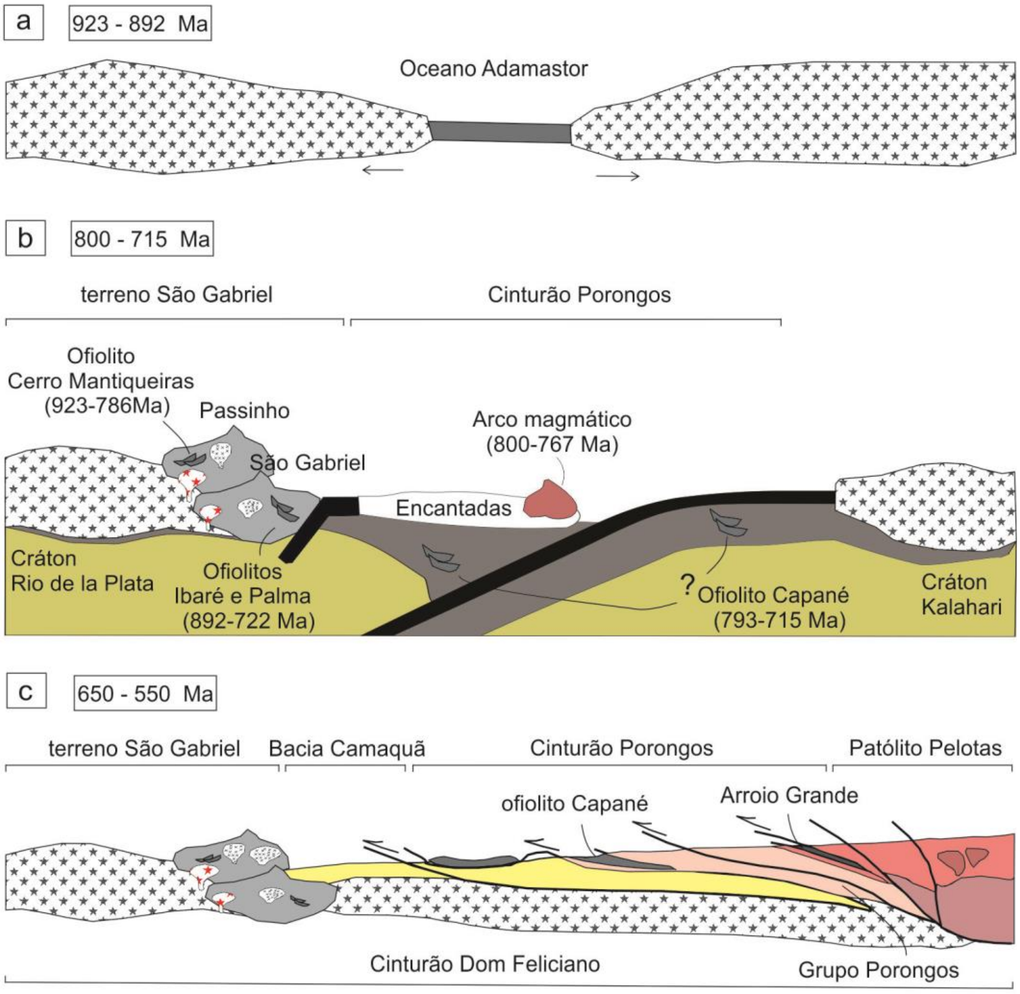

Figura 7. Modelo simplificado de evolução dos ofiolitos no Cinturão Dom Feliciano.

Embora haja uma idade um pouco mais antiga que as idades conhecidas para o Batólito Pelotas (680 ±3 Ma - Vieira et al., 2016), há um intervalo de 87 Ma entre a geração dos gnaisses do arco magmático e os granitóites do Batólito e um intervalo de 35 Ma entre a idade mais jovem de geração do ofiolito Capané e sua colocação.

Esse intervalo pode representar período de quiescência entre geração-acresção-colisão, a exemplo do que se tem em outros orógenos. Os ofiolitos no Escudo Sul-Riograndense registram a quebra do Supercontinente Rodinia e a aglomeração do Supercontinente Gondwana.

1.8 Interpretações e conclusões

O estudo de zircões de metassomatitos em serpentinitos causou um avanço no entendimento do tempo de evolução dos ofiolitos. A região do Escudo Sul-Riograndense formou em um processo prolongado de geração e colocação de ofiolitos, zona de subducção, magmas graníticos e basálticos juvenis. Isótopos de Hf, química do zircão e isótopos de boro da turmalina indicam característica juvenil com assinatura de litosfera oceânica para os ofiolitos.

Na porção oeste do Cinturão Dom Feliciano (terreno São Gabriel) os ofiolitos Cerro Mantiqueiras, Ibaré e Palma foram gerados na crosta oceânica no Toniano (923 ±3, 892 ±3, 880 ±12 Ma). A idade metamórfica do ofiolito Cerro Mantiqueiras é 786 ±13 Ma. A serpentinização dos peridotitos dos ofiolitos começou na cadeia meso-oceânica no início do Toniano (880 ±12 Ma). Serpentinização pode ter continuado até a zona de subducção e a colocação final em 722 ±3 Ma no arco intra-oceânico São Gabriel (758 ±4 Ma). O terreno São Gabriel evoluiu a partir de sucessiva formação de arcos de ilhas que foram subsequentemente amalgamados ao Cráton Rio de la Plata.

Na parte central-leste (Grupo Porongos), o ofiolito Capané de idade entre 793-715 Ma estabelece um limite para a evolução tectônica do Gondwana Oeste envolvendo a amalgamação de crátons. O ofiolito marca o fechamento final do oceano que precedeu a formação do cinturão de montanha formado pelo Batólito Pelotas (680-550 Ma). A obducção ocorreu durante a colisão que formou o cinturão de dobramentos e cavalgamentos Porongos em 650-570 Ma.

Durante o ciclo Neoproterozóico Brasiliano, a história tectônica do Cinturão Dom Feliciano no Escudo Sul-Riograndense demonstra uma evolução do Ciclo de Wilson com duração de aproximadamente 200 Ma começando em 923-892 Ma (albititos oceânicos; artigo 1). Magmatismo de crosta oceânica, subducção e construção de arcos de ilhas ocorreram no oceano Adamastor em 879 ±14 Ma (arco Passinho) e 758 ±4 Ma (arco São Gabriel) que resultaram na obdução dos ofiolitos (artigos 1, 2) formados durante a expansão, na cadeia oceânica conforme registro nos ofiolitos Cerro Mantiqueiras (923-786 Ma), Ibaré e Palma (892-722 Ma). Durante essa fase convergente do Orógeno Brasiliano, no leste do cinturão, o ofiolito Capané (793-715

Ma) registra a última fatia de litosfera mantélica (artigo 3) empurrada sobre o continente (650-570 Ma) durante a orogenia colisional (Kalahari-Encantadas-Rio de la Plata) marcando o fechamento do oceano Adamastor.

A composição química da turmalina do ofiolito Ibaré indica dravita e sua composição isotópica $\delta^{11}B$ = 3 a 5‰ liga sua origem a crosta oceânica alterada (artigo 4). A natureza oceânica do ofiolito fica assim corroborada. Esta Tese de Doutorado solucionou os objetivos propostos e significa uma contribuição para o entendimento da geologia do Escudo Sul-Riograndense. Os dados e as interpretações aqui reportados poderão servir de base para estudos futuros.

Referências:

Abd El-Rahman, Y., Polat, Y., Dilek, Y., Fryer, B.J., El-Sharkawy, M., Sakran, S. 2009. Geochemistry and tectonic evolution of the Neoproterozoic incipient arc–forearc crust in the Fawakhir area, Central Eastern Desert of Egypt. Precambrian Research 175, 116–134.

Ague, J.J. 2003. Fluid infiltration and transport of major, minor and trace elements during regional metamorphism of carbonate rocks, Wepawaug Schist, Connecticut, USA. American Journal of Science 30, 753–816.

Ali, K.A., Azer, M.K., Gahlan, H.A. 2010. Age constraints on the formation and emplacement of Neoproterozoic ophiolites along the Allaqi-Heiani suture, South Eastern Desert of Egypt. Gondwana Research 18, 583–595.

Almeida, F.F.M., Hasui, Y., Broto Neves, B.B., Fuck, R.A. 1981. Brazilian structural provinces: na intridution. Earth Sciences Reviews 17, 1–29.

Aspden, J.A., McCourt, W.J., Brook, M. 1987. Geometrical control of subduction-related magmatism: The Mesozoic and Cenozoic plutonic history of western Colombia. Journal ofthe Geological Society, London 144, 893–905.

Babinski, M., Chemale Jr.,F., Hartmann, L.A., van Schmus, W.R., Silva, L.C. 1996. Juvenile accretion at 750–700 Ma in Southern Brazil. Geology 24, 439–442.

Bach, W., Jons N., Klein, F. 2013. Metasomatism within the ocean crust. In: Metasomatism and the chemical transformation of rock the role of fluids in terrestrial and extraterrestrial processes (Eds.), Harlov, D.E. & Austrheim, 253–288.

Basei, M.A.S., Siga Jr.,O., Masquelin, H., Harara, O.M., Reis Neto, J.M., Precozzi, F. 2000. The Dom Feliciano belt (Brazil-Uruguay) and its foreland (Rio de la Plata Craton): framework, tectonic evolution and correlations with similar terranes of southwestern Africa. In Proceeding in 31st International Geological Congress, Sociedade Brasileira de Geologia, Rio de Janeiro 49p.

Basei, M.A.S., Frimmel, H.E., Nutman, A.P., Preciozzi, F., Jacob, J. 2005. A connection between the Neoproterozoic Dom Feliciano (Brazil/Uruguay) and Gariep (Namibia/South Africa) orogenic belts–evidence from a reconnaissance study. Precambrian Research 139, 195–221.

Basei, M.A.S., Frimmel, H.E., Nutman, A.P., Preciozzi, F. 2008. West Gondwana amalgamation based on detrital zircon ages from Neoproterozoic Ribeira and Dom Feliciano Belts of South America and comparison with coeval sequences from SW Africa. In: Pankhurst, R.J., Trouw, R.A.J., Brito Neves, B.B., De Wit, M.J. (Eds.), west Gondwana Pre-Cenozoic correlations across the south Atlantic region. Geological Society Special Publication 294, 239–256.

Basei, M.A.S, Campos Neto, M.C., Castro, N.A., Nutman, A.P., Wemmer, K., Yamamoto, M.T., Hueck, M., Osako, L., Siga, O., Passarelli, C.R. 2011. Tectonic evolution of the Brusque Group, Dom Feliciano belt, Santa Catarina, Southern Brazil. Journal of South American Earth Sciences 32, 324–350.

Camozzato, E., Klein, C., Iglesias, C.M.F. 2014. Bagé, Folha SH.21-Z-D-III. Estado do RS. Porto Alegre: CPRM. Carta geológica, escala 1:100.000. Programa geologia do Brasil – PGB.

Chemale Jr., F. 1982. Geologia da região de Palma, São Gabriel, Rio Grande do Sul. Programa de Pós-Graduação em Geociências, Universidade Federal do Rio Grande do Sul, 136p.

Chemale Jr., F., Hartmann, L.A., da Silva, L.C. 1995. Stratigraphy and tectonism of the Brasiliano Cycle in southern Brazil. Communs geol. Surv. Namibia 10,153–168.

Chemale Jr., F. 2000. Evolução Geológica do Escudo Sul-rio-grandense, in Holz, M., De Ros, L.F. (Eds.), Geologia do Rio Grande do Sul: Centro de investigação do Gondwana- Universidade Federal do Rio Grande do Sul, Porto Alegre, Brazil, 13–55.

Coleman, R.G. 1977. Emplacement and metamorphism of ophiolltes. Societá Italiana di mineralogia e petrologia 33, 161–190.

Corfield, R.I., Searle, M.P., Pedersen, R.B. 2001. Tectonic Setting, Origin, and Obduction History of the Spontan Ophiolite, Ladakh Himalaya, NW India. The Journal of Geology 109, 715–736.

De Souza, S., Tremblay, A., Daoust, C., Gauthier, M. 2008. Stratigraphy and geochemistry of the Lac-Brompton ophiolite, Canada: evidence for extensive forearc magmatism and mantle exhumation in the Southern Quebec Ophiolite Belt. Canadian Journal of Earth Sciences 45, 9993–1014.

Dewey, F.J., Kidd, W.S.F. 1974. Continental collisions in the Appalachian-Caledonian orogenic belt: Variations related to complete and incomplete suturing. Geology 2, 543–546.

Dilek, Y., Thy, P., Moores, E.M., Ramsden, T.W., 1990. Tectonic evolution of the Troodos Ophiolite within the Tethyan Framework. Tectonics 9, 811–823.

Dilek, Y. 2003a. Ophiolite concept and its evolution, in Dilek, Y., Newcomb, S. (Eds.) Ophiolite concept and the evolution of geological thought. Geological Society of America Special Paper 373, 1–16.

Dilek, Y., 2003b. Ophiolite pulses, mantle plumes and orogeny, in Dilek, Y., Robinson P.T. (Eds.), Ophiolites in Earth History. Geological Society, London, Special Publications 218, 9–19.

Dilek, Y., Furnes, H. 2011. Ophiolite genesis and global tectonics: geochemical and tectonic fingerprinting of ancient oceanic lithosphere. GSA Bulletin 123, 387–411.

Dilek, Y., Furnes, H. 2014. Ophiolites and their origins. Elements 10, 93–100.

Dubińska, E., Bylina, P., Kozłowski, A., Dörr,W., Nejbert, K., Schastokc, J., Kulickie, C. 2004. U-Pb dating of serpentinization-hydrothermal zircon from a metassomatic rodingite shell (Sudetic ophiolite, SW Poland). Chemical Geology 203, 183–203.

Fauqué, L.E., Villar, L.M. 2003. Stratigraphic reinterpretation and petrology of the Cerro Chuscho Formation. Precordillera of La Rioja. A Revista de la Asociación Geológica Argentina 58, 218–232.

Fernandes, L.A.D., Tommasi, A., Porcher, C.C. 1992. Deformation patterns in the southern Brazilian branch of the Dom Feliciano Belt: A reappraisal. Journal of South American Earth Sciences 5, 77–96.

Fernandes, L.A.D.,Menegat, R., Costa A.F.U., Koester, E., Porcher, C.C., Tommasi, A., Kraemer, G., Ramgrab, G.E, Camozzatto, E. 1995a. Evolução tectônica do Cinturão Dom Feliciano no Escudo Sul-Rio-Grandense: Parte I – uma contribuição a partir do registro geológico. Revista Brasileira de Geociências 25, 351–374.

Fernandes, L.A.D., Menegat, R., Costa A.F.U., Koester, E., Porcher, C.C., Tommasi, A., Kraemer, G., Ramgrab, G.E, Camozzatto, E. 1995b. Evolução tectônica do Cinturão Dom Feliciano no Escudo Sul-Rio-Grandense: Parte II – uma contribuição a partir das assinaturas geofísicas. Revista Brasileira de Geociências 25, 375–384.

Furnes, H., Pedersen, R.B., Stillman, C.J. 1988. The Leka Ophiolite Complex, central Norwegian Caledonides: field characteristics and geotectonic significance. Journal of the Geological Society, London 145, 401–412.

Furnes, H., Pedersen, R.B., Hertogen, J., Albrektsen, B.A. 1992. Magma development of the Leka Ophiolite Complex, central Norwegian Caledonides. Lithos 27, 259–277.

Furnes, H., Wit, M., Dilek, Y. 2014. Four billion years of ophiolites reveal secular trends in oceanic crust formation. Geoscience Frontiers 5, 571–603.

Gaggero, L., Spadea, P., Cortesogno, L., Savelieva, G.N., Pertsev, A.N. 1997. Geochemical investigation of the igneous rocks from the Nurali ophiolitic mélange zone, Southern Urals. Tectonophysics 276, 139–161.

Garcia, M.A.M. 1980. Petrologia do complexo Palma, RS. Porto Alegre. Dissertação de Mestrado. Programa de Pós Graduação em Geociências, Universidade Federal do Rio Grande do Sul, 133p.

Garcia, M.A.M., Hartmann, L.A. 1981. Petrologia do Complexo Palma-RS. Acta Geologica Leopondensia 9, 51-122.

Garfunkel, Z. 2015. The relations between Gondwana and the adjacent peripheral Cadomian domain–constrains on the origin, history, and paleogeography of the peripheral domain. Gondwana Research 28, 1257–1281.

Gastal, M.C., Ferreira, F.J.F., Cunha, J.U., Esmeris, C., Koester, E., Raposo, M.B., Rossetti, M.M.M. 2015. Alojamento do granito Lavras e a mineralização aurífera durante evolução de centro vulcano-plutônico pós-colisional, oeste do Escud Sulriograndense: dados geofísicos e estruturais. Brazilian Journal of Geology 45, 217–241.

Gollmann, K., Marques, J.C., Frantz, J.C., Chemale, Jr.F. 2008. Geoquímica e isotópos de Nd de rochas metavulcânicas da Antiforme Capané, Complexo Metamórfico Porongos, RS. Revista Pesquisas em Geociências 35, 83–95.

Goncalves, P., Marquer, D., Oliot, E., Durand, C. 2013. Thermodynamic modeling and thermobarometry of metasomatized rocks In: Metasomatism and the chemical transformation of rock the role of fluids in terrestrial and extraterrestrial processes (Eds.), Harlov, D.E. & Austrheim, 53–92.

Goscombe, B., Gray, D., Armstrong, R., Foster, D.A., Vogl, J. 2005. Event geochronology of the Pan-African Kaoko Belt, Namibia. Precambrian Research 140, 1–41.

Gubert, M.L., Philipp, R.P., Basei, M.A.S. 2016. The Bossoroca Complex, São Gabriel Terrane, Dom Feliciano Belt, southernmost Brazil. U-Pb geochronology and tectonic implications for the neoproterozoic São Gabriel Arc. Journal of South American Earth Sciences 70, 1–17.

Guivel, C., Lagabrielle, Y., Bourgois, J., Maury, R.C., Fourcade, S., Martin, H., Arnaud, N. 1999. New geochemical constraints for the origin of ridgesubducted- related plutonic and volcanic suites from the Chile Triple Junction (Taitao Peninsula and Site 862, LEG ODP141 on the Taitao Ridge). Tectonophysics 311, 83–111.

Harlov, D.E. & Austrheim, H. 2013. Metasomatism and the chemical transformation of rock: rock-mineral-fluid Interaction in Terrestrial and Extraterrestrial Environments. In: Metasomatism and the chemical transformation of rock the role of fluids in terrestrial and extraterrestrial processes (Eds.), Harlov, D.E. & Austrheim, 1–16.

Hartmann, L.A., Leite, J.A.D., Silva, L.C., Remus, M.V.D., McNaughton, N.J., Groves, D.I., Fletcher, I.R., Santos, J.O.S., Vasconcellos, M.A.Z. 2000. Advances in SHRIMP geochronology and their impact on understanding the tectonic and metallogenic evolution of southern Brazil. Australian Journal of Earth Sciences 47, 829–844.

Hartmann, L.A., Remus, M.V.D. 2000. Origem e evolução das rochas ultramáficas do Rio Grande do Sul desde o Arqueano até o Cambriano. In: Holz, M., De Ros, L.F. (Eds.), Geologia do Rio Grande do Sul, Porto Alegre: Ed. CECO/UFRGS, 55–78.

Hartmann, L.A, Chemale Jr.,F. 2003. Mid amphibolite facies metamorphism of harzburgites in the Neoproterozoic Cerro Mantiqueiras Ophiolite, southernmost Brazil. Anais da Academia Brasileira de Ciências 75, 109–128.

Hartmann, L.A., Philipp, R.P., Liu, D., Wan, Y., Wang, Y., Santos, J.O.S., Vasconcellos, M.A.Z. 2004. Paleoproterozoic magmatic provenance of detrital zircons, porongos complex quartzites, southern Brazilian shield. International Geology Review 46, 127–157.

Hartmann, L.A., Chemale Jr., F., Philipp, R.P. 2007. Evolução geotectônica do Rio Grande do Sul no Pré-Cambriano. In: Iannuzzi, R., Frantz, J.C. (Eds.), 50 Anos de Geologia. Universidade Federal do Rio Grande do Sul, Porto Alegre, Brazil, 97–123.

Hartmann, L.A., Liu, D., Wang, Y., Massonne, H.J., Santos, J.O.S. 2008. Protolith age of Santa Maria Chico granulites dated on zircons from an associated amphibolite-facies granodiorite in southernmost Brazil. Anais da Academia Brasileira de Ciências 80, 543–551.

Hartmann, L.A., Philipp, R.P., Santos, J.O.S., McNaughton, N.J. 2011. Time frame of the 753–680 Ma juvenile accretion during the São Gabriel orogeny, southern Brazilian shield. Gondwana Research 19, 84–99.

Jian, P., Kröner, A., Windley, B.F., Shi, Y., Zhang, F., Miao, L., Tomurhuu, D., Zhang, W., Liu, D. 2010. Zircon ages of the Bayankhongor ophiolitr mélange and associated rocks: time constraints on Neoproterozoic to Cambrian accretionary and collisional orogenesis in Central Mongolia. Precambrian Research 177, 162–180.

Jian, P., Kröner, A., Windley, B.F., Shi, Y., Zhang, W., Zhang, L., Yang, W. 2012. Carboniferous and Cretaceous mafic-ultramafic massifs in Inner Mongolia (China): a SHRIMP zircon and geochemical study of the previous presumed integral “Hegenshan ophiolite”. Lithos 142–143, 48–66.

Jost, H., Hartmann, L.A. 1979. Rodingitos do Rio Grande do Sul. Acta Geológica Leopoldensia 3, 77–91.

Jost, H., Bitencourt, M.F. 1980. Estratigrafia e tectônica de uma fração da Faixa de Dobramentos de Tijucas no Rio Grande do Sul. Acta Geologica Leopoldensia 4, 27–60.

Khain, E.V., Bibikova, E.V., Kröner, A., Zhuravlev, D.Z., Sklyarov, E.V., Fedotova A.A., Kravchenko-Berezhnoy, I.R. 2002. The most ancient ophiolite of the Central Asian fold belt: U-Pb and Pb-Pb zircon ages for the Dunzhugur Complex, Eastern Sayan, Siberia, and geodynamic implications. Earth and PlanetaryScience Letters 199, 311–325.

Koester, E., Porcher, C.C., Pimentel, M.M., Fernandes, L.A.D., Vignol-Lelarge, M.L., Oliveira, L.D., Ramos, R.C. 2016. Further evidence of 777 Ma subduction-related continental arc magmatism in Eastern Dom Feliciano Belt, southern Brazil: The Chácara das Pedras Orthogneiss. Journal of South American Earth Sciences 68, 155–166.

Kounov, A., Graf, J., von Quadt, A., Bernoulli, D., Burgd, J.P., Seward, D., Ivanov, Z., Fanning, M. 2012. Evidence for a “Cadomian” ophiolite and magmatic-arc complex in SW Bulgaria. Precambrian Research 212–213, 275–295.

Kovalenko, V.I., Yarmolyuk, V.V., Kovach, V.P., Kotov, A.B., Kozakov, I.K., Salnikova, E.B., Larin, A.M. 2004. Isotope provinces, mechanisms of generation and sources of the continental crust in the Central Asian mobile belt: geological and isotopic evidence. Journal of Asian Earth Sciences 23, 605–627.

Kroner, U., Romer, R.L. 2013. Two plates e many subduction zones: the Variscan orogeny reconsidered. Gondwana Research 24, 298–329.

Lagabrielle, Y., Guivel,C., Maury, R.C, Bourgois, J., Fourcade, S., Martin, H. 2000 Magmatic–tectonic effects of high thermal regime at the site o active ridge subduction: the Chile Triple Junction model. Tectonophysics 326, 255–268.

Laux, J.H., Bongiolo, E.M., Klein, C., Iglesias, C.M.F. 2012. Lagoa da Meia Lua, Folha SH.21-Z-B-VI. Estado do RS. Porto Alegre: CPRM. Carta Geológica, Escala 1:100.000. Programa Geologia do Brasil – PGB.

Leblanc, M., Lbouabi, M. 1988. Native silver mineralisation along a rodingite tectonic contact between serpentinite and quartz-diorite (Bon Azzer, Morocco). Economic Geology 83,1379–1391.

Leite, J.D. 1997. A origem dos harzburgitos da Sequência Cerro Mantiqueiras e implicações tectônicas para o desenvolvimento do Neoproterozóico da porção oeste do Escudo Sul Riograndense. Dissertação de mestrado. Programa de Pós-Graduação em Geociências, Universidade Federal do Rio Grande do Sul, 161p.

Leite, J.A.D., Hartmann, L.A., McNaughton, N.J., Chemale Jr., F. 1998. SHRIMP U/Pb zircon geochronology of Neoproterozoic juvenile and crustal-reworked terranes in southernmost Brazil. International Geology Review 40, 688–705.

Le Moigne, J., Lagabrielle, Y., Whitechurch, H., Girardeau, J., Bourgois, J., Maury, R.C. 1996. Petrology and geochemistry of the Ophiolitic and Volcanic Suites of the Taitao Peninsula e Chile Triple Juction Area. Journal of South American Earth Sciences 9, 43–58.

Lena, L.O.F., Pimentel, M.M., Philipp, R.P., Armstrong, R., Sato, K. 2014. The evolution of the Neoproterozoic São Gabriel juvenile terrane, southern Brazil based on high spatial resolution U-Pb ages and $\delta^{18}O$ data from detrital zircons. Precambrian Research 247, 126–138.

Lenz, C., Porcher, C.C., Fernandes, L.A.D., Masquelin, H., Koester, E., Conceição R.V. 2013. Geochemistry of the Neoproterozoic (800–767 Ma) Cerro Bori orthogneisses, Dom Feliciano Belt in Uruguay: tectonic evolution of an ancient continental arc. Mineralogy and Petrology 107, 785–806.

Li, X-P., Zhang, L-F., Wilde, S.A., Song, B., Liu, X-M. 2010. Zircons from rodingite in the Western Tianshan serpentinite complex: Mineral chemistry and U–Pb ages define nature and timing of rodingitization. Lithos 118, 17–34.

Machado, N., Koppe, J.C., Hartmann, L.A. 1990. A late Proterozoic U-Pb age for the Bossoroca belt, Rio Grande do Sul, Brazil. Journal of South American Earth Sciences 3, 87–90.

Marques, J.C., Jost, H., Roisenberg, A., Frantz, J.C. 1998. Eventos ígneos da Suíte Metamórfica Porongos na área da Antiforme Capané, Cachoeira do Sul – RS. Revista Brasileira de Geociências 28, 419–430.

Marques, J.C., Roisenberg, A., Jost, H., Frantz, J.C., Teixeira, R.S. 2003, Geologia e geoquímica das rochas metaultramáficas da Antiforme Capané, Suíte Metamórfica Porongos, RS. Revista Brasileira de Geociências 33, 95–107.

Martil, M.M.D., Bitencourt, M.F., Nardi, L.V.S., Koester, E., Pimentel, M.M. 2017. Pre-collisional, Neoproterozoic (ca. 790 Ma) continental arc magmatism in southern Mantiqueira Province, Brazil. Geochemical and isotopic constraints from the Várzea do Capivarita Complex. Lithos 274–275, 39–52.

Naumann, M.P., Hartmann, L.A., 1984. Cornubianitos ultramáficos e matassomatitos associados da região do Arroio Corticeiras. In: Congresso Brasileiro de Geologia 33, Rio de Janeiro 9, 4279–4290.

Naumann, M.P. 1985. O complexo Vulcano-sedimentar-ultramáfico e granitoides da região de Ibaré, RS. Programa de Pós-Graduação em Geociências, Universidade Federal do Rio Grande do Sul, 161p.

Neubauer, F. 2002. Evolution of late Neoproterozoic to early Paleozoic tectonic elements in Central and Southeast European Alpine mountain belts: review and synthesis. Tectonophysics 352, 87–103.

Oliver, G.J.H., Corfu, F., Krogh, T.E. 1993. U–Pb ages from SW Poland: evidence for a Caledonian suture zone between Baltica and Gondwana. Journal of the Geological Society London 150, 355–369.

Paim, P.S.G., Chemale Jr., F., Lopes, R.C. 2000. A Bacia do Camaquã. In: Holz,M., De Ros, L.F. (Eds.), Geologia do Rio Grande do Sul: Centro de Investigação do Gondwana. Universidade Federal do Rio Grande do Sul, Porto Alegre, Brazil, 231–274.

Pallister, J.S., Stacey, J.S., Fischer, L.B., Premo, W.R. 1988. Precambrian ophiolites of Arabia: geologic settings, U-Pb geochronology, Pb-isotope characteristics, and implications for continental accretion. Precambrian Research 38, 1–54.

Pearce, J.A., Robinson, P.T. 2010. The Troodos ophiolitic complex probably formed in a subduction initiation, slab edge setting. Gondwana Research 18, 60–81.

Pedersen, R.B., Searle, M.P., Carter, A., Bandopadhyay, P.C. 2010. U–Pb zircon age of the Andaman ophiolite: implications for the beginning of subduction beneath the Andaman–Sumatra arc. Journal of the Geological Society 167, 1105–1112.

Penniston-Dorland S.C., Ferry, J.M. 2008. Element mobility and scale of mass transport in the formation of quartz veins during regional metamorphism of the Waits river formation, eastcentral Vermont. American Mineralogy 93, 7–21.

Pertille, J., Hartmann, L.A., Philipp, R.P., Petry, T.S., Lana, C.C. 2015a. Origin of the Ediacaran Porongos Group, Dom Feliciano Belt, southern Brazilian Shield, with emphasis on whole rock and detrital zircon geochemistry and U-Pb, Lu-Hf isotopes. Journal of South American Earth Sciences 64, 69–93.

Pertille, J., Hartmann, L.A., Philipp, R.P. 2015b. Zircon U-Pb age constraints on the Paleoproterozoic sedimentary basement of the Ediacaran Porongos Group, Sul-Riograndense Shield, southern Brazil. Journal of South American Earth Sciences 63, 334–345.

Pertille, J., Hartmann, L.A., Santos, J.O.S., McNaughton, N.J., Armstrong, R. 2017. Reconstructing the Cryogenian-Ediacaran evolution of the Porongos fold and thrust belt, Southern Brasiliano orogen, based on zircon U-Pb-Hf-O isotopes. International Geology Review 59, 1532–1560.

Philipp, R.P., Machado, R., Nardi, L.V.S., Lafon, J.M. 2002. O magmatismo granítico Neoproterozóico do Batólito Pelotas no sul do Brasil: Novos dados e revisão de geocronologia regional. Revista Brasileira De Geociências 32, 277–290.

Philipp, R.P., Massonne, H.J., Campos, R.S. 2013, Peraluminous leucogranites of the Cordilheira Suite: A record of Neoproterozoic collision and the generation of the Pelotas Batholith, Dom Feliciano Belt, Southern Brazil. Journal of South American Earth Sciences 43, 8–24.

Philipp, R.P., Pimentel, M.M., Chemale Jr., F. 2016. Tectonic evolution of the Dom Feliciano Belt in southern Brazil. Geological relationships and U-Pb geochronology. Brazilian Journal of Geology 46, 83–104.

Pirajno, F. 2013. Effects ofMetasomatism onMineral Systems and Their Host Rocks: Alkali Metasomatism, Skarns, greisens, tourmalinites, rodingites, black-wall alteration and listvenites. In: Metasomatism and the chemical transformation of rock the role of fluids in terrestrial and extraterrestrial processes (Eds.), Harlov, D.E. & Austrheim, 203–252.

Porcher, C.C, Fernandes, L.A.D. 1990. Relações embasamento/cobertura na porção ocidental do cinturão Dom Feliciano: Um esboço estrutural. Revista Pesquisas 17, 72–84.

Porcher, C. C., Mcnaughton, N.J., Leite, J.A.D., Hartmann, L.A., Fernandes, L. A.D. 1999. Idade SHRIMP em zircão: vulcanismo ácido do Complexo Metamórfico Porongos. In: Simpósio de vulcanismo e ambientes associados, 1 Gramado, resumos p. 110.

Pushkov, V.N. 2009. The evolution of the Uralian orogen. In: Murphy, J.B., Keppie, J.D., Hynes, A.J. (Eds.), Ancient Orogens and Modern Analogues, The Geological Society, London, Special Publications 327, 161–195.

Putnis, A., Austrheim, H. 2013. Mechanisms of metasomatism and metamorphism on the local mineral scale: The role of dissolution-reprecipitation during mineral re-equilibration. In: Metasomatism and the chemical transformation of rock the role of fluids in terrestrial and extraterrestrial processes (Eds.), Harlov, D.E. & Austrheim, 141–170.

Queiroga, G.N., Pedrosa-Soares, A.C., Noce, C.M., Alkmim, F.F., Pimentel, M.M., Dantas, E., Martins, M., Castañeda, C., Suita, M.T.F., Prichard, F. 2007. Age of the Ribeirão da Folha ophiolite, Araçuaí Orogen: the U-Pb zircon dating of a plagiogranite. Geonomos 15, 61–65.

Ramos, R.C. 2014. complexo ofiolítico arroio grande, sudeste do Escudo Sul-Rio-grandense: caracterização e discussões das unidades ortoderivadas. Dissertação de mestrado. Programa de Pós-Graduação em Geociências, Universidade Federal do Rio Grande do Sul, 43p.

Ramos, R.C., Koester, E. 2014. Geologia da associação metamáfica-ultramáfica da região de Arroio Grande, sudeste do Escudo Sul-Rio-grandense. Instituto de Geociências, Universidade Federal do Rio Grande do Sul, Porto Alegre, RS, Brasil. Pesquisas em Geociências 41, 25–38.

Ramos, V.A., Escayola, M., Mutti, D.I., Vujovich, G.I. 2000. Proterozoic-early Paleozoic ophiolites of the Andean basement of southern South America. In: Dilek, Y., Moores, E.M., Elthon, D., Nicolas, A. (Eds.), Ophiolites and oceanic crust: New insights from field studies and the ocean drilling program. Boulder, Colorado, Geological Society of America, Special Paper 349, 331–349.

Rautenschlein, M., Jenner, G.A., Hertogen, J., Hofmann, A.W., Kerrich, R., Schmincke, H.U., White,W.M. 1985. Isotopic and trace element composition of volcanic glasses from the Akaki Canyon, Cyprus: implications for the origin of the Troodos ophiolite. Earth and Planetary Science Letters 75, 369–383.

Remus, M.V.D. 1990. Geologia e Geoquímica do Complexo Cambaizinho, São Gabriel, RS. Geologia da região de Palma, São Gabriel, Rio Grande do Sul. Dissertação de mestrado. Programa de Pós-Graduação em Geociências, Universidade Federal do Rio Grande do Sul, 267p.

Remus, M.V.D., Hartmann, L.A., Ribeiro, M. 1991. Nota sobre a geologia dos metamorfitos de pressão intermediária e granitóides associados da região de Pinheiro Machado/RS. Acta Geologica Leopoldensia 34, 175–90.

Remus, M.V.D., McNaughton, N.J., Hartmann, L.A., Koppe, J.C., Fletcher, I.R., Groves, D.I., Pinto, V.M. 1999. Gold in the Neoproterozoic juvenile Bossoroca Volcanic Arc of Southernmost Brazil: isotopic constraints on timing and sources. Journal of South American Earth Sciences 12, 349–366.

Remus, M.V.D., Hartmann, L.A., McNaughton, N.J., Groves, D.I., Fletcher, I.R. 2000. The link between hydrothermal epigenetic copper mineralization and the Caçapava Granite of the Brasiliano Cycle in Southern Brazil. Journal of South American Earth Sciences 13, 191–216.

Rioux, M., Bowring, S., Kelemen, P., Gordon, S., Miller, R., Dudás, F. 2013. Tectonic development of the Semail ophiolite: high-precision U-Pb zircon geochronology and Sm-Nd isotopic constraints on crustal growth and emplacement. Journal of Geophysical Research: Solid Earth 118, 2085–2101.

Robinson, P.T, Zhou, M-F., Hu, X-F., Reynolds, P., Wenji, B., Yang, J. 1999. Geochemical constraints on the origin of the Hegensha Ophiolite, Inner Mongolia, China. Journal of Asian Earth Sciences 17, 423–442.

Rubenach, M. 2013. Structural controls of metasomatism on a regional scale. In: Metasomatism and the chemical transformation of rock the role of fluids in terrestrial and extraterrestrial processes (Eds.), Harlov, D.E. & Austrheim, 93-140.

Saalmann, K., Hartmann, L.A., M.V.D., Remus, M.V.D., Koester, E, Conceição, R.V., 2005a. Sm–Nd isotope geochemistry of metamorphic volcano-sedimentary successions in the São Gabriel Block, southernmost Brazil: evidence for the existence of juvenile Neoproterozoic oceanic crust to the east of the Rio de la Plata craton. Precambrian Research 136, 159–175.

Saalmann, K., Remus, M.V.D., Hartmann, L.A. 2005b. Geochemistry and Crustal Evolution of Volcano-sedimentary Successions and Orthogneisses in the São Gabriel Block, Southernmost Brazil - Relics of Neoproterozoic Magmatic Arcs. Gondwana Research 8, 143–161.

Saalmann, K., Remus, M.V.D., Hartmann, L.A. 2006. Structural evolution and tectonic setting of the Porongos belt, Southern Brazil. Geological Magazine 143, 59–88.

Saalmann, K., Gerdes, A., Lahaye, Y., Hartmann, L.A., Remus, M.V.D., Läufer, A. 2011. Multiple accretion at the eastern margin of the Rio de la Plata craton: The prolonged Brasiliano orogeny in southernmost Brazil. International Journal of Earth Sciences 100, 355–378.

Saccani, E., Pricipi, G., Garfagnoli, F., Menna, F. 2008. Corsica ophiolites: geochemistry and petrogenesis of basaltic and metabasaltic rocks. Ofioliti 33, 187–207.

Saccocia, P.J., Ding, K., Berndt, M.E., Seewald, J.S., Seyfried Jr.,W.E. 1994. Experimental and theoretical perspectives on crustal alteration atmid-ocean ridges. In: Lentz, D.R. (Ed.), Alteration and Alteration Processes AssociatedWith Ore-forming Systems Geological Association of Canada. Waterloo, Canada, Short Course Notes 11, 403–431.

Samson, S.D., Inglis, J.D., D' Lemos, R.S., Admou, H., Blichert-Toft, J., Hefferan, K. 2004. Geochronological, geochemical, and Nd–Hf isotopic constraints on the origin of Neoproterozoic plagiogranites in the Tasriwine ophiolite, Anti-Atlas orogen, Morocco. Precambrian Research 135, 133–147.

Santos, J.O.S., Chernicoff, C.J., Zappettini, E.O., McNaughton, N.J., Hartmann, L.A. 2017. Large geographic and temporal extensions of the Río de la Plata Craton, South America and its metacratonic eastern margin. International Geology Review (aceito para publicação).

Searle M.P., Law, R.D., Jessup, M. 2006. Crustal structure, restoration and evolution of the Greater Himalaya in Nepal–South Tibet: implications for channel flow and ductile extrusion of the middle crust. Geological Society, London, Special Publications 268, 355–378.

Silva, L.C., McNaughton, N.J., Armstrong, R., Hartmann, L.A., Fletcher, I.R. 2005. The neoproterozoic Mantiqueira Province and its African connections: A zircon-based U-Pb geochronologic subdivision for the Brasilian/Pan-African systems of orogens. Precambrian Research 136, 203–240.

Silveira, D.F.S. 2017. Sequências Porongos I e II: Depósitos Ediacaranos sinorogênicos do Complexo Porongos (RS) e as implicações para o SW Gondwana. Dissertação de Mestrado. Programa de Pós Graduação em Geociências, Universidade Federal do Rio Grande do Sul, 153p.

Spadea, P., Delaloye, M., Espinosa, A., Orrego, A., Wagner, J.J. 1987. Ophiolite complex from La Tetilla, Southwestern Colombia, South America. The Journal of Geology 95, 377–395.

Stern, R.J., Johanson, P.R., Kroner, A., Yibas, B. 2004. Neoproterozoic ophiolites of the Arabian-Nubian Shield. In: Kusky, T.M. (Ed.), Precambrian Ophiolites and Related Rocks. Elsevier, Amsterdam 13, 95–128.

Suita, M.T.F., Pedrosa-Soares, A.C., Leite, C.A.S., Nilson, A.A., Prichard, H.M. 2004. Complexos ofiolíticos do Brasil e a metalogenia comparada das faixas araçuaí e brasília. In: Pereira, E.S., Castroviejo, R., Ortiz, F. (Eds.), Complejos ofiolíticos en IberoAmérica: Edita Proyecto XIII.1, Madrid-España 379, 101–132.

Vedana, L.A., Philipp, R.P., Basei, M.A.S. 2017. Tonian to early Cryogenian synorogenic basin of the São Gabriel Terrane, Dom Feliciano Belt, southernmost Brazil. International Geology Review doi.org/10.1080/00206814.2017.1328709

Villa, I.M., Williams, M.L. 2013. Geochronology of metasomatic events. In: Metasomatism and the chemical transformation of rock the role of fluids in terrestrial and extraterrestrial processes (Eds.), Harlov, D.E. & Austrheim, 171–202.

Yao, J., Cawood, P.A., Shu, L., Santosh, M., Li, J. 2016. An Early Neoproterozoic Accretionary Prism Ophiolitic Mélange from the Western Jiangnan Orogenic Belt, South China. The Journal of Geology 124, 587–601.

Zharikov, V.A., Pertsev, N.N., Rusinov, V.L., Callegari, E., Fettes, D.J. 2007. Metasomatism and metasomatic rocks. Recommendations by the IUGS subcommission on the systematics of metamorphic rocks, 9. http://www.bgs.ac.uk/scmr/docs/papers/paper_9.pdf

2. ARTIGOS PUBLICADOS E SUBMETIDO A PERIÓDICOS INTERNACIONAIS

Precambrian Research 285 (2016) 299–314

Contents lists available at ScienceDirect

Precambrian Research

journal homepage: www.elsevier.com/locate/precamres

Evolution of Neoproterozoic ophiolites from the southern Brasiliano Orogen revealed by zircon U-Pb-Hf isotopes and geochemistry

Karine R. Arena [a], Léo A. Hartmann [a,*], Cristiano Lana [b]

[a] Instituto de Geociências, Universidade Federal do Rio Grande do Sul, Avenida Bento Gonçalves, 9500, 91501-970 Porto Alegre, Rio Grande do Sul, Brazil
[b] Departamento de Geologia, Escola de Minas, Universidade Federal de Ouro Preto, Morro do Cruzeiro, 35400-000 Ouro Preto, Minas Gerais, Brazil

ARTICLE INFO

Article history:
Received 17 November 2015
Revised 4 July 2016
Accepted 11 September 2016
Available online 20 September 2016

Keywords:
Zircon
Albitite
U-Pb-Hf isotopes
Ophiolite
São Gabriel terrane
Brasiliano Orogen

ABSTRACT

U-Pb and Lu-Hf isotopic analyses of zircon from albitites, southern Brasiliano Orogen, indicate Neoproterozoic ages for two ophiolites. The difficulty of dating ophiolites is overcome by finding zircon in albitites contained in serpentinite. Two key areas were selected for the study, the Cerro Mantiqueiras and the Ibaré ophiolites, both in the juvenile São Gabriel terrane, Rio Grande do Sul, Brazil. Two distinct U-Pb SHRIMP ages are registered in the Cerro Mantiqueiras ophiolite zircons, respectively 923 ± 3 Ma in the cores and 786 ± 13 Ma in the rims. In the Ibaré ophiolite, the dating of zircon grains resulted in a single age of 892 ± 3 Ma. Distinctive depleted mantle Hf isotope signatures characterize the zircons; in the Cerro Mantiqueiras sample, εHf = +8 to +13 and Hf T_{DM} = 0.91–1.23 Ga, whereas the Ibaré sample displays εHf = +13 to +15 and Hf T_{DM} = 0.75–0.93 Ga. Ophiolite accretion in the São Gabriel terrane of the southern Brasiliano Orogen occurred in the Tonian, which establishes the age of a significant event in the tectonic evolution of the continent. The Hf data indicate that the ophiolites were derived from juvenile depleted mantle. This first direct dating of ophiolites sets new limits to the evolution of the Brasiliano Orogen.

1. Introduction

Zircon U-Pb-Hf isotopic studies are a powerful tool for unravelling the history of the incorporation of ophiolites into continental crust (Lissenberg et al., 2009; Furnes et al., 2014). The dating of ophiolites is commonly hampered by the lack of datable minerals in ultramafic rocks. This leads to the dating of zircon from associated oceanic plagiogranites and gabbros, interpreted as part of the ophiolite (e.g., Samson et al., 2004; Dilek and Thy, 2006; Queiroga et al., 2007; Pedersen et al., 2010; Karaoglan et al., 2013; Rioux et al., 2013). An advance was the discovery of zircon in albitites associated with ophiolites (e.g., Schaltegger et al., 2002). Dating of zircon from albitites can lead to the determination of the crystallization and alteration age and therefore of magma genesis and rock alteration in the oceanic crust.

Neoproterozoic ophiolites are voluminous in the Arabian-Nubian Shield (e.g., Stern et al., 2004; Gahlan et al., 2015). As an example, zircon U-Pb dating from plagiogranites yielded an igneous age of 762 Ma (Samson et al., 2004), early in the Panafrican Orogeny. The Hf isotopic composition of the same crystals, εHf (762 Ma) = +14, indicates melt batches that originated in the depleted mantle. The coeval Cadomian terranes in the southeast-European Alpine–Mediterranean mountain belt also contain ophiolites (e.g., Kounov et al., 2012; Garfunkel, 2015). In South America, the equivalent Brasiliano Orogen has a large number of ophiolites in the early portion, particularly in the Goiás arc (e.g., Pimentel and Fuck, 1992) and in the São Gabriel terrane in southernmost Brazil (e.g., Hartmann and Chemale, 2003). These two juvenile terranes represent only 5% of the exposed area of the Brasiliano Orogen, but are significant for the reconstruction of Rodinia and Gondwana.

The São Gabriel terrane is the most intensely studied juvenile section of the Brasiliano Orogen (Babinski et al., 1996; Saalmann et al., 2006; Hartmann et al., 2011; Lena et al., 2014; Lopes et al., 2015). The terrane evolved from 948 Ma to 660 Ma but the ages of the contained ophiolites remain unresolved.

This is the first study of zircons from Neoproterozoic ophiolites from the Brasiliano Orogen, collected from albitites enveloped by serpentinites. The difficulty of dating ophiolites is presently overcome by finding zircon in albitites that originated in the oceanic crust. Two key areas were selected for the study, the Cerro Mantiqueiras and the Ibaré ophiolites, because they contain albitites (>90% albite, some plagioclase), immersed in serpentinite.

We studied the zircons with multiple spot analytical techniques on the same crystal, guided by backscattered electron images. Zircons were dated with U-Pb isotopes determined with the

---

* Corresponding author.
E-mail addresses: karinearena@gmail.com (K.R. Arena), leo.hartmann@ufrgs.br (L.A. Hartmann), cristianodeclana@gmail.com (C. Lana).

http://dx.doi.org/10.1016/j.precamres.2016.09.014
0301-9268/

sensitive high-resolution ion microprobe (SHRIMP-IIe) and Hf isotopes by laser ablation inductively coupled plasma mass spectrometer (LA-ICP-MS). Trace elements of zircon were analyzed by laser ablation.

2. Geological setting

2.1. São Gabriel terrane

The São Gabriel terrane is commonly included in the Dom Feliciano belt (Fernandes et al., 1992, 1995; Tommasi et al., 1994; Lenz et al., 2013; Lena et al., 2014; Lopes et al., 2015; Hartmann et al., 2016), which is the southernmost segment of the 1000-km wide Brasiliano Orogen that extends for 3000 km along the Atlantic coast of South America (Fig. 1a). The terrane is mostly covered by the Paraná basin to the north and west; its exposure is approximately 50–100 km, smaller than the coeval, juvenile, 500-km long Goiás magmatic arc of central Brazil (Pimentel and Fuck, 1992) or the 2000-km long Arabian-Nubian shield (Ali et al., 2010; Morag et al., 2011). Nevertheless, the terrane is a significant marker of juvenile processes of mantle accretion to the crust in the Neoproterozoic (Fig. 1a, b).

The São Gabriel terrane occurs in the western portion of the local Sul-Riograndense shield (Babinski et al., 1996; Leite et al., 1998; Saalmann et al., 2005a,b; Hartmann et al., 2011; Lena et al., 2014; Lopes et al., 2015). In the southwest of the shield in Rio Grande do Sul state, older La Plata Craton rocks occur, mostly the Santa Maria Chico granulitic complex (2.55–2.02 Ga). The terrane was intruded by numerous Ediacaran granitic bodies and covered extensively by sedimentary and volcanic rocks of the Camaquã basin in the foreland of the Pelotas batholith (Pertille et al., 2015; Hartmann et al., 2016).

The Sul-Riograndense Shield is the result of processes of generation and deformation of continental crust, with a maximum growth during the Transamazonian (2.26–2.00 Ga) and Brasiliano (900–535 Ma) orogenic cycles. Each cycle included magma extraction and possibly also solid portions from the mantle, with the consequent construction of oceanic crust (basaltic plain and abyssal sediments, oceanic plateaus, oceanic islands), presence of microcontinents and continental margins (e.g., Hartmann et al., 2007).

The São Gabriel terrane was divided (Jost and Hartmann, 1984; Chemale, 2000; Hartmann et al., 2000, 2007; Hartmann and Remus, 2000) into the petrotectonic associations designated orthogneisses Cambaí, supracrustal rocks (Passo Feio, Cambaizinho, Palma and Bosssoroca complex), and the Cerro Mantiqueiras sequence, Ibaré Complex (Naumann, 1985) and postectonic granites.

Ophiolites were recognized in the São Gabriel terrane on the basis of field geology, mainly metabasalts, amphibolites and ultramafic rocks (magnesian schists, serpentinites and harzburgites) and zircon ages (890–700 Ma) associated with Nd model ages close to magmatic ages. But the data were obtained from associated granitic rocks, lacking the direct study of zircon from ultramafic rocks. In the Palma region, the ultramafic complex was considered an ophiolite by Szubert et al. (1977) and Ribeiro and Fantinel (1978), and the Cerro Mantiqueiras as an ophiolite by Leite (1997) and Hartmann and Chemale (2003). The Cerro Mantiqueiras ophiolite is embedded in a tonalite-trondhjemite-granodiorite association, both deformed and metamorphosed in middle amphibolite facies conditions (Hartmann and Remus, 2000; Hartmann and Chemale, 2003). Previous dating of zircon with the U-Pb SHRIMP method established some of the most significant ages in the evolution of the São Gabriel terrane (Table 1).

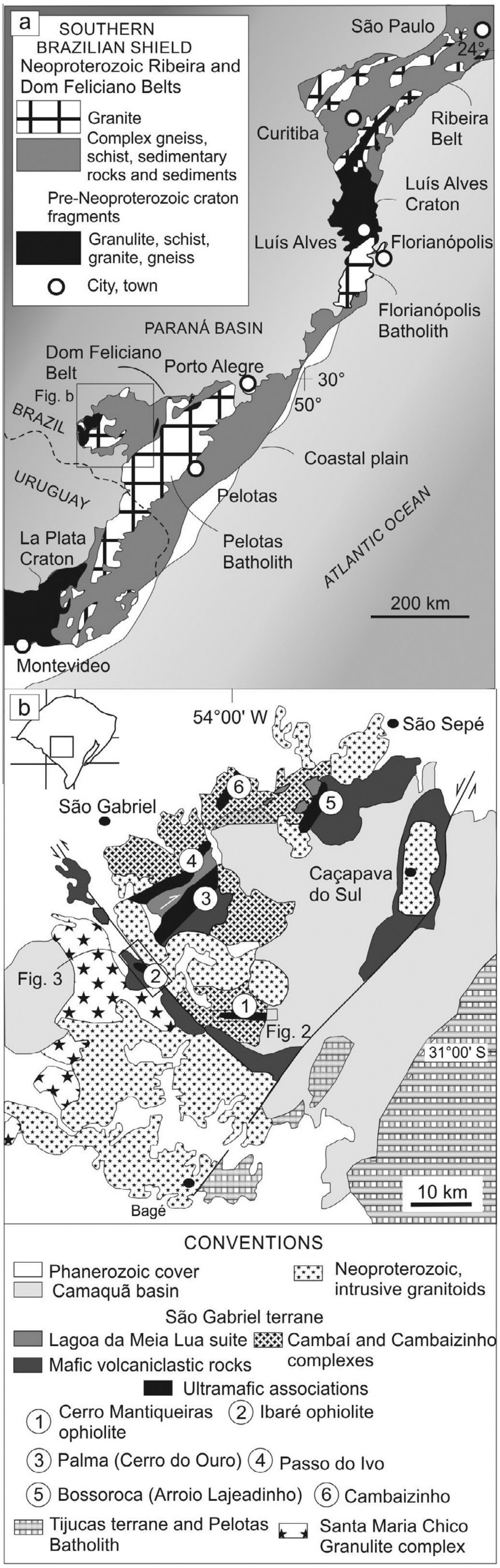

Fig. 1. (a) Geological map of the Brasiliano Orogen in southern Brazil and Uruguay (modified from Salazar et al., 2013); (b) geological map of the São Gabriel terrane and limits (modified from Hartmann et al., 2007).

Table 1
U-Pb geochronological and Nd isotopic data available for the São Gabriel terrane, including this work.

Stratigraphic unit	Rock type	Zircon age (Ma)	εNd	$T_{(DM)}$, Ga
Palma Complex-Campestre Formation	Intermediate volcanic and volcanoclastic rocks	753 ± 2 (rhyolite)[1], 757 ± 17 (dacite) [2]	5.0 – 6.4[7] ($t = 750$)	∼0.9 and 0.77[7]
Palma Complex-Cerro do Ouro Formation	Serpentinite		+6.8[7]	0.65[7]
	Amphibolite		+5.6[7]	0.85[7]
	Magnesian schist		+3.1[7]	1.35[7]
Cambaizinho Complex	Metassedimentary rocks – Felsic gneisses, magnesian schists, serpentinites		2.5[7]	1.18[7]
	Metassedimentary gneisses	840–650[3]		
Passo Feio Complex	Metapelites	948–803[4]		
Cambaí Complex	Diorite – tonalite –trondhjemite – granodiorite gneisses and Santa Zélia granite	750 ± 16 (metatonalite)[5], 735 ± 5 (diorite)[6], 718 ± 2 (tonalite)[6], 690 ± 2 (tonalite)[6], 680 ± 2 (tonalite)[6], 682 ± 1 (granodiorite)[6]	4.3 – 6.3[7]	0.7 and 0.9[7]
Passinho event	Metadiorite	879 ± 14[5]		
	Cerro Mantiqueiras	733 ± 10 (amphibolite)[6]		
	Cerro Mantiqueiras (ophiolite)	923.2 ± 3 (albitite)[8]		
	Ibaré (ophiolite)	892.4 ± 2.8 (albitite)[8]		

[1] Machado et al. (1990; U-Pb conventional), [2] Remus et al. (1999), [3] Lena et al. (2014), [4] Lopes et al. (2015), [5] Leite et al. (1998), [6] Hartmann et al. (2011), [7] Saalmann et al. (2005a), [8] This work. All ages by U-Pb SHRIMP, except as indicated.

The progressive metamorphism of serpentinite led to newly-formed harzburgite in the middle amphibolite facies of orogenic metamorphism (Vance and Dungan, 1977) as described for the Cerro Mantiqueiras ophiolite (Hartmann and Chemale, 2003). The Cerro Mantiqueiras is the largest ultramafic body (Fig. 2) in the southern Brazilian Shield (9.0 × 0.5 km) and its mineral assemblage of olivine + orthopyroxene + chlorite + tremolite characterizes the middle amphibolite facies of orogenic metamorphism that recrystallized the original serpentinite and that preceded the presently observed low to medium intensity serpentinization (Jost and Hartmann, 1984; Leite, 1997).

The Ibaré ophiolite is a volcano-sedimentary succession with voluminous ultramafic rocks (Fig. 3), initially deformed in the greenschist facies of orogenic metamorphism but with a strong overprint of contact metamorphism caused by the intrusion of the Santa Rita Granite (Naumann and Hartmann, 1984; Naumann, 1985). The mineral assemblage olivine + talc (jackstraw texture) indicates low hornblende hornfels facies for large tracts of the ophiolite.

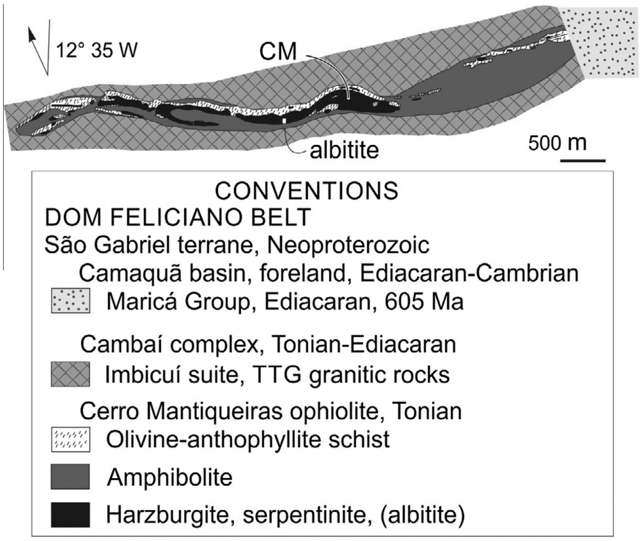

Fig. 2. Geological map of Cerro Mantiqueiras ophiolite (Leite, 1997).

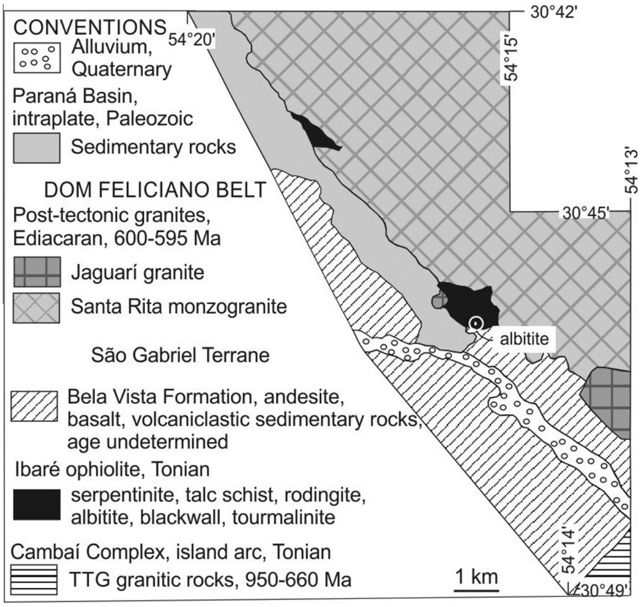

Fig. 3. Geological map of the Ibaré ophiolite (Naumann, 1985).

2.2. Sample description

In this study, the classification of the rocks as albitites is based on the modal composition (>90 vol.% albite). Albitites are commonly considered the product of fractionation or alteration of plagiogranites (e.g., Tilton et al., 1981; Ohnenstetter et al., 1981; Li et al., 2013, 2015). Other origins have been proposed for albitite, including metasomatism of granitic rocks by hydrothermal fluids, direct crystallization from Na rich magma (Schwartz, 1992) and direct precipitation from solution (Harlow, 1994; Johnson and Harlow, 1999). The term oceanic plagiogranite is a general descriptive classification for trondhjemites, tonalites and albite granites associated with ophiolites (Coleman and Peterman, 1975).

In the Cerro Mantiqueiras ophiolite (CM3 sample), albitite occurs in two blocks up to 0.5 m large (6578064 N, 216413 E; datum WGS84) immersed in the harzburgite (Fig. 4a, b, c); the contact of the two rock types was not observed. The albitite is considered part of the ophiolite, because no albitites are

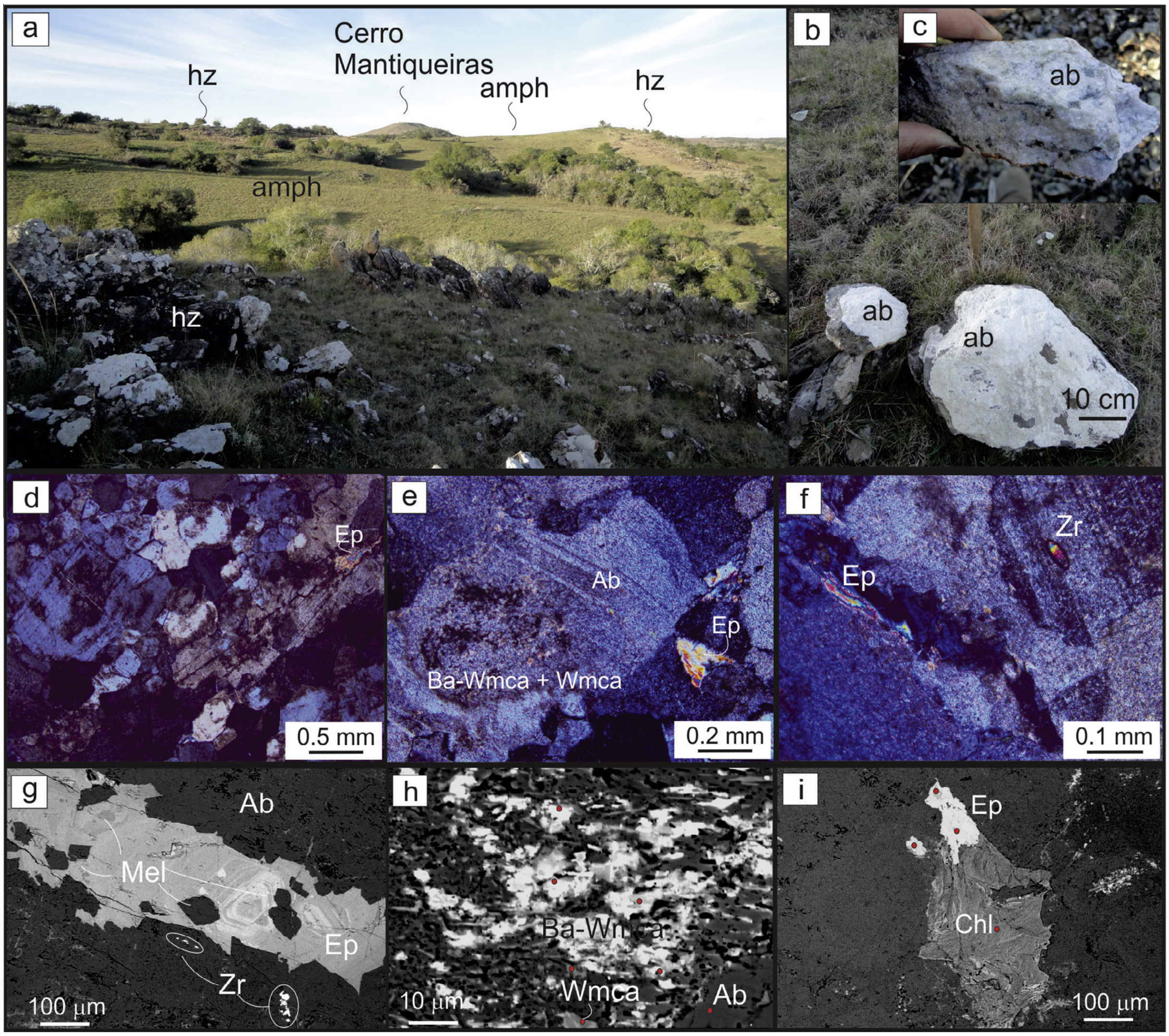

Fig. 4. Selected field photographs, photomicrographies and backscattered electron (BSE) images from the Cerro Mantiqueiras albitite sample (CM3), (a) Harzburgite blocks (white crust are lichens); one of the small blocks is an albitite; (b) Albitite block, broken; hammer handle = 0.5 m; white color = albite; (c) albitite samples; (d) intergrown and polygonal contact between albite crystals; (e) intense alteration of albite to white mica and Ba feldspar; (f) epidote filling fracture and euhedral zircon included in albite; (g) zoned epidote rich in Fe (higher iron = light gray), associated euhedral high relief = soda melilite; (h) detail of contact showing Ba-white mica (light gray) and white mica (medium gray); (i) epidote grain replaced by Mg-Fe chlorite (Chl).

recognized in the TTG association of the São Gabriel Terrane; also, the albitite is not intensely altered that it could have TTG as protolith. The medium-grained albitite is characterized by granoblastic, equigranular to inequigranular texture. The contacts between grains of albite are interlobate to polygonal (Fig. 4d). Albite shows intense alteration to white mica, epidote and other minerals. Ba-white mica (2.92–4.33 wt.% Ba) replaces partly albite (Fig. 4e, h) and a white mica without Ba (medium gray). Zoned epidote occurs filling fractures and associated euhedral soda melilite (Fig. 4g) and replacing albite. Fe-Mg chlorite (Table 2) is associated with epidote (Fig. 4i). The accessory minerals are zircon, apatite, opaques and minor amounts of titanite. Zircon occurs as euhedral crystals included in albite (Fig. 4f) and as minute fragmented crystals; tiny oval zircon grains surrounding epidote are also occasionally observed (Fig. 4g).

The Ibaré albitite (IB2 sample) is 20 × 10 m large (6591173 N, 762629 E; datum WGS 84) and is surrounded by blackwall, the entire metasomatic association immersed in ultramafic rocks (Fig. 5a, b). The TTG association of the São Gabriel Terrane is not present in the region. The albitite is fine-grained showing a hiatale texture and the contact between grains is lobate to interfingered, marked especially by albite (Fig. 5c). Prehnite occurs as subhedral grains replaced by aggregates of Fe-Mg chlorite (Fig. 5d, f; Table 2). Epidote is associated with barite and Ba-feldspar (possibly hyalophane, see Table 2) and occurs replacing albite; white mica also occurs with Ba-white mica (Fig. 5e, g). The accessory minerals are abundant titanite and lesser zircon, apatite and opaque. Chlorite aggregates occasionally surround minute titanite clasts and tiny zircon (Fig. 5f); minute oval titanite grains surrounding prehnite (Fig. 5f) and chlorite (Fig. 5h) are also observed. The Ibaré albitite has significantly more titanite than the Cerro Mantiqueiras albitite.

Quartz is minor in the albitites. The predominant mineral is albite but calcic plagioclase also occurs. Albitization of calcic plagioclase is the most widely recognized metamorphic alteration. The bulk of the plagioclase was altered to cloudy albite and commonly contains patches of the assemblage chlorite, epidote, white mica and Ba-feldspar (Figs. 4 and 5; Table 2).

Table 2
Chemical compositions (wt.%) by electron microprobe of selected silicates from albitites, Cerro Mantiqueiras and Ibaré Ophiolites. (–) = below detection limit, blank = not analyzed.

Albitites	Cerro Mantiqueiras ophiolite					Ibaré ophiolite				
Sample	CM3-C5	CM3-C2	CM3-C5	CM3-C2	CM3-C2	IB2-C2	IB2-C6	IB2-C2	IB2-C7	IB2-C5
Mineral	Oligoclase	Albite	Chlorite	Soda Melilite	Epidote	Albite	Chlorite	Prehnite	Ba-feldspar	Epidote
Dataset/point	1/1	4/1	1/1	4/1	4/1	3/1	10/1	4/1	1/1	8/1
SiO_2	63.86	66.74	26.56	64.39	37.08	67.70	27.32	43.29	56.04	37.30
Al_2O_3	22.53	20.44	22.74	21.66	23.43	19.47	20.96	24.21	20.76	24.77
MgO	–	0.01	21.11	0.01	–	–	20.68	–	–	0.04
K_2O	0.05	0.16	–	0.07	–	0.05	–	–	11.09	–
FeO	0.02	–	16.47	0.25	10.93	0.10	16.25	0.03	0.14	9.37
MnO	–	–	0.20	–	0.05	–	0.70	0.03	–	0.16
CaO	3.99	0.76	0.04	2.62	22.64	–	0.01	26.45	–	22.90
Na_2O	9.65	11.18	–	10.04	0.01	11.70	–	–	0.90	0.02
TiO_2	–	0.01	0.03	0.02	0.02	–	0.04	–	0.25	0.16
BaO	0.04	0.03	–	–	–	–	–	–	10.60	–
Cr_2O_3					–					–
P_2O_5					0.02					0.05
PbO					0.01					0.06
Sum	99.58	99.40	87.14	99.03	94.17	99.05	85.96	93.86	99.45	94.72

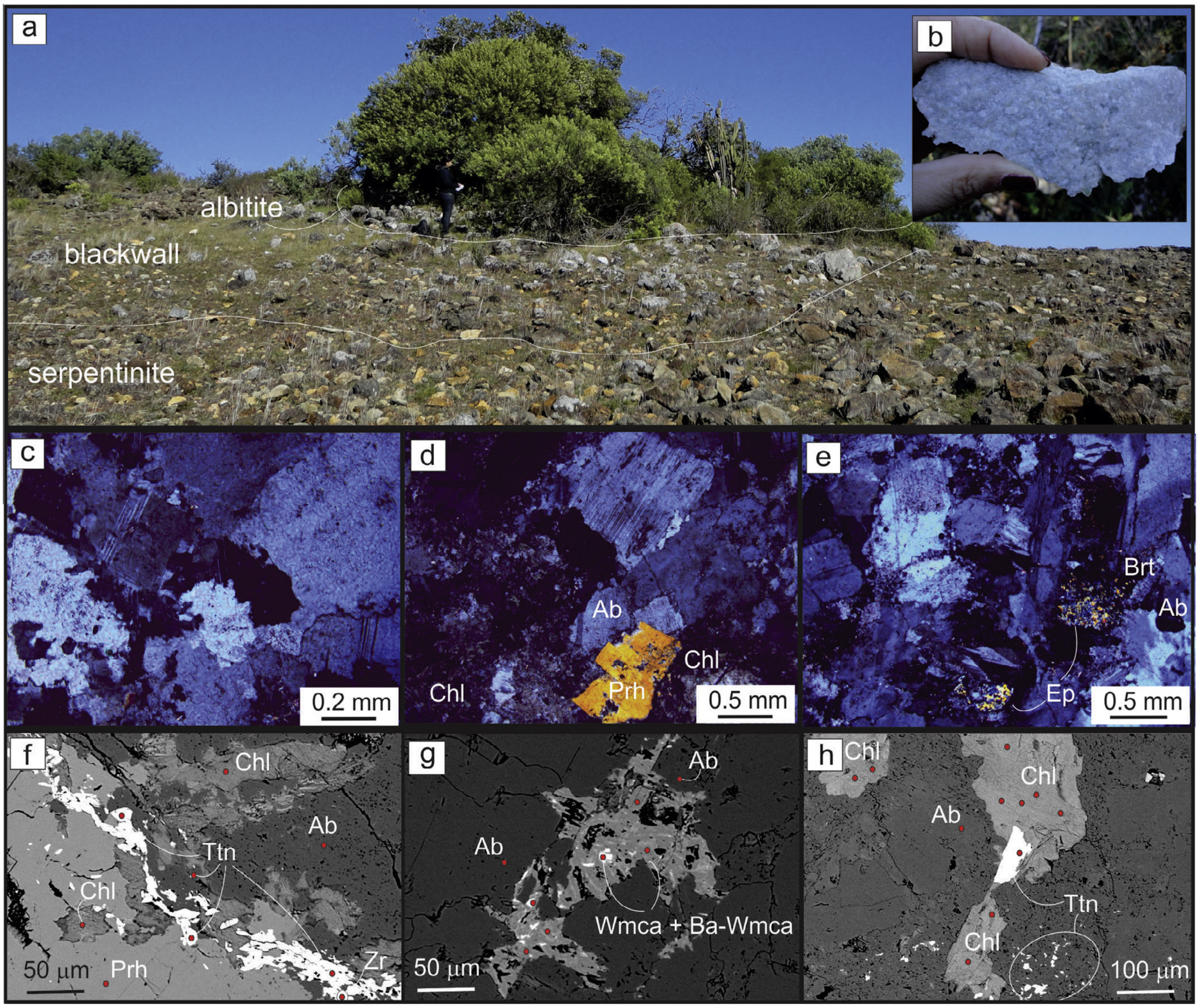

Fig. 5. Selected field photographs, photomicrographs and backscattered electron (BSE) images from the Ibaré albitite sample (IB2); (a) Geological relationships between the albitite and surrounding blackwall and serpentinite; (b) albitite sample; (c) lobate to interfingered contact of albite crystals; (d) prehnite replaced by aggregates of chlorite (e) intense alteration of albite to epidote and associated barite; (f) subhedral prehnita grain partially replaced by Fe-Mg chlorite and associated titanite and a zircon grain; (g) Ba-white mica (Ba = 10 wt.%, light gray) and white mica (k = 14 wt.%; Ba = 0.5–2 wt.%, medium gray).

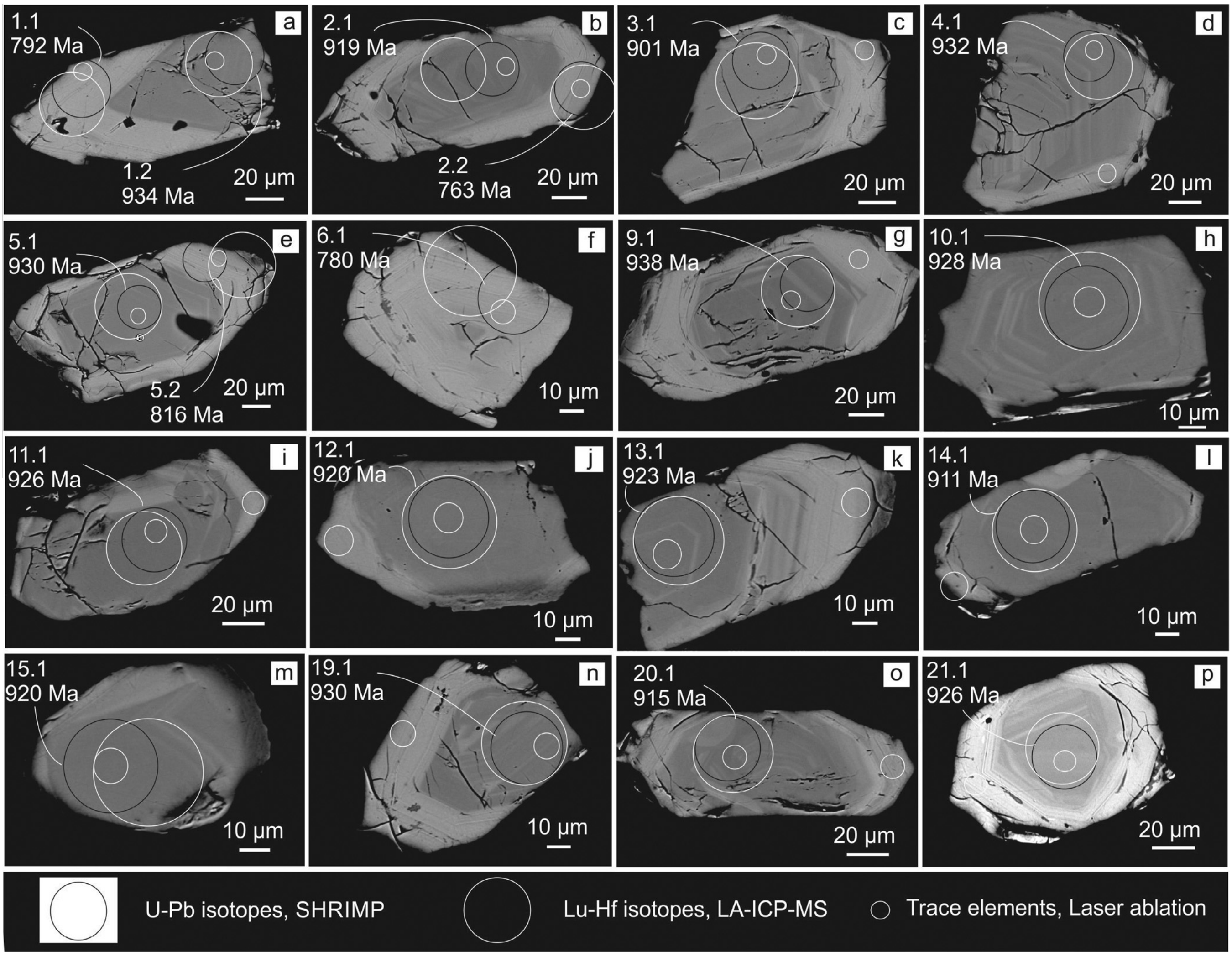

Fig. 6. Cerro Mantiqueiras albitite, CM3 sample. (a–p) Back-scattered electron images with analyzed spots. Black circle = U-Pb ages (Ma); greater white circle = Hf isotopes; smaller white circle = trace elements.

3. Methods

Field studies in the Ibaré and Cerro Mantiqueiras ophiolites led to the discovery of two occurrences of albitite, which were studied for their petrographic, chemical and zircon isotopic characteristics. Zircon separation was made with standard procedures of crushing and milling, heavy liquids and Frantz isodynamic equipment. The zircon grains of each sample were hand-picked and mounted on an epoxy disc together with chips of TEMORA2 (417 Ma) standard and polished to half their thicknesses to reveal the internal structure. Carbon coating of the mount was followed by the documentation of backscattered electron images (BSE) of each crystal at the Laboratório de Geologia Isotópica, Universidade Federal do Rio Grande do Sul. After re-coating with gold, these images were used to guide the isotopic and elemental determinations with probes. The BSE images guided the spot isotopic analyses. Several techniques were used for the characterization of the zircon, as follows.

3.1. Electron microscopy and microprobe

Identification of minerals and their textural relationships were undertaken with a transmission petrographic microscope Olympus BX51, UC30 and also in one polished thin section of each albitite. Chemical compositions of selected silicates from the albitites were obtained using a Cameca SXFive electron microprobe at Laboratório de Microssonda Eletrônica, Universidade Federal do Rio Grande do Sul, with accelerating voltage at 15.0 kV, beam current 15 nA and beam size 5 μm. The minerals were analyzed on the basis of feldspar = 32 O, chlorite = 28 O, prehnite = 22 O, epidote = 25 O, Na-melilite = 14 O. The H_2O content was not determined. Data correction was made using software Peak Sight/ version 5.1.

3.2. U-Pb geochronology

Zircon U-Pb geochronology was performed with the USP SHRIMP-IIe equipment at the Centro de Pesquisas Geocronológicas, Universidade de São Paulo, Brazil. TEMORA2 (417 Ma) standard was used. Weighed mean standard Pb/U:UO/U2 (n = 12) = 00.00354, 2σ error of mean = 1.01%, Calc. 2σ external spot-to-spot error = 2.8%, MSWD = 5.22. The data acquisition was done in bracketing mode and consisted of 1 analysis of standard for each 4 analyses of sample. U-Pb isotopes were determined on 45 zircon crystals separated from the two albitites. In sample CM3, the analyzed zircon grains (n = 24) are euhedral to subhedral, in sample IB2 subhedral (n = 21). Operational conditions of the sensitive high-resolution ion microprobe used spot size of 30 μm, all results

Table 3
SHRIMP U-Pb isotopic analyses (n = 28) of zircon grains from an albitite (CM3), Cerro Mantiqueiras ophiolite.

	U (ppm)	Th/U	Pb (ppm)	Pb_c (%)	Isotopic ratios				Ages		
					$^{206}Pb/^{238}U$	$^{207}Pb/^{235}U$	$^{207}Pb/^{206}Pb$	$^{208}Pb/^{232}Th$	$^{206}Pb/^{238}U$	$^{207}Pb/^{206}Pb$	Disc. (%)
Spot											
CM3-1.1*	3041	0.19	341.9	−0.01	0.1309 ± 1.4	1.17 ± 1.5	0.0647 ± 0.3	0.0393 ± 1.6	792.9 ± 10	764 ± 6	−4
CM3-1.2	81	0.28	10.9	−0.06	0.1559 ± 1.7	1.54 ± 2.3	0.0718 ± 1.6	0.0498 ± 3.8	934.1 ± 14	980 ± 33	5
CM3-2.1	115	0.37	15.2	0.07	0.1533 ± 1.6	1.47 ± 2.1	0.0697 ± 1.3	0.0448 ± 2.8	919.4 ± 13	920 ± 26	0
CM3-2.2*	1613	0.11	174.2	−0.01	0.1258 ± 1.4	1.11 ± 1.5	0.0642 ± 0.4	0.0378 ± 1.9	763.6 ± 10	748 ± 8	−2
CM3-3.1	111	0.35	14.3	0.14	0.1500 ± 1.6	1.43 ± 2.1	0.0690 ± 1.3	0.0453 ± 2.9	901.1 ± 13	900 ± 27	0
CM3-4.1	237	0.55	31.7	0.02	0.1556 ± 1.5	1.51 ± 1.8	0.0703 ± 0.9	0.0478 ± 2.0	932.3 ± 13	937 ± 19	1
CM3-5.1	111	0.34	14.9	0.15	0.1554 ± 1.6	1.49 ± 2.2	0.0693 ± 1.5	0.0471 ± 3.2	930.9 ± 14	909 ± 32	−2
CM3-5.2*	1395	0.07	162.0	0.00	0.1351 ± 1.4	1.23 ± 1.6	0.0658 ± 0.7	0.0499 ± 5.6	816.9 ± 11	799 ± 15	−2
CM3-6.1*	1463	0.18	163.5	0.94	0.1287 ± 1.4	1.18 ± 2.4	0.0663 ± 1.8	0.0399 ± 6.1	780.7 ± 10	816 ± 40	5
CM3-7.1	74	0.25	9.4	−0.16	0.1493 ± 2.3	1.40 ± 7.2	0.0682 ± 6.9	0.0490 ± 4.2	897.3 ± 19	876 ± 142	−2
CM3-8.1*	229	0.09	26.4	0.19	0.1339 ± 1.5	1.21 ± 2.3	0.0658 ± 1.7	0.0435 ± 8.6	810.1 ± 11	799 ± 35	−1
CM3-8.2*	1343	0.10	143.1	0.51	0.1233 ± 1.5	1.09 ± 2.0	0.0640 ± 1.3	0.0376 ± 5.7	749.6 ± 10	741 ± 29	−1
CM3-9.1	102	0.23	13.7	0.02	0.1568 ± 2.1	1.54 ± 2.5	0.0711 ± 1.5	0.0503 ± 4.0	938.9 ± 18	959 ± 30	2
CM3-10.1	87	0.33	11.6	0.09	0.1548 ± 1.7	1.49 ± 2.4	0.0699 ± 1.7	0.0489 ± 3.6	928.0 ± 14	926 ± 36	0
CM3-11.1	36	0.31	4.8	0.36	0.1546 ± 2.0	1.48 ± 3.9	0.0695 ± 3.4	0.0528 ± 6.1	926.5 ± 16	915 ± 70	−1
CM3-12.1	89	0.26	11.7	0.09	0.1535 ± 1.7	1.47 ± 2.2	0.0695 ± 1.5	0.0453 ± 3.6	920.4 ± 14	912 ± 31	−1
CM3-13.1	132	0.43	17.5	0.00	0.1540 ± 1.6	1.46 ± 2.0	0.0687 ± 1.2	0.0473 ± 2.5	923.3 ± 13	891 ± 24	−3
CM3-14.1	94	0.36	12.3	−0.04	0.1519 ± 1.6	1.50 ± 2.1	0.0716 ± 1.3	0.0478 ± 3.0	911.6 ± 14	975 ± 27	7
CM3-15.1	51	0.24	6.7	0.29	0.1535 ± 1.8	1.46 ± 2.9	0.0689 ± 2.3	0.0421 ± 5.8	920.4 ± 15	897 ± 48	−3
CM3-16.1*	2406	0.10	274.0	0.24	0.1322 ± 1.4	1.18 ± 1.6	0.0648 ± 0.6	0.0452 ± 2.7	800.3 ± 10	767 ± 13	−4
CM3-17.1	111	0.40	14.0	0.19	0.1466 ± 1.6	1.39 ± 2.8	0.0689 ± 2.2	0.0446 ± 3.8	881.9 ± 13	894 ± 46	1
CM3-18.1	46	0.25	5.6	0.32	0.1430 ± 1.9	1.38 ± 4.5	0.0699 ± 4.1	0.0427 ± 9.7	861.7 ± 15	925 ± 84	7
CM3-19.1	116	0.36	15.5	0.08	0.1552 ± 1.6	1.50 ± 2.2	0.0701 ± 1.5	0.0476 ± 3.1	930.0 ± 13	931 ± 32	0
CM3-20.1	129	0.43	16.9	0.07	0.1526 ± 1.8	1.50 ± 2.2	0.0711 ± 1.3	0.0447 ± 2.8	915.5 ± 15	960 ± 26	5
CM3-21.1	172	0.42	22.9	0.07	0.1546 ± 1.6	1.48 ± 2.0	0.0695 ± 1.3	0.0453 ± 2.6	926.8 ± 13	915 ± 26	−1
CM3-22.1	138	0.38	17.5	0.10	0.1480 ± 1.6	1.41 ± 2.1	0.0692 ± 1.4	0.0450 ± 3.0	889.5 ± 13	904 ± 28	2
CM3-23.1	164	0.30	22.3	0.22	0.1574 ± 1.6	1.52 ± 2.4	0.0701 ± 1.8	0.0543 ± 3.5	942.2 ± 13	931 ± 37	−1
CM3-24.1*	242	0.23	27.3	0.25	0.1309 ± 1.5	1.19 ± 2.3	0.0656 ± 1.8	0.0398 ± 4.3	793.2 ± 11	795 ± 37	0

All Pb in ratios is radiogenic component. All are corrected for 204Pb; Pb = radioactive Pb; Pb_c = Common Pb; * = dating on rim.

corrected for ^{204}Pb. Data were plotted on concordia diagrams using ISOPLOT/Ex (Ludwig, 2003). Error ellipses on Concordia plots are shown at the 1σ level.

3.3. Zircon Hf isotope analyses

Hf isotopic measurements used a Thermo-Finnigan Neptune multicollector ICP-MS coupled to a Photon-Machines 193 nm laser system, at Departamento de Geologia, Universidade Federal de Ouro Preto, Minas Gerais, Brazil. Data were collected in static mode during 60 s of ablation with a spot size of 50 μm. Nitrogen (∼0.080 l/min) was introduced into the Ar sample-carrier gas. Typical signal intensity was ca. 10 V for ^{180}Hf. The isotopes ^{172}Yb, ^{173}Yb and ^{175}Lu were simultaneously monitored during each analysis step to allow for correction of isobaric interferences of Lu and Yb isotopes on mass 176. The ^{176}Yb and ^{176}Lu were calculated using a $^{176}Yb/^{173}Yb$ of 0.796218 (Chu et al., 2002) and $^{176}Lu/^{175}Lu$ of 0.02658 (JWG in-house value). The correction for instrumental mass bias utilized an exponential law and a $^{179}Hf/^{177}Hf$ value of 0.7325 (Patchett and Tatsumoto, 1980) for correction of Hf isotopic ratios. The mass bias of Yb isotopes generally differs slightly from that of the Hf isotopes with a typical offset of the βHf/βYb of ca. 1.04 to 1.06 when using the $^{172}Yb/^{173}Yb$ value of 1.35274 from Chu et al. (2002). This offset was determined for each analytical session by averaging the βHf/βYb of multiple analyses of the JMC 475 solution doped with variable Yb amounts and all laser ablation analyses (typically n > 50) of zircon with a ^{173}Yb signal intensity of >60 mV. The mass bias behavior of Lu was assumed to follow that of Yb. The Yb and Lu isotopic ratios were corrected using the βHf of the individual integration steps (n = 60) of each analysis divided by the average offset factor of the complete analytical session. The results were calibrated with the standard zircon TEMORA 415 (Hf 0.282680), MUD TANK 730 Ma (Hf 0.282501) and 91500, 1065 Ga (Hf 0.282307). Initial epsilon hafnium value εHf(t) was calculated using a decay constant of 1.865×10^{-11} yr^{-1} (Scherer et al., 2001). The average MORB (DM) 176Lu/177Hf and 176Hf/177Hf of 0.0384 and 0.283165 respectively and a value of 0.0113 for the average continental crust (Taylor and McLennan, 1985; Wedepohl, 1995), 176Lu/177Hf = 0.0336, and 176Hf/177Hf = 0.282785 for CHUR (Bouvier et al., 2008).

3.4. Trace element chemistry of zircon

The zircon chemical composition, particularly rare earth elements and Sr, Y, Nb, Ba, Ta, Th, U, were obtained via LA-ICP-MS (a New Wave 213 laser ablation coupled to a Agilent 7700) at Departamento de Geologia, Universidade Federal de Ouro Preto, Minas Gerais, Brazil (Takenaka et al., 2015). The laser was set to produce spot sizes of 25 μm in diameter, during a period of 30 s at 10 Hz frequency. The data acquisition was done in bracketing mode and consisted of 3 to 4 analyses of standards (NIST 612 and NIST 610) bracketing 10–15 unknowns. The data reduction was done via the Glitter software (GEMOC Laser ICP MS Total Trace Element Reduction), which provides an interactive environment for analytic selection of background and sample signals (Van Achterbergh et al., 2001; Jackson et al., 2004). Instrumental mass bias and ablation depth-dependent elemental fractionation were corrected by tying the time-resolved signal for the unknown zircon to the identical integration window of the primary standard NIST612. NIST 610 was used as a secondary control standard. Errors are derived from the averaged counts for each mass for both the standards and values are then compared to those of the primary and secondary standards, to determine concentrations. For Si, Sr, Nb, Ba, and Y precision is <2.4% (excluding Zr in NIST612 = 17% and Nb in NIST 610 = 9%); for the measured REE, Hf, Th, and U, precision <1.5% (NIST612) and ranges from 0.6 to 5.5% (NIST 610). The precision for Gd is 7.2% and Tm is 7%.

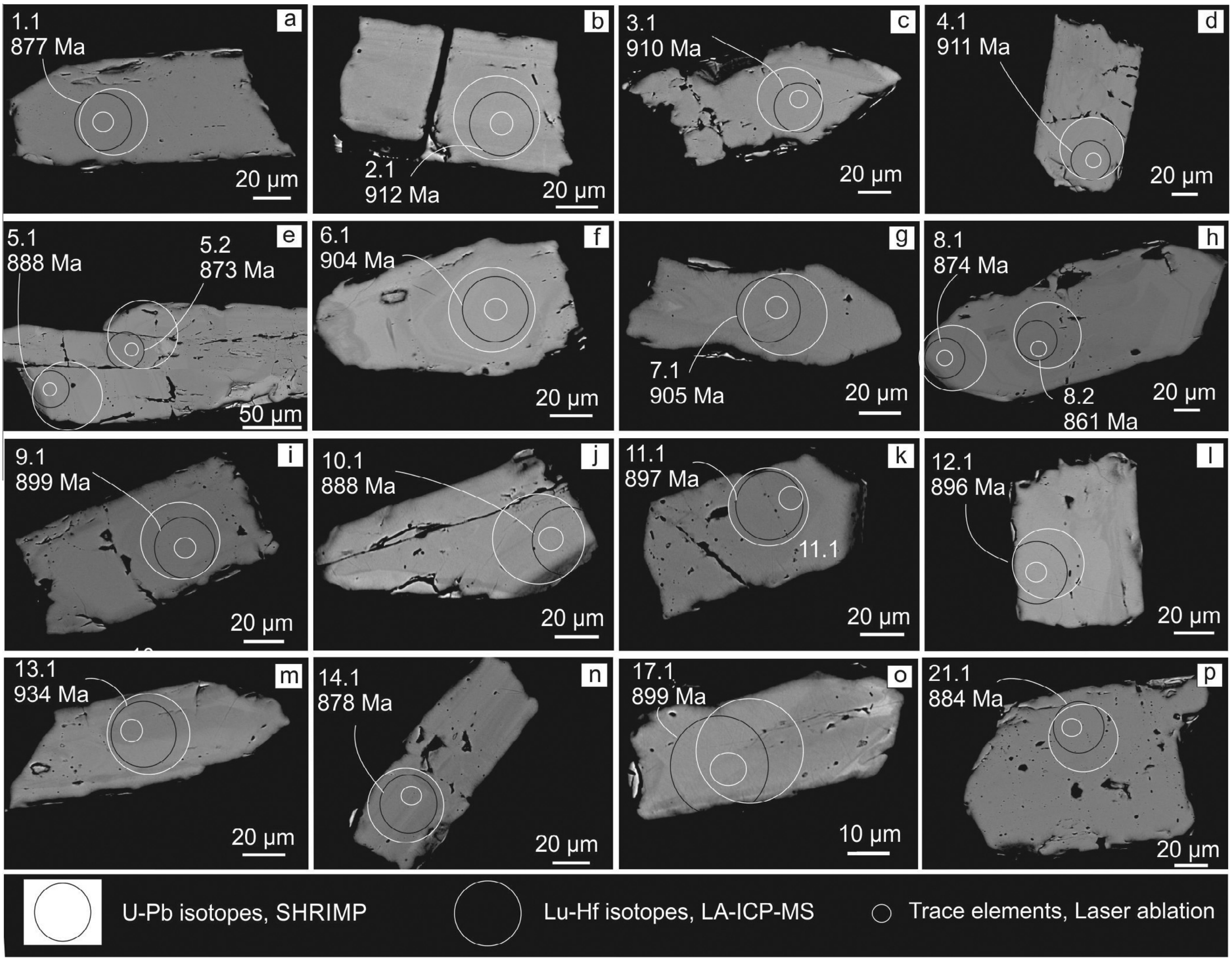

Fig. 7. Ibaré albitite, IB2 sample. (a–p) Back-scattered electron images with analyzed spots. Black circle = U-Pb ages (Ma); greater white circle = Hf isotope; smaller white circle = trace elements.

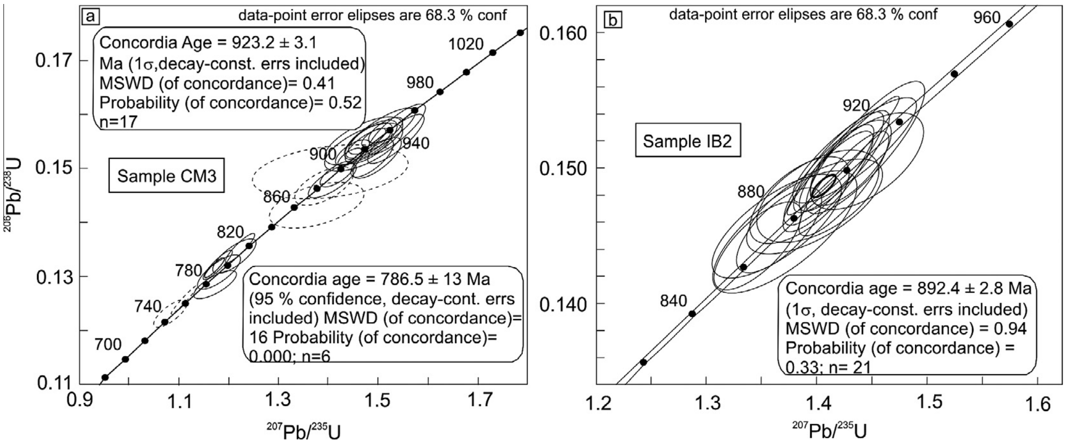

Fig. 8. Concordia ages. (a) Isotopic analyses of CM3 zircon crystals displayed in a concordia diagram; (b) isotopic analyses of IB2 zircon crystals displayed in a concordia diagram. Dotted line ellipses are not included in the average.

4. Results

4.1. Description of zircon

In the Cerro Mantiqueiras albitite (CM3), all zircon grains have a homogeneous to incipiently zoned core (medium gray tone in BSE image) surrounded by a wide, fractured, bright rim (Fig. 6a–p). The zoned cores are characteristic of inherited magmatic grains. The overgrowth occurs commonly along well developed surfaces, but also over corroded and embayed zoned cores (Fig. 6i, l). The rim is richer in U than the core (Table 3), making the rim brighter than the core in BSE images. The zircon

Table 4

SHRIMP U-Pb isotopic analyses (n=21) of zircon grains from an albitite (IB2) sample, Ibaré ophiolite.

	U (ppm)	Th/U	Pb (ppm)	Pb_c (%)	Isotopic ratios				Ages		
					$^{206}Pb/^{238}U$	$^{207}Pb/^{235}U$	$^{207}Pb/^{206}Pb$	$^{208}Pb/^{232}Th$	$^{206}Pb/^{238}U$	$^{207}Pb/^{206}Pb$	Disc. (%)
Spot											
IB2-1.1	111	0.32	13.9	0.08	0.1458 ± 1.6	1.37 ± 2.2	0.0684 ± 1.5	0.0436 ± 3.4	877.6 ± 13	879 ± 31	0
IB2-2.1	122	0.24	15.9	−0.01	0.1521 ± 1.9	1.45 ± 2.2	0.0691 ± 1.2	0.0460 ± 3.4	912.5 ± 16	901 ± 25	−1
IB2-3.1	170	0.28	22.2	0.10	0.1516 ± 1.6	1.44 ± 2.2	0.0690 ± 1.6	0.0451 ± 3.7	910.1 ± 13	897 ± 33	−1
IB2-4.1	395	0.42	51.6	−0.01	0.1518 ± 1.5	1.44 ± 1.6	0.0687 ± 0.7	0.0461 ± 1.9	911.2 ± 12	890 ±14	−2
IB2-5.1	254	0.24	32.5	0.63	0.1478 ± 1.5	1.40 ± 2.7	0.0687 ± 2.2	0.0421 ± 5.2	888.6 ± 12	890 ± 47	0
IB2-5.2	165	0.32	20.6	0.32	0.1451 ± 2.0	1.37 ± 3.0	0.0684 ± 2.3	0.0433 ± 4.5	873.6 ± 16	882 ± 47	1
IB2-6.1	315	0.39	40.8	0.01	0.1506 ± 1.5	1.42 ± 1.8	0.0685 ± 0.9	0.0441 ± 2.2	904.4 ± 13	883 ± 19	−2
IB2-7.1	346	0.28	44.7	−0.04	0.1508 ± 1.5	1.42 ± 1.9	0.0685 ± 1.1	0.0443 ± 2.3	905.2 ± 13	883 ± 23	−2
IB2-8.1	272	0.21	33.9	0.14	0.1452 ± 1.5	1.35 ± 2.4	0.0677 ± 1.8	0.0427 ± 3.5	874.1 ± 12	858 ± 38	−2
IB2-8.2	156	0.27	19.3	0.29	0.1430 ± 1.6	1.36 ± 2.9	0.0688 ± 2.5	0.0410 ± 5.8	861.6 ± 13	892 ± 51	3
IB2-9.1	366	0.27	47.0	−0.04	0.1497 ± 1.5	1.42 ± 1.7	0.0686 ± 0.7	0.0452 ± 2.2	899.2 ± 12	887 ± 15	−1
IB2-10.1	239	0.27	30.4	0.18	0.1477 ± 1.5	1.38 ± 2.1	0.0680 ± 1.5	0.0433 ± 3.5	888.2 ± 13	868 ± 31	−2
IB2-11.1	266	0.32	34.2	0.15	0.1494 ± 1.8	1.42 ± 2.4	0.0689 ± 1.5	0.0437 ± 3.5	897.5 ± 15	895 ± 31	0
IB2-12.1	284	0.32	36.4	0.15	0.1493 ± 1.5	1.42 ± 1.9	0.0691 ± 1.2	0.0430 ± 2.7	896.9 ± 13	903 ± 24	1
IB2-13.1	152	0.32	20.3	−0.12	0.1559 ± 1.6	1.49 ± 1.9	0.0694 ± 1.1	0.0490 ± 3.1	934.2 ± 14	912 ± 22	−2
IB2-14.1	148	0.35	19.1	2.71	0.1460 ± 1.7	1.37 ± 11.7	0.0681 ± 11.4	0.0469 ± 11.7	878.4 ± 14	872 ± 240	−1
IB2-16.1	101	0.24	13.0	0.20	0.1504 ± 1.6	1.45 ± 2.4	0.0698 ± 1.7	0.0493 ± 5.6	903.3 ± 14	924 ± 35	2
IB2-17.1	223	0.21	28.7	0.06	0.1497 ± 1.5	1.41 ± 1.9	0.0684 ± 1.2	0.0442 ± 3.4	899.2 ± 13	880 ± 24	−2
IB2-19.1	329	0.40	42.2	−0.02	0.1492 ± 1.5	1.41 ± 1.8	0.0687 ± 0.9	0.0449 ± 2.2	896.4 ± 12	891 ± 20	−1
IB2-20.1	258	0.26	32.1	0.14	0.1443 ± 1.5	1.35 ± 2.0	0.0677 ± 1.3	0.0412 ± 3.4	868.8 ± 12	860 ± 27	−1
IB2-21.1	114	0.26	14.4	0.23	0.1471 ± 1.6	1.40 ± 2.9	0.0689 ± 2.4	0.0432 ± 5.6	884.6 ± 13	895 ± 49	1

All Pb in ratios is the radiogenic component. All analyses are corrected for 204Pb; Pb = radioactive Pb; Pb_c = Common Pb.

Table 5

LA-MC-ICPMS Lu-Hf isotopes of zircon grains. Ages from U-Pb SHRIMP (Table 3).

Spot	$^{176}Y/^{177}Hf$[a]	±2 s	$^{176}Lu/^{177}Hf$	±2 s	$^{178}Hf/^{177}Hf$	$^{180}Hf/^{177}Hf$	SigHf[b]	$^{176}Hf/^{177}Hf$	±2 s [c]	$^{176}Hf/^{177}Hf(t)$	εHf(t)[d]	±2 s[c]	T_{DM2}[e] (Ga)	Age[f] (Ma)
Cerro Mantiqueiras albitite (sample CM3)														
1.1*	0.0248	29	0.00096	9	1.46723	1.88611	12	0.282605	19	0.282592	9.5	0.7165	0.97	792.9 ± 10
1.2	0.1066	92	0.00399	26	1.46727	1.88601	8	0.282652	26	0.282582	13.7	0.7168	0.91	934.1 ± 14
2.1	0.0750	62	0.00279	17	1.46721	1.88634	9	0.282631	17	0.282583	13.5	0.7168	0.91	919.4 ± 13
2.2*	0.0194	16	0.00080	5	1.46726	1.88602	10	0.282463	20	0.282452	5.3	0.7162	1.23	763.6 ± 10
3.1	0.0302	28	0.00115	8	1.46724	1.88570	11	0.282495	18	0.282476	9.2	0.7165	1.13	901.1 ± 13
4.1	0.0172	14	0.00071	4	1.46719	1.88592	9	0.282486	17	0.282474	9.9	0.7165	1.12	932.3 ± 13
5.1	0.0286	25	0.00109	7	1.46731	1.88649	10	0.282510	20	0.282491	10.5	0.7166	1.08	930.9 ± 14
5.2*	0.0369	40	0.00134	12	1.46725	1.88602	12	0.282516	16	0.282496	8.0	0.7164	1.12	816.9 ± 11
6.1*	0.0868	71	0.00319	20	1.46718	1.88582	12	0.282651	19	0.282604	11.1	0.7166	0.93	780.7 ± 10
7.1	0.0248	20	0.00099	6	1.46722	1.88648	10	0.282584	22	0.282567	12.4	0.7167	0.95	897.3 ± 19
8.1*	0.0339	30	0.00131	9	1.46723	1.88612	15	0.282570	17	0.282550	9.8	0.7165	1.02	810.1 ± 11
8.2*	0.0814	71	0.00309	21	1.46721	1.88517	7	0.282658	21	0.282614	10.7	0.7166	0.92	749.6 ± 10
9.1	0.0214	17	0.00084	5	1.46724	1.88612	11	0.282521	19	0.282506	11.2	0.7166	1.05	938.9 ± 18
10.1	0.0205	16	0.00087	5	1.46719	1.88648	11	0.282543	17	0.282527	11.7	0.7167	1.01	928.0 ± 14
11.1	0.0108	9	0.00046	2	1.46719	1.88592	11	0.282494	18	0.282486	10.2	0.7166	1.10	926.5 ± 16
12.1	0.0235	20	0.00097	6	1.46726	1.88516	9	0.282564	22	0.282547	12.2	0.7167	0.98	920.4 ± 14
13.1	0.0191	15	0.00077	4	1.46724	1.88664	12	0.282560	18	0.282547	12.3	0.7167	0.98	923.3 ± 13
14.1	0.0288	23	0.00116	7	1.46721	1.88518	9	0.282578	19	0.282558	12.4	0.7167	0.96	911.6 ± 14
15.1	0.0179	15	0.00071	4	1.46721	1.88643	13	0.282600	14	0.282587	13.6	0.7168	0.90	920.4 ± 15
16.1*	0.0669	59	0.00257	18	1.46723	1.88498	9	0.282600	19	0.282561	10.0	0.7165	1.00	800.3 ± 10
17.1	0.0271	22	0.00109	6	1.46728	1.88556	9	0.282591	20	0.282573	12.2	0.7167	0.95	881.9 ± 13
18.1	0.0257	22	0.00098	6	1.46725	1.88614	8	0.282557	23	0.282541	10.7	0.7166	1.02	861.7 ± 15
19.1	0.0278	23	0.00110	6	1.46725	1.88600	11	0.282586	21	0.282567	13.1	0.7168	0.94	930.0 ± 13
20.1	0.0148	13	0.00063	4	1.46717	1.88626	10	0.282521	25	0.282510	10.8	0.7166	1.05	915.5 ± 15
21.1	0.0305	30	0.00119	9	1.46724	1.88613	10	0.282512	14	0.282492	10.4	0.7166	1.08	926.8 ± 13
22.1	0.0241	21	0.00093	6	1.46736	1.88567	8	0.282547	24	0.282532	11.0	0.7166	1.02	889.5 ± 13
23.1	0.0569	48	0.00217	14	1.46723	1.88580	10	0.282618	21	0.282579	13.8	0.7168	0.91	942.2 ± 13
24.1*	0.0136	11	0.00054	3	1.46727	1.88611	12	0.282572	20	0.282564	9.9	0.7165	1.00	793.2 ± 11

[a] $^{176}Yb/^{177}Hf = (^{176}Yb/^{173}Yb)$ true × $(^{173}Yb/^{177}Hf)$ meas × (M ^{173}(Yb)/M ^{177}(Hf))b(Hf), b(Hf) = ln ($^{179}Hf/^{177}Hf$ true/$^{179}Hf/^{177}Hf$ measured)/ln ($M^{179}(Hf)/M^{177}(Hf)$), M = mass of respective isotope. The $^{176}Lu/^{177}Hf$ were calculated in a similar way by using the $^{175}Lu/^{177}Hf$ and b(Yb).

[b] Mean Hf signal in volt.

[c] Uncertainties are quadratic additions of the within-run precision and the daily reproducibility of the 40 ppb-JMC475 solution. Uncertainties for the JMC475 quoted at 2SD (2 standard deviation).

[d] Initial $^{176}Hf/^{177}Hf$ and εHf calculated using the apparent Pb-Pb age determined by LA-ICP-MS dating (see column f), and the CHUR parameters: 176Lu/177Hf = 0.0336 and 176Hf/177Hf = 0.282785 (Bouvier et al., 2008).

[e] Two stage model age in billion years using the measured 176Lu/177Hf of each spot (first stage = age of zircon), a value of 0.0113 for the average continental crust (second stage), and average MORB (DM) 176Lu/177Hf and 176Hf/177Hf of 0.0388 and 0.28325, respectively.

[f] $^{206}Pb/^{238}U$ age.

[*] rim.

grains are euhedral to subhedral, aspect ratio 3:1 to 2:1 with length 70–140 μm.

In the Ibaré albitite (IB2), the subhedral zircon grains have aspect ratio 2:1 to 3:1 with lengths 60–100 μm, two grains reaching 180 and 200 μm. In backscattered electron images, the grains are homogeneous without core and rim. The crystals have well developed surfaces, but also present embayements and dissolution features (Fig. 7c,g,h,i,p) and are porous over large portions (Fig. 7a–p).

4.2. U-Pb geochronology

U-Pb isotopic analyses (n = 49) of zircons by SHRIMP are concordant and display ⩽7% discordance for all Cerro Mantiqueiras analyses and ⩽3% discordance in Ibaré (Fig. 8). In the CM3, isotopic analyses (n = 28) of 24 zircon grains were performed on euhedral to subhedral zircon grains. Two distinct Concordia ages are found for the Cerro Mantiqueiras albitite zircons, 923 ± 3 Ma in the cores and 786 ± 13 Ma in the rims (Fig. 8a). Magmatic Th/U = 0.2–0.4 is present in the cores and metamorphic Th/U ⩽ 0.1 in the rims (Table 3). The Th/U ratio is commonly used to distinguish metamorphic from igneous grains (e.g., Hoskin and Black, 2000; Hartmann et al., 2000).

In Ibaré, isotopic determinations (n = 21) on 19 zircon grains resulted in a single age of 892.4 ± 2.8 Ma (Fig. 8b). Th/U = 0.2–0.4 suggest a magmatic origin for the grains (Table 4).

4.3. Lu-Hf isotopic systematics of zircon

In a first evaluation, the calculated Hf-models ages were younger by 1–192 Ma than the U-Pb ages. For instance, the CM3 zircons displayed Hf-model ages between 0.7–0.9 Ga in zircon cores and rims, younger than the corresponding U-Pb ages. The IB2 zircons showed Hf-model ages between 0.6–0.7 Ma, 134–278 Ma younger than U-Pb ages. This occurred because the following ratios were used in the calculation: ^{176}Lu/^{177}Hf = 0.0113 for continental crust, ^{176}Lu/^{177}Hf = 0.0384 and ^{176}Hf/^{177}Hf = 0.283165 for depleted mantle. The Hf-model age data in this study were recalculated according to the current values assumed for depleted mantle ^{176}Hf/^{177}Hf = 0.28325 and ^{176}Lu/^{177}Hf = 0.0388 by Andersen et al. (2009), that we regard as the best estimates for CM3 and IB2 zircons (see Tables 5 and 6).

The ^{176}Hf/^{177}Hf isotopic results for CM3 zircons (n = 24) (Table 5) display a large range in initial Hf isotopes (0.282452–0.282614). In contrast, IB2 zircons (n = 22) (Table 6) have initial ^{176}Hf/^{177}Hf ratios with limited variation (0.282599–0.282673). IB2 zircons show more radiogenic ^{176}Hf/^{177}Hf isotopic ratios than CM3 zircons (Fig. 9a). We obtained Hf-model ages with a range between 0.91–1.23 Ga in CM3 (Table 5). In IB2, Hf-model ages range from 0.75 to 0.93 Ga (Table 6). Some zircon analyses have lower Hf-model age (Tables 5 and 6), but Hf model ages of these analyses are not significantly lower and agree with the U-Pb ages (Fig. 9b). Model ages are only approximations dependent on simplified assumptions about the crust and mantle. The important result is that the Hf data show that the samples are juvenile.

Combining the zircon ages with the zircon εHf(t) results provides evidence that zircon grains in the Cerro Mantiqueiras (CM3) and Ibaré (IB2) crystallized from a juvenile magma. Positive εHf between +8 and +13 (CM3) and between +13 and +15 (IB2) are characteristic of depleted mantle-derived magmas (Fig. 9d).

4.4. Zircon trace elements

Negative Eu and pronounced positive Ce anomalies are observed in all analyzed zircon grains CM3 (Fig. 10a). Samples CM3 (cores) and IB2 (Tables 7 and 8) have similar contents of LREE, but the Ibaré zircons are more enriched in HREE. In sample CM3, the zircon rims are greatly enriched in LREE contents compared to cores. Enrichment is also observed in HREE (Fig. 10a). In the U

Table 6
LA-MC-ICPMS Lu-Hf isotopes of zircon grains. Ages from U-Pb SHRIMP determinations (see Table 4).

Spot name	^{176}Y/^{177}Hf	±2 s	^{176}Lu/^{177}Hf[a]	±2 s	^{178}Hf/^{177}Hf	^{180}Hf/^{177}Hf	SigHf[b]	^{176}Hf/^{177}Hf	±2 s[c]	^{176}Hf/^{177}Hf(t)	εHf(t)[d]	±2 s[c]	T_{DM2}[e] (Ga)	Age[f] (Ma)
Ibaré albitite (sample IB2)														
1.1	0.08794	72	0.00376	23	1.46718	1.88612	10	0.282735	23	0.282673	15.7	0.7169	0.75	877.6 ± 13
2.1	0.05277	43	0.00231	14	1.46725	1.88585	13	0.282650	19	0.282610	14.3	0.7168	0.86	912.5 ± 16
3.1	0.09224	74	0.00374	23	1.46719	1.88596	13	0.282690	20	0.282626	14.8	0.7169	0.83	910.1 ± 13
4.1	0.08589	91	0.00353	32	1.46723	1.88594	13	0.282688	17	0.282628	14.9	0.7169	0.83	911.2 ± 12
5.1	0.05949	76	0.00246	26	1.46722	1.88625	13	0.282661	16	0.282620	14.1	0.7168	0.85	888.6 ± 12
5.2	0.04152	39	0.00181	14	1.46722	1.88542	14	0.282630	19	0.282600	13.0	0.7168	0.90	873.6 ± 16
6.1	0.08958	72	0.00365	22	1.46723	1.88616	13	0.282673	17	0.282610	14.1	0.7168	0.86	904.4 ± 13
7.1	0.10471	84	0.00433	26	1.46732	1.88411	12	0.282722	28	0.282648	15.4	0.7169	0.79	905.2 ± 13
8.1	0.06773	63	0.00282	21	1.46724	1.88557	12	0.282652	18	0.282605	13.2	0.7168	0.89	874.1 ± 12
8.2	0.06461	53	0.00282	18	1.46720	1.88633	14	0.282672	19	0.282627	13.7	0.7168	0.85	861.6 ± 13
9.1	0.06551	73	0.00274	27	1.46724	1.88578	13	0.282664	17	0.282617	14.2	0.7168	0.85	899.2 ± 12
10.2	0.07781	63	0.00322	20	1.46721	1.88568	17	0.282674	19	0.282620	14.1	0.7168	0.86	888.2 ± 13
11.1	0.09339	75	0.00382	23	1.46727	1.88612	16	0.282699	16	0.282634	14.8	0.7169	0.82	897.5 ± 15
12.1	0.07714	64	0.00309	20	1.46719	1.88661	19	0.282687	16	0.282635	14.8	0.7169	0.93	896.9 ± 13
13.1	0.06695	69	0.00280	25	1.46725	1.88576	18	0.282653	20	0.282604	14.5	0.7169	0.86	934.2 ± 14
14.1	0.07718	63	0.00327	20	1.46723	1.88636	18	0.282662	16	0.282608	13.4	0.7168	0.88	878.4 ± 14
16.1	0.07478	60	0.00312	19	1.46718	1.88544	6	0.282652	29	0.282599	13.7	0.7168	0.89	903.3 ± 14
17.1	0.05127	42	0.00221	14	1.46719	1.88623	15	0.282655	15	0.282618	14.2	0.7168	0.85	899.2 ± 13
19.1	0.06168	59	0.00255	20	1.46723	1.88610	16	0.282649	14	0.282606	13.7	0.7168	0.88	896.4 ± 12
20.1	0.06258	57	0.00271	19	1.46728	1.88606	16	0.282688	16	0.282644	14.5	0.7169	0.81	868.8 ± 12
21.1	0.07801	63	0.00337	20	1.46726	1.88622	13	0.282705	18	0.282649	15.0	0.7169	0.80	884.6 ± 13

[a] ^{176}Yb/^{177}Hf = (^{176}Yb/^{173}Yb) true × (^{173}Yb/^{177}Hf) meas × (M ^{173}(Yb)/M ^{177}(Hf))b(Hf). b(Hf) = ln (^{179}Hf/^{177}Hf true/^{179}Hf/^{177}Hf measured)/ln (M^{179}(Hf)/M^{177}(Hf)). M = mass of respective isotope. The ^{176}Lu/^{177}Hf were calculated in a similar way by using the 175Lu/177Hf and b(Yb).

[b] Mean Hf signal in volt.

[c] Uncertainties are quadratic additions of the within-run precision and the daily reproducibilityof the 40 ppb-JMC475 solution. Uncertainties for the JMC475 quoted at 2SD (2 standard deviation).

[d] Initial ^{176}Hf/^{177}Hf and ƐHf calculated using the apparent Pb-Pb age determined by LA-ICP-MS dating (see column f) and the CHUR parameters: 176Lu/177Hf = 0.0336 and 176Hf/177Hf = 0.282785 (Bouvier et al., 2008).

[e] Two stage model age in billion years using the measured 176Lu/177Hf of each spot (first stage = age of zircon), a value of 0.0113 for the average continental crust (second stage), and average MORB (DM) 176Lu/177Hf and 176Hf/177Hf of 0.0388 and 0.28325, respectively.

[f] ^{206}Pb/^{238}U age.

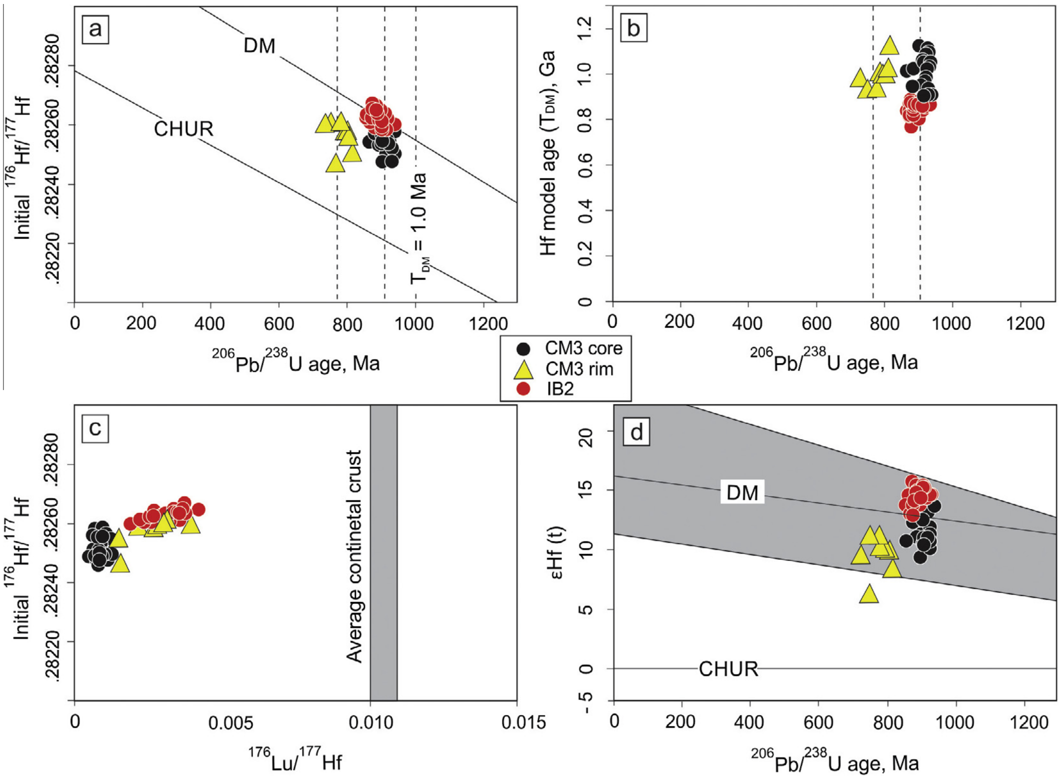

Fig. 9. Crustal evolution diagram with Lu-Hf isotopic system analyses versus U-Pb ages. (a) U-Pb age versus initial $^{176}Hf/^{177}Hf$ showing that IB2 zircons have a more depleted initial Hf isotope signature than CM3 zircons; (b) U-Pb age versus Hf-model age, highlighting igneous and metamorphic events; (c) $^{176}Lu/^{177}Hf$ versus initial $^{176}Hf/^{177}Hf$ showing the difference between the Lu-Hf system of CM3 (core and rim) and IB2; IB2 zircon has higher Lu/Hf ratios; (d) U-Pb ages versus εHf values showing characteristic mantle-derived magma fingerprint. Diagram of Hf compositional field from Gerdes and Zeh (2006). DM = depleted mantle, CHUR = chondrite uniform reservoir.

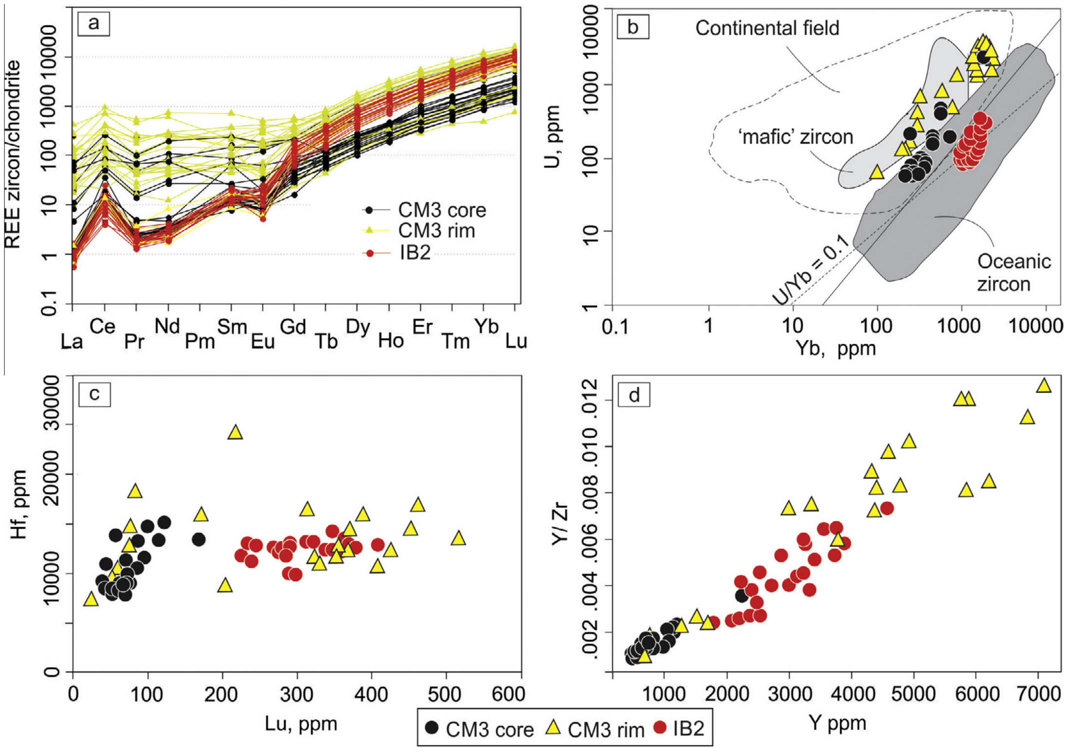

Fig. 10. Geochemical discriminant diagram for zircon trace elements. (a) Chondrite-normalized REE (Boynton, 1984); (b) Yb × U variation diagram for modern oceanic zircon. Light gray field corresponds to 'mafic' zircon continental field (Grimes et al., 2009); (c) Lu versus Hf diagram displaying high concentration of Lu in IB2 zircons and Lu-enrichment in the CM3 rim compared to cores; (d) Y versus Y/Zr diagram showing Y-enrichment in IB2 zircons and in CM3 rims compared with CM3 cores.

Table 7
Major and trace element analyses of zircon from the CM3 sample. * = rim.

Spot	Th	Zr	Y	La	Ce	Pr	Nd	Sm	Eu	Gd	Tb	Dy	Ho	Er	Tm	Yb	Lu	Si	Hf	Pb	U	Sc	Sr	Nb	Ba
1.1*	418.98	480031	5760.91	28.92	153.66	11.40	88.20	27.15	9.28	91.07	33.10	447.91	186.05	913.52	209.63	2134.41	426.41	149580	12284	33.71	3059.05	728.38	11.07	26.25	4.53
1.2	16.55	489334	551.50	2.57	48.39	2.02	18.63	14.16	4.59	21.62	3.51	44.72	16.86	82.25	20.14	209.97	47.00	149580	10890	4.45	66.88	433.52	1.55	6.49	3.5
2.1	296.96	483082	4914.74	22.81	112.89	8.56	66.34	17.29	8.98	58.27	25.65	372.80	154.37	773.83	177.66	1769.76	353.23	149580	12074	21.69	2088.56	669.45	10.0	29.96	3.78
2.2*	43.68	481794	542.65	0.30	8.38	0.24	1.64	1.95	0.65	9.14	2.61	38.49	15.32	86.36	21.39	232.67	51.26	149580	8105	4.58	113.77	256.66	0.33	5.68	1.86
3.1	274.94	624598	2269.01	7.73	116.94	5.79	53.13	28.94	10.76	52.63	16.42	168.81	69.39	320.77	78.51	722.84	167.95	149580	13529	11.89	220.13	389.73	6.98	22.61	12.69
3.2*	34.85	484558	649.99	0.45	12.41	0.40	2.30	2.44	0.53	8.16	3.61	44.87	18.70	96.54	23.62	248.55	55.90	149580	9428	4.50	101.23	233.47	0.41	5.91	2.95
4.1	122.83	499913	614.06	0.39	29.16	0.31	1.72	2.22	0.85	9.68	3.31	44.85	18.47	95.26	24.21	256.09	58.79	149580	8252	9.59	217	228.94	0.38	8.44	3.02
4.2*	116.82	557864	573.23	3.19	37.20	1.97	7.34	11.45	3.57	19.82	2.06	41.43	18.73	92.72	21.49	275.85	58.25	149580	10222	11.81	243.98	246.7	1.87	6.43	19.28
5.1	35.16	509094	858.54	0.32	11.91	0.31	1.80	2.31	0.60	10.88	5.05	62.56	25.77	137.81	30.82	302.16	68.45	149580	8038	1.57	99.99	294.97	0.32	8.09	2.76
5.2*	50.91	592947	1253.88	5.29	66.14	5.78	27.44	18.83	23.32	43.75	5.05	88.86	19.80	60.03	14.15	102.23	24.20	149580	7329	23.14	64.81	303.62	7.74	9.56	42.44
6.1	245.72	545134	4396.15	9.08	81.80	5.34	45.19	11.07	5.30	59.11	22.80	327.04	135.23	675.62	161.52	1576.86	330.84	149580	11003	21.65	1192.42	816.12	2.28	28.82	5.58
7.1	16.64	525130	680.11	0.25	8.39	0.27	2.12	1.99	0.59	9.40	3.63	52.25	21.83	112.06	27.21	277.24	65.40	149580	10550	3.35	69.86	459.34	0.40	5.4	3.24
7.2*	82.55	805452	1756.77	7.80	16.61	6.82	35.05	46.98	11.00	65.06	14.69	167.06	68.27	305.52	75.89	808.54	217.21	149580	24277	24.36	419.68	705.55	5.13	7.09	62.29
8.1*	19.06	545329	515.00	0.28	7.87	0.32	2.27	2.32	0.62	4.12	2.81	37.75	15.25	85.06	21.45	240.07	57.42	149580	13846	2.70	215.90	301.41	0.60	7.36	2.42
8.2*	258.78	613562	4363.50	17.60	324.79	11.43	117.00	50.68	11.33	101.89	28.94	360.66	165.74	728.63	168.78	1680.62	369.71	149580	14486	35.89	1592.93	697.93	6.01	20.64	6.81
9.1	22.64	585448	583.12	76.73	217.61	29.38	149.87	32.05	1.85	26.81	28.94	48.87	18.38	88.67	21.51	218.03	58.01	149580	10885	2.31	88.21	290.11	100.9	6.66	4.04
9.2*	200.03	564231	7108.53	13.72	205.07	13.55	120.96	69.72	26.18	129.53	39.16	565.71	231.89	1131.83	267.84	2531.72	517.41	149580	13476	27.41	1788.77	965.68	4.59	28.61	6.02
10.1	28.79	551748	634.48	0.30	11.15	0.25	1.73	2.10	0.84	11.25	3.79	44.39	18.72	94.54	23.43	242.98	61.43	149580	9494	3.13	85.25	321.64	0.31	5.42	2.60
11.2	28.03	577475	438.93	0.36	7.24	0.32	1.54	2.47	0.93	8.52	2.55	33.14	13.76	68.73	17.35	176.46	45.13	149580	8843	2.84	65.15	309.62	0.4	4.44	2.79
11.1*	54.65	769434	697.87	8.48	46.04	7.96	48.80	22.31	2.93	18.99	4.14	59.69	25.94	115.19	31.09	294.10	81.86	149580	18191	8.37	260.13	492.59	1.91	7.76	8.89
12.1	28.85	576840	766.88	0.29	8.36	0.25	1.70	2.13	0.61	6.73	4.58	58.40	23.19	115.62	28.04	333.84	67.92	149580	10659	3.13	78.43	456.55	0.51	4.19	2.41
12.2*	17.05	601702	527.40	0.28	8.21	0.22	1.70	2.08	0.47	6.31	2.03	37.91	16.16	90.94	24.51	296.95	75.57	149580	12826	2.71	739.03	335.83	0.75	5.49	2.94
13.1	51.67	610297	885.82	0.42	12.25	0.26	2.24	4.63	0.63	17.83	5.71	72.33	30.59	134.91	30.50	306.45	71.06	149580	11377	6.07	123.49	494.36	0.93	6.12	3.27
13.2*	666.83	743376	6207.33	42.85	560.37	31.79	143.52	45.53	25.85	131.95	29.22	402.53	213.80	981.28	227.89	2128.80	462.47	149580	16866	57.56	3307.73	820.56	10.14	51.69	69.52
14.1	28.54	625549	872.96	0.41	11.33	0.29	1.68	2.83	0.52	15.48	5.01	64.99	28.09	135.06	32.96	315.77	80.58	149580	10626	2.08	82.31	500.56	0.40	5.68	3.47
14.2*	53.88	628073	1554.23	14.57	109.48	6.45	34.25	13.31	2.70	24.66	7.90	121.00	52.42	265.95	69.37	713.34	170.59	149580	15948	5.41	699.33	497.11	1.94	9.19	54.55
16.1*	184.70	645946	3772.81	6.92	55.93	2.70	25.32	13.90	4.07	49.27	18.35	286.44	119.38	609.56	153.83	1564.71	359.41	149580	13181	21.21	1906.45	693.15	1.71	29.74	5.55
17.1	53.61	667218	1035.72	1.46	13.09	0.62	2.74	12.61	1.42	18.06	5.80	83.15	32.91	157.94	39.71	366.86	88.13	149580	10467	8.60	157.74	493.03	0.90	4.43	3.11
17.2*	730.54	731030	5845.83	128.62	586.83	65.95	358.76	40.57	20.55	94.06	34.44	477.78	196.22	914.01	216.44	2006.99	452.16	149580	14493	99.24	3598.8	855.12	67.8	42.63	28.98
18.1	32.39	471054	998.93	19.30	214.64	12.33	116.12	46.50	13.34	55.30	5.59	71.26	29.57	159.70	39.13	425.08	99.70	149580	14701	41.29	208.13	475.51	3.8	7.28	17.33
18.2*	126.37	448247	3352.62	84.96	753.97	55.76	441.67	139.17	37.05	148.18	19.29	249.55	96.17	519.05	126.63	1450.10	313.24	149580	16402	252.77	1811.51	637.14	53.81	18.68	101.88
19.1	44.37	456174	992.27	3.49	40.14	1.69	16.19	5.28	2.45	23.46	5.93	81.11	31.54	154.16	34.31	329.68	75.66	149580	9267	4.57	106.10	440.76	0.38	3.95	3.43
19.2*	307.93	415765	2989.51	11.50	143.76	5.09	34.82	8.65	4.32	43.25	15.95	240.12	95.08	471.82	113.49	983.31	202.68	149580	8812	23.88	1326.98	486.51	13.31	24.05	9.15
20.1	32.04	520494	1212.13	0.50	15.38	0.57	3.29	2.96	1.43	14.74	4.89	79.41	33.07	213.75	51.82	514.12	122.22	149580	15286	6.45	473.84	503.06	1.13	9.44	5.82
20.2*	36.46	501308	799.17	32.15	337.69	25.29	173.52	73.13	31.65	95.40	8.45	72.60	24.06	116.22	31.22	316.35	77.39	149580	14697	16.73	416.81	359.84	24.35	7.19	12.39
21.1	13.58	495083	1094.39	15.86	69.08	8.22	44.67	4.66	1.50	11.98	4.29	76.86	32.09	189.46	50.40	504.67	114.66	149580	13419	9.59	407.34	395.19	2.48	4.37	6.23
21.2*	178.37	583450	4775.16	34.51	317.81	27.13	165.28	28.75	14.79	70.58	25.93	397.77	152.99	804.12	201.40	1854.95	389.06	149580	15833	40.35	2580.26	754.82	18.2	24.57	12.29
22.1	69.00	562148	1107.61	0.42	12.97	0.26	2.10	2.86	0.99	20.25	6.85	92.74	34.41	175.34	41.44	402.05	96.86	149580	11611	6.98	189.16	510.53	0.43	4.67	2.77
22.2*	128.41	477881	4590.38	40.55	234.20	21.10	172.63	43.52	13.15	68.93	21.18	336.10	138.12	774.21	179.03	1741.00	367.06	149580	12417	18.39	2004.45	697.39	7.85	27.67	4.41
23.1	34.90	477549	616.20	0.23	10.98	0.22	1.73	2.45	0.84	13.02	3.87	49.47	19.42	98.31	24.08	239.20	60.70	149580	8436	3.46	82.12	256.93	0.42	4.65	1.90
23.2*	485.77	486142	5860.08	10.70	61.99	3.44	24.11	12.22	4.16	83.47	35.55	512.31	193.69	926.08	209.50	1905.23	408.08	149580	10812	42.75	2307.34	846.76	4.79	27.43	4.05
24.1	23.74	467917	451.21	0.32	10.43	0.21	2.23	1.53	0.85	7.68	2.87	35.93	14.49	70.87	17.08	183.15	39.83	149580	9151	5.42	72.53	330.46	0.67	4.03	2.07
24.2*	264.63	482825	4315.57	43.79	96.43	4.89	30.81	8.91	12.12	50.09	19.98	333.37	137.27	694.47	167.21	1584.75	322.50	149580	11546	28.93	2092.7	667.68	10.79	28.59	3.48

Table 8
Major and trace element analyses of zircon from the IB2 sample.

Spot	Th	Zr	Y	La	Ce	Pr	Nd	Sm	Eu	Gd	Tb	Dy	Ho	Er	Tm	Yb	Lu	Si	Hf	Pb	U	Sc	Sr	Nb	Ba
1.1	34.42	534614	2828.27	0.25	7.01	0.187	2.15	3.28	1.48	31.76	11.63	203.49	84.52	458.09	117.11	1211.23	297.30	149580	9831	3.45	105.79	633.07	0.49	3.25	2.03
2.1	37.48	537269	2203.64	0.23	5.04	0.166	1.45	2.30	1.24	26.70	11.02	152.14	64.81	351.14	89.92	966.59	239.97	149580	11358	3.14	116.56	568.91	0.34	4.12	6.50
3.1	34.79	526956	3215.35	0.27	11.78	0.176	1.19	2.15	1.51	34.61	13.62	226.50	96.06	510.20	123.99	1255.01	298.99	149580	9739	4.07	127.92	544.42	0.45	6.98	1.85
4.1	72.09	555128	3532.49	0.25	10.43	0.237	1.27	3.25	0.88	45.08	15.60	247.27	106.10	554.63	144.11	1485.11	351.13	149580	13152	7.25	216.83	615.14	0.40	6.42	2.21
5.1	64.34	570678	3256.09	0.19	8.66	0.232	1.44	2.97	1.21	38.47	14.86	230.42	98.63	510.14	125.89	1301.36	312.03	149580	13178	5.96	218.1	513.8	1.00	6.21	2.78
5.2	60.99	555180	2529.68	0.51	10.63	0.244	1.28	3.15	1.59	31.81	11.82	179.34	72.49	396.44	107.17	1136.88	285.37	149580	11585	7.37	165.42	486.66	0.88	4.66	15.21
6.1	130.47	580173	3754.21	0.20	20.18	0.207	1.51	2.54	1.11	44.38	17.36	277.24	112.88	593.98	146.00	1523.40	354.00	149580	12198	12.62	352.65	517.85	0.81	10.6	1.94
7.1	77.60	626050	4533.99	0.35	12.8	0.42	2.48	3.09	1.82	50.44	19.35	315.44	129.75	689.17	172.21	1805.54	408.53	149580	12882	6.83	322.2	658.05	0.58	8.97	3.71
8.1	53.48	665927	3379.31	0.46	11.41	0.45	4.97	3.50	0.76	28.86	12.58	223.65	98.32	526.58	141.98	1474.63	349.31	149580	14231	4.91	287.89	652.88	0.84	11.62	4.69
8.2	41.38	634758	2395.94	0.29	5.40	0.227	1.47	2.65	0.88	23.59	9.31	160.10	68.70	383.45	100.44	1134.43	280.73	149580	12355	2.95	134.69	560.26	0.93	3.91	1.67
9.1	68.61	665683	3817.29	0.27	10.89	0.243	1.70	3.12	1.03	37.25	16.05	271.40	109.18	585.53	149.69	1558.60	371.96	149580	12630	6.58	258.75	562.05	0.71	9.93	6.23
10.1	54.03	683901	2691.12	0.32	8.33	0.209	2.03	2.12	1.23	24.15	10.81	173.89	76.58	419.18	109.46	1229.13	292.31	149580	12746	5.71	209.85	568.74	0.90	6.49	2.61
11.1	62.42	707451	3710.99	0.23	10.72	0.183	1.69	4.32	0.97	34.81	15.38	252.72	108.53	566.92	145.87	1556.23	362.02	149580	12784	6.03	248.68	608.9	0.55	8.89	2.53
12.1	70.73	716513	3214.06	0.25	11.67	0.28	1.76	3.85	1.39	34.88	15.43	236.42	93.01	480.92	120.05	1254.89	291.54	149580	13238	6.06	210.21	472.24	0.60	6.77	29.44
13.1	58.54	751778	3153.36	0.25	9.34	0.336	1.91	2.89	1.05	28.92	12.92	228.75	92.11	491.18	125.09	1333.21	322.54	149580	13110	6.07	194.21	619.86	1.13	5.32	1.60
14.1	43.83	763121	2981.47	0.27	7.90	0.24	1.82	2.09	1.18	25.57	12.29	194.31	84.06	468.13	126.57	1378.82	338.34	149580	12580	5.21	180.17	661.58	0.76	3.31	7.07
16.1	24.03	755300	1761.59	0.21	3.27	0.252	1.22	2.17	0.54	18.03	6.79	115.74	50.83	288.73	78.22	880.02	226.45	149580	11872	2.84	94.11	522.59	0.77	2.72	2.16
16.2	36.54	776856	2479.25	0.20	7.51	0.209	0.98	1.69	0.43	24.71	10.13	164.72	71.37	387.46	102.01	1121.16	268.13	149580	12751	4.57	172.13	513.44	0.46	7.79	1.88
17.1	25.07	821902	2051.96	0.23	3.60	0.155	1.12	2.69	0.38	15.59	7.63	126.11	56.53	327.84	87.90	988.90	245.99	149580	12972	3.24	145.99	537.47	0.48	3.25	1.90
19.1	55.06	878654	2426.64	0.46	11.12	0.201	1.26	3.25	1.02	24.93	11.50	172.12	70.07	364.73	91.38	986.90	235.22	149580	13195	6.44	201.1	386.54	0.36	6.15	2.55
19.2	56.56	891240	3300.58	0.17	8.23	0.219	1.72	2.72	1.02	28.39	13.64	225.62	94.70	509.85	132.90	1425.51	346.23	149580	12538	4.69	226.31	589.02	3.47	6.81	32.19
20.1	37.39	912161	2245.07	0.30	6.88	0.23	1.18	2.13	0.74	19.79	8.02	140.75	61.33	350.89	94.49	1082.40	274.56	149580	12087	3.19	182.44	524.62	0.90	3.5	17.82
21.1	25.74	956294	2531.17	0.26	5.71	0.169	1.77	3.73	1.01	24.39	10.54	171.15	71.01	404.82	108.13	1164.00	288.56	149580	9997	2.93	98.7	620.62	0.40	2.95	2.16

versus Yb diagram (Fig. 10b), CM3 zircons have compositions overlapping the oceanic and continental fields (Grimes et al., 2007) with U/Yb (core) = 0.23–0.92 and U/Yb (rim) = 0.41–2.49. The IB2 zircons plot in the oceanic zircon field with U/Yb = 0.08–0.18 and three analyses with U/Yb = 0.2. According to Grimes et al. (2015), "approximately 10% of the available MOR zircons analyzed do exhibit uncharacteristically high U/Yb values and overlap the more enriched 'continental survey' of Grimes et al. (2007)." This may be the case for some of the analyzed zircons in this study, particularly from sample CM3.

Lutetium shows a range of zircon compositions. The bivariate diagram Lu versus Hf (Fig. 10c) displays the higher content of Lu in CM3 rim (lower in core) and in IB2 zircons. The concentration of Y is lower in the CM3 than IB2 and rim of CM3. Y versus Y/Zr shows increase in the ratio with increasing Y (Fig. 10d). Closer inspection of zircon grains shows several features indicative of a mechanism of fluid-assisted alteration (without change in the Th/U ratio in IB2). The early stage of transformation generated pores and small dissolution embayments in the zircon crystals (Fig. 7). Local transport of Zr at the thin-section scale is also indicated by the presence of small zircon ($\leqslant 1\ \mu m$) crystals in the matrix (Figs. 4g, 5f).

Enrichment in HREE and Y is observed preferentially in CM3 rim as compared to cores (Fig. 10). In chondrite-normalized Sm/La ratio versus La (ppm), not shown here, CM3 and IB2 zircons plot between the fields defined for magmatic and hydrothermal/porous zircons (Hoskin, 2005; Grimes et al., 2009). This indicates the probable magmatic origin for CM3 core and IB2 zircon compositions probably associated with fluid-assisted alteration. We argue that the IB2 zircons are magmatic with possible early xenotime-type alteration.

5. Discussion

The integration of field studies with BSE images of zircon, U-Pb dating, Lu-Hf isotopic analyses and trace element geochemistry allowed the characterization of ophiolite zircon from the southern Brasiliano Orogen. Early Neoproterozoic ages were obtained from all the zircon.

The Hf isotope data of this study (Fig. 9) are consistent with a major contribution of material derived from a depleted mantle source in CM3 and IB2 zircons. The IB2 zircons have the most depleted initial Hf isotope signature, plotting slightly above the depleted mantle curve relative to CM3 (Fig. 9a, d). This suggests a regional variation, with slightly more radiogenic mantle in Ibaré ophiolite than Cerro Mantiqueiras ophiolite.

CM3 zircons have trace-element compositions overlapping the oceanic and continental fields of Grimes et al. (2007, 2015), but IB2 zircons are oceanic with U/Yb ~0.1 (Fig. 10b). Portner et al. (2011) interpreted a subset of zircons from an E-MORB ophiolite that displays higher U/Yb overlapping the continental field of Grimes et al. (2007) as originating from parent melts with variably enriched mantle sources. Low U/Yb (<0.1) appears to be diagnostic of zircons from differentiated melts of the depleted MORB mantle and higher U/Yb values suggest enriched geochemical reservoirs (Grimes et al., 2015 and references therein). We interpret that the studied Cerro Mantiqueiras and Ibaré zircons crystallized in melts derived from depleted (IB2) or enriched (CM3) mantle.

Different degrees of LREE enrichment are typical of altered or metamict zircons (e.g., Belousova et al., 2015). There is evidence such as the porous aspect of IB2 zircon and metamorphic CM3 rim enrichment in HREE and Y. Only IB2 shows pores, which may be early fluid or melt inclusions. IB2 shows a single age with no evidence for resetting. Therefore, alteration if present must be close in age to magmatic crystallization.

The $^{176}Hf/^{177}Hf$ ratios of the metamorphic zircon component (CM3 rim) are indistinguishable from ratios in the igneous zircon (CM3 core), which is at least 100 Ma older. This suggests that the source of the Zr in the metamorphic zircon was dissolution of the older zircon core. According to Gerdes and Zeh (2009) “zircon overgrowths always have higher initial $^{176}Hf/^{177}Hf$ than previously grown domains, due to the incorporation of additional radiogenic ^{176}Hf formed by ^{176}Lu decay in the rock’s matrix between successive zircon growth events. Incorporation of such ^{176}Hf into zircon domains affected by post-growth alteration is negligible.” Thus, it should be emphasized that the rim component of CM3 zircon grew from a metamorphic fluid, not from a magma, so it may not be meaningful to compare its chemistry to fields established by magmatic zircon (Grimes et al., 2007). The Lu enrichment in the CM3 rims (Fig. 10c) is due to zircon growth from a late metamorphic fluid, so this new metamorphic zircon grew with different Lu/Hf ratios (Fig. 9c). The CM3 zircons show a wide range in the $^{176}Hf/^{177}Hf$ ratios, whereas IB2 shows higher value but limited Hf isotopic variation. This is interpreted as originating from parent melts with variably enriched mantle sources or inhomogeneity in the depleted mantle reservoir.

Ages from the Cerro Mantiqueiras region include amphibolites and associated granitic rocks (Leite, 1997; Leite et al., 1998). Some igneous rocks (750–733 Ma) are younger than the presently-obtained metamorphic age (786 ± 13 Ma). This suggests that the region formed in a protracted process of ophiolite generation, emplacement and subduction-zone generation of juvenile granitic and basaltic magmas.

A younger metamorphic event at 700 Ma recorded in the Cerro Mantiqueiras amphibolite (Leite, 1997; Leite et al., 1998) was not recognized in the studied zircons from the albitites. Geochemical and textural changes in the albitites may have been caused by other metamorphic events between 786–700 Ma (younger than the dated zircons). The zircons do not register low temperature late recrystallization. The Brasiliano evolution in the São Gabriel terrane started (Leite et al., 1998; Saalmann et al., 2011; Philipp et al., 2014) with the creation of intra-oceanic Passinho arc (948–850 Ma), first identified in a metadiorite (ca. 880 Ma), followed by subduction of oceanic crust. This intra-oceanic arc formed due to subduction under the Rio de La Plata craton.

Following the oceanic Passinho arc incorporation into the continental crust, a gap in tectonic activity occurred between 850–786 Ma. The São Gabriel orogeny (Hartmann et al., 2011) occurred afterwards and was responsible for the construction of large sectors of the juvenile terrane. The Cerro Mantiqueiras ophiolite cannot be younger than 786 ± 13 Ma. The results are most significant for the evolution of the Brasiliano Orogen. The two studied ophiolites were generated in the oceanic crust in the Tonian (approximately 923 and 892 Ma) and the Cerro Mantiqueiras ophiolite deformed approximately at 786 Ma, possibly during accretion to the continental crust. The metamorphic zircons (786) may have grown due to burial during the São Gabriel orogeny.

The intense deformation and alteration of Precambrian ophiolites commonly hinder the direct study of mantle-derived minerals, such as olivine, orthopyroxene and spinel (e.g., Hartmann and Chemale, 2003; Stern et al., 2004). The resilient nature of zircon leads to the preservation of U-Pb isotopic compositions for age determination (e.g., Hartmann et al., 2000). Hf isotopic ratios are also preserved and useful for crustal residence studies even in metamorphic cores and rims (e.g., Gerdes and Zeh, 2006, 2009). Trace element compositions of zircon help discriminate between oceanic and continental crust environments of crystallization (Grimes et al., 2007, 2009, 2015).

The combined U-Pb-Hf isotopic and trace-elements data here presented lead to a better understanding of the origin and evolution of the two ophiolites in the Tonian, constraining more tightly the early processes that formed the Brasiliano Orogen.

6. Conclusions

We determined from zircon studies of albitites, integrated with field observations, that both the Ibaré and the Cerro Mantiqueiras rock associations are ophiolites. The data strongly suggest generation in the oceanic crust from a depleted mantle. Hf isotopic data indicate the juvenile character of the ophiolites but from mantle of different compositions in Ibaré compared to Cerro Mantiqueiras. The metamorphic age in the Cerro Mantiqueiras ophiolite is Tonian 786 ± 13 Ma.

We have thus demonstrated the presence of Neoproterozoic ophiolites in the Brasiliano Orogen in the southern Brazilian Shield.

Acknowledgements

This article is part of the PhD thesis by Karine da Rosa Arena at the Programa de Pós-Graduação em Geociências, Universidade Federal do Rio Grande do Sul, Brazil. The investigation was supported financially through a scholarship to Karine R. Arena and grant number 479555/2012-5 to Léo A. Hartmann by Conselho Nacional do Desenvolvimento Científico e Tecnológico (CNPq, Brazilian Government). Support by Colombo C. G. Tassinari and Kei Sato at USP is gratefully acknowledged. Significant contributions to the improvement of the article by two anonymous journal reviewers are gratefully acknowledged. We are grateful to associate editor Wilson Teixeira of the journal for his careful and efficient handling of the manuscript.

References

Ali, K.A., Azer, M.K., Gahlan, H.A., 2010. Age constraints on the formation and emplacement of Neoproterozoic ophiolites along the Allaqi-Heiani suture, South Eastern Desert of Egypt. Gondwana Res. 18, 583–595.

Andersen, T., Andersson, U.B., Graham, S., Aberg, G., Simonsen, S.L., 2009. Granitic magmatism by melting of juvenile continental crust: new constraints on the source of Palaeoproterozoic granitoids in Fennoscandia from Hf isotopes in zircon. J. Geol. Soc. 166, 233–247.

Babinski, M., Chemale Jr., F., Hartmann, L.A., Van Schmus, W.R., Silva, L.C., 1996. Juvenile accretion at 750–700 Ma in Southern Brazil. Geology 24, 439–442.

Belousova, E.A., Jiménez, J.M.G., Graham, I., Griffin, W.L., O’Reilly, S.Y., Pearson, N., Martin, L., Craven, S., Talavera, C., 2015. The enigma of crustal zircons in upper-mantle rocks: Clues from the Tumut ophiolite, southeast Australia. Geology 43, 119–122.

Bouvier, A., Vervoort, J.D., Patchett, P.J., 2008. The Lu–Hf and Sm–Nd isotopic composition of CHUR: constraints from unequilibrated chondrites and implications for the bulk composition of terrestrial planets. Earth Planet. Sci. Lett. 273, 48–57.

Boynton, W.V., 1984. Cosmochemistry of the rare earth elements; meteorite studies. In: Henderson, P. (Ed.), Rare Earth Element Geochemistry. Elsevier Sci. Publ. Co., Amsterdam, pp. 63–114.

Chemale Jr., F., 2000. Evolução Geológica do Escudo Sul-Rio-Grandense. In: Holz, M., De Ros, L.F. (Eds.), Geologia do Rio Grande do Sul. Editora UFRGS, Porto Alegre, pp. 13–52.

Chu, N.C., Taylor, R.N., Chavagnac, V., Nesbitt, R.W., Boella, R.M., Milton, J.A., German, C.R., Bayon, G., Burton, K., 2002. Hf isotope ratio analysis using multi-collector inductively coupled plasma mass spectrometry: an evaluation of isobaric interference corrections. J. Anal. At. Spectrom. 17, 1567–1574.

Coleman, R.G., Peterman, Z.E., 1975. Oceanic plagiogranite. J. Geophys. Res. 80, 1099–1108.

Dilek, Y., Thy, P., 2006. Age and petrogenesis of plagiogranite intrusions in the Ankara mélange, central Turkey. Isl. Arc 15, 44–57.

Fernandes, L.A.D., Tommasi, A., Porcher, C.C., 1992. Deformation patterns in the southern Brazilian branch of the Dom Feliciano belt: a reappraisal. J. South Am. Earth Sci. 5, 77–96.

Fernandes, L.A.D., Menegat, R., Costa, A.F.U., Koester, E., Porcher, C.C., Tommasi, A., Kraemer, G., Ramgrab, G.R., Camozzato, E., 1995. Evolução tectônica do Cinturão Dom Feliciano no Escudo Sul-riograndense: Parte I – uma contribuição a partir do registro geológico. Rev. Bras. Geosci. 25, 351–374.

Furnes, H., de Wit, M., Dilek, Y., 2014. Four billion years of ophiolites reveal secular trends in oceanic crust formation. Geosci. Front. 5, 571–603.

Gahlan, H.A., Azer, M.K., Khalil, A.E.S., 2015. The Neoproterozoic Abu Dahr ophiolite, South Eastern Desert, Egypt: petrological characteristics and tectonomagmatic evolution. Mineral. Petrol. http://dx.doi.org/10.1007/s00710-015-0397-z.

Garfunkel, Z., 2015. The relations between Gondwana and the adjacent peripheral Cadomian domain—constraints on the origin, history, and paleogeography of the peripheral domain. Gondwana Res. 28, 1257–1281.

Gerdes, A., Zeh, A., 2006. Combined U-Pb and Hf isotope LA-(MC)-ICP-MS analyses of detrital zircons: comparison with SHRIMP and new constraints for the provenance and age of an Armorican metasediment in Central Germany. Earth Planet. Sci. Lett. 249, 47–61.

Gerdes, A., Zeh, A., 2009. Zircon formation versus zircon alteration — new insights from combined U-Pb and Lu–Hf in-situ LA-ICP-MS analyses, and consequences for the interpretation of Archean zircon from the Central Zone of the Limpopo Belt. Chem. Geol. 261, 230–243.

Grimes, C.B., John, B.E., Kelemen, P.B., Mazdab, F., Wooden, J.L., Cheadle, M.J., Hanghøj, K., Schwartz, J.J., 2007. The trace element chemistry of zircons from oceanic crust: a method for distinguishing detrital zircon provenance. Geology 35, 643–646.

Grimes, C.B., John, B.E., Cheadle, M.J., Mazdab, F.K., Wooden, J.L., Swapp, S., Schwartz, J.J., 2009. On the occurrence, trace element geochemistry, and crystallization history of zircon from in situ ocean lithosphere. Contrib. Mineral. Petrol. 158, 757–783.

Grimes, C.B., Wooden, J.L., Cheadle, M.J., John, B.E., 2015. ''Fingerprinting'' tectono-magmatic provenance using trace elements in igneous zircon. Contrib. Mineral. Petrol. 170, 46. http://dx.doi.org/10.1007/s00410-015-1199-3.

Harlow, G.E., 1994. Jadeitites, albitites and related rocks from the Motagua fault zone, Guatemala. J. Metamorph. Geol. 12, 49–68.

Hartmann, L.A., Chemale Jr., F., 2003. Mid amphibolite facies metamorphism of harzburgites in the Neoproterozoic Cerro Mantiqueiras Ophiolite, southernmost Brazil. Anais Acad. Bras. Ciênc. 75, 109–128.

Hartmann, L.A., Remus, M.V.D., 2000. Origem e evolução das rochas ultramáficas do Rio Grande do Sul desde o Arqueano até o Cambriano. In: Holz, M., De Ros, L.F. (Eds.), Geologia do Rio Grande do Sul, Porto Alegre: Ed. CECO/UFRGS p. 55–78.

Hartmann, L.A., Leite, J.A.D., Silva, L.C., Remus, M.V.D., McNaughton, N.J., Groves, D.I., Fletcher, I.R., Santos, J.O.S., Vasconcellos, M.A.Z., 2000. Advances in SHRIMP geochronology and their impact on understanding the tectonic and metallogenic evolution of southern Brazil. Aust. J. Earth Sci. 47, 829–843.

Hartmann, L.A., Chemale Jr, F., Philipp, R.P., 2007. Evolução geotectônica do Rio Grande do Sul no Pré-Cambriano. In: Iannuzzi, R., Frantz, J.C. (Eds.), 50 Anos de Geologia. Instituto de Geociências, Porto Alegre, pp. 97–123.

Hartmann, L.A., Philipp, R.P., Santos, J.O.S., McNaughton, N.J., 2011. Time frame of the 753–680 Ma juvenile accretion during the São Gabriel orogeny, southern Brazilian Shield. Gondwana Res. 19, 84–99.

Hartmann, L.A., Lopes, W.R., Savian, J.F., 2016. Integrated evaluation of the geology, aerogammaspectrometry and aeromagnetometry of the Sul-Riograndense Shield, southernmost Brazil. Ann. Braz. Acad. Sci. 88, 75–92.

Hoskin, P.W.O., 2005. Trace-element composition of hydrothermal zircon and the alteration of Hadean zircon from the Jack Hills, Australia. Geochim. Cosmochim. Acta 69, 637–648.

Hoskin, P.W.O., Black, L.P., 2000. Metamorphic zircon formation by solid-state recrystallization of protolith igneous zircon. J. Metamorph. Geol. 18, 423–439.

Jackson, S.E., Pearson, N.J., Griffin, W.L., Belousova, E.A., 2004. The application of laser ablation inductively coupled plasma mass spectrometry to in situ U-Pb zircon geochronology. Chem. Geol. 211, 47–69.

Johnson, C.A., Harlow, G.E., 1999. Guatemala jadeitites and albitites were formed by deuterium-rich serpentinizing fluids deep within a subduction zone. Geology 27, 629–632.

Jost, H., Hartmann, L.A., 1984. Província Mantiqueira – Setor Meridional. In: Almeida, F.F.M., Hasui, Y. (Eds.), O Pré-Cambriano do Brasil. Edgard Blücher, São Paulo, pp. 345–368.

Karaoglan, F.G., Parlak, O., Klotzli, U., Thoni, M., Koller, F., 2013. U-Pb and Sm–Nd geochronology of the Kizildag (Hatay, Turkey) ophiolite: implications for the timing and duration of suprasubduction zone type oceanic crust formation in the southern Neotethys. Geol. Mag. 150, 283–299.

Kounov, A., Graf, J., von Quadt, A., Bernoulli, D., Burg, J.-P., Seward, D., Ivanov, Z., Fanning, M., 2012. Evidence for a ''Cadomian'' ophiolite and magmatic-arc complex in SW Bulgaria. Precambrian Res. 212–213, 275–295.

Leite, J.D., 1997. A origem dos harzburgitos da Sequência Cerro Mantiqueiras e implicações tectônicas para o desenvolvimento do Neoproterozóico da porção oeste do Escudo Sul Riograndense. Porto Alegre. Programa de Pós-Graduação em Geociências, Universidade Federal do Rio Grande do Sul. PhD thesis (in Portuguese).161p.

Leite, J.A.D., Hartmann, L.A., McNaughton, N.J., Chemale Jr., F., 1998. SHRIMP U/Pb zircon geochronology of Neoproterozoic juvenile and crustal-reworked terranes in southernmost Brazil. Int. Geol. Rev. 40, 688–705.

Lena, L.O.F., Pimentel, M.M., Philipp, R.P., Armstrong, R., Sato, K., 2014. The evolution of the Neoproterozoic São Gabriel juvenile terrane, southern Brazil based on high spatial resolution U-Pb ages and $\partial^{18}O$ data from detrital zircons. Precambrian Res. 247, 126–138.

Lenz, C., Porcher, C.C., Fernandes, L.A.D., Masquelin, H., Koester, E., Conceição, R.V., 2013. Geochemistry of the Neoproterozoic (800–767 Ma) Cerro Bori orthogneisses, Dom Feliciano Belt in Uruguay: tectonic evolution of an ancient continental arc. Mineral. Petrol. 107, 785–806.

Li, X.-H., Faure, M., Lin, W., Manatschal, G., 2013. New isotopic constraints on age and magma genesis of an embryonic oceanic crust: The Chenaillet Ophiolite in the Western Alps. Lithosphere 160–161, 283–291.

Li, X.-H., Faure, M., Rossi, P., Lin, W., Lahondère, D., 2015. Age of Corsica ophiolites revisited: Insights from in situ zircon U-Pb age and O–Hf isotopes. Lithosphere 220–223, 179–190.

Lissenberg, C.J., Rioux, M., Shimizu, N., Bowring, S.A., Mével, C., 2009. Zircon dating of oceanic crustal accretion. Science 323, 1048–1050.

Lopes, C.G., Pimentel, M.M., Philipp, R.P., Gruber, L., Armstrong, R., Junges, S., 2015. Provenance of the Passo Feio Complex, Dom Feliciano Belt: implications for the age of supracrustal rocks of the São Gabriel Arc, southern Brazil. J. South Am. Earth Sci. 58, 9–17.

Ludwig, K.R., 2003. Isoplot/Ex Version 3.00: A Geochronological Toolkit for Microsoft Excel. Berkeley Geochronology Center, Berkeley, CA.

Machado, N., Koppe, J.C., Hartmann, L.A., 1990. A late Proterozoic U-Pb age for the Bossoroca belt, Rio Grande do Sul, Brazil. J. South Am. Earth Sci. 3, 87–90.

Morag, N., Avigad, D., Gerdes, A., Belousova, E., Harlavan, Y., 2011. Crustal evolution and recycling in the northern Arabian-Nubian Shield: new perspectives from zircon Lu–Hf and U-Pb systematics. Precambrian Res. 186, 101–116.

Naumann, M.P., 1985. O complexo Vulcano-sedimentar-ultramáfico e granitoides da região de Ibaré, RS. Porto Alegre. Programa de Pós-Graduação em Geociências, Universidade Federal do Rio Grande do Sul. Master's thesis (in Portuguese). 161p.

Naumann, M.P., Hartmann, L.A., 1984. Cornubianitos ultramáficos e matassomatitos associados da região do Arroio Corticeiras. In: Congresso Brasileiro de Geologia 33, Rio de Janeiro. Brazilian Society of Geology. In Portuguese. 9, 4279–4290.

Ohnenstetter, M., Ohnenstetter, D., Vidal, P., Cornichet, J.D.H., Mace, J., 1981. Crystallization and age of zircon from Corsican ophiolitic albitites: consequences for oceanic expansion in Jurassic times. Earth Planet. Sci. Lett. 54, 397–408.

Patchett, P.J., Tatsumoto, M., 1980. A routine high-precision method for Lu-Hf isotope geochemistry and chronology. Contrib. Miner. Petrol. 75, 263–267.

Pedersen, R.B., Searle, M.P., Carter, A., Bandopadhyay, P.C., 2010. U-Pb zircon age of the Andaman ophiolite: implications for the beginning of subduction beneath the Andaman-Sumatra arc. J. Geol. Soc. (London) 167, 1105–1112.

Pertille, J., Hartmann, L.A., Philipp, R.P., Petry, T.S., Lana, C.C., 2015. Origin of the Ediacaran Porongos Group, Dom Feliciano Belt, southern Brazilian Shield, with emphasis on whole rock and detrital zircon geochemistry and U-Pb, Lu-Hf isotopes. J. South Am. Earth Sci. 64, 69–93.

Philipp, R.P., Lusa, M., Basei, M.A.S., Hartmann, L.A., Santos, J.O.S., 2014. Oldest age of magmatism in the Passinho arc in the southwestern portion of Gondwana, Rio Grande do Sul, Brazil. IX South American Symposium on Isotope Geology, São Paulo, p. 1.

Pimentel, M.M., Fuck, R.A., 1992. Neoproterozoic crustal accretion in central Brazil. Geology 20, 375–379.

Portner, R.A., Daczko, N.R., Murphy, M.J., Pearson, N.J., 2011. Enriching mantle melts within a dying mid-ocean spreading ridge: Insights from Hf-isotope and trace element patterns in detrital oceanic zircon. Lithosphere 126, 355–368.

Queiroga, G.N., Pedrosa-Soares, A.C., Noce, C.M., Alkmim, F.F., Pimentel, M.M., Dantas, E., Martins, M., Castañeda, C., Suita, M.T.F., Prichard, F., 2007. Age of the Ribeirão da Folha ophiolite, Araçuaí Orogen: The U-Pb zircon dating of a plagiogranite. Geonomos 15, 61–65.

Remus, M.V.D., McNaughton, N.J., Hartmann, L.A., Koppe, J.C., Fletcher, I.R., Groves, D.I., Pinto, V.M., 1999. Gold in the Neoproterozoic juvenile Bossoroca Volcanic Arc of Southernmost Brazil: isotopic constraints on timing and sources. J. South Am. Earth Sci. 12, 349–366.

Ribeiro, M., Fantinel, L.M.A., 1978. Associações petrotectônicas do Escudo Sul-Riograndense. Iheringia, Série Geológica. Porto Alegre (In Portuguese) 5, 19–54.

Rioux, M., Bowring, S., Keleme, P., Gordon, S., Miller, R., Dudás, F., 2013. Tectonic development of the Semail ophiolite: high-precision U-Pb zircon geochronology and Sm-Nd isotopic constraints on crustal growth and emplacement. J. Geophys. Res. Solid Earth 118, 2085–2101.

Saalmann, K., Hartmann, L.A., Remus, M.V.D., Koester, E., Conceição, R.V., 2005a. Sm–Nd isotope geochemistry of metamorphic volcano-sedimentary successions in the São Gabriel belt, southernmost Brazil: evidence for the existence of juvenile Neoproterozoic oceanic crust to the east of the La Plata Craton. Precambrian Res. 136, 159–175.

Saalmann, K., Remus, M.V.D., Hartmann, L.A., 2005b. Geochemistry and crustal evolution of volcano-sedimentary successions and orthogneisses in the São Gabriel belt, southernmost Brazil – relics of Neoproterozoic magmatic arcs. Gondwana Res. 8, 143–162.

Saalmann, K., Remus, M.V.D., Hartmann, L.A., 2006. Tectonic evolution of the Neoproterozoic São Gabriel block, southern Brazil: Constrain on Brasiliano orogenic evolution of the Rio de La Plata. J. South Am. Earth Sci. 21, 204–227.

Saalmann, K., Gerdes, A., Lahaye, Y., Hartmann, L.A., Remus, M.V.D., Läufer, A., 2011. Multiple accretion at the eastern margin of the Rio de la Plata craton: the prolonged Brasiliano orogeny in southernmost Brazil. Int. J. Earth Sci. 100, 355–378.

Salazar, E., Coloma, F., Creixell, C., 2013. Geología del área El Tránsito-Lagunillas, Región de Atacama. Servicio Nacional de Geología y Minería, Carta Geológica de Chile, Serie Geología Básica 149.

Samson, S.D., Inglis, J.D., D'Lemos, R.S., Admou, H., Blichert-Toft, J., Hefferan, K., 2004. Geochronological, geochemical, and Nd–Hf isotopic constraints on the origin of Neoproterozoic plagiogranites in the Tasriwine ophiolite, Anti-Atlas orogen, Morocco. Precambrian Res. 135, 133–147.

Schaltegger, U., Desmurs, L., Manatschal, G., Müntener, O., Meier, M., Frank, M., Bernoulli, D., 2002. The transition from rifting to sea-floor spreading within a magma-poor rifted margin: field and isotopic constraints. Terra Nova 14, 156–162.

Scherer, E.E., Münker, C., Mezger, K., 2001. Calibration of the lutetium–hafnium clock. Science 293, 683–687.

Schwartz, M.O., 1992. Geochemical criteria for distinguishing magmatic and metasomatic albite-enrichment in granitoids: examples from Ta-Li granite Yivhun (China) and the Sn-W deposit Tikus (Indonesia). Mineral. Dep. 27, 101–108.

Stern, R.J., Johnson, P.R., Kröner, A., Yibas, B., 2004. Neoproterozoic ophiolites of the Arabian-Nubian Shield. In: Kusky, T. (Ed.) Precambrian Ophiolites and Related Rocks. Developments in Precambrian Geology, Vol. 13 (K.C. Condie, Series Editor), Elsevier. 3, 95–128.

Szubert, C.C., Kirchner, C.A., Garcia, C.A., Andreotti, J.L.S., Shintaku, I., 1977. Projeto Cobre nos Corpos Básico-Ultrabásicos e Efusivas do Rio Grande do Sul. Porto Alegre, CPRM/DNPM (In Portuguese). 2, 113 p.

Takenaka, L.B., Lana, C., Scholz, R., Nalini, H.A. (Jr.), Abreu, A.T., 2015. Optimization of the in-situ U-Pb age dating method via LA-Quadrupole-ICP-MS with applications to the timing of U-Zr-Mo mineralization in the Poços de Caldas Alkaline Complex, SE Brazil. J. South Am. Earth Sci. http://dx.doi.org/10.1016/j.jsames.2015.04.007.

Taylor, S.R., McLennan, S.M., 1985. The Continental Crust: Its Composition and Evolution. Blackwell Scientific Publication, Carlton, p. 312.

Tilton, G.R., Hopson, C.A., Wright, J.E., 1981. Uranium-lead isotopic ages of the Samail Ophiolite, Oman, with applications to Tethyan ocean ridge tectonics. J. Geophys. Res. 86, 2763–2775.

Tommasi, A., Fernandes, L.A.D., Pinheiro Machado, R., Kraemer, R., Koester, E., 1994. Incorporação de lascas do manto à crosta continental nas porções externas do Cinturão Dom Feliciano – evidências de uma zona de cisalhamento litosférica. Pesquisas (Porto Alegre) 21, 79–84.

Van Achterbergh, E., Ryan, C.G., Jackson, S.E., Griffin, W.L., 2001. Data reduction software for LA–ICP–MS. In: Sylvester, P.J. (Eds.), Laser ablation-ICP mass spectrometry in the Earth Sciences: Principles and applications, Mineralogical Association of Canada, Short Course, [Ottawa, Ontario] v. 29, p. 239–243.

Vance, J.A., Dungan, M.A., 1977. Formation of peridotites by deserpentinization in the Darrington and Sultan areas, Cascade Mountains, Washington. Geol. Soc. Am. 88, 1497–1508.

Wedepohl, K.H., 1995. The compositions of the continental crust. Geochim. Cosmochim. Acta 59, 1217–1232.

Gondwana Research 49 (2017) 296–332

Contents lists available at ScienceDirect

Gondwana Research

journal homepage: www.elsevier.com/locate/gr

Tonian emplacement of ophiolites in the southern Brasiliano Orogen delimited by U-Pb-Hf isotopes of zircon from metasomatites

Karine R. Arena [a],*, Léo A. Hartmann [a], Cristiano Lana [b]

[a] Instituto de Geociências, Universidade Federal do Rio Grande do Sul, Avenida Bento Gonçalves, 9500, 91501-970 Porto Alegre, Rio Grande do Sul, Brazil
[b] Departamento de Geologia, Escola de Minas, Universidade Federal de Ouro Preto, Morro do Cruzeiro, 35400-000 Ouro Preto, Minas Gerais, Brazil

ARTICLE INFO

Article history:
Received 18 November 2016
Received in revised form 17 May 2017
Accepted 29 May 2017
Available online 15 June 2017

Editor. A.S. Collins

Keywords:
Ophiolite
Metasomatite
Zircon
U-Pb-Hf isotopes
Brasiliano Orogen

ABSTRACT

Key parameters in the evolution of the oceanic crust in the little-known Tonian period of the Brasiliano Orogen are presently established through the finding and characterization of zircon in chloritite and tourmalinite enclosed in serpentinite. The Ibaré and Palma ophiolites were selected for the study and both are from the juvenile São Gabriel terrane, Rio Grande do Sul state, Brazil. U-Pb and Lu-Hf isotopic analyses of zircon from metasomatites and a volcanoclastic rock with laser ablation indicate similar ages in both ophiolites, respectively 726 ± 2 Ma and 722 ± 3 Ma (metasomatites) and 758 ± 4 Ma (volcanoclastic rock). Other three representative ages recorded in the metasomatites are 880 ± 12, 836 ± 6 and 780 ± 5 Ma, interpreted as successive serpentinization events. Mantle Hf isotope compositions of zircon in the metasomatites range from εHf = +12.1 to +1.4 and in the volcanoclastic rock the sample displays εHf = +11.7 to +6.7. Zircon geochemistry is close to the mantle array. This direct dating of ophiolites sets new limits to the evolution of the Brasiliano Orogen during formation of Gondwana. The youngest possible age for ophiolite accretion is 722 Ma.

1. Introduction

The timing of ophiolite generation and emplacement into the continental crust is a significant parameter for the reconstruction of supercontinents. Reconstructing the travel history of the oceanic crust from mid-ocean spreading center to accretion into intra-oceanic island arc is a significant challenge in the geological evolution of continents.

The emplacement and deformation age of Precambrian ophiolites is commonly limited to dating of associated oceanic plagiogranites (e.g., Samson et al., 2004; Dilek and Thy, 2006; Queiroga et al., 2007; Pedersen et al., 2010; Karaoglan et al., 2013; Rioux et al., 2013) or albitite (Arena et al., 2016). Field relationships commonly indicate the tectonic relations between serpentinized peridotite and adjacent rocks (Froitzheim and Rubatto, 1998). The study of zircon from metasomatites in serpentinites caused an advance in the correct timing of ophiolite evolution (Schaltegger et al., 2002; Beard et al., 2002; Dubińska and Wiewióra, 1999; Dubińska et al., 2004; Li et al., 2013) and this has led to the direct dating of the alteration process of the serpentinite in the oceanic crust. Large bodies of serpentinite are commonly ascribed to mantle sections of ophiolites (e.g., Deschamps et al., 2013), so the dating of zircon in rodingite or chloritite from the blackwall can be a decisive age parameter. The metasomatic rocks contain information regarding the origin and evolution of the serpentinite in the mantle and crust, as well as the geological environment of formation. The rocks may indicate the tectonic environment of generation and also provide information on the alteration path along their incorporation into the continental crust. The Tonian terranes of the Brasiliano Orogen and their relationship with Rodinia or with the processes of Gondwana fusion have been characterized in some regions (Rapela et al., 2007; Rapela et al., 2011; Casquet et al., 2012; Brito Neves et al., 2014; Philipp et al., 2016), and the direct dating of the oceanic crust in southwest Gondwana has been done by Arena et al. (2016).

We selected two ophiolites from the juvenile Neoproterozoic São Gabriel terrane because they are remnants of the oceanic crust and mantle formed during the rupture of Supercontinent Rodinia at 900–750 Ma and agglomeration of Gondwana at 750–600 Ma. In the ophiolites, we investigated metasomatites, particularly chloritite and tourmalinite from serpentinites but also associated a volcanoclastic rock and an intrusive granite, to delimit the accretion of the oceanic crust to an intra-oceanic arc. This paper presents a combined zircon U–Pb and Lu–Hf isotopic and trace element geochemical study by laser ablation. The spot analyses on the same crystals were controlled by backscattered electron images. This first direct dating of the alteration process of serpentinite in the oceanic crust and its emplacement

---

* Corresponding author.
E-mail addresses: karinearena@gmail.com (K.R. Arena), leo.hartmann@ufrgs.br (L.A. Hartmann), cris.lana@pq.cnpq.br (C. Lana).

http://dx.doi.org/10.1016/j.gr.2017.05.018
1342-937X/

in the southern Brasiliano Orogen establishes the age of 722 Ma for the main peak during the collision of the ophiolites with the arc.

2. Geological setting

The Brazilian Shield underlies discontinuously a large extent of South America to the east of the Andes (e.g., Hartmann and Delgado, 2001), including the Brasiliano Orogen (3000 km N-S and 1000 km E-W) and was part of Gondwana (Fig. 1a, b). This orogen is comparable in extent and timing (900–500 Ma) to the Pan-African Orogen (Stern et al., 2004). Numerous ophiolites were described in NE Africa and dated from associated granitic and volcanic rocks (Samson et al., 2004; Ali et al., 2010).

The Brasiliano Orogen includes mobile belts of Neoproterozoic and Cambrian rocks in addition to Pre-Neoproterozoic basement reworked during collision. The ophiolites in Brazil (Fig. 1b) represent remnants of Neoproterozoic oceanic crust, and in southern Brazil they are concentrated in the juvenile São Gabriel terrane. The ophiolites contain metasomatites (rodingite, chloritite, tourmalinite) formed during the serpentinization process (Garcia, 1980; Naumann, 1985). The oceanic rocks are enclosed in volcanoclastic rocks, considered an intra-oceanic arc.

The selected ophiolites from southernmost Brazil are part of the Sul-Riograndense shield, in the southern portion of the Brazilian Shield (Fig. 1b, c). They are part of the Neoproterozoic Dom Feliciano Belt. This belt has a Paleoproterozoic basement with small volumes of Archean rocks that constitute overall the Rio de la Plata Craton. The main recognized craton exposures occur in Argentina (Tandilia Belt; Cingolani et al., 2002), in the basement of Uruguay (Piedra Alta and Nico Pérez terranes; Dalla Salda et al., 1988) and in southern Brazil (Taquarembó terrane; Hartmann, 1998; Hartmann et al., 1999) to the southwest of the São Gabriel terrane. The Dom Feliciano Belt includes four main units from west to east, namely the São Gabriel terrane, Camaquã Basin, the Porongos fold and thrust belt and the Pelotas Batholith (Paim et al., 2000; Pertille et al., 2015, 2017; Fragoso César et al., 1986; Philipp and Machado, 2005).

The São Gabriel terrane (Figs. 1c, 2) is the most intensely studied (Chemale et al., 1995; Babinski et al., 1996; Saalmann et al., 2005a, 2005b, 2006; Hartmann et al., 2011; Lena et al., 2014; Lopes et al., 2015) juvenile section of the Brasiliano Orogen and evolved from 948 Ma to 660 Ma (Fig. 3). In the terrane, serpentinization and

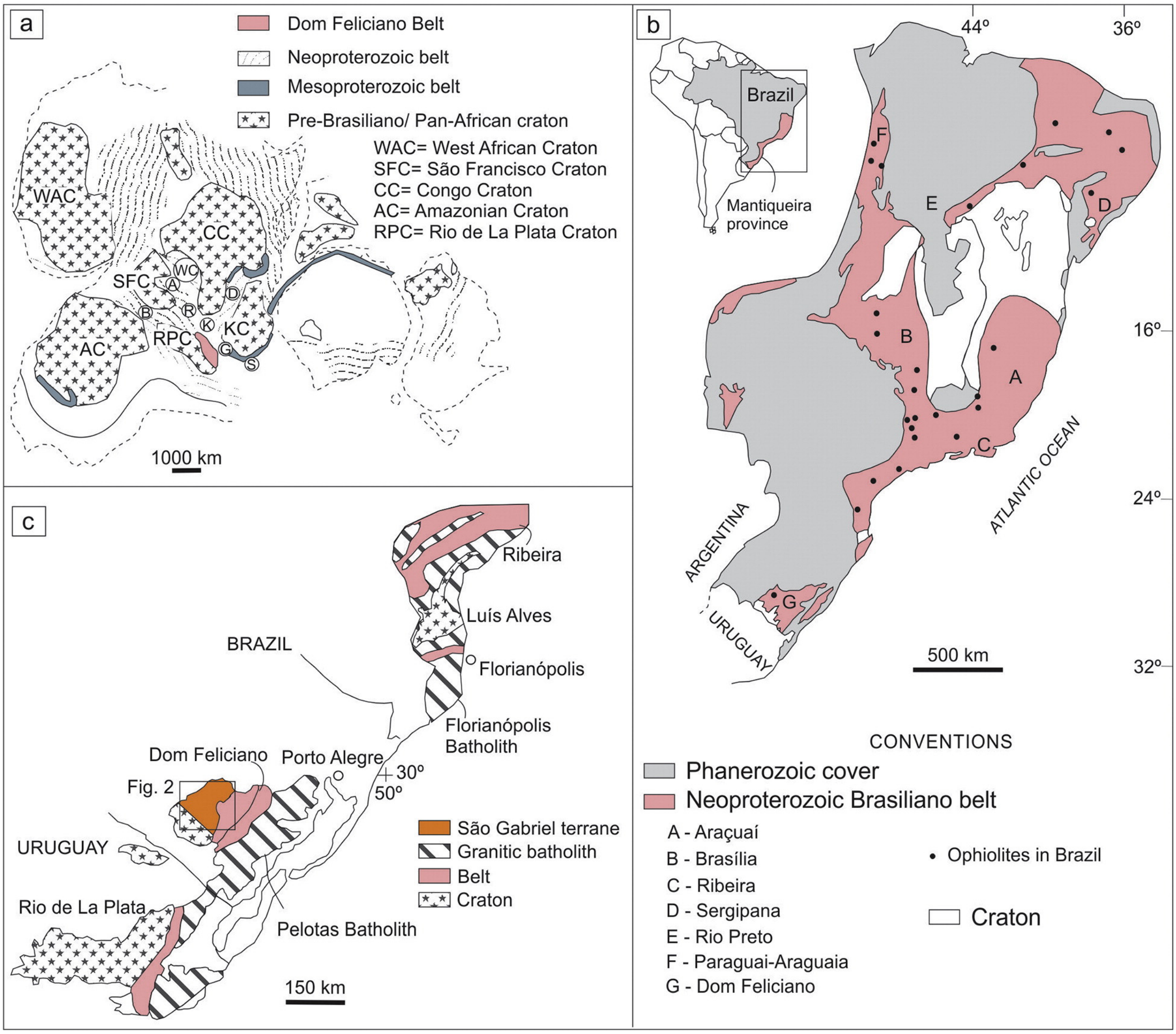

Fig. 1. (a) Reconstruction (500 Ma) of Gondwana with its Meso and Neoproterozoic mobile belts (adapted from Unrug, 1997; Saalmann et al., 2005b). Dom Feliciano Belt highlighted; A = Araçuaí, B = Brasília, D = Damara, G = Gariep, K = Kaoko, R = Ribeira, S = Saldania, WC = West Congo; (b) Geological map of Brazil to the east of the Amazon Craton showing location of ophiolites in the Neoproterozoic belts (after Suita et al., 2004); (c) Geologic map of southern part of Mantiqueira province showing domains in Brazil and Uruguay (adapted from Chemale et al., 1995; Rapela et al., 2007).

metasomatic zoning are intense in all units, especially in the Cerro Mantiqueiras, Ibaré, Palma and Bosssoroca ophiolites.

The Ibaré and Palma ophiolites are the two key areas selected for the study in the juvenile São Gabriel terrane (Fig. 2). In Ibaré, the north-northeast boundary of Ibaré ophiolite and associated volcano-sedimentary rocks is marked by a strong overprint of contact metamorphism (Naumann and Hartmann, 1984; Naumann, 1985), produced by the intrusion of the Santa Rita Granite (Fig. 4). There are also superimposed changes caused by regional metamorphic events ranging from low to medium grade metamorphism that affected the unit. Bands and boudins in rodingites, chloritites and magnesian schists follow a northwest preferred orientation corresponding to the direction of the main metamorphic foliation (Naumann, 1985). The volcano-sedimentary succession has mostly intercalated phyllite, quartzite, meta-arkose, metagraywacke, metarhythmite, metasiltite, metaandesite and metavolcanoclastic rocks.

The Palma ophiolite consists of metabasalt, amphibolite, serpentinite, magnesian schist, quartzite and pelitic paragneiss. Chloritites occur as metasomatic bodies and the host serpentinites exhibit size of approximately 1 × 0.2 km (Garcia, 1980; Chemale, 1982; Remus et al., 1993). The metavolcanic rocks are interleaved with amphibole gneiss, chert, quartzite and minor marble. The bodies generally form elongate lenses and boudins (Fig. 5).

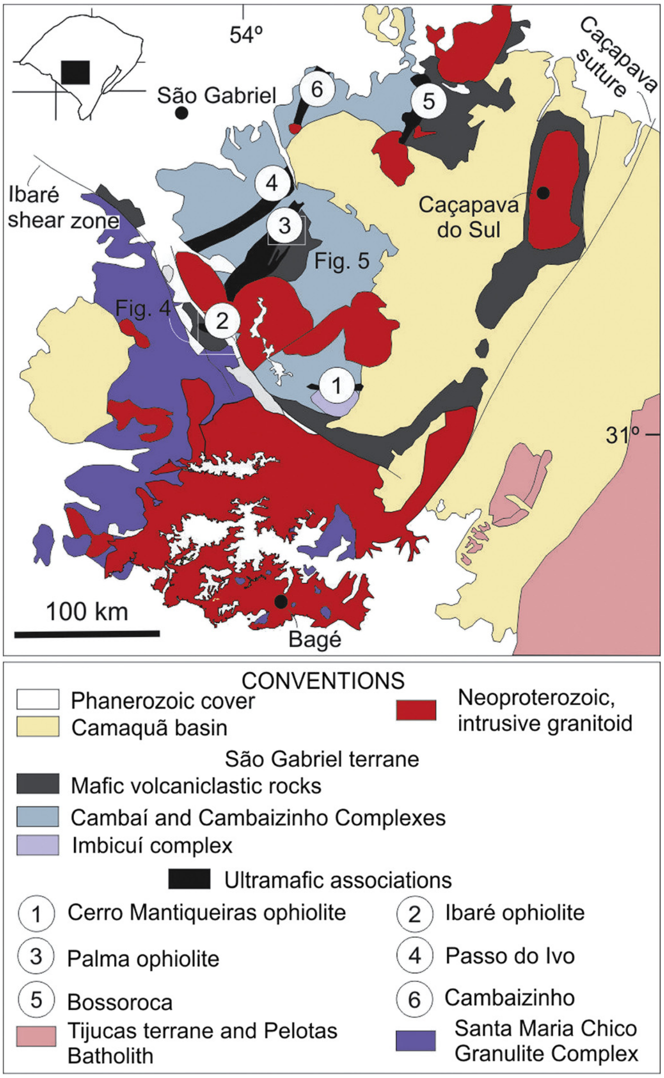

Fig. 2. Geological map of the São Gabriel terrane (after Hartmann et al., 2007, Laux et al., 2012, Camozzato et al., 2014). Inset shows location of study area in the southern Brasiliano Orogen.

The Ibaré serpentinite comprises also talc serpentinite, tremolite-talc serpentinite and olivine-talc serpentinite and chrysotile, lizardite and minor antigorite were described (Naumann, 1985). The same group of serpentines was reported for Palma serpentinite by Garcia (1980). The serpentinite mineralogy suggests that early low-temperature serpentinization (zeolite facies) produced widespread chrysotile and lizardite pseudomorphic serpentinites. Late stage (greenschist facies) may have occurred with recrystallization producing antigoritic serpentinites that characterize low metamorphic grade in the Ibaré and Palma ophiolites. Additionally, in Ibaré the mineral assemblage olivine + talc (jackstraw texture) indicates low hornblende hornfels facies for large tracts of the ophiolite (Naumann and Hartmann, 1984). The initial deformation in the greenschist facies of orogenic metamorphism was succeeded by a strong overprint of contact metamorphism caused by the intrusion of the Santa Rita Granite (Naumann, 1985).

2.1. Sample description

The samples were collected from the Ibaré and Palma ophiolites (Figs. 4, 5; Table 1). The tourmalinite (IB14 sample) body (2.0 × 5 m large) occurs in the extreme northwestern part of the ophiolite, and is in contact with chloritite (IB15 sample) (Figs. 6a–c, 7b), both surrounded by serpentinite. The chloritites from Ibaré (IB15) and Palma (PA18) have similar aspect in the field, and occur as blocks (10 × 20 cm) in serpentinite (Fig. 6a, c, g, h, i). The Ibaré and Palma chloritites and Ibaré tourmalinite are composed of Fe-Mg chlorites (Table 2). IB15 displays euhedral magnetite (1 to 3 mm in size) in hand samples (Fig. 6c). In the matrix of IB5, euhedral magnetite occurs with minor replacement by ilmenite. In addition, ilmenite occurs associated with apatite. Zircon occurs as euhedral crystals and as tiny oval grains (Fig. 7d–f). In the tourmalinite, zircon occurs both in the associated chlorite matrix and included in tourmaline (Fig. 7b–c). In the matrix of PA18, minor skeletal magnetite occurs with intense replacement by ilmenite and major amounts of apatite. Zircon occurs as euhedral crystals and as tiny oval zircon grains (Fig. 7g–i). The fine-grained volcanoclastic rock (IB1 sample) is located ~700 m distant from the Ibaré ophiolite (Fig. 4b). The outcrop is exposed in a dirt road cutting and in the road bed (Fig. 6d–f).

3. Analytical methods

Field study was followed by petrography with a petrographic microscope Olympus BX51, UC30 at Instituto de Geociências, Universidade Federal do Rio Grande do Sul, in one polished thin section of each studied rock. One polished thin section of the each sample (IB14, IB15, PA18) was studied with scanning electron microscope at Laboratório de Geologia Isotópica, Universidade Federal do Rio Grande do Sul. Chemical compositions of chlorites from the samples (Table 2) were obtained using a Cameca SXFive electron microprobe at Laboratório de Microssonda Eletrônica, Universidade Federal do Rio Grande do Sul, with accelerating voltage at 15.0 kV, beam current 15 nA and beam size 5 μm. The minerals were analyzed on the basis of chlorite = 28 O; the H_2O content was not determined. Data correction was made using software Peak Sight/version 5.1.

The analytical technique used in the zircon isotopic (U-Pb and Lu-Hf) analyses from IB19 are reported in Appendix A. Zircon isotopic (U-Pb and Lu-Hf) and trace element chemistry from metasomatic and volcanoclastic rocks were determined by laser ablation in four rock samples, including 387 zircon U-Pb isotopic analyses (Appendices B–E), 314 Lu-Hf analyses (Appendices F–J) and 237 trace element analyses (Appendices K–N). Zircon crystals were separated from sample IB14 (Ibaré tourmalinite, n = 67), sample IB15 (Ibaré chloritite, n = 41), sample IB1 (volcanoclastic rock, n = 158 crystals) and sample IB19 (Santa Rita Granite, n = 35).

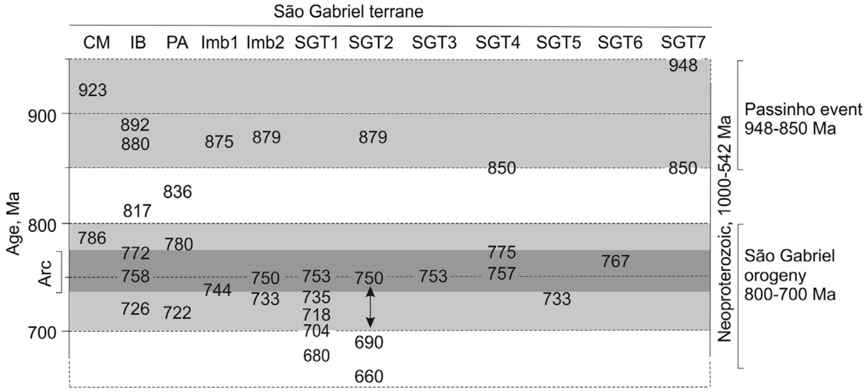

Fig. 3. U-Pb ages (SHRIMP, SIMS, LA-ICP-MS) of igneous, metamorphic and detrital zircon from the São Gabriel terrane. CM = Cerro Mantiqueiras ophiolite, albitite (Arena et al., 2016); IB = Ibaré ophiolite, albitite (Arena et al., 2016), metasomatites and volcanoclastic rock (this work); PA = chloritite (this work); Imb1 = Imbicuí Complex gneiss (Philipp et al., 2014); Imb2 = Imbicuí Complex gneiss (Leite et al., 1998); SGT1 = São Gabriel terrane (Hartmann et al., 2011); SGT2 = São Gabriel terrane (Lena et al., 2014); SGT3 = São Gabriel terrane (Machado et al., 1990); SGT4 = São Gabriel terrane (Remus et al., 1999, 2000); SGT5 = São Gabriel terrane (Laux et al., 2010); SGT6 = São Gabriel terrane (Gubert et al., 2016); SGT7 = São Gabriel terrane (Lopes et al., 2015).

Zircon crystals from the Palma ophiolite were separated from sample PA18 (chloritite, n = 54). All zircon crystals were imaged prior to analysis using backscattered electrons at the Laboratório de Geologia Isotópica (UFRGS, Brazil) to evaluate zoning patterns and locate mineral inclusions and cracks (Fig. 8).

Whole-rock chemical analyses were performed in the Bureau Veritas Laboratory (Vancouver, Canada) (Appendices O, P) with the methods of Group LF300 and LF100. Out of 31 chemical analyses, 18 are from Ibaré volcanoclastic rocks and 13 from Cerro Mantiqueiras metabasalts. The analyses were used for rock classification, geochemical characterization and tectonic setting of the ophiolites (sample location indicated in Appendix Q). Ibaré section is shown in Fig. 4a.

3.1. Zircon LA-ICP-MS U-Pb dating

Zircon U–Pb isotope analyses were undertaken at the Departamento de Geologia of Universidade Federal de Ouro Preto, Minas Gerais, Brazil. The analytical technique used a ThermoScientific Element 2 sector field (SF) ICP-MS coupled to a CETAC LSX-213 G2+ laser system. Calibration was performed using the GJ-1 zircon standard (Jackson et al., 2004). In addition, zircon BB was analyzed in four analytical sessions. In the first session, GJ-1 yielded a mean average age ^{206}U/^{238}Pb of 602 ± 2.1 Ma (2SD, n = 19; MSWD = 1.1) and BB a mean average age ^{206}U/^{238}Pb of 562.8 ± 2 Ma (2SD, n = 35; MSWD = 1.9). In the second session, GJ-1 yielded a mean average age ^{206}U/^{238}Pb of 603 ± 3.8 Ma (2SD, n = 10; MSWD = 1.2) and BB a mean average age ^{206}U/^{238}Pb of 560 ± 4.8 Ma (2SD, n = 8; MSWD = 1.4). In the third session, GJ-1 yielded a mean average age ^{206}U/^{238}Pb of 601 ± 1.8 Ma (2SD, n = 14; MSWD = 1.4) and BB a mean average age ^{206}U/^{238}Pb of 561 ± 1.3 (2SD, n = 16; MSWD = 1.19). In the fourth session, GJ-1 yielded a mean average age ^{206}U/^{238}Pb of 602 ± 3 (2SD, n = 11; MSWD = 0.63) and BB a mean average age ^{206}U/^{238}Pb of 563 ± 2 (2SD, n = 20; MSWD = 0.64). This is in agreement with the LA-ICP-MS long-term average of BB (562 Ma; Santos et al., 2017) reference zircon at Universidade Federal de Ouro Preto and GJ-1 (602 Ma; Horstwood et al., 2016). Operational conditions of the sensitive high-resolution ion microprobe used spot size of 20 μm, laser energy of 15%, laser shot frequency of 10 Hz and shutter delay of 15. The LA-ICPMS data were reduced using the software Glitter (Van

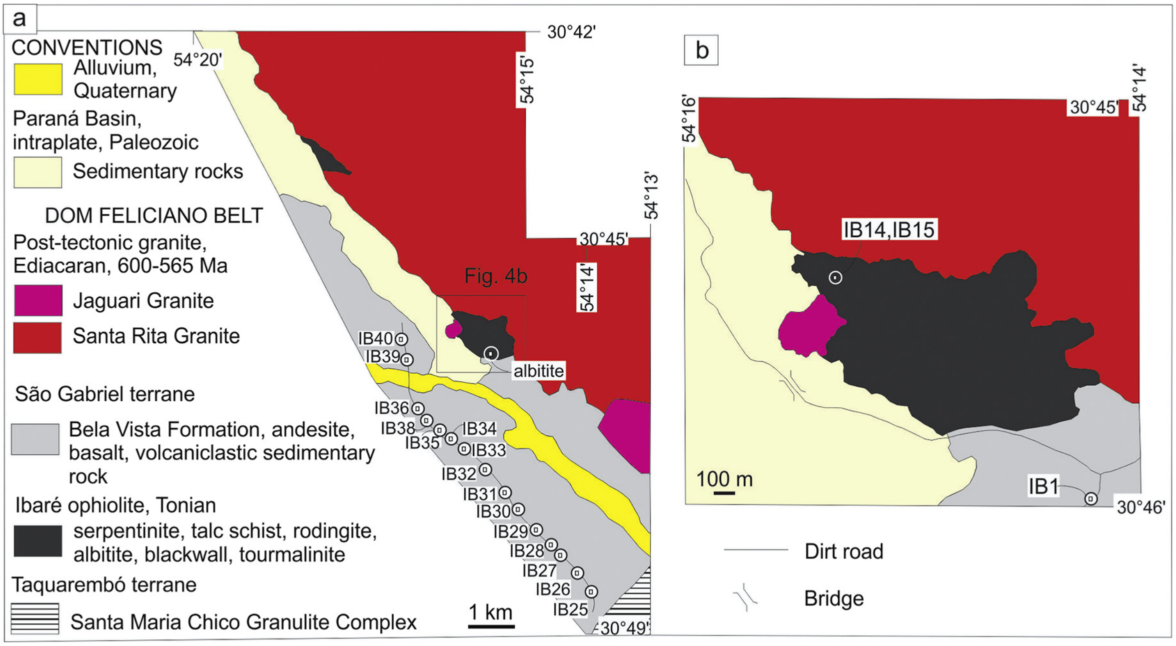

Fig. 4. Geological map of the Ibaré ophiolite showing sample location (after Naumann, 1985; Laux et al., 2012). (a) Albitite location from Arena et al. (2016); Sample locations of IB25 to IB40, this work (see Appendices P–Q); (b) IB1, IB14 and IB15 sample location.

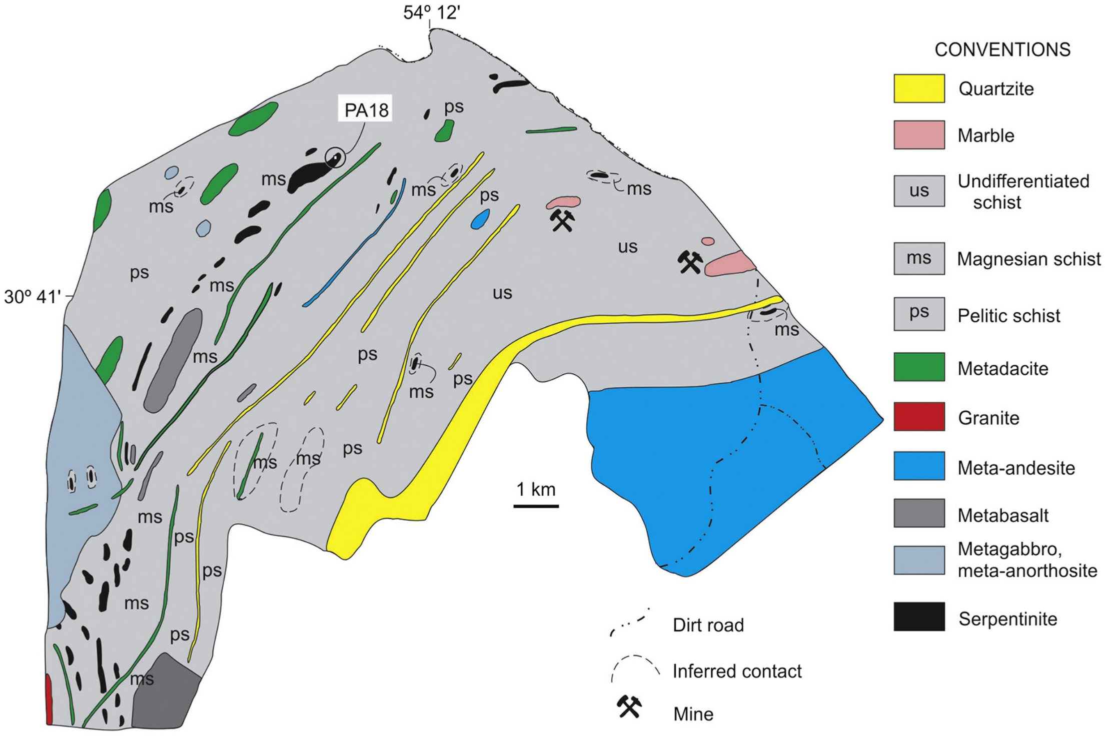

Fig. 5. Geological map of the Palma ophiolite showing sample location (after Garcia, 1980). Location of sample PA18 indicated.

Achterbergh et al., 2001) with ages calculated and plotted on Concordia diagrams using the IsoplotEx 4 program (Ludwig, 2003). Uncertainties given for individual analyses (ratios and ages) are at the 2 sigma level.

3.2. Zircon Lu-Hf isotope analyses

Hf isotopic measurements used a Thermo-Finnigan Neptune multicollector ICP-MS coupled to a Photon-Machines 193 nm laser system, at Departamento de Geologia, Universidade Federal de Ouro Preto. Data were collected in static mode during 60 s of ablation with a spot size of 50 μm. Nitrogen (~0.080 L/min) was introduced into the Ar sample-carrier gas. Typical signal intensity was ca. 10 V for ^{180}Hf. The isotopes ^{172}Yb, ^{173}Yb and ^{175}Lu were simultaneously monitored during each analysis step to allow for correction of isobaric interferences of Lu and Yb isotopes on mass 176. The ^{176}Yb and ^{176}Lu were calculated using a ^{176}Yb/^{173}Yb of 0.796218 (Chu et al., 2002) and ^{176}Lu/^{175}Lu of 0.02658 (JWG in-house value). The correction for instrumental mass bias utilized an exponential law and a ^{179}Hf/^{177}Hf value of 0.7325 (Patchett and Tatsumoto, 1980) for correction of Hf isotopic ratios. The mass bias of Yb isotopes generally differs slightly from that of the Hf isotopes with a typical offset of the βHf/βYb of ca. 1.04 to 1.06 when using the ^{172}Yb/^{173}Yb value of 1.35274 from Chu et al. (2002). This offset was determined for each analytical session by averaging the βHf/βYb of multiple analyses of the JMC 475 solution doped with variable Yb amounts and all laser ablation analyses (typically $n > 50$) of zircon with a ^{173}Yb signal intensity of >60 mV. The mass bias behavior of Lu was assumed to follow that of Yb. The Yb and Lu isotopic ratios were corrected using the βHf of the individual integration steps ($n = 60$) of each analysis divided by the average offset factor of the complete analytical session. The results were calibrated with the standard zircon Temora, 416 Ma (176Hf/177Hf: 0.282680 ± 0.000031), MUDTANK, 732 Ma (176Hf/177Hf: 0.282504 ± 0.000044), Plesovice, 337 Ma (76Hf/177Hf: 0.282482 ± 0.000013) and 91,500, 1065 Ma (176Hf/177Hf: 0.282307 ± 0.000031). Initial epsilon hafnium value εHf(t) was calculated using a decay constant of 1.865×10^{-11} yr^{-1} (Scherer et al., 2001). We used the average MORB (DM) 176Lu/177Lu and 176Hf/177Hf of 0.0384 and 0.283165 respectively, and a value of 0.0113 for the average continental crust (Taylor and McLennan, 1985; Wedepohl, 1995), 176Lu/177Hf = 0.0336, and 176Hf/177Hf = 0.282785 for CHUR (Bouvier et al., 2008).

3.3. Trace element chemistry of zircon

Trace element compositions were obtained from the same mounts used for U-Pb isotopic determinations. Zircon chemical composition, particularly rare earth elements and U, was determined with a LA-ICP-MS (a New Wave 213 laser ablation coupled to a Agilent 7700) at Departamento de Geologia, Universidade Federal de Ouro Preto

Table 1
Summary of rock types, analyses and sample location.

Sample	Lithology	Age (Ma)	U-Pb (n)	Lu-Hf (n)	Trace elements (n)	Lat (N)	Long (W)
IB1	Volcanoclastic	758 ± 4	159	133	98	6,591,173	762,629
IB14	Tourmalinite	726 ± 2	86	68	50	6,592,673	761,835
IB15	Chloritite	726 ± 2	48	41	57	6,592,673	761,835
PA18	Chloritite	722 ± 3	59	52	32	6,602,561	766,429
IB19	Granite	584.7 ± 2	20	20	–	6,593,321	763,301

Ages quoted are 95% confidence, all 2σ except IB19 which are 1σ.
(n) = number of concordant U–Pb, Lu-Hf zircon isotopic and trace element analyses.
Lat/Long = datum WGS 84 hand-held GPS used.
(–) not analyzed.

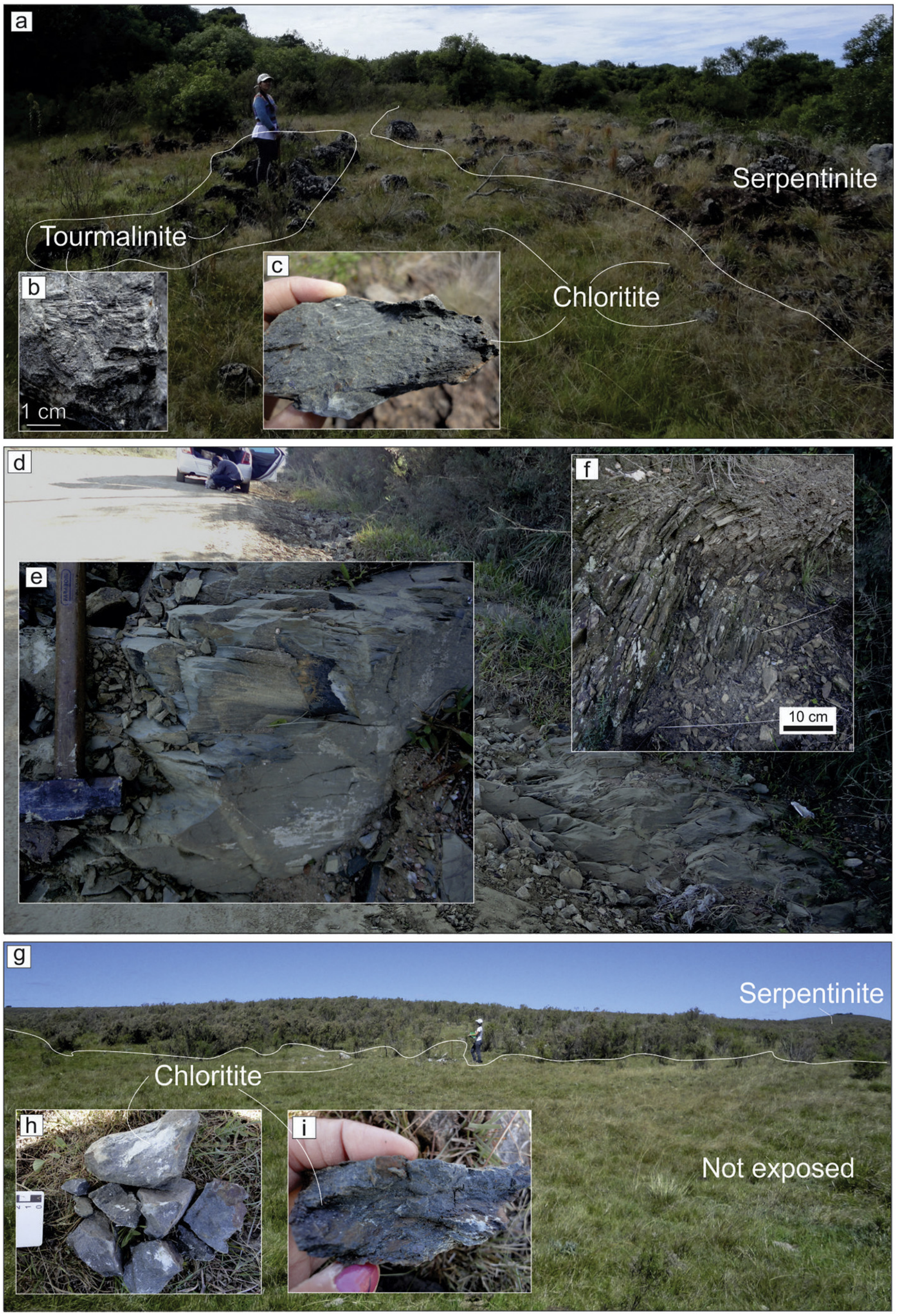

Fig. 6. Selected field photographs of Ibaré and Palma. (a) Ibaré tourmalinite body approximately 2 × 5 m; blocks of chloritite approximately 10 × 20 cm, samples IB14, IB15; (b) detail of tourmalinite; (c) chloritite, euhedral magnetite visible; (d) volcanoclastic rock outcrop, IB1 sample; (e) detail of IB1 sample; (f) vertical detail; fractures and fold of volcanoclastic rock (IB1 sample); (g) Palma chloritic blackwall around serpentinite; (h) blocks of chloritite 10 × 20 cm; (i) chloritite PA18 hand sample.

(Takenaka et al., 2015). The laser was set to produce spot sizes of 25 μm in diameter, during a period of 30 s at 10 Hz frequency. The data acquisition was done in bracketing mode and consisted of 3 to 4 analyses of standards (NIST 612 and NIST 610) bracketing 10–15 unknowns. The data reduction was done via the Glitter software (GEMOC Laser ICP MS Total Trace Element Reduction), which provides an interactive environment for analytic selection of background and sample signals (Van Achterbergh et al., 2001; Jackson et al., 2004). Instrumental mass bias and ablation depth-dependent elemental fractionation were corrected by tying the time-resolved signal for the unknown zircon to the identical integration window of the primary standard NIST612. Additional details on methodology can be found in Appendix A. NIST 610 was used as a secondary control standard. Error was derived from the averaged counts for each mass for both the standards and values are then compared to those of the primary and secondary standards, to determine concentrations.

4. Results

4.1. Zircon description

The internal structure of zircon (Fig. 8) from metasomatites displays patchy and oscillatory zoning in euhedral to subhedral zircon. Some crystals have embayments and show porous portions and overgrowths of tiny xenotime and monazite. In the Ibaré metasomatites, zircon crystals have sizes 80–250 μm (aspect ratio 3:1 to 6:1), larger than Palma

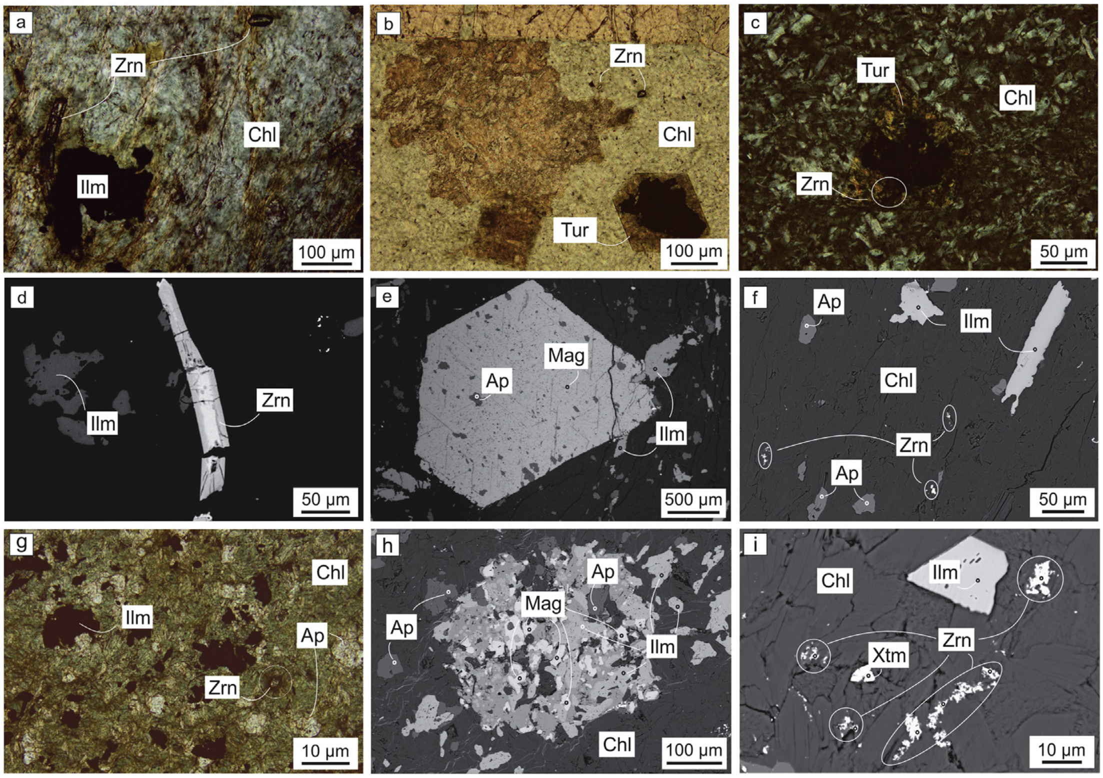

Fig. 7. Selected photomicrographs and backscattered electron (BSE) images of the metasomatites from the ophiolites of the São Gabriel terrane. (a) Zircon crystals in matrix of IB15 choritite; (b) tourmalinite IB14 with chlorite in the matrix and zircon inset; (c) zircon inclusion in tourmaline in IB14; (d) euhedral zircon in IB15 matrix; (e) euhedral magnetite with apatite inclusion and associated ilmenite in IB15 matrix; (f) ilmenite, apatite and tiny oval zircon grains in IB15 matrix; (g) small zircon crystals in matrix of PA18 choritite and major amounts of apatite; (h) skeletal magnetite (light gray) with intense replacement by ilmenite (medium gray) in PA18 matrix; (i) ilmenite, xenotime and tiny oval zircon grains in PA18 matrix. Zrn = zircon, Tur = tourmaline, Chl = chlorite, Ap = apatite, Mag = magnetite, Ilm = ilmenite, Xtm = xenotime.

(100–190 µm; aspect ratio 1:1 to 3:1), possibly because some crystals are broken fragments. The volcanoclastic rock shows subhedral to anhedral zircons (50–100 µm with few closer to185 µm; aspect ratio 2:1); embayments are present. Euhedral apatite inclusions are common in the core in all zircons in the studied rocks.

Some young crystals show oscillatory zoning (e.g., IB14-58, IB15-19, IB15-52, IB15-53) which can be either formed by magmatic or metasomatic processes. On the other hand, the presence of curved zones, commonly starting at the crystal edge and advancing toward the core, can be explained by interaction of the crystal surface with fluids (e.g. IB14-67, IB15-14, IB15-21, PA18-19). The BSE images show that some older zircons do not show zoning (e.g., Fig. 8m). Possibly comparable internal structures of euhedral zircon with oscillatory zoning were described by Dubińska et al. (2004) for zircon formed during serpentinization in metasomatic rocks (rodingite and their chloritic blackwall). Another observation was made by Hu et al. (2017) by which euhedral to subhedral zircon grains from rodingite and serpentinite, displaying elongated or irregular, prismatic or ellipsoidal shape exhibit oscillatory or banded zoning. A hydrothermal origin for zircon can be inferred by its presence in low-SiO_2 rocks, such as peridotite, pyroxenite and eclogite, which should normally be devoid of zircon (Schaltegger, 2007). Extensive evidence has been presented that hydrothermal zircon (metasomatic) forms in volatile-rich partial melts from metasomatized mantle beneath old continental roots, e.g., kimberlites (Griffin et al., 2000). Hydrothermal zircon may form during metasomatism of harzburgite by basaltic liquid and accompanying fluids (Grieco et al., 2001) and also during alteration of ophiolitic rocks (Dubińska et al., 2004). The zircon crystals presently studied are metasomatic and similar in some aspects to these descriptions.

4.2. Zircon LA-ICP-MS U-Pb dating

A weighted mean $^{206}Pb/^{238}U$ age (Ludwig, 1998) was calculated (with 2s and absolute input errors) for zircon from each metasomatic and volcanoclastic rock (Appendices B–D). This yields (Fig. 9a–f) the dates of 726 ± 2 Ma (IB14, IB15; interval 700–751 Ma, n = 90), 722 ± 3 Ma (PA18; interval 702–749 Ma, n = 37) and 758 ± 4 Ma (IB1; interval 702–800 Ma, n = 132). Other three representative ages recorded in the metasomatites are 780 ± 5 Ma, 836 ± 6 Ma and 880 ± 12 Ma. In the IB14, IB15 zircons, the younger ages (699–680 Ma) are concordant, but may be due to variable Pb loss. The 650–600 Ma ages may represent a last alteration process (Figs. 9a–d, 10a–b; Appendices B, C). This suggests that zircon in Ibaré and Palma ophiolites crystallized and recrystallized during more than one event. Partial reorganization of the U-Pb system occurred in specific zircon grains, because a few grains have younger cores than rims (Fig. 8g, r). The volcanoclastic rock shows a range of ages between 600 and 907 Ma and one crystal at 1032 Ma, but the most significant range is between ~800 and 700 Ma (Fig. 9e, f; Appendix D). For the Santa Rita Granite, a calculated Concordia age (n = 20) of zircons (>90% concordant) displays an age of 584.7 ± 1.9 Ma; some analyses (n = 15) were not used in the calculation (Fig. 11a; Appendix E). In the IB1 zircons, the Th/U ratios range from 0.2 to 1.3. In the metasomatic rocks, the ratios range from 0.01 to 1.9 (Ibaré ophiolite) and from 0.2 to 1.3 (Palma ophiolite).

4.3. Zircon Lu-Hf isotope analyses

The Hf-isotope data (Appendices F–H) determined in Ibaré and Palma ophiolite zircons (Fig. 10a) are consistent with a major

Table 2
Chemical compositions (wt%) by electron microprobe of chlorites from a tourmalinite and chloritites, Ibaré and Palma ophiolites.

	Ibaré ophiolite										Palma ophiolite				
	Chloritite (IB15)					Tourmalinite (IB14)					Chloritite (PA18)				
Sample spot	14/2	14/3	8/1	8/2	4/3	1/2	1/7	1/8	1/11	1/12	1/3	1/5	3/1	3/3	3/4
DataSet/Point	2/1	3/1	4/1	5/1	10/1	2/1	7/1	8/1	11/1	12/1	3/1	5/1	6/1	8/1	9/1
SiO_2	26.39	27.27	26.35	26.94	26.8	26.69	26.81	26.25	26.9	27.32	24.8	24.52	25.22	24.29	24.76
TiO_2	0.05	0.09	0.09	0.06	0.08	0.02	0.01	0.04	0.01	0.03	0.08	0.05	0.07	0.04	0.05
Al_2O_3	23.02	22.01	22.5	21.93	22.37	23.37	23.26	23.16	22.58	22.46	21.76	21.64	20.92	21.66	21.25
Cr_2O_3	0.01	–	–	–	–	–	–	–	–	–	0.02	0.03	0.02	0.03	0.01
FeO	14.64	14.47	14.59	14.58	14.81	13.37	13.07	13.06	12.94	12.7	26.57	25.67	25.93	25.67	25.95
MgO	22.97	23.04	22.18	22.49	22.77	23.46	23.82	23.17	23.93	24.49	14.65	15.11	15.05	14.43	14.58
MnO	0.37	0.36	0.35	0.36	0.36	0.31	0.3	0.33	0.33	0.32	0.39	0.3	0.35	0.3	0.3
NiO	0.05	0.03	0.04	–	–	–	0.05	–	0.03	–	–	0.02	0.01	0.06	–
Na_2O	0.01	0.02	–	–	–	0.03	–	–	–	0.03	0.01	–	–	0.01	0.01
K_2O	–	–	–	0.02	–	–	–	–	–	–	–	0.01	0.01	–	0.01
CaO	0.01	0.01	0.03	0.04	0.01	–	–	–	0.01	–	–	0.01	0.01	0.04	0.02
BaO	0.05	0.01	0.07	–	–	0.06	–	–	–	–	–	0.06	–	0.08	–
CoO	0.04	0.04	0.05	–	0.04	–	0.03	–	–	0.03	0.02	–	–	0.02	–
Sum	87.62	87.34	86.25	86.42	87.24	87.31	87.36	86.01	86.72	87.37	88.29	87.43	87.6	86.63	86.93

(–) = below detection limit.

contribution from a depleted mantle source. IB1 zircons (Appendix I) show more radiogenic $^{176}Hf/^{177}Hf$ isotopic ratios than IB14, IB15, PA18 zircons (Fig. 10b, d). The initial $^{176}Hf/^{177}Hf$ increases with decreasing age in the metasomatites (Fig. 10a, b). The obtained dataset of the zircons also indicates an εHf(t) evolutionary trend from early to the end of the Tonian (between ~880 and ~722 Ma) characterized by a decrease in εHf(t) from about +12 to +1 (Fig. 10a). For the IB19, Santa Rita Granite (Fig. 11b, Appendix J), εHf(t) data are negative (−14.1 to −32.6) and indicate a substantial component of evolved crust in the magma from which the zircons crystallized.

4.4. Trace elements

Geochemical characteristics of oceanic crust zircon (negative Eu anomaly and pronounced positive Ce-anomaly) are observed in all analyzed grains (Appendices K–N). In the metasomatic rocks, the negative Eu anomaly is small, and zircons from all samples show similar REE distributions (Fig. 12a). The data display U/Yb = 0.6–1.4 (IB14), U/Yb = 0.5–1.6 (IB15), U/Yb = 0.2–2.0 (PA18) and U/Yb = 0.1–1.0 (IB1), (Fig. 12b). Chondrite-normalized Sm/La ratios of zircon vary from 0.5–13 (IB14), 0.7–11 (IB15), 0.1–10 (PA18) and 01–42 (IB1). These low values reflect enrichment in La (Fig. 12c). The distribution of least-mobile trace elements in zircon (Nb/Yb × U/Yb) can be used for the understanding of tectono-magmatic setting of ophiolite rocks (Grimes et al., 2015). Our data are shown in Fig. 12d. The volcanoclastic rock (IB1) exhibits a prominent population similar to mid-ocean ridge (MOR-type) rocks.

4.5. Classification, geochemical characteristics and tectonic setting.

Based on whole rock chemical composition (immobile elements), the ophiolitic volcanoclastics and metavolcanics are classified on a TAS proxy diagram (Pearce, 1996). The rocks are classified as basalt to andesite (Fig. 13a). In Ibaré, the SiO_2 content varies from 57.13 to 66.04 wt%, whereas in the Cerro Mantiqueiras from 48.62 to 60 wt%. Incompatible trace-element concentrations normalized to the N-MORB composition (Sun and McDonough, 1989) are shown in Fig. 13b. Significant enrichment is observed in large ion lithophile elements (LILEs: Cs, Ba, Rb, K) and light rare earth elements (LREEs: La, Ce, Pr, Nd, Sm) relative to high-field strength elements (HFSE: Nb, Ta, Zr, Hf, Ti, Y) and heavy rare-earth-elements (HREE: Tb, Dy, Ho, Er, Tm, Yb Lu). Similar feature is also exhibited by primitive basalts (Green, 2006, and references therein). The studied samples (Fig. 13b, Appendices O and P) have similar contents of HREE, but the Ibaré volcanoclastics are more enriched in LILE and LREE. Some of the LILE (Rb, Ba, K) (Fig. 13b) and Na and Si may have been modified by seafloor hydrothermal processes as described by Basta et al. (2011). The discrimination diagram Th/Yb versus Nb/Yb (Fig. 13c) illustrates the distinction between oceanic basalts and oceanic subduction-related basalts (Pearce, 2008, 2014). The V versus Ti plot (Fig. 13d) consolidates the fingerprinting of origin of the two ophiolites. The Ibaré Ti/V ratio varies from 18.3 to 52.6 and the Cerro Mantiqueiras from 11.41 to 36.6 (Fig. 13d), although sample CM31 has low ratio (6.5).

5. Discussion

5.1. U-Pb geochronology

The results obtained on 162 zircon grains from three samples of metasomatites indicate a protracted process of oceanic crust evolution and accretion to continent. Ages are near 880 Ma, 836 Ma, 780 Ma, but a strong mode occurs at 722 Ma. These ages are observed in all samples, including chloritites and tourmalinite. The volcanoclastic rock has an age of 758 Ma and an intrusive granite has the age of 585 Ma.

Partial reorganization of the U-Pb system (Fig. 8g, r) can be due to metamorphism or low-temperature fluid-rock interaction. This led to U-Pb isotope fractionation in the zircon, possibly in a fluid phase, causing dissolution–reprecipitation in different domains (Gebauer and Grünenfelder, 1976; Geisler et al., 2003). We interpret the heterogeneity of the Th/U ratio (0.01–1.9) in the metasomatic rocks as a process similar to the description by Zhiwei et al. (2009). These authors showed that U, Th and Pb from the dissolution of pristine zircons and leaching of other minerals may be enriched and unevenly distributed in the newly formed hydrothermal zircons. For example, Th may have been leached from the rocks related to the ultramafics and migrated, in a process similar to the transference of Zr from external sources along sheared blackwall, as described by Dubińska et al. (2004). Heterogeneity of the hydrothermal zircons is also supported by Hoskin (2005). Previous Ibaré albitite age of 890 Ma (Arena et al., 2016) and new 880 Ma age (this work) suggest that the serpentinization of the mantle peridotites from the Ibaré ophiolite started at a mid-ocean ridge in the early Tonian. Following many studies (Klein, 2009; and references therein), we interpret these rocks as a result of alteration processes in the oceanic crust. Serpentinization may also have occurred during movement of the oceanic crust toward the subduction zone, with the overriding plate comprising mantle tectonites transported from the mid-ocean spreading center and thrusted onto the intra-oceanic island arc. The emplacement of ophiolite associated with the São Gabriel volcanic arc occurred late in the Tonian (722 Ma), as shown here. This suggests

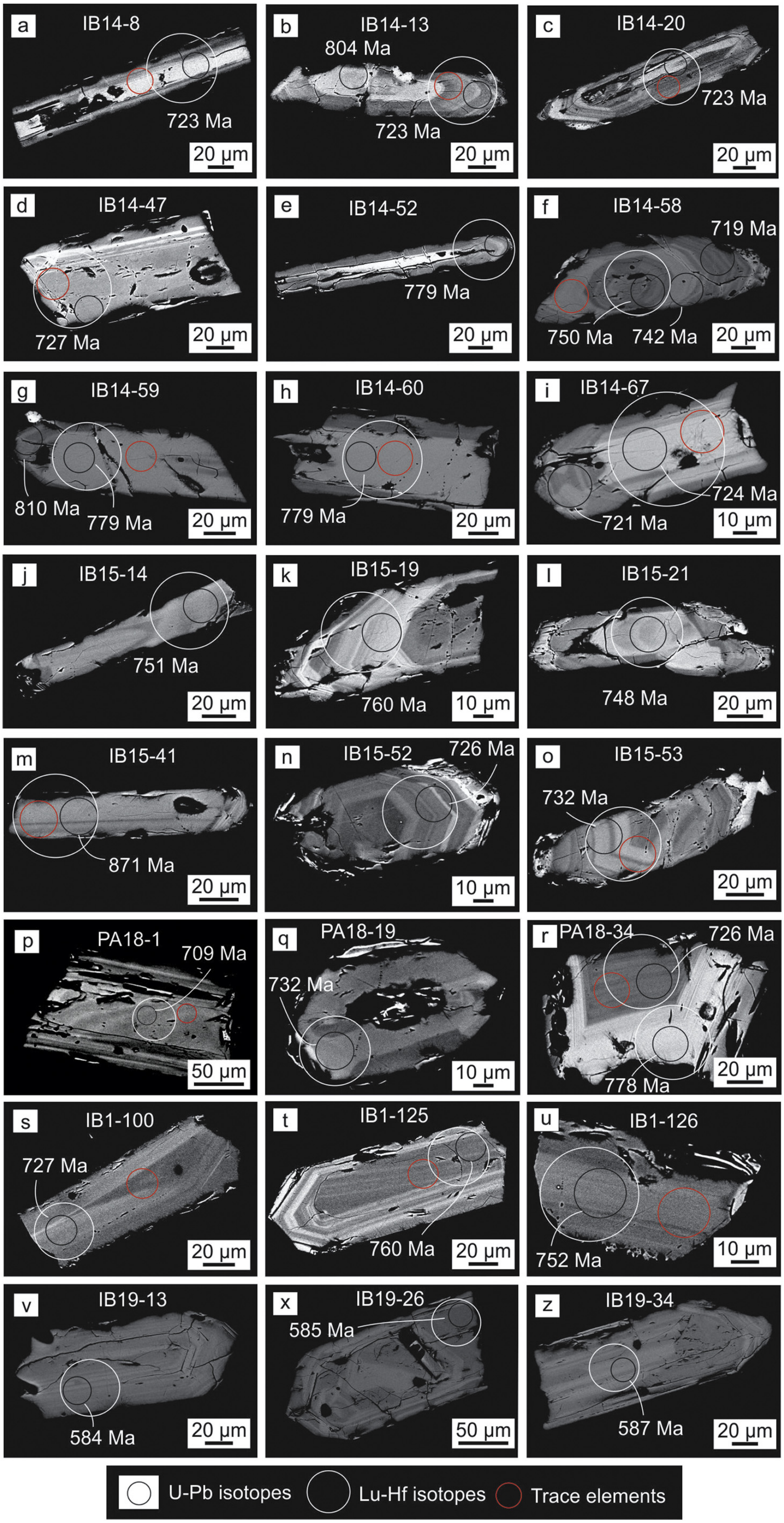
a
IB14-8
723 Ma
20 µm
b
IB14-13
804 Ma
723 Ma
20 µm
c
IB14-20
723 Ma
20 µm
d
IB14-47
727 Ma
20 µm
e
IB14-52
779 Ma
20 µm
f
IB14-58
719 Ma
750 Ma
742 Ma
20 µm
g
IB14-59
810 Ma
779 Ma
20 µm
h
IB14-60
779 Ma
20 µm
i
IB14-67
724 Ma
721 Ma
10 µm
j
IB15-14
751 Ma
20 µm
k
IB15-19
760 Ma
10 µm
l
IB15-21
748 Ma
20 µm
m
IB15-41
871 Ma
20 µm
n
IB15-52
726 Ma
10 µm
o
IB15-53
732 Ma
20 µm
p
PA18-1
709 Ma
50 µm
q
PA18-19
732 Ma
10 µm
r
PA18-34
726 Ma
778 Ma
20 µm
s
IB1-100
727 Ma
20 µm
t
IB1-125
760 Ma
20 µm
u
IB1-126
752 Ma
10 µm
v
IB19-13
584 Ma
20 µm
x
IB19-26
585 Ma
50 µm
z
IB19-34
587 Ma
20 µm
U-Pb isotopes
Lu-Hf isotopes
Trace elements

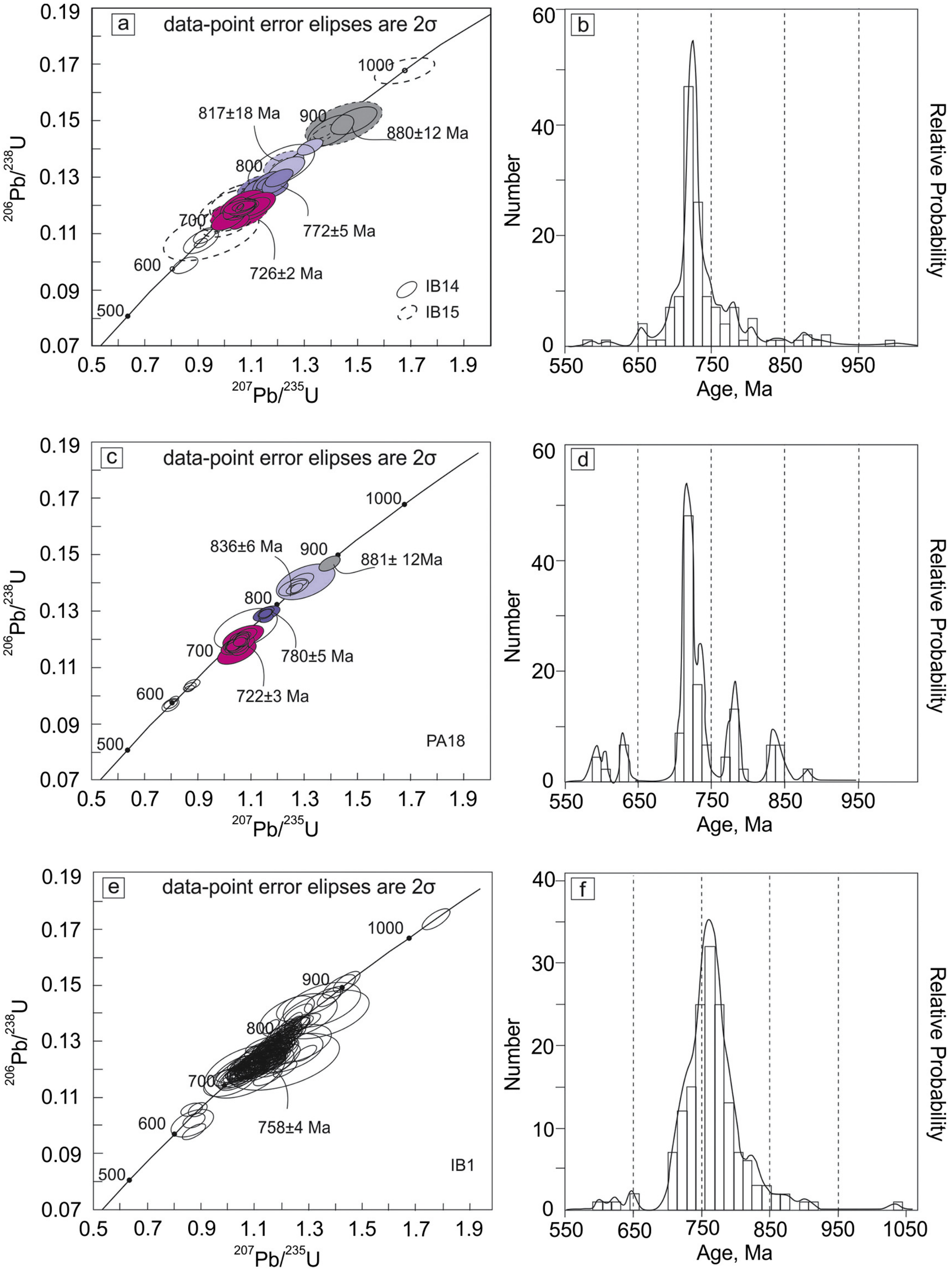

Fig. 9. U-Pb isotopic diagrams of zircon from Ibaré and Palma. (a) Isotopic analyses of IB14 and IB15 in concordia diagram; (b) relative probability versus age diagram of IB14 and IB15; (c) isotopic analyses of PA18 in concordia diagram; (d) relative probability versus age diagram of PA18; (e) isotopic analyses of IB1 in concordia diagram; (f) relative probability versus age diagram of IB1.

that the region formed in a protracted process of ophiolite generation, emplacement and subduction-zone of juvenile granitic and basaltic magmas.

The intra-arc (~758 Ma) reported herein indicates a long period (~120 Ma) between the generation of the oceanic crust and the formation of the island arc. The age of the Ibaré volcanoclastic rock IB1 is

Fig. 8. Selected BSE images of zircon from Ibaré and Palma. (a–u) Back-scattered electron images showing analyzed spots. IB14 = tourmalinite; IB15 = chloritite; IB1 = volcanoclastic rock; PA = chloritite; IB19 = granite. Black circle = U-Pb analysis displaying age; large white circle = Hf isotope analysis; small red circle = trace element analysis.

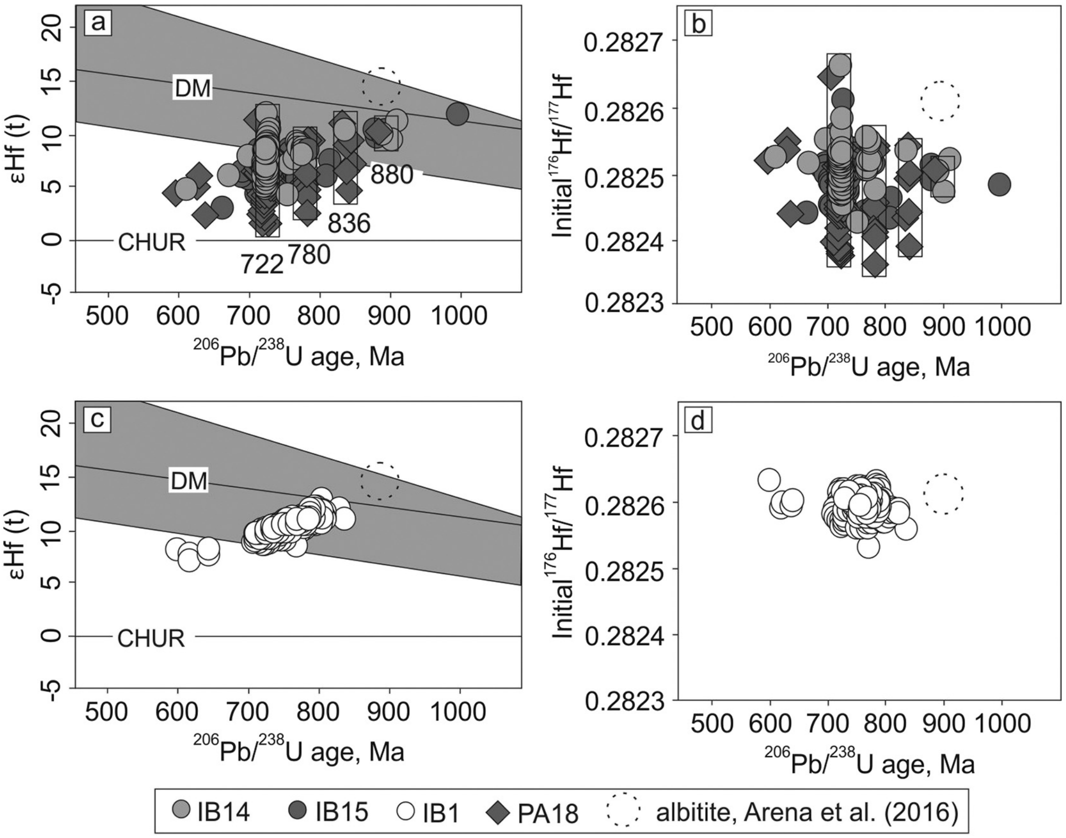

Fig. 10. Hf isotopic system versus U-Pb ages. (a) U-Pb ages versus εHf values showing characteristic mantle-derived magma fingerprint; (b) Initial ^{176}Hf/^{177}Hf showing increase with decreasing U-Pb age in the metasomatites; (c) εHf evolution diagram showing the result of analyses of IB1; (d) U-Pb ages versus initial ^{176}Hf/^{177}Hf in IB1. DM = depleted mantle, CHUR = chondrite uniform reservoir. Depleted Mantle evolution from Gerdes and Zeh (2006) indicated by highlighted field.

coeval with the U-Pb zircon age determination at 753 ± 2 Ma (Machado et al., 1990), 757 ± 17 Ma (Remus et al., 1999) and 767 ± 3 Ma (Gubert et al., 2016) from rocks in the island-arc containing the Bossoroca ophiolite (location in Fig. 2). An age of 733 ± 13 Ma was obtained in a volcanoclastic rock from Ibaré by Laux et al. (2010) and interpreted as the deposition of the metasedimentary rocks of the São Gabriel terrane. A few ages (Fig. 9a–f, Appendices B–D) near 699–680 Ma in the IB14, IB15 zircons are concordant but could be due to variable Pb loss (e.g. Bomparola et al., 2007). In addition, the 650–600 Ma ages may represent a late alteration process coinciding with an accretionary orogeny (Babinski et al., 1997; Lena et al., 2014) that may have caused some alteration of the serpentinite and the zircons contained in the chloritites. Granite intrusion occurred during late deformation, e.g., Santa Rita and Jaguari Granites. The U-Pb zircon age of the Jaguari Granite is 569 ± 6 Ma (Gastal et al., 2015) and the ^{207}Pb/^{206}Pb age is 567 ± 4 Ma (Gastal et al., 2006). In the studied region, the intrusion of the Santa Rita Granite occurred at 584.7 ± 1.9 Ma.

In the eastern part of the São Gabriel terrane, the Cerro Mantiqueiras ophiolite had a life span of ~140 Ma, between the formation of the albitite (923–786 Ma) in the mid-ocean spreading ridge and its accretion (Arena et al., 2016) to the intra-oceanic island arc (Passinho arc, 879 Ma). The Ibaré and Palma ophiolites had a life span of 170 Ma

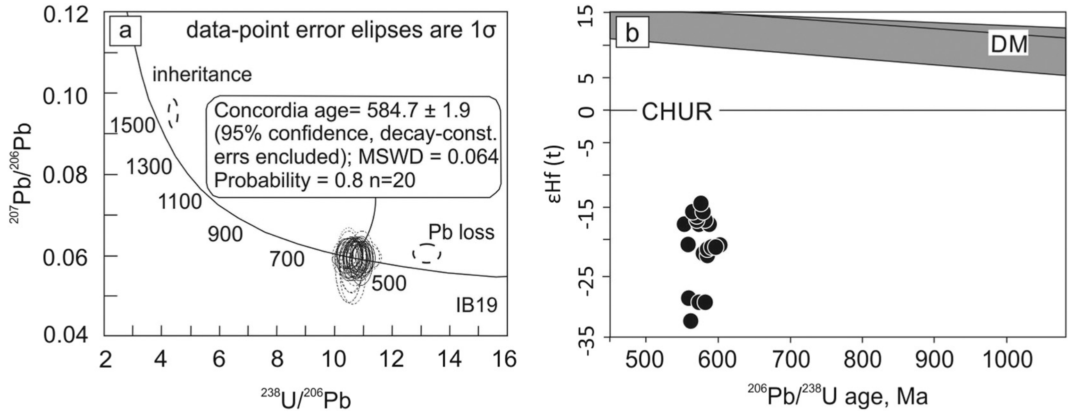

Fig. 11. U-Pb geochronology and Lu-Hf isotopes of the Santa Rita Granite, sample IB19. (a) Isotopic analyses in concordia diagram; (b) comparative εHf evolution diagram showing the result of analyses of the Santa Rita Granite. DM = depleted mantle, CHUR = chondrite uniform reservoir.

starting between 892 Ma (albitite; Arena et al., 2016) and 880 Ma (first serpentinization of metasomatites, this work) in the mid-ocean ridge and its accretion of the intra-oceanic island arc (São Gabriel arc, 758 Ma) at 722 Ma.

The Neoproterozoic São Gabriel terrane started as a primitive island arc at 948–850 Ma (e.g., Passinho arc). Arc-type magmatism continued through the Neoproterozoic (e.g., 800–700 Ma São Gabriel arc) with emplacement of ophiolites at 722 Ma. TTG rocks intruded the terrane continuously up to 660 Ma (Hartmann et al., 2011; Lena et al., 2014). Throughout the Sul-Riograndense Shield, a younger continental collisional event occurred at 650–600 Ma (Babinski et al., 1997; Pertille et al., 2015) and this may be registered in some younger ages of zircon from the metasomatites and other rocks. Younger granites (Santa Rita and Jaguari) close the geological history of the region and are the temporal link with the large Pelotas Batholith in the east of the shield.

The ophiolites from the São Gabriel terrane are dispersed and occur in a small area, but processes can be compared with the Himalaya-Alpine orogen. In the eastern Neo-Tethys, U-Pb zircon age of ophiolite is 177 Ma and its emplacement age near 75–65 Ma, therefore a duration of 112 Ma between the generation and emplacement in the Spontang ophiolite (Pedersen et al., 2010). Sutures containing ophiolites can be >3000 km long in the Himalayas and the timing of two different sutures can be 46 Ma apart (Liu et al., 2016). Accretionary orogens such as the Andes also contain ophiolites (Ramos et al., 2010). The evolution of the eastern Neoproterozoic–Early Cambrian Pampean belt occurred during a period of 60 Ma (600–540 Ma) coeval with the late stages of the Brasiliano Orogen in Brazil (Escayola et al., 2007).

5.2. Lu-Hf isotopic systematics of zircon

Lu–Hf isotopic analyses of all metasomatic zircon domains display evolving ^{176}Hf/^{177}Hf ratios along time (Fig. 10b). The heterogeneity of ^{176}Hf/^{177}Hf ratio and the decrease in εHf(t) from about +12 to +1 (Fig. 10a) indicates that some zircon domains were contaminated with an older crustal component, possibly in a process comparable to the studies of Morag et al. (2011) in the Arabian-Nubian Shield. And yet, the contamination may have occurred in an even older event (Gladkochub et al., 2006).

The positive εHf(t) suggests that the source of Zr in the chloritites was ultimately a juvenile mantle-derived magma at ca. 880–722 Ma. This is interpreted as early serpentinization at the spreading ridge (880 Ma), close to intersection with ridge fracture zone. Fresh and altered rocks, including albitites (~890 Ma, Arena et al., 2016) and partly serpentinized and chloritized metamorphic peridotite, were transported away from the mid-ocean spreading center and thrusted into the island arc. Metasomatism and extensive re-equilibration with crustal material also occurred during the emplacement of the ophiolite mainly at the end of the Tonian (722 Ma) with approximation to the craton.

The Santa Rita Granite belongs to the post-collisional event and is characterized by negative εHf(t) of −14.1 to −32.6. These negative εHf(t) data indicate that the granitic magmas formed to a large extent by recycling of older Rio de la Plata continental crust.

Zircons of the oldest group (~880 Ma) display no evidence of continental-derived influence, only a strictly mantle-derived range from εHf +12.1 to +9.1. This is coeval with a mantle-derived range

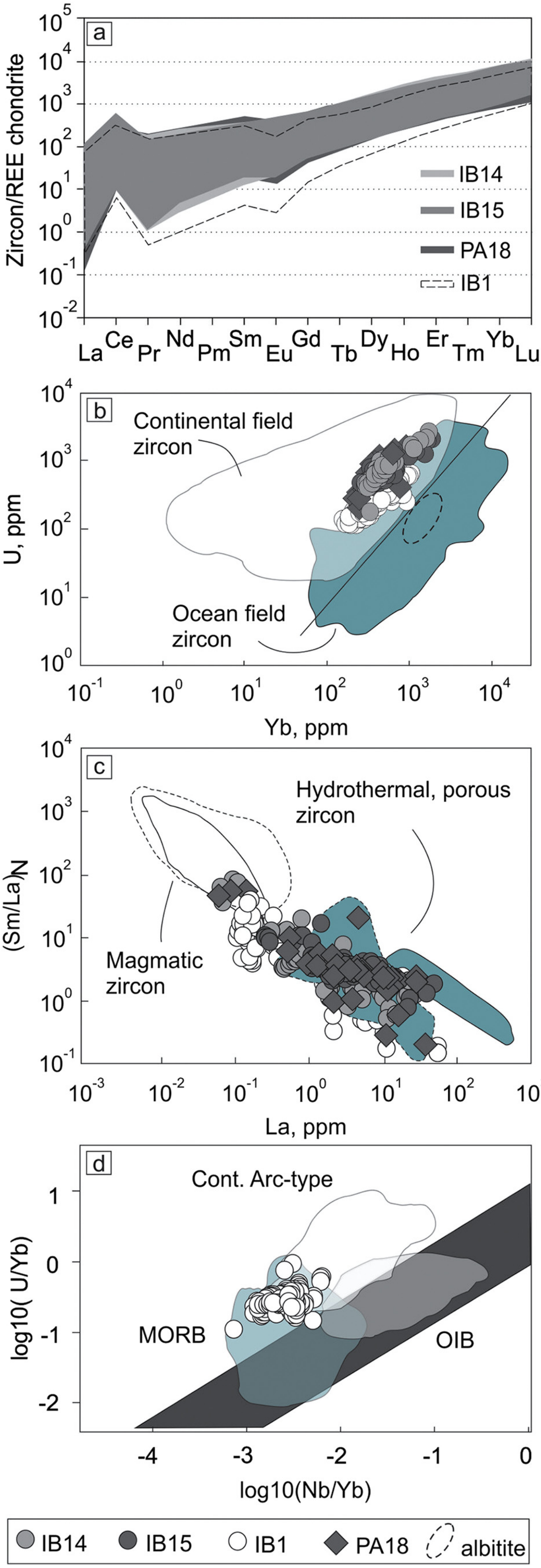

Fig. 12. Geochemical discrimination diagram using zircon trace elements. (a) Chondrite-normalized REE (Boynton, 1984); (b) Yb × U variation diagram for modern oceanic zircon (e.g., Grimes et al., 2009); dotted circle = albitite from Arena et al. (2016); (c) (Sm/La)$_N$ versus La (ppm); fields proposed by Hoskin (2005) for the discrimination of magmatic and hydrothermal zircons shown; comparison with overlapping fields from Grimes et al. (2009) (dotted circle) for magmatic and porous zircons; chondrite normalized Sm/La ratio from Boynton (1984); (d) diagram of log$_{10}$ Nb/Yb versus log$_{10}$ U/Yb used for tectono-magmatic setting of ophiolites (Grimes et al., 2015). The volcanoclastic rock (IB1) is similar to suprasubduction zone type ophiolites.

from Ibaré albitite (Arena et al., 2016) εHf +15 to +13. However, the age groups between 836 and 722 Ma exhibit influence of mantle plus hydrothermally-altered crust with εHf values varying between +12.0 and +1.4. The youngest age group (650–600 Ma) shows εHf values between +6.2 and +1.9. All the age groups, therefore, have juvenile signature with some continent-derived influence. It is well established that the upper mantle is heterogeneous (Hofmann et al., 2003). Several studies have argued for contamination of the MORB source either by the crustal or mantle part of the continental lithosphere (e.g. Hanan et al., 2004; Janney et al., 2005; Hamelin et al., 2013). Heterogeneous MORB includes incompatible element-depleted normal MORB, relatively undepleted transitional MORB and incompatible element-enriched (*E*-type) MORB (Janney et al., 2005). Our data display unusual (+12 to +1) Hf isotope signature in metasomatic rocks. Although we cannot specify which component acted, this component may have mixed with the depleted mantle in the São Gabriel oceanic portion as it approached the subduction zone. The limited Hf isotope data available for the southern Brasiliano Orogen allow a preliminary delimitation of the extent of the particular heterogeneous Hf signature recognized in our studies.

The ability to analyze Lu–Hf isotope ratios in the same spot of a zircon crystal that was previously dated with U–Pb isotopes allows the linking of known geological events (igneous or metamorphic). The application of Hf isotopes in zircon was developed in the past three decades to trace rock origin and the evolution of crust and mantle along time (Patchett et al., 1981; Andersen et al., 2002; Petersson, 2010; Gerdes and Zeh, 2006; Gerdes and Zeh, 2009). In contrast, much less attention has been paid to the Hf isotope composition of zircon that grew during metamorphism (Zheng et al., 2005). The effect of serpentinization and hydrothermal (metasomatic) zircon Lu–Hf and U–Pb isotope systems needs additional studies.

5.3. Zircon trace elements

Our U/Yb data are consistent with the compositions of oceanic crust zircon but overlap the continental field. According to Grimes et al. (2015), "approximately 10% of the available MOR zircons analyzed do exhibit uncharacteristically high U/Yb values and overlap the more enriched 'continental survey' of Grimes et al. (2007, 2009)." The ratio U/Yb < ~0.1 characterizes zircon from differentiated melts originating from the depleted MORB mantle (Grimes et al., 2007; Grimes et al., 2009; Grimes et al., 2015). Such low $(Sm/La)_N$ values as shown here are typically associated with zircon thought to have formed from, or been altered by, hydrothermal fluids (Hoskin, 2005) and are similar to porous oceanic crust zircon (Grimes et al., 2009). Our interpretation is that the zircons are metasomatic. Most of the zircons from metasomatites show hydrothermal composition (Sm/La < 20). High LREE and low $(Sm/La)_N$ ratios may reflect, in part, the composition of sub-micron inclusions or residues in the pores, however such characteristics may also be indicative of interaction with saline aqueous fluids (Grimes et al., 2009).

The integrated evaluation of trace elements with the depleted mantle εHf shows that the zircons evolved from an 880 Ma ocean ridge, with successive pulses of serpentinization at 836, 780 and 722 Ma. Zircon from the metasomatic and volcanoclastic rocks is enriched in some trace elements (e.g., U) causing overlapping between oceanic and continental compositions (U/Yb > 0.1). In addition, the wide range in $^{176}Hf/^{177}Hf$ ratios indicates extensive re-equilibration with crustal material. The zircons have trace-element compositions overlapping the oceanic and continental fields of Grimes et al. (2007, 2015). But Portner et al. (2011) interpreted a subset of zircons from an E-MORB ophiolite that displays higher U/Yb overlapping the continental field of Grimes et al. (2007) as originating from parent melts with variably enriched mantle sources. Low U/Yb (<0.1) appears to be diagnostic of zircons from differentiated melts of the depleted MORB mantle and higher U/Yb values suggest enriched geochemical reservoirs (Grimes et al., 2015, and references therein). Zircon studies in albitite (Arena et al., 2016) from the Ibaré ophiolite showed oceanic zircon with U/Yb ≤0.1 but from Cerro Mantiqueiras ophiolite showed trace-element compositions overlapping the oceanic and continental fields of Grimes et al. (2007, 2015), while zircon rims plotted in the continental field. This may be due to variation in the mantle reservoir. Ibaré albitite zircons crystallized in melts derived from depleted and Cerro Mantiqueiras albitite zircons from enriched mantle and with interference of crustal fluids in the metamorphic zircon rims. Zircon from both Cerro Mantiqueiras and Ibaré albitites formed on the oceanic spreading ridge (920 to 890 Ma; Arena et al., 2016) with crustal influence registered only in Cerro Mantiqueiras albitite. The tectono-magmatic setting obtained from the immobile trace elements in zircon (Grimes et al., 2015) from IB1 exhibit a prominent population of mid-ocean ridge compositions (MOR-type) (Fig. 12d). Zircons from the IB1 sample show similar characteristics to several suprasubduction zone ophiolites, e.g., Semail, Troodos and Ekecikdag, analyzed by Grimes et al. (2015) for tectono-magmatic studies.

Integrated U-Pb age, Hf isotopic signature and trace elements of the metasomatic zircons of Ibaré and Palma show some crustal interference on rock formation. The arc may have been close to the continental crust at the time of ophiolite emplacement. Timing and sources of zircon are thus constrained and help define the evolution of the Brasiliano Orogen and Gondwana agglomeration.

5.4. Classification, geochemical characteristics and tectonic setting of the ophiolite

The information obtained from zircon studies is now integrated with whole-rock geochemistry to interpret the geological environment of ophiolite obduction. Whole-rock geochemistry can yield significant information regarding the type of ophiolite (Pearce, 2008; Dilek et al., 2008; Basta et al., 2011; Dilek and Furnes, 2011; Dilek and Furnes, 2014; Pearce, 2014). In a first approximation, ophiolites are classified either as non-subduction ophiolites or suprasubduction zone ophiolites (Pearce, 2008, 2014; Dilek and Furnes, 2014). Th and Nb are both immobile from weathering to low amphibolite facies metamorphism, and they behave similarly during most petrogenetic processes (Pearce, 2008). In Th and Nb diagrams, non-subduction ophiolites plot predominantly within the MORB-OIB array and suprasubduction zone related plot above the array. For the ophiolites from suprasubduction zone settings, the V versus Ti plot provides the extra information needed to improve the fingerprinting of ophiolite origin (Pearce, 2014, following Shervais, 1982 and Pearce, 2008). Our analyzed rocks compositions plot above the MORB array in the Th/Yb–Nb/Yb diagram (Fig. 13c). Some of the samples plot in the MORB array and others above it in the Nb/Yb versus U/Yb diagram (Fig. 13e) and Nb/Yb versus La/Yb (not shown), indicating subduction zone influence. The proportions of HFSE-REE (Nb, Yb, Ta, Zr, Hf) plot invariably within the MORB array (Fig. 13e–h), similar to Green (2006). The Ti/V ratio of the volcanoclastics (18–52) is typical of MORB and metabasalts (11–36), transitional between MORB and island arc tholeiite (Fig. 13d). Additionally, Pearce (2014) highlighted the distinct trend along time from MORB-like ratios at the beginning of subduction to more island-arc tholeiite-like with increasing subduction influence.

A volcanoclastic metaandesite from the Palma ophiolite (Saalmann et al., 2005b) shows similarity with the studied samples from Ibaré (Fig. 13). Saalmann et al. (2005b) considered the rock typical of arc basalts or active continental margin. The rock would thus be formed from juvenile subduction-related magma with little reworked old continental crust (negative Sm anomaly) typical of accretionary orogens.

We made an integrated evaluation of field geology, U-Pb and εHf isotopic and trace element composition of zircons from metasomatic and selected volcanoclastic (IB1) rocks from Ibaré and Palma. The integrated evaluation with additional whole-rock geochemistry from

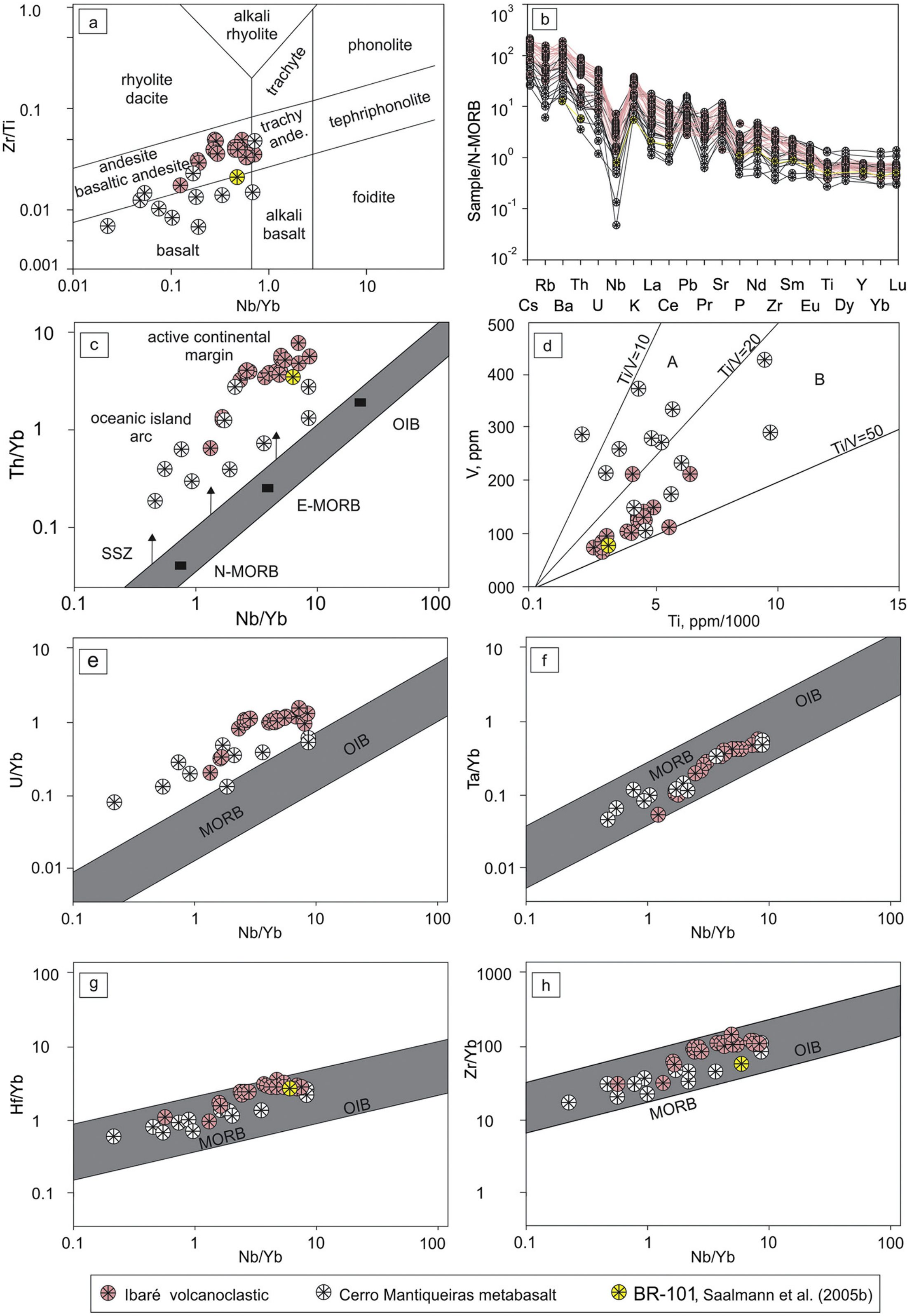

Fig. 13. Whole rock geochemical diagrams. (a) Immobile element–based TAS diagram from Pearce (1996); (b) N-MORB normalized spider diagram (from Sun and McDonough, 1989) from volcanoclastic and metabasalts; (c) the Th/Nb used to distinguish suprasubduction zone (SSZ) from mid-ocean ridge (MORB-OIB array) ophiolites by Pearce (2014); (d) V versus Ti diagram (Pearce, 2014, following Shervais, 1982 and Pearce, 2008). A = Island arc tholeiite (and slab proximal BABB and FAB), B = MORB (and slab distal BABB and FAB); (e–h) plots of selected high-field strength elements (U, Ta, Hf, Zr)/Yb versus Nb/Yb for volcanoclastic and metabasalt rocks. Range of incompatible element ratios MORB-OIB array from Green (2006) indicated by highlighted field.

volcanoclastics (Ibaré; this work), metaandesite (Palma; Saalmann et al., 2005b) and metabasaltic rocks (Cerro Mantiqueiras, this work) allows us to interpret the rock association as subduction-initiation ophiolites. Thus, we interpret the collage of the ophiolites to the eastern margin of the Rio de la Plata Craton with continued progressive accretion, altogether between 836 and 722 Ma in the studied region.

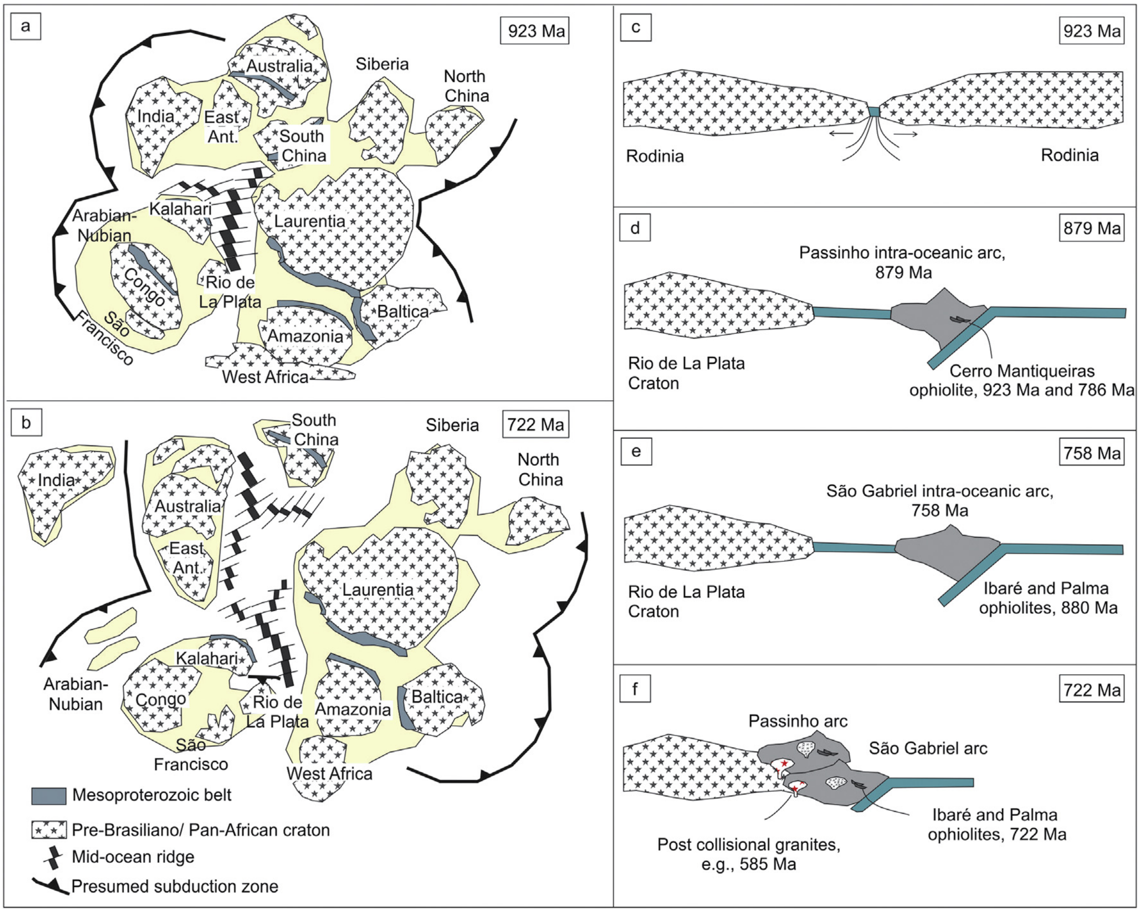

Fig. 14. (a) and (b) Reconstruction configurations of Rodinia at the assembly (923 Ma) and (722 Ma) time (modified after Li et al., 2008 and Bogdanova et al., 2009); (c–f) Neoproterozoic–Early Tonian tectonic model for São Gabriel terrane evolution. See text for details.

5.5. Zr-mobility and chloritic blackwall

Acid fluid activity, frequently considered as responsible for Zr transfer, is not consistent with serpentinization, because fluids concomitant with the serpentinization process are highly alkaline ($pH = 8–12$) (e.g., Neal and Stanger, 1985). However, the crystallization of zircon in the blackwall was possibly due to a pH decrease during chlorite and corrensite formation related to fixing of OH groups by chlorite and corrensite, which could locally reduce the pH of the fluid (Saccocia et al., 1994). Otherwise, Zr may be mobilized by CO_2-rich fluids. Zr may be transferred from both external source and associated rodingite protolith (Dubińska et al., 2004) into the blackwall. With boron introduced into the system by fluids, tourmalinite formed along with chloritite. Similarly, zircon from the chloritic blackwall from the southern Brazilian Shield ophiolites may have co-precipitated with chlorite and tourmaline from highly alkaline water genetically related to serpentinization. Four pulses occurred over time, from the ocean ridge (880 Ma) to the final incorporation of the ophiolite (722 Ma) in the volcanic arc, because the chloritites contain zircons of different ages. Chloritite has a potential for the direct dating of serpentinization.

5.6. Evolution of Brasiliano orogen and inheritance

The Neoproterozoic Earth was shaped largely by the Grenvillian (Sunsás in South America) and Brasiliano (also Pan-African, Cadomian) orogenies. Both the Brasiliano and Grenvillian Orogens are widely recognized in many continental fragments. The normalized frequency distribution of zircon ages from river mouth sand over the world demonstrates that Mesoproterozoic (1.3–1.0 Ga) (Howard et al., 2015, and references therein) and Neoproterozoic (0.9–0.6 Ga) peaks are the largest populations. This means that plate tectonics was active in these periods with extensive subduction.

The Brasiliano Orogen is one of the main Neoproterozoic orogens formed during the assembly of West Gondwana. It comprises the Dom Feliciano (Uruguay and southern Brazil), Ribeira and Araçuaí belts among others (Fig. 1b). Its African counterpart includes the Gariep, Damara, West Congo and Kaoko belts (Goscombe et al., 2005; Philipp et al., 2016 and references therein). Several models have been presented to explain the tectonic evolution of this orogen and its role in the assembly of West Gondwana (Chemale, 2000; Cordani et al., 2003; Basei et al., 2008; Pertille et al., 2017). A rift system was documented between the Kalahari and Congo cratons of Africa, displaying an age range of 1.1–0.95 Ga (Unrug, 1995).

Similar late Mesoproterozoic (1200–1000 Ma) ages from detrital zircons of the Rocha Formation (supracrustal rocks of the Punta del Este terrane) in Uruguay and of the Gariep Belt in southern Africa suggest that they were probably deposited in the same basin, according to Basei et al. (2005). Also, the age of 1100 Ma was obtained on zircon grains from the Punta del Este terrane basement rocks and interpreted as remnant from the Namaqua Belt of Namibia, southern Africa (Basei et al., 2011).

Other correlated Mesoproterozoic ages (1300–1000 Ma) between Brazil and South Africa were obtained, e.g., from West Congo Belt, comparable to the Araçuaí Belt (Espinhaço Supergroup, Brazil) by Frimmel et al. (2006). Additionally, Meso and Neoproterozoic deformed cover in reworked basement terranes were described by Heilbron et al. (2008) for the Ribeira Belt and its southwestern African counterparts.

The formation of Gondwana in the Neoproterozoic resulted from a series of events registered in the Pan-African–Brasiliano belts. These events include subduction of oceanic lithosphere, accretion of terranes, collision of continental blocks and mantle plume activity (Unrug, 1997; Schmitt et al., 2004). The Ribeira Belt is among the younger products of the Pan-African–Brasiliano collage with collisional events taking place from the late Neoproterozoic through the Paleozoic (Schmitt et al., 2004, 2008, and references therein).

In the central-northern part of Brazil, extensional regimes (1.1–0.97 Ga) caused the development of the Grenville orogeny in the Amazonas plate (Bettencourt et al., 1999). In the Goiás massif, southeast of the Amazonian craton, protoliths of orthogneisses have Neoproterozoic crystallization ages of 899 Ma and metavolcanic rocks have ages of 929 to 877 Ma and 764 Ma (Pimentel and Fuck, 1992). A Sm-Nd whole-rock isochron age of 863 ± 97 Ma and model ages of 1.13–0.94 Ga were obtained for Goiás magmatic arc by Pimentel et al. (2000).

In southern Brazil, Mesoproterozoic crust was reported in the basement of the Pelotas Batholith by Pertille et al. (2017). Mesoproterozoic associations also include the Capivarita Anorthosite (1.57 Ga; Chemale et al., 2011) and the Tupi Silveira amphibolite (1.56 Ga; Camozzato et al., 2013). In addition to Neoproterozoic ages (see Fig. 3), this work shows Neoproterozoic ages (880–722, 650 Ma) for ophiolitic rocks. The zircon U-Pb ages and εHf of ophiolites indicate a mantle composition with variable crustal contamination. These data record the onset of the broad taphrogeny in the Tonian for Rodinia break-up and later reconstruction of Gondwana.

The following geotectonic model for the São Gabriel terrane is suggested. The tectonic evolution started at the end of Rodinia, with oceanic opening and crust generation with formation of the ophiolites (ca. 923 Ma Cerro Mantiqueiras and ca. 892 Ma Ibaré) (Fig. 14c). Following, an intra-oceanic arc (ca. 879 Ma Passinho arc) had westward subduction (Fig. 14d) causing the accretion of this arc to the eastern margin of the Rio de la Plata Craton. The Cerro Mantiqueiras ophiolite deformed approximately at 786 Ma, possibly during accretion to the continental crust (Arena et al., 2016). A new intra-oceanic arc was formed (ca. 758 Ma, São Gabriel arc). After the beginning of convergence of a newly subducting plate, an intra-oceanic arc was formed in a subduction-initiation setting (Fig. 14e). Subsequent subduction to the west occurred, and thus the Ibaré and Palma ophiolites were thrusted onto the intra-oceanic island arc (ca. 722 Ma) (Fig. 14f). We position the ophiolite emplacement into the intra-arc close to the craton. The ophiolites were not adjacent to the craton, because the 880–722 Ma juvenile rocks (including youngest ages of 650 Ma) have positive εHf(t) values. This model explains the heterogeneity of ^{176}Hf/^{177}Hf ratios, suggesting that some zircon domains were slightly contaminated by an older crustal component.

5.7. Prolonged break-up process of Rodinia

Rodinia supercontinent existed during the time span ~1000–850 Ma (Bogdanova et al., 2009) or possibly shorter. The Rio de La Prata Craton is commonly proposed as a component of the Rodinia supercontinent associated with Kalahari, Antarctica, Australia and South China (Li et al., 1999). In this configuration, the oceanic albitites (Arena et al., 2016) are suggested to be related to a beginning rifting of the supercontinent.

Previous and present data indicate that the onset of rifting occurred at 923 Ma (Cerro Mantiqueiras ophiolite) and continued until 892 Ma (Ibaré ophiolite) (Arena et al., 2016). This suggests that Rodinia rifting started earlier in southern Brazil than in South China (830–740 Ma) by (Hoffman, 1999; Li et al., 1999).

Four major stages of break-up, which affected to a varying extent separate blocks of Rodinia, occurred at 825–800, 780–755, 740–720, and 650–550 Ma ago (Li et al., 1999, 2008). Geochronological data for rocks of the South China block characterized the period 820 to 720 Ma (Li et al., 2004). The overall mean age of 828 Ma from the mafic intrusives in South China is identical to the 827 Ma age of the dyke swarm of southeast Australia, thought to be of mantle plume origin (Zhao et al., 1994). But on the other hand, Xia et al. (2012) examined ~900 Ma rift-related volcanism in China and suggested that this event temporally coincided with the separation of Australia, East Antarctica, South China and Laurentia, as part of the wider Rodinia break-up. Also ca. ~900–750 Ma, protracted rifting in the Neoproterozoic was concentrated in Scottish promontory of Laurentia (Dalziel and Soper, 2001). Similar ages were also obtained in the Congo and Kalahari margins (880–750 Ma; Johnson et al., 2005) and east Africa (880–740 Ma; Frimmel et al., 2001). Li et al. (2008 and references therein) and Pirajno and Santosh (2015) suggested that these records could have been the first sign of a Rodinia superplume, and the break-up occurring at ~760 Ma (Li et al., 1999).

Crustal thinning is a long-lasting process (Frimmel et al., 2001) during which several pulses of magmatism occur over a period of some hundred million years. According to these authors, it is difficult to compare ages as a tool to reconstruct the configuration of the Neoproterozoic supercontinent. If crustal thinning and eventual break-up were more or less coeval throughout the supercontinent, the arrival of a centrally located superplume head would provide a plausible cause for such extensional tectonism as suggested by Frimmel et al. (2001). The postulated plume head beneath south China and a comparable plume near east Africa would not be possible because the respective areas were at almost opposite ends of the supercontinent. Furthermore, it is important to highlight that Cawood et al. (2013) do not share the plume model.

We highlight evidence of oceanic crust in the time period 923–892 Ma for albitites (Arena et al., 2016) and 880–722 Ma for metasomatites (this work). This is a contribution to the evolution of West Gondwana, suggesting that the beginning of Rodinia break-up was at 923 Ma in the Rio de la Plata Craton (Fig. 14a, b).

6. Conclusion

The southern Brasiliano Orogen formed in a protracted process of generation and emplacement of ophiolites in subduction-initiation zone, granitic magmas and juvenile basaltic rocks. Hf isotopes indicate juvenile mantle depleted signature of the ophiolites. The Ibaré and Palma ophiolites were generated in the oceanic crust and they are part of the same suture. The serpentinization of peridotites of ophiolites began in mid-ocean ridge in the early Tonian (880 Ma). The serpentinization may have continued until the subduction-initiation zone and emplacement onto the intra-oceanic arc (dated at 758 Ma) at 722 Ma. The younger ages may be associated with late alteration processes coinciding with the accretionary orogeny near 650–600 Ma in the southern Brasiliano Orogen. Post-collisional Santa Rita Granite is presently dated at 585 Ma and represents the final major geological event in the region except for shear zone development.

Acknowledgements

This article is part of the PhD thesis by Karine da Rosa Arena at Programa de Pós-Graduação em Geociências, Universidade Federal do Rio Grande do Sul, Brazil. The investigation was supported financially through a scholarship to Karine R. Arena, a grant number 479555/2012-5 to Léo A. Hartmann by Conselho Nacional de Desenvolvimento Científico e Tecnológico (CNPq) and by a FAPERGS grant (Processo 2225-2551/14-8) to Léo A. Hartmann (Rio Grande do Sul State Government). Significant contributions to the improvement of the article by two anonymous journal reviewers are gratefully acknowledged. We are grateful to Associate Editor Professor Alan Collins and Editor-in-Chief Professor Santosh for their careful and efficient handling of the manuscript.

Appendix A. Methodology IB19 sample and trace elements of other samples

Zircon LA-ICP-MS U-Pb dating

Selected sample of granite from Ibaré were prepared for LA-ICP-MS U-Pb zircon analyses at the Institute of Geosciences, University of São Paulo. Backscattered electron (BSE) images of zircons were obtained before isotopic analyses to guide spot selection.

Isotopic data were obtained using a NEPTUNE inductively coupled plasma-mass spectrometer (LA-ICP-MS) coupled with an excimer laser ablation system. The cup configurations optimized for U-Pb data acquisition were IC3 = ^{202}Hg, IC4 = ^{204}(Hg + Pb), L4 = ^{206}Pb, IC6 = ^{207}Pb, L3 = ^{208}Pb, H2 = ^{232}Th and H4 = ^{238}U where L and H were low, with a high mass to Faraday cup position and ICs are ion counting (continuous dynode system). The ICP configurations were: Radio Frequency power = 1100 W; cool gas flow rate ~ 15 L/min (Ar); auxiliary gas flow rate ~ 0.7 L/min (Ar); sample gas flow rate ~ 0.9 L/min. Laser Setup: energy = 6 mJ, repetition rate = 6 Hz, spot size = 32 μm, helium carrier gás = 0.25 + 0.5 L/min. The routine U-Pb analysis consists of 2 blanks, 2 NIST 612, 3 external standard (GJ1 standard), 13 unknown samples, 2 external standards, 2 NIST 612 and 2 blanks measurement. Each run consisted of 40 cycles, with 1 s/cycle. The ^{204}Hg interference on ^{204}Pb was corrected by ^{202}Hg where the value of ^{204}Pb/^{202}Hg ratio is 4.2. The normalization of the ^{207}Pb/^{206}Pb ratio was achieved by combined NIST and external standards. The normalization of ^{206}Pb/^{238}U ratio was achieved by external standards. The GJ1 standard was utilized for mass bias correction.

The residual common Pb was corrected according to the measured 204Pb concentration using the known terrestrial composition (Stacey and Kramers, 1975). The uncertainty introduced by laser-induced fractionation of elements and mass instrumental discrimination were corrected using a reference standard of zircon (GJ-1) (608.5 ± 0.4 Ma, Jackson et al., 2004). The isotope ratios and interelement fractionation of data obtained by the ICP-MS instrument were evaluated by interspersing the GJ-1 zircon standard in every set of thirteen zircon samples (spots). The GJ-1 standard meets the requirements for the methods used in the laboratory, and the ratios of 206Pb*/238U, 207Pb*/206Pb* and 232Th/238U were homogeneous throughout the application of bracket technique. External errors were calculated using error propagation of the individual measurements of the standard GJ-1 and measurements of the individual zircon samples (spots). Ages calculation were made using Isoplot version 4 based mainly on 206Pb/238U (Ludwig, 2008).

Zircon Lu-Hf isotopes analyses

All Lu–Hf zircon analysis were carried out at the Institute of Geosciences, University of São Paulo, on a Neptune multicollector inductively coupled plasma mass spectrometer equipped with a 193 nm laser–ablation Photon system. Lu–Hf isotopic analyses were performed in the same zircon grains that were previously dated. The used spot was 47 μm in diameter; ablation time of 60s; repetition rate of 7 Hz, and He was used as carrier gas.

The 176Hf isotope has interferences from 176Yb (abundance 12.7%) and 176Lu (5.2%) with the interfering factor of 176Yb affecting 4 times more than 176Lu. To eliminate the interferences on 176Hf the abundance constants: 173Yb/171Yb = 1.123456; 174Yb/173Yb = 1.972124; 176Yb/173Yb = 0.786956; 176Lu/175Lu = 0.2645; 178Hf/177Hf = 1.46735 and 179Hf/177Hf 0.7325 (Thirlwall and Walder, 1995) are reported to NEPTUNE reduction software to make the interference corrections and normalization of the ratio 176H/177Hf using "ON LINE" mode.

The 176Lu and 176Yb isobaric interferences on 176Hf are corrected by monitoring the 175Lu, 173Yb and 171Yb signals. On 176Hf/177Hf ratio is also taken into account the corrections of "mass bias" of Lu and Yb. Normalization of 176Hf/177Hf ratio is based on reason 179Hf/177Hf = 0.7325 and reason 178Hf/177Hf is calculated as a quality control test to be around 1467. All the errors of the reasons measures are 2 sigma.

Cup configuration and instrument operating parameters are presented below. The isotopes 171Yb, 173Yb, 174Yb, 175Lu, 176(Hf + Yb + Lu), 177Hf, 178Hf, 179Hf and 181Ta were collected simultaneously on Faraday cups. 176Lu/175Lu ratio of 0.02669 was used to calculate 176Lu/177Hf. Mass bias corrections of Lu–Hf isotopic ratios were calculated using the variations of GJ 82C standard.

A decay constant for 176Lu of 1.865×10^{-11} yr^{-1} (Söderlund et al., 2004), the present–day chondritic ratios of 176Hf/177Hf = 0.282772 and 176Lu/177Hf = 0.0332 (Blichert-Toft and Albarède, 1997) were adopted to calculate εHf values. A two–stage continental model (TDM2) was calculated using the initial 176Hf/177Hf of zircon and the 176Lu/177Hf = 0.022 ratio for the lower continental crust (Griffin et al., 2004).

Analyses of Lu-Hf in zircon do not use any treatment off line. It is used only the Thermo software where the interference from Lu and Yb on the 176Hf, corrections back ground, calculation of reasons and statistics, are made automatically in online mode by the software itself.

Cup configuration and interferences

L4	L3	L2	L1	Axial	H1	H2	H3	H4
^{171}Yb	^{173}Yb	^{174}Yb	^{175}Lu	^{176}Hf	^{177}Hf	^{178}Hf	^{179}Hf	^{181}Ta

Instrument operating parameters

MC–ICP–MS		*Laser ablation*	
Model	ThermoFinnigan Neptune	Type	193 nm Ar–F excimer laser
Forward power	952 W	Model	Analyte G2 – Photon Machines
Mass resolution	Low (400)	Repetition rate	7 Hz
		Laser fluence	8.55 J/m^2
		Spot size	47 μm

Gas flows-laser ablation		*Data reduction*		
Cool/plasma (Ar)	16 L/min	Mass bias	^{173}Yb/^{171}Yb	1.123456
			^{179}Hf/^{177}Hf	0.7325
Auxiliary (Ar)	0.80 L/min	Interference correction	^{176}Yb/^{173}Yb	0.786956
Sample cell gas (He)	~1 L/min		^{176}Lu/^{175}Lu	0.026549
Nitrogen	1.4 mL/min		^{174}Yb/^{173}Yb	1.973000

Cup configuration and instrument operating parameters for Hf analyses, following guidelines from Fisher et al. (2014).

References

Blichert-Toft, J., Albarède, F., 1997. The Lu—Hf isotope geochemistry of chondrites and the evolution of the mantle–crust system. Earth and Planetary Science Letters 148, 243–258.

Fisher, C. M., Vervoort, J.D., Hanchar, J.M., 2014. Guidelines for reporting zircon Hf isotopic data by LA–MC–ICPMS and potential pitfalls in the interpretation of these data. Chemical Geology 363, 125–133.

Griffin, W.L., Belousova, E.A Shee, S.R., Pearson, N.J., O'Reilly, S.Y., 2004. Archean crust evolution in the northern Yilgarn Craton: U—Pb and Hf–isotope evidence from detrital zircons. Precambrian Research 131, 231–282.

Jackson, S.E., Pearson, N.J., Griffin, W.L., Belousova, E.A., 2004. The application of laser ablation inductively coupled plasma mass spectrometry to in situ U—Pb zircon geochronology. Chemical Geology 211, 47–69.

Ludwig, K.R., 2008. Manual for Isoplot 3.7. Berkeley Geochronology Center, Special Publication 4, 77.

Thirlwall, M.F., Walder, A.J., 1995. In situ Hafnium isotope analysis of zircon by inductively coupled plasma multiple collector mass spectrometer. Chemical Geology 122, 241–247.

Söderlund, U., Patchett, P.J., Vervoort, J.D., Isachsen, C.E., 2004. The ^{176}Lu decay constant determined by Lu—Hf and U—Pb isotope systematics of Precambrian mafic intrusions. Earth and Planetary Science Letters 219, 311–324.

Stacey, J.S., Kramers, J.D., 1975. Approximation of Terrestrial Lead Isotope Evolution by a 2-Stage Model. Earth and Planetary Science Letters 26, 207–221.

At Universidade Federal de Ouro de Preto, instrumental mass bias and ablation depth-dependent elemental fractionation were corrected using the primary standard NIST612. This is as recommended by Van Achterbergh et al. (2001) by choosing the time-resolved signal for the unknown zircon that is the identical integration window of the primary standard NIST612. The mass dependent drift is calculated based on the chosen integration window of the time-dependent signal. The yield for each element relative to the yield of the internal standard for each analysis is plotted relative to the same ratio for the first standard analysis according to the equation: (Yieldi / Yieldistd)n/(Yieldi / Yieldistd)1(std) where Yieldistd = yield for the internal standard trace element concentrations calculated using the following equations: concni = (cpsnij /abundancej) / (yieldni) 1 where concni = the concentration of element i in analysis n, cpsnij = the mean count rate (background-subtracted) of isotope j of i in analysis n, abundancej = natural abundance of isotope j, yieldni = cps per ppm of element i in analysis n. The yield of element i in analysis n is determined by: yieldni = yieldns * Int(yieldni / yieldns)std 2 where yieldns = cps per ppm of the internal standard s in analysis n, Int(yieldni / yieldns)std = the ratio of the yield of element i in analysis n to the yield of the internal standard s in analysis n, interpolated over the standard analyses. For more information on the data reduction method see Van Achterbergh et al. (2001).

Appendix B. LA-ICP-MS U-Pb geochronological data of zircon grains of chloritite (IB15) and tourmalinite (IB14) samples from Ibaré ophiolite

Spot	Pbc (%)	U (ppm)	Th/U	Ages				Isotopic ratios						Rho	Conc (%)
				^{206}Pb/^{238}U	2s	^{207}Pb/^{235}U	2s	^{207}Pb/^{206}Pb	2s	^{207}Pb/^{235}U	2s	^{206}Pb/^{238}U	2s		
IB14-56*	0.60	255	0.09	607.6	15.1	626.0	21.1	0.06255	3.6	0.85245	4.5	0.09884	2.6	0.58	97
IB14-17	0.27	434	0.82	655.1	9.6	657.0	10.7	0.06170	1.6	0.90997	2.2	0.10697	1.5	0.70	100
IB14-29*	0.39	689	0.57	656.2	20.9	655.8	29.2	0.06143	4.9	0.90755	6.0	0.10716	3.3	0.56	100
IB15-51	−0.49	549	0.34	662.2	45.7	678.4	79.4	0.06372	13.6	0.95053	15.4	0.10818	7.2	0.47	98
IB14-61	0.25	117	0.57	668.2	13.6	664.5	18.0	0.06136	3.0	0.92406	3.7	0.10921	2.1	0.58	101
IB15-30	−0.05	283	0.22	680.0	10.6	699.0	12.8	0.06458	1.9	0.99053	2.5	0.11124	1.6	0.65	97
IB15-36	−0.02	252	0.46	690.3	12.1	696.6	15.2	0.06326	2.4	0.98577	3.0	0.11302	1.8	0.62	99
IB15-20	0.03	877	0.61	692.1	8.8	712.4	9.0	0.06507	1.1	1.01692	1.8	0.11334	1.3	0.77	97
IB15-3*	0.15	218	0.73	693.8	29.9	709.9	44.0	0.06460	7.1	1.01205	8.4	0.11363	4.5	0.54	98
IB15-15	0.05	392	0.90	695.3	9.1	702.2	9.3	0.06348	1.2	0.99680	1.8	0.11388	1.4	0.75	99
IB14-5	0.14	154	0.05	696.5	11.5	731.3	14.3	0.06705	2.1	1.05481	2.7	0.11409	1.7	0.64	95
IB15-1	0.38	41	0.10	698.7	14.1	708.2	20.7	0.06390	3.4	1.00862	4.0	0.11448	2.1	0.53	99
IB15-57*	−0.12	511	0.79	699.9	12.0	708.0	15.6	0.06377	2.4	1.00837	3.0	0.11468	1.8	0.59	99
IB15-11	0.26	317	0.75	700.2	11.7	705.0	14.6	0.06337	2.2	1.00237	2.9	0.11473	1.8	0.62	99
IB15-10*	0.18	251	0.48	702.3	16.0	703.9	22.1	0.06302	3.6	1.00020	4.3	0.11511	2.4	0.56	100
IB14-65*	0.44	265	0.63	704.1	20.5	712.7	28.2	0.06395	4.5	1.01764	5.4	0.11542	3.1	0.57	99
IB15-35	0.02	1248	0.78	705.4	9.6	708.6	10.0	0.06331	1.3	1.00946	2.0	0.11564	1.4	0.73	100
IB15-2	0.36	301	0.47	705.5	12.0	715.0	14.6	0.06410	2.2	1.02216	2.8	0.11566	1.8	0.63	99
IB15-13	0.27	326	0.57	707.0	12.4	711.7	15.8	0.06355	2.4	1.01563	3.1	0.11591	1.9	0.61	99
IB15-6*	0.35	440	1.15	710.4	14.1	721.7	18.4	0.06447	2.8	1.03559	3.5	0.11650	2.1	0.59	98
IB15-7	−0.15	158	0.51	712.2	11.2	699.3	13.9	0.06155	2.2	0.99123	2.7	0.11681	1.7	0.61	102
IB15-3	0.29	80	0.32	713.3	37.9	721.9	56.9	0.06422	9.1	1.03593	10.7	0.11700	5.6	0.52	99
IB14-51	0.32	227	0.62	714.1	10.7	727.3	12.2	0.06481	1.7	1.04676	2.3	0.11715	1.6	0.68	98
IB15-6	0.29	423	0.61	715.2	10.5	712.7	11.8	0.06290	1.7	1.01768	2.3	0.11734	1.5	0.68	100
IB14-50*	0.43	352	0.58	716.4	16.4	721.2	21.5	0.06383	3.3	1.03447	4.1	0.11755	2.4	0.59	99
IB14-4*	0.24	465	0.83	717.0	9.9	739.9	11.0	0.06612	1.5	1.07243	2.1	0.11764	1.5	0.70	97
IB14-50	0.37	337	0.20	717.4	11.3	712.4	13.4	0.06266	2.0	1.01702	2.6	0.11772	1.7	0.64	101
IB14-36*	0.31	298	0.66	717.9	15.5	745.3	20.5	0.06670	3.1	1.08334	3.8	0.11781	2.3	0.60	96
IB14-37	0.30	373	0.78	718.0	11.2	737.9	12.8	0.06577	1.8	1.06835	2.4	0.11782	1.6	0.68	97
IB14-68	0.26	135	0.48	718.2	13.2	716.1	16.5	0.06303	2.5	1.02436	3.2	0.11786	1.9	0.61	100
IB14-58**	0.41	313	0.93	719.1	13.2	722.6	16.7	0.06376	2.6	1.03734	3.2	0.11800	1.9	0.61	100
IB14-40	0.30	555	0.57	719.2	11.0	733.0	12.5	0.06503	1.8	1.05826	2.4	0.11803	1.6	0.67	98
IB14-49	0.34	200	0.53	719.7	11.0	736.7	12.7	0.06544	1.8	1.06580	2.4	0.11812	1.6	0.67	98
IB14-54	0.29	173	0.56	719.9	16.5	732.2	21.7	0.06486	3.3	1.05661	4.1	0.11814	2.4	0.59	98
IB14-21	0.19	258	0.68	720.0	10.4	744.7	12.0	0.06642	1.7	1.08226	2.3	0.11817	1.5	0.67	97
IB14-39	0.29	420	0.66	720.2	10.7	731.1	11.9	0.06471	1.6	1.05453	2.3	0.11819	1.6	0.69	98
IB14-30*	0.35	331	0.57	720.2	10.4	726.8	11.5	0.06417	1.6	1.04576	2.2	0.11820	1.5	0.69	99

(continued on next page)

(*continued*)

Spot	Pbc (%)	U (ppm)	Th/U	Ages				Isotopic ratios						Rho	Conc (%)
				$^{206}Pb/^{238}U$	2s	$^{207}Pb/^{235}U$	2s	$^{207}Pb/^{206}Pb$	2s	$^{207}Pb/^{235}U$	2s	$^{206}Pb/^{238}U$	2s		
IB14-26	0.41	286	0.77	720.3	10.7	746.3	12.3	0.06659	1.7	1.08542	2.3	0.11821	1.6	0.68	97
IB14-22	0.24	206	0.69	720.6	10.1	726.5	11.1	0.06410	1.5	1.04523	2.1	0.11827	1.5	0.70	99
IB14-31	0.35	904	1.22	720.6	10.3	748.3	11.3	0.06681	1.5	1.08958	2.1	0.11828	1.5	0.71	96
IB14-19	0.21	372	0.89	721.1	11.2	742.6	13.4	0.06605	1.9	1.07780	2.5	0.11835	1.6	0.65	97
IB15-48*	−0.05	309	0.73	721.1	11.7	722.6	14.3	0.06357	2.2	1.03739	2.8	0.11835	1.7	0.62	100
IB14-67*	0.35	159	0.66	721.2	20.0	730.6	27.3	0.06455	4.3	1.05356	5.2	0.11837	2.9	0.57	99
IB14-13*	0.27	377	0.69	721.6	10.1	723.4	10.7	0.06362	1.4	1.03897	2.1	0.11844	1.5	0.72	100
IB14-14	0.23	140	0.65	721.9	11.2	716.1	13.0	0.06269	1.9	1.02432	2.5	0.11850	1.6	0.65	101
IB14-46	0.28	347	0.15	722.0	10.4	709.3	11.5	0.06186	1.6	1.01083	2.2	0.11851	1.5	0.68	102
IB14-27	0.25	642	0.08	722.1	11.4	744.7	13.2	0.06621	1.8	1.08218	2.5	0.11853	1.7	0.67	97
IB14-23	0.21	527	1.02	722.5	10.1	721.0	11.1	0.06324	1.5	1.03410	2.1	0.11859	1.5	0.69	100
IB14-29	0.28	189	0.64	722.5	10.5	730.1	11.7	0.06436	1.6	1.05243	2.2	0.11860	1.5	0.69	99
IB14-69	0.46	168	0.67	722.5	13.4	744.8	17.2	0.06619	2.6	1.08238	3.2	0.11860	2.0	0.61	97
IB14-42*	0.28	519	1.06	722.6	13.7	738.7	17.1	0.06542	2.5	1.06999	3.2	0.11861	2.0	0.62	98
IB14-28	0.25	330	0.22	722.7	10.2	725.1	11.3	0.06373	1.6	1.04243	2.2	0.11864	1.5	0.69	100
IB14-10	0.34	424	0.44	722.7	10.7	733.2	12.0	0.06472	1.7	1.05865	2.3	0.11864	1.6	0.68	99
IB14-53	0.59	484	0.61	722.8	14.4	784.5	19.2	0.07124	2.8	1.16551	3.5	0.11866	2.1	0.60	92
IB14-36	0.30	175	0.57	722.8	10.6	720.8	11.7	0.06319	1.7	1.03377	2.3	0.11866	1.5	0.68	100
IB14-8	0.36	1638	1.26	723.0	10.5	718.2	11.7	0.06285	1.6	1.02849	2.3	0.11869	1.5	0.68	101
IB14-43	0.27	395	0.50	723.1	10.9	722.7	12.2	0.06339	1.7	1.03747	2.3	0.11870	1.6	0.68	100
IB14-9	0.33	431	0.74	723.3	11.1	740.7	12.9	0.06560	1.8	1.07400	2.4	0.11875	1.6	0.66	98
IB14-20	0.23	461	0.72	723.4	13.0	722.0	15.6	0.06328	2.3	1.03608	3.0	0.11875	1.9	0.63	100
IB14-71	0.29	145	0.51	723.6	11.6	737.7	13.6	0.06520	1.9	1.06783	2.6	0.11878	1.7	0.66	98
IB14-12*	0.35	298	0.57	723.9	10.8	731.0	12.3	0.06434	1.7	1.05420	2.3	0.11884	1.6	0.67	99
IB14-44	0.38	401	1.01	723.9	12.4	732.6	15.4	0.06453	2.3	1.05742	2.9	0.11884	1.8	0.62	99
IB14-67	0.33	1459	1.23	724.1	10.3	727.7	11.2	0.06391	1.5	1.04763	2.1	0.11888	1.5	0.70	100
IB14-32	0.27	1669	1.13	724.2	9.9	721.5	10.3	0.06314	1.4	1.03510	2.0	0.11890	1.4	0.73	100
IB14-15	0.18	507	0.96	724.4	10.8	718.5	12.4	0.06277	1.8	1.02924	2.4	0.11893	1.6	0.66	101
IB14-34*	0.28	347	0.86	724.5	11.3	747.7	13.4	0.06636	1.9	1.08842	2.5	0.11895	1.6	0.65	97
IB14-18	0.22	331	0.19	724.6	10.8	747.9	12.5	0.06637	1.8	1.08878	2.4	0.11897	1.6	0.67	97
IB14-42	0.29	355	0.93	725.0	10.2	723.6	11.1	0.06332	1.5	1.03929	2.1	0.11904	1.5	0.70	100
IB14-57	0.35	297	0.77	725.4	10.6	737.4	11.7	0.06500	1.6	1.06728	2.2	0.11910	1.5	0.69	98
IB14-35	0.30	253	0.55	725.5	10.4	748.0	11.4	0.06630	1.5	1.08892	2.1	0.11912	1.5	0.70	97
IB14-32*	0.37	1916	0.95	726.2	13.3	734.3	16.2	0.06453	2.4	1.06088	3.1	0.11924	1.9	0.63	99
IB15-52	−0.04	270	0.54	726.2	12.9	760.5	16.6	0.06780	2.4	1.11481	3.1	0.11925	1.9	0.61	95
IB14-1	−0.05	298	0.75	726.3	11.9	746.2	14.9	0.06599	2.2	1.08522	2.8	0.11926	1.7	0.62	97
IB15-22	0.03	250	0.59	726.6	9.6	744.8	9.9	0.06579	1.2	1.08231	1.9	0.11931	1.4	0.75	98
IB15-17	0.05	291	0.64	727.3	9.5	722.1	9.6	0.06293	1.2	1.03630	1.9	0.11943	1.4	0.74	101
IB14-16*	0.13	1574	0.26	727.4	16.0	761.2	21.2	0.06778	3.2	1.11624	3.9	0.11944	2.3	0.59	96
IB14-6	−0.02	184	0.07	727.4	14.0	744.7	18.2	0.06571	2.8	1.08212	3.4	0.11945	2.0	0.59	98
IB14-47	0.30	68	0.01	727.6	21.6	760.5	29.7	0.06767	4.5	1.11484	5.5	0.11949	3.1	0.57	96
IB14-12	0.25	186	0.65	728.0	12.0	721.2	14.3	0.06276	2.1	1.03455	2.7	0.11956	1.7	0.63	101
IB14-56	0.37	1421	0.75	729.6	11.3	721.4	12.6	0.06264	1.8	1.03502	2.4	0.11983	1.6	0.68	101
IB15-26	−0.01	464	0.72	730.0	9.4	732.8	9.6	0.06399	1.2	1.05787	1.8	0.11991	1.4	0.75	100
IB15-12	0.81	153	1.01	731.3	32.6	729.1	45.6	0.06341	7.2	1.05034	8.6	0.12014	4.7	0.55	100
IB14-63	0.44	291	0.58	731.7	12.3	715.7	15.0	0.06176	2.3	1.02349	2.9	0.12019	1.8	0.61	102
IB15-53	−0.06	306	0.61	732.0	9.8	745.4	10.4	0.06536	1.4	1.08371	2.0	0.12025	1.4	0.72	98
IB15-33	−0.06	273	0.63	732.6	10.3	746.8	11.7	0.06548	1.6	1.08660	2.2	0.12035	1.5	0.68	98
IB15-37	−0.02	168	0.55	732.6	10.0	743.0	10.7	0.06500	1.4	1.07875	2.0	0.12036	1.4	0.71	99
IB15-57	−0.10	654	0.90	733.0	9.9	745.9	10.5	0.06533	1.4	1.08462	2.0	0.12042	1.4	0.72	98
IB15-25	0.05	218	0.88	734.2	10.1	754.1	10.9	0.06622	1.4	1.10154	2.0	0.12064	1.5	0.72	97
IB14-34	0.27	422	0.92	734.3	10.2	724.4	10.7	0.06258	1.5	1.04096	2.1	0.12064	1.5	0.71	101
IB14-60*	0.22	74	0.75	735.3	22.5	738.6	31.7	0.06421	5.0	1.06971	6.0	0.12082	3.2	0.54	100
IB15-34	−0.03	239	0.61	736.2	9.8	764.5	10.4	0.06733	1.3	1.12317	1.9	0.12098	1.4	0.73	96
IB15-64	−0.08	219	0.45	737.2	12.6	735.2	15.4	0.06362	2.3	1.06285	2.9	0.12116	1.8	0.62	100
IB15-32	−0.08	983	1.03	740.2	11.9	759.7	14.6	0.06636	2.1	1.11326	2.7	0.12167	1.7	0.62	97
IB15-16*	0.05	199	0.45	741.0	9.9	746.9	10.5	0.06470	1.4	1.08668	2.0	0.12181	1.4	0.72	99
IB15-28	0.02	303	0.68	741.2	11.3	741.8	12.8	0.06406	1.8	1.07635	2.4	0.12186	1.6	0.66	100
IB14-58*	0.28	232	0.67	742.5	11.2	770.8	12.7	0.06752	1.7	1.13648	2.3	0.12207	1.6	0.68	96
IB15-30*	0.00	272	0.92	745.5	9.8	762.9	10.1	0.06625	1.3	1.11980	1.9	0.12259	1.4	0.74	98
IB15-9	−0.11	520	0.88	745.8	10.1	761.0	10.8	0.06599	1.4	1.11596	2.0	0.12265	1.4	0.71	98
IB15-16	0.04	1321	1.10	746.6	9.4	750.0	9.3	0.06457	1.1	1.09313	1.7	0.12279	1.3	0.77	100
IB15-21	0.03	373	0.79	748.6	9.7	741.6	9.6	0.06337	1.2	1.07585	1.8	0.12313	1.4	0.75	101
IB15-50	−0.04	122	0.65	748.8	16.1	766.9	21.5	0.06643	3.2	1.12821	4.0	0.12317	2.3	0.57	98
IB14-58	0.26	199	0.76	750.2	13.2	778.5	16.2	0.06775	2.3	1.15274	3.0	0.12341	1.9	0.63	96
IB15-14	0.05	229	0.73	751.7	10.0	755.7	10.3	0.06479	1.3	1.10480	1.9	0.12367	1.4	0.73	99
IB14-65	0.32	162	0.69	756.9	21.2	775.7	29.0	0.06675	4.3	1.14663	5.3	0.12458	3.0	0.56	98
IB14-72	0.27	484	0.34	759.1	11.2	763.0	12.5	0.06501	1.7	1.12012	2.3	0.12497	1.6	0.68	99
IB14-70	0.34	348	0.61	759.7	14.4	768.2	17.5	0.06558	2.5	1.13090	3.2	0.12507	2.0	0.62	99
IB15-19	0.03	552	0.06	760.1	9.8	754.5	9.5	0.06388	1.1	1.10230	1.8	0.12515	1.4	0.76	101
IB15-31	−0.05	247	0.51	760.5	21.4	763.0	29.0	0.06488	4.4	1.12007	5.3	0.12521	3.0	0.56	100
IB14-4	0.36	553	0.75	762.8	13.4	797.5	16.2	0.06890	2.2	1.19322	2.9	0.12561	1.9	0.64	96
IB14-41	0.27	479	0.60	765.7	11.9	756.5	13.3	0.06362	1.8	1.10642	2.5	0.12613	1.6	0.67	101
IB14-48	0.31	1035	1.29	770.0	11.1	757.1	12.3	0.06333	1.7	1.10780	2.3	0.12687	1.5	0.67	102
IB14-73*	0.55	1105	2.23	771.8	13.0	792.1	16.1	0.06738	2.3	1.18162	2.9	0.12719	1.8	0.61	97

(*continued*)

Spot	Pbc (%)	U (ppm)	Th/U	Ages				Isotopic ratios						Rho	Conc (%)
				^{206}Pb/^{238}U	2s	^{207}Pb/^{235}U	2s	^{207}Pb/^{206}Pb	2s	^{207}Pb/^{235}U	2s	^{206}Pb/^{238}U	2s		
IB14-45	0.18	329	0.66	776.4	21.2	789.5	27.8	0.06665	4.1	1.17618	5.0	0.12799	2.9	0.58	98
IB14-73	0.44	1138	1.50	777.5	12.0	773.0	14.0	0.06456	2.0	1.14110	2.6	0.12818	1.6	0.64	101
IB14-59	0.30	815	1.10	779.1	11.8	775.1	13.2	0.06467	1.8	1.14554	2.4	0.12847	1.6	0.66	101
IB14-33	0.27	2454	0.31	779.2	11.2	788.2	11.8	0.06624	1.5	1.17343	2.1	0.12848	1.5	0.71	99
IB14-60	0.27	778	0.87	779.7	12.2	789.9	13.6	0.06639	1.8	1.17701	2.5	0.12858	1.7	0.67	99
IB14-52	0.34	602	0.76	779.8	11.1	777.8	12.0	0.06493	1.6	1.15114	2.2	0.12858	1.5	0.69	100
IB15-24	0.03	202	0.67	782.5	10.4	784.1	10.7	0.06545	1.3	1.16458	2.0	0.12905	1.4	0.72	100
IB14-24	0.46	549	0.40	789.4	13.2	807.7	15.9	0.06767	2.2	1.21547	2.8	0.13027	1.8	0.63	98
IB14-16	0.29	1896	0.46	801.2	10.7	810.4	11.0	0.06694	1.4	1.22140	2.0	0.13234	1.4	0.72	99
IB14-13	0.23	130	1.13	804.4	20.5	813.9	26.5	0.06708	3.8	1.22912	4.7	0.13290	2.7	0.58	99
IB15-12*	0.22	321	0.34	806.4	12.5	807.2	14.4	0.06609	2.0	1.21430	2.6	0.13325	1.7	0.64	100
IB15-29	−0.07	129	0.56	809.6	22.8	811.1	30.7	0.06628	4.5	1.22295	5.4	0.13381	3.0	0.55	100
IB14-59*	0.34	317	1.13	810.4	35.6	806.2	47.8	0.06564	7.0	1.21230	8.4	0.13395	4.7	0.56	101
IB14-38	0.32	241	1.26	834.7	12.3	851.8	13.3	0.06893	1.7	1.31391	2.3	0.13825	1.6	0.69	98
IB14-31*	0.23	67	0.84	847.4	14.5	853.9	17.1	0.06807	2.3	1.31856	2.9	0.14049	1.8	0.62	99
IB15-41	0.06	515	0.09	871.1	14.8	879.0	16.7	0.06901	2.2	1.37661	2.8	0.14468	1.8	0.64	99
IB15-10	0.27	606	1.97	876.2	12.3	879.0	13.1	0.06858	1.6	1.37664	2.2	0.14558	1.5	0.68	100
IB14-30	0.75	140	0.84	880.6	26.0	888.1	32.9	0.06927	4.5	1.39801	5.5	0.14637	3.1	0.58	99
IB15-18	−0.71	226	0.91	892.8	34.6	909.9	51.0	0.07080	7.2	1.45005	8.3	0.14855	4.1	0.50	98
IB14-11	0.38	47	0.77	901.3	22.8	923.7	29.1	0.07170	3.9	1.48352	4.7	0.15006	2.7	0.57	98
IB14-25	4.48	199	0.91	910.3	57.5	945.1	92.3	0.07348	12.7	1.53660	14.3	0.15166	6.7	0.47	96
IB15-27	0.07	20	0.19	998.5	25.0	1002.5	37.1	0.07290	5.0	1.68397	5.7	0.16753	2.7	0.47	100

All analyses are corrected for 204Pb; Pbc = Common Pb. * = altered portion, commonly near rim.

Appendix C. LA-ICP-MS U-Pb geochronology data of zircon grains of chloritite (PA18) sample from Palma ophiolite

Spot	Pbc (%)	U (ppm)	Th/U	Ages				Isotopic ratios						Rho	Conc (%)
				^{206}Pb/^{238}U	2s	^{207}Pb/^{235}U	2s	^{207}Pb/^{206}Pb	2s	^{207}Pb/^{235}U	2s	^{206}Pb/^{238}U	2s		
PA18-57	0.22	234	0.50	592.8	10.8	594.3	15.2	0.05990	2.8	0.79551	3.3	0.09632	1.9	0.57	100
PA18-15	−0.01	337	1.59	595.1	8.1	594.6	12.1	0.05970	2.3	0.79603	2.7	0.09670	1.4	0.53	100
PA18-27	0.03	137	0.79	604.8	5.2	601.5	7.7	0.05960	1.4	0.80835	1.7	0.09837	0.9	0.53	101
PA18-37	0.03	220	0.74	627.3	5.3	633.7	7.8	0.06150	1.4	0.86650	1.6	0.10219	0.9	0.54	99
PA18-35	0.03	185	0.86	630.1	7.6	634.4	11.0	0.06130	1.9	0.86791	2.3	0.10268	1.3	0.55	99
PA18-10	0.08	794	0.93	635.2	8.9	639.7	13.0	0.06147	2.3	0.87768	2.7	0.10356	1.5	0.54	99
PA18-46	0.11	250	0.75	702.3	20.9	726.7	29.6	0.06589	4.7	1.04565	5.6	0.11509	3.1	0.56	97
PA18-24	0.06	1122	1.23	707.9	9.3	733.1	13.1	0.06614	2.1	1.05848	2.5	0.11607	1.4	0.55	97
PA18-63	0.02	134	1.24	708.0	6.5	717.8	9.1	0.06421	1.5	1.02779	1.8	0.11609	1.0	0.55	99
PA18-1	0.03	319	0.69	709.5	9.4	729.0	13.0	0.06547	2.0	1.05024	2.5	0.11634	1.4	0.56	97
PA18-11	0.04	537	0.68	713.5	5.0	716.7	6.9	0.06354	1.1	1.02549	1.3	0.11704	0.7	0.55	100
PA18-28	0.06	427	0.52	713.8	6.4	724.4	8.7	0.06447	1.4	1.04089	1.7	0.11710	0.9	0.57	99
PA18-50	−0.10	165	0.29	714.1	15.0	722.1	21.4	0.06416	3.5	1.03642	4.1	0.11715	2.2	0.54	99
PA18-12	0.05	311	2.02	714.2	5.2	731.6	7.3	0.06533	1.2	1.05540	1.4	0.11716	0.8	0.56	98
PA18-49	0.02	408	1.64	714.7	5.5	727.2	7.6	0.06473	1.2	1.04656	1.5	0.11725	0.8	0.56	98
PA18-16	0.02	508	1.52	715.4	5.9	732.9	8.3	0.06538	1.3	1.05815	1.6	0.11737	0.9	0.55	98
PA18-40	0.05	86	0.27	715.7	14.5	720.5	20.6	0.06381	3.3	1.03312	4.0	0.11742	2.1	0.54	99
PA18-2	0.03	544	1.24	715.7	5.2	725.6	7.3	0.06445	1.2	1.04347	1.4	0.11743	0.8	0.54	99
PA18-42	0.02	216	1.40	717.3	5.8	727.4	7.9	0.06451	1.3	1.04691	1.5	0.11769	0.9	0.56	99
PA18-22	0.09	978	0.59	717.3	8.2	727.3	11.3	0.06451	1.8	1.04690	2.2	0.11770	1.2	0.56	99
PA18-48	0.03	182	0.44	718.0	10.3	719.3	14.2	0.06345	2.3	1.03068	2.7	0.11781	1.5	0.55	100
PA18-60	0.34	512	0.90	718.0	14.6	734.4	20.1	0.06532	3.1	1.06123	3.8	0.11783	2.2	0.57	98
PA18-32*	0.03	322	0.46	718.8	5.9	729.3	8.0	0.06461	1.3	1.05087	1.5	0.11796	0.9	0.56	99
PA18-47	0.06	619	0.78	719.5	6.3	720.9	8.4	0.06351	1.3	1.03396	1.6	0.11808	0.9	0.57	100
PA18-18	0.03	342	0.72	720.1	5.3	732.2	7.3	0.06485	1.2	1.05674	1.4	0.11818	0.8	0.56	98
PA18-17	0.05	498	0.75	720.5	5.6	727.0	7.5	0.06416	1.2	1.04621	1.4	0.11826	0.8	0.56	99
PA18-31	0.07	1166	0.54	721.1	5.4	726.1	7.2	0.06399	1.1	1.04434	1.4	0.11836	0.8	0.57	99
PA18-21	−0.07	466	1.18	721.9	9.8	724.7	13.8	0.06375	2.2	1.04153	2.6	0.11849	1.4	0.54	100
PA18-59	0.09	340	0.41	722.7	8.9	729.0	12.2	0.06420	1.9	1.05018	2.3	0.11864	1.3	0.56	99
PA18-30	0.03	551	0.75	723.7	5.4	735.3	7.4	0.06489	1.2	1.06294	1.4	0.11880	0.8	0.56	98
PA18-26	0.03	820	0.81	724.8	5.1	728.0	6.9	0.06389	1.1	1.04823	1.3	0.11899	0.7	0.56	100
PA18-33	0.05	179	0.35	724.9	8.8	725.7	12.1	0.06359	1.9	1.04358	2.3	0.11902	1.3	0.55	100
PA18-34	0.06	247	0.30	726.1	6.6	727.3	8.9	0.06369	1.4	1.04690	1.7	0.11922	1.0	0.56	100
PA18-19	0.03	139	1.09	732.3	6.0	738.1	8.3	0.06443	1.3	1.06872	1.6	0.12030	0.9	0.55	99
PA18-43	0.00	108	0.30	732.4	8.9	733.5	12.4	0.06385	2.0	1.05934	2.4	0.12033	1.3	0.54	100
PA18-55	0.02	129	0.61	733.6	8.3	738.3	11.6	0.06432	1.9	1.06901	2.2	0.12053	1.2	0.54	99
PA18-29	0.00	515	0.72	733.9	6.3	729.6	8.6	0.06324	1.4	1.05149	1.7	0.12059	0.9	0.55	101
PA18-13*	0.03	38	3.70	734.6	20.5	737.7	31.1	0.06416	5.0	1.06778	5.8	0.12071	2.9	0.51	100
PA18-25	0.05	351	0.59	734.9	7.7	726.7	10.5	0.06280	1.7	1.04566	2.0	0.12076	1.1	0.55	101
PA18-39	0.03	171	0.46	737.3	6.0	734.0	8.2	0.06347	1.3	1.06032	1.6	0.12117	0.9	0.55	100
PA18-62	−0.05	476	0.27	738.8	11.1	744.5	15.3	0.06461	2.4	1.08172	2.9	0.12143	1.6	0.55	99
PA18-10*	0.01	819	0.98	739.7	5.3	737.6	7.3	0.06368	1.2	1.06767	1.4	0.12159	0.8	0.55	100

(*continued on next page*)

(*continued*)

Spot	Pbc (%)	U (ppm)	Th/U	Ages				Isotopic ratios						Rho	Conc (%)
				$^{206}Pb/^{238}U$	2s	$^{207}Pb/^{235}U$	2s	$^{207}Pb/^{206}Pb$	2s	$^{207}Pb/^{235}U$	2s	$^{206}Pb/^{238}U$	2s		
PA18-56	0.09	86	0.90	749.8	34.2	743.4	48.9	0.06347	7.7	1.07949	9.1	0.12334	4.8	0.53	101
PA18-67	0.01	242	0.35	770.8	6.4	780.8	8.5	0.06610	1.3	1.15747	1.6	0.12701	0.9	0.57	99
PA18-32	0.04	994	0.95	772.4	7.0	778.1	9.2	0.06562	1.4	1.15178	1.7	0.12730	1.0	0.57	99
PA18-34*	0.00	472	0.97	778.7	8.5	781.6	11.5	0.06548	1.8	1.15915	2.1	0.12839	1.2	0.55	100
PA18-53	−0.03	388	0.90	779.4	7.2	778.3	9.7	0.06502	1.5	1.15217	1.8	0.12851	1.0	0.55	100
PA18-41	0.05	46	0.45	780.1	12.2	780.0	18.9	0.06517	3.0	1.15592	3.4	0.12864	1.7	0.48	100
PA18-58	0.02	193	0.76	781.5	6.5	775.6	8.7	0.06452	1.3	1.14661	1.6	0.12888	0.9	0.56	101
PA18-18*	0.05	406	1.05	782.3	5.9	781.5	7.7	0.06515	1.2	1.15907	1.4	0.12902	0.8	0.56	100
PA18-36	−0.02	194	0.78	786.7	7.5	779.8	10.3	0.06456	1.6	1.15551	1.9	0.12980	1.0	0.54	101
PA18-23	0.04	462	0.83	788.0	5.6	784.3	7.4	0.06499	1.1	1.16509	1.3	0.13003	0.8	0.56	100
PA18-44	−0.02	139	1.64	831.5	8.6	828.4	11.3	0.06643	1.7	1.26107	2.0	0.13768	1.1	0.55	100
PA18-35*	0.07	136	1.25	832.0	8.2	834.6	10.6	0.06712	1.5	1.27488	1.8	0.13777	1.1	0.57	100
PA18-54	0.00	58	0.38	834.2	15.3	827.8	20.9	0.06614	3.1	1.25984	3.7	0.13815	2.0	0.54	101
PA18-14	−0.03	580	0.96	839.7	7.9	835.3	10.4	0.06655	1.5	1.27657	1.8	0.13913	1.0	0.56	101
PA18-45	−0.37	361	1.58	845.1	30.2	846.5	41.0	0.06739	5.9	1.30166	7.0	0.14008	3.8	0.54	100
PA18-64	0.00	172	1.25	847.0	13.2	840.1	17.3	0.06649	2.5	1.28732	3.0	0.14042	1.7	0.56	101
PA18-20	0.08	97	0.50	881.7	12.2	886.0	15.4	0.06893	2.1	1.39305	2.6	0.14657	1.5	0.57	100

All analyses are corrected for 204Pb; Pbc = Common Pb. * = altered portion, commonly near rim.

Appendix D. LA-ICP-MS U-Pb geochronology data of zircon grains of volcanoclastic rock (IB1) sample from Ibaré ophiolite

Spot	Pbc (%)	U (ppm)	Th/U	Ages				Isotopic ratios					2s	Rho	Conc (%)
				$^{206}Pb/^{238}U$	2s	$^{207}Pb/^{235}U$	2s	$^{207}Pb/^{206}Pb$	2s	$^{207}Pb/^{235}U$	2s	$^{206}Pb/^{238}U$			
IB1-94	0.07	130	0.72	600.1	14.0	637.2	19.1	0.06491	3.2	0.87310	4.0	0.09756	2.4	0.61	94
IB1-116	0.00	93	0.43	618.5	23.6	633.2	36.0	0.06234	6.4	0.86556	7.5	0.10070	4.0	0.53	98
IB1-46	0.22	194	0.48	624.3	13.2	638.0	18.6	0.06237	3.2	0.87447	3.9	0.10168	2.2	0.57	98
IB1-50	0.22	122	0.43	647.6	12.0	645.5	16.2	0.06098	2.8	0.88844	3.4	0.10567	1.9	0.58	100
IB1-39	0.08	309	0.57	648.0	11.7	632.9	18.4	0.05933	3.4	0.86500	3.9	0.10574	1.9	0.49	102
IB1-35	0.00	54	0.35	702.8	24.2	705.1	38.8	0.06313	6.6	1.00257	7.5	0.11518	3.6	0.48	100
IB1-91	0.29	102	0.39	705.7	16.9	713.9	21.8	0.06394	3.4	1.01989	4.2	0.11569	2.5	0.60	99
IB1-47	0.01	159	0.50	706.2	13.3	703.5	18.0	0.06260	2.9	0.99942	3.5	0.11578	2.0	0.57	100
IB1-111	−0.02	183	0.57	711.3	14.8	721.9	18.4	0.06441	2.8	1.03602	3.5	0.11666	2.2	0.62	99
IB1-7	0.14	96	0.39	712.9	12.6	705.9	14.7	0.06228	2.2	1.00418	2.9	0.11693	1.9	0.65	101
IB1-53	0.22	115	0.64	713.0	11.6	703.9	13.0	0.06203	1.9	1.00028	2.5	0.11695	1.7	0.67	101
IB1-178	−0.06	351	1.13	714.8	16.0	775.9	21.2	0.07095	3.1	1.14707	3.9	0.11726	2.4	0.61	92
IB1-122	0.14	77	0.48	716.3	20.9	714.1	28.3	0.06297	4.5	1.02036	5.4	0.11753	3.1	0.57	100
IB1-27	0.23	44	0.37	716.9	16.0	732.8	23.8	0.06523	3.8	1.05785	4.5	0.11762	2.4	0.52	98
IB1-132	0.03	61	0.34	719.5	18.2	705.3	24.3	0.06161	3.9	1.00299	4.7	0.11808	2.7	0.57	102
IB1-164	−0.07	152	1.35	719.6	25.4	769.1	36.9	0.06956	5.6	1.13274	6.7	0.11810	3.7	0.55	94
IB1-1	0.15	31	0.31	720.0	14.5	717.6	20.6	0.06306	3.3	1.02739	4.0	0.11817	2.1	0.54	100
IB1-140	0.06	73	0.30	721.6	16.6	731.2	21.6	0.06458	3.3	1.05459	4.1	0.11844	2.4	0.59	99
IB1-124	0.09	108	0.32	722.8	16.8	734.5	21.6	0.06488	3.3	1.06140	4.1	0.11865	2.4	0.60	98
IB1-151	0.02	123	0.55	722.8	12.9	752.2	14.9	0.06709	2.0	1.09767	2.8	0.11865	1.9	0.68	96
IB1-80	0.22	413	0.75	724.5	11.7	735.5	12.2	0.06484	1.6	1.06345	2.3	0.11895	1.7	0.73	99
IB1-100	0.22	183	0.74	727.4	16.7	749.4	21.2	0.06630	3.1	1.09194	4.0	0.11945	2.4	0.61	97
IB1-129	0.01	59	0.53	727.9	21.9	716.5	30.4	0.06220	4.9	1.02520	5.8	0.11955	3.2	0.55	102
IB1-18	0.16	65	0.48	728.3	13.3	725.1	22.7	0.06320	3.9	1.04229	4.3	0.11961	1.9	0.44	100
IB1-167	0.28	88	1.19	728.8	46.8	741.1	68.7	0.06512	10.7	1.07474	12.6	0.11970	6.8	0.54	98
IB1-104	0.04	112	0.57	729.2	15.5	735.4	19.1	0.06438	2.8	1.06311	3.6	0.11977	2.2	0.62	99
IB1-143	0.02	168	0.41	729.4	13.6	750.8	15.6	0.06628	2.1	1.09476	2.9	0.11980	2.0	0.68	97
IB1-48	0.14	71	0.41	729.8	12.8	805.2	16.6	0.07322	2.3	1.21005	3.0	0.11987	1.9	0.63	91
IB1-52	0.13	121	0.40	731.1	12.1	731.6	13.6	0.06375	1.9	1.05549	2.6	0.12009	1.7	0.67	100
IB1-93	0.26	128	0.40	731.4	13.1	735.6	14.8	0.06420	2.1	1.06364	2.8	0.12015	1.9	0.68	99
IB1-120	−0.07	124	0.45	731.8	13.2	738.0	15.3	0.06446	2.2	1.06844	2.9	0.12022	1.9	0.66	99
IB1-185	−0.08	38	0.33	733.3	26.4	748.9	39.2	0.06566	6.2	1.09074	7.3	0.12048	3.8	0.52	98
IB1-24	0.17	59	0.62	736.9	13.0	735.2	17.0	0.06365	2.6	1.06278	3.2	0.12111	1.9	0.58	100
IB1-153	0.03	46	0.24	737.0	13.2	745.4	16.5	0.06488	2.5	1.08352	3.1	0.12113	1.9	0.61	99
IB1-14	0.16	61	0.41	737.8	13.3	723.0	17.7	0.06209	2.8	1.03814	3.4	0.12126	1.9	0.56	102
IB1-108	0.06	80	0.45	739.0	15.4	744.1	18.9	0.06454	2.8	1.08098	3.6	0.12147	2.2	0.62	99
IB1-149	0.04	198	0.47	740.0	11.6	773.5	11.7	0.06809	1.4	1.14205	2.1	0.12165	1.7	0.77	96
IB1-152	0.00	46	0.23	741.2	25.6	771.0	36.6	0.06766	5.6	1.13673	6.7	0.12185	3.6	0.55	96
IB1-49	0.17	154	0.34	743.0	11.5	750.9	11.8	0.06501	1.5	1.09493	2.2	0.12216	1.6	0.74	99
IB1-186	0.00	40	0.36	743.3	19.0	773.7	25.6	0.06780	3.8	1.14254	4.7	0.12222	2.7	0.58	96
IB1-169	0.14	102	0.37	743.7	13.8	768.6	15.3	0.06713	2.0	1.13179	2.8	0.12228	2.0	0.70	97
IB1-147	0.03	140	0.44	745.2	12.9	780.5	14.1	0.06847	1.8	1.15680	2.6	0.12254	1.8	0.71	95
IB1-115*	−0.01	60	0.40	745.2	48.4	812.3	73.3	0.07253	10.6	1.22545	12.6	0.12255	6.9	0.54	92
IB1-115	0.09	130	0.45	745.4	12.8	748.0	13.5	0.06443	1.8	1.08891	2.5	0.12258	1.8	0.72	100
IB1-173	0.07	71	0.36	746.1	14.4	759.9	16.6	0.06583	2.3	1.11367	3.1	0.12270	2.0	0.66	98
IB1-121	0.04	89	0.51	746.2	12.3	769.6	13.0	0.06702	1.6	1.13398	2.4	0.12272	1.7	0.73	97
IB1-12	0.16	82	0.46	746.3	12.2	737.7	14.5	0.06310	2.1	1.06791	2.8	0.12274	1.7	0.63	101
IB1-150	0.04	97	0.38	747.1	12.2	761.0	12.8	0.06586	1.6	1.11587	2.4	0.12288	1.7	0.73	98

(*continued*)

Spot	Pbc (%)	U (ppm)	Th/U	Ages				Isotopic ratios					2s	Rho	Conc (%)
				^{206}Pb/^{238}U	2s	^{207}Pb/^{235}U	2s	^{207}Pb/^{206}Pb	2s	^{207}Pb/^{235}U	2s	^{206}Pb/^{238}U			
IB1-113	0.06	289	0.58	747.9	11.5	769.8	11.1	0.06687	1.2	1.13431	2.0	0.12302	1.6	0.80	97
IB1-168	−0.14	24	0.47	748.4	29.5	778.6	45.1	0.06792	7.0	1.15284	8.1	0.12311	4.2	0.51	96
IB1-59	0.15	177	0.40	749.4	11.7	744.6	11.9	0.06366	1.5	1.08205	2.2	0.12329	1.7	0.74	101
IB1-78	0.15	71	0.36	749.5	13.7	760.9	14.9	0.06563	2.0	1.11568	2.8	0.12329	1.9	0.70	98
IB1-170	0.01	108	0.38	749.9	13.0	778.1	14.5	0.06771	1.9	1.15176	2.7	0.12336	1.8	0.69	96
IB1-144	0.04	316	0.69	750.5	11.6	770.7	11.2	0.06674	1.3	1.13613	2.1	0.12347	1.6	0.79	97
IB1-176	0.07	78	0.40	751.7	12.7	767.4	13.4	0.06623	1.7	1.12930	2.5	0.12367	1.8	0.72	98
IB1-158	0.11	47	0.49	752.3	13.4	787.0	15.5	0.06859	2.1	1.17074	2.8	0.12379	1.9	0.67	96
IB1-26	0.13	167	0.52	752.6	12.4	754.1	12.8	0.06451	1.6	1.10148	2.4	0.12383	1.7	0.73	100
IB1-126	0.05	131	0.63	752.7	12.0	779.5	12.1	0.06762	1.4	1.15476	2.2	0.12385	1.7	0.76	97
IB1-134	0.04	198	0.62	754.6	11.7	773.2	11.4	0.06667	1.3	1.14147	2.1	0.12418	1.6	0.78	98
IB1-162	0.04	175	0.46	754.9	12.1	800.4	12.3	0.07003	1.4	1.19960	2.2	0.12424	1.7	0.77	94
IB1-156	0.06	47	0.28	755.0	18.2	762.5	23.9	0.06532	3.6	1.11907	4.4	0.12425	2.5	0.58	99
IB1-136	−0.05	80	0.53	755.3	18.3	760.8	23.9	0.06509	3.6	1.11552	4.4	0.12430	2.6	0.58	99
IB1-30	0.18	62	0.35	756.2	13.8	764.0	17.0	0.06539	2.5	1.12205	3.1	0.12446	1.9	0.62	99
IB1-85	0.33	49	0.42	756.4	17.6	769.5	22.2	0.06603	3.2	1.13359	4.1	0.12450	2.5	0.61	98
IB1-133	0.06	173	0.82	756.5	11.8	791.7	11.8	0.06878	1.3	1.18085	2.1	0.12452	1.7	0.78	96
IB1-51	0.15	140	0.43	756.9	12.9	753.4	13.5	0.06404	1.8	1.10007	2.5	0.12459	1.8	0.71	100
IB1-110	−0.11	88	0.79	757.6	24.7	764.2	34.3	0.06529	5.2	1.12251	6.3	0.12470	3.5	0.55	99
IB1-77	0.17	48	0.36	757.6	13.1	763.8	14.0	0.06523	1.8	1.12171	2.6	0.12471	1.8	0.71	99
IB1-165	0.08	70	0.61	757.8	12.9	789.9	13.9	0.06843	1.8	1.17702	2.5	0.12475	1.8	0.72	96
IB1-128	0.04	203	0.65	757.9	11.8	771.9	11.6	0.06620	1.3	1.13880	2.1	0.12476	1.7	0.78	98
IB1-137	0.03	174	0.56	758.2	12.1	776.6	12.0	0.06675	1.4	1.14871	2.2	0.12481	1.7	0.76	98
IB1-175	0.06	120	0.41	758.3	12.5	792.7	12.8	0.06873	1.5	1.18293	2.3	0.12482	1.7	0.75	96
IB1-160	0.05	79	0.25	759.5	13.4	778.5	14.8	0.06686	2.0	1.15266	2.7	0.12504	1.9	0.69	98
IB1-34	0.18	310	0.49	760.0	11.8	770.3	11.4	0.06582	1.3	1.13542	2.1	0.12512	1.6	0.78	99
IB1-125	0.04	164	0.36	760.2	11.9	758.7	11.6	0.06439	1.4	1.11111	2.2	0.12515	1.7	0.77	100
IB1-148	−0.01	98	0.63	760.4	12.7	787.7	13.9	0.06792	1.8	1.17229	2.5	0.12519	1.8	0.71	97
IB1-57	0.15	85	0.40	760.4	12.6	762.5	13.1	0.06482	1.7	1.11893	2.4	0.12520	1.8	0.72	100
IB1-37	−0.22	143	0.65	760.7	27.0	784.5	38.3	0.06749	5.8	1.16550	6.9	0.12525	3.8	0.55	97
IB1-114	−0.94	122	0.69	760.8	36.2	801.7	58.7	0.06962	9.0	1.20236	10.3	0.12526	5.0	0.49	95
IB1-81	0.14	29	0.25	761.1	15.0	783.6	17.6	0.06734	2.4	1.16360	3.2	0.12532	2.1	0.65	97
IB1-22	0.23	141	0.36	761.5	12.4	764.2	13.5	0.06494	1.8	1.12264	2.5	0.12538	1.7	0.69	100
IB1-25	0.16	128	0.37	761.6	12.1	754.3	12.3	0.06373	1.6	1.10201	2.3	0.12541	1.7	0.73	101
IB1-90	0.11	136	0.43	762.6	13.8	840.8	15.9	0.07443	2.0	1.28891	2.8	0.12559	1.9	0.70	91
IB1-157	0.04	255	0.88	763.7	11.9	786.1	11.6	0.06739	1.3	1.16874	2.1	0.12578	1.7	0.78	97
IB1-127	−0.03	93	0.43	764.8	19.3	775.6	25.3	0.06602	3.8	1.14658	4.6	0.12596	2.7	0.58	99
IB1-155	0.03	201	0.52	765.1	12.0	790.9	11.8	0.06786	1.3	1.17904	2.1	0.12601	1.7	0.78	97
IB1-9	0.13	220	0.28	766.0	12.1	766.6	12.6	0.06482	1.6	1.12767	2.3	0.12618	1.7	0.72	100
IB1-11	0.11	69	0.53	766.3	15.2	762.6	21.9	0.06431	3.5	1.11931	4.0	0.12623	2.1	0.52	100
IB1-182	0.05	185	0.64	766.8	12.7	783.6	13.1	0.06680	1.6	1.16349	2.4	0.12632	1.8	0.74	98
IB1-123	0.02	61	0.84	767.3	19.8	772.1	25.8	0.06537	3.8	1.13919	4.7	0.12640	2.7	0.58	99
IB1-145	0.04	112	0.54	767.9	12.4	796.0	12.6	0.06823	1.5	1.19000	2.3	0.12650	1.7	0.75	96
IB1-97	0.19	53	0.29	768.2	13.0	789.5	13.6	0.06740	1.7	1.17618	2.5	0.12656	1.8	0.73	97
IB1-102	−0.01	40	0.22	768.3	15.9	789.5	20.1	0.06740	2.9	1.17614	3.6	0.12657	2.2	0.61	97
IB1-187	0.07	282	0.62	768.9	12.2	788.5	11.6	0.06721	1.3	1.17389	2.1	0.12668	1.7	0.79	98
IB1-44	0.22	440	0.60	769.4	12.1	764.9	12.6	0.06430	1.6	1.12393	2.3	0.12677	1.7	0.71	101
IB1-96	0.16	74	0.48	770.1	13.1	795.1	13.1	0.06791	1.5	1.18807	2.4	0.12688	1.8	0.76	97
IB1-163	0.07	169	0.41	770.2	12.3	801.4	12.1	0.06868	1.4	1.20186	2.2	0.12692	1.7	0.78	96
IB1-36	0.17	95	0.55	770.5	12.6	766.9	13.5	0.06445	1.8	1.12824	2.5	0.12697	1.7	0.70	100
IB1-99	0.07	73	0.51	770.8	18.3	788.7	23.3	0.06706	3.4	1.17450	4.2	0.12701	2.5	0.60	98
IB1-172	0.06	255	0.52	771.1	12.2	796.3	11.7	0.06797	1.3	1.19082	2.1	0.12707	1.7	0.79	97
IB1-179	0.01	61	0.47	773.3	20.8	782.2	27.6	0.06604	4.1	1.16042	5.0	0.12744	2.9	0.57	99
IB1-159	0.08	602	1.03	773.6	11.9	799.9	11.2	0.06817	1.2	1.19856	2.0	0.12751	1.6	0.81	97
IB1-112	0.05	204	0.50	773.7	12.0	792.8	11.5	0.06730	1.3	1.18315	2.1	0.12751	1.6	0.79	98
IB1-177	0.10	106	0.60	774.9	15.6	805.8	18.2	0.06878	2.4	1.21122	3.2	0.12772	2.1	0.66	96
IB1-76	0.16	153	0.40	775.1	12.5	773.3	11.9	0.06481	1.4	1.14169	2.2	0.12776	1.7	0.78	100
IB1-31	0.14	39	0.32	775.2	15.8	764.6	23.7	0.06376	3.8	1.12334	4.4	0.12778	2.2	0.49	101
IB1-82	0.13	139	0.57	775.3	12.9	766.1	12.1	0.06393	1.4	1.12651	2.2	0.12780	1.8	0.79	101
IB1-161	0.06	112	0.48	775.3	12.6	799.5	12.6	0.06796	1.5	1.19757	2.3	0.12781	1.7	0.76	97
IB1-183	0.04	93	0.43	775.5	15.2	792.3	17.5	0.06707	2.4	1.18215	3.1	0.12784	2.1	0.66	98
IB1-139	0.04	383	0.51	776.4	11.9	783.1	11.2	0.06587	1.2	1.16235	2.0	0.12799	1.6	0.80	99
IB1-98	0.30	122	0.62	776.7	19.2	789.1	23.9	0.06657	3.4	1.17518	4.3	0.12804	2.6	0.61	98
IB1-88	0.16	72	0.35	777.4	12.9	795.8	12.8	0.06732	1.5	1.18969	2.3	0.12817	1.8	0.77	98
IB1-21	0.15	26	0.46	777.7	17.6	784.5	27.2	0.06592	4.3	1.16535	4.9	0.12821	2.4	0.49	99
IB1-56	0.15	96	0.24	778.2	12.7	782.5	12.4	0.06564	1.4	1.16121	2.3	0.12830	1.7	0.77	99
IB1-32	0.26	137	0.64	778.4	13.3	789.8	14.8	0.06650	2.0	1.17676	2.7	0.12834	1.8	0.67	99
IB1-4	0.20	109	0.35	778.8	13.8	774.7	13.7	0.06465	1.7	1.14465	2.5	0.12841	1.9	0.75	101
IB1-72	0.14	85	0.48	780.5	12.9	781.8	12.4	0.06535	1.4	1.15976	2.3	0.12871	1.8	0.78	100
IB1-131	0.12	353	0.41	780.8	13.0	798.3	13.0	0.06731	1.5	1.19495	2.3	0.12876	1.8	0.75	98
IB1-103	−0.96	106	0.85	781.1	33.7	820.4	54.0	0.07000	8.1	1.24331	9.3	0.12882	4.6	0.49	95
IB1-171	0.01	109	0.39	781.8	18.2	799.5	23.0	0.06737	3.3	1.19764	4.1	0.12893	2.5	0.60	98
IB1-73	0.15	63	0.33	784.1	13.3	812.5	13.1	0.06875	1.5	1.22606	2.3	0.12933	1.8	0.77	96
IB1-68	0.16	84	0.56	785.8	13.2	799.9	12.6	0.06706	1.4	1.19856	2.3	0.12963	1.8	0.78	98

(*continued on next page*)

(*continued*)

Spot	Pbc (%)	U (ppm)	Th/U	Ages				Isotopic ratios					2s	Rho	Conc (%)
				$^{206}Pb/^{238}U$	2s	$^{207}Pb/^{235}U$	2s	$^{207}Pb/^{206}Pb$	2s	$^{207}Pb/^{235}U$	2s	$^{206}Pb/^{238}U$			
IB1-107	0.10	240	0.62	786.6	12.8	787.8	12.6	0.06552	1.5	1.17243	2.3	0.12979	1.7	0.76	100
IB1-86	0.15	120	0.38	788.4	13.0	789.4	12.3	0.06556	1.4	1.17595	2.2	0.13009	1.8	0.79	100
IB1-65	0.17	396	0.70	789.0	12.9	805.6	11.8	0.06745	1.2	1.21084	2.1	0.13020	1.7	0.82	98
IB1-67	0.17	93	0.52	790.0	13.3	799.4	12.5	0.06661	1.4	1.19738	2.2	0.13037	1.8	0.79	99
IB1-105	0.28	152	0.37	790.7	17.7	805.9	20.9	0.06734	2.9	1.21159	3.7	0.13049	2.4	0.64	98
IB1-79	0.15	286	0.82	791.3	12.8	793.5	11.7	0.06580	1.2	1.18479	2.1	0.13060	1.7	0.81	100
IB1-54	0.17	52	0.47	791.5	13.3	800.1	16.6	0.06656	2.4	1.19905	3.0	0.13065	1.8	0.60	99
IB1-87	0.15	66	0.38	792.9	13.2	789.0	12.9	0.06511	1.5	1.17513	2.3	0.13089	1.8	0.76	100
IB1-109	0.37	661	0.98	793.9	16.5	810.5	19.3	0.06760	2.6	1.22160	3.4	0.13106	2.2	0.65	98
IB1-92	0.15	123	0.68	794.7	13.1	799.3	12.3	0.06618	1.3	1.19711	2.2	0.13119	1.8	0.80	99
IB1-38	0.15	336	0.42	795.0	12.7	796.1	14.0	0.06577	1.9	1.19022	2.5	0.13126	1.7	0.67	100
IB1-63	0.15	171	0.33	797.8	12.8	784.4	11.7	0.06415	1.3	1.16528	2.1	0.13175	1.7	0.80	102
IB1-101	0.16	369	1.09	798.6	13.0	802.7	12.6	0.06625	1.4	1.20458	2.3	0.13187	1.7	0.77	99
IB1-84	0.16	280	0.51	800.9	12.9	813.9	11.9	0.06738	1.2	1.22896	2.1	0.13229	1.7	0.81	98
IB1-184	0.08	83	0.58	802.5	14.6	817.4	15.7	0.06765	2.0	1.23667	2.8	0.13257	1.9	0.70	98
IB1-19	0.14	288	0.64	804.0	12.6	826.4	12.6	0.06862	1.4	1.25671	2.2	0.13283	1.7	0.76	97
IB1-83	0.15	256	0.33	805.4	13.0	801.6	11.8	0.06552	1.3	1.20229	2.1	0.13309	1.7	0.81	100
IB1-61	0.17	99	0.35	809.8	13.3	816.5	12.4	0.06690	1.3	1.23474	2.2	0.13386	1.8	0.79	99
IB1-64	0.17	236	0.47	815.2	13.3	804.7	11.9	0.06505	1.2	1.20896	2.1	0.13480	1.7	0.82	101
IB1-3	0.18	53	0.41	817.7	13.8	828.7	13.9	0.06766	1.7	1.26174	2.4	0.13524	1.8	0.73	99
IB1-60	0.16	144	0.51	817.9	13.0	781.7	12.1	0.06217	1.4	1.15955	2.2	0.13528	1.7	0.77	105
IB1-55	0.22	89	0.38	822.8	15.2	826.2	16.2	0.06692	2.1	1.25610	2.8	0.13613	2.0	0.69	100
IB1-89	0.15	236	0.40	823.9	13.4	817.6	12.0	0.06581	1.2	1.23707	2.1	0.13633	1.7	0.81	101
IB1-74	0.16	57	0.35	824.6	14.0	836.2	13.5	0.06796	1.5	1.27857	2.3	0.13645	1.8	0.77	99
IB1-62	0.16	73	0.72	827.7	14.6	845.8	15.5	0.06883	1.9	1.30018	2.7	0.13701	1.9	0.70	98
IB1-71	0.14	225	0.36	831.9	13.4	821.0	11.9	0.06553	1.2	1.24461	2.1	0.13775	1.7	0.81	101
IB1-66	0.17	204	0.60	834.6	13.6	836.0	12.3	0.06706	1.2	1.27804	2.1	0.13821	1.7	0.81	100
IB1-15	0.33	66	0.43	838.8	36.4	827.8	54.3	0.06575	8.1	1.25970	9.3	0.13896	4.6	0.49	101
IB1-130	−0.94	109	0.46	843.2	39.6	869.0	62.3	0.07024	9.1	1.35334	10.3	0.13974	5.0	0.48	97
IB1-15	0.31	29	0.49	844.3	16.2	827.5	19.1	0.06526	2.6	1.25919	3.3	0.13994	2.0	0.61	102
IB1-4	0.13	46	0.36	856.6	21.4	823.1	26.3	0.06376	3.8	1.24933	4.6	0.14211	2.7	0.58	104
IB1-174	−0.15	190	0.64	860.9	38.4	866.5	52.9	0.06840	7.5	1.34749	8.8	0.14287	4.8	0.54	99
IB1-5	0.30	66	0.47	869.1	19.9	867.6	23.9	0.06785	3.2	1.35006	4.0	0.14432	2.4	0.60	100
IB1-146	0.14	173	0.71	878.6	16.1	878.8	16.8	0.06835	2.0	1.37608	2.8	0.14601	2.0	0.69	100
IB1-118	−0.03	106	0.80	898.0	18.8	894.3	21.4	0.06855	2.8	1.41268	3.6	0.14947	2.2	0.63	100
IB1-69	0.15	125	0.43	907.7	18.5	905.6	17.8	0.06906	2.0	1.43983	2.9	0.15121	2.2	0.74	100
IB1-138	0.12	190	1.35	1032.7	17.4	1035.4	16.1	0.07399	1.7	1.77243	2.5	0.17375	1.8	0.74	100

All analyses are corrected for 204Pb; Pbc = Common Pb. * = altered portion, commonly near rim.

Appendix E. LA-ICP-MS U-Pb geochronological data of zircon grains of Santa Rita Granite (IB19) sample from Ibaré

Spot	Pbc (%)	U (ppm)	Th/U	Ages				Isotopic ratios					1s	Rho	Conc (%)
				$^{206}Pb/^{238}U$	1s	$^{207}Pb/^{206}Pb$	1s	$^{206}Pb/^{238}U$	1s	$^{238}U/^{206}Pb$	1s	$^{207}Pb/^{206}Pb$			
IB19-1	1.87	271	0.57	0.553	0.008	0.586	0.056	0.0895	0.0014	11.1671	0.1727	0.0595	0.0016	0.92	94
IB19-17	0.40	265	0.36	0.554	0.009	0.587	0.044	0.0898	0.0016	11.1373	0.1932	0.0595	0.0012	0.71	94
IB19-5	0.61	330	0.64	0.559	0.008	0.580	0.047	0.0906	0.0013	11.0353	0.1640	0.0594	0.0013	0.93	96
IB19-23	1.73	247	0.40	0.559	0.009	0.595	0.048	0.0907	0.0016	11.0292	0.1936	0.0598	0.0013	0.66	93
IB19-36	0.45	369	0.64	0.562	0.005	0.568	0.048	0.0911	0.0009	10.9779	0.1086	0.0590	0.0013	0.82	98
IB19-4	0.27	154	1.63	0.563	0.009	0.608	0.088	0.0913	0.0016	10.9548	0.1894	0.0601	0.0024	0.30	92
IB19-8	0.34	140	0.44	0.566	0.010	0.545	0.088	0.0917	0.0016	10.9002	0.1914	0.0584	0.0024	0.69	103
IB19-27	0.00	72	0.62	0.566	0.007	0.602	0.071	0.0919	0.0011	10.8872	0.1318	0.0600	0.0019	0.27	94
IB19-31	0.27	147	0.92	0.567	0.009	0.616	0.077	0.0920	0.0015	10.8681	0.1803	0.0603	0.0021	0.39	92
IB19-7	0.95	304	0.48	0.569	0.008	0.543	0.047	0.0923	0.0013	10.8314	0.1545	0.0584	0.0013	0.37	104
IB19-35	0.00	95	0.88	0.570	0.008	0.577	0.098	0.0924	0.0014	10.8189	0.1623	0.0593	0.0027	0.35	98
IB19-15	1.21	140	0.37	0.575	0.012	0.539	0.065	0.0934	0.0020	10.7089	0.2276	0.0583	0.0018	0.85	106
IB19-22	1.39	359	0.62	0.576	0.009	0.570	0.041	0.0934	0.0016	10.7082	0.1800	0.0591	0.0011	0.67	100
IB19-24	0.90	197	0.48	0.577	0.011	0.635	0.063	0.0937	0.0019	10.6748	0.2122	0.0609	0.0019	0.78	90
IB19-29	1.89	164	1.31	0.577	0.008	0.561	0.099	0.0936	0.0014	10.6853	0.1549	0.0588	0.0027	0.81	102
IB19-13	1.22	267	0.51	0.578	0.009	0.584	0.039	0.0938	0.0016	10.6658	0.1812	0.0595	0.0011	0.93	98
IB19-21	1.42	349	0.48	0.578	0.009	0.569	0.037	0.0937	0.0015	10.6673	0.1751	0.0590	0.0010	0.56	101
IB19-34	1.49	305	0.86	0.578	0.005	0.587	0.048	0.0938	0.0009	10.6567	0.1053	0.0595	0.0013	0.90	98
IB19-10	1.90	77	0.90	0.579	0.011	0.456	0.129	0.0940	0.0018	10.6391	0.2043	0.0561	0.0034	0.01	127
IB19-6	0.35	97	0.73	0.582	0.010	0.541	0.119	0.0945	0.0018	10.5775	0.1986	0.0583	0.0031	0.51	107
IB19-26	1.50	334	0.99	0.582	0.005	0.585	0.043	0.0945	0.0009	10.5812	0.0976	0.0595	0.0012	0.96	99
IB19-20	0.72	226	0.37	0.583	0.011	0.609	0.064	0.0946	0.0019	10.5731	0.2107	0.0602	0.0018	0.21	95
IB19-18	0.00	157	0.87	0.585	0.010	0.625	0.050	0.0951	0.0017	10.5180	0.1857	0.0606	0.0014	0.94	93
IB19-11	3.97	911	0.69	0.586	0.009	0.560	0.052	0.0952	0.0015	10.5083	0.1636	0.0588	0.0014	0.89	104
IB19-30	0.53	60	0.83	0.586	0.011	0.501	0.139	0.0952	0.0018	10.5001	0.1972	0.0572	0.0038	0.59	117
IB19-32	1.52	311	0.98	0.586	0.007	0.614	0.069	0.0952	0.0011	10.4992	0.1264	0.0603	0.0019	0.84	95
IB19-12	0.49	507	0.93	0.589	0.008	0.560	0.037	0.0956	0.0014	10.4600	0.1497	0.0588	0.0010	0.95	105
IB19-33	3.33	114	0.89	0.589	0.006	0.559	0.057	0.0957	0.0010	10.4517	0.1112	0.0588	0.0015	0.88	105

(*continued*)

Spot	Pbc (%)	U (ppm)	Th/U	Ages				Isotopic ratios					1s	Rho	Conc (%)
				$^{206}Pb/^{238}U$	1s	$^{207}Pb/^{206}Pb$	1s	$^{206}Pb/^{238}U$	1s	$^{238}U/^{206}Pb$	1s	$^{207}Pb/^{206}Pb$			
IB19-9	1.50	365	1.01	0.590	0.008	0.543	0.043	0.0959	0.0014	10.4305	0.1505	0.0583	0.0012	0.48	108
IB19-14	0.39	462	0.96	0.591	0.009	0.572	0.034	0.0960	0.0016	10.4214	0.1692	0.0591	0.0009	0.92	103
IB19-25	2.51	252	0.63	0.594	0.006	0.615	0.053	0.0965	0.0010	10.3592	0.1067	0.0603	0.0015	0.62	96
IB19-16	1.58	775	0.79	0.597	0.009	0.555	0.029	0.0971	0.0015	10.3000	0.1549	0.0587	0.0008	0.97	107
IB19-28	1.02	141	0.53	0.602	0.006	0.577	0.062	0.0979	0.0011	10.2121	0.1131	0.0593	0.0017	0.77	104
IB19-19	0.00	650	1.05	0.474	0.008	0.636	0.042	0.0763	0.0014	13.1139	0.2333	0.0609	0.0012	0.90	74
IB19-2	0.28	83	0.48	1.325	0.019	1.550	0.041	0.2283	0.0036	4.3809	0.0687	0.0961	0.0020	0.99	85

All analyses are corrected for 204Pb; Pbc = Common Pb.

Appendix F. LA-MC-ICPMS Lu-Hf isotopes data on zircon grains. Ibaré tourmalinite (IB14 sample)

Spot	$^{176}Yb/^{177}Hf$[a]	±2s	$^{176}Lu/^{177}Hf$[a]	±2s	$^{178}Hf/^{177}Hf$	$^{180}Hf/^{177}Hf$	Sig_{Hf}[b]	$^{176}Hf/^{177}Hf$	±2s[c]	$^{176}Hf/^{177}Hf_{(t)}$[d]	eHf(t)[d]	±2s[c]	T_{DM}[e] (Ga)	Age[f] (Ma)
IB14-1	0.0276	24	0.00109	8	146,721	188,673	10	0.282517	22	0.282502	6.23	0.7163	1.00	726.3
IB14-4	0.0482	53	0.00185	17	146,726	188,652	9	0.282547	24	0.282520	7.70	0.7164	0.95	762.8
IB14-4*	0.0564	47	0.00202	13	146,725	188,652	10	0.282527	18	0.282499	5.94	0.7162	1.10	717.0
IB14-5	0.0510	61	0.00210	23	146,724	188,671	9	0.282590	18	0.282562	7.70	0.7164	0.89	696.5
IB14-6	0.0389	47	0.00144	16	146,724	188,629	12	0.282525	19	0.282505	6.37	0.7163	0.99	727.4
IB14-8	0.0549	97	0.00200	28	146,719	188,662	8	0.282551	41	0.282524	6.92	0.7163	0.96	723.0
IB14-9	0.0791	79	0.00292	28	146,739	188,359	7	0.282524	44	0.282484	5.53	0.7162	1.04	723.3
IB14-10	0.0753	66	0.00257	18	146,743	188,332	8	0.282517	33	0.282482	5.44	0.7162	1.04	722.7
IB14-11	0.0651	123	0.00229	43	146,729	188,612	10	0.282511	24	0.282472	9.12	0.7165	0.98	901.3
IB14-12	0.0471	42	0.00183	13	146,720	188,642	9	0.282537	21	0.282512	6.62	0.7163	0.98	728.0
IB14-13*	0.0672	62	0.00240	18	146,729	188,604	10	0.282535	16	0.282502	6.13	0.7163	1.00	721.6
IB14-14	0.0615	58	0.00216	18	146,728	188,598	10	0.282529	29	0.282499	6.04	0.7162	1.01	721.9
IB14-15	0.0689	62	0.00267	19	146,731	188,519	9	0.282547	23	0.282511	6.49	0.7163	0.98	724.4
IB14-18	0.0429	35	0.00176	11	146,728	188,608	11	0.282544	21	0.282520	6.83	0.7163	0.97	724.6
IB14-19	0.0649	56	0.00242	15	146,724	188,576	11	0.282567	25	0.282534	7.25	0.7163	0.94	721.1
IB14-20	0.0524	46	0.00205	14	146,722	188,610	13	0.282566	27	0.282538	7.44	0.7163	0.93	723.4
IB14-21	0.0484	46	0.00185	13	146,732	188,487	10	0.282545	30	0.282519	6.72	0.7163	0.97	720.0
IB14-22	0.0670	59	0.00259	17	146,732	188,547	9	0.282571	28	0.282536	7.30	0.7163	0.94	720.6
IB14-23	0.0737	69	0.00267	20	146,726	188,593	12	0.282569	22	0.282533	7.23	0.7163	0.94	722.5
IB14-24	0.0484	39	0.00179	12	146,730	188,558	12	0.282508	24	0.282481	6.92	0.7163	1.01	789.4
IB14-25	0.0913	122	0.00309	34	146,734	188,513	11	0.282587	24	0.282534	11.51	0.7166	0.86	910.3
IB14-26	0.0460	39	0.00178	12	146,729	188,555	9	0.282528	27	0.282504	6.16	0.7163	1.00	720.3
IB14-27	0.0465	38	0.00174	11	146,726	188,521	12	0.282571	20	0.282547	7.74	0.7164	0.91	722.1
IB14-28	0.0714	62	0.00268	18	146,726	188,575	15	0.282622	16	0.282585	9.10	0.7165	0.84	722.7
IB14-29	0.0892	90	0.00251	20	146,721	188,518	5	0.282491	45	0.282457	4.54	0.7162	1.09	722.5
IB14-30	0.0698	67	0.00240	19	146,728	188,641	11	0.282552	21	0.282512	10.07	0.7165	0.91	880.6
IB14-31	0.0942	92	0.00343	27	146,725	188,595	10	0.282573	25	0.282526	6.97	0.7163	0.95	720.6
IB14-32*	0.1235	114	0.00457	34	146,729	188,604	12	0.282608	33	0.282545	7.77	0.7164	0.95	726.2
IB14-32	0.1507	150	0.00575	51	146,722	188,603	10	0.282652	28	0.282570	8.72	0.7164	0.86	724.2
IB14-33	0.1939	270	0.00643	84	146,732	188,520	9	0.282610	34	0.282516	7.90	0.7164	0.95	779.2
IB14-34	0.0575	57	0.00196	14	146,729	188,450	9	0.282547	30	0.282520	7.04	0.7163	0.96	734.3
IB14-34*	0.0726	118	0.00229	16	14,683	187,883	6	0.282555	112	0.282524	6.96	0.7163	0.96	724.5
IB14-35	0.0431	40	0.00165	12	146,727	188,585	11	0.282542	18	0.282519	6.83	0.7163	0.97	725.5
IB14-36	0.0444	37	0.00175	11	146,729	188,546	7	0.282511	25	0.282487	5.62	0.7162	1.03	722.8
IB14-37	0.0673	56	0.00238	16	146,722	188,636	13	0.282524	20	0.282492	5.68	0.7163	1.02	718.0
IB14-38	0.0617	52	0.00239	15	146,733	188,458	9	0.282586	22	0.282548	10.32	0.7165	0.86	834.7
IB14-39	0.0527	43	0.00195	12	146,727	188,561	13	0.282547	18	0.282521	6.74	0.7163	0.97	720.2
IB14-40	0.0435	36	0.00166	10	146,724	188,462	9	0.282536	25	0.282513	6.47	0.7163	0.98	719.2
IB14-41	0.0531	53	0.00187	14	146,724	188,630	15	0.282565	16	0.282538	8.39	0.7164	0.91	765.7
IB14-42	0.0541	46	0.00207	14	146,727	188,638	12	0.282579	18	0.282551	7.92	0.7164	0.90	725.0
IB14-43	0.0288	26	0.00097	7	146,724	188,639	17	0.282560	18	0.282547	7.74	0.7164	0.91	723.1
IB14-44	0.0664	54	0.00237	15	146,720	188,617	16	0.282559	16	0.282527	7.05	0.7163	0.95	723.9
IB14-45	0.0626	55	0.00230	16	146,728	188,566	14	0.282576	18	0.282542	8.79	0.7164	0.90	776.4
IB14-46	0.1338	131	0.00549	46	146,728	188,617	12	0.282744	26	0.282669	12.06	0.7167	0.67	722.0
IB14-47	0.0559	52	0.00224	17	146,724	188,579	11	0.282572	15	0.282541	7.65	0.7164	0.92	727.6
IB14-48	0.1051	102	0.00393	30	146,723	188,606	12	0.282622	22	0.282565	9.44	0.7165	0.86	770.0
IB14-49	0.0540	45	0.00197	12	146,721	188,613	15	0.282546	20	0.282519	6.69	0.7163	0.97	719.7
IB14-50	0.058	54	0.00209	15	146,721	188,575	10	0.282543	28	0.282515	6.48	0.7163	0.98	717.4
IB14-51	0.0569	48	0.00208	14	146,728	188,501	10	0.282534	27	0.282507	6.09	0.7162	1.00	714.1
IB14-52	0.0635	61	0.00225	16	146,740	188,532	7	0.282573	39	0.282540	8.78	0.7164	0.90	779.8
IB14-54	0.0693	62	0.00251	18	146,726	188,536	10	0.282548	22	0.282514	6.51	0.7163	0.98	719.9
IB14-56	0.1181	117	0.00429	34	146,731	188,567	9	0.282664	30	0.282605	9.95	0.7165	0.80	729.6
IB14-56*	0.0500	43	0.00171	12	146,724	188,594	14	0.282555	20	0.282535	4.74	0.7161	0.98	607.6
IB14-57	0.0646	57	0.00237	17	146,724	188,590	12	0.282560	17	0.282527	7.11	0.7163	0.95	725.4
IB14-58	0.0515	43	0.00195	12	146,724	188,468	9	0.282541	25	0.282513	7.17	0.7163	0.97	750.2

(*continued on next page*)

(*continued*)

Spot	^{176}Yb/^{177}Hf[a]	±2s	^{176}Lu/^{177}Hf[a]	±2s	^{178}Hf/^{177}Hf	^{180}Hf/^{177}Hf	Sig_{Hf}[b]	^{176}Hf/^{177}Hf	±2s[c]	^{176}Hf/^{177}Hf$_{(t)}$[d]	eHf(t)[d]	±2s[c]	T_{DM}[e] (Ga)	Age[f] (Ma)
IB14-59	0.1079	114	0.00385	33	146,728	188,610	14	0.282586	28	0.282529	8.39	0.7164	0.92	779.1
IB14-60	0.0874	81	0.00325	24	146,727	188,616	12	0.282578	18	0.282530	8.43	0.7164	0.92	779.7
IB14-61	0.0490	91	0.00175	30	146,718	188,605	12	0.282548	28	0.282526	5.77	0.7162	0.98	668.2
IB14-63	0.0441	42	0.00175	12	146,728	188,456	8	0.282536	32	0.282512	6.70	0.7163	0.98	731.7
IB14-65	0.0504	45	0.00192	13	146,733	188,595	10	0.282557	22	0.282529	7.89	0.7164	0.93	756.9
IB14-67	0.0816	108	0.00296	35	146,722	188,671	10	0.282596	28	0.282555	8.08	0.7164	0.90	724.1
IB14-68	0.0352	30	0.00142	10	146,722	188,625	9	0.282515	17	0.282496	5.82	0.7162	1.02	718.2
IB14-69	0.0612	53	0.00237	16	146,733	188,536	8	0.282556	29	0.282524	6.91	0.7163	0.96	722.5
IB14-70	0.1636	144	0.00618	43	146,733	188,456	9	0.282662	29	0.282574	9.52	0.7165	0.84	759.7
IB14-71	0.0533	43	0.00204	13	146,726	188,577	11	0.282547	19	0.282519	6.77	0.7163	0.97	723.6
IB14-72	0.0488	42	0.00177	12	146,718	188,527	10	0.282555	24	0.282529	7.95	0.7164	0.93	759.1
IB14-73	0.2914	247	0.01012	66	146,724	188,554	9	0.282667	35	0.282519	7.98	0.7164	0.94	777.5
IB14-73*	0.2878	251	0.00982	66	146,721	188,648	9	0.282680	37	0.282537	8.51	0.7164	0.91	771.8

Quoted uncertainties (absolute) relate to the last quoted figure. The effect of the inter-element fractionation on the Lu/Hf was estimated to be about 6% or less based on analyses of the GJ-1 and Plesoviče zircon. Accuracy and reproducibility was checked by repeated analyses (n = 30 and 20 respectively) of reference zircon GJ-1 and Plesoviče (data given as mean with 2 standard deviation uncertainties).

* = altered portion, commonly near rim.

[a] 176Yb/177Hf = (176Yb/173Yb)true × (173Yb/177Hf)meas × (M173(Yb)/M177(Hf))b(Hf). b(Hf) = ln(179Hf/177Hf true / 179Hf/177Hfmeasured) / ln (M179(Hf)/M177(Hf)). M = mass of respective isotope. The 176Lu/177Hf were calculated in a similar way by using the 175Lu/177Hf and b(Yb).

[b] Mean Hf signal in volt.

[c] Uncertainties are quadratic additions of the within-run precision and the daily reproducibility of the 40 ppb-JMC475 solution. Uncertainties for the JMC475 quoted at 2SD (2 standard deviation).

[d] Initial 176Hf/177Hf and eHf calculated using the apparent Pb-Pb age determined by LA-ICP-MS dating (see column f) and the CHUR parameters: 176Lu/177Hf = 0.0336 and 176Hf/177Hf = 0.282785 (Bouvier et al., 2008).

[e] Two stage model age in billion years using the measured 176Lu/177Hf of each spot (first stage = age of zircon) a value of 0.0113 for the average continental crust (second stage) and an average MORB (DM) 176Lu/177Hf and 176Hf/177Hf of 0.0384 and 0.283165 respectively.

[f] ^{206}Pb/^{238}U age.

Appendix G. LA-MC-ICPMS Lu-Hf isotopes data on zircon grains. Ibaré chloritite (IB15 sample)

Spot	^{176}Yb/^{177}Hf[a]	±2s	^{176}Lu/^{177}Hf[a]	±2s	^{178}Hf/^{177}Hf	^{180}Hf/^{177}Hf	Sig_{Hf}[b]	^{176}Hf/^{177}Hf	±2s[c]	^{176}Hf/^{177}Hf$_{(t)}$[d]	eHf(t)[d]	±2s[c]	T_{DM}[e] (Ga)	Age[f] (Ma)
IB15-1	0.0234	28	0.00096	10	146,729	188,509	10	0.282540	22	0.282527	6.50	0.7163	0.96	698.7
IB15-2	0.0439	47	0.00160	13	146,727	188,632	11	0.282505	19	0.282484	5.11	0.7162	1.04	705.5
IB15-3	0.0333	28	0.00127	8	146,730	188,609	18	0.282597	11	0.282580	8.69	0.7164	0.85	713.3
IB15-3*	0.038	32	0.00125	8	146,722	188,650	16	0.282537	17	0.282521	6.15	0.7163	0.98	693.8
IB15-6*	0.0948	91	0.00340	28	146,726	188,581	9	0.282532	21	0.282486	5.32	0.7162	1.04	710.4
IB15-6	0.0520	43	0.00197	13	146,731	188,587	10	0.28253	21	0.282503	6.03	0.7162	1.00	715.2
IB15-10	0.1277	223	0.00446	75	146,729	188,557	7	0.282565	40	0.282491	9.23	0.7165	0.96	876.2
IB15-10*	0.0539	46	0.00188	12	146,729	188,591	11	0.282480	23	0.282455	4.03	0.7161	1.10	702.3
IB15-11	0.0531	43	0.00207	13	146,730	188,561	8	0.282549	35	0.282522	6.33	0.7163	0.97	700.2
IB15-12*	0.0953	78	0.00329	21	146,732	188,555	13	0.282484	24	0.282434	5.62	0.7162	1.10	806.4
IB15-12	0.0533	48	0.00204	15	146,724	188,612	10	0.282529	31	0.282501	6.30	0.7163	1.00	731.3
IB15-13	0.0752	61	0.00273	17	146,731	188,427	7	0.282494	42	0.282458	4.22	0.7161	1.10	707.0
IB15-14	0.0732	59	0.00263	16	146,722	188,615	7	0.282593	41	0.282556	8.70	0.7164	0.88	751.7
IB15-15	0.0628	61	0.00248	20	146,727	188,536	10	0.282551	22	0.282518	6.11	0.7163	0.98	695.3
IB15-16*	0.0996	105	0.00345	32	146,726	188,242	10	0.282549	31	0.282501	6.52	0.7163	1.00	741.0
IB15-16	0.1376	141	0.00523	45	146,743	188,338	5	0.282608	28	0.282535	7.84	0.7164	0.93	746.6
IB15-17	0.0534	50	0.00193	13	146,738	188,475	9	0.282541	31	0.282515	6.69	0.7163	0.97	727.3
IB15-18	0.0826	71	0.00298	21	146,731	188,385	6	0.282558	44	0.282508	10.19	0.7165	0.92	892.8
IB15-19	0.0564	46	0.00195	12	146,731	188,581	14	0.282564	23	0.282536	8.20	0.7164	0.92	760.1
IB15-20	0.0623	101	0.00217	32	146,736	188,549	8	0.282530	50	0.282502	5.45	0.7162	1.01	692.1
IB15-21	0.0655	53	0.00237	14	146,725	188,633	9	0.282543	38	0.282510	7.00	0.7163	0.98	748.6
IB15-24	0.0544	125	0.00194	46	146,757	188,249	5	0.282553	79	0.282524	8.29	0.7164	0.93	782.5
IB15-26	0.0870	101	0.00323	36	146,722	188,634	10	0.282516	26	0.282472	5.23	0.7162	1.06	730.0
IB15-27	0.0565	89	0.00210	28	146,722	188,548	8	0.282530	35	0.282490	11.97	0.7167	0.90	998.5
IB15-28	0.0598	57	0.00227	18	146,740	188,543	8	0.282518	35	0.282486	6.01	0.7162	1.02	741.2
IB15-29	0.0839	150	0.00203	14	146,783	188,224	6	0.282504	125	0.282473	7.08	0.7163	1.02	809.6
IB15-30	0.0421	35	0.00165	11	146,733	188,586	8	0.282538	30	0.282517	5.71	0.7162	0.99	680.0
IB15-31	0.0782	78	0.00287	26	146,728	188,564	8	0.282486	34	0.282445	4.97	0.7162	1.10	760.5
IB15-32	0.0806	78	0.00281	23	146,725	188,624	11	0.282500	29	0.282461	5.08	0.7162	1.07	740.2
IB15-33	0.0641	73	0.00237	25	146,720	188,558	8	0.282528	28	0.282495	6.13	0.7163	1.01	732.6
IB15-34	0.0608	68	0.00215	20	146,728	188,540	10	0.282526	29	0.282496	6.24	0.7163	1.10	736.2
IB15-35	0.0677	64	0.00241	17	146,727	188,404	7	0.282523	39	0.282491	5.37	0.7162	1.03	705.4
IB15-36	0.0496	44	0.00180	13	146,730	188,493	9	0.282557	25	0.282534	6.53	0.7163	0.95	690.3
IB15-37	0.0423	43	0.00151	13	146,725	188,540	8	0.282479	25	0.282458	4.82	0.7162	1.08	732.6
IB15-41	0.1797	166	0.00656	51	146,751	188,416	6	0.282640	54	0.282532	10.57	0.7166	0.88	871.1
IB15-48	0.0584	66	0.00227	24	146,728	188,522	8	0.282564	24	0.282533	7.50	0.7164	0.94	735.0
IB15-50	0.0364	31	0.00137	9	146,724	188,597	11	0.282548	22	0.282529	7.68	0.7164	0.94	748.8

(*continued*)

Spot	^{176}Yb/^{177}Hf[a]	±2s	^{176}Lu/^{177}Hf[a]	±2s	^{178}Hf/^{177}Hf	^{180}Hf/^{177}Hf	Sig_{Hf}[b]	^{176}Hf/^{177}Hf	±2s[c]	^{176}Hf/$^{177}Hf_{(t)}$[d]	eHf(t)[d]	±2s[c]	T_{DM}[e] (Ga)	Age[f] (Ma)
IB15-51	0.1548	161	0.00532	48	146,719	188,593	6	0.282511	28	0.282445	2.76	0.7160	1.14	662.2
IB15-52	0.0255	21	0.00097	6	146,724	188,591	12	0.282642	21	0.282629	10.71	0.7166	0.75	726.2
IB15-53	0.0792	91	0.00280	28	146,728	188,606	9	0.282527	23	0.282488	5.87	0.7162	1.02	732.0
IB15-64	0.0583	69	0.00222	24	146,728	188,513	7	0.282471	29	0.282440	4.28	0.7161	1.12	737.2

Quoted uncertainties (absolute) relate to the last quoted figure. The effect of the inter-element fractionation on the Lu/Hf was estimated to be about 6% or less based on analyses of the GJ-1 and Plesoviče zircon. Accuracy and reproducibility was checked by repeated analyses (n = 30 and 20. respectively) of reference zircon GJ-1 and Plesoviče (data given as mean with 2 standard deviation uncertainties).

* = altered portion, commonly near rim.

[a] 176Yb/177Hf = (176Yb/173Yb)true × (173Yb/177Hf)meas × (M173(Yb)/ M177(Hf))b(Hf). b(Hf) = ln(179Hf/177Hf true / 179Hf/177Hfmeasured) / ln (M179(Hf)/M177(Hf)). M = mass of respective isotope. The 176Lu/177Hf were calculated in a similar way by using the 175Lu/177Hf and b(Yb).

[b] Mean Hf signal in volt.

[c] Uncertainties are quadratic additions of the within-run precision and the daily reproducibility of the 40 ppb-JMC475 solution. Uncertainties for the JMC475 quoted at 2SD (2 standard deviation).

[d] Initial 176Hf/177Hf and eHf calculated using the apparent Pb-Pb age determined by LA-ICP-MS dating (see column f) and the CHUR parameters: 176Lu/177Hf = 0.0336 and 176Hf/177Hf = 0.282785 (Bouvier et al., 2008).

[e] Two stage model age in billion years using the measured 176Lu/177Hf of each spot (first stage = age of zircon) a value of 0.0113 for the average continental crust (second stage) and an average MORB (DM) 176Lu/177Hf and 176Hf/177Hf of 0.0384 and 0.283165 respectively.

[f] ^{206}Pb/^{238}U age.

Appendix H. LA-MC-ICPMS Lu-Hf isotopes data on zircon grains. Palma chloritite (PA18 sample)

Spot	^{176}Yb/^{177}Hf[a]	±2s	^{176}Lu/^{177}Hf[a]	±2s	^{178}Hf/^{177}Hf	^{180}Hf/^{177}Hf	Sig_{Hf}[b]	^{176}Hf/^{177}Hf	±2s[c]	^{176}Hf/$^{177}Hf_{(t)}$[d]	eHf(t)[d]	±2s[c]	T_{DM}[e] (Ga)	Age[f] (Ma)
PA18-1	0.0534	43	0.00187	11	146,721	188,636	15	0.282678	19	0.282653	11.20	0.7166	0.71	709.5
PA18-2	0.0605	50	0.00192	14	146,724	188,621	13	0.282510	22	0.282484	5.35	0.7162	1.04	715.7
PA18-10	0.0765	81	0.00223	19	146,720	188,589	10	0.282465	22	0.282438	1.92	0.716	1.16	635.2
PA18-10*	0.0534	44	0.00185	11	146,718	188,556	9	0.282478	22	0.282452	4.77	0.7162	1.09	739.7
PA18-11	0.0759	61	0.00216	13	146,722	188,516	11	0.282407	20	0.282378	1.55	0.7159	1.25	713.5
PA18-12	0.0530	51	0.00174	14	146,719	188,578	13	0.282525	17	0.282502	5.94	0.7162	1.01	714.2
PA18-14	0.0528	43	0.00180	11	146,720	188,585	19	0.282415	14	0.282387	4.69	0.7162	1.18	839.7
PA18-15	0.0370	31	0.00136	9	146,718	188,670	13	0.282539	16	0.282524	4.04	0.7161	1.01	595.1
PA18-16	0.1116	90	0.00364	22	146,723	188,660	11	0.282513	21	0.282464	4.64	0.7162	1.08	715.4
PA18-17	0.0409	38	0.00134	10	146,723	188,690	11	0.282547	19	0.282529	7.05	0.7163	0.95	720.5
PA18-18*	0.0398	33	0.00140	9	146,725	188,622	16	0.282445	14	0.282424	4.74	0.7162	1.13	782.3
PA18-19	0.0461	38	0.00159	10	146,724	188,575	9	0.282484	21	0.282462	4.95	0.7162	1.08	732.3
PA18-20	0.1259	106	0.00401	26	146,728	188,604	10	0.282582	18	0.282515	10.21	0.7166	0.91	881.7
PA18-21	0.0390	34	0.00132	9	146,727	188,630	14	0.282465	20	0.282447	4.18	0.7161	1.11	721.9
PA18-22	0.0481	44	0.00160	11	146,728	188,567	14	0.282508	15	0.282486	5.47	0.7162	1.03	717.3
PA18-23	0.0520	51	0.00172	14	146,730	188,516	10	0.282442	20	0.282416	4.59	0.7162	1.14	788.0
PA18-24	0.0449	40	0.00156	12	146,730	188,641	12	0.282425	17	0.282404	2.35	0.716	1.20	707.9
PA18-26	0.0351	36	0.00113	10	146,725	188,599	12	0.282520	21	0.282505	6.28	0.7163	1.00	724.8
PA18-28	0.0565	53	0.00181	14	146,725	188,619	11	0.282580	17	0.282556	7.85	0.7164	0.9	713.8
PA18-29	0.0501	42	0.00175	11	146,729	188,626	16	0.282557	17	0.282533	7.49	0.7164	0.94	733.9
PA18-30	0.0648	57	0.00204	14	146,730	188,565	13	0.282396	19	0.282368	1.43	0.7159	1.26	723.7
PA18-31	0.0350	29	0.00129	8	146,726	188,628	16	0.282481	18	0.282464	4.74	0.7162	1.08	721.1
PA18-32	0.0330	33	0.00109	9	146,729	188,504	10	0.282466	26	0.282450	5.43	0.7162	1.08	772.4
PA18-32*	0.0263	28	0.00098	9	146,734	188,605	10	0.282479	23	0.282466	4.77	0.7162	1.07	718.8
PA18-33	0.0294	42	0.00106	13	146,727	188,592	15	0.282440	17	0.282426	3.49	0.7161	1.15	724.9
PA18-34	0.0346	29	0.00118	7	146,729	188,610	14	0.282579	17	0.282563	8.38	0.7164	0.88	726.1
PA18-34*	0.0333	30	0.00115	8	146,727	188,631	12	0.282574	15	0.282557	9.36	0.7165	0.87	778.7
PA18-35	0.0721	60	0.00231	15	146,729	188,615	11	0.282589	19	0.282562	6.17	0.7163	0.92	630.1
PA18-35*	0.0702	60	0.00235	16	146,728	188,497	6	0.282595	23	0.282558	10.60	0.7166	0.84	832.0
PA18-36	0.0420	41	0.00138	10	146,726	188,609	14	0.282566	16	0.282545	9.13	0.7165	0.89	786.7
PA18-37	0.0610	59	0.00193	16	146,725	188,653	13	0.282563	15	0.28254	5.35	0.7162	0.97	627.3
PA18-39	0.0606	99	0.00177	26	146,725	188,652	14	0.282556	14	0.282531	7.52	0.7164	0.94	737.3
PA18-41	0.0225	33	0.00078	11	146,725	188,651	10	0.282469	20	0.282458	5.86	0.7162	1.06	780.1
PA18-43	0.0204	17	0.00070	5	146,723	188,681	12	0.282564	19	0.282554	8.22	0.7164	0.89	732.4
PA18-44	0.0445	51	0.00157	15	146,723	188,673	9	0.282464	20	0.282439	6.38	0.7163	1.08	831.5
PA18-45	0.0395	32	0.00122	7	146,727	188,624	15	0.282471	16	0.282452	7.12	0.7163	1.05	845.1
PA18-46	0.0768	96	0.00249	30	146,726	188,580	12	0.282556	21	0.282523	6.43	0.7163	0.97	702.3
PA18-47	0.0735	70	0.00250	19	146,725	188,636	13	0.282453	17	0.282419	3.14	0.716	1.17	719.5
PA18-48	0.0279	23	0.00102	7	146,722	188,632	15	0.282429	16	0.282415	2.96	0.716	1.17	718.0
PA18-49	0.0681	59	0.00235	15	146,726	188,525	12	0.282524	22	0.282492	5.62	0.7162	1.02	714.7
PA18-50	0.0226	20	0.00075	5	146,726	188,627	13	0.282560	16	0.28255	7.65	0.7164	0.91	714.1
PA18-53	0.0365	31	0.00130	9	146,723	188,613	15	0.282420	18	0.282401	3.84	0.7161	1.18	779.4
PA18-54	0.0544	51	0.00166	12	146,722	188,636	12	0.282529	22	0.282503	8.69	0.7164	0.95	834.2
PA18-55	0.0401	34	0.00139	9	146,718	188,624	11	0.282485	19	0.282466	5.11	0.7162	1.07	733.6
PA18-56	0.0661	70	0.00194	18	146,726	188,637	9	0.282467	23	0.28244	4.54	0.7161	1.11	749.8
PA18-58	0.0298	28	0.00100	7	146,723	188,601	10	0.282370	21	0.282355	2.27	0.716	1.26	781.5
PA18-59	0.0594	63	0.00197	18	146,726	188,611	12	0.282423	20	0.282396	2.40	0.716	1.21	722.7
PA18-60	0.0583	66	0.00192	18	146,723	188,601	10	0.282552	21	0.282526	6.89	0.7163	0.96	718.0

(*continued on next page*)

(*continued*)

Spot	^{176}Yb/^{177}Hf[a]	±2s	^{176}Lu/^{177}Hf[a]	±2s	^{178}Hf/^{177}Hf	^{180}Hf/^{177}Hf	Sig_{Hf}[b]	^{176}Hf/^{177}Hf	±2s[c]	^{176}Hf/^{177}Hf$_{(t)}$[d]	eHf(t)[d]	±2s[c]	T_{DM}[e] (Ga)	Age[f] (Ma)
PA18-62	0.0788	95	0.00098	28	146,724	188,646	11	0.282458	21	0.282444	4.46	0.7161	1.11	738.8
PA18-63	0.0594	51	0.00204	14	146,725	188,615	10	0.282483	18	0.282456	4.18	0.7161	1.1	708.0
PA18-64	0.0163	15	0.00064	5	146,723	188,664	12	0.282526	18	0.282516	9.44	0.7165	0.92	847.0
PA18-67	0.0324	27	0.00110	7	146,727	188,618	12	0.282571	18	0.282555	9.11	0.7165	0.88	770.8

Quoted uncertainties (absolute) relate to the last quoted figure. The effect of the inter-element fractionation on the Lu/Hf was estimated to be about 6% or less based on analyses of the GJ-1 and Plesoviče zircon. Accuracy and reproducibility was checked by repeated analyses (n = 30 and 20. respectively) of reference zircon GJ-1 and Plesoviče (data given as mean with 2 standard deviation uncertainties).

* = altered portion, commonly near rim.

[a] 176Yb/177Hf = (176Yb/173Yb)true × (173Yb/177Hf)meas × (M173(Yb)/
M177(Hf))b(Hf). b(Hf) = ln(179Hf/177Hf true / 179Hf/177Hfmeasured) / ln (M179(Hf)/M177(Hf)). M = mass of respective isotope. The 176Lu/177Hf were calculated in a similar way by using the 175Lu/177Hf and b(Yb).

[b] Mean Hf signal in volt.

[c] Uncertainties are quadratic additions of the within-run precision and the daily reproducibility of the 40 ppb-JMC475 solution. Uncertainties for the JMC475 quoted at 2SD (2 standard deviation).

[d] Initial 176Hf/177Hf and eHf calculated using the apparent Pb-Pb age determined by LA-ICP-MS dating (see column f) and the CHUR parameters: 176Lu/177Hf = 0.0336 and 176Hf/177Hf = 0.282785 (Bouvier et al., 2008).

[e] Two stage model age in billion years using the measured 176Lu/177Hf of each spot (first stage = age of zircon) a value of 0.0113 for the average continental crust (second stage) and an average MORB (DM) 176Lu/177Hf and 176Hf/177Hf of 0.0384 and 0.283165 respectively.

[f] ^{206}Pb/^{238}U age.

Appendix I. LA-MC-ICPMS Lu-Hf isotopes data on zircon grains. Ibaré volcanoclastic rock (IB1 sample)

Spot	^{176}Yb/^{177}Hf[a]	±2s	^{176}Lu/^{177}Hf[a]	±2s	^{178}Hf/^{177}Hf	^{180}Hf/^{177}Hf	Sig_{Hf}[b]	^{176}Hf/^{177}Hf	±2s[c]	^{176}Hf/^{177}Hf$_{(t)}$[d]	eHf(t)[d]	±2s[c]	T_{DM}[e] (Ga)	Age[f] (Ma)
IB1-3	0.0173	14	0.00064	4	146,721	188,622	13	0.282583	16	0.282573	10.81	0.7166	0.82	817.7
IB1-4	0.0299	34	0.00106	10	146,722	188,634	15	0.282606	17	0.282590	10.54	0.7166	0.80	778.8
IB1-7	0.0330	27	0.00116	7	146,725	188,627	14	0.282636	15	0.282620	10.12	0.7165	0.77	712.9
IB1-9	0.0330	28	0.00128	9	146,727	188,628	16	0.282624	12	0.282606	10.79	0.7166	0.78	766.0
IB1-11	0.0251	25	0.00089	7	146,729	188,561	14	0.282589	19	0.282576	9.75	0.7165	0.84	766.3
IB1-12	0.0412	39	0.00149	13	146,728	188,607	14	0.282604	23	0.282583	9.55	0.7165	0.83	746.3
IB1-14	0.0200	17	0.00073	5	146,730	188,592	16	0.282587	17	0.282577	9.14	0.7165	0.85	737.8
IB1-15	0.0257	22	0.00095	7	146,723	188,583	15	0.282570	16	0.282555	10.64	0.7166	0.85	838.8
IB1-18	0.0366	30	0.00130	8	146,728	188,582	14	0.282613	16	0.282595	9.57	0.7165	0.82	728.3
IB1-19	0.0446	37	0.00158	11	146,741	188,313	10	0.282588	37	0.282564	10.18	0.7166	0.84	804.0
IB1-21	0.0385	39	0.00140	12	146,740	188,255	10	0.282592	39	0.282572	9.85	0.7165	0.84	777.7
IB1-22	0.0337	30	0.00125	9	146,733	188,428	14	0.282593	21	0.282575	9.61	0.7165	0.84	761.5
IB1-24	0.0315	32	0.00120	10	146,728	188,598	16	0.282619	16	0.282602	10.02	0.7165	0.80	736.9
IB1-25	0.0322	27	0.00118	7	146,731	188,477	16	0.282594	13	0.282577	9.68	0.7165	0.84	761.6
IB1-26	0.0413	37	0.00140	10	146,720	188,606	17	0.282643	14	0.282623	11.11	0.7166	0.75	752.6
IB1-27	0.0213	17	0.00079	5	146,727	188,555	14	0.282576	17	0.282565	8.26	0.7164	0.88	716.9
IB1-30	0.0254	37	0.00085	10	146,725	188,593	18	0.282572	14	0.282560	8.95	0.7165	0.87	756.2
IB1-31	0.0228	26	0.00082	8	146,723	188,352	11	0.282629	27	0.282617	11.4	0.7166	0.75	775.2
IB1-32	0.0635	85	0.00204	22	146,726	188,614	16	0.282611	22	0.282581	10.20	0.7166	0.82	778.4
IB1-34	0.0309	27	0.00113	8	146,735	188,428	11	0.282583	21	0.282567	9.28	0.7165	0.86	760.0
IB1-35	0.0198	18	0.00072	5	146,725	188,597	17	0.282589	14	0.282579	8.44	0.7164	0.86	702.8
IB1-36	0.0336	39	0.00116	11	146,725	188,615	16	0.282600	13	0.282583	10.10	0.7165	0.82	770.5
IB1-37	0.0554	60	0.00188	19	146,729	188,512	15	0.282616	18	0.282589	10.09	0.7165	0.81	760.7
IB1-38	0.0269	27	0.00090	8	146,726	188,578	17	0.282621	13	0.282608	11.51	0.7166	0.76	795.0
IB1-39	0.0410	38	0.00134	10	146,718	188,637	16	0.282622	14	0.282606	8.13	0.7164	0.83	648.0
IB1-44	0.0404	35	0.00136	10	146,723	188,622	18	0.282620	13	0.282600	10.68	0.7166	0.79	769.4
IB1-46	0.0304	25	0.00102	6	146,722	188,597	17	0.282616	16	0.282604	7.54	0.7164	0.84	624.3
IB1-47	0.0284	26	0.00107	8	146,724	188,589	15	0.282600	15	0.282586	8.74	0.7164	0.84	706.2
IB1-49	0.0430	43	0.00162	14	146,724	188,457	11	0.282621	17	0.282598	10.01	0.7165	0.80	743.0
IB1-50	0.0423	35	0.00158	11	146,721	188,584	15	0.282612	19	0.282593	7.67	0.7164	0.85	647.6
IB1-51	0.0302	35	0.00104	10	146,724	188,598	13	0.282611	19	0.282596	10.25	0.7166	0.80	756.9
IB1-52	0.0665	60	0.00243	17	146,729	188,543	15	0.282636	20	0.282603	9.90	0.7165	0.80	731.1
IB1-53	0.054	45	0.00193	13	146,724	188,458	10	0.282641	23	0.282615	9.93	0.7165	0.78	713.0
IB1-55	0.0345	30	0.00121	9	146,728	188,445	12	0.282602	18	0.282583	11.28	0.7166	0.80	822.8
IB1-56	0.0367	30	0.00141	9	146,718	188,625	15	0.282625	13	0.282604	11.02	0.7166	0.78	778.2
IB1-57	0.0219	18	0.00078	5	146,723	188,625	16	0.282613	16	0.282602	10.53	0.7166	0.79	760.4
IB1-59	0.0272	22	0.00104	6	146,726	188,601	17	0.282606	15	0.282591	9.91	0.7165	0.81	749.4
IB1-60	0.0436	36	0.00174	11	146,726	188,491	13	0.282613	18	0.282586	11.27	0.7166	0.79	817.9
IB1-61	0.0345	30	0.00127	8	146,730	188,447	15	0.282602	25	0.282583	10.97	0.7166	0.80	809.8
IB1-63	0.0255	21	0.00105	7	146,730	188,507	13	0.282602	18	0.282586	10.82	0.7166	0.80	797.8
IB1-64	0.0793	70	0.00293	21	146,728	188,581	12	0.282620	31	0.282575	10.82	0.7166	0.82	815.2
IB1-67	0.0330	30	0.00116	10	146,728	188,608	16	0.282633	15	0.282616	11.69	0.7167	0.75	790.0
IB1-68	0.0367	33	0.00121	9	146,721	188,631	14	0.282587	15	0.282569	9.94	0.7165	0.84	785.8
IB1-72	0.0230	19	0.00077	5	146,727	188,645	17	0.282592	13	0.282581	10.23	0.7165	0.82	780.5
IB1-73	0.0262	21	0.00097	6	146,724	188,589	19	0.282621	17	0.282607	11.24	0.7166	0.77	784.1
IB1-74	0.0245	20	0.00093	6	146,727	188,460	13	0.282588	22	0.282574	10.98	0.7166	0.82	824.6
IB1-76	0.0289	25	0.00109	7	146,724	188,621	18	0.282606	14	0.282590	10.44	0.7166	0.81	775.1
IB1-77	0.0400	34	0.00133	8	146,723	188,455	9	0.282626	27	0.282607	10.65	0.7166	0.78	757.6
IB1-78	0.0189	16	0.00073	5	146,722	188,630	16	0.282565	16	0.282555	8.61	0.7164	0.89	749.5

(*continued*)

Spot	^{176}Yb/^{177}Hf[a]	±2s	^{176}Lu/^{177}Hf[a]	±2s	^{178}Hf/^{177}Hf	^{180}Hf/^{177}Hf	Sig_{Hf}[b]	^{176}Hf/^{177}Hf	±2s[c]	^{176}Hf/$^{177}Hf_{(t)}$[d]	eHf(t)[d]	±2s[c]	T_{DM}[e] (Ga)	Age[f] (Ma)
IB1-80	0.0592	58	0.00210	17	146,731	188,367	13	0.282641	21	0.282612	10.09	0.7165	0.78	724.5
IB1-81	0.0225	18	0.00089	6	146,719	188,611	16	0.282620	16	0.282607	10.74	0.7166	0.78	761.1
IB1-82	0.0260	21	0.00098	6	146,726	188,481	15	0.282582	19	0.282568	9.66	0.7165	0.85	775.3
IB1-83	0.0620	52	0.00217	15	146,723	188,560	16	0.282638	19	0.282605	11.66	0.7167	0.76	805.4
IB1-84	0.0488	40	0.00186	11	146,723	188,546	14	0.282597	27	0.282569	10.28	0.7166	0.84	800.9
IB1-85	0.0452	43	0.00159	13	146,732	188,591	17	0.282652	19	0.282629	11.42	0.7166	0.74	756.4
IB1-86	0.0396	40	0.00149	13	146,725	188,640	20	0.282631	16	0.282609	11.41	0.7166	0.76	788.4
IB1-87	0.0187	15	0.00073	5	146,725	188,484	16	0.282599	21	0.282588	10.78	0.7166	0.80	792.9
IB1-88	0.0249	22	0.00093	7	146,729	188,507	17	0.282624	14	0.282610	11.22	0.7166	0.76	777.4
IB1-91	0.0281	25	0.00111	8	146,724	188,625	19	0.282590	19	0.282575	8.36	0.7164	0.86	705.7
IB1-92	0.0299	25	0.00100	7	146,723	188,605	18	0.282599	17	0.282584	10.67	0.7166	0.81	794.7
IB1-93	0.0235	21	0.00088	6	146,723	188,585	15	0.282601	13	0.282589	9.42	0.7165	0.83	731.4
IB1-94	0.0779	66	0.00253	16	146,721	188,546	14	0.282663	25	0.282634	8.08	0.7164	0.79	600.1
IB1-96	0.0316	26	0.00115	7	146,727	188,394	11	0.282638	23	0.282621	11.44	0.7166	0.75	770.1
IB1-97	0.0359	31	0.00131	9	146,726	188,646	16	0.282636	21	0.282617	11.24	0.7166	0.75	768.2
IB1-98	0.0433	38	0.00171	12	146,742	188,175	6	0.282581	48	0.282556	9.27	0.7165	0.87	776.7
IB1-99	0.0358	36	0.00137	14	146,729	188,559	10	0.282626	34	0.282606	10.92	0.7166	0.78	770.8
IB1-100	0.0334	32	0.00121	10	146,731	188,591	11	0.282605	22	0.282588	9.31	0.7165	0.83	727.4
IB1-101	0.0590	69	0.00216	20	146,740	188,476	7	0.282631	50	0.282599	11.27	0.7166	0.78	798.6
IB1-104	0.0397	37	0.00142	11	146,725	188,561	13	0.282600	17	0.282581	9.07	0.7165	0.84	729.2
IB1-107	0.0454	37	0.00178	11	146,720	188,524	8	0.282606	25	0.282580	10.34	0.7166	0.82	786.6
IB1-108	0.0394	34	0.00149	10	146,723	188,465	8	0.282601	27	0.282580	9.28	0.7165	0.84	739.0
IB1-109	0.0842	78	0.00292	21	146,740	188,282	6	0.282609	50	0.282565	10.00	0.7165	0.85	793.9
IB1-110	0.0767	64	0.00265	16	146,742	188,243	4	0.282647	45	0.282609	10.73	0.7166	0.77	757.6
IB1-111	0.0419	37	0.00152	10	146,746	188,236	7	0.282644	44	0.282624	10.20	0.7166	0.77	711.3
IB1-112	0.0363	35	0.00141	11	146,729	188,300	7	0.282633	33	0.282612	11.21	0.7166	0.76	773.7
IB1-113	0.0463	58	0.00172	18	146,724	188,409	9	0.282606	29	0.282582	9.54	0.7165	0.83	747.9
IB1-114	0.0533	48	0.00187	14	146,733	188,490	13	0.282592	29	0.282565	9.24	0.7165	0.86	760.8
IB1-115*	0.0263	23	0.00098	7	146,728	188,493	9	0.282612	26	0.282598	10.06	0.7165	0.80	745.2
IB1-115	0.0501	41	0.00178	11	146,726	188,588	13	0.282648	20	0.282623	10.94	0.7166	0.75	745.4
IB1-116	0.0333	31	0.00110	7	146,727	188,483	13	0.282598	20	0.282585	6.74	0.7163	0.88	618.5
IB1-120	0.0385	35	0.00149	10	146,722	188,577	14	0.282590	15	0.282570	8.74	0.7164	0.86	731.8
IB1-121	0.0536	44	0.00199	12	146,725	188,572	15	0.282620	14	0.282592	9.86	0.7165	0.81	746.2
IB1-122	0.0328	32	0.00120	10	146,724	188,562	15	0.282609	14	0.282593	9.22	0.7165	0.83	716.3
IB1-123	0.0246	21	0.00091	6	146,730	188,476	10	0.282593	23	0.282580	9.91	0.7165	0.83	767.3
IB1-124	0.0411	80	0.00139	22	146,732	188,496	11	0.282592	23	0.282573	8.66	0.7164	0.86	722.8
IB1-125	0.0319	33	0.00118	10	146,722	188,621	16	0.282586	13	0.282569	9.37	0.7165	0.85	760.2
IB1-126	0.0296	28	0.00105	8	146,727	188,583	15	0.282610	22	0.282595	10.12	0.7165	0.80	752.7
IB1-127	0.0789	67	0.00280	19	146,724	188,535	8	0.282660	30	0.282620	11.26	0.7166	0.75	764.8
IB1-128	0.0405	34	0.00152	10	146,730	188,472	10	0.282630	23	0.282608	10.70	0.7166	0.78	757.9
IB1-129	0.0231	20	0.00078	5	146,724	188,564	13	0.282622	16	0.282611	10.13	0.7165	0.78	727.9
IB1-132	0.0279	32	0.00099	8	146,718	188,650	12	0.282599	17	0.282586	9.03	0.7165	0.84	719.5
IB1-133	0.0407	35	0.00145	10	146,730	188,578	11	0.282623	19	0.282602	10.46	0.7166	0.79	756.5
IB1-134	0.0387	32	0.00138	9	146,723	188,654	12	0.282598	17	0.282578	9.57	0.7165	0.84	754.6
IB1-136	0.0342	29	0.00127	8	146,732	188,455	7	0.282616	26	0.282598	10.28	0.7166	0.80	755.3
IB1-137	0.0299	33	0.00109	9	146,733	188,263	10	0.282603	33	0.282587	9.97	0.7165	0.82	758.2
IB1-139	0.0417	42	0.00149	13	146,721	188,532	13	0.282626	20	0.282604	10.98	0.7166	0.78	776.4
IB1-140	0.0260	29	0.00084	6	146,726	188,609	13	0.282638	19	0.282627	10.53	0.7166	0.76	721.6
IB1-143	0.0379	31	0.00141	9	146,724	188,573	13	0.282603	24	0.282584	9.19	0.7165	0.84	729.4
IB1-144	0.0583	48	0.00213	14	146,728	188,411	11	0.282600	33	0.282570	9.18	0.7165	0.86	750.5
IB1-145	0.0243	20	0.00094	6	146,730	188,528	11	0.282581	21	0.282567	9.48	0.7165	0.85	767.9
IB1-147	0.0232	22	0.00094	8	146,721	188,632	14	0.282582	16	0.282569	9.02	0.7165	0.86	745.2
IB1-148	0.0275	24	0.00102	8	146,727	188,590	12	0.282568	23	0.282553	8.81	0.7165	0.88	760.4
IB1-149	0.0259	21	0.00106	6	146,725	188,613	11	0.282582	20	0.282567	8.85	0.7165	0.87	740.0
IB1-150	0.0161	15	0.00061	4	146,732	188,569	13	0.282600	19	0.282591	9.86	0.7165	0.81	747.1
IB1-151	0.0216	21	0.00088	7	146,720	188,513	10	0.282568	24	0.282556	8.06	0.7164	0.89	722.8
IB1-152	0.0268	24	0.00106	8	146,722	188,585	13	0.282635	17	0.282620	10.75	0.7166	0.76	741.2
IB1-153	0.0505	51	0.00179	16	146,723	188,473	7	0.282650	31	0.282625	10.83	0.7166	0.75	737.0
IB1-155	0.0440	52	0.00158	16	146,729	188,533	14	0.282615	20	0.282592	10.30	0.7166	0.81	765.1
IB1-157	0.0451	42	0.00158	12	146,730	188,381	8	0.282625	36	0.282602	10.62	0.7166	0.79	763.7
IB1-158	0.0174	14	0.00063	4	146,729	188,507	10	0.282597	23	0.282588	9.86	0.7165	0.82	752.3
IB1-159	0.0966	81	0.00351	23	146,733	188,434	7	0.282634	77	0.282583	10.16	0.7166	0.82	773.6
IB1-160	0.0238	20	0.00093	6	146,721	188,633	12	0.282641	17	0.282628	11.43	0.7166	0.74	759.5
IB1-161	0.0541	48	0.00188	12	146,719	188,600	13	0.282649	23	0.282622	11.57	0.7167	0.74	775.3
IB1-162	0.0459	39	0.00161	11	146,720	188,493	9	0.282605	35	0.282582	9.71	0.7165	0.83	754.9
IB1-163	0.0259	30	0.00096	11	146,722	188,498	12	0.282589	26	0.282575	9.80	0.7165	0.84	770.2
IB1-164	0.0657	82	0.00233	23	146,743	188,344	8	0.282631	43	0.282599	9.53	0.7165	0.81	719.6
IB1-165	0.0523	47	0.00171	13	146,723	188,620	15	0.282632	16	0.282608	10.68	0.7166	0.78	757.8
IB1-167	0.0644	59	0.00226	17	146,726	188,536	9	0.282644	24	0.282613	10.21	0.7166	0.78	728.8
IB1-168	0.0190	16	0.00064	4	146,716	188,628	13	0.282597	19	0.282588	9.77	0.7165	0.82	748.4
IB1-169	0.0238	19	0.00091	6	146,722	188,543	13	0.282576	18	0.282563	8.79	0.7165	0.87	743.7
IB1-170	0.0248	30	0.00087	10	146,725	188,503	13	0.282609	18	0.282597	10.11	0.7165	0.80	749.9
IB1-172	0.0298	25	0.00110	7	146,727	188,470	6	0.282541	37	0.282525	8.05	0.7164	0.94	771.1
IB1-173	0.0197	17	0.00071	5	146,724	188,627	13	0.282574	20	0.282564	8.87	0.7165	0.87	746.1
IB1-175	0.0323	28	0.00123	8	146,728	188,596	13	0.282592	14	0.282574	9.51	0.7165	0.84	758.3

(*continued on next page*)

(*continued*)

Spot	^{176}Yb/^{177}Hf[a]	±2s	^{176}Lu/^{177}Hf[a]	±2s	^{178}Hf/^{177}Hf	^{180}Hf/^{177}Hf	Sig$_{Hf}$[b]	^{176}Hf/^{177}Hf	±2s[c]	^{176}Hf/^{177}Hf$_{(t)}$[d]	eHf(t)[d]	±2s[c]	T$_{DM}$[e] (Ga)	Age[f] (Ma)
IB1-176	0.0289	24	0.00104	7	146,722	188,631	14	0.282579	14	0.282564	9.00	0.7165	0.87	751.7
IB1-177	0.0336	28	0.00121	8	146,729	188,613	14	0.282598	17	0.282580	10.09	0.7165	0.82	774.9
IB1-178	0.0586	66	0.00190	20	146,730	188,313	8	0.282617	44	0.282591	9.13	0.7165	0.83	714.8
IB1-179	0.0494	51	0.00184	16	146,729	188,279	6	0.282594	42	0.282567	9.59	0.7165	0.85	773.3
IB1-182	0.0314	30	0.00123	9	146,731	188,469	11	0.28258	23	0.282562	9.27	0.7166	0.86	766.8
IB1-183	0.0336	28	0.00124	8	146,731	188,450	10	0.282595	29	0.282577	9.99	0.7165	0.83	775.5
IB1-185	0.0274	27	0.00109	10	146,721	188,556	11	0.282626	26	0.282611	10.24	0.7166	0.78	733.3
IB1-186	0.0245	21	0.00091	6	146,731	188,481	8	0.282626	30	0.282613	10.55	0.7166	0.77	743.3
IB1-187	0.0479	40	0.00190	12	146,734	188,404	8	0.282623	33	0.282596	10.5	0.7166	0.80	768.9

Quoted uncertainties (absolute) relate to the last quoted figure. The effect of the inter-element fractionation on the Lu/Hf was estimated to be about 6% or less based on analyses of the GJ-1 and Plesovičе zircon. Accuracy and reproducibility was checked by repeated analyses (n = 30 and 20. respectively) of reference zircon GJ-1 and Plesovičе (data given as mean with 2 standard deviation uncertainties).

* = altered portion, commonly near rim.

[a] 176Yb/177Hf = (176Yb/173Yb)true × (173Yb/177Hf)meas × (M173(Yb)/ M177(Hf))b(Hf). b(Hf) = ln(179Hf/177Hf true / 179Hf/177Hfmeasured) / ln (M179(Hf)/M177(Hf)). M = mass of respective isotope. The 176Lu/177Hf were calculated in a similar way by using the 175Lu/177Hf and b(Yb).

[b] Mean Hf signal in volt.

[c] Uncertainties are quadratic additions of the within-run precision and the daily reproducibility of the 40 ppb-JMC475 solution. Uncertainties for the JMC475 quoted at 2SD (2 standard deviation).

[d] Initial 176Hf/177Hf and eHf calculated using the apparent Pb-Pb age determined by LA-ICP-MS dating (see column f) and the CHUR parameters: 176Lu/177Hf = 0.0336 and 176Hf/177Hf = 0.282785 (Bouvier et al., 2008).

[e] Two stage model age in billion years using the measured 176Lu/177Hf of each spot (first stage = age of zircon) a value of 0.0113 for the average continental crust (second stage) and an average MORB (DM) 176Lu/177Hf and 176Hf/177Hf of 0.0384 and 0.283165 respectively.

[f] ^{206}Pb/^{238}U age.

Appendix J. LA-MC-ICPMS Lu-Hf isotopes data on zircon grains. Ibaré Santa Rita Granite (IB19 sample)

Spot	176Hf/177Hf	±2s	176Lu/177Hf	±2s	^{206}Pb/^{238}U age	eHf(0)	176Hf/177Hf	eHf	176Hf/177Hf	TDM	176Hf/177Hf	eHf
					(T1) Ma		(T1)	(T1)	DM(T)	(Ga)	DM(T)	(TDM)
5.1	0.281851	0.000057	0.0014402	0.0000295	559	−32.55	0.281836	−20.80	0.282821	2767	0.281184	6.12
7.1	0.281992	0.000048	0.0010714	0.0000119	569	−27.57	0.281981	−15.45	0.282814	2442	0.281429	7.32
8.1	0.281991	0.000027	0.0006930	0.0000345	566	−27.62	0.281984	−15.43	0.282816	2438	0.281432	7.33
11.1	0.281788	0.000053	0.0018840	0.0000520	586	−34.80	0.281767	−22.65	0.282801	2902	0.281081	5.62
12.1	0.281817	0.000057	0.0025847	0.0000876	589	−33.78	0.281788	−21.84	0.282799	2855	0.281117	5.80
13.1	0.281986	0.000053	0.0012511	0.0000083	578	−27.78	0.281973	−15.54	0.282807	2455	0.281420	7.27
17.1	0.281937	0.000057	0.0010897	0.0000340	554	−29.53	0.281926	−17.75	0.282825	2573	0.281330	6.84
20.1	0.281944	0.000039	0.0009474	0.0000269	583	−29.28	0.281934	−16.82	0.282804	2538	0.281357	6.96
21.1	0.281595	0.000085	0.0018817	0.0000175	578	−41.64	0.281574	−29.66	0.282807	3328	0.280757	4.03
22.1	0.281922	0.000055	0.0009440	0.0000216	576	−30.07	0.281912	−17.76	0.282809	2591	0.281317	6.77
23.1	0.281616	0.000062	0.0011397	0.0000335	559	−40.89	0.281604	−29.04	0.282821	3275	0.280797	4.23
25.1	0.281818	0.000076	0.0012855	0.0000243	594	−33.75	0.281803	−21.19	0.282796	2818	0.281145	5.93
26.1	0.281594	0.000062	0.0020134	0.0000844	582	−41.67	0.281572	−29.66	0.282804	3331	0.280754	4.02
28.1	0.281825	0.000060	0.0016998	0.0000574	602	−33.50	0.281806	−20.93	0.282790	2808	0.281152	5.97
29.1	0.282028	0.000060	0.0014683	0.0000301	577	−26.29	0.282013	−14.16	0.282808	2367	0.281485	7.59
32.1	0.281811	0.000081	0.0011629	0.0000260	586	−33.99	0.281798	−21.56	0.282801	2835	0.281132	5.87
34.1	0.281801	0.000064	0.0017702	0.0000382	578	−34.34	0.281782	−22.31	0.282807	2875	0.281102	5.72
33.1	0.281923	0.000049	0.0012277	0.0000399	589	−30.02	0.281909	−17.54	0.282799	2588	0.281319	6.78
35.1	0.281961	0.000035	0.0007588	0.0000050	570	−28.70	0.281952	−16.44	0.282813	2504	0.281382	7.09
36.1	0.281528	0.000075	0.0025097	0.0000448	562	−43.99	0.281501	−32.59	0.282819	3495	0.280629	3.41

Appendix K. LA-ICPMS trace elements data on zircon grains. Ibaré tourmalinite (IB14 sample)

Spot	La	Ce	Pr	Nd	Sm	Eu	Gd	Tb	Dy	Ho	Er	Tm	Yb	Lu	U
IB14-1	3.91	40.78	3.42	19.76	8.26	2.7	15.35	4.45	58.44	25.63	146.13	36.94	413.55	94.22	597.76
IB14-4	0.518	40.68	0.341	3.5	10.09	5.0	44.02	13.63	148.2	53.67	259.6	56.2	562.17	122.33	384.4
IB14-8	21.13	188.5	11.18	80.23	51.24	23.68	146.68	38.76	383.48	129.24	536.3	110.45	1013.37	208.62	959.23
IB14-9	2.25	35.6	1.52	12.11	11.86	6.12	49.67	13.5	124.97	47.03	219.96	48.26	478.17	109.28	335.8
IB14-10	4.39	36.3	2.63	18.7	12.21	8.06	29.5	8.93	97.07	40.05	194.62	45.81	469.35	104.82	306.02
IB14-11	10.6	46.26	3.58	21.01	8.86	3.88	21.4	6.51	70.97	26.63	121.46	26.88	270.11	60.84	229.02
IB14-12	<0.068	23.75	0.138	2.04	3.75	2.42	26.26	8.11	91.72	36.62	177.49	40.44	407.6	91.01	281.97
IB14-13*	8.71	89.12	5.72	40.96	18.37	10.9	43.09	12.79	128.52	50.19	228.07	49.58	505.28	109.15	378.19
IB14-14	1.42	38.73	0.831	5.76	8.46	4.91	36.62	12.15	133.03	48.45	222.55	49.26	496.07	109.42	486.44
IB14-15	<0.112	47.2	0.192	4.97	13.08	6.9	59.51	17.47	180.57	67.64	297.4	64.23	629.79	135.92	452.78
IB14-18	0.18	13.77	0.214	2.49	3.78	2.44	18.78	6.27	74.82	29.78	145.51	34.61	378.29	85.85	226.8
IB14-20	2.19	28.79	1.25	10.41	6.99	3.77	26.19	7.72	81.27	32.21	151.66	35.34	364.83	84.87	213.04
IB14-21	2.32	23.24	1.17	8.9	7.87	4.29	34.99	9.92	106.8	40.6	175.62	39.16	399.86	90.31	255.45

(*continued*)

Spot	La	Ce	Pr	Nd	Sm	Eu	Gd	Tb	Dy	Ho	Er	Tm	Yb	Lu	U
IB14-22	1.98	22.22	1.1	5.79	5.4	3.33	28.3	8.47	106.17	41.08	206.04	46.64	486.28	115.32	322.97
IB14-23	4.27	45.4	2.56	18.49	15.09	7.45	46.5	12.24	118.53	43.86	189.3	41.29	417.6	88.81	321.46
IB14-24	1.79	13.27	0.681	4.82	3.77	2.9	21.89	11.45	149.5	62.76	305.94	69.4	716.15	154.76	611.01
IB14-26	15.86	88.01	6.88	34.72	15.73	5.93	32.92	9.68	105.84	41.2	208.13	47.46	496.85	111.9	368.36
IB14-27	0.44	8.85	0.235	3.14	2.57	1.56	15.43	5.29	75.22	32.02	165.97	36.67	376.68	83.62	353.82
IB14-31	29.93	252.68	22.61	152.19	61.44	25.27	80.17	15.65	114.75	35.27	159.67	40.54	479.5	108.34	668.98
IB14-32*	4.27	53.31	2.76	16.68	13.64	7.61	42.07	11.7	124.68	46.9	218.38	48.26	487.98	108.4	396.27
IB14-32	18.87	139.09	9.99	58.71	36.43	14.95	99.6	28.17	305.28	115.23	509.44	107.97	1066.26	220.38	966.74
IB14-34	0.97	45.14	1.00	8.34	9.66	5.31	43.8	13.31	145.41	54.52	249.13	54.45	532.74	117.64	465.74
IB14-34*	4.39	60.48	4.02	24.07	14.04	5.9	49.8	12.9	143.68	49.02	224.62	48.79	504.97	111.11	361.72
IB14-35	0.566	10.7	0.341	3.3	4.13	1.68	15.35	4.65	60.65	22.48	116.6	26.19	304.31	70.61	161.1
IB14-36	0.185	17.59	0.2	1.8	3.84	2.21	18.57	6.36	76.35	30.22	143.82	32.84	343.8	76.74	215.9
IB14-38	0.744	17.7	0.82	5.95	5.53	3.72	23.58	9.81	118.19	46.98	229.00	50.23	507.23	107.81	342.26
IB14-40	1.55	16.7	0.93	4.93	3.3	2.67	16.33	4.99	57.85	23.74	116.61	27.1	318.16	72.77	184.25
IB14-41	8.67	71.31	4.33	30.57	17.99	9.3	54.58	16.31	153.6	54.43	239.82	52.36	525.7	111.31	711.99
IB14-42	3.29	44.69	2.92	21.67	12.99	6.02	28.02	7.84	77.72	30.83	142.62	31.89	338.88	76.86	180.57
IB14-44	<0.086	48.81	0.296	6.22	12.84	8.63	60.87	16.8	188.2	69.39	301.46	64.09	676.96	147.44	524.27
IB14-46	3.59	28.41	2.13	13.8	8.32	7.59	31.06	9.85	112.97	44.79	207.81	47.53	497.43	111.06	441.54
IB14-47	5.58	28.96	4.02	24.37	12.81	7.27	40.71	12.22	131.38	46.59	180.24	34.26	338.15	70.39	63.08
IB14-48	20.68	251.39	17.64	113.01	70.14	32.73	159.01	39.91	411.24	144.79	608.74	120.16	1182.41	241.93	1213.95
IB14-49	<0.061	31.06	0.177	2.86	6.14	4.13	32.14	10.74	120.16	44.78	208.93	44.92	490.41	108.75	347.48
IB14-50	2.33	26.94	1.52	9.25	7.78	5.83	30.17	9.77	109.66	38.68	177.18	39.26	413.67	89.54	431.82
IB14-51	13.13	79.68	5.66	33.29	14.53	5.13	30.39	8.71	95.53	37.67	176.77	41.16	432.52	97.34	331.16
IB14-55	11.15	61.66	5.97	40.37	17.39	6.97	34.58	7.32	73.21	26.27	128.15	29.06	323.12	73.29	261.26
IB14-57	1.48	29.42	0.66	8.12	10.24	4.68	37.15	10.29	116.26	44.27	213.8	47.89	537.12	121.9	331.85
IB14-58*	0.312	26.35	0.297	3.03	6.01	2.73	23.29	7.78	96.08	36.37	166.6	36.84	393.75	85.83	309.99
IB14-59	5.66	97.63	3.29	27.18	29.59	12.36	98.11	29.37	309.45	118.09	505.06	106.92	1088.54	230.02	890.56
IB14-60	2.89	93.36	1.69	16.59	19.82	12.59	88.26	27.37	301.86	113.31	503.38	107.42	1095.49	238.47	917.53
IB14-62	3.24	19.65	1.66	8.76	4.18	2.15	16.26	4.84	62.19	24.34	125.77	28.37	315.63	71.58	247.6
IB14-63	0.72	31.32	0.99	7.87	6.55	2.69	22.91	6.09	77.13	27.74	134.36	30.39	331.97	74.01	217.57
IB14-65	0.89	45.95	0.64	5.71	10.83	5.31	48.3	15.32	163.35	56.03	247.79	53.42	543.84	115.11	410.46
IB14-66	1.9	39.72	1.22	10.45	13.03	6.44	44.68	12.89	129.22	45.65	198.96	45.05	474.5	102.81	338.1
IB14-67	2.99	182.08	3.68	32.84	39.06	19.75	157.39	47.31	550.45	201.74	871.04	174.55	1742.51	358.66	1687.96
IB14-69	5.45	45.92	1.87	10.5	8.89	4.37	33.76	11.12	124.73	46.28	218.71	47.68	512.94	112.48	339.7
IB14-70	0.81	122.21	1.04	16.3	27.51	13.26	127.07	38.6	426.42	159.43	706.22	146.6	1516.31	320.77	1362.79
IB14-71	4.71	57.37	2.13	16.03	12.67	7.6	47.85	14.93	154.1	54.06	242.29	51.1	541.11	114.93	449.2
IB14-72	21.53	155.1	11.73	69.98	30.67	8.6	33.4	7.69	91.08	36.14	170.76	40.69	428.02	94.06	600.86

* = altered portion, commonly near rim.

Appendix L. LA-ICPMS trace elements data on zircon grains. Ibaré chloritite (IB15 sample)

Spot	La	Ce	Pr	Nd	Sm	Eu	Gd	Tb	Dy	Ho	Er	Tm	Yb	Lu	U
IB15-2	1.48	57.77	1.45	10.67	9.39	3.35	24.32	8.41	94.26	37.36	174.82	41.4	420.2	91.01	300.27
IB15-3	1.58	32.45	1.6	10.86	8.27	3.43	19.99	6.52	85.05	38.77	203.25	51.41	566.87	117.78	349.03
IB15-5	5.69	160.59	4.67	36.98	39.53	15.81	121.76	34.4	355.72	132.15	561.85	120.61	1203.8	245.96	841.98
IB15-6	2.54	79.79	2.48	20.72	15.12	8.8	64.25	16.73	180.77	63.94	279.73	60.15	596.12	124.65	547.97
IB15-7	2.01	16.88	1.36	8.61	6.09	3.11	28.84	11.07	147.18	64.15	301.12	69.36	706.05	150.01	443.67
IB15-8	6.16	73.69	4.02	28.26	20.18	8.26	51.18	13.85	140.49	48.87	222.34	52.05	547.39	116.21	395.3
IB15-9	1.4	51.09	1.63	15.84	21.98	8.22	56.13	16.36	159.73	60.99	268.79	59.95	616.07	137.7	413.37
IB15-10	48.74	709.17	36.83	252.00	143.01	46.82	265.73	68.67	675.5	238.64	974.09	196.13	1855.33	357.89	1667.35
IB15-11	1.18	46.6	1.48	11.76	14.17	6.04	46.68	14.2	143.7	52.28	233.6	52.17	512.39	111.79	383.61
IB15-14	8.05	207.85	10.13	81.09	54.64	24.47	128.14	32.14	277.79	88.57	346.52	71.14	660.17	127.58	346.16
IB15-15	0.558	19.32	0.505	5.48	7.08	4.15	31.87	11.65	143.71	61.53	282.52	64.7	661.99	142.56	410.08
IB15-16	14.78	196.86	10.91	80.09	56.8	23.69	169.93	48.02	492.99	178.47	752.51	156.16	1558.89	316.49	1393.58
IB15-17	0.232	18.42	0.268	3.18	4.13	2.07	21.58	6.9	75.4	30.16	148.34	34.71	371.99	79.93	211.65
IB15-24	1.08	36.75	1.3	11.07	11.48	5.11	39.8	9.7	109.18	38.03	170.56	38.6	418.12	92.79	310.93
IB15-25	9.81	100.37	8.62	64.62	47.56	17.87	91.19	20.43	163.33	51.42	189.53	38.16	369.77	77.86	264.55
IB15-26	2.23	126.36	2.31	14.3	10.56	4.06	29.67	8.53	90.64	31.39	142.15	31.58	330.91	73.28	460.85
IB15-29	7.62	93.14	5.06	32.99	22.58	11.08	60.65	16.09	156.96	58.27	243.36	54.13	552.67	120.29	421.13
IB15-30	3.35	31.14	3.9	26.94	19.13	6.85	37.24	10.29	95.24	33.22	155.18	34.04	348.61	74.32	262.12
IB15-31	11.92	249.69	9.88	63.26	39.46	18.65	72.85	14.84	123.46	37.84	147.49	31.65	307.61	64.82	254.25
IB15-32	7.88	70.91	7.64	52.26	40.82	13.86	76.32	18.29	167.01	54.2	239.23	49.32	527.37	111.69	361.09
IB15-33	1.58	25.42	1.09	8.51	7.11	3.27	25.39	8.92	115.26	46.68	218.48	51.45	541.98	116.00	421.82
IB15-34	20.74	94.5	9.84	56.36	23.83	9.61	41.98	11.37	116.51	44.91	203.32	46.36	473.38	108.97	404.71
IB15-36	14.38	479.33	15.01	86.17	43.54	13.75	73.81	18.27	167.36	56.94	247.58	52.42	535.43	108.98	463.59
IB15-37	1.43	11.46	0.956	9.36	6.83	2.94	21.05	7.38	101.63	43.11	217.77	51.11	563.33	121.72	437.27
IB15-38	1.09	31.14	0.513	4.77	8.13	5.23	37.52	11.82	122.31	43.86	203.1	45.63	459.58	100.26	316.2
IB15-39	3.08	175.72	2.87	18.89	15.72	7.93	54.9	16.48	164.35	57.98	257.77	55.58	561.49	122.22	427.82
IB15-40	2.89	45.76	1.85	13.34	9.00	5.17	40.9	12.42	129.71	49.25	218.54	48.95	513.53	106.25	382.23
IB15-41	0.171	8.35	0.288	3.32	4.95	3.66	39.43	22.35	326.73	149.07	710.58	163.7	1595.5	318.9	726.94
IB15-45	4.33	59.51	3.34	20.15	15.8	8.6	36.49	10.73	103.69	38.16	178.36	38.92	409.01	89.25	314.03
IB15-46	0.93	73.79	1.08	10.48	14.92	7.75	57.76	17.8	176.53	64.33	271.18	59.31	586.76	122.59	549.9

(*continued on next page*)

(*continued*)

Spot	La	Ce	Pr	Nd	Sm	Eu	Gd	Tb	Dy	Ho	Er	Tm	Yb	Lu	U
IB15-47	6.83	49.87	4.42	29.26	19.00	9.49	51.9	15.35	161.98	60.5	273.45	62.02	643.94	131.67	621.34
IB15-48	0.58	33.87	0.412	3.56	8.07	4.79	36.31	10.96	122.3	46.24	223.13	52.2	516.92	113.79	336.91
IB15-50	0.234	17.62	0.364	3.22	3.75	1.43	14.27	4.65	51.66	20.93	101.12	23.08	250.96	55.99	230.73
IB15-53	1.8	36.1	1.22	7.09	9.79	4.17	32.69	10.42	110.28	42.64	197.97	44.43	476.69	103.13	333.33
IB15-54	4.00	56.23	2.39	13.02	14.34	5.66	40.29	11.3	108.98	35.71	153.38	32.94	341.33	75.26	258.13
IB15-55	1.05	27.74	0.91	6.59	4.97	2.54	14.23	4.82	52.88	19.67	92.00	19.88	225.15	51.89	249.31
IB15-56	6.36	160.21	5.92	54.51	45.97	20.27	133.65	35.35	339.36	119.57	507.51	105.91	1027.56	210.02	864.85
IB15-57	4.4	114.31	3.71	27.98	25.49	11.57	71.79	18.97	190.45	68.47	291.06	65.53	651.2	136.49	528.82
IB15-58	2.16	44.84	1.78	15.9	14.95	5.37	36.89	11.66	121.93	47.88	223.33	52.36	537.59	120.24	324.26
IB15-59	1.19	38.29	1.26	8.52	9.72	4.46	25.31	8.76	95.42	39.01	181.01	40.55	419.14	89.25	326.55
IB15-60	21.43	148.81	11.87	68.79	34.06	10.54	55.04	12.53	108.91	36.59	167.07	38.22	391.53	83.5	278.78
IB15-61	4.18	84.26	2.63	26.59	25.67	11.36	86.19	24.26	256.86	94.35	413.41	89.05	910.84	191.16	740.11
IB15-62	0.727	42.57	0.739	7.46	12.6	5.78	47.94	14.64	159.69	60.57	267.23	58.21	595.58	127.44	399.83
IB15-63	0.95	31.82	0.94	9.72	7.83	4.2	30.19	8.71	101.16	39.67	186.24	43.29	471.21	106.84	273.54
IB15-64	12.63	119.99	10.42	63.93	45.07	17.97	76.06	15.29	134.93	43.86	197.58	44.46	477.04	103.01	360.3
IB15-66	1.07	47.64	3.91	8.95	15.13	7.9	56.78	16.62	173.84	61.92	273.44	58.29	630.04	132.98	470.81
IB15-67	13.4	204.44	9.75	66.58	44.06	16.93	72.12	13.74	103.78	33.31	137.8	30.46	317.16	68.17	521.26
IB15-68	1.19	53.21	0.97	8.57	15.22	7.3	62.36	18.4	194.24	69.18	301.68	65.7	656.92	135.17	392.61
IB15-69	1.2	35.35	1.03	7.67	5.86	3.43	29.28	8.97	94.49	36.62	167.96	38.13	416.16	87.99	297.82
IB15-70	4.07	40.04	2.27	16.07	14.66	6.41	40.49	11.28	120.38	47.37	224.19	50.62	519.62	109.29	309.51
IB15-71	0.303	20.09	0.203	2.89	4.05	2.16	16.92	5.86	71.42	29.18	138.8	33.23	341.39	78.08	196.48
IB15-72	8.9	116.74	6.73	44.33	33.17	12.53	63.47	14.76	127.13	42.25	180.02	40.16	402.12	88.41	243.44
IB15-73	1.83	44.06	1.4	11.81	13.04	6.48	52.51	13.84	151.46	56.08	237.04	53.05	538.01	115.07	387.68
IB15-75	35.68	174.77	17.69	118.48	68.32	34.39	129.86	28.1	258.94	75.7	281.97	58.16	548.95	101.56	472.3
IB15-77	16.66	121.88	12.05	85.71	52.93	18.98	88.28	19.02	163.48	53.78	229.56	51.17	524.1	110.24	314.6
IB15-78	2.86	50.42	3.12	23.93	23.25	10.03	56.95	15.03	145.07	49.15	211.87	45.52	472.5	99.22	355.65
IB15-79	8.6	178.22	6.29	45.52	31.02	12.23	62.08	14.3	133.01	41.98	180.7	39.15	384.09	84.51	347.9

Appendix M. LA-ICPMS trace elements data on zircon grains. Palma chloritite (PA18 sample)

Spot	La	Ce	Pr	Nd	Sm	Eu	Gd	Tb	Dy	Ho	Er	Tm	Yb	Lu	U
PA18-1	4.58	53.92	4.77	31.19	18.99	4.61	43.57	12.25	126.16	43.79	185.48	38.15	357.61	70.67	212.31
PA18-3	2.56	57.56	2.1	14.2	13.18	4.89	31.24	10.28	115.01	41.87	198.48	43.12	441.69	90.74	324.77
PA18-6	37.25	117.21	8.28	33.27	9.03	3.51	29.24	9.76	102.15	40.86	188.63	42.61	438.16	92.56	321.98
PA18-8	2.05	48.81	0.94	5.98	6.71	3.37	30.9	11.73	144.15	59.53	254.97	56.13	538.56	106.17	418.41
PA18-10*	5.91	116.53	5.74	33.17	21.52	13.16	47.46	13.96	135.73	50.59	224.54	52.14	544.09	117.81	909.79
PA18-13	5.42	39.47	5.01	30.3	20.64	10.23	41.09	12.98	117.54	40.1	165.5	36.76	365.88	70.8	295.14
PA18-14	1.31	110.57	1.38	11.28	11.23	5.69	42.26	13.44	137.46	47.77	197.7	40.59	377.43	71.64	511.26
PA18-15	4.36	108.83	4.43	29.03	27.75	7.27	77.92	26.13	258.73	89.71	375.9	78.51	761.63	145.69	694.89
PA18-16	0.052	28.25	<0.082	2.62	3.55	1.4	15.24	4.91	57.11	21.84	98.98	21.53	214.35	42.35	143.45
PA18-17	3.72	39.94	3.4	21.17	15.83	4.13	34.53	10.93	116.77	42.67	190.78	39.64	397.35	81.52	307.78
PA18-20	<0.145	13.73	0.311	3.59	12.69	4.00	84.12	30.99	349.58	124.71	500.46	91.59	796.85	137.36	190.42
PA18-22	14.46	74.08	11.24	66.41	35.97	9.6	60.87	17.34	156.03	45.97	186.96	38.52	387.24	76.68	570.18
PA18-24	6.00	61.24	6.22	33.39	27.73	12.94	50.3	15.12	138.75	41.93	173.06	37.48	391.27	86.91	784.65
PA18-26	2.59	91.81	2.64	14.01	13.64	4.77	46.73	15.58	174.98	66.15	297.35	66.44	639.92	123.68	588.68
PA18-30	14.3	108.48	13.65	81.47	51.94	12.15	98.8	27.35	240.89	73.74	276.83	54.46	503.95	89.98	416.78
PA18-31	27.5	177.93	27.46	165.08	109.25	32.78	188.15	50.92	418.82	116.9	431.65	84.74	838.55	161.59	1226.64
PA18-32	0.467	32.11	0.194	2.6	4.21	1.67	15.43	5.29	56.99	22.21	100.91	22.4	230.91	47.25	142.00
PA18-33	26.11	149.03	22.61	131.56	82.94	26.59	159.39	41.44	373.13	106.21	381.45	69.67	615.13	110.59	554.19
PA18-34	2.05	19.56	0.853	3.5	3.19	0.315	13.02	5.53	65.93	28.64	138.1	31.42	317.18	62.5	216.22
PA18-35	5.00	38.69	4.81	30.85	22.5	5.09	55.99	15.8	155.62	50.51	206.73	40.21	369.52	68.47	200.87
PA18-36	16.33	62.63	6.73	32.59	14.05	5.84	32.84	10.72	127.01	44.91	202.21	39.52	388.1	72.72	295.44
PA18-43	1.36	17.36	1.5	9.25	6.6	3.93	16.4	5.29	62.81	21.91	101.55	20.93	200.65	40.7	123.33
PA18-46	3.88	53.64	4.04	25.74	18.24	5.04	45.56	14.51	155.15	50.14	213.84	43.49	409.66	75.57	474.15
PA18-47	0.891	48.97	1.18	7.39	4.77	2.58	17.85	5.24	63.99	23.9	117.72	28.24	310.43	68.98	364.8
PA18-48	11.66	53.16	8.8	49.01	22.1	9.07	42.8	8.87	76.62	26.51	119.18	27.35	304.78	72.78	494.06
PA18-50	10.55	35.87	2.91	13.95	4.1	0.442	15.75	5.82	78.02	32.66	151.89	33.33	334.31	63.79	190.68
PA18-55	<0.081	25.35	0.268	4.38	7.1	2.79	22.01	6.39	77.19	26.23	110.02	24.71	242.15	46.25	74.33
PA18-56	9.26	84.39	9.17	59.76	38.87	23.77	81.96	23.25	187.61	50.92	179.9	32.19	270.02	44.95	359.91
PA18-58	0.503	46.17	0.688	7.24	8.72	4.71	23.71	7.91	77.47	26.91	115.23	24.25	235.46	46.72	142.04
PA18-59	2.13	142.5	2.41	16.23	15.66	5.18	52.02	14.44	155.2	53.3	223.44	44.8	437.64	82.96	743.16
PA18-65	0.6	82.68	0.729	6.37	9.06	3.7	30.02	9.54	102.54	38.32	159.94	32.4	309.05	57.86	222.95
PA18-67	3.97	22.56	1.23	5.83	6.6	0.56	21.9	9.06	111.16	44.1	208.32	44.27	402.72	77.89	302.34

* = altered portion, commonly near rim.

Appendix N. LA-ICPMS trace elements data on zircon grains. Ibaré volcanoclastic rock (IB1 sample)

Spot	La	Ce	Pr	Nd	Sm	Eu	Gd	Tb	Dy	Ho	Er	Tm	Yb	Lu	U
IB1-3	52.88	140.43	17.82	75.35	14.36	1.84	17.44	4.57	44.11	16.3	76.73	16.24	165.58	35.23	42.84
IB1-4	0.133	8.95	0.163	0.63	1.74	0.37	10.74	4.37	55.17	21.6	105.58	24.58	258.52	55.63	77.01
IB1-7	15.28	46.82	5.23	30.39	11.44	1.82	25.89	8.92	102.44	41.24	188.04	40.75	416.17	79.58	75.68
IB1-9	0.12	10.35	0.126	0.78	0.82	0.38	6.71	3.12	41.12	19.00	98.71	25.28	286.84	66.4	126.36
IB1-11	0.77	11.09	0.85	5.87	4.99	1.43	25.52	8.74	99.01	37.05	160.56	34.86	343.23	67.78	75.45
IB1-12	7.79	39.76	7.85	51.68	36.38	8.64	53.54	10.95	90.51	24.96	111.57	22.84	244.43	53.32	162.6
IB1-14	0.099	7.48	0.076	0.58	1.45	0.46	5.47	2.39	32.09	13.23	67.27	14.93	158.28	35.2	54.17
IB1-15	0.14	12.38	0.126	2.08	3.22	1.07	18.8	7.69	96.27	37.75	169.78	35.77	368.76	73.49	73.64
IB1-16	18.77	53.9	7.58	37.04	20.14	4.42	34.56	10.1	95.28	33.69	156.35	35.83	384.26	87.05	181.73
IB1-17	7.96	16.61	2.9	11.7	6.25	0.96	15.64	6.02	63.48	26.66	130.25	31.49	330.9	76.2	149.44
IB1-18	0.81	19.02	1.15	6.44	4.6	0.77	15.12	5.52	71.27	29.74	142.27	32.5	327.93	67.94	68.92
IB1-19	5.26	79.81	3.93	22.48	19.27	4.06	37.97	11.2	131.56	47.5	217.05	49.53	520.86	112.54	276.65
IB1-21	19.46	64.32	7.59	48.36	22.32	3.9	61.59	16.04	170.99	58.22	262.47	58.07	615.84	132.13	139.92
IB1-22	0.322	8.67	0.313	2.82	4.51	1.13	17.91	6.44	82.44	32.61	151.9	32.94	333.11	68.61	96.25
IB1-24	0.108	8.77	0.095	0.86	1.7	0.29	10.31	3.77	58.46	25.82	131.64	31.61	357.81	84.35	78.79
IB1-32	6.84	53.77	4.06	23.93	20.26	4.67	64.44	18.62	193.64	65.26	281.95	58.78	558.28	109.25	227.24
IB1-34	0.211	11.54	0.132	1.77	2.29	0.65	9.34	3.97	49.39	22.52	115.27	29.01	327.29	75.99	151.66
IB1-37	4.55	29.65	3.54	21.33	19.89	2.78	56.08	15.97	153.72	57.51	241.08	48.19	460.09	89.81	157.31
IB1-41	0.426	16.64	0.635	4.77	8.57	2.16	43.04	13.71	159.44	58.3	254.24	54.33	513.92	102.86	122.75
IB1-39	0.159	15.87	0.381	4.13	4.33	1.36	28.26	9.84	110.32	42.28	187.51	41.13	398.71	80.24	136.08
IB1-42	1.56	25.17	1.04	5.98	6.36	1.61	41.49	14.71	194.56	77.07	361.58	77.33	738.39	151.85	144.39
IB1-43	0.127	6.33	0.072	0.61	1.02	0.47	7.8	2.81	38.42	14.73	67.46	15.92	159.28	34.4	39.4
IB1-44	0.124	11.31	0.061	2.48	4.27	0.63	18.4	8.48	94.16	36.24	163.72	34.53	334.01	63.86	104.4
IB1-46	0.135	11.46	0.129	2.78	4.73	1.49	22.88	8.59	95.48	38.85	173.87	37.00	368.09	76.26	97.93
IB1-51	25.29	91.21	15.65	100.89	52.04	10.26	86.99	19.9	203.73	73.52	325.11	73.32	715.42	151.88	219.39
IB1-52	0.132	5.34	0.121	1.15	1.92	0.45	10.04	3.36	44.04	17.4	87.06	22.23	222.21	51.92	82.82
IB1-53	0.19	12.79	0.28	3.94	8.51	2.13	33.4	12.97	155.31	59.49	264.26	54.53	504.88	100.98	96.79
IB1-57	0.103	7.58	0.091	1.07	2.14	0.28	10.3	3.46	42.33	16.72	80.17	17.61	171.15	35.38	42.43
IB1-63	2.14	15.11	0.616	3.4	1.03	0.44	8.4	3.87	51.74	22.91	118.04	28.47	318.3	72.43	227.44
IB1-64	2.43	44.04	1.91	9.95	15.67	2.75	53.11	20.36	246.22	101.98	491.74	107.53	1103.43	225.28	356.91
IB1-68	2.49	35.45	1.9	12.36	11.99	2.1	34.12	9.48	105.74	37.81	171.86	36.04	336.68	70.29	154.87
IB1-72	0.149	7.79	0.202	0.94	1.39	0.38	7.21	2.88	35.74	12.83	66.96	15.99	169.51	35.45	64.33
IB1-76	7.49	40.26	5.01	32.18	15.07	4.00	28.96	9.75	108.34	39.86	199.52	45.85	498.15	110.9	201.31
IB1-77	0.147	5.81	0.123	0.86	1.22	0.36	10.93	4.47	52.4	22.64	111.66	22.00	232.06	48.62	35.17
IB1-78	4.85	22.67	1.29	5.8	3.62	1.06	17.48	6.08	71.65	29.39	150.95	36.12	374.75	84.58	125.39
IB1-80	17.57	70.95	16.37	89.09	56.64	12.62	100.17	26.6	252.24	82.96	346.63	73.78	694.86	139.52	430.35
IB1-81	0.164	5.19	0.118	1.21	1.27	0.6	6.05	2.57	33.6	16.37	84.93	19.97	221.93	52.96	37.42
IB1-82	0.28	9.97	0.465	2.7	3.00	0.97	13.15	4.02	47.46	18.35	97.22	20.67	232.82	52.03	88.12
IB1-84	0.73	34.48	0.82	6.99	12.55	1.81	33.75	14.00	157.19	65.28	306.96	67.08	672.54	138.42	303.23
IB1-87	9.72	30.6	2.77	12.27	4.66	1.18	14.01	4.62	60.02	24.65	116.46	25.64	278.59	57.9	79.46
IB1-90	4.01	52.93	3.00	23.7	22.66	4.34	65.71	19.88	207.06	75.59	326.61	65.21	619.04	122.62	210.47
IB1-91	2.03	17.42	0.8	5.56	5.25	1.32	22.53	7.17	85.29	33.16	153.64	34.25	366.17	81.18	153.93
IB1-92	0.179	8.96	0.125	1.16	5.56	0.44	21.49	7.04	83.87	29.96	133.7	27.65	268.19	52.4	61.58
IB1-93	2.14	11.38	1.09	5.82	6.35	0.89	16.83	3.85	46.97	18.31	90.97	21.09	223.98	50.04	72.47
IB1-98	0.168	19.69	0.193	5.13	5.28	2.7	32.09	11.62	131.00	52.64	252.55	59.39	619.31	134.77	153.21
IB1-99	0.14	19.85	0.261	3.99	7.57	2.02	46.64	15.49	188.84	75.57	326.87	69.94	626.22	124.79	149.79
IB1-100	0.41	9.42	0.247	3.44	3.65	1.18	18.54	6.2	76.38	30.26	128.85	27.7	272.32	56.29	68.52
IB1-104	0.149	15.77	0.159	4.47	9.95	1.8	42.14	14.33	178.47	70.32	315.27	62.34	604.51	118.79	131.28
IB1-107	0.157	12.1	0.132	1.31	3.55	0.96	24.9	8.61	106.84	41.11	200.94	43.55	415.39	87.87	106.63
IB1-108	0.223	15.89	0.357	4.03	10.11	1.64	40.09	13.75	169.99	68.22	301.5	64.15	584.54	123.55	94.64
IB1-109	16.78	110.63	13.66	76.02	60.45	11.45	110.81	25.81	186.56	50.19	203.18	41.37	414.05	89.33	125.55
IB1-110	1.52	13.35	1.16	7.03	5.82	1.65	20.43	6.04	78.68	34.38	168.7	40.44	423.87	97.45	90.29
IB1-113	8.53	50.42	5.99	37.62	26.29	4.39	62.14	14.47	144.14	49.58	227.42	49.68	507.4	108.25	273.54
IB1-115	2.06	30.66	2.45	10.00	12.77	1.72	27.51	9.2	109.61	45.65	213.63	47.66	464.61	99.08	117.02
IB1-116	4.53	36.31	4.19	23.9	16.15	3.75	30.55	8.93	95.64	34.41	161.04	38.24	386.14	88.54	228.66
IB1-120	3.28	27.29	1.63	12.42	10.75	2.35	26.58	7.08	67.21	26.62	130.28	33.74	352.02	80.63	217.44
IB1-121	3.78	25.97	3.24	18.71	12.3	3.77	36.39	11.01	140.65	55.12	261.18	61.58	611.68	134.63	214.05
IB1-122	55.47	117.6	13.08	51.2	11.47	2.04	36.63	11.06	138.95	53.58	244.72	51.28	492.29	100.66	126.22
IB1-123	9.12	38.22	5.43	36.19	15.58	2.13	22.81	6.00	52.33	18.22	88.32	17.84	180.56	38.89	51.05
IB1-124	6.55	23.79	2.7	11.23	5.12	1.07	13.74	4.23	46.43	18.54	92.54	22.08	230.99	56.23	77.54
IB1-125	1.68	14.02	0.563	3.59	2.66	1.28	16.89	5.91	80.03	31.43	153.65	36.64	401.93	92.77	165.13
IB1-126	2.33	23.57	1.81	13.27	14.08	3.46	42.65	13.03	145.77	56.56	261.24	59.37	577.88	126.54	188.68
IB1-128	7.87	60.29	6.09	16.45	46.81	6.28	45.00	14.92	137.21	43.45	222.64	56.86	517.56	126.4	333.87
IB1-129	15.76	58.74	5.66	25.97	12.86	1.55	48.5	15.11	182.13	66.87	289.04	55.73	497.84	96.36	134.83
IB1-132	0.138	5.95	0.112	0.94	0.94	0.36	4.87	1.71	22.34	9.94	51.1	12.67	142.71	35.17	58.92
IB1-133	0.516	15.04	0.518	6.3	9.2	1.48	36.75	12.69	144.73	56.5	247.68	50.09	462.94	89.6	167.39
IB1-134	0.93	16.2	0.583	4.36	5.76	1.62	21.34	8.41	99.6	41.94	187.19	41.24	394.68	80.09	89.55
IB1-136	0.37	8.37	0.269	1.84	3.03	0.43	12.99	5.66	65.69	28.97	143.7	33.26	355.48	79.04	58.53
IB1-139	0.406	23.04	0.444	4.5	7.95	1.89	35.92	11.85	136.14	55.45	250.8	54.17	557.92	117.47	204.26
IB1-140	4.81	19.85	1.72	18.37	9.6	0.99	30.61	8.09	71.77	23.4	119.58	25.21	303.7	66.53	99.61
IB1-143	0.119	8.57	0.141	0.97	3.48	1.16	12.34	4.91	64.05	26.19	136.23	31.00	340.84	73.94	99.18
IB1-144	1.54	35.91	1.46	10.71	13.42	2.5	37.38	13.68	149.12	58.66	274.19	59.03	576.84	122.91	276.6
IB1-145	2.53	24.18	1.04	6.45	4.11	1.09	24.48	7.25	101.22	40.52	187.54	39.92	395.11	79.34	130.94

(continued on next page)

(*continued*)

Spot	La	Ce	Pr	Nd	Sm	Eu	Gd	Tb	Dy	Ho	Er	Tm	Yb	Lu	U
IB1-147	0.117	12.58	0.126	1.42	2.43	0.49	11.73	4.33	60.71	27.27	143.29	34.5	387.67	88.72	177.94
IB1-149	1.74	12.79	1.53	7.88	4.9	1.05	10.93	3.35	38.79	14.04	75.36	18.64	204.19	46.73	85.77
IB1-150	0.2	9.02	0.142	1.64	4.27	0.84	14.55	4.85	64.79	25.51	125.95	28.26	294.86	65.44	89.86
IB1-151	1.83	10.28	0.66	8.19	4.72	1.34	18.68	5.16	55.43	20.88	99.3	23.34	253.1	57.5	117.13
IB1-152	2.05	9.19	0.68	3.82	1.82	0.98	9.19	3.56	43.72	20.21	113.64	27.1	303.49	76.09	43.90
IB1-153	0.87	10.79	0.63	6.02	10.33	1.46	58.06	21.68	272.1	109.39	504.38	103.9	983.13	191.65	105.43
IB1-155	0.644	39.24	0.579	7.26	10.77	2.13	42.04	14.12	166.71	63.34	298.13	64.7	658.04	132.22	279.05
IB1-157	1.49	15.18	0.47	4.47	4.78	0.9	21.85	7.23	91.06	35.05	167.46	34.04	357.66	74.2	108.11
IB1-162	0.315	26.04	0.23	6.21	10.01	1.87	55.23	19.62	228.41	85.75	381.62	76.52	699.69	130.42	168.93
IB1-163	0.191	29.49	0.363	3.98	10.01	2.02	51.4	17.63	217.3	80.43	357.9	71.86	657.54	129.81	185.14
IB1-165	0.111	7.45	0.098	0.78	1.64	0.7	12.3	4.14	51.88	21.82	107.42	22.8	233.84	51.79	61.57
IB1-167	3.2	45.59	3.56	25.48	21.42	3.82	56.67	15.62	167.91	58.41	257.06	55.21	544.45	104.87	250.72
IB1-168	0.122	7.94	0.104	0.83	0.9	0.209	7.24	3.64	41.26	18.05	76.77	16.93	172.2	35.04	37.39
IB1-170	0.199	8.17	0.142	1.85	2.22	0.91	10.69	4.05	53.53	21.43	109.16	25.23	277.73	60.36	81.88
IB1-172	1.67	24.85	1.56	11.49	13.84	2.58	55.8	20.04	237.06	91.04	432.26	91.78	856.97	169.9	138.36
IB1-173	2.04	17.55	0.487	5.76	4.59	0.86	10.00	3.4	42.38	19.32	110.23	30.04	347.91	88.6	371.20
IB1-175	2.57	53.49	2.08	14.2	14.09	5.2	48.06	15.79	194.74	77.37	377.8	88.78	960.00	212.06	295.89
IB1-176	0.161	15.15	0.242	3.32	6.48	1.78	36.5	12.97	161.05	61.15	277.3	55.79	524.4	102.32	149.09
IB1-177	10.94	11.85	0.466	0.92	2.63	0.42	10.13	3.42	47.12	19.88	93.74	21.73	232.83	49.13	79.87
IB1-178	16.12	49.82	5.63	30.55	8.29	1.54	21.93	5.89	75.36	29.67	146.85	34.47	352.43	76.08	97.21
IB1-182	0.15	13.48	0.265	2.54	5.29	1.75	27.05	10.35	140.68	56.94	279.86	62.95	650.98	136.91	127.02
IB1-183	0.37	12.68	0.105	1.53	2.61	0.77	14.35	5.64	72.64	30.95	161.48	36.51	406.06	90.14	111.28
IB1-185	0.172	10.56	0.105	0.57	0.99	0.24	3.78	2.05	24.09	10.04	54.35	14.14	158.28	39.00	36.65
IB1-186	0.143	7.59	0.156	0.91	1.95	0.5	14.91	5.37	69.74	27.94	134.34	30.24	303.18	64.85	48.02
IB1-187	0.139	9.3	0.169	0.74	2.81	0.78	16.51	5.75	69.76	29.03	142.15	33.00	357.09	79.22	139.11

Appendix O. Chemical analyses of the Ibaré volcanoclastic rocks. Oxides in wt%, trace elements in ppm

	IB1	IB25	IB26	IB27	IB28	IB29	IB30	IB31	IB32A	IB32B	IB33A	IB33B	IB34	IB35	IB36	IB38B	IB39B	IB40
SiO_2	59.2	61.4	62.0	60.6	60.0	57.2	60.8	60.1	60.3	66.0	63.2	63.9	61.6	61.3	64.2	64.2	57.1	60.4
Al_2O_3	18.3	13.8	15.0	15.8	15.6	11.3	14.5	16.6	16.6	15.7	14.8	14.4	15.8	17.1	16.8	15.5	17.2	17.6
Fe_2O_3	7.2	7.7	5.8	6.7	6.5	6.3	7.2	7.1	7.0	4.4	5.6	4.0	5.5	5.5	5.3	5.6	8.2	7.0
MgO	2.9	3.4	3.3	3.2	4.0	10.0	3.8	3.9	3.8	2.5	2.6	1.7	3.2	2.1	1.5	2.6	3.3	2.7
CaO	2.8	4.9	4.4	4.5	3.7	5.8	5.1	1.8	2.3	1.4	3.1	4.3	2.3	2.5	1.4	1.9	5.5	1.9
Na_2O	3.0	3.5	3.6	3.3	3.6	2.1	3.2	3.8	3.3	5.5	4.2	3.1	5.1	3.0	3.0	4.0	3.2	3.6
K_2O	1.4	1.3	2.2	2.0	2.2	2.7	2.1	2.2	2.2	1.4	2.0	2.9	1.1	2.9	3.4	2.2	0.7	1.3
TiO_2	0.7	0.8	0.6	0.7	0.7	0.5	0.8	0.8	0.7	0.5	0.8	0.5	0.9	0.8	0.7	0.7	0.7	0.7
P_2O_5	0.1	0.2	0.2	0.2	0.2	0.3	0.2	0.2	0.2	0.1	0.1	0.1	0.3	0.5	0.1	0.1	0.2	0.1
MnO	0.1	0.1	0.1	0.1	0.1	0.1	0.1	0.1	0.1	0.1	0.1	0.1	0.1	0.1	0.1	0.1	0.2	0.1
Cr_2O_3	0.0	0.0	0.0	0.0	0.0	0.1	0.0	0.0	0.0	0.0	0.0	–	0.0	0.0	0.0	0.0	0.0	0.0
LOI	4.1	2.5	2.6	2.7	3.0	3.3	1.9	3.2	3.2	2.0	3.4	4.9	3.9	4.1	3.5	2.9	3.6	4.4
Sum	99.9	99.9	99.9	99.9	99.9	99.8	99.9	99.9	99.9	100	99.9	100	99.9	99.9	100	99.9	99.9	99.9
Ba	437	804	1037	798	824	1224	1011	694	713	552	820	869	526	792	720	816	250	372
Be	–	3.0	–	–	2.0	3.0	2.0	2.0	1.0	2.0	2.0	–	2.0	–	3.0	2.0	–	–
Co	14.8	21.6	17.5	18.9	20.6	33.5	22.2	9.3	16.2	8.6	14.2	9.2	17.1	7.1	8.5	12.2	19.5	6.1
Cs	0.9	0.7	1.4	1.0	1.4	0.6	1.5	1.1	1.7	0.3	0.6	1.3	1.1	1.1	1.3	1.1	0.9	0.9
Ga	18.0	15.4	14.8	16.8	16.5	15.4	16.4	17.9	17.9	15.7	14.9	14.6	17.5	18.3	17.1	15.8	18.5	18.9
Hf	3.3	6.5	3.7	4.4	4.1	4.1	4.7	4.2	4.5	3.1	4.8	3.9	5.1	5.3	5.6	4.8	1.8	3.5
Nb	3.0	10.1	9.5	7.2	7.6	9.4	10.9	8.1	9.3	6.0	5.5	3.7	14.1	5.9	6.0	4.9	2.6	3.5
Rb	29.7	29.0	57.0	47.7	63.8	66.9	56.4	60.5	59.9	21.7	38.9	73.6	36.6	76.3	93.9	53.9	17.1	28.9
Sn	–	1.0	1.0	1.0	1.0	2.0	1.0	1.0	1.0	1.0	1.0	–	2.0	1.0	1.0	1.0	–	–
Sr	312	1011	998	811	641	929	945	375	428	548	450	312	441	255	114	330	768	275
Ta	0.2	0.7	0.7	0.5	0.5	0.7	0.7	0.6	0.7	0.5	0.5	0.3	0.8	0.5	0.5	0.4	0.1	0.2
Th	2.6	6.6	6.7	5.6	5.6	10.4	7.2	6.3	8.4	4.9	7.4	5.2	7.5	9.0	9.4	7.8	1.3	2.7
U	0.6	1.6	1.5	1.6	1.5	2.3	1.4	2.0	2.0	1.1	2.1	1.3	1.6	2.2	2.5	2.0	0.4	0.7
V	132	150	104	137	124	101	150	130	123	73	120	81	106	132	100	120	216	127
W	–	0.6	0.7	1.0	0.8	0.5	0.6	0.8	1.0	0.6	0.9	2.2	1.2	1.4	1.6	0.8	–	0.6
Zr	113	265	144	170	157	152	189	160	164	114	166	148	204	190	210	172	62	121
Y	15.8	17.7	14.7	17.1	16.3	14.7	16.8	16.9	16.2	12.1	18.3	14.6	19.0	23.1	21.9	17.5	21.4	20.2
La	10.0	36.1	33.8	26.2	25.1	29.2	37.3	19.7	30.7	21.5	15.3	11.6	39.4	24.2	20.7	15.2	10.6	12.3
Ce	16.3	71.4	63.2	50.7	50.1	58.6	71.7	36.2	56.2	37.6	32.0	24.4	73.8	46.2	42.0	32.3	21.5	21.6
Pr	2.8	8.5	7.6	5.9	5.9	7.0	8.5	5.2	6.9	4.6	3.9	3.0	8.4	6.0	5.1	3.9	3.0	3.1
Nd	11.9	32.0	28.0	22.8	22.4	26.9	32.0	20.9	25.6	17.8	15.2	12.1	31.2	23.4	19.5	15.7	13.2	13.2
Sm	2.8	5.7	4.9	4.2	4.2	5.1	5.6	4.0	4.6	3.2	3.3	2.4	5.3	4.7	4.2	3.3	3.4	2.8
Eu	0.9	1.4	1.3	1.2	1.1	1.3	1.5	1.1	1.3	1.0	0.9	0.6	1.3	1.0	0.8	0.9	1.0	0.9
Gd	3.0	4.5	3.8	3.7	3.7	4.1	4.4	3.6	4.0	2.7	3.3	2.6	4.4	4.6	4.0	3.3	3.6	3.3
Tb	0.5	0.6	0.5	0.6	0.5	0.5	0.6	0.5	0.6	0.4	0.5	0.4	0.6	0.7	0.6	0.5	0.6	0.5
Dy	3.1	3.4	2.9	3.2	2.9	3.0	3.4	3.2	3.2	2.3	3.3	2.7	3.6	4.3	3.9	3.2	3.7	3.4
Ho	0.6	0.7	0.5	0.6	0.6	0.5	0.6	0.6	0.6	0.4	0.7	0.5	0.6	0.8	0.8	0.6	0.8	0.7
Er	1.9	1.9	1.5	1.8	1.6	1.4	1.8	1.8	1.6	1.2	1.8	1.6	1.8	2.4	2.2	2.0	2.2	2.1
Tm	0.3	0.3	0.2	0.3	0.3	0.2	0.3	0.3	0.3	0.2	0.3	0.2	0.3	0.4	0.3	0.3	0.3	0.3
Yb	1.9	1.8	1.4	1.7	1.7	1.3	1.5	1.7	1.6	1.2	1.9	1.6	1.7	2.3	2.2	1.9	2.0	2.1
Lu	0.3	0.3	0.2	0.3	0.3	0.2	0.3	0.3	0.3	0.2	0.3	0.3	0.3	0.4	0.4	0.3	0.3	0.4

IB = samples; (–) = below detection limit in ppm: $Cr_2O_3 < 0.002$, Be < 1, Cs < 0.1, Sn < 1, Ta < 0.1, Th < 0.2, 0.1, W < 0.5.

Appendix P. Chemical analyses of the Cerro Mantiqueiras metabasalts. Oxides in wt%, trace elements in ppm

	CM20	CM21	CM26	CM27	CM29	CM31	CM33	CM34	CM35	CM36	CM37	CM38	CM39
SiO_2	50.3	60	55.39	50.93	56.19	57.17	48.62	54	50.33	59.37	53.09	53.94	48.74
Al_2O_3	12.8	15.92	15.98	16.65	17.27	14.59	13.91	19.12	14.27	15.91	14.82	15.37	14.3
Fe_2O_3	10.8	7.6	9.99	10.28	8.67	10.77	13.25	8.34	10.95	7.21	12.96	11.05	12.76
MgO	8.3	2.98	5.31	6.39	3.72	4.32	8.94	3.38	7.2	4.15	4.53	4.99	7.89
CaO	9.8	5.5	8	10.57	7.45	7.55	8.26	5.3	10.67	8.18	7.45	8.45	11.32
Na_2O	2.4	3.65	1.48	2.6	3.29	2.22	2.9	4.37	3.49	3.17	3.53	3.19	1.61
K_2O	2.1	1.19	0.91	0.56	0.5	1.31	0.95	1.25	0.75	0.47	0.86	0.51	0.72
TiO_2	1.6	0.67	0.57	0.86	0.76	0.31	0.94	0.93	1	0.49	1.58	0.8	0.71
P_2O_5	0.3	0.23	0.07	0.08	0.08	0.08	0.08	0.08	0.08	0.08	0.08	0.08	0.08
MnO	0.2	0.13	0.14	0.17	0.2	0.16	0.21	0.16	0.22	0.12	0.24	0.17	0.22
Cr_2O_3	0.018	0.002	0.046	0.012	0.009	0.008	0.019	–	0.047	0.028	0.005	0.032	0.022
LOI	1	1.8	1.9	0.7	1.5	1.2	1.6	2.7	0.7	0.7	0.6	1.2	1.1
Sum	99.8	99.9	99.9	99.9	99.9	99.9	99.8	99.9	99.8	99.9	99.9	99.9	99.8
Ba	580	712	352	109	151	371	284	357	302	136	242	89	165
Be	1	–	–	–	–	1	–	–	1	–	2	1	–
Co	42.4	18.3	38.3	32.4	18.6	30	56.4	30	41.8	27.7	34.5	36.5	41
Cs	0.6	0.5	0.7	0.6	0.4	1	0.3	0.7	–	0.2	0.2	0.3	0.6
Ga	16.4	16.1	12.7	14.1	14.3	13.1	14.5	19.5	16	12.8	17.9	13.9	16.3
Hf	3.7	4.6	0.8	1.6	2	1.2	1.4	2.1	2.5	1.2	3.9	1.7	1
Nb	15.2	15.3	0.3	1.3	1.7	1.5	2.1	2.9	6.9	0.1	3.5	1	1.9
Rb	30.2	18.7	17.4	5.4	7.8	27.2	17.2	26.2	3.2	4.9	12.1	8	9.3
Sn	1	–	–	–	–	–	–	–	–	–	2	2	–
Sr	655	1198	203	414	429	626	267	574	373	281	392	274	825
Ta	0.9	0.8	–	0.2	0.2	0.1	0.2	0.2	0.6	–	0.3	0.1	0.1
Th	2.3	4.9	–	1.1	1.2	1.1	–	0.6	1.4	1.8	1.1	0.4	2.4
U	0.9	1	0.1	0.5	0.4	0.4	–	0.2	0.7	0.8	0.7	–	0.3
V	289	153	259	272	106	287	334	174	232	213	427	280	373
W	0.6	–	–	–	–	–	–	–	–	–	–	–	–
Zr	147	201	23	53	67	45	48	77	84	42	146	65	30
Y	21.3	19.6	14	17.6	30	9.1	20.9	16.5	21	11.7	38.9	20.7	10
La	28.5	44.1	2.8	7.1	7.8	7.6	3.6	6.5	12.8	3.6	13.1	5	8.1
Ce	54.8	88.6	5.7	17.7	18.5	17.8	8.1	16.6	25.5	5.8	32	12.2	18.4
Pr	7.44	10.27	0.86	2.24	2.75	2.27	1.24	2.57	3.48	0.68	4.61	1.85	2.53
Nd	29.8	38	4.3	9.7	13.1	9.7	6.3	12.5	14.5	3.3	20.9	8.7	11.4
Sm	6.16	6.26	1.26	2.29	3.73	2.14	1.96	3.13	3.53	0.99	4.96	2.49	2.76
Eu	1.83	1.51	0.5	0.86	1.19	0.58	0.8	1.07	1.12	0.43	1.87	0.87	0.79
Gd	5.73	4.79	1.87	2.8	4.37	1.86	2.83	3.13	3.71	1.44	5.8	3.1	2.49
Tb	0.79	0.64	0.32	0.47	0.75	0.26	0.52	0.49	0.58	0.28	0.95	0.54	0.33
Dy	4.59	3.67	2.2	2.91	5.22	1.57	3.43	3.09	3.57	1.96	6.27	3.7	1.92
Ho	0.78	0.66	0.49	0.61	1.07	0.32	0.74	0.62	0.73	0.4	1.3	0.78	0.37
Er	2.07	1.84	1.41	1.83	3.05	0.89	2.21	1.61	2.08	1.31	3.94	2.27	1.06
Tm	0.29	0.29	0.22	0.27	0.51	0.13	0.33	0.25	0.31	0.19	0.58	0.34	0.14
Yb	1.78	1.78	1.36	1.72	3.07	0.89	2.11	1.54	1.92	1.28	3.78	2.15	0.89
Lu	0.28	0.28	0.22	0.29	0.5	0.15	0.34	0.24	0.31	0.2	0.61	0.33	0.13

CM = samples name; (–) = below detection limit in ppm: $Cr_2O_3 < 0.002$, Be < 1, Cs < 0.1, Sn < 1, Ta < 0.1, Th < 0.2, 0.1, W < 0.5.

Appendix Q. Coordinates of the volcanoclastics and metabasalts. Datum = WGS 84. Hand-held GPS used

Samples	North coordinate	South coordinate
IB1	6,591,173	762,629
IB25	6,587,669	764,873
IB26	6,587,723	764,814
IB27	6,588,111	764,420
IB28	6,588,304	764,194
IB29	6,588,598	763,896
IB30	6,588,979	763,557
IB31	6,589,364	763,147
IB32A	6,589,784	762,663
IB32B	6,589,784	762,663
IB33A	6,590,287	762,173
IB33B	6,590,287	762,173
IB34	6,590,350	762,094
IB35	6,590,461	761,893
IB36	6,590,792	761,353
IB38B	6,590,572	761,687
IB39B	6,591,949	760,755
IB40	6,592,564	760,706
CM20	6,578,038	215,727
CM21	6,578,090	215,229

(continued on next page)

(*continued*)

Samples	North coordinate	South coordinate
CM26	6,579,144	220,496
CM27	6,579,205	220,486
CM29	6,578,961	220,497
CM31	6,578,816	220,181
CM33	6,578,733	220,221
CM34	6,578,758	220,540
CM35	6,578,720	220,864
CM36	6,579,209	221,084
CM37	6,579,387	221,094
CM38	6,578,839	222,219
CM39	6,578,564	222,472

IB = Ibaré samples name; CM = Cerro Mantiqueiras samples name.

References

Ali, K.A., Azer, M.K., Gahlan, H.A., 2010. Age constraints on the formation and emplacement of Neoproterozoic ophiolites along the Allaqi-Heiani suture, South Eastern Desert of Egypt. Gondwana Research 18, 583–595.

Andersen, T., Griffin, W.L., Pearson, N.J., 2002. Crustal evolution in the SW part of the Baltic Shield: the Hf isotope evidence. Journal of Petrology 43, 1725–1747.

Arena, K.R., Hartmann, L.A., Lana, C., 2016. Evolution of Neoproterozoic ophiolites from the southern Brasiliano Orogen revealed by zircon U-Pb-Hf isotopes and geochemistry. Precambrian Research 285, 299–314.

Babinski, M., Chemale, Jr.F., Hartmann, L.A., Van Schmus, W.R., Silva, L.C., 1996. Juvenile accretion at 750–700 Ma in Southern Brazil. Geology 24, 439–442.

Babinski, M., Chemale Jr., F., Van Schmus, W.R., Hartmann, L.A., Da Silva, L.C., 1997. U–Pb and Sm–Nd geochronology of the Neoproterozoic granitic–gneissic Dom Feliciano Belt, southern Brazil. Journal of South American Earth Sciences 3–4, 263–274.

Basei, M.A.S., Frimmel, H.E., Nutman, A.P., Preciozzi, F., Jacob, J., 2005. A connection between the Neoproterozoic Dom Feliciano (Brazil/Uruguay) and Gariep (Namibia/SouthAfrica) orogenic belts–evidence from a reconnaissance study. Precambrian Research 139, 195–221.

Basei, M.A.S., Frimmel, H.E., Nutman, A.P., Preciozzi, F., 2008. West Gondwana amalgamation based on detrital zircon ages from Neoproterozoic Ribeira and Dom Feliciano Belts of South America and comparison with coeval sequences from SW Africa. In: Pankhurst, R.J., Trouw, R.A.J., Brito Neves, B.B., De Wit, M.J. (Eds.), West Gondwana Pre-Cenozoic Correlations Across the south Atlantic Region. Geological Society Special Publication Vol. 294, pp. 239–256.

Basei, M.A.S., Campos Neto, M.C., Castro, N.A., Nutman, A.P., Wemmer, M.T., Yamamoto, M.T., Hueck, M., Osako, L., Siga Jr., O., Passarelli, C.R., 2011. Tectonic evolution of the Brusque Group, Dom Feliciano Belt, Santa Catarina. Journal of South American Earth Sciences 32, 324–350.

Basta, F.F., Maurice, A.E., Bakhit, B.R., Ali, K.A., Manton, W.I., 2011. Neoproterozoic contaminated MORB of Wadi Ghadir ophiolite, NE Africa: geochemical and Nd and Sr isotopic constraints. Journal of African Earth Sciences 59, 227–242.

Beard, J.S., Fullagar, P.D., Sinha, A.K., 2002. Gabbroic pegmatite intrusions, Iberia Abyssal Plain, ODP Leg 173, Site 1070: magmatism during a transition from non-volcanic rifting to sea-floor spreading. Journal of Petrology 43 (5), 885–905.

Bettencourt, J.S., Tosdal, R.M., Leite, W.B., Payolla, B.L., 1999. Mesoproterozoic rapakivi granites of the Rondônia Tin Province, southwestern border of the Amazonian craton, Brazil - I. Reconnaissance U-Pb geochronology and regional implications. Precambrian Research 95, 41–67.

Bogdanova, S.V., Pisarevsky, S.A., Li, Z.X., 2009. Assembly and breakup of Rodinia (some results of IGCP project 440). Stratigraphy and Geological Correlation 17, 259–274.

Bomparola, R.M., Ghezzo, C., Belousova, E., Griffin, W.L., O'Reilly, S.Y., 2007. Resetting of the U-Pb zircon system in Cambro-Ordovician intrusives of the Deep Freeze Range, Northern Victoria Land, Antarctica. Journal of Petrology 48, 327–364.

Bouvier, A., Vervoort, J.D., Patchett, P.J., 2008. The Lu–Hf and Sm–Nd isotopic composition of CHUR: constraints from unequilibrated chondrites and implications for the bulk composition of terrestrial planets. Earth and Planetary Science Letter 273, 48–57.

Boynton, W.V., 1984. Cosmochemistry of the rare earth elements; meteorite studies. In: Henderson, P. (Ed.), Rare Earth Element Geochemistry. Elsevier Science Publishing Company, Amsterdam, pp. 63–114.

Brito Neves, B.B., Fuck, R.A., Pimentel, M.M., 2014. The Brasiliano collage in South America: a review. Brazilian Journal of Geology 44, 493–518.

Camozzato, E., Philipp, R.P., Chemale Jr., F., 2013. Idades Estaterianas e Calimianas no Domo da Vigia: Complexos Vigia e Porongos, Metagranito Seival e Anfibolito Tupi Silveira, Bagé, RS. Proceedings of the Simpósio Nacional de Estudos Tectônicos 14th, Chapada dos Guimarães, Mato Grosso Brazil, pp. 1–4.

Camozzato, E., Klein, C., Iglesias, C.M.F., 2014. Geological map of Bagé, Rio Grande do Sul, Porto Alegre. Brazil Geological Survey SH.21-Z-D-III, Scale 1:100,000.

Casquet, C., Rapela, C.W., Pankhurst, R.J., Baldo, E.G., Galindo, C., Fanning, C.M., Dahlquist, J.A., Saavedra, J., 2012. A history of Proterozoic terranes in southern South America: from Rodinia to Gondwana. Geoscience Frontiers 3, 137–145.

Cawood, P.A., Wang, Y.J., Xu, Y.J., Zhao, G.C., 2013. Locating South China in Rodinia and Gondwana: a fragment of greater India lithosphere? Geology 41, 903–906.

Chemale Jr., F., 1982. Geologia da região de Palma, São Gabriel, Rio Grande do Sul. Master thesis. Universidade Federal do Rio Grande do Sul.

Chemale Jr., F., 2000. Evolução Geológica do Escudo Sul-rio-grandense. In: Holz, M., De Ros, L.F. (Eds.), Geologia do Rio Grande do Sul: Centro de Investigação do Gondwana. Universidade Federal do Rio Grande do Sul. Porto Alegre, Brazil, pp. 13–55.

Chemale Jr., F., Hartmann, L.A., da Silva, L.C., 1995. Stratigraphy and tectonism of Precambrian to early Paleozoic units in southern Brazil and Uruguay. Acta Geológica Leopoldensia 44, 1–111.

Chemale Jr., F., Philipp, R.P., Dussin, A.I., Formoso, M.L.L., Kawashita, K., Bertotti, A.L., 2011. Lu–Hf and U–Pb age determination of Capivarita Anorthosite in the Dom Feliciano Belt, Brazil. Precambrian Research 186, 117–126.

Chu, Nan-Chin, Taylor, R.N., Chavagnac, V., Nesbitt, R.W., Boella, R.M., Milton, J.A., German, C.R., Bayon, G., Burton, K., 2002. Hf isotope ratio analysis using multi-collector inductively coupled plasma mass spectrometry: an evaluation of isobaric interference corrections. Journal of Analytical Atomic Spectrometry 17, 1567–1574.

Cingolani, C.A., Hartmann, L.A., Santos, J.O.S., McNaughton, N.J., 2002. U-Pb SHRIMP dating of zircons from the Buenos Aires Complex of the Tandilia Belt, Río de La Plata Craton. Proceedings of the Congreso Geológico Argentino 15th, Argentina, pp. 149–154.

Cordani, U.G., Brito Neves, B.B., D'Agrella-Filho, M.S., 2003. From Rodinia to Gondwana: a review of the available evidence from South America. Gondwana Research 6, 275–283.

Dalla Salda, L., Bossi, J., Cingolani, C.A., 1988. The Rio de la Plata cratonic region of southwestern Gondwanaland. Episodes 11, 263–269.

Dalziel, I.W.D., Soper, N.J., 2001. Neoproterozoic extension on the Scottish Promontory of Laurentia; paleogeographic and tectonic implications. The Journal of Geology 109, 299–317.

Deschamps, F., Godard, M., Guillot, S., Hattori, K., 2013. Geochemistry of subduction zone serpentinites: a review. Lithos 178, 96–127.

Dilek, Y., Furnes, H., 2011. Ophiolite genesis and global tectonics: geochemical and tectonic fingerprinting of ancient oceanic lithosphere. GSA Bulletin 123, 387–411.

Dilek, Y., Furnes, H., 2014. Ophiolites and their origins. Elements 10, 93–100.

Dilek, Y., Thy, P., 2006. Age and petrogenesis of plagiogranite intrusions in the Ankara mélange, central Turkey. Island Arc 15, 44–57.

Dilek, Y., Furnes, H., Shallo, M., 2008. Geochemistry of the Jurassic Mirdita Ophiolite (Albania) and the MORB to SSZ evolution of a marginal basin oceanic crust. Lithos 100, 174–209.

Dubińska, E., Wiewióra, A., 1999. Layer silicates from a rodingite and its blackwall from Przemilow (Lower Silesia, Poland): mineralogical record of metasomatic processes during serpentinization and serpentinite recrystallization. Mineralogy and Petrology 67, 223–237.

Dubińska, E., Bylina, P., Kozłowski, A., Dörr, W., Nejbert, K., Schastokc, J., Kulickie, C., 2004. U-Pb dating of serpentinization-hydrothermal zircon from a metassomatic rodingite shell (Sudetic ophiolite, SW Poland). Chemical Geology 203, 183–203.

Escayola, M.P., Pimentel, M.M., Armstrong, R., 2007. Neoproterozoic backarc basin: sensitive high-resolution ion microprobe U-Pb and Sm-Nd isotopic evidence from the Eastern Pampean ranges, Argentina. Geology 35, 495–498.

Fragoso César, A.R.S., Figueiredo, M.C.H., Soliani Jr., E., Faccini, U.F., 1986. O Batólito Pelotas (Proterozóico Superior/Eo-Paleozóico) no Escudo do Rio Grande do Sul, Brasil. Proceedings of the Congresso Brasileiro de Geologia 34th, Goiânia, Brazil, pp. 1322–1343.

Frimmel, H.E., Zartman, R.E., Spath, A., 2001. The Richtersveld Igneous Complex South Africa: U–Pb zircon and geochemical evidence for the beginning of Neoproterozoic continental breakup. The Journal of Geology 109, 493–508.

Frimmel, H.E., Tack, L., Basei, M.S., Nutman, A.P., Boven, A., 2006. Provenance and chemostratigraphy of the Neoproterozoic West Congolian Group in the Democratic Republic of Congo. Journal of African Earth Sciences 46, 221–239.

Froitzheim, N., Rubatto, D., 1998. Continental breakup by detachment faulting: field evidence and geochronological constraints (Tasna nappe, Switzerland). Terra Nova 10, 171–176.

Garcia, M.A.M., 1980. Petrologia do Complexo Palma Rio Grande do Sul. Master thesis. Universidade Federal do Rio Grande do Sul.

Gastal, M.C., Lafon, J.M., Ferreira, F.J.F., Magro, F.U.S., Remus, M.V.D., Sommer, C.A., 2006. Reinterpretação do Complexo Intrusivo Lavras do Sul – RS, de acordo com os sistemas vulcano-plutônicos de subsidência. Parte I: Geologia, geofísica e geocronologia (207Pb/206Pb e 206Pb/238U). Revista Brasileira de Geociencias 36, 109–124.

Gastal, M.C., Ferreira, F.J.F., Cunha, J.U., Esmeris, C., Koester, E., Raposo, M.B., Rossetti, M.M.M., 2015. Alojamento do granito Lavras e a mineralização aurífera durante evolução de centro vulcano-plutônico pós-colisional, oeste do Escud Sul-riograndense: dados geofísicos e estruturais. Brazilian Journal of Geology 45, 217–241.

Gebauer, D., Grünenfelder, M., 1976. U-Pb zircon and Rb-Sr whole-rock dating of low-grade metasediments. Example: Montagne Noire (Southern France). Contribution to Mineralogy and Petrology 59, 13–32.

Geisler, T., Pidgeon, R.T., Kurtz, R., Bronswijk, W., Schleicher, H., 2003. Experimental hydrothermal alteration of partially metamict zircon. American Mineralogist 88, 1496–1513.

Gerdes, A., Zeh, A., 2006. Combined U–Pb and Hf isotope LA-(MC)-ICP-MS analyses of detrital zircons: comparison with SHRIMP and new constraints for the provenance and age of an Armorican metasediment in Central Germany. Earth and Planetary Sciences Letters 249, 47–61.

Gerdes, A., Zeh, A., 2009. Zircon formation versus zircon alteration – new insights from combined U-Pb and Lu–Hf in-situ LA-ICP-MS analyses, and consequence for the interpretation of Archean zircon from the Central Zone of the Limpopo Belt. Chemical Geology 261, 230–243.

Gladkochub, D.P., Wingate, M.T.D., Pisarevsky, S.A., Donskaya, T.V., Mazukabzov, A.M., Ponomarchuk, V.A., Stanevich, A.M., 2006. Mafic intrusions in southwestern Siberia and implications for a Neoproterozoic connection with Laurentia. Precambrian Research 147, 260–278.

Goscombe, B., Gray, D., Armstrong, R., Foster, D.A., Vogl, J., 2005. Event geochronology of the Pan-African Kaoko Belt, Namibia. Precambrian Research 140, 1–41.

Green, N.L., 2006. Influence of slab thermal structure on basalt source regions and melting conditions: REE and HFSE constraints on from the garibaldi volcanic belt, northern Cascadia subduction system. Lithos 87, 23–49.

Grieco, G., Ferrario, A., Von Quadt, A., Koeppel, V., Mathez, E.A., 2001. The zircon-bearing chromitites of the phlogopite peridotite of Finero (Ivrea Zone, Southern Alps): evidence and geochronology of a metasomatized mantle slab. Journal of Petrology 42, 89–101.

Griffin, W.L., Pearson, N.J., Belousova, E., Jackson, S.E., Van Achterbergh, E., O'Reilly, S.Y., Shee, S.R., 2000. The Hf isotope composition of cratonic mantle: LAM-MC-ICPMS analysis of zircon megacrysts in kimberlites. Geochimica et Cosmochimica Acta 64, 133–147.

Grimes, C.B., John, B.E., Kelemen, P.B., Mazdab, F., Wooden, J.L., Cheadle, M.J., Hanghøj, K., Schwartz, J.J., 2007. The trace element chemistry of zircons from oceanic crust: a method for distinguishing detrital zircon provenance. Geology 35, 643–646.

Grimes, C.B., John, B.E., Cheadle, M.J., Mazdab, F.K., Wooden, J.L., Swapp, S., Schwartz, J.J., 2009. On the occurrence, trace element geochemistry, and crystallization history of zircon from in situ ocean lithosphere. Contribution to Mineralogy and Petrology 158, 757–783.

Grimes, C.B., Wooden, J.L., Cheadle, M.J., John, B.E., 2015. “Fingerprinting” tectono-magmatic provenance using trace elements in igneous zircon. Contribution to Mineralogy and Petrology. 170:46. http://dx.doi.org/10.1007/s00410-015-1199-3.

Gubert, M.L., Philipp, R.P., Basei, M.A.S., 2016. The Bossoroca Complex, São Gabriel Terrane, Dom Feliciano Belt, southernmost Brazil: U-Pb geochronology and tectonic implications for the neoproterozoic São Gabriel Arc. Journal of South American Earth Sciences 70, 1–17.

Hamelin, C., Bezos, A., Dosso, L., Escartin, J., Cannat, M., Mevel, C., 2013. Atypically depleted upper mantle component revealed by Hf isotopes at Lucky Strike segment. Chemical Geology 341, 128–139.

Hanan, B.B., Blichert-Toft, J., Pyle, D.G., Christie, D.M., 2004. Contrasting origins of the upper mantle revealed by hafnium and lead isotopes from the Southeast Indian Ridge. Nature 432, 91–94.

Hartmann, L.A., 1998. Deepest exposed crust of Brazil - geochemistry of Paleoproterozoic depleted Santa Maria Chico Granulites. Gondwana Research 3–4, 331–341.

Hartmann, L.A., Delgado, I.M., 2001. Cratons and orogenic belts of the Brazilian Shield and their contained gold deposits. Mineralium Deposita 36, 207–217.

Hartmann, L.A., Leite, J.A.D., McNaughton, N.J., Santos, J.O.S., 1999. Deepest exposed crust of Brazil - SHRIMP establishes three events. Geology 27, 947–950.

Hartmann, L.A., Chemale Jr., F., Philipp, R.P., 2007. Evolução geotectônica do Rio Grande do Sul no Pré-Cambriano. In: Iannuzzi, R., Frantz, J.C. (Eds.), 50 Anos de Geologia. Universidade Federal do Rio Grande do Sul, Porto Alegre, Brazil, pp. 97–123.

Hartmann, L.A., Philipp, R.P., Santos, J.O.S., McNaughton, N.J., 2011. Time frame of the 753–680 Ma juvenile accretion during the São Gabriel orogeny, southern Brazilian shield. Gondwana Research 19, 84–99.

Heilbron, M., Valeriano, C.M., Tassinari, C.C.G., Almeida, J., Tupinambá, M., Siga Jr., O., Trouw, R., 2008. Correlation of Neoproterozoic terranes between the Ribeira Belt, SE Brazil and its African counterpart: comparative tectonic evolution and open questions. Geological Society, Special Publications, London 294, 211–237.

Hoffman, P.F., 1999. The breakup of Rodinia, birth of Gondwana, true polar wanderand the snowball. Journal of African Earth Sciences 28, 17–33.

Hofmann, A.W., Heinrich, D.H., Karl, K.T., 2003. Sampling mantle heterogeneity through oceanic basalts: isotopes and trace elements. Treatise on Geochemistry. Pergamon, Oxford, pp. 1–44.

Horstwood, M.S.A., Košler, J., Gehrels, G., Jackson, S.E., McLean, N.M., Paton, C., Pearson, N.J., Sircombe, K., Sylvester, P., Vermeesch, P., Bowring, J.F., Condon, D.J., Schoene, B., 2016. Community-Derived Standards for LA-ICP-MS U-(Th-)Pb Geochronology – Uncertainty Propagation, Age Interpretation and Data Reporting. Geostandards and Geoanalytical Research 40, 311–332.

Hoskin, P.W.O., 2005. Trace-element composition of hydrothermal zircon and the alteration of Hadean zircon from the Jack Hills, Australia. Geochimica et Cosmochimica Acta 69, 637–648.

Howard, A.L., Farmera, G.L., Amato, J.M., Fedo, C.M., 2015. Zircon U–Pb ages and Hf isotopic compositions indicate multiple sources for Grenvillian detrital zircon deposited in western Laurentia. Earth and Planetary Science Letters 432, 300–310.

Hu, C.N., Santosh, M., Yang, Q.Y., Kimd, S.W., Nakagawa, M., Maruyama, S., 2017. Magmatic and metasomatic imprints in a long-lasting subduction zone: evidence from zircon in rodingite and serpentinite of Kochi, SW Japan. Lithos 274–275, 349–362.

Jackson, S.E., Pearson, N.J., Griffin, W.L., Belousova, E.A., 2004. The application of laser ablation inductively coupled plasma mass spectrometry to in situ U-Pb zircon geochronology. Chemical Geology 211, 47–69.

Janney, P.E., Le Roex, A.P., Carlson, R.W., 2005. Hafnium isotope and trace element constraints on the nature of mantle heterogeneity beneath the Central Southwest Indian ridge (13°E to 47°E). Journal of Petrology 46, 2427–2464.

Johnson, S.P., Rivers, T., De Waele, B., 2005. A review of the Mesoproterozoic to early Palaeozoic magmatic and tectonothermal history of south-central Africa: implications for Rodinia and Gondwana. Journal of the Geological Society 162, 433–450.

Karaoglan, F.G., Parlak, O., Klotzli, U., Thoni, M., Koller, F., 2013. U–Pb and Sm–Nd geochronology of the Kizildag (Hatay, Turkey) ophiolite: implications for the timing and duration of suprasubduction zone type oceanic crust formation in the southern Neotethys. Geological Magazine 150, 283–299.

Klein, F., 2009. Petrology of Serpentinites and Rodingites in the Oceanic Lithosphere. Ph.D. thesis. Universität Bremen.

Laux, J.H., Bongiolo, E.M., Chemale, Jr.F., Santos, T.C., 2010. U-Pb data from Ibaré Formation: a volcano-sedimentary sequence of São Gabriel Arc, Rio Grande do Sul – Brazil. Proceedings of the South American Symposium on Isotope Geology 7th, Brasilia, Brazil, pp. 74–77.

Laux, J.H., Bongiolo, E.M., Klein, C., Iglesias, C.M.F., 2012. Geological map of Lagoa da Meia Lua, Rio Grande do Sul, Porto Alegre. Brazil Geological Survey SH.21-Z-B-VI, Scale 1: 100,000.

Leite, J.A.D., Hartmann, L.A., McNaughton, N.J., Chemale Jr., F., 1998. SHRIMP U/Pb zircon geochronology of Neoproterozoic juvenile and crustal-reworked terranes in southernmost Brazil. International Geology Review 40, 688–705.

Lena, L.O.F., Pimentel, M.M., Philipp, R.P., Armstrong, R., Sato, K., 2014. The evolution of the Neoproterozoic São Gabriel juvenile terrane, southern Brazil based on high spatial resolution U-Pb ages and δ^{18}O data from detrital zircons. Precambrian Research 247, 126–138.

Li, Z.X., Li, X.H., Kinny, P.D., Wang, J., 1999. The breakup of Rodinia: did it start with a mantle plume beneath South China? Earth and Planetary Science Letters 173, 171–181.

Li, Z.X., Evans, D.A.D., Zhang, S., 2004. A 90° spin on Rodinia: possible causal links between the Neoproterozoic supercontinent, superplume, true polar wander and low-latitude glaciation. Earth and Planetary Science Letters 220, 409–421.

Li, Z.X., Bogdanova, S.V., Collins, A.S., Davidson, A., De Waele, B., Ernst, R.E., Fitzsi-mons, I.C.W., Fuck, R.A., Gladkochub, D.P., Jacobs, J., Karlstrom, K.E., Lu, S., Natapov, L.M., Pease, V., Pisarevsky, S.A., Thrane, K., Vernikovsky, V., 2008. Assembly, configuration, and break-up history of Rodinia: a synthesis. Precambrian Research 160, 179–210.

Li, X.H., Faure, M., Lin, W., Manatschal, G., 2013. New isotopic constraints on age and magma genesis of an embryonic oceanic crust: the Chenaillet Ophiolite in the Western Alps. Lithos 160–161, 283–291.

Liu, C.Z., Chung, S.L., Wu, F.Y., Zhang, C., Xu, Y., Wang, J.G., Chen, Y., Guo, S., 2016. Tethyan suturing in Southeast Asia: zircon U-Pb and Hf-O isotopic constraints from Myanmar ophiolites. Geology 44, 311–314.

Lopes, C.G., Pimentel, M.M., Philipp, R.P., Gruber, L., Armstrong, R., Junges, S., 2015. Provenance of the Passo Feio Complex, Dom Feliciano Belt: implications for the age of supracrustal rocks of the São Gabriel Arc, southern Brazil. Journal of South American Earth Sciences 58, 9–17.

Ludwig, K.R., 1998. On the treatment of concordant uranium–lead ages. Geochimica et Cosmochimica Acta 62, 665–676.

Ludwig, K.R., 2003. Isoplot/Ex Version 3.00: A Geochronological Toolkit for MicrosoftExcel. Berkeley Geochronology Center, Berkely, CA (Special Publication 4, 71 http://bgc.org/isoplot_etc/isoplot.html).

Machado, N., Koppe, J.C., Hartmann, L.A., 1990. A late Proterozoic U-Pb age for the Bossoroca belt, Rio Grande do Sul, Brazil. Journal of South American Earth Sciences 3, 87–90.

Morag, N., Avigad, D., Gerdes, A., Belousova, E., Harlavan, Y., 2011. Crustal evolution and recycling in the northern Arabian Nubian Shield: new perspectives from zircon Lu–Hf and U–Pb systematics. Precambrian Reserach 186, 101–116.

Naumann, M.P., 1985. O complexo Vulcano-sedimentar-ultramáfico e granitoides da região de Ibaré. Master thesis. Universidade Federal do Rio Grande do Sul.

Naumann, M.P., Hartmann, L.A., 1984. Cornubianitos ultramáficos e metassomatitos associados da região do Arroio Corticeira. Proceedings of the Congresso Brasileiro de Geologia 33th, Rio de Janeiro, Brazil, pp. 4279–4290.

Neal, C., Stanger, G., 1985. Past and present serpentinization of ultramafic rocks; an example from the Semail ophiolite nappe of the northern Oman. In: Drever, J.I. (Ed.), The Chemistry of Weathering. D. Reidel Publishing Company, pp. 249–275.

Paim, P.S.G., Chemale Jr., F., Lopes, R.C., 2000. A Bacia do Camaquã. In: Holz, M., De Ros, L.F. (Eds.), Geologia do Rio Grande do Sul: Centro de Investigação do Gondwana. Universidade Federal do Rio Grande do Sul, Porto Alegre, Brazil, pp. 231–274.

Patchett, P.J., Tatsumoto, M., 1980. A routine high-precision method for Lu-Hf isotope geochemistry and chronology. Contribution to Mineralogy and Petrology 75, 263–267.

Patchett, P.J., Kuovo, O., Hedge, C.E., Tatsumoto, M., 1981. Evolution of the continental crust and mantle heterogeneity: evidence from hafnium isotopes. Contribution to Mineralogy and Petrology 78, 279–297.

Pearce, J.A., 1996. A user's guide to basalt discrimination diagrams. Geological Association of Canada Special Publication 12, 79–113.

Pearce, J.A., 2008. Geochemical fingerprinting of oceanic basalts with applications to ophiolite classification and the search for Archean oceanic crust. Lithos 100, 14–48.

Pearce, J.A., 2014. Immobile element fingerprinting of ophiolites. Elements 10, 101–108.

Pedersen, R.B., Searle, M.P., Carter, A., Bandopadhyay, P.C., 2010. U–Pb zircon age of the Andaman ophiolite: implications for the beginning of subduction beneath the Andaman–Sumatra arc. Journal of the Geological Society 167, 1105–1112.

Pertille, J., Hartmann, L.A., Philipp, R.P., Petry, T.S., Lana, C.C., 2015. Origin of the Ediacaran Porongos group, Dom Feliciano Belt, southern Brazilian Shield, with emphasis on whole rock and detrital zircon geochemistry and U-Pb, Lu-Hf isotopes. Journal of South American Earth Sciences 64, 69–93.

Pertille, J., Hartmann, L.A., Santos, J.O.S., McNaughton, N.J., Armstrong, R., 2017. Reconstructing the Cryogenian-Ediacaran evolution of the Porongos fold and thrust belt, Southern Brasiliano orogen, based on zircon U-Pb-Hf-O isotopes. International Geology Review http://dx.doi.org/10.1080/00206814.2017.1285257.

Petersson, M.A., 2010. Zircon U-Pb, Hf and O Isotope Constraints on the Growth Versus Recycling of Continental Crust in the Grenville Orogen, Ohio, USA. Master thesis. Lund University.

Philipp, R.P., Machado, R., 2005. The Late Neoproterozoic granitoid magmatism of the Pelotas Batholith, southern Brazil. Journal of South American Earth Sciences 19, 461–478.

Philipp, R.P., Hartmann, L.A., Lusa, M., Basei, M.A.S., Santos, J.O.S., 2014. Oldest age of magmatism in the Passinho Arc in the southwestern portion of Gondwana, Rio Grande do Sul, Brazil. Proceedings of the South American Symposium on Isotope Geology 9th, São Paulo, Brazil, p. 186.

Philipp, R.P., Pimentel, M.M., Chemale Jr., F., 2016. Tectonic evolution of the Dom Feliciano Belt in Southern Brazil: geological relationships and U-Pb geochronology. Brazilian Journal of Geology 46, 83–104.

Pimentel, M.M., Fuck, R.A., 1992. Neoproterozoic crustal accretion in central Brazil. Geology 203, 375–379.

Pimentel, M.M., Fuck, R.A., Gioia, S.M.C.L., 2000. The Neoproterozoic Goiás magmatic arc, Central Brazil: a review and new Sm-Nd isotopic data. Brazilian Journal of Geology 30, 35–39.

Pirajno, F., Santosh, M., 2015. Mantle plumes, supercontinents, intracontinental riftingand mineral systems. Precambrian Research 259, 243–261.

Portner, R.A., Daczko, N.R., Murphy, M.J., Pearson, N.J., 2011. Enriching mantle melts within a dying mid-ocean spreading ridge: Insights from Hf-isotope and trace element patterns in detrital oceanic zircon. Lithos 126, 355–368.

Queiroga, G.N., Pedrosa-Soares, A.C., Noce, C.M., Alkmim, F.F., Pimentel, M.M., Dantas, E., Martins, M., Castañeda, C., Suita, M.T.F., Prichard, F., 2007. Age of the Ribeirão da Folha ophiolite, Araçuaí Orogen: the U-Pb zircon dating of a plagiogranite. Geonomos 15, 61–65.

Ramos, V.A., Escayola, M., Mutti, D.I., Vujovich, G.I., 2010. Proterozoic-early Paleozoic ophiolites of the Andean basement of southern South America. Geological Society of America Special Papers 349, 331–349.

Rapela, C.W., Pankhurst, R.J., Casquet, C., Fanning, C.M., Baldo, E.G., González-Casado, J.M., Galindo, C., Dahlquist, J., 2007. The Río de la Plata craton and the assembly of SW Gondwana. Earth-Science Reviews 8, 49–82.

Rapela, C.W., Fanning, C.M., Casquet, C., Pankhurst, R.J., Spalletti, L., Poiré, D., Baldo, E.G., 2011. The Rio de la Plata craton and the adjoining Pan-African/brasiliano terranes: their origins and incorporation into south-west Gondwana. Gondwana Research 20, 673–690.

Remus, M.V.D., Hartmann, L.A., Formoso, M.L.L., 1993. Os Padrões de Elementos Terras Raras (ETR) e afinidade geoquímica komatiítica dos xistos magnesianos e rochas associadas do Complexo Cambaizinho, São Gabriel-RS. Revista Brasileira de Geociências 23, 370–387.

Remus, M.V.D., McNaughton, N.J., Hartmann, L.A., Koppe, J.C., Fletcher, I.R., Groves, D.I., Pinto, V.M., 1999. Gold in the Neoproterozoic juvenile Bossoroca Volcanic Arc of Southernmost Brazil: isotopic constraits on timing and sources. Journal of South American Earth Sciences 12, 349–366.

Remus, M.V.D., Hartmann, L.A., Mcnaughton, N.J., Groves, D.I., Fletcher, I.R., 2000. The link between hydrothermal epigenetic copper mineralization and the Caçapava Granite of the Brasiliano Cycle in southern Brazil. Journal of South American Earth Sciences 13, 191–216.

Rioux, M., Bowring, S., Keleme, P., Gordon, S., Miller, R., Dudás, F., 2013. Tectonic development of the Semail ophiolite: high-precision U-Pb zircon geochronology and Sm-Nd isotopic constraints on crustal growth and emplacement. Journal of Geophysical Research: Solid Earth 118, 2085–2101.

Saalmann, K., Hartmann, L.A., Remus, M.V.D., Koester, E., Conceição, R.V., 2005a. Sm–Nd isotope geochemistry of metamorphic volcano-sedimentary successions in the São Gabriel Block, southernmost Brazil: evidence for the existence of juvenile Neoproterozoic oceanic crust to the east of the Rio de la Plata craton. Precambrian Research 136, 159–175.

Saalmann, K., Remus, M.V.D., Hartmann, L.A., 2005b. Geochemistry and crustal evolution of volcano-sedimentary successions and orthogneisses in the São Gabriel block, Southernmost Brazil - relics of Neoproterozoic magmatic arcs. Gondwana Research 8, 143–161.

Saalmann, K., Remus, M.V.D., Hartmann, L.A., 2006. Tectonic evolution of the Neoproterozoic São Gabriel block, southern Brazil: constraints on Brasiliano orogenic evolution of the Rio de la Plata cratonic margin. Journal of South American Earth Sciences 21, 204–227.

Saccocia, P.J., Ding, K., Berndt, M.E., Seewald, J.S., Seyfried Jr., W.E., 1994. Experimental and theoretical perspectives on crustal alteration at mid-ocean ridges. In: Lentz, D.R. (Ed.), Alteration and Alteration Processes Associated With Ore-forming Systems Geological Association of Canada. Waterloo, Canada, Short Course Notes Vol. 11, pp. 403–431.

Samson, S.D., Inglis, J.D., D'Lemos, R.S., Admou, H., Blichert-Toft, J., Hefferan, K., 2004. Geochronological, geochemical, and Nd–Hf isotopic constraints on the origin of Neoproterozoic plagiogranites in the Tasriwine ophiolite, Anti-Atlas orogen, Morocco. Precambrian Research 135, 133–147.

Santos, M.M., Lana, C., Scholz, R., Buick, I., Schmitz, M.D., Kamo, S.L., Gerdes, A., Corfu, F., Tapster, S., Lancaster, P., Storey, C.D., Basei, M.A.S., Tohver, E., Alkmim, A., Nalini, H., Krambrock, K., Fantini, C., Wiedenbeck, M., 2017. A New Appraisal of Sri Lankan BB Zircon as a Reference Material for LA-ICP-MS U-Pb Geochronology and Lu-Hf Isotope Tracing. Geostandards and Geoanalytical Research http://dx.doi.org/10.1111/ggr.12167.

Schaltegger, U., 2007. Hydrothermal zircon. Elements 3, 51–79.

Schaltegger, U., Desmurs, L., Manatschal, G., Müntener, O., Meier, M., Frank, M., Bernoulli, D., 2002. The transition from rifting to sea-floor spreading within a magma-poor rifted margin: field and isotopic constraints. Terra Nova 14, 156–162.

Scherer, E.E., Münker, C., Mezger, K., 2001. Calibration of the lutetium-hafnium clock. Science 293, 683–687.

Schmitt, R.S., Trouw, R.A.J., Van Schmus, W.R., Pimentel, M.M., 2004. Late amalgamation in the central part of Western Gondwana: new geochronological data and the characterization of a Cambrian collision orogeny in the Ribeira Belt (SE Brazil). Precambrian Research 133, 29–61.

Schmitt, R.S., Trouw, R.A.J., Medeiros, S.R., Dantas, E.L., 2008. Age and geotectonic setting of Late Neoproterozoic juvenile mafic gneisses and associated paragneisses from the Ribeira belt (SE Brazil) based on geochemistry and Sm–Nd data—implications on Gondwana assembly. Gondwana Research 13, 502–515.

Shervais, J.W., 1982. Ti–V plots and the petrogenesis of modern and ophiolitic lavas. Earth and Planetary Science Letters 59, 101–118.

Stern, R.J., Johanson, P.R., Kroner, A., Yibas, B., 2004. Neoproterozoic ophiolites of the Arabian-Nubian Shield. In: Kusky, T.M. (Ed.), Precambrian Ophiolites and Related Rocks. 13. Elsevier, Amsterdam, pp. 95–128.

Suita, M.T.F., Pedrosa-Soares, A.C., Leite, C.A.S., Nilson, A.A., Prichard, H.M., 2004. Complexos ofiolíticos do Brasil e a metalogenia comparada das faixas araçuaí e brasília. In: Pereira, E.S., Castroviejo, R., Ortiz, F. (Eds.), Complejos ofiolíticos em Ibero América: Edita Proyecto XIII.1, Madrid-España. 379, pp. 101–132.

Sun, S.S., McDonough, W.F., 1989. Chemical and isotopic systematics of oceanic basalts: implications for mantle composition and processes. In: Saunders, A.D., Norry, M. (Eds.), Magmatism in Ocean Basins, Geological Society of London Special Publication. 42, pp. 313–345.

Takenaka, L.B., Lana, C., Scholz, R., Nalini Jr., H.A., Abreu, A.T., 2015. Optimization of the in-situ U-Pb age dating method via LA-Quadrupole-ICP-MS with applications to the timing of U-Zr-Mo mineralization in the Poços de Caldas Alkaline Complex, SE Brazil. Journal of South America Earth Sciences 62, 70–79.

Taylor, S.R., McLennan, S.M., 1985. The Continental Crust: Its Composition and Evolution. Blackwell Scientific Publication, Carlton, p. 312.

Unrug, R., 1995. Rodinia and Gondwana: a record of supercontinent configuration change. In: Yoshida, M., Santosh, M. (Eds.), India and Antarctica during the Precambrian. Geological Society of India Memoir Vol. 34, pp. 1–9.

Unrug, R., 1997. Rodinia to Gondwana: the geodynamic map of Gondwana Supercontinent Assembly. GSA Today 7, 1–6.

Van Achterbergh, E., Ryan, C.G., Jackson, S.E., Griffin, W.L., 2001. Data reduction software for LA–ICP–MS. In: Sylvester, P.J. (Ed.), Laser Ablation-ICP Mass Spectrometry in the Earth Sciences: Principles and Applications. Mineralogical Association of Canada, Short Course, Ottawa, Ontario Vol. 29, pp. 239–243.

Wedepohl, K.H., 1995. The compositions of the continental crust. Geochimica et Cosmochimica Acta 59, 1217–1232.

Xia, L.Q., Xia, Z.C., Xu, X.Y., Li, X.M., Ma, Z.P., 2012. Mid-late proterozoic rift-relatedvolcanic rocks in China: geological records of rifting and break-up of Rodinia. Geoscience Frontiers 3, 375–399.

Zhao, J.X., Malcolm, M.T., Korsch, R.J., 1994. Characterisation of a plume-related ~800 Ma magmatic event and its implications for basin formation in central-southern Australia. Earth and Planetary Science Letters 121, 349–367.

Zheng, Y.F., Wu, Y.B., Zhao, Z.F., Zhang, S.B., Xu, P., Wu, F.Y., 2005. Metamorphic effect on zircon Lu–Hf and U–Pb isotope systems in ultrahigh-pressure eclogite-facies metagranite and metabasite. Earth and Planetary Science Letters 240, 378–400.

Zhiwei, B., Qiang, W., Guodian, B., Zhenhua, Z., 2009. Impact of hydrothermal alteration on the U-Pb isotopic system of zircons from the Fangcheng syenites in the Qinling orogen, Henan Province. Chinese Journal of Geochemistry 28, 163–171.

International Geology Review

ISSN: 0020-6814 (Print) 1938-2839 (Online) Journal homepage: http://www.tandfonline.com/loi/tigr20

U–Pb–Hf isotopes and trace elements of metasomatic zircon delimit the evolution of neoproterozoic Capané ophiolite in the southern Brasiliano Orogen

Karine R. Arena, Léo A. Hartmann & Cristiano Lana

To cite this article: Karine R. Arena, Léo A. Hartmann & Cristiano Lana (2017): U–Pb–Hf isotopes and trace elements of metasomatic zircon delimit the evolution of neoproterozoic Capané ophiolite in the southern Brasiliano Orogen, International Geology Review, DOI: 10.1080/00206814.2017.1355269

To link to this article: http://dx.doi.org/10.1080/00206814.2017.1355269

INTERNATIONAL GEOLOGY REVIEW, 2017
https://doi.org/10.1080/00206814.2017.1355269

Taylor & Francis
Taylor & Francis Group

U–Pb–Hf isotopes and trace elements of metasomatic zircon delimit the evolution of neoproterozoic Capané ophiolite in the southern Brasiliano Orogen

Karine R. Arena[a], Léo A. Hartmann[a] and Cristiano Lana[b]

[a]Instituto de Geociências, Universida de Federal do Rio Grande do Sul, Porto Alegre, Brazil; [b]Departamento de Geologia, Escola de Minas, Universidade Federal de Ouro Preto, Ouro Preto, Brazil

ABSTRACT
The Capané ophiolite is a fragment of oceanic lithosphere obducted into the Ediacaran Porongos fold and thrust belt, southern Brasiliano Orogen. A studied rodingite blackwall contained in serpentinite has metasomatic zircon that displays multiple U–Pb ages from Tonian to Cryogenian (793 ± 0.9, 757 ± 2.1, 715 ± 2.2 Ma). The ages are interpreted as corresponding to multiple alteration events in the mantle. Multiple U–Pb–Hf isotopes and trace element analyses on the same crystals by laser ablation were controlled by backscatered electron images. Hf isotopes indicate zircon origin from a depleted mantle (εHf = +15 to +10.7), and trace elements point to an oceanic origin. The Capané ophiolite thus marks the evolution of the Adamastor ocean during the Tonian and Cryogenian, a significant result for the reconstruction of Rodinia and Gondwana supercontinents.

ARTICLE HISTORY
Received 25 January 2017
Accepted 11 July 2017

KEYWORDS
Capané ophiolite;
zircon U–Pb–Hf isotopes;
zircon trace elements;
Tonian; ocean closure

1. Introduction

Ophiolites are common in juvenile terranes accreted to the continents, both in the Phanerozoic (e.g. northern California – Shervais *et al*. 2004) and in the Tonian (e.g. Fuchuan ophiolite, China – Zhang *et al*. 2012; Bi'r Umq-Nakasib ophiolite belt, Arabian-Nubian Shield – Johnson *et al*. 2003; Cerro Mantiqueiras and Ibaré ophiolites, São Gabriel terrane – Arena *et al*. 2016, 2017). Slabs of oceanic lithosphere are also found in Phanerozoic fold and thrust belts (e.g. Kermanshah ophiolite in the Zagros belt – Navabpour *et al*. 2014; Ajirlu *et al*. 2016) but this overall rock association is poorly known in Precambrian orogens.

Zircon can be either present or newly formed in metasomatites during serpentinization, leading to the direct dating of the alteration process close to the incorporation of the serpentinite into the oceanic crust or later during its incorporation into continental crust (Dubińska and Wiewióra 1999; Arena *et al*. 2017; references therein). The study of rodingites helps determining the crystallization age of zircon and therefore of magma genesis in the oceanic crust. Rodingite is a common metasomatic rock in serpentinized oceanic lithosphere (Klein 2009) and has been found in a range of tectonic settings, including seafloor spreading centers (Bach and Klein 2009) and ophiolites (Barriga and Fyfe 1983; Austrheim and Prestvik 2008) besides subduction zone (Li *et al*. 2007). In general, unless tectonically displaced, rodingite is enveloped by chlorite or, less commonly, an amphibole-rich shell labeled as blackwall (Frost 1975). Rodingites are altered, calcium-enriched, country rocks that are in contact with altered peridotites; protoliths include basalt, gabbro, mafic cumulates, volcanic rocks, granitic rocks, serpentinites, or sediments (Frost 1975; Dubińska *et al*. 2004; references therein). Rodingites are formed by the migration of calcium carried in serpentinizing fluids from peridotite into country rock (Dubińska *et al*. 2004; Evans *et al*. 2013). Zircon from rodingite blackwall has therefore the potential to yield the age of oceanic crust.

The Neoproterozoic-Cambrian Brasiliano Orogen is a major geotectonic feature of South America and has many detrital schist belts associated with granitic plutons and batholiths, and minor foreland basins. In the southern portion of the Dom Feliciano Belt, the orogenic triad 'granitic core-fold and thrust belt-foreland basin' has been characterized by Pertille *et al*. (2015a, 2017). The triad includes mostly the Pelotas Batholith-Porongos Group-Camaquã Basin.

Serpentinites occur along the Porongos fold and thrust belt as small (100–500 m) disrupted fragments

CONTACT Karine R. Arena karinearena@gmail.com Instituto de Geociências, Universida de Federal do Rio Grande do Sul, Avenida Bento Gonçalves, 9500, Porto Alegre, Rio Grande do Sul 91501-970, Brazil.
Supplemental data for this article can be accessed here.

and are interpreted as the mantle section of an ophiolite. The intense low-grade metamorphic alteration of the rocks precludes decisive geochemical characterization of the ophiolite. The geotectonic significance of the presence of ophiolites in the Neoproterozoic fold and thrust belt led us to select the Capané ophiolite for a U–Pb–Hf isotope and trace element study of metasomatic zircon from a rodingite blackwall. Multiple spots were analysed in the same crystal, guided by backscattered electron images.

The obtained zircon ages are Tonian and Cryogenian (793, 757, 715 Ma) and the zircon is related to melt batches originated in the depleted mantle. Trace elements of zircon indicate oceanic affinity. This is the first characterization of an ophiolite inserted tectonically in a fold and thrust belt of the Brasiliano Orogen.

2. Geological characterization

The Brasiliano Orogen extends for 4000 km from northeastern Brazil to southern Uruguay and approximately 1000 km between the Atlantic Ocean coast to central Brazil. The Dom Feliciano Belt (Figure 1(a,b)) is a local designation of the orogen in the southern portion (Hartmann *et al.* 2000) and comprises four different units, aside from the basement Rio de la Plata Craton. The São Gabriel terrane (923–650 Ma) has Neoproterozoic juvenile characteristics (Babinski *et al.* 1996; Leite *et al.* 1998;

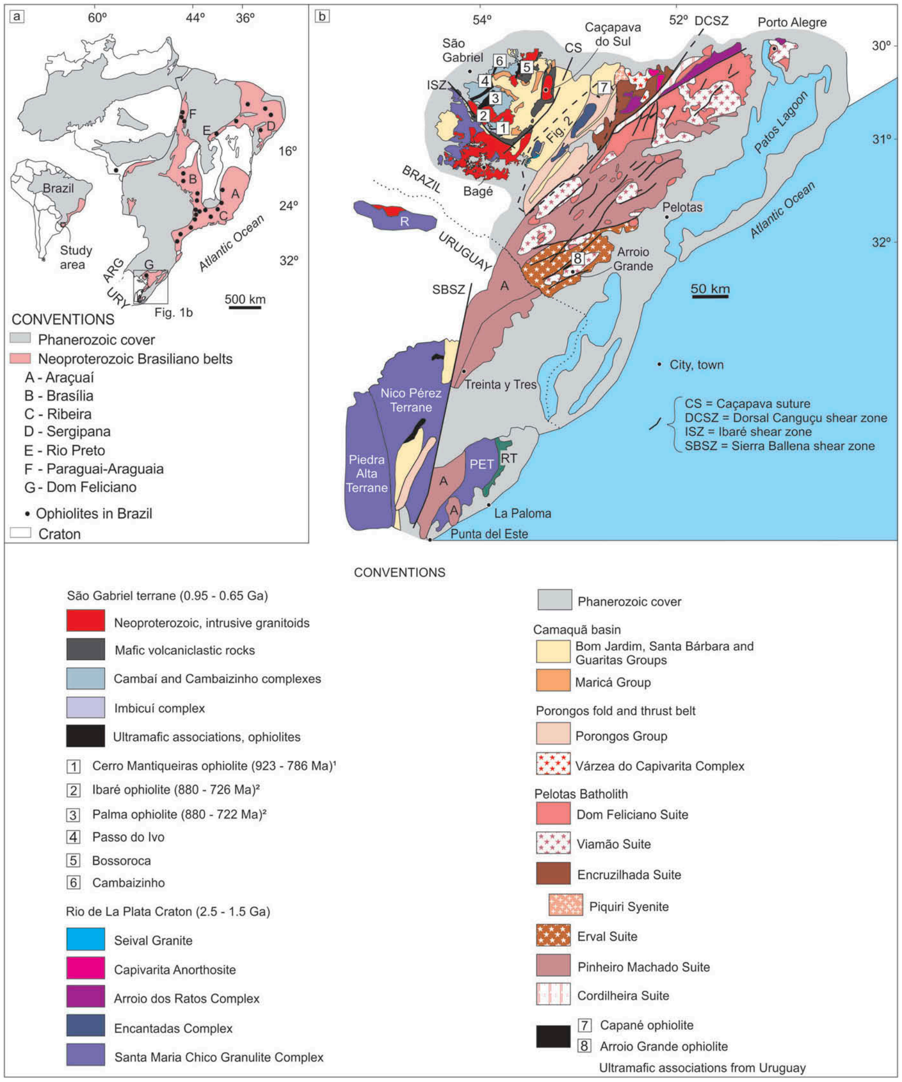

Figure 1. (a) Geological map of Brazil showing the distribution of Neoproterozoic ophiolitic rocks in the Brasiliano Orogen (after Suita *et al.* 2004). ARG = Argentina, URY = Uruguay; (b) geological map of the Precambrian-Cambrian Sul-Riograndense Shield (Dom Feliciano Belt and basement) southern Brazil (after Chemale 2000; Hartmann et al. 2007; Laux et al. 2012; Camozzato et al. 2014; Pertille et al. 2015a; [1]Arena et al. 2016, [2]2017; Philipp et al. 2016b) and part of Uruguay (Rapela et al. 2011). R = Riveira; PET = Punta del Este terrane; RT = Rocha terrane; A = Aiguá, undifferentiated granite belt (660–540 Ma).

Saalmann *et al*. 2005a, 2005b; Hartmann *et al*. 2011; Lena *et al*. 2014; Arena *et al*. 2016), whereas the granitic rocks of the Pelotas Batholith correspond to a crustally-reworked unit (Fragoso-César *et al*. 1986; Philipp and Machado 2005). The schists and gneisses of the Porongos fold and thrust belt are dominated by deformed sedimentary rocks but the belt also includes quartzites and ultramafic lenses (e.g. Saalmann *et al*. 2006; Pertille *et al*. 2017) and the Camaquã foreland Basin (Paim *et al*. 2000; Pertille *et al*. 2015a) as the least deformed unit. The integration of the São Gabriel terrane with the Porongos fold and thrust belt (Pertille *et al*. 2017) as part of Dom Feliciano belt was proposed by Fernandes *et al*. (1995b). Both regions are delimited by the Caçapava suture (Chemale 2000 and references therein) (Figure 1(b)).

The Neoproterozoic Dom Feliciano Belt trends NE–SW and is 1200 km long and up to 150 km wide. The belt is parallel to the Atlantic coast, from its northern limit in Santa Catarina state in Brazil to its southern extension in Uruguay. It is a remnant of the much wider orogen present in Gondwana before rupture of the supercontinent. The origin is related to the convergence and the subsequent final collision between the Rio de la Plata and Kalahari Cratons (e.g. Fernandes *et al*. 1992, 1995a, 1995b; Babinski *et al*. 1997; Leite *et al*. 1998; Silva *et al*. 1999; Chemale 2000; Basei *et al*. 2005; Hartmann *et al*. 2007; Lenz *et al*. 2011). The orogeny produced intense magmatic activity in the Tonian to Cambrian. Tonian accretionary processes in this belt are recorded in the São Gabriel terrane (923–892 Ma, Arena *et al*. 2016, 2017; 880–722 Ma), and in the Porongos fold and thrust belt (789 Ma, Saalmann *et al*. 2011, 790 Ma, Martil *et al*. 2017). In the eastern portion of the Dom Feliciano Belt, the Piratini Gneiss includes all locally named Tonian units, e.g. Chácara das Pedras (777 ± 4 Ma; Koester *et al*. 2016), Cerro Bori Orthogneiss (802–767 Ma, Lenz *et al*. 2011), Várzea do Capivarita Complex (790 Ma, Martil *et al*. 2017) and the Piratini Gneiss in the type locality (781 ± 5 Ma, Silva *et al*. 1999).

In the southeastern portion of the Dom Feliciano Belt, the Arroio Grande ophiolite (Figure 1(b)) is immersed in the granitoids of the Pinheiro Machado Complex, Pelotas Batholith (Ramos and Koester 2015). Additionally, the La Tuna ophiolite from Uruguay (Peel *et al*. 2009) may be part of a larger ophiolite belt (Ramos and Koester 2014). A granitic rock in the Arroio Grande region (Vieira *et al*. 2016) displays a crystallization age of 680 ± 2.9 Ma and 660 ± 2.8 for zircon rims. The Hf model ages vary from 1.8 to 1.9 Ma and εHf from −15.16 to −14.66.

The Pelotas Batholith is composed of five main granitic suites, namely pre-collisional Cordilheira, syn-collisional Pinheiro Machado and post-collisional Herval, Viamão and Dom Feliciano suites (Figure 1(b)). The magmatic and tectonic evolution of the Pelotas Batholith occurred between 650 and 550 Ma (Babinski *et al*. 1997; Basei *et al*. 2005; Silva *et al*. 2005; Philipp *et al*. 2013). This continental collision (650–600) was denominated Dom Feliciano event by Babinski *et al*. (1997). Sr and Nd isotopic data suggest reworking of Palaeoproterozoic continental crust (Philipp *et al*. 2016b and references therein). The filling of the palaeo-Porongos basin occurred at 650–570 Ma, coeval with the formation of the Pelotas Batholith. The maximum depositional age of the youngest portions of the Porongos basin in the Capané region is 570 Ma (Pertille *et al*. 2015a).

The Porongos Group (Figure 2) is the major component of a fold and thrust belt located in the central portion of the Dom Feliciano Belt in the Sul-Riograndense Shield. The group was established as part of a foreland basin of Ediacaran age (Pertille *et al*. 2015a, 2017) and comprises metasedimentary rocks (metapelite, schist, and thin quartzite layers). The lithotypes include quartzite and felsic to intermediate metavolcanic rocks with subordinate intercalations of marble, graphite schist, meta-arkose and metaconglomerate, as well as lenses of ultramafic rocks such as serpentinite, talc schist and chlorite schist (Jost and Bitencourt 1980; Porcher and Fernandes 1990; Remus *et al*. 1991; Marques *et al*. 2003; Gollmann *et al*. 2008) that belong to the Porongos fold and thrust belt (Pertille *et al*. 2017). The group was affected by metamorphism in the chlorite to staurolite zone (greenschist to low amphibolite facies) (Jost 1982). The supracrustal sequence of the Porongos belt overlies the basement of the Encantadas Complex including quartzites of Santana Formation (Hartmann *et al*. 2004; Pertille *et al*. 2015b). Regional-scale folding of the Porongos Group generated four antiforms (Jost and Bitencourt 1980), named from north to south Capané (10 × 20 km), Serra dos Pedrosas (5 × 30 km), Santana da Boa Vista (7 × 20 km), and Godinho (3 × 4 km).

The Capané antiform (Figure 2) is in the northern portion of the Porongos Group and is composed of detrital schist with lenses of serpentinite, magnesian schist, talc schist and some chloritite, rodingite and podiform chromitite (Jost and Hartmann 1979; Marques *et al*. 2003). The 500 × 100 m-large slices of Capané ophiolite occur imbricated in the Porongos Group.

2.1. *Sample description*

The CP3 rodingite blackwall is a block (20 × 40 cm) in direct contact with serpentinite, close to talc schist. A marble quarry is located approximately 400 m from CP3

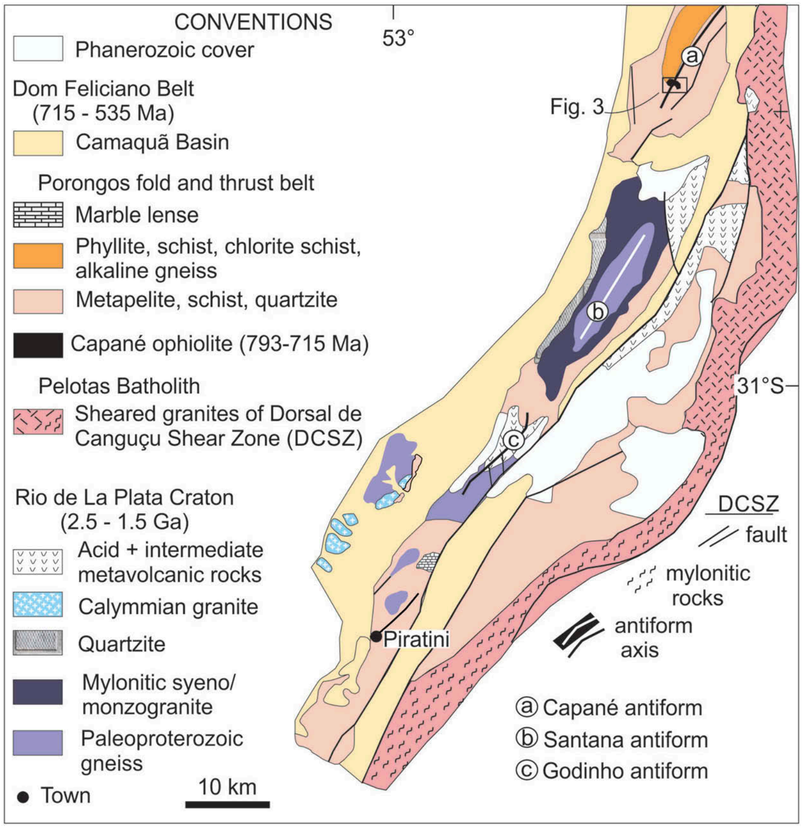

Figure 2. Geological map of Porongos Belt (after Chemale 2000; Hartmann *et al.* 2004; Pertille et al. 2017).

(Figure 3(a,b)). Serpentinite is only present in one side of the loose block (Figure 3(c)).

CP3 blackwall rodingite consists of clinochlore in the matrix and also well-formed crystals (Supplementary Table 1; Figure 4(a–g)) associated with abundant magnetite, ilmenite and a large number of zircon crystals (up to 0.1 mm in size) (Figure 4(a,b)). Lesser amounts of apatite and rutile also occur. Euhedral to subhedral crystals (Figure 5(a–c)) of calcium silicate compositions rich in Al_2O_3 and FeO (Figure 5(d–o)) represent coarse-grained clasts, composed of vesuvianite e.g. possibly allanite-Ce ($CaCeAl_2Fe_2 + (Si_2O_7) (SiO_4) O (OH)$) and Mg-vesuvianite.

3. Material and methods

Field study in the Capané ophiolite resulted in the discovery of the studied block of rodingite blackwall. Petrography of the CP3 sample preceded the determination of chemical and isotopic compositions of zircon crystals. Petrography was done with a transmission petrographic microscope Olympus BX51, UC30. One polished thin section of the sample was studied with scanning electron microscope at Laboratório de Geologia Isotópica, Universidade Federal do Rio Grande do Sul. Chemical compositions of chlorite from the sample were obtained using a Cameca SXFive electron microprobe at Laboratório de Microssonda Eletrônica, Universidade Federal do Rio Grande do Sul, with accelerating voltage at 15 kV, beam current 15 nA and beam size 5 µm. The minerals were analysed on the basis of chlorite = 28O; the H_2O content was calculated by stoichiometry with Excel spread sheet.

Whole-rock chemical analyses were performed in the Bureau Veritas Laboratory (Vancouver, Canada) with the methods of Group LF300 and LF100. Two samples were analysed (Supplementary Table 2), one serpentinite (CP1 sample) and one rodingite blackwall (CP3 sample). The analyses were used for geochemical characterization and tectonic setting interpretation (Figure 6) of the ophiolite. Sample locations are indicated in Figure 3.

Zircon compositions were determined by LA-ICP-MS, adding to 131 zircon U–Pb isotopic analyses, 79 concordant (out of 131 total) Lu–Hf isotopic analyses and 76 trace element analyses. All zircon crystals were imaged prior to analysis using backscattered electrons to evaluate zoning patterns and locate mineral inclusions and cracks (Figure 7).

3.1. *Zircon U–Pb dating*

Zircon U–Pb isotopic analyses were undertaken at the Departamento de Geologia, Universidade

Figure 3. (a) Satellite image 3D (Landsat 7) of study area; (b) selected field photographs; (c) rodingite blackwall block with remnants of serpentinite (0.5 cm) on one side, white line dividing serpentinite and rodingite blackwall; (d) CP3 hand sample.

Federal de Ouro Preto, Minas Gerais, Brazil. The analytical technique used a ThermoScientific Element 2 sector field (SF) ICP-MS coupled to a CETAC LSX-213 G2+ laser system. Calibration was performed using the BB9 standard. In addition, GJ-1 (Jackson *et al.* 2004) was analysed. The BB9 standard yielded a mean average age 561 ± 0.83 Ma (2SD, *n* = 27, MSWD = 2.4) and the GJ-1 secondary standard yielded an average age ^{206}U/^{238}Pb 601 ± 1.2 Ma (2SD, *n* = 21, MSWD = 2.5). This is in agreement with the LA-ICP-MS long-term average of BB (562 ± 6 Ma; Santos *et al.* 2017) reference zircon at Universidade Federal de Ouro Preto and with the GJ-1 (602 ± 5 Ma; Horstwood *et al.* 2016). During analyses the laser was set with a spot size of 20 μm, energy of 15%, shot frequency of 10 Hz and shutter delay of 15s. The LA-ICP-MS data were initially reduced on-line using the software Glitter (Van Achterbergh *et al.* 2001) and then exported and corrected for common Pb using an in-house spread sheet. The ages calculated and plotted on concordia diagrams using the IsoplotEx 4 program (Ludwig 2003). Uncertainties given for individual analyses (ratios and ages) are at the 2 sigma level.

3.2. Zircon Lu–Hf isotopic analyses

Hf isotopic measurements used a Thermo-Finnigan Neptune multicollector ICP-MS coupled to a Photon-Machines 193 nm laser system, at Departamento de Geologia, Universidade Federal de Ouro Preto. Data were collected in static mode during 60 s of ablation with a spot size of 50 μm, coinciding with location of previous U–Pb analyses. Nitrogen (~0.080 l/min) was introduced into the Ar sample-carrier gas. Typical signal intensity was ca. 10 V for ^{180}Hf. The isotopes ^{172}Yb, ^{173}Yb, and ^{175}Lu were simultaneously monitored during each analysis step to allow for correction of isobaric interferences of Lu and Yb isotopes on mass 176. The ^{176}Yb and ^{176}Lu were calculated using a ^{176}Yb/^{173}Yb of 0.796218 (Chu *et al.* 2002) and ^{176}Lu/^{175}Lu of 0.02658 (JWG in-house value). The correction for instrumental mass bias utilized an exponential law and a ^{179}Hf/^{177}Hf value of 0.7325 (Patchett

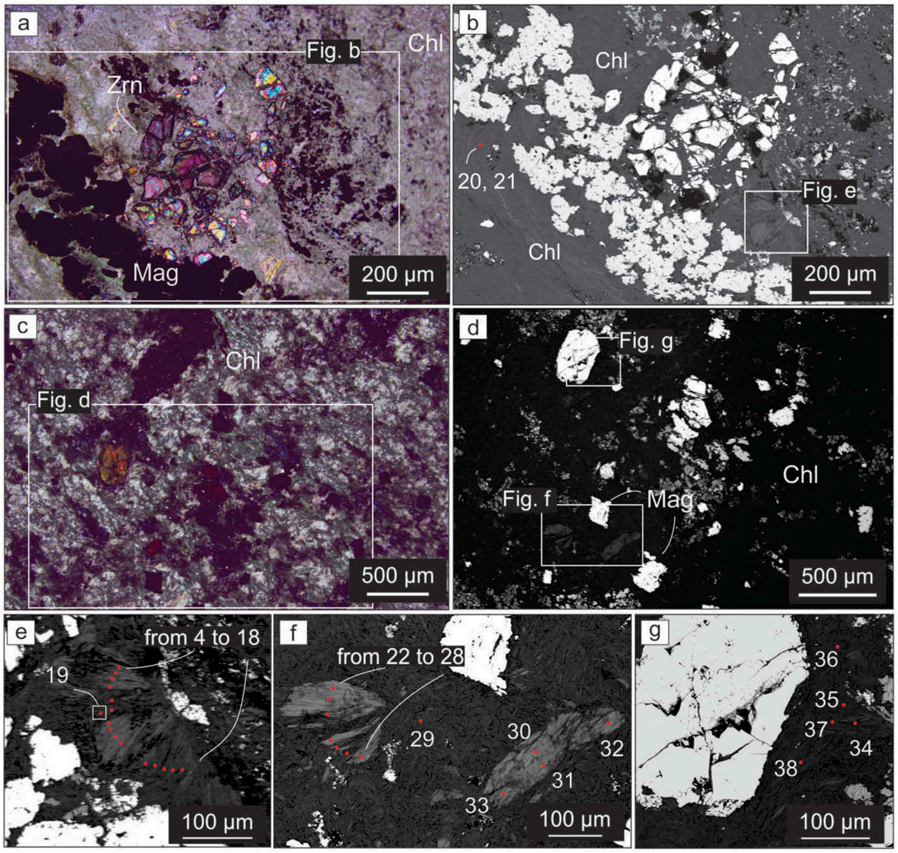

Figure 4. Photomicrographs and backscattered electron images of CP3 sample. (a,b) Zircon in the matrix up to 200 µm; (c,d) euhedral opaque minerals and calcium silicates in chlorite matrix; (e–g) analysed chlorite microprobe points indicated in red (see Supplementary Table 1). Zrn = zircon, Mag = Magnetite, Chl = chlorite.

and Tatsumoto 1981) for correction of Hf isotopic ratios. The mass bias of Yb isotopes generally differs slightly from that of the Hf isotopes with a typical offset of the βHf/βYb of ca. 1.04–1.06 when using the ^{172}Yb/^{173}Yb value of 1.35274 from Chu *et al.* (2002). This offset was determined for each analytical session by averaging the βHf/βYb of multiple analyses of the JMC 475 solution doped with variable Yb amounts and all laser ablation analyses (typically n >50) of zircon with a ^{173}Yb signal intensity of >60 mV. The mass bias behaviour of Lu was assumed to follow that of Yb. The Yb and Lu isotopic ratios were corrected using the βHf of the individual integration steps (n = 60) of each analysis divided by the average offset factor of the complete analytical session. The results were calibrated with the standard zircon Temora, 416 Ma (^{176}Hf/^{177}Hf: 0.282680 ± 0.000031), Mud Tank, 732 Ma (^{176}Hf/^{177}Hf: 0.282504 ± 0.000044) and 91,500, 1065 Ma (176Hf/177Hf: 0.282307 ± 0.000031). Initial epsilon hafnium value εHf(t) was calculated using a decay constant of 1.865 × 10^{-11} year^{-1} (Scherer *et al.* 2001). We used the average MORB (DM) ^{176}Lu/^{177}Lu and ^{176}Hf/^{177}Hf of 0.0384 and 0.283165 respectively, and a value of 0.0113 for the average continental crust (Taylor and McLennan 1985; Wedepohl 1995), ^{176}Lu/^{177}Hf = 0.0336, and ^{176}Hf/^{177}Hf = 0.282785 for CHUR (Bouvier *et al.* 2008).

3.3. Trace element chemistry of zircon

Trace element compositions were obtained from the same crystal analysed for U–Pb isotopes. The zircon chemical composition, particularly rare earth elements and U, was determined with a LA-ICP-MS (a New Wave 213 laser ablation coupled to an Agillent 7700) at Departamento de Geologia, Universidade Federal de Ouro Preto (Takenaka *et al.* 2015). The laser was set to produce spot sizes of 25 µm in diameter, during a period of 30 s at 10 Hz frequency. The data acquisition was done in bracketing mode and consisted of 3–4 analyses of standards (NIST 612 and NIST 610) bracketing 10–15 unknowns. The data reduction was done via the Glitter software (GEMOC Laser ICP- MS Total Trace Element Reduction), (Van Achterbergh *et al.* 2001; Jackson *et al.* 2004). Instrumental mass bias and ablation depth-dependent elemental fractionation were corrected by

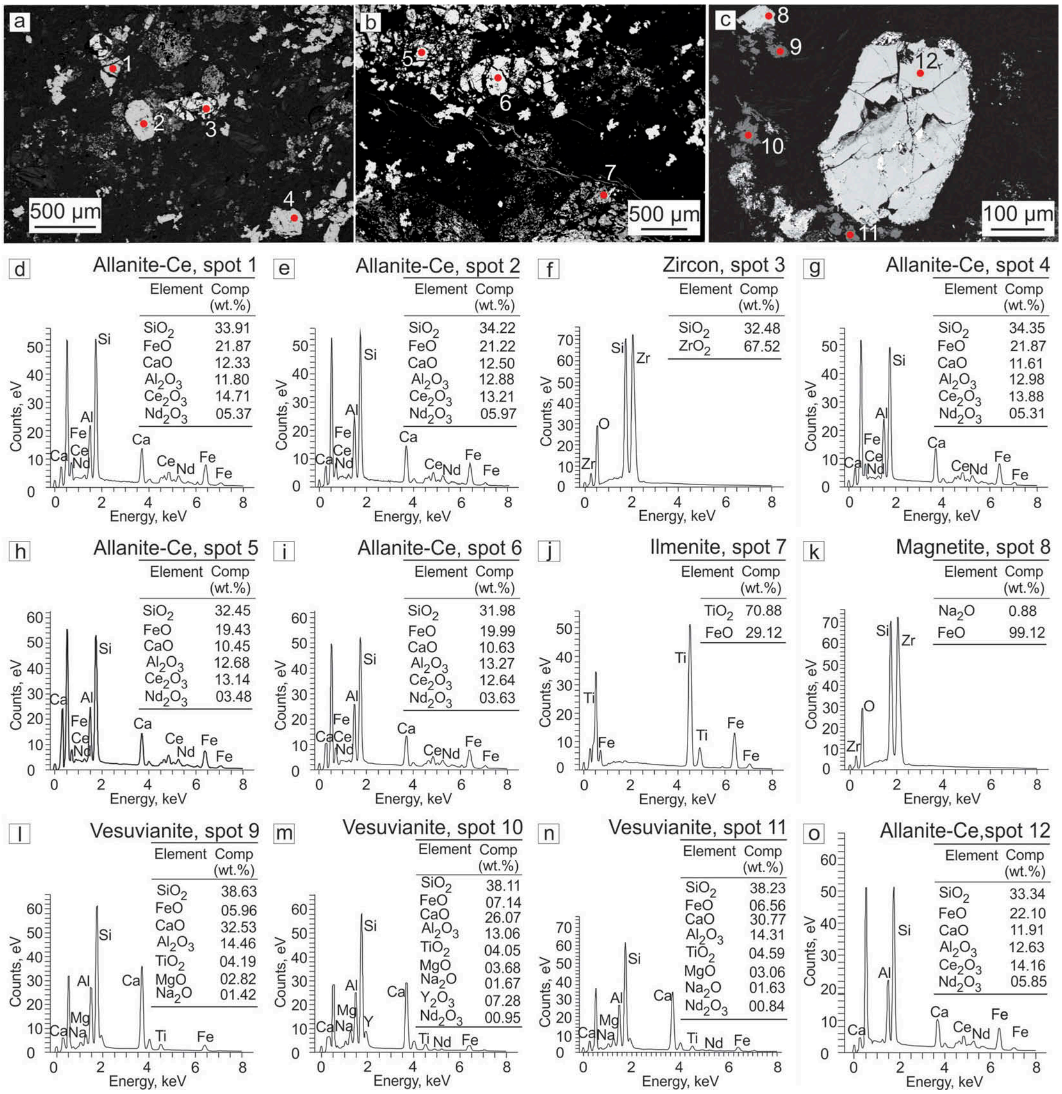

Figure 5. (a–c) Backscattered electron images and (d–o) energy dispersive X-ray spectroscopy (EDS) from CP3 silicates with the characteristic peaks of SiO_2, CaO, Al_2O_3, and others. Analysed points indicated in red.

tying the time-resolved signal for the unknown zircon to the identical integration window of the primary standard NIST612. NIST 610 was used as a secondary control standard. Error was derived from the averaged counts for each mass for both the standards.

4. Results

Whole-rock geochemistry, major and trace element composition of the two samples from selected rocks are used to classify and interpret the tectonic setting of Capané ophiolite. Sample CP3 contains (wt.%) SiO_2 = 25.76, MgO = 17.56, Al_2O_3 = 16.55, Fe_2O_3 = 26.64 and CaO = 0.17 (Supplementary Table 2) classified as rodingite blackwall. The sample is enriched in REE and has pronounced negative Eu anomaly (Figure 6(a)). Sample CP1 (Figure 6(c)) contains SiO_2 = 45.58, MgO = 33.2, and Fe_2O_3 = 5.84. Except for La-enrichment (La = 0.2, Supplementary Table 2), CP1 shows homogeneous distribution of REE such that REE patterns are relatively flat (Figure 6(b)).

Zircon from CP3 was studied to investigate the age, isotopic and geochemical signatures of mantle composition. Most significant results were obtained on zircon from backscattered electron images (*n* = 131), U–Pb (*n* = 131) and Lu–Hf (*n* = 79) isotopic analyses and trace element geochemistry (*n* = 76).

The internal structure of zircon crystals from sample CP3 is homogeneous and shows no zoning (Figure 7(a–o)). A few crystals have xenotime on the rims of zircon (e.g. Figure 8(a,d,e)), high content of Al and Mg (Figure 8(f,h,i)) and also Ca, Fe, Na (Figure 8(h,i)) in some portions. One euhedral KCl (sylvite) inclusion was found inside a zircon crystal (Figure 8(f,g)).

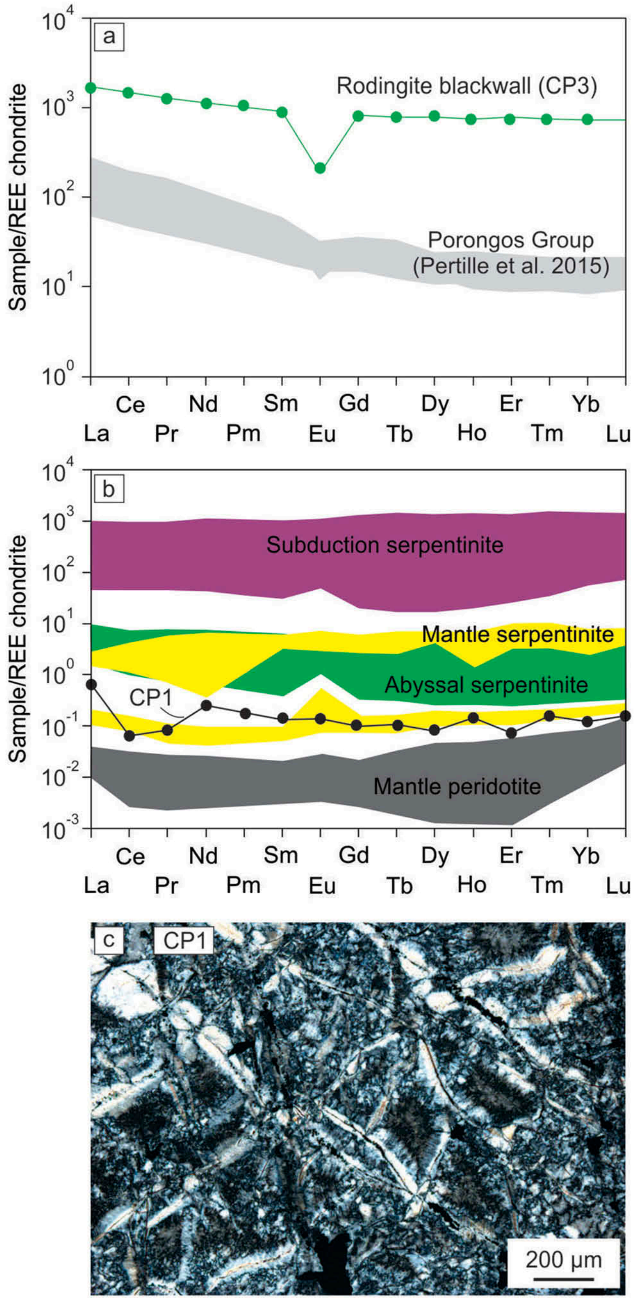

Figure 6. (a) REE compositions of the rodingite blackwall (CP3) and Capané schist and chlorite schist (Pertille *et al.* 2015a); (b) REE compositions of the serpentinite (CP1), subduction serpentinite (De Hoog *et al.* 2009), abyssal serpentinite (Jöns et al. 2010), mantle wedge serpentinite (Deschamps et al. 2010) and mantle peridotite (Marchesi et al. 2009); (c) photomicrograph of serpentinite (CP1). Chondrite-normalized REE patterns by Boynton (1984).

Weighted mean $^{206}Pb/^{238}U$ ages are distributed in the rodingite blackwall in three main groups at 793 ± 0.9, 757 ± 2.1, and 715 ± 2.2 Ma. One oldest grain was dated at 862 ± 6 Ma and other three older zircon grains range in age between 808–802 (Figure 9, Supplementary Table 3).

The isotopic results for Lu–Hf indicate Hf T_{DM} = 0.74–0.91 and positive εHf between +10.7 and +15, characteristic of depleted mantle-derived magmas (Figure 10 (a,b)). The $^{176}Hf/^{177}Hf$ isotopic ratios range from 0.282649 to 0.282748. The Hf-model age data in this study were recalculated according to the current values assumed for the depleted mantle ($^{176}Hf/^{177}Hf = 0.28325$ and $^{176}Lu/^{177}Hf = 0.0388$) by Andersen *et al.* (2009), which we regard as the best estimates for CP3 zircons (see Supplementary Table 4).

Pronounced positive Ce anomaly and negative Eu anomaly are observed in all analysed grains (Figure 11(a)). CP3 zircon is enriched in HREEs and also in Hf (5426–8146 ppm) and Y (494–5692 ppm) (Supplementary Table 5). Plots of trace elements Yb × iU, Nb/Yb × iU/Yb, Y × iU/Yb show distinct fields for zircons crystallized in the ocean and continent (Figure 11(b–d)).

5. Discussion and interpretation

5.1. Geochemical and geological setting

Information obtained on chemical composition by electron microprobe (WDS and EDS) are now integrated with whole-rock geochemistry of samples CP3 and CP1 to classify and interpret the geological environment of Capané ophiolite obduction. In CP3 sample, calcium silicate minerals, rich in Al_2O_3 and FeO, are well preserved (Figure 5) and allow the identification of rodingite extensively altered to chloritic blackwall. The CP3 clinochlore shows large crystals more enriched in Fe than those in the matrix (Supplementary Table 1, Figure 4(e–g)). The MgFe-chlorite (Supplementary Table 1) and Mg-rich vesuvianite (Figure 5(l–n)) possibly reflect increasing Mg/Ca in the fluid phase during formation of rodingite blackwall. In CP3, the altered mineralogy was not preserved and clinochlore is abundant.

Integrated with WDS and EDS (Supplementary Table 1, Figure 5), chemical analyses of CP3 (Supplementary Table 2) show that Mg-enrichment converted extensively the rodingite to chloritite blackwall. Besides, high concentration of Zr in the rodingite blackwall (4836 ppm, Supplementary Table 2) is observed. Zircon crystallization in the blackwall is possibly due to pH decrease during chlorite formation related to fixing of OH which could locally reduce pH of the fluid (Dubińska *et al.* 2004 and references therein).

REE patterns of CP3 display REE-enrichment. REE of schist and chlorite schist (surrounding serpentinite body; Figure 3) of Capané (Pertille *et al.* 2015a) are compared with the rodingite blackwall (Figure 6(a)). Pertille *et al.* (2015a) interpreted the schists as derived

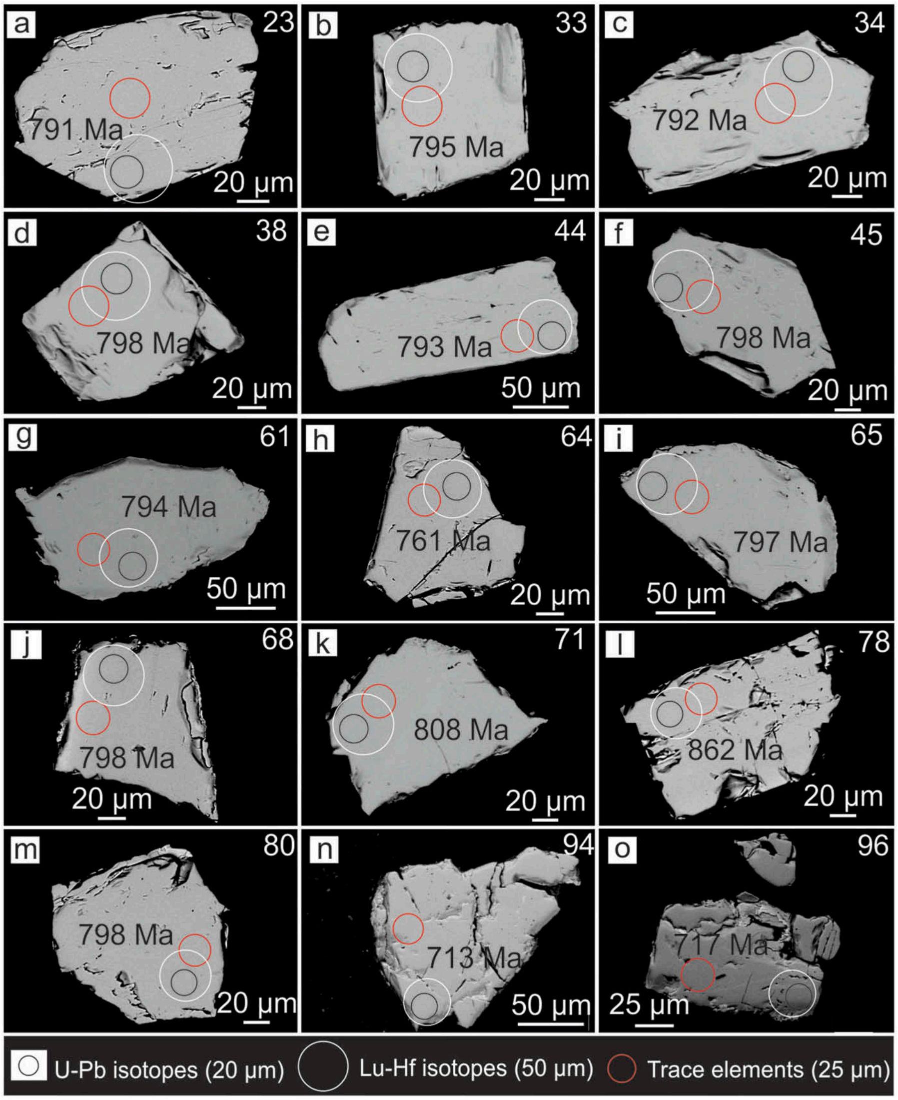

Figure 7. (a–o) Backscattered electron zircon images, CP3 sample. Grain numbers and U–Pb analyses indicated, e.g. 23 and 791 Ma. Black circle = U–Pb ages (Ma); larger white circle = Hf isotopes; red circle = trace elements. Size of each analysis spot indicated.

from Pelotas Batholith and reinforced the interpretation of the Porongos Group as essentially continental.

Additionally, the CaO content of CP3 is similar to the rodingite blackwall (Na18) described by Dubińska *et al.* (2004), but CP3 has lower SiO_2 content and higher Al_2O_3–Fe_2O_3 (Supplementary Table 2) compared to Na18. CP3 is also more enriched in REE than Na18 of Dubińska *et al.* (2004). The differences possibly reflect the protolith rock and geological setting during metasomatism. This leads to the interpretation that the protolith of rodingite CP3 (rodingite blackwall) may have been disrupted during emplacement into the Porongos fold and thrust belt.

Chemical composition of CP1 provides information on the environment in which it was formed. The geodynamic setting in which serpentinites formed has significant influence on rock geochemistry (Deschamps *et al.* 2013). The composition depends of the nature of fluids and temperature. Three groups of serpentinites are distinguished. Subduction zone-related serpentinite (De Hoog *et al.* 2009) is found mostly in suture zones associated with HP–LT metamorphic rocks. Abyssal serpentinites (Jöns *et al.* 2010) represent oceanic peridotites altered by seawater. Mantle wedge serpentinites (Deschamps *et al.* 2010) are mantle peridotites altered by fluids released from the subducted slab.

According to Deschamps *et al.* (2013 and references therein), aqueous fluids in equilibrium with peridotites are enriched in SiO_2 compared to MgO although this point remains controversial. But, additionally, the REE reflect the geochemical signature of the original protolith because these elements are little mobile during serpentinization.

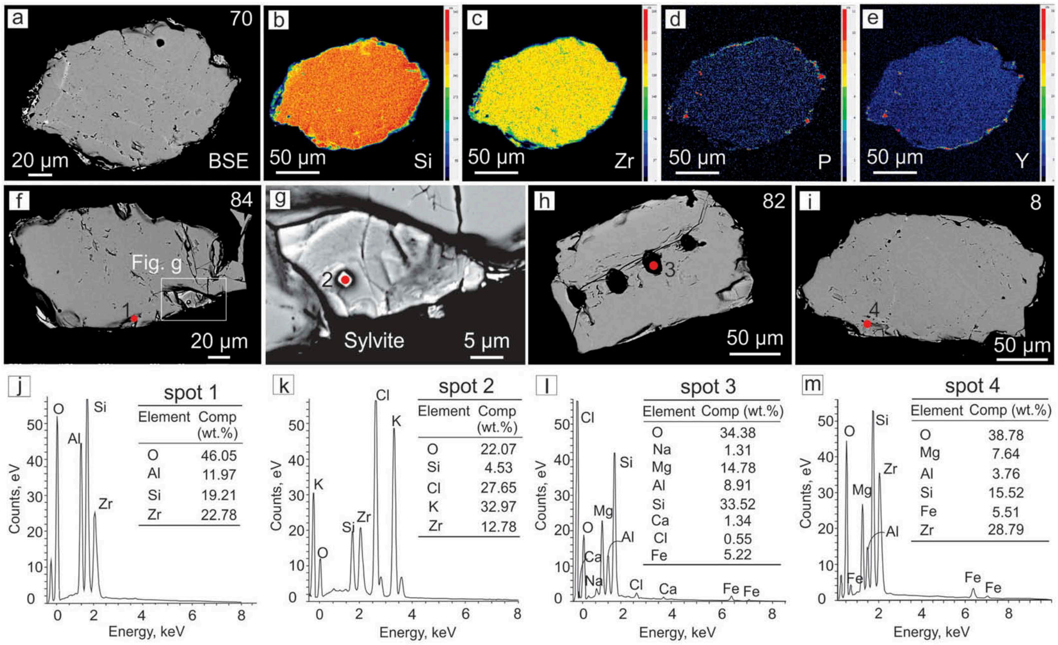

Figure 8. (a–e) Element distribution map, showing P, Y in zircon rim from CP3; (f–i) backscattered electron images; figure grain number indicated, e.g. 70; (j–m) energy dispersive X-ray spectroscopy (EDS) from CP3 zircon inclusion. Analysed points indicated in red.

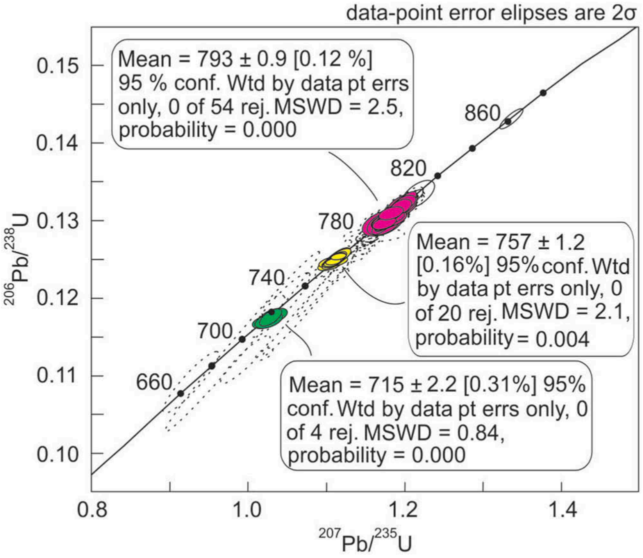

Figure 9. U–Pb isotopic analyses of CP3 zircon in concordia diagram. Dotted line ellipses are not included in the mean ages (discordant data of Pb loss along concordia).

Chondrite-normalized REE (Boynton 1984) of whole-rock compositions of the three groups of serpentinites are shown in Figure 6(b). Serpentinite CP1 displays LREE and HREE in agreement with mantle wedge composition of Deschamps *et al.* (2010) (Figure 6(b)). Our interpretation is based on scant information, so additional studies are required. We prefer to position the ophiolite as depleted mantle in the more general scenario.

5.2. Zircon U–Pb–Hf isotopes and trace elements

The study of zircon from the CP3 rodingite blackwall, using multiple techniques, indicates three main age groups, namely 793 ± 0.9, 757 ± 2.1, and 715 ± 2.2 Ma. The analysed neoproterozoic zircon grains have Hf-model age = 0.91–0.74, corresponding to a rock-section of juvenile signature (εHf = +10.7 to +15). These compositions are coeval with São Gabriel terrane ophiolites (εHf = +8 to +15 and Hf T_{DM} = 1.23–0.75 Ga; Arena *et al.* 2016). Integrated evaluation of U–Pb age and trace elements with the Hf-model age and depleted mantle εHf shows that the zircons evolved from a ~ 793 Ma mantle. This array of data is attributed to three continued pulses of serpentinization. The $^{176}Hf/^{177}Hf$ ratios of all analysed zircons are effectively identical (0.282649–0.282748) (Gerdes and Zeh 2009; Vervoort and Kemp 2016), indicating that zircons from the ophiolite have a single Hf isotopic composition.

The trace element analyses of U and Yb exhibit compatibility in magmatic systems according to Grimes *et al.* (2007, 2009). HREEs (e.g. Yb) as well as Hf and Y concentrations are enriched in MORB relative to continental crust. The REEs are similar to the São Gabriel terrane ophiolites (Figure 11(a)). The affinity of zircon with U, Yb, and other HREEs permits these elements to be incorporated into zircon such that the U/Yb ratios of zircon reflects the chemical environment of crystallization. Additional phases crystallizing with zircon (e.g. xenotime) (Figure 8(a–e)) likely compete for U

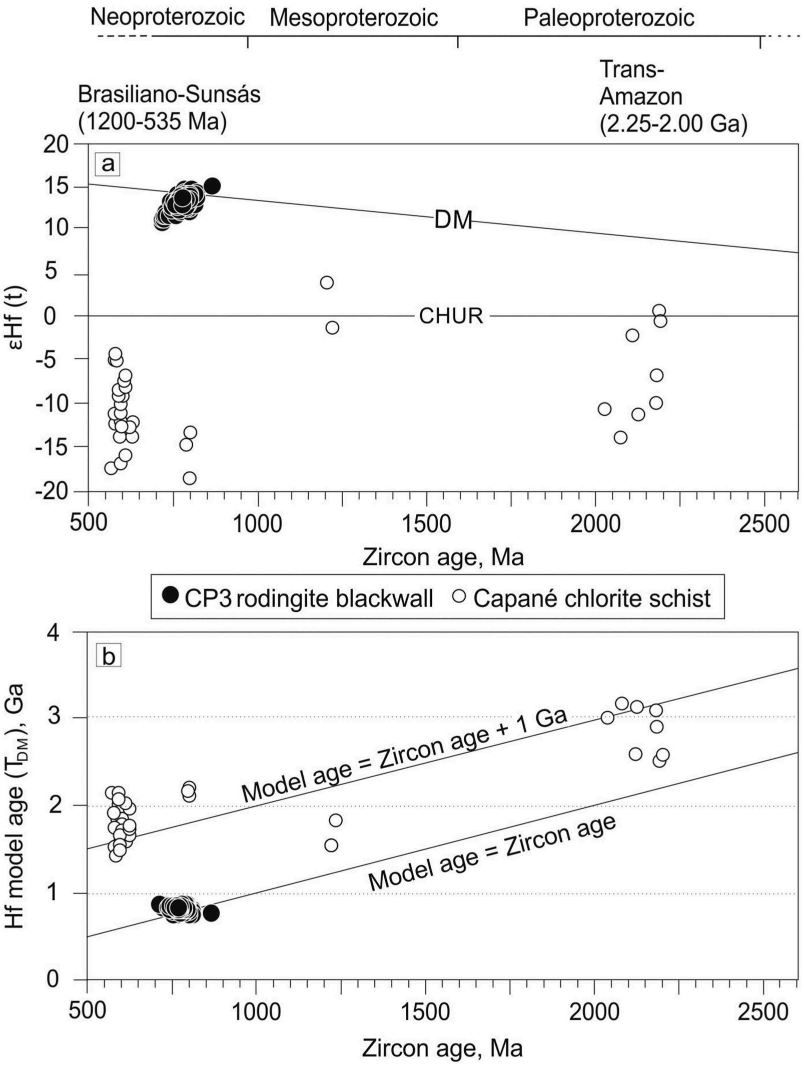

Figure 10. Lu–Hf data. (a) εHf values versus concordant zircon U–Pb age of CP3 compared with Capané chlorite schist; (b) Hf model ages versus U–Pb age CP3 zircon compared to Capané chlorite schist. Data for Capané chlorite schist are from Pertille *et al*. (2015a).

and Yb. These elements can therefore vary within an individual sample, although typically by much less than one order of magnitude (Grimes *et al*. 2007). Zircon grains may undergo multiple episodes of sedimentation, magmatism, and/or metamorphism while retaining isotopic age and chemical information of trace elements (e.g. Hoskin and Ireland 2000; Belousova *et al*. 2002; Grimes *et al*. 2015). Zircon from Capané chlorite schist (Pertille *et al*. 2015a) has a signature of trace elements of continental zircon (Figure 11(d)). In contrast, in the CP3 rodingite blackwall the signature is oceanic (Figure 11(b–d)).

All zircon ages from the Capané rodingite blackwall are older than the maximum depositional age of the Porongos Group in which the ophiolite is contained. This requires that the ophiolite was emplaced tectonically into the sedimentary rocks. The emplacement age is interpreted as approximately between 650–570 Ma when Porongos fold and thrust belt formed (Pertille *et al*. 2017). The youngest age in the zircons of the Capané ophiolite, as here shown, is 715 Ma. The youngest ages were not used in the average age because they represent Pb loss (Figure 9; Supplementary Table 3). The zircons from 793 to 715 Ma were not disturbed during fold and thrust belt advance over the Craton. The CP3 zircon shows positive εHf and trace element signature of oceanic zircon from Grimes *et al*. (2009) diagrams. Lu–Hf isotopes and trace elements of zircon from the Capané ophiolite are similar to relatively undisturbed mantle. This interpretation of lack of disturbance is based on the constant composition of εHf and trace elements.

The Capané schists display well-developed schistosity; some phyllites are present with slaty cleavage where the S_0 structure is still preserved (Saalmann *et al*. 2006, 2011; Pertille *et al*. 2015a). The Capané

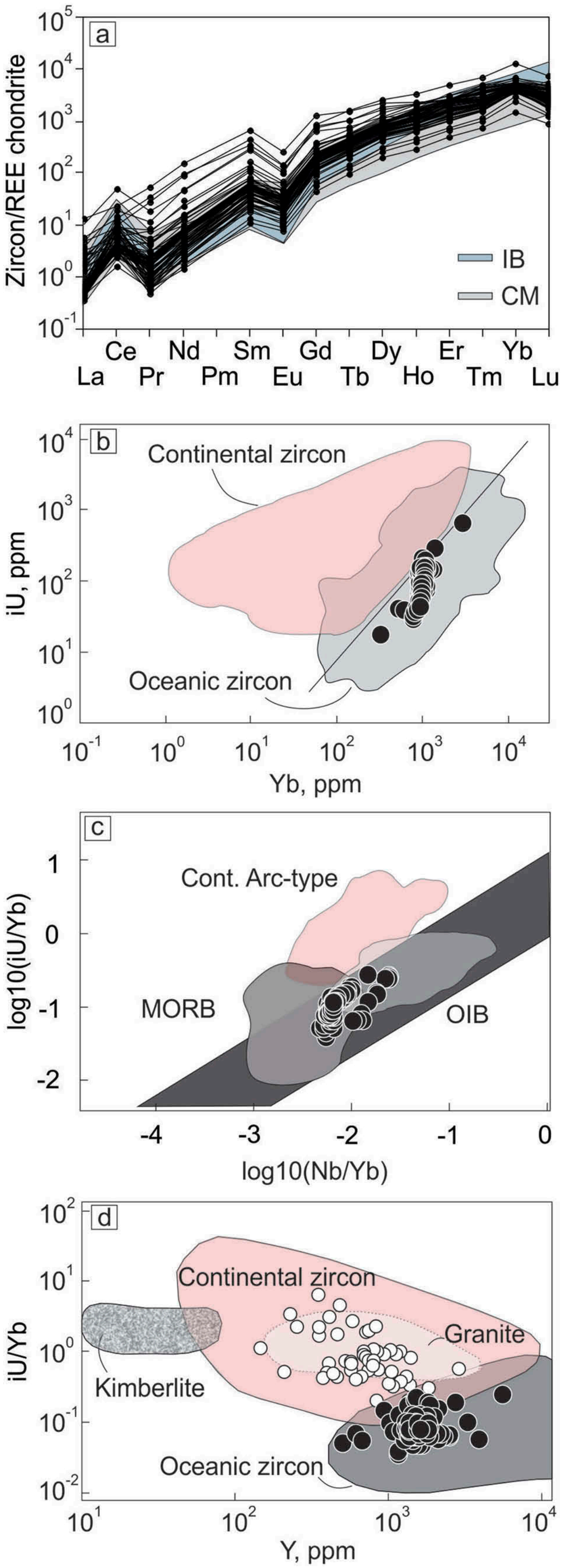

Figure 11. Geochemical tectonic discrimination diagrams for continental and oceanic zircon grains using zircon trace elements. (a) Chondrite-normalized REE (Boynton 1984); IB and CM = oceanic zircon from Arena *et al.* (2016) for comparison; (b) plot of Yb against iU; (c) plot of $\log_{10}$ Nb/Yb against $\log_{10}$ iU/Yb; (d) Y against iU/Yb. Capané chlorite schist is from Pertille et al. (2015a). iU = initial U.

ophiolite represents the last piece of dismembered oceanic lithosphere during continental collision obducted into the continent. The ophiolite was intensely deformed during the evolution of the fold and thrust belt.

Because of the occurrence of ultramafic rocks (Marques *et al*. 2003) and of mafic and felsic metavolcanic rocks with negative to slightly negative εNd values (Gollmann *et al*. 2008), the Capané region was previously discussed separately from the Porongos fold and thrust belt and interpreted as the basal section of an ophiolite (Marques *et al*. 1998). A metarhyolite from the Capané antiform with U–Pb SHRIMP age of 783 ± 6 Ma was dated by Porcher *et al*. (1999) and interpreted as the age of crystallization. Also, zircon U–Pb SHRIMP ages for a Capané chlorite schist indicated two populations. One Neoproterozoic population is 800–570 Ma old, and a Palaeo to Mesoproterozoic population is 2250–1200 Ma. Both populations derived from recycled crust, showing sources (Pertille *et al*. 2015a) with εHf between −18 and −4 and Hf T_{DM} = 2.2–1.5 Ga (Figure 10).

In the Porongos fold and thrust belt, U–Pb (TIMS) ages of zircons from a meta-andesite in the Santana area are 783 ± 8 Ma (Chemale 2000). Metavolcanic rocks from the Porongos Group were also studied by Saalmann *et al*. (2006). The isotopic data led these authors to recognize two distinct groups. In the northwestern region, εNd(t = 780 Ma) values are between −20.6 and −21.7, and in the southeastern region εNd (t = 780) is close to −6.9. The high $^{87}Sr/^{86}Sr(i)$ values (0.7064–0.7286) and trace element data support the interpretation of partial melting or considerable contamination by old continental crust during magma generation and evolution. A U–Pb rhyolite zircon age of 789 ± 7 Ma obtained by Saalmann *et al*. (2011) was indicated as crystallization age. The continental origin for the Tonian zircon grains (809, 801, 773 Ma) from rhyodacites of Porongos fold and thrust belt was also recently detected by Lu–Hf (εHf = −20 and −10; Hf T_{DM} = 2.18–1.77 Ga) and $\delta^{18}O$ (7.8 and 9.7 ‰) by Pertille *et al*. (2017).

A rift setting around 800 Ma was suggested by Saalmann *et al*. (2011) for the Porongos Group, formed over the Encantadas basement. But ages of a magmatic event from 802 to 767 Ma were also recognized within the Dom Feliciano Belt. In the Rocha region, Uruguay (Cerro Bori Orthogneisses), in Piratini region (mafic xenoliths, Piratini Gneiss) and in granitoids in the Porto Alegre region (Chácara das Pedras Orthogneiss), rocks show subduction-related continental magmatic arc affinity (Silva *et al*. 1999; Lenz *et al*. 2011; Koester *et al*. 2016).

The contact between the Porongos Group and the Pelotas Batholith is delimited by the Dorsal de Canguçu Shear Zone (e.g. Hartmann *et al*. 2016 and references therein) (Figure 1(b)). Several authors consider this shear zone a suture (e.g. Fragoso-César *et al*. 1986; Saalmann *et al*. 2011) or intra-continental fault (Fernandes and Koester 1999). Therefore, the origin of Dorsal de Canguçu shear zone and associated environment are a subject of controversy. Zircons close to 800 Ma may be either part of thrust slices or detrital, originated in either case from the Pelotas Batholith.

The youngest possible age for Capané ophiolite obduction is 715 Ma. During the advance of the fold and thrust belt, parts of ophiolites remained near the roots of the thrust, e.g. the Arroio Grande ophiolite (surrounded by Pelotas Batholith) and parts were thrusted into the Porongos fold and thrust belt, e.g. Capané ophiolite (Figure 12). The thrust wedges were progressively deformed in the depositional zones, thus forming the Porongos and Camaquã basins (Figure 12).

After Gondwana stabilization and the end of orogeny, orogenic wedge migration ceased in the Sul-Riograndense Shield (Figure 12). This model inserts the evolution of the ophiolite into the proposal for the Porongos fold and thrust belt by Saalmann *et al*. (2006) and Pertille *et al*. (2017). Our model explains the presence of an ophiolite within a continental schist belt

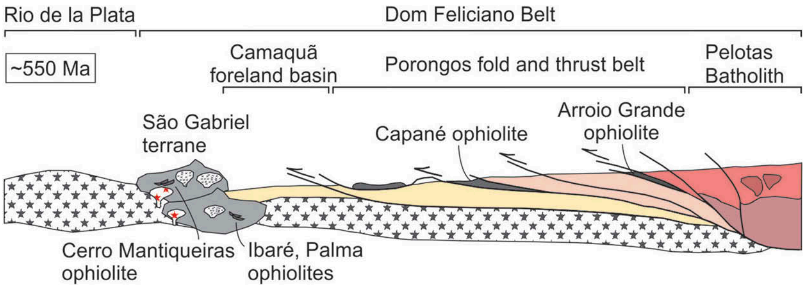

Figure 12. Tectonic model for the Brasiliano evolution of the Porongos fold and thrust belt. Representation of the final stage of the Brasiliano Orogen in the Sul-Riograndense Shield including Capané and Arroio Grande ophiolites.

(Figures 2 and 3) and uses the presence of the ophiolite to propose a new scenario for the evolution of the Brasiliano Orogen in its southern segment.

The Capané ophiolite emplacement was related to the development of the Brasiliano Orogenic Cycle. Ophiolite obduction occurred during ocean closure. This event was coeval with ophiolite emplacement in the juvenile São Gabriel terrane, in the western portion of the Dom Feliciano Belt. The emplacement age in the western terrane was interpreted as approximately 722 Ma at the end of a protracted evolution of the ophiolite during 880–722 Ma (Arena *et al*. 2017). Similar and coeval processes occurred in the western and eastern portions of the Dom Feliciano Belt. The continental collision between the Rio the La Plata and Kalahari Cratons that followed the final closure of the Adamastor ocean is recorded the metamorphic events (650–620 Ma) and in emplacement of the Pelotas Batholith (Philipp *et al*. 2016a).

With the erosional decay after tectonic convergence and interruption of crustal thickening, there occurred the continued post-orogenic development of a mountain range and its foreland as proposed by Tucker and Van Der Beek (2013) and Pertille *et al.* (2017). The suture zone of a mountain belt is a fundamental structure inherited from subduction and indicates the contact of passive margin rocks with terrane or accretionary wedge material. This zone also contains deformed rocks that were thrusted together (Van Der Pluijm and Marshak 1997). This zone in this work is signalled by the displaced Capané ophiolite indicating an active continental margin collision on the eastern portion of the Dom Feliciano Belt, related to the Brasiliano cycle.

6. Conclusions

The mantle section of the Capané ophiolite is a piece of depleted mantle, presently occurring in the Porongos fold and thrust belt. Zircon from a rodingite blackwall, contained in serpentinite, yields εHf between +10.7 and + 15.0, with trace element composition similar to derivation from depleted mantle. This overall composition indicates that zircon is related to melt batches originated in the depleted mantle. The U–Pb dating of the zircon from this ophiolite at 793 ± 0.9 to 715 ± 2.2 Ma in the Dom Feliciano Belt, southern Brasiliano Orogen, sets a limit to the tectonic evolution of West Gondwana involving the amalgamation of the Rio de la Plata and Kalahari cratons and closure of Adamastor Ocean. The ophiolite marks the final closure of the ocean preceding the formation of a mountain belt. The obduction occurred during the collision that formed the Porongos fold and thrust belt at 650–570 Ma.

Acknowledgements

This study is part of the PhD thesis of Karine da Rosa Arena at Programa de Pós-Graduação em Geociências, Universidade Federal do Rio Grande do Sul, Brazil. We acknowledge the major contribution from João Orestes S. Santos to the improvement of the manuscript, and also to three anonymous reviewers. Editor Robert J. Stern conducted efficiently the evaluation procedures.

Disclosure statement

No potential conflict of interest was reported by the authors.

Funding

The investigation was supported financially through a scholarship to Karine and a grant to Léo A. Hartmann by Conselho Nacional do Desenvolvimento Científico e Tecnológico (CNPq) of Brazil; Edital Universal-2012. Support from a FAPERGS grant 'Edital Pesquisador Gaúcho' is also acknowledged.

References

Ajirlu, M.J., Moazzen, M., and Hajialioghli, R., 2016, Tectonic evolution of the Zagros Orogen in the realm of the Neotethys between the Central Iran and Arabian Plates: An ophiolite perspective: Central European Geology, v. 59, p. 1–27. doi:10.1556/24.59.2016.001

Andersen, T., Andersson, U.B., Graham, S., Åberg, G., and Simonsen, S.L., 2009, Granitic magmatism by melting of juvenile continental crust: New constraints on the source of Palaeoproterozoic granitoids in Fennoscandia from Hf isotopes in zircon: Journal of the Geological Society, London, v. 166, p. 233–247. doi:10.1144/0016-76492007-166

Arena, K.R., Hartmann, L.A., and Lana, C., 2016, Evolution of Neoproterozoic ophiolites from the southern Brasiliano Orogen revealed by zircon U-Pb-Hf isotopes and geochemistry: Precambrian Research, v. 285, p. 299–314. doi:10.1016/j.precamres.2016.09.014

Arena, K.R., Hartmann, L.A., and Lana, C., 2017, Tonian emplacement of ophiolites in the southern Brasiliano Orogen delimited by U-Pb-Hf isotopes of zircon from metasomatites: Gondwana Research, v. 49, p. 296–332. doi:10.1016/j.gr.2017.05.018

Austrheim, H., and Prestvik, T., 2008, Rodingitization and hydration of the oceanic lithosphere as developed in the Leka ophiolite, north–central Norway: Lithos, v. 104, p. 177–198. doi:10.1016/j.lithos.2007.12.006

Babinski, M., Chemale, Jr., F. Van Schmus, W.R., and Silva, L.C., 1997, U-Pb and Sm-Nd geochronology of the Neoproterozoic granitic gneissic Dom Feliciano Belt, Southern Brazil: Journal of South American Earth Sciences, v. 10, p. 263–274. doi:10.1016/S0895-9811(97)00021-7

Babinski, M., Chemale, Jr., F. Hartmann, L.A., Van Schmus, W.R., and Silva, L.C., 1996, Juvenile accretion at 750–700 Ma in Southern Brazil: Geology, v. 24, p. 439–442. doi:10.1130/0091-7613(1996)024<0439:JAAMIS>2.3.CO;2

Bach, W., and Klein, F., 2009, The petrology of seafloor rodingites: Insights fromgeochemical reaction pathmodeling: Lithos, v. 112, p. 103–117. doi:10.1016/j.lithos.2008.10.022

Barriga, F., and Fyfe, W.S., 1983, Development of rodingite in basaltic rocks in serpentinites, East Liguria, Italy: Contributions to Mineralogy and Petrology, v. 84, p. 146–151. doi:10.1007/BF00371281

Basei, M.A.S., Frimmel, H.E., Nutman, A.P., Preciozzi, F., and Jacob, J., 2005, A connection between the Neoproterozoic Dom Feliciano (Brazil/Uruguay) and Gariep (Namibia/South Africa) orogenic belts–evidence from a reconnaissance provenance study: Precambrian Research, v. 139, p. 195–221. doi:10.1016/j.precamres.2005.06.005

Belousova, E.A., Griffin, W.L., O'Reilly, S.Y., and Fisher, N.J., 2002, Igneous zircon: Trace element composition as an indicator of source rock type: Contributions to Mineralogy and Petrology, v. 143, p. 602–622. doi:10.1007/s00410-002-0364-7

Bouvier, A., Vervoort, J.D., and Patchett, P.J., 2008, The Lu–Hf and Sm–Nd isotopic composition of CHUR: Constraints from unequilibrated chondrites and implications for the bulk composition of terrestrial planets: Earth and Planetary Science Letters, v. 273, p. 48–57. doi:10.1016/j.epsl.2008.06.010

Boynton, W.V., 1984, Cosmochemistry of the rare earth elements; meteorite studies, *in* Henderson, P., ed., Rare earth element geochemistry: Amsterdam, Elsevier Science Publishing Company, p. 63–114.

Camozzato, E., Klein, C., and Iglesias, C.M.F., 2014, Geological map of Bagé, Rio Grande do Sul, Porto Alegre: Brazil Geological Survey SH.21-Z-D-III, scale 1:100,000.

Chemale, Jr., F. 2000, Evolução Geológica do Escudo Sul-rio-grandense, *in* Holz, M., and De Ros, L.F., eds., Geologia do Rio Grande do Sul: Porto Alegre, Brazil, Centro de Investigação do Gondwana- Universidade Federal do Rio Grande do Sul, p. 13–55.

Chu, N.C., Taylor, R.N., Chavagnac, V., Nesbitt, R.W., Boella, R. M., Milton, J.A., German, C.R., Bayon, G., and Burton, K., 2002, Hf isotope ratio analysis using multi-collector inductively coupled plasma mass spectrometry: An evaluation of isobaric interference corrections: Journal of Analytical Atomic Spectrometry, v. 17, p. 1567–1574. doi:10.1039/b206707b

De Hoog, J.C.M., Janák, M., Vrabec, M., and Froitzheim, N., 2009, Serpentinised peridotites from an ultrahigh-pressure terrane in the Pohorje Mts. (Eastern Alps, Slovenia): Geochemical constraints on petrogenesis and tectonic setting: Lithos, v. 109, p. 209–222. doi:10.1016/j.lithos.2008.05.006

Deschamps, F., Godard, M., Guillot, S., and Hattori, K., 2013, Geochemistry of subduction zone serpentinites: A review: Lithos, v. 178, p. 96–127. doi:10.1016/j.lithos.2013.05.019

Deschamps, F., Guillot, S., Godard, M., Chauvel, C., Andreani, M., and Hattori, K., 2010, In situ characterization of serpentinites from forearc mantle wedges: Timing of serpentinization and behavior of fluid-mobile elements in subduction zones: Chemical Geology, v. 269, p. 262–277. doi:10.1016/j.chemgeo.2009.10.002

Dubińska, E., Bylina, P., Kozłowski, A., Dörr, W., Nejbert, K., Schastok, J., and Kulicki, C., 2004, U-Pb dating of serpentinization - hydrothermal zircon from a metassomatic rodingite shell (Sudetic ophiolite, SW Poland): Chemical Geology, v. 203, p. 183–203. doi:10.1016/j.chemgeo.2003.10.005

Dubińska, E., and Wiewióra, A., 1999, Layer silicates from a rodingite and its blackwall from Przemiłow (Lower Silesia, Poland): Mineralogical record of metasomatic processes during serpentinization and serpentinite recrystallization: Mineralogy and Petrology, v. 67, p. 223–237. doi:10.1007/BF01161523

Evans, B.W., Hattori, K., and Baronnet, A., 2013, Serpentinite: What, why, where?: Elements, v. 9, p. 99–106. doi:10.2113/gselements.9.2.99

Fernandes, L.A.D., and Koester, E., 1999, The Neoproterozoic Dorsal de Canguçu strike-slip shear zone: Its nature and role in the tectonic evolution of southern Brazil: Journal of African Earth Sciences, v. 29, p. 3–24. doi:10.1016/S0899-5362(99)00076-7

Fernandes, L.A.D., Menegat, R., Costa, A.F.U., Koester, E., Porcher, C.C., Tommasi, A., Kramer, G., Ramgrab, G.E., and Camozzato, E., 1995a, Evolução tectônica do Cinturão Dom Feliciano no Escudo Sul-riograndense: Parte I- Uma contribuição a partir do registro geológico: Revista Brasileira De Geociências, v. 25, p. 351–374.

Fernandes, L.A.D., Menegat, R., Costa, A.F.U., Koester, E., Porcher, C.C., Tommasi, A., Kramer, G., Ramgrab, G.E., and Camozzato, E., 1995b, Evolução tectônica do Cinturão Dom Feliciano no Escudo Sul-rio-grandense: Parte II- Uma contribuição a partir do registro geofísico: Revista Brasileira De Geociências, v. 25, p. 375–384.

Fernandes, L.A.D., Tommasi, A., and Porcher, C.C., 1992, Deformation patterns in the southern Brazilian branch of the DFB: A reappraisal: Journal of South American Earth Sciences, v. 5, p. 77–96. doi:10.1016/0895-9811(92)90061-3

Fragoso-César, A.R.S., Figueiredo, M.C.H., Soliani ., E., Jr., and Faccini., U.F., 1986, O Batólito Pelotas (Proterozóico Superior/Eo-Paleozóico) no Escudo do Rio Grande do Sul, *in* Proceedings Congresso Brasileiro de Geologia, 34th, Goiânia: Goiás, Sociedade Brasileira de Geologia, p. 1322–1343.

Frost, B.R., 1975, Contact metamorphism of serpentinite, chloritic blackwall and rodingite at Paddy-Go-Easy Pass, Central Cascades, Washington: Journal of Petrology, v. 16, p. 272–313. doi:10.1093/petrology/16.2.272

Gerdes, A., and Zeh, A., 2009, Zircon formation versus zircon alteration – new insights from combined U-Pb and Lu–Hf in-situ LA-ICP-MS analyses, and consequence for the interpretation of Archean zircon from the Central Zone of the Limpopo Belt: Chemical Geology, v. 261, p. 230–243. doi:10.1016/j.chemgeo.2008.03.005

Gollmann, K., Marques, J.C., Frantz, J.C., and Chemale, Jr., F. 2008, Geoquímica e isotópos de Nd de rochas metavulcânicas da Antiforme Capané, Complexo Metamórfico Porongos, RS: Revista Pesquisas Em Geociências, v. 35, p. 83–95.

Grimes, C.B., John, B.E., Cheadle, M.J., Mazdab, F.K., Wooden, J. L., Swapp, S., and Schwartz, J.J., 2009, On the occurrence, trace element geochemistry, and crystallization history of zircon from in situ ocean lithosphere: Contributions to Mineralogy and Petrology, v. 158, p. 757–783. doi:10.1007/s00410-009-0409-2

Grimes, C.B., John, B.E., Kelemen, P.B., Mazdab, F., Wooden, J. L., Cheadle, M.J., Hanghøj, K., and Schwartz, J.J., 2007, The trace element chemistry of zircons from oceanic crust: A method for distinguishing detrital zircon provenance: Geology, v. 35, p. 643–646. doi:10.1130/G23603A.1

Grimes, C.B., Wooden, J.L., Cheadle, M.J., and John, B.E., 2015, "Fingerprinting" tectono-magmatic provenance using trace elements in igneous zircon: Contributions to Mineralogy and Petrology, v. 170, 46 p. doi:10.1007/s00410-015-1199-3

Hartmann, L.A., Chemale, Jr., F. and Philipp, R.P., 2007, Evolução Geotectônica do Rio Grande do Sul no Pré-Cambriano, *in* Iannuzzi, R., and Frantz, J.C., eds., 50 Anos de Geologia: Porto Alegre, Instituto de Geociências, Universidade Federal do Rio Grande do Sul, Vol. 396, p. 97–123.

Hartmann, L.A., Leite, J.A.D., Silva, L.C., Remus, M.V.D., McNaughton, N.J., Groves, D.I., Fletcher, I.R., Santos, J.O.S., and Vasconcellos, M.A.Z., 2000, Advances in SHRIMP geochronology and their impact on understanding the tectonic and metallogenic evolution of southern Brazil: Australian Journal of Earth Sciences, v. 47, p. 829–844. doi:10.1046/j.1440-0952.2000.00815.x

Hartmann, L.A., Lopes, W.R., and Savian, J.F., 2016, Integrated evaluation of the geology, aerogammaspectrometry and aeromagnetometry of the Sul-Riograndense Shield, southernmost Brazil: Anais Da Academia Brasileira De Ciências, v. 88, p. 75–92. doi:10.1590/0001-3765201520140495

Hartmann, L.A., Philipp, R.P., Liu, D., Wan, Y., Wang, Y., Santos, J.O.S., and Vasconcellos, M.A.Z., 2004, Paleoproterozoic magmatic provenance of detrital zircons, porongos complex quartzites, southern Brazilian shield: International Geology Review, v. 46, p. 127–157. doi:10.2747/0020-6814.46.2.127

Hartmann, L.A., Philipp, R.P., Santos, J.O.S., and McNaughton, N.J., 2011, Time frame of 753-680 Ma juvenile accretion during the São Gabriel orogeny, southern Brazilian Shield: Gondwana Research, v. 19, p. 84–99. doi:10.1016/j.gr.2010.05.001

Horstwood, M.S.A., Košler, J., Gehrels, G., Jackson, S.E., McLean, N.M., Paton, C., Pearson, N.J., Sircombe, K., Sylvester, P., Vermeesch, P., Bowring, J.F., Condon, D.J., and Schoene, B., 2016, Community-derived standards for la-icp-ms u-(th-)pb geochronology – uncertainty propagation, age interpretation and data reporting: Geostandards and Geoanalytical Research, v. 40, p. 311–332. doi:10.1111/j.1751-908X.2016.00379.x

Hoskin, P.W.O., and Ireland, T.R., 2000, Rare earth element chemistry of zircon and its use as a provenance indicator: Geology, v. 28, p. 627–630. doi:10.1130/0091-7613(2000)28<627:REECOZ>2.0.CO;2

Jackson, S.E., Pearson, N.J., Griffin, W.L., and Belousova, E.A., 2004, The application of laser ablation inductively coupled plasma mass spectrometry to in situ U-Pb zircon geochronology: Chemical Geology, v. 211, p. 47–69. doi:10.1016/j.chemgeo.2004.06.017

Johnson, P.R., Abdelsalam, M.G., and Stern, R.J., 2003, The Bi'r Umq-Nakasib suture zone in the Arabian-Nubian shield: A key to understanding crustal growth in the East African Orogen: Gondwana Research, v. 6, p. 523–530. doi:10.1016/S1342-937X(05)71003-0

Jöns, N., Bach, W., and Klein, F., 2010, Magmatic influence on reaction paths and element transport during serpentinisation: Chemical Geology, v. 274, p. 196–211. doi:10.1016/j.chemgeo.2010.04.009

Jost, H., 1982, Condições do metamorfismo regional de uma parte da faixa de dobramentos de Tijucas no Rio Grande do Sul-RS: Acta Geologica Leopoldensia, v. 12, p. 3–32.

Jost, H., and Bitencourt, M.F., 1980, Estratigrafia e tectônica de uma fração da Faixa de Dobramentos de Tijucas no Rio Grande do Sul: Acta Geologica Leopoldensia, v. 4, p. 27–60.

Jost, H., and Hartmann, L.A., 1979, Rodingitos do Rio Grande do sul, Brasil: Acta Geologica Leopoldensia, v. 3, p. 77–91.

Klein, F., 2009, Petrology of serpentinites and rodingites in the oceanic lithosphere [Ph.D. thesis]: Bremen, Universität Bremen, 185 p.

Koester, E., Porcher, C.C., Pimentel, M.M., Fernandes, L.A.D., Vignol-Lelarge, M.L., Oliveira, L.D., and Ramos, R.C., 2016, Further evidence of 777 Ma subduction-related continental arc magmatism in Eastern Dom Feliciano Belt, southern Brazil: The Chácara das Pedras Orthogneiss: Journal of South American Earth Sciences, v. 68, p. 155–166. doi:10.1016/j.jsames.2015.12.006

Laux, J.H., Bongiolo, E.M., Klein, C., and Iglesias, C.M.F., 2012, Geological map of Lagoa da Meia Lua, Rio Grande do Sul, Porto Alegre: Brazil Geological Survey SH.21-Z-B-VI, scale 1:100,000.

Leite, J.A.D., Hartmann, L.A., McNaughton, N.J., and Chemale, Jr., F. 1998, SHRIMP U/Pb zircon geochronology of Neoproterozoic juvenile and crustal-reworked terranes in southernmost Brazil: International Geology Review, v. 40, p. 688–705. doi:10.1080/00206819809465232

Lena, L.O.F., Pimentel, M.M., Philipp, R.P., Armstrong, R., and Sato, K., 2014, The evolution of the Neoproterozoic São Gabriel juvenile terrane, southern Brazil based on high spatial resolution U-Pb ages and $\delta^{18}O$ data from detrital zircons: Precambrian Research, v. 247, p. 126–138. doi:10.1016/j.precamres.2014.03.010

Lenz, C., Fernandes, L.A.D., McNaughton, N.J., Porcher, C.C., and Masquelin, H., 2011, U-Pb SHRIMP ages for the Cerro Bori orthgneisses, Dom Feliciano Belt in Uruguay: Evidences of a 800 Ma magmatic and 650 Ma metamorphic event: Precambrian Research, v. 185, p. 149–163. doi:10.1016/j.precamres.2011.01.007

Li, X.P., Zhang, L., Wei., C., Ai, Y., and Chen, J., 2007, Petrology of rodingite derived from eclogite in western Tianshan, China: Journal of Metamorphic Geology, v. 25, p. 363–382. doi:10.1111/j.1525-1314.2007.00700.x

Ludwig, K.R., 2003, Isoplot/Ex Version 3.00: A Geochronological Toolkit for MicrosoftExcel: Berkeley, C.A., Berkeley Geochronology Center. Special Publication 4, 71: http://bgc.org/isoplot_etc/isoplot.html.

Marchesi, C., Garrido, C.J., Godard, M., Belley, F., and Ferré, E., 2009, Migration and accumulation of ultra-depleted subduction-related melts in the Massif du Sud ophiolite (New Caledonia): Chemical Geology, v. 266, p. 171–186. doi:10.1016/j.chemgeo.2009.06.004

Marques, J.C., Jost, H., Roisenberg, A., and Frantz, J.C., 1998, Eventos ígneos da Suíte Metamórfica Porongos na área da Antiforme Capané, Cachoeira do Sul – RS: Revista Brasileira De Geociências, v. 28, p. 419–430.

Marques, J.C., Roisenberg, A., Jost, H., Frantz, J.C., and Teixeira, R. S., 2003, Geologia e geoquímica das rochas metaultramáficas da Antiforme Capané, Suíte Metamórfica Porongos, RS: Revista Brasileira De Geociências, v. 33, p. 95–107.

Martil, M.M.D., Bitencourt, M.F., Nardi, L.V.S., Koester, E., and Pimentel, M.M., 2017, Pre-collisional, Neoproterozoic (ca. 790 Ma) continental arc magmatism in southern Mantiqueira Province, Brazil: Geochemical and isotopic constraints from the Várzea do Capivarita Complex: Lithos, v. 274–275, p. 39–52. doi:10.1016/j.lithos.2016.11.011

Navabpour, P., Barrier, E., and McQuillan, H., 2014, Oblique oceanic opening and passive margin irregularity, as inherited in the Zagros fold-and-thrust belt: Terra Nova, v. 26, p. 208–215. doi:10.1111/ter.2014.26.issue-3

Paim, P., Chemale, Jr., F. and Lopes, R.C., 2000, A Bacia do Camaquã, *in* Holz, M., and De Ros, L.F., eds., Geologia do Rio Grande do Sul: Porto Alegre, Centro de Investigação do Gondwana- Universidade Federal do Rio Grande do Sul, p. 231–274.

Patchett, P.J., and Tatsumoto, M., 1981, A routine high-precision method for Lu-Hf isotope geochemistry and chronology: Contributions to Mineralogy and Petrology, v. 75, p. 263–267. doi:10.1007/BF01166766

Peel, E., Basei, M., and Sanchez Bettucci, L., 2009, La Tuna Complex: A possible Neoproterozoic ophiolite: American Geophysical Union, Spring Meeting, Abstract #T31A-06.

Pertille, J., Hartmann, L.A., and Philipp, R.P., 2015b, Zircon U-Pb age constraints on the Paleoproterozoic sedimentary basement of the Ediacaran Porongos Group, Sul-Riograndense Shield, southern Brazil: Journal of South American Earth Sciences, v. 63, p. 334–345. doi:10.1016/j.jsames.2015.08.005

Pertille, J., Hartmann, L.A., Philipp, R.P., Petry, T.S., and Lana, C. C., 2015a, Origin of the Ediacaran Porongos Group, Dom Feliciano Belt, southern Brazilian Shield, with emphasis on whole rock and detrital zircon geochemistry and U-Pb, Lu-Hf isotopes: Journal of South American Earth Sciences, v. 64, p. 69–93. doi:10.1016/j.jsames.2015.09.001

Pertille, J., Hartmann, L.A., Santos, J.O.S., McNaughton, N.J., and Armstrong, R., 2017, Reconstructing the Cryogenian-Ediacaran evolution of the Porongos fold and thrust belt, Southern Brasiliano Orogen, based on zircon U-Pb-Hf-O isotopes: International Geology Review, v. 59, p. 1532–1560. doi:10.1080/00206814.2017.1285257

Philipp, R.P., Bom, F.M., Pimentel, M.M., Junges, S.L., and Zvirtes, G., 2016a, SHRIMP U-Pb age and high temperature conditions of the collisional metamorphism in the Várzea do Capivarita Complex: Implications for the origin of Pelotas Batholith, Dom Feliciano Belt, Southern Brazil: Journal of South American Earth Sciences, v. 66, p. 196–207. doi:10.1016/j.jsames.2015.11.008

Philipp, R.P., and Machado, R., 2005, The late neoproterozoic granitoid magmatism of the Pelotas Batholith, southern Brazil: Journal of South American Earth Sciences, v. 19, p. 461–478. doi:10.1016/j.jsames.2005.06.010

Philipp, R.P., Massonne, H.J., and Campos, R.S., 2013, Peraluminous leucogranites of the Cordilheira Suite: A record of Neoproterozoic collision and the generation of the Pelotas Batholith, Dom Feliciano Belt, Southern Brazil: Journal of South American Earth Sciences, v. 43, p. 8–24. doi:10.1016/j.jsames.2012.10.006

Philipp, R.P., Pimentel, M.M., and Chemale Jr., F., 2016b, Tectonic evolution of the Dom Feliciano Belt in southern Brazil: Geological relationships and U-Pb geochronology: Brazilian Journal of Geology, v. 46, p. 83–104. doi:10.1590/2317-4889201620150016

Porcher, C.C., and Fernandes, L.A.D., 1990, Relações embasamento-cobertura na porção ocidental do Cinturão Dom Feliciano: Um esboço estrutural: Revista Pesquisas Em Geociências, v. 17, p. 72–84.

Porcher, C.C., McNaughton, N.J., Leite, J.A.D., Hartmann, L.A., and Fernandes, L.A.D., 1999, Idade SHRIMP em zircão: Vulcanismo ácido do Complexo Metamórfico Porongos, *in* Proceedings Simpósio sobre vulcanismo e ambientes associados, 1st, Gramado: Rio Grande do Sul, Sociedade Brasileira de Geologia, 110 p.

Ramos, R.C., and Koester, E., 2014, Geologia da associação metamáfica-ultramáfica da região de Arroio Grande, sudeste do Escudo Sul-rio-grandense: Pesquisas Em Geociências, v. 41, p. 25–38.

Ramos, R.C., and Koester, E., 2015, Lithogeochemistry of the meta-igneous units from Arroio Grande Ophiolitic Complex, southernmost Brazil: Brazilian Journal of Geology, v. 45, p. 65–78. doi:10.1590/23174889201500010005

Rapela, W.C., Fanning, C.M., Casquet, C., Pankhurst, R.J., Spalletti, L., Poiré, D., and Baldo, E.G., 2011, The Rio de la Plata craton and the adjoining Pan-African/brasiliano terranes: Their origins and incorporation into South-West Gondwana: Gondwana Research, v. 20, p. 673–690. doi:org/10.1016/j.gr.2011.05.001

Remus, M.V.D., Hartmann, L.A., and Ribeiro, M., 1991, Nota sobre a geologia dos metamorfitos de pressão intermediária e granitóides associados da região de Pinheiro Machado/RS: Acta Geologica Leopoldensia, v. 34, p. 175–190.

Saalmann, K., Gerdes, A., Lahaye, Y., Hartmann, L.A., Remus, M. V.D., and Läufer, A., 2011, Multiple accretion at the eastern margin of the Rio de la Plata craton: The prolonged Brasiliano orogeny in southernmost Brazil: International Journal of Earth Sciences, v. 100, p. 355–378. doi:10.1007/s00531-010-0564-8

Saalmann, K., Hartmann, L.A., Remus, M.V.D., Koester, E., and Conceição, R.V., 2005a, Sm–Nd isotope geochemistry of metamorphic volcano-sedimentary successions in the São Gabriel Block, southernmost Brazil: Evidence for the existence of juvenile Neoproterozoic oceanic crust to the east of the Rio de la Plata craton: Precambrian Research, v. 136, p. 159–175. doi:10.1016/j.precamres.2004.10.006

Saalmann, K., Remus, M.V.D., and Hartmann, L.A., 2005b, Geochemistry and crustal evolution of volcano-sedimentary successions and orthogneisses in the São Gabriel Block, southernmost Brazil - Relics of Neoproterozoic Magmatic Arcs: Gondwana Research, v. 8, p. 143–161. doi:10.1016/S1342-937X(05)71114-X

Saalmann, K., Remus, M.V.D., and Hartmann, L.A., 2006, Structural evolution and tectonic setting of the Porongos belt, southern Brazil: Geological Magazine, v. 143, p. 59–88. doi:10.1017/S0016756805001433

Santos, M.M., Lana, C., Scholz, R., Buick, I., Schmitz, M.D., Kamo, S.L., Gerdes, A., Corfu, F., Tapster, S., Lancaster, P., Storey, C. D., Basei, M.A.S., Tohver, E., Alkmim, A., Nalini, H., Krambrock, K., Fantini, C., and Wiedenbeck, M., 2017, A new appraisal of Sri Lankan BB zircon as a reference material for LA-ICP-MS U-Pb geochronology and Lu-Hf isotope tracing: Geostandards and Geoanalytical Research. doi:10.1111/ggr.12167

Scherer, E.E., Münker, C., and Mezger, K., 2001, Calibration of the lutetium-fafnium clock: Science, v. 293, p. 683–687. doi:10.1126/science.1061372

Shervais, J.W., Kimbrough, D.L., Renne, P., Hanan, B.B., Murchey, B., Snow, C.A., Schuman, M.M.Z., and Beaman, J., 2004, Multi-stage origin of the Coast Range ophiolite, California: Implications for the life cycle of supra-subduction zone ophiolites: International Geology Review, v. 46, p. 289–315. doi:10.2747/0020-6814.46.4.289

Silva, L.C., Hartmann, L.A., McNaughton, N.J., and Fletcher, I.R., 1999, SHRIMP U-Pb Zircon dating of Neoproterozoic granitic magmatism and collision in the Pelotas Batholith, southernmost Brazil: International Geology Review, v. 41, p. 531–551. doi:10.1080/00206819909465156

Silva, L.C., McNaughton, N.J., Armstrong, R., Hartmann, L.A., and Fletcher, I.R., 2005, The neoproterozoic Mantiqueira Province and its African connections: A zircon-based U-Pb geochronologic subdivision for the Brasilian/Pan-African systems of orogens: Precambrian Research, v. 136, p. 203–240. doi:10.1016/j.precamres.2004.10.004

Suita, M.T.F., Pedrosa-Soares, A.C., Leite, C.A.S., Nilson, A.A., and Prichard, H.M., 2004, Complexos ofiolíticos do Brasil e a metalogenia comparada das faixas Araçuaí e Brasília, *in* Pereira, E.S., Castroviejo, R., and Ortiz, F., eds., Complejos ofiolíticos em Ibero América: Madrid-España, Edita Proyecto XIII, Vol. 379, p. 101–132.

Takenaka, L.B., Lana, C., Scholz, R., Nalini, H.A., Jr., and Abreu, A.T., 2015, Optimization of the *in-situ* U-Pb age dating method via LA-Quadrupole-ICP-MS with applications to the timing of U-Zr-Mo mineralization in the Poços de Caldas Alkaline Complex, SE Brazil: Journal of South American Earth Sciences, v. 62, p. 70–79. doi:10.1016/j.jsames.2015.04.007

Taylor, S.R., and McLennan, S.M., 1985, The continental crust: Its composition and evolution: Carlton, Blackwell Scientific Publication, 312 p.

Tucker, G.E., and van der Beek, P., 2013, A model for post-orogenic development of a mountain range and its foreland: Basin Research, v. 25, p. 241–259. doi:10.1111/j.1365-2117.2012.00559.x

Van Achterbergh, E., Ryan, C.G., Jackson, S.E., and Griffin, W.L., 2001, Data reduction software for LA–ICP–MS, *in* Sylvester, P.J., eds., Laser ablation-ICP mass spectrometry in the earth sciences: Principles and applications: Ottawa, Ontario, Mineralogical Association of Canada, Short Course, Vol. 29, p. 239–243.

Van Der Pluijm, B.A., and Marshak, S., 1997, Earth structure: An introduction to structural geology and tectonics: United States, McGraw-Hill College, 672 p.

Vervoort, J.D., and Kemp, A.I.S., 2016, Clarifying the zircon Hf isotope record of crust–mantle evolution: Chemical Geology, v. 425, p. 65–75. doi:10.1016/j.chemgeo.2016.01.023

Vieira, D.T., Koester, E., and Porcher, C.C., 2016, Magmatismo Neoproterozóico (680 Ma) no sudeste do escudo Sul-Rio-Grandense: U-Pb e Lu-Hf LA-MC-ICP-MS em zircão, *in* Proceedings Congresso Brasileiro de Geologia, 48th, Porto Alegre: http://sbg.sitepessoal.com/anais48cbg/sts/st13.htm (ID 8889).

Wedepohl, K.H., 1995, The compositions of the continental crust: Geochimica Cosmochimica Acta, v. 59, p. 1217–1232. doi:10.1016/0016-7037(95)00038-2

Zhang, S.B., Wu, R.X., and Zheng, Y.F., 2012, Neoproterozoic continental accretion in South China: Geochemical evidence from the Fuchuan ophiolite in the Jiangnan orogen: Precambrian Research, v. 220–221, p. 45–64. doi:10.1016/j.precamres.2012.07.010

Supplementary Table 1. Chemical composition by electron microprobe (WDS) of chlorites from CP3 rodingite blackwall, Capané ophiolite.

Sample spot	4-4d	4-5d	4-6d	4-7d	4-8d	4-9d	4-10d	4-11d	4-12d	4-13d	4-14d	4-15d	4-16d	4-17d	4-18d	4-19d	4-20	4-21
DataSet/Point	4/1	5/1	6/1	*7/1	*8/1	*9/1	10/1	11/1	12/1	13/1	14/1	15/1	16/1	17/1	*18/1	*19/1	*20/1	*21/1
SiO_2	26.32	24.95	27.01	26.94	27.28	27.23	25.08	24.87	24.50	24.38	27.29	26.64	26.83	26.93	25.80	26.95	27.32	27.55
TiO_2	0.00	0.03	0.02	0.03	0.02	0.02	0.01	0.03	0.03	0.04	0.04	0.01	0.03	0.01	0.00	0.03	0.03	0.03
Al_2O_3	18.85	19.94	20.07	19.30	20.24	19.67	21.29	21.42	21.22	21.66	19.33	18.99	19.06	19.91	20.11	20.64	19.90	19.81
Cr_2O_3	0.01	0.00	0.00	0.00	0.00	0.00	0.01	0.00	0.00	0.00	0.00	0.02	0.01	0.01	0.01	0.00	0.00	0.00
FeO	21.80	24.39	19.82	17.40	18.67	16.38	24.98	26.73	26.87	25.92	21.19	18.45	18.28	19.15	18.09	18.71	17.23	17.24
MnO	0.27	0.35	0.31	0.62	0.28	0.30	0.38	0.38	0.42	0.39	0.29	0.28	0.26	0.27	0.29	0.32	0.33	0.35
MgO	17.69	15.72	20.09	20.91	20.83	22.03	15.20	14.26	13.21	13.63	19.54	20.17	20.55	20.02	19.16	20.61	21.51	21.42
NiO	0.00	0.02	0.00	0.05	0.07	0.00	0.01	0.04	0.04	0.00	0.04	0.05	0.00	0.01	0.01	0.06	0.07	0.00
CaO	0.02	0.02	0.01	0.04	0.00	0.01	0.00	0.02	0.01	0.02	0.00	0.02	0.01	0.01	0.02	0.01	0.01	0.00
Na_2O	0.03	0.05	0.04	0.02	0.03	0.01	0.00	0.00	0.02	0.07	0.00	0.00	0.00	0.02	0.02	0.00	0.02	0.00
K_2O	0.01	0.00	0.00	0.03	0.01	0.00	0.00	0.00	0.00	0.00	0.00	0.00	0.01	0.00	0.00	0.01	0.00	0.01
BaO	0.00	0.00	0.00	1.03	0.04	0.00	0.01	0.01	0.03	0.00	0.00	0.00	0.00	0.00	0.01	0.00	0.17	0.07
H_2O**	11.21	11.09	11.68	11.55	11.77	11.66	11.28	11.28	11.07	11.10	11.65	11.37	11.44	11.58	11.25	11.75	11.72	11.73
Total	96.22	96.56	99.05	97.92	99.24	97.31	98.26	99.04	97.53	97.31	99.37	96.00	96.48	97.95	94.93	99.09	98.31	98.36
Structural formula based on 28 (O)																		
Si	5.629	5.384	5.538	5.584	5.556	5.600	5.331	5.286	5.305	5.263	5.616	5.619	5.620	5.575	5.499	5.500	5.591	5.630
Al	4.753	5.085	4.857	4.725	4.862	4.771	5.334	5.370	5.419	5.516	4.693	4.723	4.709	4.859	5.056	4.967	4.802	4.774
Ti	0.000	0.005	0.003	0.005	0.003	0.003	0.002	0.005	0.005	0.006	0.006	0.002	0.005	0.002	0.000	0.005	0.005	0.005
Cr	0.002	0.000	0.000	0.000	0.000	0.000	0.002	0.000	0.000	0.000	0.000	0.003	0.002	0.002	0.002	0.000	0.000	0.000
Fe^{3+}	0.001	0.000	0.000	0.000	0.000	0.000	0.001	0.000	0.018	0.017	0.000	0.000	0.000	0.004	0.027	0.000	0.000	0.023
Fe^{2+}	3.900	4.466	3.429	3.062	3.193	2.828	4.442	4.772	4.866	4.679	3.673	3.268	3.220	3.315	3.224	3.204	2.955	2.946
Mn	0.049	0.064	0.054	0.109	0.048	0.052	0.068	0.068	0.077	0.071	0.051	0.050	0.046	0.047	0.052	0.055	0.057	0.061
Mg	5.640	5.057	6.141	6.461	6.324	6.754	4.816	4.518	4.264	4.386	5.994	6.342	6.417	6.178	6.088	6.270	6.562	6.525
Ni	0.000	0.003	0.000	0.008	0.011	0.000	0.002	0.007	0.007	0.000	0.007	0.008	0.000	0.002	0.002	0.010	0.012	0.000
Ca	0.005	0.005	0.002	0.009	0.000	0.002	0.000	0.005	0.002	0.005	0.000	0.005	0.002	0.002	0.005	0.002	0.002	0.000
Na	0.025	0.042	0.032	0.016	0.024	0.008	0.000	0.000	0.017	0.059	0.000	0.000	0.000	0.016	0.017	0.000	0.016	0.000
K	0.005	0.000	0.000	0.016	0.005	0.000	0.000	0.000	0.000	0.000	0.000	0.000	0.005	0.000	0.000	0.005	0.000	0.005

Compositions are quoted in weight% and structural formula, in atoms per formula unit. *Chlorite in matrix; ** = calculated by stoichiometry.

Supplementary Table 1. Continuation.

Sample spot	2-1	2-2	2-3	2-4	2-5	2-6	2-7	2-8	2-9	2-10	2-11	2-12	2-13	2-14	2-15	2-16	2-17
DataSet/Point	22/1	23/1	24/1	25/1	*26/1	*27/1	28/1	*29/1	30/1	31/1	32/1	33/1	*34/1	*35/1	*36/1	*37/1	*38/1
SiO_2	24.77	24.18	24.99	24.88	25.97	26.47	25.52	27.18	24.09	25.06	24.42	24.72	27.44	27.40	26.73	26.98	26.93
TiO_2	0.02	0.03	0.02	0.02	0.04	0.02	0.01	0.01	0.00	0.03	0.02	0.04	0.04	0.02	0.02	0.01	0.03
Al_2O_3	21.58	22.06	21.67	20.83	21.26	20.47	21.51	20.29	22.14	21.32	21.31	21.70	18.99	19.79	19.65	19.18	19.88
Cr_2O_3	0.00	0.01	0.01	0.01	0.01	0.03	0.00	0.01	0.00	0.00	0.00	0.01	0.01	0.01	0.01	0.00	0.00
FeO	25.03	26.35	25.75	28.46	19.95	18.46	21.07	18.27	27.15	24.06	26.16	23.76	19.73	17.47	20.66	18.79	17.82
MnO	0.38	0.37	0.33	0.43	0.36	0.33	0.37	0.30	0.43	0.40	0.43	0.47	0.24	0.27	0.33	0.31	0.29
MgO	15.29	13.86	14.45	12.51	18.87	20.54	17.88	20.93	13.26	15.83	13.97	15.83	20.42	21.30	19.11	20.34	20.96
NiO	0.03	0.02	0.03	0.00	0.03	0.04	0.02	0.00	0.04	0.00	0.00	0.02	0.01	0.01	0.00	0.02	0.03
CaO	0.02	0.00	0.01	0.02	0.03	0.02	0.01	0.00	0.01	0.03	0.04	0.00	0.00	0.00	0.00	0.00	0.00
Na_2O	0.00	0.01	0.02	0.00	0.00	0.01	0.00	0.01	0.01	0.00	0.02	0.01	0.03	0.01	0.01	0.02	0.02
K_2O	0.00	0.00	0.00	0.01	0.01	0.00	0.01	0.02	0.00	0.00	0.01	0.00	0.02	0.02	0.01	0.01	0.00
BaO	0.05	0.00	0.03	0.01	0.05	0.11	0.00	0.03	0.01	0.00	0.06	0.00	0.01	0.00	0.00	0.00	0.00
H_2O**	11.29	11.18	11.29	11.10	11.55	11.62	11.45	11.74	11.15	11.30	11.11	11.29	11.63	11.69	11.51	11.50	11.61
Total	98.46	98.07	98.73	98.46	98.14	98.12	97.85	98.79	98.29	98.03	97.55	97.85	98.57	98.07	98.04	97.16	97.57
Structural formula based on 28 (O)																	
Si	5.254	5.186	5.304	5.372	5.393	5.456	5.344	5.552	5.176	5.316	5.267	5.248	5.653	5.618	5.570	5.625	5.563
Al	5.402	5.581	5.424	5.304	5.205	4.981	5.309	4.887	5.611	5.333	5.422	5.435	4.617	4.784	4.829	4.716	4.842
Ti	0.003	0.005	0.003	0.003	0.006	0.003	0.002	0.002	0.000	0.005	0.003	0.006	0.006	0.003	0.003	0.002	0.005
Cr	0.000	0.002	0.002	0.002	0.002	0.005	0.000	0.002	0.000	0.000	0.000	0.002	0.002	0.002	0.002	0.000	0.000
Fe^{3+}	0.000	0.000	0.019	0.030	0.002	0.000	0.000	0.000	0.000	0.000	0.000	0.000	0.000	0.012	0.000	0.000	0.000
Fe^{2+}	4.475	4.743	4.572	5.138	3.465	3.224	3.691	3.126	4.896	4.279	4.738	4.242	3.429	2.996	3.612	3.291	3.088
Mn	0.068	0.067	0.059	0.079	0.063	0.058	0.066	0.052	0.078	0.072	0.079	0.085	0.042	0.047	0.058	0.055	0.051
Mg	4.835	4.432	4.572	4.026	5.842	6.311	5.581	6.373	4.247	5.005	4.491	5.010	6.271	6.510	5.936	6.321	6.455
Ni	0.005	0.003	0.005	0.000	0.005	0.007	0.003	0.000	0.007	0.000	0.000	0.003	0.002	0.002	0.000	0.003	0.005
Ca	0.005	0.000	0.002	0.005	0.007	0.004	0.002	0.000	0.002	0.007	0.009	0.002	0.007	0.002	0.002	0.004	0.004
Na	0.000	0.008	0.016	0.000	0.000	0.008	0.000	0.008	0.008	0.000	0.017	0.000	0.016	0.016	0.008	0.008	0.000
K	0.000	0.000	0.000	0.006	0.005	0.000	0.005	0.010	0.000	0.000	0.006	0.000	0.005	0.000	0.000	0.000	0.000

Compositions are quoted in weight% and structural formula, in atoms per formula unit. *Chlorite in matrix; ** = calculated by stoichiometry.

Supplementary Table 2. Chemical analysis of serpentinite CP1 and rodingite blackwall CP3.

	CP1	CP3
SiO_2	45.58	25.76
TiO_2	<0.01	1.99
P_2O_5	<0.01	0.55
Al_2O_3	0.89	16.55
Fe_2O_3	5.84	26.64
K_2O	<0.01	<0.01
CaO	0.01	0.79
Na_2O	<0.01	<0.01
MgO	33.2	17.56
MnO	0.07	0.27
Cr_2O_3	0.377	0.003
LOI	13.2	8.5
Sum	99.46	99.48
Zr	0.2	4836.7
Y	0.2	1442.6
Co	102.1	90
Ga	<0.5	6.8
Hf	<0.1	149
Nb	<0.1	170
Ni	2185	111
Rb	0.2	0.4
Sc	7	84
Sr	1	69.6
Ta	<0.1	19.2
Th	<0.2	83.2
U	<0.1	20.3
V	33	47
W	<0.5	1.3
Sn	<0.1	<0.1
Ba	5	10
Be	<0.1	<0.1
Cs	<0.1	<0.1
Ce	<0.1	1199
Dy	<0.05	255.99
Er	<0.03	165.47
Eu	<0.02	13.59
Gd	<0.05	216.92
Ho	<0.02	54.19
La	0.2	533.8
Lu	<0.01	23.89
Nd	<0.3	688.8
Pr	<0.02	158.88
Sm	<0.05	178.5
Tb	<0.01	37.82
Tm	<0.01	24.6
Yb	<0.05	154.02

Oxides in wt.% and trace elements in ppm.

Supplementary Table 3. U-Pb isotopic data by LA-ICP-MS of zircon grains from CP3 rodingite blackwall, Capané ophiolite.

					Ages						Isotopic ratios							
Spot	Pbc (%)	U (ppm)	iU (ppm)	Th/U	^{206}Pb/^{238}U	2s	^{207}Pb/^{235}U	2s	^{207}Pb/^{206}Pb	2s	^{207}Pb/^{206}Pb	2s	^{207}Pb/^{235}U	2s	^{206}Pb/^{238}U	2s	Rho	Conc. (%)
78	0.0	163	188	0.51	862	6	862	5	861	11	0.0678	0.6	1.3376	0.9	0.1432	0.7	0.79	100
71	0.7	41	47	0.59	808	7	809	9	810	26	0.0661	1.2	1.2179	1.6	0.1336	0.9	0.59	100
42	0.2	57	65	0.61	805	3	806	4	809	14	0.0661	0.6	1.2125	0.8	0.1331	0.5	0.58	100
76	0.2	56	64	0.56	802	5	803	5	806	13	0.0660	0.6	1.2061	0.9	0.1326	0.7	0.74	100
75	0.2	53	60	0.52	800	8	801	8	804	19	0.0659	0.9	1.2011	1.4	0.1322	1.1	0.79	100
97	0.3	133	152	0.48	800	4	801	5	805	15	0.0660	0.7	1.2007	0.9	0.1320	0.5	0.60	99
83	0.3	75	86	0.45	799	5	800	6	803	17	0.0659	0.8	1.1996	1.0	0.1320	0.6	0.61	100
72	0.9	130	148	0.55	799	8	800	9	803	28	0.0659	1.3	1.1991	1.7	0.1320	1.0	0.61	99
104	0.5	33	37	0.37	798	6	800	9	805	29	0.0659	1.4	1.1988	1.6	0.1318	0.8	0.50	99
38	0.2	115	131	0.54	798	4	800	4	804	13	0.0659	0.6	1.1982	0.8	0.1318	0.5	0.62	99
63	0.3	110	126	0.46	799	4	800	5	800	14	0.0658	0.7	1.1981	0.9	0.1320	0.6	0.64	100
80	0.1	65	74	0.59	798	5	799	5	802	13	0.0659	0.6	1.1972	0.9	0.1318	0.6	0.70	99
81	0.3	35	40	0.38	797	6	799	6	806	18	0.0660	0.9	1.1972	1.1	0.1316	0.8	0.66	99
77	0.1	63	72	0.58	798	6	799	6	803	14	0.0659	0.7	1.1967	1.0	0.1318	0.8	0.78	99
68	0.1	149	170	0.53	798	6	799	5	802	11	0.0659	0.5	1.1966	1.0	0.1318	0.8	0.83	100
45	0.0	84	96	0.50	798	4	799	4	801	13	0.0658	0.6	1.1958	0.8	0.1317	0.5	0.64	100
65	0.2	166	189	0.59	797	6	798	5	801	11	0.0658	0.5	1.1947	1.0	0.1316	0.8	0.83	100
87	0.2	108	124	0.44	797	4	798	5	800	12	0.0658	0.6	1.1937	0.8	0.1316	0.6	0.70	100
67	0.0	134	153	0.55	796	5	797	5	801	10	0.0658	0.5	1.1930	0.8	0.1315	0.7	0.81	99
51	0.2	151	172	0.56	796	4	797	4	799	12	0.0658	0.6	1.1918	0.8	0.1314	0.5	0.65	100
69	0.2	95	108	0.57	795	9	797	8	800	13	0.0658	0.6	1.1916	1.4	0.1313	1.3	0.90	99
107	0.1	62	71	0.62	796	6	796	6	797	16	0.0657	0.8	1.1908	1.1	0.1314	0.8	0.71	100
66	0.2	98	112	0.59	795	4	796	5	799	12	0.0658	0.6	1.1906	0.8	0.1313	0.6	0.70	99
33	0.4	82	93	0.70	795	4	796	5	799	17	0.0658	0.8	1.1904	0.9	0.1312	0.5	0.51	99
73	0.2	131	150	0.54	795	6	796	6	798	14	0.0657	0.7	1.1900	1.0	0.1313	0.8	0.74	100
86	0.1	226	259	0.67	795	5	796	4	798	10	0.0657	0.5	1.1897	0.8	0.1313	0.6	0.79	100
70	0.0	54	62	0.64	794	6	796	6	800	15	0.0658	0.7	1.1894	1.0	0.1311	0.8	0.73	99
37	0.2	113	129	0.62	794	3	796	5	799	15	0.0658	0.7	1.1891	0.8	0.1311	0.5	0.56	99
113	0.2	612	698	0.74	794	4	795	4	798	11	0.0658	0.5	1.1879	0.8	0.1310	0.6	0.73	99
74	0.4	133	151	0.57	794	6	795	6	797	17	0.0657	0.8	1.1878	1.1	0.1311	0.8	0.71	100
61	0.4	83	95	0.56	794	4	795	6	798	19	0.0658	0.9	1.1875	1.0	0.1310	0.5	0.48	99

129	0.3	160	183	0.46	793	4	795	4	798	14	0.0657	0.7	1.1871	0.8	0.1310	0.5	0.58	99
50	0.2	62	70	0.39	794	4	794	5	797	16	0.0657	0.8	1.1867	0.9	0.1310	0.5	0.56	100
40	0.0	73	83	0.57	794	4	794	4	795	13	0.0656	0.6	1.1865	0.8	0.1311	0.5	0.61	100
89	0.1	109	124	0.62	793	5	794	5	797	13	0.0657	0.6	1.1859	0.9	0.1309	0.7	0.77	99
44	0.3	84	96	0.45	793	4	794	5	798	14	0.0657	0.7	1.1859	0.9	0.1308	0.6	0.64	99
29	0.2	259	296	0.60	792	3	794	4	798	12	0.0657	0.6	1.1852	0.7	0.1308	0.4	0.58	99
101	0.2	57	65	0.60	793	7	793	7	795	17	0.0657	0.8	1.1845	1.2	0.1309	0.9	0.76	100
103	0.3	111	126	0.76	792	6	793	6	798	16	0.0657	0.8	1.1841	1.1	0.1307	0.8	0.74	99
34	0.2	74	85	0.46	792	3	793	5	796	16	0.0657	0.8	1.1827	0.9	0.1306	0.4	0.46	99
28	0.5	37	42	0.54	789	5	793	9	801	33	0.0658	1.6	1.1827	1.7	0.1303	0.7	0.39	99
54	0.2	40	46	0.41	792	3	792	6	794	20	0.0656	0.9	1.1818	1.0	0.1306	0.4	0.42	100
23	0.1	65	74	0.66	791	4	792	5	796	15	0.0657	0.7	1.1816	0.9	0.1305	0.5	0.56	99
60	0.2	104	118	0.57	790	6	792	6	795	14	0.0656	0.6	1.1807	1.0	0.1304	0.8	0.78	99
128	0.5	70	80	0.65	790	4	792	6	795	20	0.0656	0.9	1.1805	1.1	0.1304	0.5	0.49	99
49	0.4	109	124	0.58	790	3	791	5	795	15	0.0656	0.7	1.1803	0.8	0.1304	0.4	0.52	99
108	0.4	25	29	0.32	790	6	791	9	794	29	0.0656	1.4	1.1800	1.6	0.1304	0.8	0.52	100
24	0.3	54	61	0.63	789	4	791	6	799	21	0.0658	1.0	1.1798	1.1	0.1301	0.6	0.51	99
52	0.3	53	60	0.60	790	4	791	6	796	18	0.0657	0.8	1.1797	1.0	0.1303	0.6	0.55	99
41	0.4	59	67	0.56	790	8	791	8	794	18	0.0656	0.9	1.1789	1.4	0.1303	1.1	0.78	99
93	0.0	214	244	0.60	789	5	791	4	795	11	0.0656	0.5	1.1788	0.8	0.1303	0.6	0.78	99
84	0.2	113	129	0.56	789	5	790	5	793	13	0.0656	0.6	1.1771	0.9	0.1302	0.7	0.72	99
46	0.2	179	204	0.62	789	4	790	4	793	13	0.0656	0.6	1.1771	0.8	0.1301	0.5	0.63	99
90	0.1	108	123	0.54	788	5	790	5	794	14	0.0656	0.7	1.1762	1.0	0.1300	0.7	0.74	99
55	0.2	172	196	0.61	788	5	789	5	793	13	0.0656	0.6	1.1758	0.9	0.1300	0.6	0.71	99
109	0.2	24	27	0.40	788	7	789	9	792	30	0.0656	1.4	1.1757	1.7	0.1301	0.9	0.56	100
35	0.1	128	146	0.54	788	3	789	4	793	14	0.0656	0.7	1.1753	0.8	0.1300	0.4	0.49	99
99	0.0	16	18	0.33	788	8	789	12	792	38	0.0655	1.8	1.1753	2.1	0.1301	1.1	0.52	100
122*	0.4	158	181	0.49	788	2	789	4	793	16	0.0656	0.7	1.1749	0.8	0.1299	0.3	0.41	99
120*	0.0	1292	1473	0.39	787	14	789	10	795	09	0.0656	0.4	1.1747	1.9	0.1298	1.8	0.97	99
43*	0.4	54	61	0.36	787	4	789	5	794	17	0.0656	0.8	1.1742	1.0	0.1298	0.5	0.56	99
119*	0.3	44	50	0.57	787	6	789	7	793	21	0.0656	1.0	1.1740	1.3	0.1299	0.8	0.61	99
85*	0.1	103	117	0.56	787	4	788	4	792	12	0.0655	0.6	1.1737	0.8	0.1299	0.5	0.66	99
57*	0.2	176	201	0.58	787	6	788	5	792	13	0.0655	0.6	1.1729	1.0	0.1298	0.8	0.78	99
27*	0.3	85	97	0.59	787	3	788	5	792	17	0.0656	0.8	1.1729	0.9	0.1298	0.4	0.47	99

138*	0.0	41	47	0.34	787	4	788	6	789	18	0.0655	0.9	1.1725	1.0	0.1299	0.6	0.57	100
82*	0.4	30	34	0.32	787	4	787	7	789	22	0.0655	1.1	1.1715	1.2	0.1298	0.5	0.46	100
137*	0.3	187	214	0.62	787	5	787	5	788	14	0.0654	0.7	1.1708	1.0	0.1298	0.7	0.72	100
102*	0.6	41	47	0.58	786	5	788	7	795	21	0.0656	1.0	1.1735	1.2	0.1297	0.6	0.52	99
92*	0.3	76	86	0.57	786	4	788	5	793	16	0.0656	0.7	1.1723	0.9	0.1297	0.5	0.58	99
32*	0.4	63	72	0.60	786	3	788	6	791	19	0.0655	0.9	1.1720	1.0	0.1297	0.4	0.41	99
47*	0.3	62	70	0.54	786	3	787	5	791	16	0.0655	0.8	1.1714	0.9	0.1297	0.5	0.50	99
36*	0.3	107	122	0.50	785	3	786	5	789	15	0.0655	0.7	1.1683	0.9	0.1295	0.4	0.52	99
48*	0.3	148	169	0.57	784	3	785	4	789	14	0.0655	0.7	1.1670	0.8	0.1293	0.5	0.57	99
91*	0.3	72	81	0.40	784	5	785	6	789	17	0.0655	0.8	1.1668	1.1	0.1293	0.7	0.62	99
22*	0.5	137	156	0.54	783	3	785	5	789	18	0.0655	0.9	1.1659	1.0	0.1292	0.5	0.48	99
59*	0.0	49	56	0.53	783	4	784	6	788	22	0.0654	1.0	1.1651	1.2	0.1292	0.6	0.49	99
135*	0.0	261	297	0.65	782	9	784	7	793	11	0.0656	0.5	1.1654	1.3	0.1289	1.2	0.92	99
58*	0.4	73	83	0.58	781	4	783	6	789	18	0.0654	0.9	1.1622	1.0	0.1288	0.6	0.56	99
62*	0.1	111	126	0.66	781	4	782	4	786	12	0.0654	0.6	1.1606	0.8	0.1288	0.5	0.65	99
110*	0.5	386	439	0.51	780	5	784	6	797	17	0.0657	0.8	1.1647	1.1	0.1286	0.7	0.67	98
133*	0.0	111	126	0.75	780	4	783	5	794	14	0.0656	0.7	1.1630	0.9	0.1286	0.6	0.65	98
56*	0.3	104	118	0.50	780	4	782	5	786	14	0.0654	0.7	1.1598	0.9	0.1287	0.5	0.63	99
39*	0.4	76	86	0.61	780	4	782	5	788	16	0.0654	0.7	1.1598	0.9	0.1286	0.6	0.59	99
31*	0.1	80	91	0.68	780	3	781	5	785	15	0.0653	0.7	1.1578	0.8	0.1285	0.4	0.50	99
121*	1.7	89	102	0.71	778	4	784	15	799	56	0.0658	2.7	1.1633	2.7	0.1283	0.6	0.20	97
30*	0.3	174	197	0.60	778	3	779	5	784	16	0.0653	0.7	1.1546	0.8	0.1283	0.4	0.47	99
53*	0.0	73	83	0.53	776	4	777	5	781	15	0.0652	0.7	1.1502	0.9	0.1279	0.5	0.57	99
88*	0.2	22	25	0.33	774	5	775	9	780	29	0.0652	1.4	1.1459	1.6	0.1275	0.7	0.45	99
21*	0.3	80	91	0.42	773	3	775	5	780	16	0.0652	0.8	1.1445	0.9	0.1274	0.4	0.48	99
114*	0.6	76	86	0.47	772	4	780	6	803	18	0.0659	0.9	1.1557	1.1	0.1272	0.6	0.57	96
111*	0.2	145	165	0.75	772	3	778	4	793	13	0.0656	0.6	1.1506	0.8	0.1273	0.5	0.60	97
139*	0.5	87	99	0.68	767	4	775	6	798	20	0.0657	1.0	1.1445	1.1	0.1263	0.6	0.51	96
132*	0.1	54	61	0.57	765	3	773	5	796	17	0.0657	0.8	1.1410	0.9	0.1260	0.4	0.46	96
131*	0.5	108	123	0.56	761	4	771	6	799	19	0.0658	0.9	1.1365	1.1	0.1253	0.5	0.48	95
64	0.3	162	184	0.52	761	3	763	4	768	14	0.0648	0.7	1.1197	0.8	0.1253	0.5	0.58	99
126	0.4	97	110	0.62	761	4	763	5	767	18	0.0648	0.8	1.1196	1.0	0.1254	0.6	0.55	99
25	0.3	97	110	0.45	761	4	762	5	767	16	0.0648	0.7	1.1187	0.9	0.1253	0.5	0.58	99
118	0.3	63	71	0.67	761	5	762	6	766	17	0.0647	0.8	1.1178	1.1	0.1252	0.7	0.66	99

105	0.4	143	162	0.59	759	3	761	5	767	16	0.0648	0.8	1.1160	0.8	0.1250	0.4	0.43	99
10	0.3	70	80	0.69	759	3	760	5	765	16	0.0647	0.8	1.1148	0.9	0.1249	0.5	0.53	99
19	0.3	116	131	0.54	759	3	761	4	765	15	0.0647	0.7	1.1149	0.8	0.1249	0.4	0.52	99
2	0.3	71	81	0.70	758	4	760	5	764	16	0.0647	0.8	1.1133	1.0	0.1248	0.6	0.63	99
12	0.3	59	66	0.60	757	6	759	6	765	18	0.0647	0.8	1.1120	1.2	0.1246	0.8	0.69	99
1	0.4	38	43	0.61	757	4	759	7	764	25	0.0647	1.2	1.1112	1.3	0.1246	0.5	0.40	99
6	0.0	66	74	0.60	758	4	759	4	764	12	0.0647	0.6	1.1127	0.8	0.1248	0.5	0.65	99
117	0.0	133	151	0.71	758	4	760	4	764	11	0.0647	0.5	1.1128	0.8	0.1248	0.6	0.77	99
15	0.3	52	59	0.58	757	3	758	5	764	15	0.0647	0.7	1.1103	0.8	0.1245	0.5	0.55	99
26	0.4	93	106	0.54	756	3	759	5	766	17	0.0647	0.8	1.1114	0.9	0.1245	0.4	0.45	99
14	0.4	60	68	0.54	754	4	756	5	763	18	0.0646	0.8	1.1062	1.0	0.1241	0.5	0.51	99
5	0.1	57	64	0.55	754	3	756	5	762	16	0.0646	0.8	1.1057	0.9	0.1241	0.4	0.49	99
7	0.4	50	56	0.51	754	4	756	6	762	18	0.0646	0.9	1.1064	1.0	0.1242	0.6	0.55	99
4	0.5	36	41	0.60	755	4	757	6	762	20	0.0646	0.9	1.1071	1.1	0.1242	0.5	0.46	99
8	0.4	75	85	0.61	754	3	756	5	762	18	0.0646	0.9	1.1060	1.0	0.1241	0.5	0.47	99
16	0.5	110	125	0.58	754	3	756	5	762	17	0.0646	0.8	1.1051	0.9	0.1241	0.4	0.46	99
11*	0.0	95	108	0.56	751	4	753	4	760	11	0.0645	0.5	1.0996	0.8	0.1236	0.6	0.74	99
123*	0.0	76	86	0.57	753	4	763	5	793	13	0.0656	0.6	1.1209	0.9	0.1240	0.6	0.68	95
17*	0.4	72	81	0.48	749	3	751	6	757	20	0.0645	1.0	1.0956	1.1	0.1232	0.4	0.42	99
130*	0.3	73	82	0.58	748	4	760	5	799	16	0.0658	0.8	1.1148	1.0	0.1230	0.6	0.59	94
112*	0.0	146	165	0.56	743	22	755	17	790	12	0.0655	0.6	1.1033	3.1	0.1222	3.1	0.98	94
141*	0.2	922	1041	0.37	734	38	749	30	794	10	0.0656	0.5	1.0911	5.5	0.1206	5.5	1.00	92
136*	0.0	93	105	0.67	726	6	721	6	707	17	0.0630	0.8	1.0345	1.2	0.1191	0.9	0.74	103
106*	0.6	133	149	0.26	726	19	727	16	729	23	0.0636	1.1	1.0456	3.0	0.1192	2.8	0.93	100
96	0.8	237	267	0.40	717	4	721	7	731	25	0.0637	1.2	1.0336	1.3	0.1177	0.7	0.49	98
79	0.5	36	40	0.34	716	6	718	7	726	21	0.0635	1.0	1.0288	1.3	0.1174	0.9	0.65	99
125	0.7	77	86	0.45	714	5	717	8	729	27	0.0636	1.3	1.0269	1.5	0.1171	0.7	0.48	98
94	0.4	51	57	0.35	713	4	715	6	721	23	0.0634	1.1	1.0224	1.2	0.1170	0.5	0.44	99
100*	0.6	259	290	0.26	699	54	701	42	710	21	0.0631	1.0	0.9954	8.2	0.1145	8.1	0.99	98
124*	0.2	231	259	0.67	691	4	715	4	793	12	0.0656	0.6	1.0222	0.8	0.1131	0.6	0.71	87
140*	0.0	90	101	1.10	685	14	703	13	761	26	0.0646	1.2	0.9989	2.5	0.1122	2.2	0.87	90
95*	0.0	96	107	0.20	669	19	667	16	662	25	0.0617	1.2	0.9293	3.2	0.1093	3.0	0.93	101

All analyses were corrected for common Pb; Pbc = Common Pb; iU = initial U; * = not included in the mean age.

Supplementary Table 4. Lu-Hf isotopic data by LA-MC-ICPMS on zircon grains from CP3 rodingite blackwall, Capané ophiolite.

Spot	^{176}Yb/^{177}Hf[a]	±2s	^{176}Lu/^{177}Hf[a]	±2s	^{178}Hf/^{177}Hf	^{180}Hf/^{177}Hf	Sig$_{Hf}$[b]	^{176}Hf/^{177}Hf	±2s[c]	^{176}Hf/^{177}Hf$_{(t)}$[d]	eHf(t)[d]	±2s[c]	T$_{DM}$[e] (Ga)	age[f] (Ma)
78	0.0395	32	0.00147	9	1.467178	1.886677	16	0.282686	23	0.282662	15.0	0.71689	0.79	862
71	0.0499	45	0.00180	13	1.467167	1.886356	15	0.282691	18	0.282664	13.8	0.71681	0.81	808
42	0.0516	43	0.00187	12	1.467178	1.886330	15	0.282726	16	0.282698	15.0	0.71689	0.74	805
76	0.0419	35	0.00157	10	1.467264	1.886841	11	0.282687	18	0.282663	13.7	0.71680	0.81	802
75	0.0388	32	0.00137	9	1.467239	1.886715	15	0.282666	19	0.282646	13.0	0.71675	0.85	800
97	0.0511	46	0.00180	13	1.467197	1.886594	16	0.282677	22	0.282650	13.1	0.71676	0.84	800
83	0.0363	29	0.00137	8	1.467238	1.886278	14	0.282711	18	0.282691	14.6	0.71687	0.76	799
72	0.0471	42	0.00171	12	1.467175	1.886355	19	0.282682	19	0.282656	13.3	0.71678	0.83	799
104	0.0293	24	0.00112	7	1.467237	1.886939	13	0.282676	14	0.282659	13.4	0.71678	0.82	798
38	0.0452	36	0.00162	10	1.467154	1.886609	18	0.282682	19	0.282657	13.3	0.71678	0.82	798
63	0.0463	39	0.00169	11	1.467152	1.886429	15	0.282694	14	0.282669	13.8	0.71681	0.80	799
80	0.0481	40	0.00177	11	1.467201	1.886598	11	0.282727	16	0.282701	14.9	0.71689	0.74	798
81	0.0164	16	0.00061	5	1.467149	1.886668	15	0.282688	23	0.282679	14.1	0.71683	0.78	797
77	0.0443	36	0.00163	10	1.467183	1.886716	16	0.282685	18	0.282661	13.5	0.71679	0.82	798
68	0.0580	53	0.00207	15	1.467210	1.886381	14	0.282710	22	0.282678	14.1	0.71683	0.78	798
45	0.0411	33	0.00149	9	1.467215	1.886787	16	0.282692	17	0.282670	13.8	0.71681	0.80	798
65	0.0643	55	0.00230	15	1.467145	1.887139	16	0.282709	17	0.282675	13.9	0.71682	0.79	797
87	0.0337	27	0.00118	7	1.467197	1.886536	16	0.282683	18	0.282666	13.6	0.71680	0.81	797
67	0.0548	47	0.00203	13	1.467208	1.886439	16	0.282688	18	0.282657	13.3	0.71678	0.82	796
51	0.0438	35	0.00158	10	1.467228	1.886648	18	0.282677	15	0.282653	13.1	0.71676	0.83	796
69	0.0452	36	0.00163	10	1.467167	1.886573	14	0.282697	16	0.282672	13.8	0.71681	0.80	795
107	0.0560	48	0.00201	13	1.467181	1.886300	15	0.282709	22	0.282679	14.1	0.71683	0.78	796
66	0.0592	55	0.00219	16	1.467053	1.886787	16	0.282699	20	0.282666	13.6	0.71680	0.81	795
33	0.0817	66	0.00294	18	1.467228	1.886441	13	0.282722	21	0.282678	14.0	0.71683	0.78	795
73	0.0480	41	0.00175	12	1.467135	1.886427	18	0.282660	15	0.282634	12.4	0.71671	0.87	795
86	0.0506	41	0.00184	11	1.467170	1.886704	17	0.282683	17	0.282656	13.2	0.71677	0.83	795
70	0.0515	42	0.00181	11	1.467224	1.886523	14	0.282690	19	0.282663	13.5	0.71679	0.81	794
37	0.0702	56	0.00250	15	1.467189	1.886500	13	0.282721	20	0.282684	14.2	0.71684	0.77	794
113	0.1182	96	0.00393	24	1.467183	1.886660	19	0.282715	23	0.282657	13.2	0.71677	0.83	794
74	0.0576	46	0.00211	13	1.467211	1.886713	16	0.282722	18	0.282691	14.4	0.71686	0.76	794
61	0.0420	34	0.00154	9	1.467182	1.886096	19	0.282668	18	0.282645	12.8	0.71674	0.85	794
129	0.0549	44	0.00188	11	1.467230	1.886475	13	0.282668	27	0.282640	12.6	0.71673	0.86	793

50	0.0269	22	0.00097	6	1.467217	1.886701	16	0.282653	16	0.282639	12.6	0.71672	0.86	794
40	0.0505	41	0.00179	11	1.467141	1.886520	15	0.282678	14	0.282651	13.0	0.71676	0.84	794
89	0.0653	59	0.00242	17	1.467210	1.886787	16	0.282708	20	0.282672	13.8	0.71681	0.80	793
44	0.0358	29	0.00131	8	1.467156	1.886528	19	0.282670	19	0.282650	13.0	0.71675	0.84	793
29	0.0592	48	0.00213	13	1.467201	1.886623	17	0.282689	16	0.282657	13.2	0.71677	0.83	792
101	0.0810	74	0.00283	20	1.467212	1.886408	13	0.282681	25	0.282639	12.6	0.71672	0.86	793
103	0.0480	39	0.00173	11	1.467182	1.887231	12	0.282700	14	0.282675	13.8	0.71681	0.79	792
34	0.0388	31	0.00146	9	1.467221	1.886748	14	0.282684	23	0.282662	13.4	0.71678	0.82	792
28	0.0491	42	0.00172	12	1.467149	1.886584	13	0.282673	17	0.282648	12.8	0.71674	0.85	789
54	0.0261	21	0.00095	6	1.467203	1.886449	13	0.282673	17	0.282659	13.3	0.71677	0.82	792
23	0.0715	57	0.00257	15	1.467218	1.886494	14	0.282705	15	0.282667	13.5	0.71679	0.81	791
60	0.0581	47	0.00212	13	1.467173	1.886762	15	0.282684	16	0.282652	13.0	0.71675	0.84	790
128	0.0617	57	0.00209	13	1.467205	1.886919	13	0.282688	19	0.282657	13.1	0.71676	0.83	790
49	0.0526	43	0.00197	12	1.467196	1.886840	16	0.282709	16	0.282680	14.0	0.71682	0.78	790
108	0.1589	129	0.00502	30	1.467044	1.886912	16	0.282690	16	0.282616	11.7	0.71666	0.91	790
24	0.0597	48	0.00218	13	1.467173	1.885866	10	0.282704	19	0.282671	13.6	0.71680	0.80	789
52	0.0355	29	0.00131	8	1.467231	1.886670	15	0.282670	17	0.282651	12.9	0.71675	0.84	790
41	0.0395	32	0.00145	9	1.467163	1.886573	18	0.282669	14	0.282648	12.8	0.71674	0.85	790
93	0.0643	59	0.00232	16	1.467209	1.886564	16	0.282724	17	0.282689	14.3	0.71685	0.76	789
84	0.0424	34	0.00150	9	1.467178	1.887066	16	0.282649	22	0.282627	12.0	0.71669	0.89	789
46	0.0603	49	0.00220	13	1.467194	1.886546	17	0.282706	21	0.282673	13.7	0.71680	0.80	789
90	0.0474	39	0.00173	11	1.467175	1.886663	16	0.282697	19	0.282671	13.6	0.71680	0.80	788
55	0.0704	58	0.00259	16	1.467190	1.886788	16	0.282722	14	0.282683	14.0	0.71683	0.78	788
109	0.0418	38	0.00142	9	1.467174	1.886640	15	0.282680	19	0.282659	13.2	0.71677	0.82	788
99	0.0431	36	0.00152	10	1.467190	1.886753	13	0.282664	23	0.282642	12.6	0.71672	0.86	788
64	0.0551	52	0.00199	15	1.467191	1.886886	17	0.282687	19	0.282659	12.6	0.71672	0.84	761
126	0.0579	54	0.00205	12	1.467202	1.886371	14	0.282689	16	0.282659	12.6	0.71672	0.84	761
25	0.0536	43	0.00197	12	1.467239	1.885340	9	0.282705	17	0.282677	13.2	0.71677	0.80	761
105	0.1025	83	0.00346	21	1.467161	1.886583	14	0.282688	32	0.282638	11.8	0.71667	0.88	759
10	0.0719	58	0.00262	16	1.467210	1.886744	13	0.282743	16	0.282706	14.2	0.71684	0.75	759
19	0.0463	37	0.00161	10	1.467184	1.886591	17	0.282679	17	0.282656	12.4	0.71671	0.85	759
2	0.0878	75	0.00309	20	1.467162	1.886688	13	0.282741	41	0.282697	13.9	0.71681	0.76	758
12	0.0537	44	0.00196	12	1.467149	1.887409	13	0.282686	16	0.282658	12.5	0.71671	0.84	757
1	0.0563	49	0.00207	14	1.467142	1.887112	13	0.282698	32	0.282669	12.8	0.71674	0.82	757

6	0.0589	57	0.00220	16	1.467216	1.886799	14	0.282712	32	0.282680	13.3	0.71677	0.80	758
117	0.1098	91	0.00383	24	1.467221	1.886773	12	0.282748	18	0.282693	13.7	0.71680	0.77	758
15	0.0423	34	0.00146	9	1.467198	1.886550	15	0.282670	18	0.282650	12.1	0.71669	0.86	757
26	0.0577	46	0.00214	13	1.467188	1.886511	12	0.282716	15	0.282685	13.4	0.71678	0.79	756
14	0.0508	41	0.00183	11	1.467194	1.886682	12	0.282712	14	0.282686	13.4	0.71678	0.79	754
5	0.0472	39	0.00176	11	1.467257	1.886722	14	0.282712	39	0.282687	13.4	0.71678	0.79	754
7	0.0368	31	0.00134	9	1.467199	1.886643	15	0.282679	21	0.282660	12.5	0.71672	0.84	754
4	0.0547	45	0.00198	12	1.467178	1.886769	13	0.282674	42	0.282646	12.0	0.71668	0.86	755
8	0.0669	59	0.00236	14	1.467217	1.886758	12	0.282732	16	0.282699	13.8	0.71681	0.76	754
16	0.0494	40	0.00178	11	1.467180	1.886458	17	0.282692	17	0.282666	12.7	0.71673	0.83	754
96	0.0591	54	0.00207	15	1.467154	1.886692	13	0.282687	16	0.282659	11.6	0.71665	0.86	717
79	0.0354	29	0.00126	8	1.467174	1.886813	13	0.282666	18	0.282649	11.2	0.71662	0.88	716
94	0.0950	78	0.00311	19	1.467205	1.886760	15	0.282682	17	0.282640	10.8	0.71660	0.90	713

Quoted uncertainties (absolute) relate to the last quoted figure. The effect of the inter-element fractionation on the Lu/Hf was estimated to be about 6% or less based on analyses of the GJ-1 and Plesoviče zircon. Accuracy and reproducibilty were checked by repeated analyses (n = 30 and 20, respectively) of reference zircon GJ-1 and Plesoviče (data given as mean with 2 standard deviation uncertainties).

(a) 176Yb/177Hf = (176Yb/173Yb)true x (173Yb/177Hf)meas x (M173(Yb)/M177(Hf))b(Hf). b(Hf) = ln(179Hf/177Hf true / 179Hf/177Hfmeasured)/ ln M=mass of respective isotope. (M179(Hf)/M177(Hf)). The 176Lu/177Hf were calculated in a similar way by using the 175Lu/177Hf and b(Yb).

(b) Mean Hf signal in volt.

(c) Uncertainties are quadratic additions of the within-run precision and the daily reproducibility of the 40ppb-JMC475 solution. Uncertainties for the JMC475 quoted at 2SD (2 standard deviation).

(d) Initial 176Hf/177Hf and eHf calculated using the apparent Pb-Pb age determined by LA-ICP-MS dating (see column f) and the CHUR parameters: 176Lu/177Hf = 0.0336 and 176Hf/177Hf = 0.282785 (Bouvier et al. 2008).

(e) Two stage model age in billion years using the measured 176Lu/177Hf of each spot (first stage = age of zircon) a value of 0.0113 for the average continental crust (second stage) and an average MORB (DM) 176Lu/177Hf and 176Hf/177Hf of 0.0388 and 0.28325 respectively.

(f) ^{206}Pb/^{238}U age.

Supplementary Table 5. Trace elements data by LA-ICPMS on zircon grains from CP3 rodingite blackwall, Capané ophiolite.

Spot	Y	Th	U	Nb	Sb	Cs	La	Ce	Pr	Nd	Sm	Eu	Gd	Dy	Er	Tm	Yb	Lu	Hf	Ta	Pb	Tb	Ho	Ca	Zn
1	1429	14.66	34.46	3.79	0.42	0.12	0.16	2.02	0.12	2.84	7.93	1.89	40.37	199	290	64	873	72	6568	1.21	1.04	14.61	63.53	2025	0.71
2	1965	23.74	52.63	4.94	0.40	0.12	0.17	2.45	0.26	4.04	10.07	2.44	52.78	269	548	93	1053	98	5965	1.70	1.71	19.39	89.00	2478	<0.30
4	1192	11.19	28.22	3.79	0.38	0.10	0.16	1.90	0.12	1.71	5.73	1.48	31.98	164	235	52	831	59	6312	1.11	0.73	12.05	53.00	3317	0.45
5	1585	20.83	52.70	4.58	0.38	0.11	0.20	2.88	0.20	3.40	9.47	2.15	46.54	223	344	75	903	86	6532	1.87	1.15	16.49	73.83	2896	0.53
6	1923	28.41	76.66	6.22	0.39	0.13	0.17	3.38	0.21	4.37	11.16	2.43	51.71	267	542	98	1027	105	6571	2.24	1.79	19.16	90.03	2894	0.36
7	1233	17.98	50.89	6.46	0.41	0.15	0.19	3.91	0.09	1.28	4.55	1.07	30.50	173	265	60	857	69	7546	2.30	0.58	11.91	57.66	2623	0.34
8	2239	30.37	79.02	6.52	0.39	0.15	0.16	2.93	0.25	4.91	10.90	2.55	56.90	305	565	132	1174	132	6267	2.29	1.92	22.14	113.11	2288	0.34
10	2557	36.42	86.54	7.12	0.37	0.18	0.15	3.02	0.29	4.99	11.89	3.31	71.04	383	530	138	1293	148	5876	2.35	2.43	26.95	146.12	1858	0.56
12	1801	24.33	59.72	5.59	0.42	0.14	0.20	2.96	0.23	4.18	10.85	2.36	48.56	250	479	87	976	94	6423	1.94	1.78	18.31	83.89	2000	0.92
14	1648	20.46	51.84	4.80	0.38	0.10	0.15	2.61	0.20	4.02	10.27	2.19	45.68	226	401	76	895	85	6218	1.71	0.39	16.41	72.88	2817	<0.33
15	1518	24.05	65.17	5.78	0.41	0.13	0.13	4.65	0.10	1.85	5.95	1.50	40.03	218	339	72	871	80	7141	2.18	1.85	15.87	72.03	2304	1.72
16	2022	39.43	111.38	8.14	0.40	0.18	0.22	6.54	0.11	2.73	9.84	2.02	55.08	293	559	108	1057	110	7452	3.09	2.29	20.94	97.45	2419	0.39
19	1855	43.22	114.91	8.19	0.38	0.17	0.17	8.21	0.11	2.12	7.78	1.57	50.23	265	521	97	1005	101	7917	3.39	1.57	18.99	90.78	2182	0.55
23	1812	21.42	46.49	4.86	0.41	0.13	0.21	2.35	0.22	3.72	10.10	2.62	55.95	272	487	84	948	92	5735	1.54	1.59	20.68	84.37	2456	0.94
24	1795	20.10	43.70	5.27	0.38	0.12	0.16	2.50	0.23	4.07	10.14	2.56	55.98	269	469	84	966	91	5610	1.46	1.47	19.98	84.08	2031	0.50
25	1176	21.56	63.62	7.65	0.39	0.17	0.21	3.25	0.15	2.73	5.67	1.44	30.29	163	254	60	852	72	5641	2.71	1.73	11.34	54.08	1716	2.69
26	1775	26.73	75.37	5.84	0.44	0.16	0.23	3.33	0.26	4.64	10.54	2.35	51.78	250	508	90	1013	103	6555	2.41	2.05	18.14	82.06	1773	3.23
28	1590	17.33	38.11	5.99	0.41	0.17	0.43	2.85	0.35	6.12	14.85	3.16	58.16	244	367	72	842	79	5953	1.31	1.40	19.59	72.97	1919	1.66
29	2778	77.63	150.74	13.67	0.40	0.21	0.45	11.83	0.54	8.34	22.86	3.53	98.60	455	652	162	1386	171	8146	5.08	5.37	32.72	155.89	2225	1.36
33	2235	29.11	60.42	6.23	0.36	0.18	0.12	2.73	0.27	5.04	12.80	3.41	73.41	349	565	134	1129	132	5559	1.81	2.15	26.39	128.06	2250	0.78
34	988	15.02	45.37	6.44	0.38	0.14	0.23	2.87	0.13	2.05	4.72	1.18	24.71	131	209	50	783	59	5877	2.19	1.15	9.32	44.92	1422	0.69
37	1981	29.91	79.99	6.33	0.41	0.14	0.15	3.40	0.24	4.44	10.77	2.40	54.57	286	578	112	1062	112	6169	2.17	2.17	20.35	97.82	2365	1.81
38	1573	31.99	101.66	7.45	0.38	0.14	0.12	6.32	0.08	2.12	6.83	1.45	43.76	231	443	81	892	86	7429	2.88	2.36	16.42	75.53	1807	0.81
40	1717	27.27	86.39	5.97	0.43	0.12	0.49	4.68	0.51	7.37	14.78	2.55	59.99	255	475	83	935	90	6724	2.39	2.00	19.72	80.32	2126	1.31
41	1379	18.44	48.12	4.83	0.35	0.15	0.17	3.41	0.07	1.84	5.88	1.47	37.34	198	310	65	802	70	6555	1.50	1.38	14.41	64.03	3517	<0.35
42	1434	17.76	42.50	4.77	0.41	0.11	0.78	2.94	0.54	7.45	14.01	2.71	53.16	216	319	66	828	74	5827	1.47	1.29	16.86	66.39	1851	1.39
44	1236	22.54	78.58	7.45	0.39	0.16	0.14	5.60	0.07	1.26	4.18	0.89	27.86	171	277	63	823	69	7615	2.70	1.66	11.38	57.44	1562	0.45
45	1326	23.63	77.06	7.35	0.38	0.11	0.19	5.40	0.10	1.75	5.15	1.05	33.64	191	311	66	857	73	7139	2.64	1.64	13.41	62.26	1887	<0.35
46	2004	46.39	113.77	12.43	0.38	0.09	0.24	6.66	0.21	4.19	11.00	2.28	55.70	300	553	119	1097	131	6562	4.02	3.39	21.31	101.70	1964	<0.35
49	1783	30.47	97.78	6.35	0.34	0.14	0.14	3.76	0.19	4.23	10.11	2.17	52.23	251	499	96	990	99	6330	2.51	2.31	18.34	84.14	2661	<0.33
50	1128	14.31	40.62	4.89	0.37	0.12	0.15	3.02	0.07	1.37	4.16	1.06	28.04	157	238	54	807	61	6661	1.60	1.38	10.81	51.49	2158	1.08
51	1644	38.63	109.12	10.25	0.37	0.19	0.64	8.43	0.38	3.42	6.97	1.35	42.97	240	482	86	918	93	7416	3.79	2.99	16.85	78.15	1355	2.02

52	1147	12.64	34.40	4.22	0.35	0.11	0.18	2.50	0.07	1.40	4.54	1.18	29.53	164	231	53	808	58	6284	1.26	0.96	11.35	51.63	2918	0.45
54	1663	18.44	43.40	4.62	0.40	0.15	0.17	2.40	0.23	3.72	9.42	2.38	50.51	241	418	77	891	82	5637	1.37	1.27	18.25	76.11	2788	0.42
55	2026	52.82	122.83	9.56	0.39	0.13	0.55	7.33	0.35	4.95	12.51	2.09	62.20	307	499	123	1081	140	7110	3.81	4.12	22.38	113.99	1893	1.20
60	1644	25.42	71.36	5.86	0.36	0.11	0.18	3.75	0.15	3.17	9.23	1.94	49.51	243	503	85	920	91	6339	2.10	1.83	17.77	77.86	2610	0.43
61	1258	13.92	37.18	4.08	0.34	0.17	0.13	2.48	0.08	1.56	5.68	1.37	34.06	179	263	58	776	63	6365	1.27	1.11	12.68	56.01	3213	<0.33
63	1132	21.08	89.91	8.20	0.40	0.12	0.20	3.92	0.16	2.51	6.21	1.36	31.99	167	268	60	825	71	5996	3.19	1.56	11.95	54.14	1935	0.40
64	2002	47.84	115.26	9.14	0.35	0.16	0.22	6.74	0.19	3.62	11.29	2.07	59.68	296	520	136	1080	132	7106	3.57	3.63	21.72	106.11	2221	1.27
65	2164	43.91	110.97	8.72	0.39	0.13	0.18	5.22	0.22	4.65	12.32	2.33	60.63	306	532	140	1151	158	6573	3.17	3.33	21.84	120.34	2086	0.54
66	1773	25.91	83.00	5.66	0.34	0.08	0.24	3.19	0.28	4.45	9.99	2.24	48.59	245	508	96	1023	108	6055	2.19	1.92	17.23	82.10	2325	<0.36
67	3353	87.21	162.79	20.61	0.47	0.15	1.13	14.90	1.38	27.67	57.27	8.01	190.14	536	650	142	1460	149	7300	5.12	6.31	48.97	146.88	1091	4.53
68	1924	49.35	122.05	9.09	0.38	0.13	0.15	7.57	0.14	2.97	10.45	1.81	56.97	286	520	121	1040	122	7120	3.76	3.96	20.81	109.17	1940	0.51
69	1391	21.61	76.00	5.47	0.35	0.13	0.16	3.18	0.15	2.69	7.98	1.73	41.37	205	364	69	831	79	6337	2.08	1.72	14.83	65.15	3107	2.67
70	1197	30.62	87.32	5.71	0.66	0.17	0.77	3.40	0.37	4.69	8.85	2.23	39.52	186	260	59	779	67	5573	1.64	2.24	13.98	57.58	2188	2.06
71	1431	16.12	37.80	4.41	0.36	0.13	0.18	2.39	0.16	2.89	7.46	1.84	40.80	214	335	67	854	73	5737	1.27	1.19	15.36	66.28	2642	<0.36
72	1686	39.23	110.88	7.68	0.37	0.12	0.14	7.34	0.13	2.37	8.02	1.55	49.58	255	487	96	928	98	7404	3.19	2.91	18.74	84.76	2341	0.59
73	1312	25.58	92.53	8.01	0.39	0.11	1.43	6.91	0.65	5.81	6.88	1.22	35.58	192	311	66	799	73	7528	2.94	1.91	13.36	62.76	1870	0.66
74	2099	36.64	105.31	7.93	0.36	0.14	0.27	4.31	0.27	5.04	11.40	2.43	56.14	300	547	144	1137	146	6076	2.81	1.88	21.36	124.55	2315	0.83
75	1014	13.59	36.20	6.04	0.35	0.16	0.29	2.61	0.13	2.03	5.82	1.31	29.79	150	214	50	823	56	6258	1.83	1.01	10.84	47.93	2398	0.97
76	1542	23.06	59.99	6.84	0.37	0.13	0.14	2.87	0.20	3.13	7.54	2.01	44.50	231	409	79	914	86	5426	2.02	1.55	16.34	72.28	1988	0.70
77	1619	26.34	75.45	5.62	0.38	0.18	0.12	4.09	0.11	2.44	8.87	1.84	48.37	238	449	81	920	84	6688	2.13	1.95	17.44	76.16	1378	1.72
78	1348	39.20	112.61	16.43	0.34	0.13	0.42	7.83	0.61	9.22	16.07	2.26	51.50	205	347	69	845	77	7055	5.44	0.95	15.41	62.46	2164	0.98
79	1417	18.58	42.70	4.07	0.29	0.17	0.46	2.66	0.26	3.98	8.82	2.17	45.97	213	345	67	859	72	5686	1.32	1.46	15.96	64.93	2610	2.67
80	1522	19.70	56.19	4.61	0.33	0.13	0.18	2.59	0.19	3.69	9.29	2.13	43.55	218	412	76	890	83	5984	1.61	1.64	15.68	70.15	2062	0.63
81	609	9.02	34.88	6.16	0.35	0.13	0.16	2.50	0.06	0.98	2.52	0.63	14.41	83	138	33	494	39	6357	1.94	0.25	5.68	28.64	2656	<0.34
83	1694	24.01	63.83	5.21	0.34	0.12	0.18	2.94	0.19	4.07	9.92	2.24	48.68	250	468	95	937	94	5769	1.76	1.89	18.09	84.21	2557	<0.34
84	1533	28.66	97.56	6.68	0.31	0.13	0.11	5.86	0.07	2.07	6.57	1.36	42.55	224	446	79	870	81	6951	2.49	1.68	15.82	70.79	1526	0.40
86	1523	68.80	145.95	22.49	0.39	0.16	0.14	9.45	0.10	2.41	6.48	1.39	39.84	227	435	88	934	97	7057	6.81	5.02	15.56	73.88	2001	0.46
87	924	22.91	102.28	13.38	0.35	0.15	0.15	6.09	0.09	1.24	3.77	0.75	22.48	134	215	51	759	60	7420	4.82	1.83	8.88	44.23	1672	<0.37
89	1963	31.02	94.11	6.25	0.36	0.17	0.16	3.48	0.25	4.69	11.39	2.39	55.96	287	498	127	1057	134	6054	2.20	2.27	20.65	109.77	2610	<0.35
90	1323	18.34	51.27	4.66	0.37	0.09	0.20	2.59	0.19	3.80	8.76	1.88	41.56	194	328	66	838	77	6035	1.68	1.34	14.54	61.23	2560	5.48
93	1823	48.39	108.68	27.24	0.36	0.16	0.21	11.32	0.16	2.94	8.15	1.69	47.57	263	556	116	1038	122	6428	6.25	2.84	18.67	90.56	1597	<0.36
94	2025	23.50	57.89	5.73	0.38	0.16	0.96	4.72	0.91	13.46	25.05	4.45	92.47	325	548	106	1013	103	5646	1.86	1.69	25.30	100.28	2611	1.40
97	2223	12.68	40.64	5.99	0.64	0.09	1.73	10.68	4.17	56.07	66.55	10.13	164.76	385	387	69	911	70	6272	1.33	1.02	36.15	88.35	1756	<0.40
99	494	4.35	15.18	3.33	0.29	0.11	0.13	1.27	0.07	0.83	2.12	0.55	11.31	63	102	24	311	28	5915	0.88	0.54	4.39	20.74	4238	0.40

101	4064	22.95	48.22	15.27	0.63	0.16	3.96	17.94	6.47	89.92	127.22	18.39	334.24	724	540	159	1124	155	6137	1.82	0.23	73.65	163.09	1884	3.85
103	1922	29.03	69.69	6.63	0.38	0.16	0.16	2.64	0.18	4.21	11.25	2.78	63.53	298	562	110	1021	113	5444	1.69	2.45	22.67	101.41	2571	2.33
104	696	8.22	31.35	6.10	0.44	0.20	0.37	2.06	0.19	2.14	3.39	0.82	17.82	100	157	38	617	44	6045	2.73	0.67	6.81	32.38	2201	0.76
105	1841	35.57	100.46	7.36	0.38	0.11	0.56	5.20	0.28	4.93	11.58	2.07	55.50	270	465	115	995	123	6329	2.70	2.66	19.58	100.58	2051	<0.38
107	2576	17.38	41.12	4.44	0.48	0.14	0.69	7.74	3.27	53.26	85.01	10.33	205.44	589	554	115	975	91	5782	1.27	1.33	48.55	152.20	2473	<0.36
109	1166	12.73	33.76	4.21	0.39	0.14	0.23	2.37	0.09	1.93	5.90	1.54	35.00	179	257	57	760	63	6209	1.13	0.89	12.75	54.17	2408	0.39
113	5692	287.32	444.18	40.73	0.84	0.14	3.10	40.03	2.23	27.45	53.33	7.13	224.97	819	1057	226	2746	236	7748	11.93	28.41	74.89	234.73	1128	4.09
117	1861	54.48	111.48	19.68	0.46	0.15	0.88	7.48	1.02	17.37	32.44	5.06	97.23	343	509	122	1021	138	5603	13.17	4.36	26.78	104.78	1673	1.28
128	1888	25.38	60.00	5.41	0.35	0.13	0.13	2.64	0.26	4.40	11.48	2.76	61.55	306	532	117	1024	116	5602	1.64	2.01	22.25	107.53	1814	1.57
129	1388	31.39	108.07	19.43	0.53	0.12	0.30	8.04	0.49	8.88	20.45	2.58	62.29	238	375	73	839	84	7114	8.52	2.57	18.61	71.88	1013	2.76

All in ppm.

Gmail **Karine Arena <karinearena@gmail.com>**

IJES-D-17-00418 : Submission Confirmation for Geochemistry and δ11B evolution of tourmaline from tourmalinite as a record of oceanic crust in the Tonian Ibaré ophiolite, southern Brasiliano Orogen

1 mensagem

Editorial Office, IJES <em@editorialmanager.com> 17 de outubro de 2017 15:05
Responder a: "Editorial Office, IJES" <monikadullo@online.de>
Para: Karine da Rosa Arena <karinearena@gmail.com>

Dear Dr Arena,

Your submission entitled "Geochemistry and δ11B evolution of tourmaline from tourmalinite as a record of oceanic crust in the Tonian Ibaré ophiolite, southern Brasiliano Orogen" has been received by journal International Journal of Earth Sciences

The submission id is: IJES-D-17-00418
Please refer to this number in any future correspondence.

You will be able to check on the progress of your paper by logging on to Editorial Manager as an author. The URL is http://ijes.edmgr.com/.

Thank you for submitting your work to this journal.

Kind regards,

International Journal of Earth Sciences

Now that your article will undergo the editorial and peer review process, it is the right time to think about publishing your article as open access. With open access your article will become freely available to anyone worldwide and you will easily comply with open access mandates. Springer's open access offering for this journal is called Open Choice (find more information on www.springer.com/openchoice). Once your article is accepted, you will be offered the option to publish through open access. So you might want to talk to your institution and funder now to see how payment could be organized; for an overview of available open access funding please go to www.springer.com/oafunding.
Although for now you don't have to do anything, we would like to let you know about your upcoming options.

International Journal of Earth Sciences

Geochemistry and δ11B evolution of tourmaline from tourmalinite as a record of oceanic crust in the Tonian Ibaré ophiolite, southern Brasiliano Orogen

--Manuscript Draft--

Manuscript Number:	
Full Title:	Geochemistry and δ11B evolution of tourmaline from tourmalinite as a record of oceanic crust in the Tonian Ibaré ophiolite, southern Brasiliano Orogen
Article Type:	Original Paper
Keywords:	Tourmalinite; Boron isotopes; Geochemistry; Ibaré ophiolite; Southern Brasiliano Orogen
Corresponding Author:	Karine da Rosa Arena Universidade Federal do Rio Grande do Sul Porto Alegre, Rio Grande do Sul BRAZIL
Corresponding Author Secondary Information:	
Corresponding Author's Institution:	Universidade Federal do Rio Grande do Sul
Corresponding Author's Secondary Institution:	
First Author:	Karine da Rosa Arena
First Author Secondary Information:	
Order of Authors:	Karine da Rosa Arena
	Léo Afraneo Hartmann, Doctor in Geology
	Cristiano de Carvalho Lana, PhD
	Gláucia Nascimento Queiroga, Doctor in Science
	Marco Paulo de Castro, Master of Science
Order of Authors Secondary Information:	
Funding Information:	
Abstract:	The isotopic and geochemical evolution of tourmaline constrain the evolution of paleo-oceanic lithosphere in ophiolites. The Brasiliano Orogen is a major structure of South America and requires characterization for the understanding of Gondwana supercontinent evolution. We made a pioneering investigation of tourmaline from a tourmalinite in the Ibaré ophiolite by integrating field work with chemical analyses of tourmaline by electron microprobe (EPMA) and δ11B determinations via laser ablation inductively coupled plasma mass spectrometer (LA-ICP-MS). Remarkably massive tourmalinite (>90 vol.% tourmaline, some chlorite) enclosed in serpentinite has homogeneous dravite in chemical and isotopic composition (δ11B = +3.5 to +5.2‰). These results indicate a geotectonic environment in the altered oceanic crust for the origin of the tourmalinite. This first δ11B characterization of tourmaline from tourmalinite sets limits to the evolution of the Neoproterozoic Brasiliano Orogen and Gondwana evolution.

Geochemistry and δ^{11}B evolution of tourmaline from tourmalinite as a record of oceanic crust in the Tonian Ibaré ophiolite, southern Brasiliano Orogen

K.R. Arena[1], L.A. Hartmann[1], C. Lana[2], G.N. Queiroga[2], M.P. Castro[2]

[1]Instituto de Geociências, Universidade Federal do Rio Grande do Sul, Avenida Bento
Gonçalves, 9500; 91501-970 Porto Alegre, Rio Grande do Sul, Brazil
[2]Departamento de Geologia, Escola de Minas, Universidade Federal de Ouro Preto,
Morro do Cruzeiro; 35400-000 Ouro Preto, Minas Gerais, Brazil

E-mail addresses:
Karine da Rosa Arena karinearena@gmail.com
Léo Afraneo Hartmann leo.hartmann@ufrgs.br
Cristiano de Carvalho Lana cris.lana@pq.cnpq.br
Gláucia Nascimento Queiroga glauciaqueiroga@yahoo.com.br
Marco Paulo de Castro marco_pcastro@yahoo.com

Abstract

The isotopic and geochemical evolution of tourmaline constrain the evolution of paleo-oceanic lithosphere in ophiolites. The Brasiliano Orogen is a major structure of South America and requires characterization for the understanding of Gondwana supercontinent evolution. We made a pioneering investigation of tourmaline from a tourmalinite in the Ibaré ophiolite by integrating field work with chemical analyses of tourmaline by electron microprobe (EPMA) and δ^{11}B determinations via laser ablation inductively coupled plasma mass spectrometer (LA-ICP-MS). Remarkably massive tourmalinite (>90 vol.% tourmaline, some chlorite) enclosed in serpentinite has homogeneous dravite in chemical and isotopic composition (δ^{11}B = +3.5 to +5.2‰). These results indicate a geotectonic environment in the altered oceanic crust for the origin of the tourmalinite. This first δ^{11}B characterization of tourmaline from tourmalinite sets limits to the evolution of the Neoproterozoic Brasiliano Orogen and Gondwana evolution.

Keywords: Tourmalinite, Boron isotopes, Geochemistry, Ibaré ophiolite, Southern Brasiliano Orogen

Introduction

Tourmaline is a most useful mineral because it is robust and can retain a record of geological processes (van Hinsberg et al. 2011). The mineral is helpful for the understanding of both continental (Chaussidon and Albarède 1992; Trumbull et al. 2008; Cabral et al. 2017) and oceanic (Smith et al. 1995; Farber et al. 2015) settings.

Most studies focused on accessory tourmaline in granitic and volcanic-sedimentary rocks, in addition to sulphide ore (e.g., Namaqualand, South Africa - Plimer 1987; Sullivan, British Columbia – Palmer and Slack 1989; Broken Hill, Australia – Slack et al. 1993). Fewer studies concentrated on oceanic lithosphere, including crust and mantle or unravelling of volatile transfer processes from the subduction setting to the mantle wedge and to arc magmatism (Palmer 1991; Rosner et al. 2003; Savov et al. 2005; Boschi et al. 2008; Yamaoka et al. 2012). In Brazil, stratiform tourmalinite occurs associated to mineralized quartz-tourmaline vein in the Mesoproterozoic Serra do Itaberaba (Ribeira belt, SE Brazil - Garda et al. 2009). Tourmaline was also described in pegmatites (Borborema Province, NE Brazil –

Trumbull et al. 2013) and as platiniferous gold–tourmaline aggregates (Gold–palladium belt of Minas Gerais, Brazil – Cabral et al. 2017).

Tourmaline (geochemistry, $\delta^{11}B$) was only studied in continental rocks in the continent. In the Brasiliano Orogen, Neoproterozoic ophiolites were only studied with zircon U-Pb isotopes in the Araçuaí Belt (oceanic plagiogranite – Queiroga et al. 2007) and Dom Feliciano Belt (albitite, chloritite, tourmalinite, rodingite blackwall – Arena et al. 2016, 2017a, b). Tourmalines from ophiolites were not studied.

We selected a massive tourmalinite (>90 vol.% tourmaline) from southern Brazil, because the rock is part of the Ibaré ophiolite. The sample was previously investigated with zircon U-Pb-Hf isotopes by Arena et al. (2017a). Large (5-30 m diameter) tourmalinites remain undescribed in the oceanic crust or ophiolites, so this is a pioneering investigation of mantle interaction with oceanic water in the Tonian.

The tourmalinite was described in the field and large tourmaline crystals (up to 10 cm) were studied by EPMA for major elements and LA-ICP-MS for $\delta^{11}B$. The results indicate a remarkably homogeneous dravite, including boron isotopes ($\delta^{11}B$ = +3.5 to +5.2‰). We interpret the tourmalinite as formed in the Tonian oceanic crust by alteration of mantle rocks in contact with oceanic water. This characterization of the geotectonic environment may have large impact on studies of the Brasiliano Orogen in the continent and reconstruction of Rodinia and Gondwana.

Geological setting

The Ibaré ophiolite from the São Gabriel terrane is part of the Dom Feliciano Belt, southern Brasiliano Orogen (Figs. 1a, b). The formation of the Dom Feliciano Belt involved the closure of the Adamastor Ocean. Corresponding subduction events resulted in the development of two intra-oceanic arcs in the São Gabriel terrane at the pre-collisional stage of the Brasiliano orogenic cycle (Machado et al. 1990; Leite et al. 1998; Remus et al. 1999; Gubert et al. 2016; Arena et al. 2017a) with subsequent ophiolite emplacement (Arena et al. 2016, 2017a). The Capané ophiolite occurs in the eastern portion of Dom Feliciano Belt (Fig. 1b) and has similar age to the São Gabriel terrane (e.g., Arena et al. 2017b). This ophiolite was emplaced into the Porongos fold and thrust belt (Pertille et al. 2015, 2017).

The main geological units of the São Gabriel terrane formed early in the Brasiliano Orogen (948 Ma to 660 Ma; Chemale et al. 1995; Babinski et al. 1996; Leite et al. 1998; Saalmann et al. 2005a, b; Hartmann et al. 2011; Lena et al. 2014; Lopes et al. 2015; Arena et al. 2016). The studied tourmalinite is part of the Ibaré ophiolite (Arena et al. 2017a), associated with volcano-sedimentary rocks which are remnants of a Neoproterozoic intra-oceanic arc.

The Ibaré ophiolite and associated rocks (Figs. 1b, 2a) show evidence of regional greenschist facies metamorphism strongly overprinted by contact metamorphism caused by the intrusion (Naumann and Hartmann 1984; Naumann 1985) of the Santa Rita Granite (584.7 ± 1.9 Ma - Arena et al. 2017a). Zircon U-Pb-Hf isotopic and geochemical characteristics of the Ibaré tourmalinite (Arena et al. 2017a) indicate the beginning of metasomatism at 880 Ma, culminating with the ophiolite emplacement at 722 Ma into intra-oceanic arc in subduction-zone setting along the margins of the Rio de la Plata craton.

Sample description

Within the Ibaré ophiolite, massive tourmalinite (>90 vol.% tourmaline) is associated with chloritite, serpentinite, magnesian schist, rodingite, and albitite (Naumann 1985; Arena et al. 2016, 2017a). Santa Rita Granite intruded the ophiolite in the northern portion and a small plug of the Jaguari Granite in the southern portion. The studied tourmalinite (2 x 5 m large) occurs immersed in chloritite and serpentinite (Figs. 2b, c). Black color of tourmalinite is distinctive and contrasts with serpentinite and the surrounding chloritite blackwall. The tourmalinite is composed of tourmaline, chlorite, some ilmenite and zircon.

Analytical methods

Field study of the Ibaré ophiolite included collection of selected tourmalinite IB14 sample. Petrography of the tourmalinite preceded the determination of chemical and boron isotopic analyses of tourmaline. Petrography was done with a transmission petrographic microscope Olympus BX51, UC30. One polished thin section of the sample was studied for elemental mapping of tourmaline by electron microprobe at Laboratório de Microssonda Eletrônica, Universidade Federal do Rio Grande do Sul. A block was cut from the massive tourmalinite sample (Figs. 2d, e) and measures 10 cm in length by ~1.5 cm in width. The block was divided into parts and placed in 5 mounts in sequential order, each measuring 2 cm x 1.5 cm (Fig. 2f). Mounts from tablets 3 and 4 (Figs. 2f, 3a, b) were selected for analyses by scanning electron microprobe and boron isotopes at Departamento de Geologia, Universidade Federal de Ouro Preto (UFOP), Minas Gerais. All these spot analyses were controlled by backscattered electron images (Fig. 3).

Electron Microprobe

Electron microprobe analyses of mounted tourmalines were performed at UFOP using a JEOL JXA-8230 Superprobe equipped with 5 spectrometers. Operating conditions were 15 kV accelerating voltage, 20 nA beam current and 10 μm beam diameter and a selection of measurement spots ensured that the stimulated volume was not contaminated by phases other than tourmaline. Counting times on the peaks/background were 10/5 s for all elements. Background intensities were collected at higher and lower energies relative to the corresponding Kα line. Appropriate natural and synthetic reference materials were used for calibration (Online Appendix 1). Tourmaline structural formulae were calculated by normalizing to 15 cations in the tetrahedral and octahedral sites (T + Z + Y) and assuming 3 boron apfu (Henry et al. 2011) using the Excel spreadsheet of Tindle et al. (2002).

Boron isotopes

Boron isotope ratio measurements were carried out at UFOP on a Thermo-Scientific Neptune Plus multi-collector ICP-MS coupled to a Photon Machines 193 Excimer laser ablation system. Samples were abladed in He atmosphere using 20 um diameter spot and 15 Hz frequency at 7 J/cm2. In the mass spectrometer, ^{10}B and ^{11}B intensities were measured (in low resolution) on the L2 and H2 detectors, respectively. The measurements consisted of 98 cycles (or integration) and 0.5 s of integration time. Data were processed after the daily run using an in-house spreadsheet by A. Gerdes (e.g., Devulder et al. 2015). The measured, background signal of the unknown sample was corrected for instrumental mass fractionation (IMF) using a standard-sample bracketing method and tourmaline B4 (schorl, δ^{11}B = -8.62 ‰) (Tonarini et al. 2003) as the primary reference material. The drift-corrected ratios were referenced to the published ^{11}B/^{10}B value of the reference material and the results are reported as δ^{11}B values relative to NIST SRM 951 boric acid using the certified ^{11}B/^{10}B value of 4.04362 ± 0.00137 (Catanzaro et al. 1970). Matrix effects, known to occur in B isotope measurements (e.g., Mikova et al. 2014) and the reproducibility of the data were monitored during the analyses using dravite (#108796) and elbaite (#98144) (Leeman and Tonarini 2001) as external reference material (Online Appendix 2). The observed internal precision for individual analyses varied between 0.3 and 0.9‰.

Results

Representative electron microprobe analyses of tourmaline are listed in Online Appendix 3. All analyzed points (n = 60) in tourmaline showed chemical homogeneity. We made 21 analyses in two basal sections of individual tourmaline grains (Figs. 3c, d), 11 random tourmaline analyses (Fig. 3d) and 28 analyses along a tourmaline of approximately 20 mm length (Fig. 3e). They show a range in MgO from 7.16 to 8.64 wt.%, FeO from 6.25 to 7.76 wt.%; CaO from 0.22 to 0.49 wt.% and Na_2O from 2.54 to 2.80 wt.%.

The basic formula of tourmaline can be written as XY_3Z_6 $(T_6O_{18})(BO_3)$ V3W, where X = Na, Ca, K, vacancy; Y = Fe^{2+}, Mg, Mn^{2+}, Li, Al, Cr^{3+}, V^{3+}, Fe^{3+}, Ti^{4+}; Z = Mg, Al, Fe^{3+}, V^{3+},Cr^{3+}; T = Si, Al, (B); V = OH, O; W = OH, F, O (Hawthorne and Henry, 1999). Chemical substitutions in tourmaline occur mainly in the X, Y and Z sites (Henry and Guidotti 1985). Some Al defficiency (<6 atoms per formula unit) in the Z site is due to Mg substitution and no Fe^{3+}. In addition, the X site occupancy is predominantly Na. The tourmaline is close dravite in composition (Online Appendix 3). Tourmalines show no chemical zoning (e.g., Fig. 4). Tourmalines are of alkali group (Na + K dominant at X site) and Mg-rich (Figs. 5a, b). The array is most consistent with operation of the $MgFe^{2+}_{-1}$ substitution (Figs. 6a, b).

The studied IB14 tourmalines show homogenous isotopic compositions ranging from $\delta^{11}B$ = +3.5 to +5.2‰ (Fig. 8b, Table 1).

Discussion

Dravite from Ibaré tourmalinite (IB14 sample) is Mg-rich and shows homogeneous chemistry and isotopic composition, $\delta^{11}B$ = +3.5 to +5.2‰. Because tourmalinites may also form during regional and contact metamorphism, careful evaluation is necessary to determine their origin relative to hydrothermal, metamorphic and granitic process. Particular care is required for the identification of processes in the oceanic realm.

A previous study of metasomatic zircon from sample IB14 indicated positive εHf = +12.06 to +4.54 over time, a signature interpreted as MORB fluid source (Arena et al. 2017a). Most intense processes of zircon formation occurred at 722 Ma.

The Jaguari (569 ± 6 Ma; Gastal et al. 2015) and Santa Rita (584.7 ± 1.9 Ma; Arena et al. 2017a) granites (Fig. 2) were possible sources in case tourmalinization occurred in the continent, after the emplacement of the ophiolite. Our results discard this hypothesis. Tourmaline in most granites and pegmatites in the continents has $\delta^{11}B$ values close to average continental crust ($\delta^{11}B = -10 \pm 3$‰; Marschall and Jiang 2011). Besides, tourmaline compositions in granitic rocks plot in fields 1 to 3 (Figs. 7a, b). In contrast, IB14 tourmalines plot in field 6 on Al–Fe–Mg(total) and Ca-Fe-Mg(total) diagrams (Henry and Guidotti 1985), unrelated to granitic rocks.

Chemistry of tourmalinite from seafloor volcano-exhalative activity (Beljavskis et al. 2005) shows that distal tourmalines plot into field 6 and proximal tourmalines overlap fields 2, 4 and 5 (Fig. 7a). In Figure 7b, distal tourmalines plot in field 7 reflecting high CaO content. Boron isotope compositions of tourmaline (Garda et al. 2009) in Ribeira belt tourmalinites previously studied by Beljavskis et al. (2005), showed $\delta^{11}B$ = −7.51 to −14.58‰. This evidences chemical and isotopic differences from the Ibaré tourmalinite (Figs 7a, b, 8b).

Tourmalines from Borborema pegmatites (Trumbull et al. 2013) overlap fields 5 and 6 on Al–Fe–Mg diagram (Fig. 7a); on Ca-Fe-Mg diagram (Fig. 7b), they overlap fields 1, 2 and 6 because of their preserved source chemical signature from surrounding rocks. The full range of $\delta^{11}B$ is −20.2 to +1.6‰ with main range −17 to −9‰ (Fig. 8b). Trumbull et al. (2013) suggest that the strong isotopic contrast between the main range and the heavy B resulted from mixing with enclosing marble and calc-silicate rocks. It is significant that the origin of IB14 tourmaline was unrelated to granitic fluids. Ibaré tourmaline is Mg-rich but no associated sedimentary or exhalative rocks were identified. Tourmalines from many environments are strongly zoned and varied in trace elements and boron isotopes, but IB14 tourmaline is chemically homogeneous (Figs. 4, 7, 8). The uniformity in composition of IB14 tourmalines is highlighted by comparison with tourmalines from tourmalinites associated with augen gneiss, leucogranite and garnet-micaschist (Fig. 7a, b) (Menderes Massif, Turkey - Yücel-Öztürk et al. 2015).

In hydrothermal systems (Slack et al. 1993), Mg-rich tourmalines may form either by pre-metamorphic replacement from seawater-derived fluids under high fluid/rock conditions, or by sulfide-silicate reactions during metamorphism. Our results are more consistent with seawater-derived fluids. The IB14 dravites are interpreted as formed from entrained seawater (Slack and Trumbull 2011) (Fig. 7c) which caused serpentinization and subsequent tourmalinization.

The IB14 dravite has boron isotope composition ($\delta^{11}B$ = + 3.5 to +5.2 ‰) typical of blackwall metasomatism between altered oceanic crust and serpentinite. The tourmalinite formed below the seawater-sediment (or volcanic) interface with no exhalative component (closely associated or in contact with chemical sediments such as metachert and iron-formation) as described by Slack et al. (1993). This is in agreement with the values of modern bulk oceanic crust (Fig. 8a) by Farber et al. (2015), which ranges between +3.7‰ and +7.9‰ (Smith et al. 1995; Yamaoka et al. 2015). The B isotope composition of IB14 tourmalinite is more enriched in δ^{11}B than the slab materials from which they likely originated (δ^{11}B MORB = −3‰ to −14‰, average −7.1‰; Chaussidon and Jambon 1994; Marschall et al. 2017). This enrichment indicates that hydrothermal marine fluids altered bulk oceanic crust in the Ibaré tourmalinite. The boron concentration of fresh MORB has a δ^{11}B value of −7‰, but when circulating seawater interacts with ocean crust at ~100 °C, then the boron is taken up into secondary minerals. Compilations of ocean cores and ophiolite sections give average boron contents of δ^{11}B = +3‰ for the upper oceanic crust (Smith et al. 1995) and the upper mantle may be altered to serpentinite by circulating seawater, particularly at slow-spreading mid-ocean ridges (Palmer 2017).

The boron isotope composition of the oceanic crust is the result of crust interaction with seawater, through capture of boron during hydrothermal alteration (Spivack and Edmond 1987; Smith et al. 1995). The average δ^{11}B calculated for altered oceanic crust is +3.7‰ (Smith et al. 1995) while serpentinite shows δ^{11}B values ranging between +8 (Boschi et al. 2008) and +15.1‰ (Benton et al. 2001). An increase in heavy δ^{11}B values (+20‰; Harvey et al. 2014) occurs by interaction with hot hydrothermal fluids at low pH in deeper levels of the oceanic crust (Seyfried and Ding 1995). Tourmaline from some geological settings may carry B enriched in ^{11}B (Table 2).

The range in sediments is typically negative (except carbonates from +13.3‰ to +31.9‰, Hemming and Hönisch 2007). The older marine sediments analyzed by Ishikawa and Nakamura (1993) showed δ^{11}B values between −17‰ and −5.6‰, systematically lower than modern sediments.

An evaluation is made of the mobility of boron in subduction-zone environments to test the hypotheses of origin of Ibaré tourmalinite. Boron isotopes can be used to unravel transfer processes from the subducting oceanic crust to the mantle wedge and to arc magmatism (Palmer 1991; Ishikawa and Tera 1999; Rosner et al. 2003; Savov et al. 2005). Studies by Ishikawa and Tera (1999) suggested a central role of altered oceanic crust and sediments as sources of fluids and boron in subduction zones. Additionally, Savov et al. (2005) and Tonarini et al. (2007) showed the potential role of subducted serpentinites as an important source of B-rich fluids to supra-subduction setting. Peacock and Hervig (1999) suggest that subduction-zone metamorphic dehydration reactions decrease the δ^{11}B value of subducted altered oceanic crust as well as subducted sediments through continuous dehydration reactions (Table 2). Boron uptake in oceanic rocks occurs by direct incorporation of boron during crystallization of structurally favorable, B-rich hydrothermal-diagenetic minerals (phyllosilicates - Williams et al. 2001) or by adsorption from seawater by secondary minerals such as clays and during low-temperature interaction of fluids with crustal, mantle and sedimentary rocks (You et al. 1996). Chemical and boron isotopic characteristics of subduction-zone mobility of elements were not observed in Ibaré samples.

The isotopic and geochemical characteristics of IB14 dravite indicate parental fluid sourced from seawater. Lithospheric mantle was intensely metasomatised by large volumes of fluids during associated serpentinization (Fig. 8b). The characteristic depleted mantle composition of zircon contained in the tourmalinite and chloritite (Arena et al. 2017a) supports the derivation of studied tourmaline from altered oceanic crust.

We envisage a geological history of the Ibaré ophiolite starting with oceanic crust formation in the Tonian during initial rupturing of Rodinia. Intense alteration of oceanic crust and mantle by interaction with heated oceanic water produced an association of serpentinite, chloritite blackwall and massive tourmalinite. This association was later accreted to an island-arc with little additional alteration of the tourmaline, which remained homogeneous in chemistry and boron isotopes. The characterization of the paleo-oceanic crust and mantle in the Ibaré ophiolite through the study of tourmalinite is most useful for the understanding of processes related to Rodinia rupturing and Gondwana assembly.

Conclusion

Dravite with no chemical zoning and with homogeneous isotopic composition ($\delta^{11}B$ = +3.5 to +5.2‰.) strengthens previous studies of mantle origin for intensely metasomatized Ibaré ophiolite. Tourmalines originated during formation of Neoproterozoic Brasiliano Orogen in oceanic altered crust prior to subduction and ophiolite obduction. Characterization of tourmalinite in Ibaré ophiolite is important to interpretations of geodynamic evolution of the southern Brasiliano Orogen.

Acknowledgements

This study is part of the PhD thesis by Karine da Rosa Arena at Programa de Pós-Graduação em Geociências, Universidade Federal do Rio Grande do Sul, Brazil. Karine held a scholarship during her PhD research from CNPq - Conselho Nacional do Desenvolvimento Científico e Tecnológico. Financial support was provided by grant from FAPERGS - Fundação de Amparo à Pesquisa do Estado do Rio Grande do Sul to Léo A. Hartmann.

References

Arena KR, Hartmann LA, Lana C (2016) Evolution of Neoproterozoic ophiolites from the southern Brasiliano Orogen revealed by zircon U-Pb-Hf isotopes and geochemistry. Precambrian Research 285:299–314. doi:10.1016/j.precamres.2016.09.014

Arena KR, Hartmann LA, Lana C (2017a) Tonian emplacement of ophiolites in the southern Brasiliano Orogen delimited by U-Pb-Hf isotopes of zircon from metasomatites. Gondwana Research 49:296-332. doi:10.1016/j.gr.2017.05.018

Arena KR, Hartmann LA, Lana C (2017b) U–Pb–Hf isotopes and trace elements of metasomatic zircon delimit the evolution of neoproterozoic Capané ophiolite in the southern Brasiliano Orogen. International Geology Review. doi.org/10.1080/00206814.2017.1355269

Babinski M, Chemale JrF, Hartmann LA et al (1996) Juvenile accretion at 750–700 Ma in Southern Brazil. Geology 24:439–442. doi.org/10.1130/0091-7613(1996)024<0439:JAAMIS>2.3.CO;2

Beljavskis P, Garda GM, Mansueto MS, Silva D (2005) Turmalinitos vulcanogênicos da Formação Morro da Pedra Preta do Grupo Serra do Itaberaba (SP): Petrografia, composição química da turmalina e implicações metalogenéticas. Geologia USP–Série Científica 5:1–18. doi.org/10.5327/S1519-874X2005000100001

Benton LD, Ryan JG, Tera F (2001) Boron isotope systematics of slab fluids as inferred from a serpentine seamount, Mariana forearc. Earth and Planetary Science Letters 187: 273–282. doi.org/10.1016/S0012-821X(01)00286-2

Boschi C, Dini A, Früh-Green GL, Kelley DS (2008) Isotopic and element exchange during serpentinization and metasomatism at the Atlantis Massif (MAR 30°N): insights from B and Sr isotope data. Geochimica et Cosmochimica Acta 72:1801–1823. doi.org/10.1016/j.gca.2008.01.013

Cabral AR, Tupinambá M, Zeh A et al (2017) Platiniferous gold–tourmaline aggregates in the gold–palladium belt of Minas Gerais, Brazil: implications for regional boron metasomatism. Mineralogy and Petrology. doi 10.1007/s00710-017-0496-0

Catanzaro EJ, Champion CE, Garner EL et al (1970) Standard reference materials: boric acid; isotopic and assay standard reference materials. U.S. National Bureau of Standards, Special Publication 260–17, 70

Chemale JrF, Hartmann LA, da Silva LC (1995) Stratigraphy and tectonism of the Brasiliano Cycle in southern Brazil. Communs geol. Surv. Namibia 10:153–168

Chemale JrF, Philipp RP, Dussin AI et al (2011) Lu–Hf and U–Pb age determination of Capivarita Anorthosite in the Dom Feliciano Belt, Brazil. Precambrian Research 186:117–126. doi.org/10.1016/j.precamres.2011.01.005

Chaussidon M, Albarède F (1992) Secular boron isotope variations in the continental crust: an ion microprobe study. Earth and Planetary Science Letters 108:229–241. doi.org/10.1016/0012-821X(92)90025-Q

Chaussidon M, Jambon A (1994) Boron content and isotopic composition of oceanic basalts: geochemical and cosmochemical implications. Earth and Planetary Science Letters 121:277–291. doi.org/10.1016/0012-821X(94)90073-6

Devulder V, Gerdes A, Vanhaecke F, Vanhaecke P (2015) Validation of the determination of the B isotopic composition in Roman glasses with laser ablation multi-collector inductively coupled plasma-mass spectrometry. Spectrochimica Acta Part B 105:116–120. doi.org/10.1016/j.sab.2014.08.038

Farber K, Dziggel A, Trumbull RB et al (2015) Tourmaline B-isotopes as tracers of fluid sources in silicified Palaeoarchaean oceanic crust of the Mendon Formation, Barberton greenstone belt, South Africa. Chemical Geology 417:134–147. doi.org/10.1016/j.chemgeo.2015.10.009

Garda GM, Trumbull RB, Beljavskis P, Wiedenbeck M (2009) Boron isotope composition of tourmalinite and vein tourmalines associated with gold mineralization, Serra do Itaberaba Group, central Ribeira Belt, SE Brazil. Chemical Geology 264:207–220. doi.org/10.1016/j.chemgeo.2009.03.013

Gastal MC, Ferreira FJF, Cunha JU et al (2015) Alojamento do granito Lavras e a mineralização aurífera durante evolução de centro vulcano-plutônico pós-colisional, oeste do Escudo Sul-riograndense: dados geofísicos e estruturais. Brazilian Journal of Geology 45:217–241. doi.org/10.1590/23174889201500020004

Gubert ML, Philipp RP, Basei MAS (2016) The Bossoroca Complex, São Gabriel Terrane, Dom Feliciano Belt, southernmost Brazil: U-Pb geochronology and tectonic implications for the neoproterozoic São Gabriel Arc. Journal of South American Earth Sciences 70:1–17. doi.org/10.1016/j.jsames.2016.04.006

Hartmann LA, Philipp RP, Santos JOS, McNaughton NJ (2011) Time frame of the 753–680 Ma juvenile accretion during the São Gabriel orogeny, southern Brazilian Shield. Gondwana Research 19:84–99. doi.org/10.1016/j.gr.2010.05.001

Harvey J, Savov IP, Agostini S et al (2014) Si-metasomatism in serpentinized peridotite: the effects of talc-alteration on strontium and boron isotopes in abyssal serpentinites from Hole 1268a, ODP Leg 209. Geochimica et Cosmochimica Acta 126:30–48. doi.org/10.1016/j.gca.2013.10.035

Hawthorne FC, Henry DJ (1999) Classification of the minerals of the tourmaline group. European Journal of Mineralogy 11:201–215. doi:10.1127/ejm/11/2/0201

Hemming NG, Hõnisch B (2007) Boron isotopes in marine carbonate sediments and the pH of the ocean. Developments in Marine Geology 1:717–734. doi10.1016/S1572-5480(07)01022-6

Henry DJ, Guidotti CV (1985) Tourmaline as a petrogenetic indicator mineral: an example from the staurolite-grade metapelites of NW Maine. American Mineralogist 70:1–15

Henry DJ, Novák N, Hawthorne FC et al (2011) Nomenclature of the tourmaline-supergroup minerals. American Mineralogist 96:895–913. doi: 10.2138/am.2011.3636

Ishikawa T, Nakamura E (1993) Boron isotope systematics of marine sediments. Earth and Planetary Science Letters 117:567-580. doi.org/10.1016/0012-821X(93)90103-G

Ishikawa T, Tera F (1999) Two isotopically distinct fluid components involved in the Mariana arc: evidences from Nb/B ratios and B, Sr, Nd, and Pb isotopes systematics. Geology 27:83–86. Doi: 10.1130/0091-7613(1999)027<0083:TIDFCI>2.3.CO;2

Leeman WP, Tonarini S (2001) Boron isotopic analysis of proposed borosilicate mineral reference samples. Geostandards and Geoanalytical Research 25:399–403. doi: 10.1111/j.1751-908X.2001.tb00614.x

Leite JAD, Hartmann LA, McNaughton NJ, Chemale JrF (1998) SHRIMP U/Pb zircon geochronology of Neoproterozoic juvenile and crustal-reworked terranes in southernmost Brazil. International Geology Review 40:688–705. doi.org/10.1080/00206819809465232

Lena LOF, Pimentel MM, Philipp RP et al (2014) The evolution of the Neoproterozoic São Gabriel juvenile terrane, southern Brazil based on high spatial resolution U-Pb ages and $\delta^{18}O$ data from detrital zircons. Precambrian Research 247:126–138. doi.org/10.1016/j.precamres.2014.03.010

Lopes CG, Pimentel MM, Philipp RP et al (2015) Provenance of the Passo Feio Complex, Dom Feliciano Belt: implications for the age of supracrustal rocks of the São Gabriel Arc, southern Brazil. Journal of South American Earth Sciences 58:9–17. doi.org/10.1016/j.jsames.2014.11.004

Machado N, Koppe JC, Hartmann LA (1990) A late Proterozoic U-Pb age for the Bossoroca belt, Rio Grande do Sul, Brazil. Journal of South American Earth Sciences 3:87–90. doi.org/10.1016/0895-9811(90)90021-R

Marschall HR, Jiang SY (2011) Tourmaline isotopes: no element left behind. Elements 7:313–319. doi: 10.2113/gselements.7.5.313

Marschall HR, Wanless VD, Shimizu N et al (2017) The boron and lithium isotopic composition of mid-ocean ridge basalts and the mantle. Geochimica et Cosmochimica Acta 207:102–138. doi.org/10.1016/j.gca.2017.03.028

Míková J, Košler J, Wiedenbeck M (2014) Matrix effects during laser ablation MC ICP-MS analysis of boron isotopes in tourmaline. Journal of Analytical Atomic Spectrometry 29:903–914. doi: 10.1039/C3JA50241D

Naumann MP, Hartmann LA (1984) Cornubianitos ultramáficos e metassomatitos associados da região do Arroio Corticeira, Proceedings of the Congresso Brasileiro de Geologia 33th, Rio de Janeiro, Brazil, pp 4279–4290

Naumann MP (1985) O complexo Vulcano-sedimentar-ultramáfico e granitoides da região de Ibaré. Master thesis, Universidade Federal do Rio Grande do Sul.

Palmer M, Slack J (1989) Boron isotopic composition of tourmaline from massive sulfide deposits and tourmalinites. Contribution Mineralogy and Petrology 103:434–451. doi.org/10.1007/BF01041751

Palmer MR (1991) Boron isotopes systematics of hydrothermal fluids and tourmalines: A synthesis. Chemical Geology 94:111–121. doi.org/10.1016/0168-9622(91)90004-G

Palmer MR (2017) Boron cycling in subduction zones. Elements 13:237–242. doi:10.2138/gselements.13.4.237

Peacock SM, Hervig RL (1999) Boron isotopic composition of subduction-zone metamorphic rocks. Chemical Geology 160:281–290. doi.org/10.1016/S0009-2541(99)00103-5

Pertille J, Hartmann LA, Philipp RP et al (2015) Origin of the Ediacaran Porongos Group, Dom Feliciano Belt, southern Brazilian Shield, with emphasis on whole rock and detrital zircon geochemistry and U-Pb, Lu-Hf isotopes. Journal of South American Earth Sciences 64:69–93. doi.org/10.1016/j.jsames.2015.09.001

Pertille J, Hartmann LA, Santos JOS et al (2017) Reconstructing the Cryogenian-Ediacaran evolution of the Porongos fold and thrust belt, Southern Brasiliano Orogen, based on zircon U-Pb-Hf-O isotopes. International Geology Review 59:1532–1560. doi.org/10.1080/00206814.2017.1285257

Philipp RP, Massonne HJ, Campos RS (2013) Peraluminous leucogranites of the Cordilheira Suite: A record of Neoproterozoic collision and the generation of the Pelotas Batholith, Dom Feliciano Belt, Southern Brazil. Journal of South American Earth Sciences 43:8–24. doi.org/10.1016/j.jsames.2012.10.006

Queiroga GN, Pedrosa-Soares AC, Noce CM et al (2007) Age of the Ribeirão da Folha ophiolite, Araçuaí Orogen: the U-Pb zircon (LA-ICPMS) dating of a plagiogranite. Geonomos 15:61–65. doi.org/10.18285/geonomos.v15i1.107

Rapela CW, Pankhurst RJ, Casquet C et al (2007) The Río de la Plata craton and the assembly of SW Gondwana. Earth-Science Reviews 8:49–82. doi.org/10.1016/j.earscirev.2007.03.004

Remus MVD, McNaughton NJ, Hartmann LA (1999) Gold in the Neoproterozoic juvenile Bossoroca Volcanic Arc of Southernmost Brazil: isotopic constraits on timing and sources. Journal of South American Earth Sciences 12:349–366. doi.org/10.1016/S0895-9811(99)00026-7

Rosner M, Erzinger J, Franz G, Trumbull RB (2003) Slab-derived boron isotope signatures in arc volcanic rocks from the Central Andes and evidence for boron isotope fractionation during progressive slab dehydration. Geochemistry Geophysics Geosystems 4:1–25. doi: 10.1029/2002GC000438

Saalmann K, Hartmann LA, Remus MVD et al (2005a) Sm–Nd isotope geochemistry of metamorphic volcano-sedimentary successions in the São Gabriel Block, southernmost Brazil: evidence for the existence of juvenile Neoproterozoic oceanic crust to the east of the Rio de la Plata craton. Precambrian Research 136:159–175. doi.org/10.1016/j.precamres.2004.10.006

Saalmann K, Remus MVD, Hartmann LA (2005b). Geochemistry and crustal evolution of volcano-sedimentary successions and orthogneisses in the São Gabriel block, Southernmost Brazil-relics of Neoproterozoic magmatic arcs. Gondwana Research 8:143–161. doi.org/10.1016/S1342-937X(05)71114-X

Savov IP, Ryan JG, D’Antonio M et al (2005). Geochemistry of serpentinized peridotites from the Mariana Forearc Conical Seamount, ODP Leg 125: Implications for the elemental recycling at subduction zones. Geochemistry Geophysics Geosystems 6:1–24. doi: 10.1029/2004GC000777

Seyfried WE, Ding K (1995) Phase Equilibria in Subseafloor Hydrothermal Systems: A Review of the Role of Redox, Temperature, pH and Dissolved Cl on the Chemistry of Hot Spring Fluids at Mid-Ocean Ridge. Physical, Chemical, Biological and Geological Interactions, AGU Geophysical Monograph 91:248–272. doi: 10.1029/GM091p0248

Slack JF, Palmer MR, Stevens BPJ, Barnes RG (1993) Origin and significance of tourmaline-rich rocks in the Broken Hill District, Australia. Economic Geology 88:505–541. doi: 10.2113/gsecongeo.88.3.505

Slack JF, Trumbull RB (2011) Tourmaline as a recorder of ore-forming processes. Elements 7:321–326. doi: 10.2113/gselements.7.5.321

Smith HJ, Spivack AJ, Staudigel H, Hart SR (1995) The boron isotopic composition of altered oceanic crust. Chemical Geology 126:119–135. doi.org/10.1016/0009-2541(95)00113-6

Spivack AJ, Edmond JM (1987) Boron isotope exchange between seawater and the oceanic crust. Geochimica et Cosmochimica Acta 51:1033–1043. doi.org/10.1016/0016-7037(87)90198-0

Tindle AG, Breaks FW, Selway JB (2002) Tourmaline in petalite-subtype granitic pegmatites: Evidence of fractionation and contamination from the Pakeagama Lake and Separation Lake areas of northwestern Ontario, Canada. The Canadian Mineralogist 40:753–788. doi.org/10.2113/gscanmin.40.3.753

Tonarini S, Pennisi M, Adorni-Braccesi A et al (2003) Intercomparison of boron isotope and concentration measurements: Part I: Selection, preparation and homogeneity tests of the intercomparison materials. Geostandards Newsletter 27:21–39. doi: 10.1111/j.1751-908X.2003.tb00710.x

Tonarini S, Agostini S, Doglioni C et al (2007) Evidence for serpentinite fluid in convergent margin systems: The example of El Salvador (Central America) arc lavas. Geochemistry Geophysics Geosystems 8:1–18. doi: 10.1029/2006GC001508

Trumbull RB, Krienitz MS, Gottesmann B, Wiedenbeck M (2008) Chemical and boron-isotope variations in tourmalines from an S-type granite and its source rocks: the Erongo granite and tourmalinites in the Damara Belt, Namibia. Contributions to Mineralogy and Petrology 155:1–18. doi:10.1007/s00410-007-0227-3

Trumbull RB, Beurlen H, Wiedenbeck M, Soares DR (2013) The diversity of B-isotope variations in tourmaline from rare-element pegmatites in the Borborema Province of Brazil. Chemical Geology 352:47–62. doi.org/10.1016/j.chemgeo.2013.05.021

van Hinsberg VJ, Henry DJ, Dutrow BL (2011) Tourmaline as a petrologic forensic mineral: a unique recorder of its geologic past. Elements 7:323–332. doi.org/10.2113/gselements.7.5.327

Williams LB, Hervig RL, Holloway JR, Hutcheon I (2001) Boron isotope geochemistry during diagenesis. Part I. Experimental determination of fractionation during illitization of smectite. Geochimica et Cosmochimica Acta 65:1769–1782. doi.org/10.1016/S0016-7037(01)00557-9

Yamaoka K, Ishikawa T, Matsubaya O et al (2012) Boron and oxygen isotope systematics for a complete section of oceanic crustal rocks in the Oman ophiolite. Geochimica et Cosmochimica Acta 84:543–559. doi.org/10.1016/j.gca.2012.01.043

Yamaoka K, Matsukura S, Ishikawa T, Kawahata H (2015) Boron isotope systematics of a fossil hydrothermal system from the Troodos ophiolite, Cyprus: water–rock interaction of oceanic crust and subseafloor ore deposits. Chemical Geology 396:61–73. doi.org/10.1016/j.chemgeo.2014.12.023

You CF, Spivack AJ, Gieskes JM et al (1996) Boron contents and isotopic compositions in pore water: a new approach to determine temperature-induced artifacts-geochemical implications. Marine Geology 129:351–361. doi.org/10.1016/0025-3227(96)83353-6

Yücel-Öztürk Y, Helvacı C, Palmer MR et al (2015) Origin and significance of tourmalinites and tourmaline-bearing rocks of Menderes Massif, western Anatolia, Turkey. Lithos 218–219:22–36. doi.org/10.1016/j.lithos.2015.01.009

Figure captions:

Figure 1. (a) Main tectonic units of southern Brazil and Uruguay (adapted from Rapela et al. 2007; Chemale et al. 2011); (b) Geological map of Dom Feliciano Belt and basement (after Philipp et al. 2013; Pertille et al. 2015; Arena et al. 2017a). Location Figure 2 indicated.

Figure 2. (a) Satellite image of study area; (b) Selected field of studied tourmalinite. Inset shows location of studied tourmalinite; (c) Studied tourmalinite outcrop; (d) Tourmalinite hand sample highlighting interfingering with chlorite; (e) Detail of tourmalinite sample, 10 cm long and 1.5 cm wide, cut from sample shown in Figure 2d; (f) Sectioned tourmalinite blocks for EPMA and LA-ICP-MS studies, shown as originally positioned in Figure 2e. Tur = tourmaline; Chl = chlorite.

Figure 3. Back-scattered electron images of studied tourmalinite sample. (a) Section of block 3 (see Figure 2f) with location of δ^{11}B analyses; location of Figures 3c, d indicated; (b) Section of block 4 (Figure 2f) with location of δ^{11}B analyses; location of Figure 3e indicated; (c) Cross-section of tourmaline crystal indicating location of EPMA analyses. (d) Prism section of tourmaline crystals indicating location of EPMA analyses; one cross-section in extreme right; (e) Prism section of tourmaline crystals indicating location of EPMA analyses.

Figure 4. (a) Back-scattered electron image; (b-e) Characteristic X-ray map displaying the distribution of Si, Al, Mg, Fe in sample IB14. No compositional zoning observed. cps = count per second. Tur = tourmaline; Chl = chlorite.

Figure 5. Ternary diagram using electron microprobe data. (a) Division according to the dominant occupancy of the X site to give the X-site vacant, alkali and calcic groups; (b) Classification of alkali group tourmaline with dominant occupancy of the Y site, highlighting dravite end-member.

Figure 6. Diagrams of tourmalines from the Ibaré tourmalinite. (a) Mg versus Fe (total = Fe^{+2}). The dotted lines represent joins between selected end members. The array of data is along the schorl–dravite join (more Mg-rich) and is most consistent with operation of the $MgFe^{2+}{}_{-1}$ substitution; (b) Al (total) versus Fe (total). The data classify the tourmaline as dravite end-member.

Figure 7. (a), (b) Plots of tourmalines on Al–Fe–Mg(total) and Ca-Fe-Mg(total) diagrams (after Yücel-Öztürk et al. 2015), 1 = Li-rich granitoid pegmatite and aplite, 2 = Li-poor granitoid and their associated pegmatiteand aplite, 3 = hydrothermally altered granite, 4 = metapelite and metapsammite coexisting with an Al-saturated phase, 5 = metapelite and metapsammite not coexisting with an Al-saturated phase, low-Ca metaultramafic and Cr, V-rich metasediment, 6 = metacarbonate, metaultramafic, Fe^{3+}-rich quartz-tourmaline rock, calc-silicate rock and Ca-poor metapelite, 7 = Ca-rich metapelite and calc-silicate rock; (c) Composition of tourmaline from the IB14 tourmalinite, indicating dominance Mg-rich seawater over Fe-rich hydrothermal fluid. DT = distal tourmaline; PT = proximal tourmaline from Garda et al. (2009); B = Borborema tourmaline by Trumbull et al. (2013); dotted area = Yücel-Öztürk et al. (2015).

Figure 8. Histogram showing $\delta^{11}B$. (a) Different geological settings of boron sources (Farber et al. 2015); (b) Frequency histogram for IB14 tourmaline and data from literature.

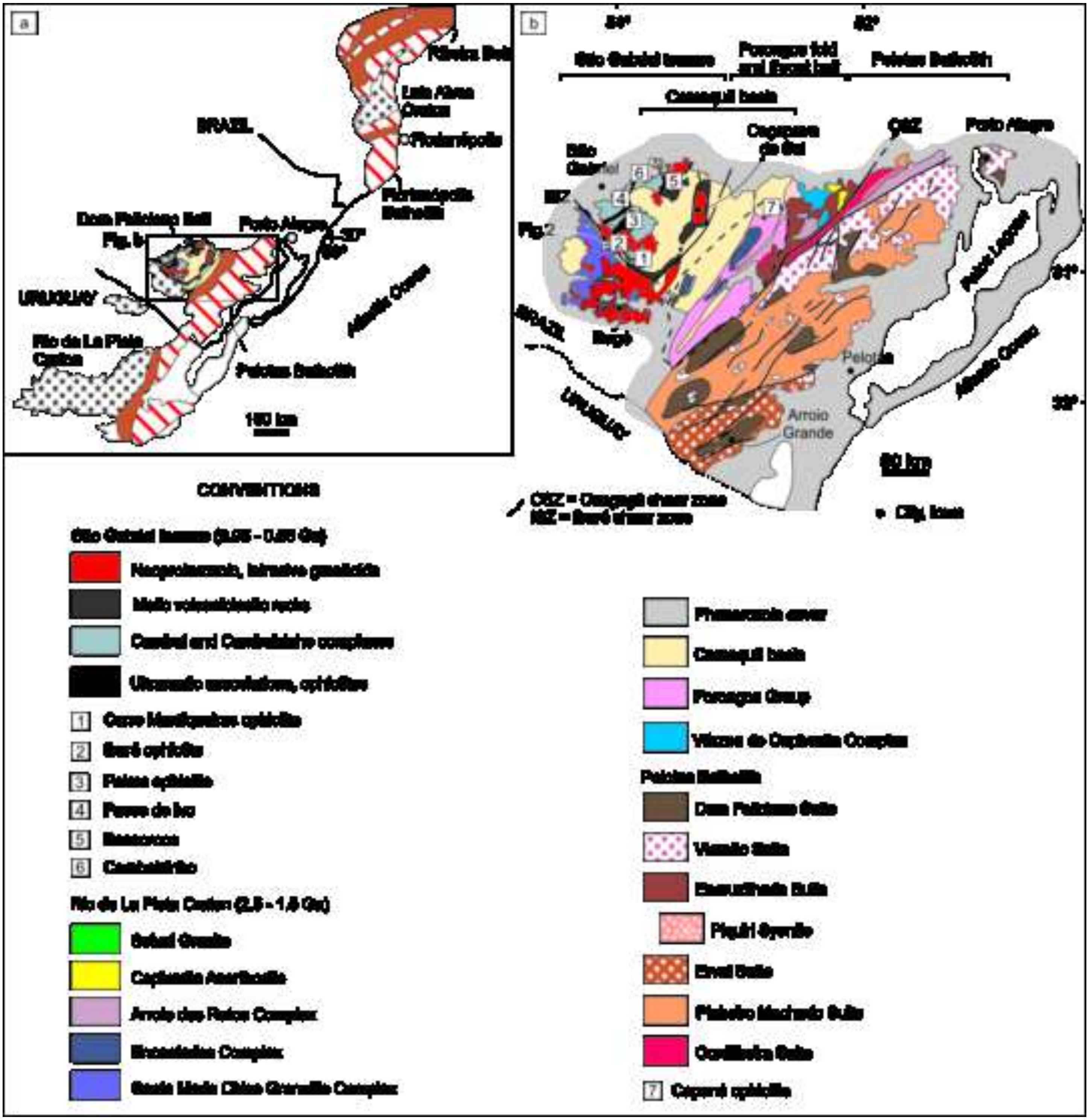
a
Ribeira Belt
Luis Alves Craton
Florianópolis
Florianópolis Batholith
BRAZIL
Dom Feliciano Belt
Fig. b
Porto Alegre
30°
51°
URUGUAY
Rio de La Plata Craton
Pelotas Batholith
Atlantic Ocean
100 km
b
54°
52°
São Gabriel terrane
Porongos fold and thrust belt
Pelotas Batholith
Camaquã basin
São Gabriel
Caçapava do Sul
CSZ
Porto Alegre
ISZ
Fig.2
Bagé
BRAZIL
URUGUAY
Pelotas
Arroio Grande
Patos Lagoon
Atlantic Ocean
31°
32°
50 km
CSZ = Caçapava shear zone
ISZ = Ibaré shear zone
City, town
CONVENTIONS
São Gabriel terrane (0.95 - 0.68 Ga)
Neoproterozoic, intrusive granitoids
Mafic volcaniclastic rocks
Cambaí and Cambaizinho complexes
Ultramafic associations, ophiolites
1 Cerro Mantiqueiras ophiolite
2 Ibaré ophiolite
3 Palma ophiolite
4 Passo do Ivo
5 Bossoroca
6 Cambaizinho
Rio de La Plata Craton (2.5 - 1.8 Ga)
Seival Granite
Capivarita Anorthosite
Arroio dos Ratos Complex
Encantadas Complex
Santa Maria Chico Granulitic Complex
Phanerozoic cover
Camaquã basin
Porongos Group
Várzea do Capivarita Complex
Pelotas Batholith
Dom Feliciano Suite
Viamão Suite
Encruzilhada Suite
Piquiri Syenite
Erval Suite
Pinheiro Machado Suite
Cordilheira Suite
7 Capané ophiolite

Figure 2

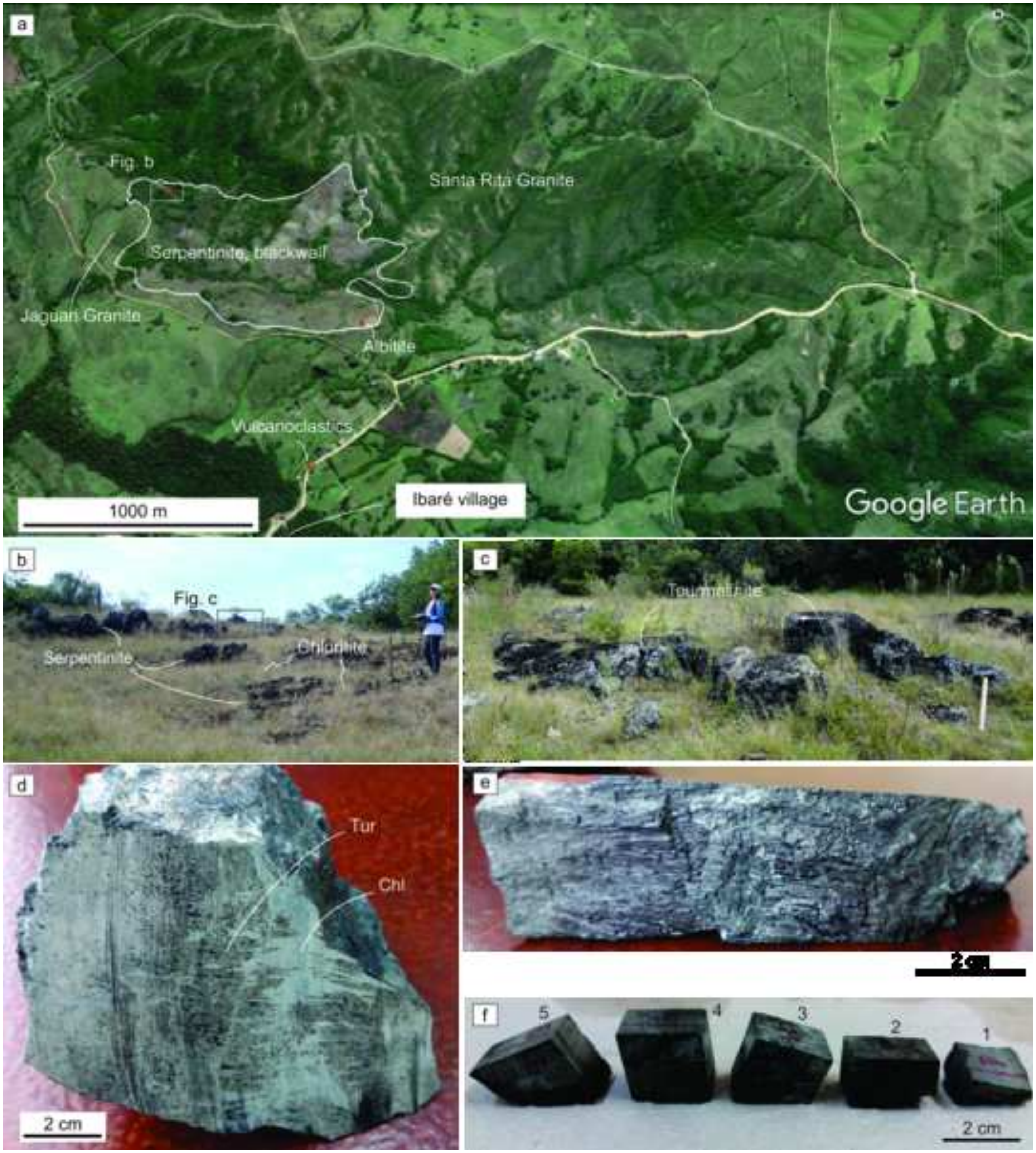
a
Fig. b
Santa Rita Granite
Serpentinite, blackwall
Jaguari Granite
Albitite
Vulcanoclastics
Ibaré village
1000 m
Google Earth
b
Fig. c
Serpentinite
Chloritite
c
Tourmalinite
d
Tur
Chl
2 cm
e
2 cm
f
5
4
3
2
1
2 cm

Figure 3

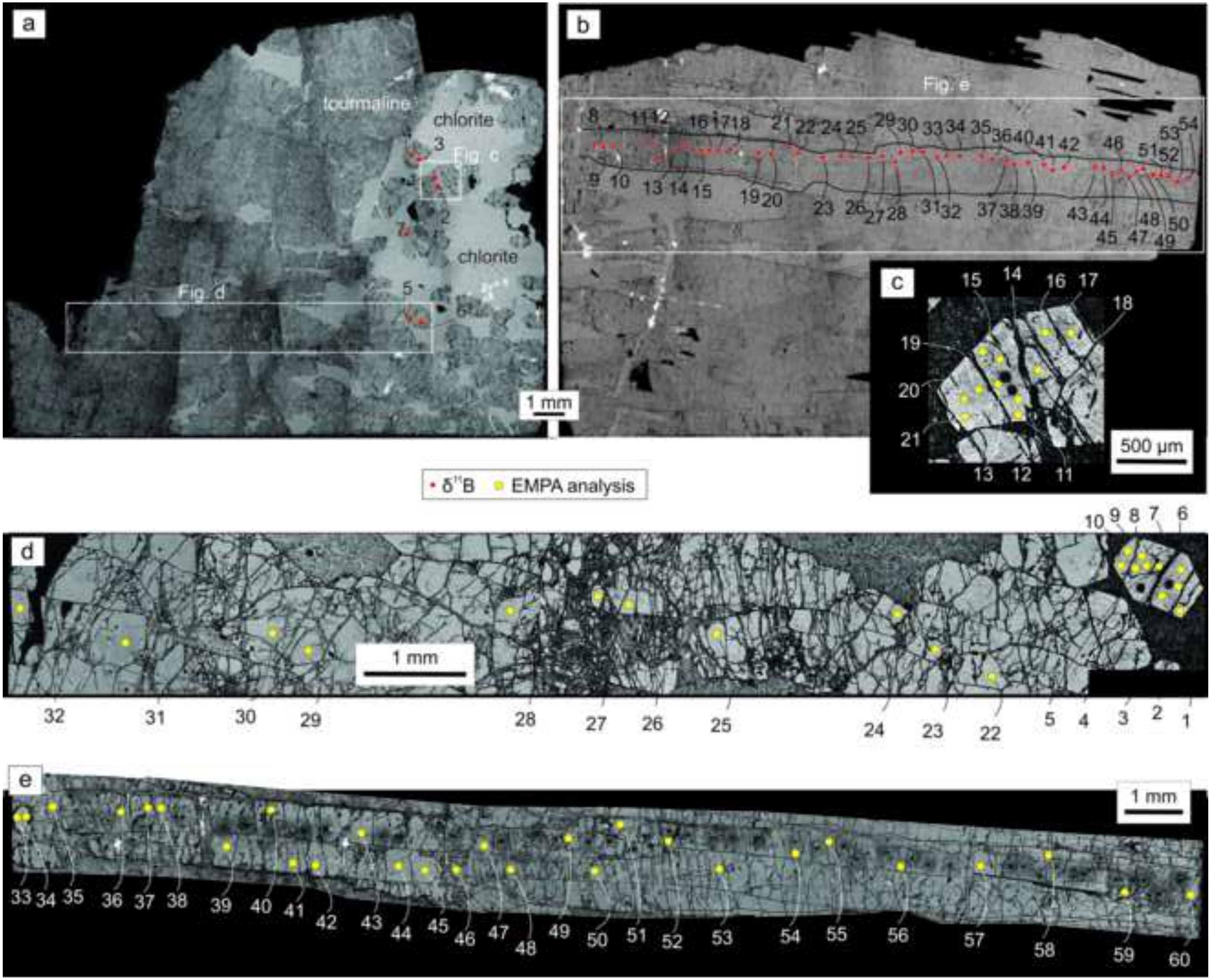
a
tourmaline
chlorite
3
Fig. c
2
chlorite
5
Fig. d
1 mm
b
Fig. e
8 11 12 16 17 18 21 22 24 25 29 30 33 34 35 36 40 41 42 46 53 54 51 52
9 10 13 14 15 19 20 23 26 27 28 31 32 37 38 39 43 44 45 47 48 49 50
c
15 14 16 17 18 19 20 21 13 12 11
500 µm
• δ11B
● EMPA analysis
d
1 mm
10 9 8 7 6
32 31 30 29 28 27 26 25 24 23 22 5 4 3 2 1
e
1 mm
33 34 35 36 37 38 39 40 41 42 43 44 45 46 47 48 49 50 51 52 53 54 55 56 57 58 59 60

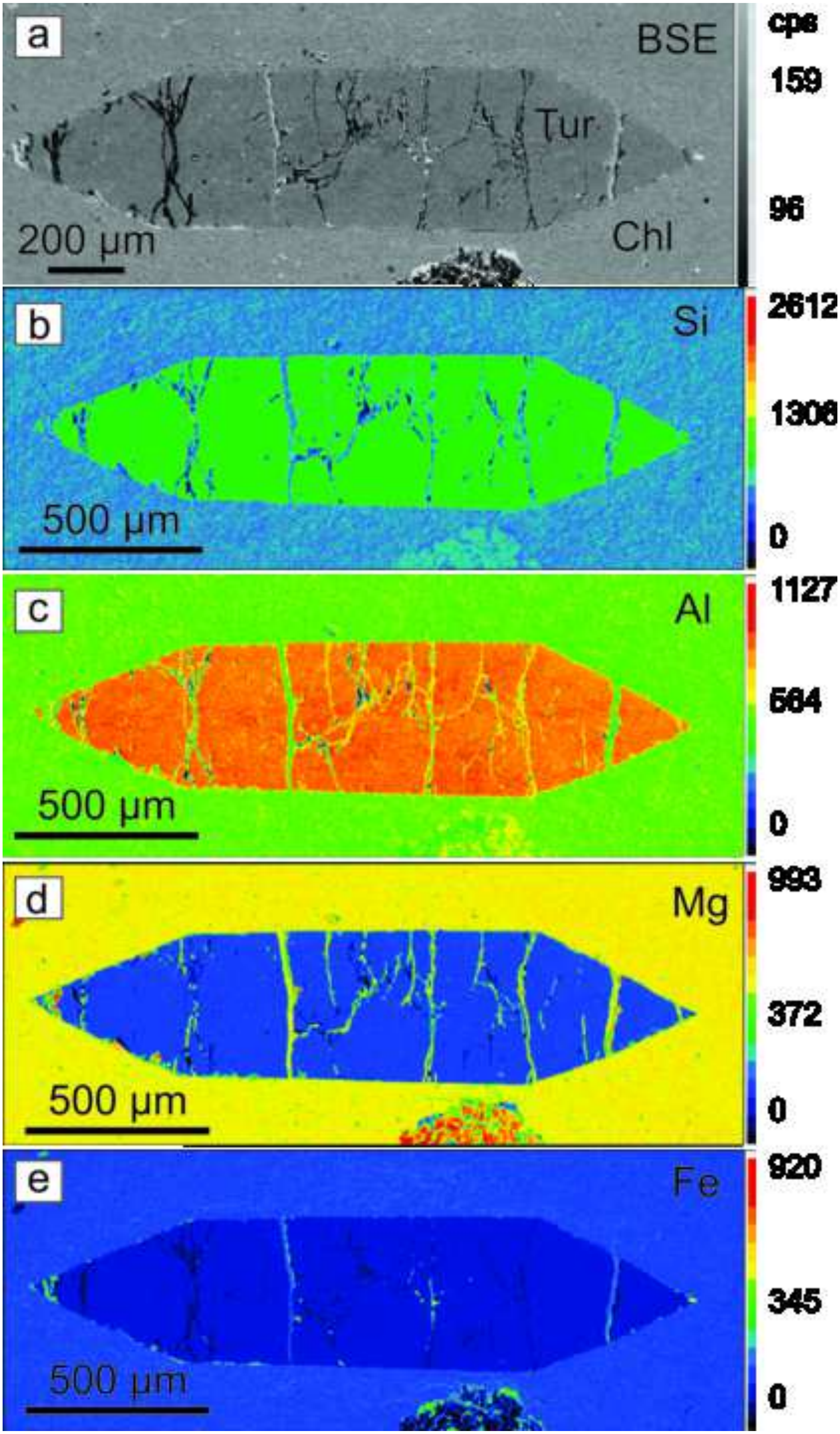
a
BSE
cps
159
96
Tur
Chl
200 µm
b
Si
2612
1306
0
500 µm
c
Al
1127
564
0
500 µm
d
Mg
993
372
0
500 µm
e
Fe
920
345
0
500 µm

Figure 5

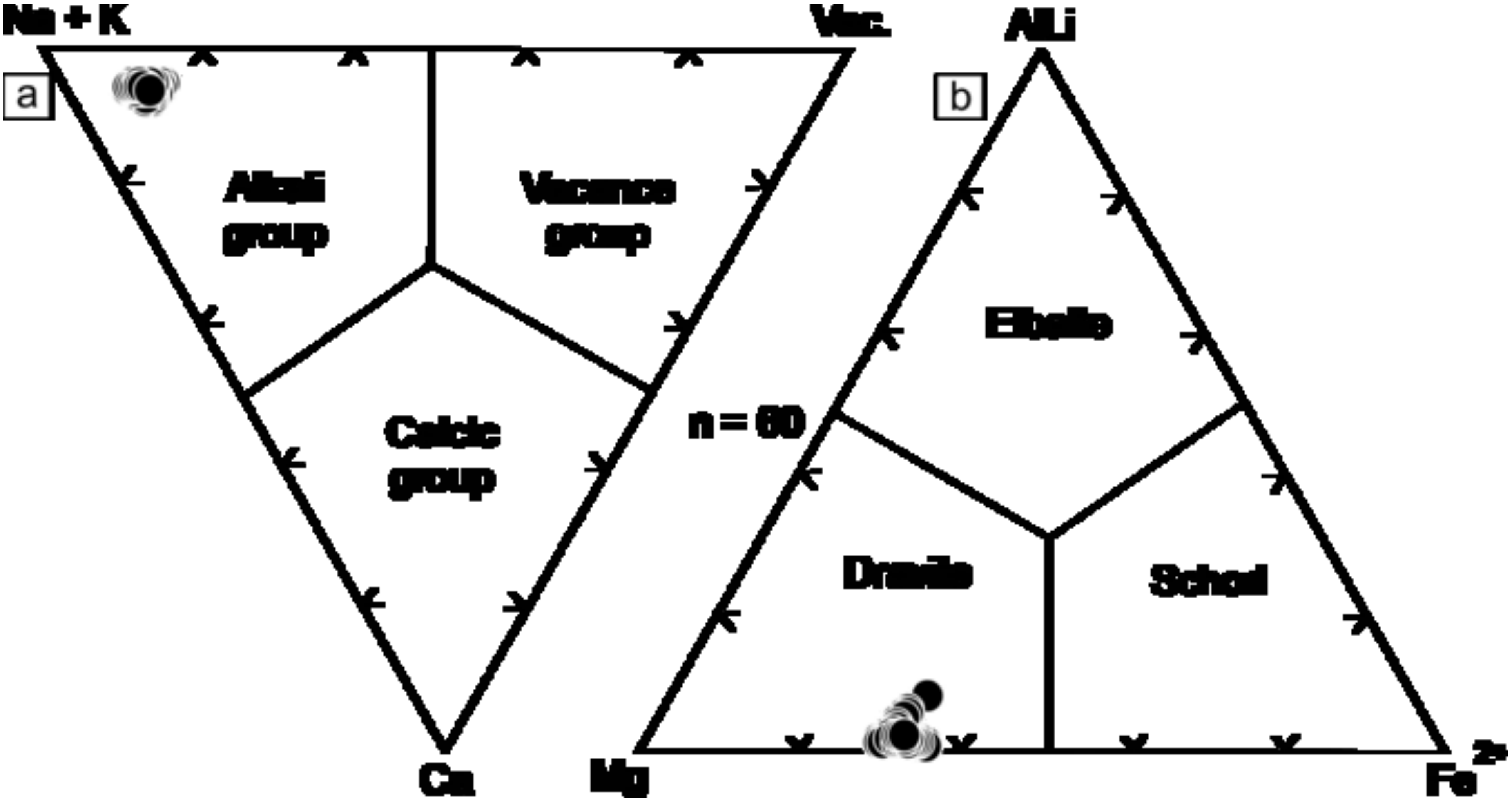
Na + K
Vac.
a
Alkali group
Vacancy group
Calcic group
Ca
n = 60
AlLi
b
Elbaite
Dravite
Schorl
Mg
Fe2+

Figure 6

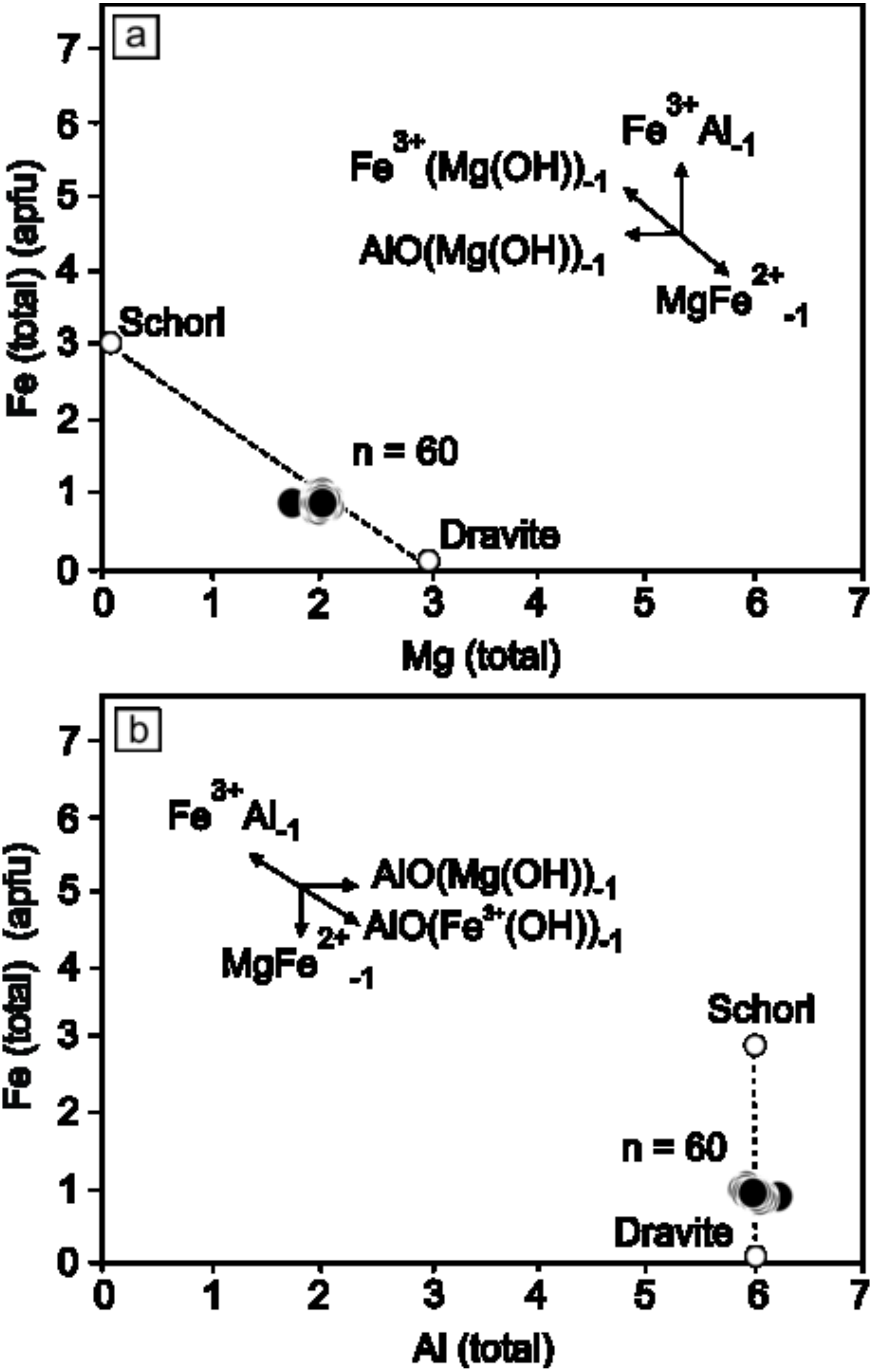
a
Fe (total) (apfu)
Mg (total)
$Fe^{3+}Al_{-1}$
$Fe^{3+}(Mg(OH))_{-1}$
$AlO(Mg(OH))_{-1}$
$MgFe^{2+}_{-1}$
Schorl
n = 60
Dravite
0
1
2
3
4
5
6
7
b
Fe (total) (apfu)
Al (total)
$Fe^{3+}Al_{-1}$
$AlO(Mg(OH))_{-1}$
$AlO(Fe^{3+}(OH))_{-1}$
$MgFe^{2+}_{-1}$
Schorl
n = 60
Dravite
0
1
2
3
4
5
6
7

Figure 7

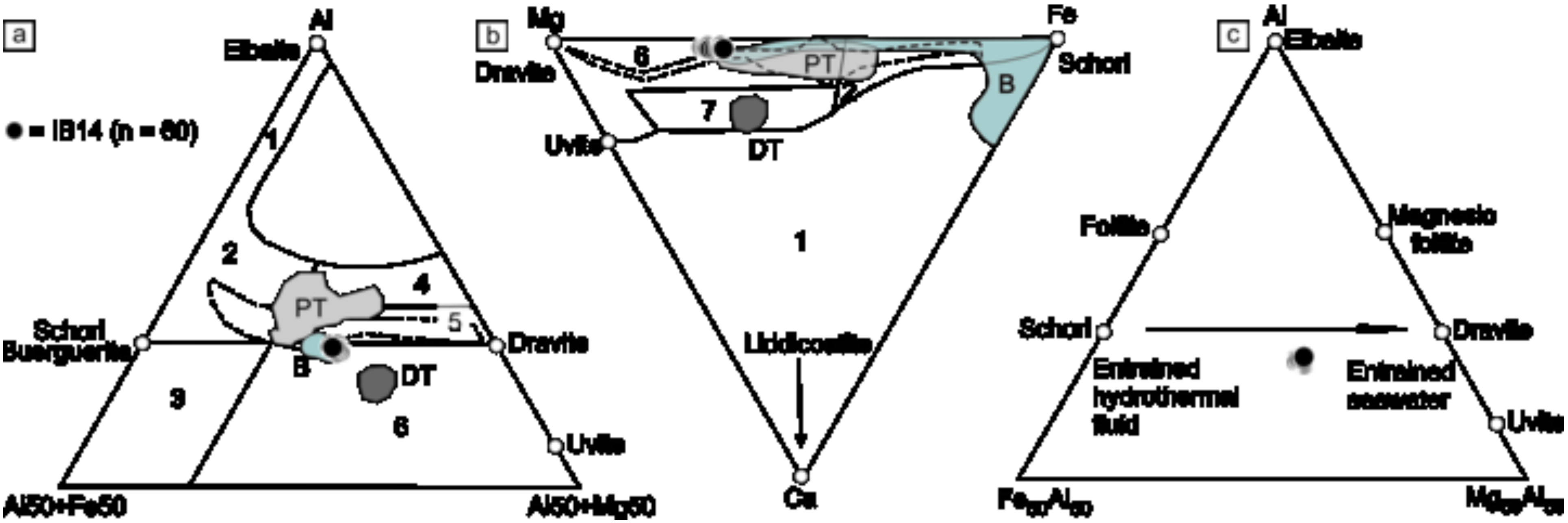
a
Al
Elbaite
● = IB14 (n = 60)
1
2
PT
4
5
Schorl
Buerguerite
B
DT
Dravite
3
6
Uvite
Al50+Fe50
Al50+Mg50
b
Mg
Dravite
6
PT
Fe
Schorl
B
7
Uvite
DT
1
Liddicoatite
Ca
c
Al
Elbaite
Foitite
Magnesio foitite
Schorl
Dravite
Entrained hydrothermal fluid
Entrained seawater
Uvite
Fe50Al50
Mg50Al50

Figure 8

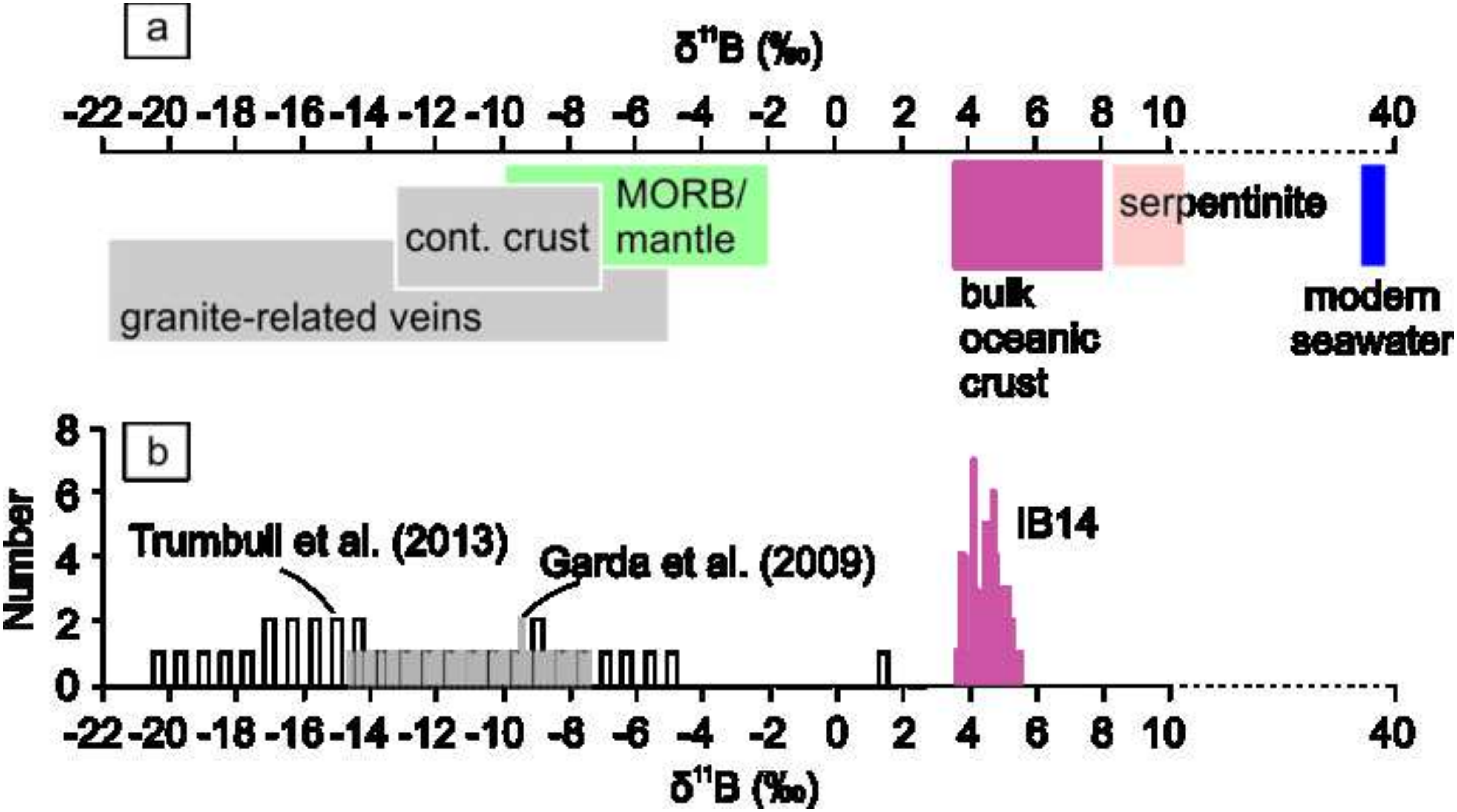
a
δ11B (‰)
-22
-20
-18
-16
-14
-12
-10
-8
-6
-4
-2
0
2
4
6
8
10
40
MORB/ mantle
cont. crust
granite-related veins
serpentinite
bulk oceanic crust
modern seawater
b
Number
8
6
4
2
0
Trumbull et al. (2013)
Garda et al. (2009)
IB14
δ11B (‰)

Table 1. δ^{11}B results for tourmaline from tourmalinite, Ibaré ophiolite

Spot	δ^{11}B (‰)	Spot	δ^{11}B (‰)
1	4.0 ± 0.18	28	4.1 ± 0.15
2	4.3 ± 0.18	29	4.0 ± 0.16
3	3.7 ± 0.19	30	4.0 ± 0.16
4	4.4 ± 0.18	31	3.9 ± 0.15
5	5.0 ± 0.19	32	3.7 ± 0.15
6	4.8 ± 0.19	33	4.0 ± 0.15
7	4.7 ± 0.20	34	3.6 ± 0.16
8	5.2 ± 0.14	35	3.6 ± 0.15
9	5.1 ± 0.14	36	3.6 ± 0.15
10	4.9 ± 0.14	37	3.5 ± 0.16
11	5.0 ± 0.13	38	3.6 ± 0.15
12	4.8 ± 0.14	39	3.7 ± 0.16
13	4.3 ± 0.17	40	3.7 ± 0.15
14	4.6 ± 0.14	41	4.1 ± 0.15
15	4.5 ± 0.15	42	4.1 ± 0.16
16	4.5 ± 0.15	43	4.0 ± 0.15
17	4.4 ± 0.15	44	4.5 ± 0.18
18	4.6 ± 0.14	45	4.4 ± 0.15
19	4.0 ± 0.15	46	4.5 ± 0.19
20	4.3 ± 0.14	47	4.6 ± 0.19
21	4.6 ± 0.13	48	4.7 ± 0.19
22	4.4 ± 0.14	49	4.5 ± 0.19
23	4.2 ± 0.14	50	4.5 ± 0.18
24	4.4 ± 0.13	51	4.9 ± 0.18
25	4.2 ± 0.14	52	4.9 ± 0.18
26	4.0 ± 0.15	53	4.7 ± 0.18
27	4.3 ± 0.15	54	4.3 ± 0.19

Table 2. B isotopes from selected geological settings.

Geological setting	$\delta^{11}B$ (‰)
Modern seawater	[a] +40‰
Marine evaporite and carbonate	[a] +18 to +32‰
Non-marine evaporite and carbonate	[a] -30 to +7‰
Terrigenous marine sediments	[a] -4 to +3‰
Altered oceanic crust	[a] 0 to +13‰
Fresh oceanic crust	[a] -3‰
Island arc volcanics	[a] -5 to +6‰
Andes arc volcanic	[b] -7 to +4‰
Continental reservoir	[c] -20 to -7‰
Subduction zone	[d] -11 to -3‰
This work	[e] +3.5 to +5.2‰

[a]Palmer and Slack, (1989); [c]Rosner et al. (2003) [c]Chaussidon and Albarède, (1992); [d]Peacock and Hervig, 1999; [e]This work.

Online Appendix 1. Reference materials used for calibration of Electron Microprobe analyses

Element	Standard	X-ray	Crystal	CH	Peak Position	BG -	BG +
Na	Anorthoclase	Ka	TAPH	1	130.25	2.594	1.464
F	CaF2	Ka	TAPH	1	199.495	4.098	2.312
Si	Quartz	Ka	TAP	2	77.45	2.752	1.609
Al	Corundum	Ka	TAP	2	90.613	2.7	1.128
Mg	Olivine	Ka	TAP	2	107.467	2.034	0.826
Zn	Gahnite	Ka	LIFH	3	99.883	1.275	0.904
Fe	Fe	Ka	LIFH	3	134.67	1.072	0.775
Cl	Scapolite(Meionite)	Ka	PETH	3	151.297	2.696	1.826
V	Glass_Rhyolitic_Corning_Glass_IR-W	Ka	LIFH	3	174.065	0.822	1.238
Ti	Rutile	Ka	PETJ	4	87.445	1.026	0.536
Ca	Fluor-Apatite	Ka	PETJ	4	106.998	0.864	0.457
Cr	Chromite	Ka	LIF	4	158.593	0.573	0.641
K	MIcrocline	Ka	PETL	5	119.279	1.055	0.529
Mn	MnO2	Ka	LIFL	5	145.597	0.476	0.677

BG = Background. CH = Spectrometer

Online Appendix 2. Boron isotopic analyses of secondary reference materials

Sample	^{11}B/1^{0}Bm	SE	corr factor	^{11}B/^{10}Bc	±s(%)	δ^{11}B (‰)
Dravite	4,629	0,001	0,868	4,018	0,015	-6,18
Dravite	4,631	0,001	0,868	4,019	0,013	
Dravite	4,63	0,001	0,868	4,019	0,013	
Elbaite	4,611	0,001	0,868	4,002	0,014	-10,36
Elbaite	4,611	0,001	0,868	4,002	0,016	
Elbaite	4,611	0,001	0,868	4,002	0,015	
Dravite	4,632	0,001	0,867	4,016	0,016	-6,67
Dravite	4,632	0,001	0,867	4,016	0,015	
Dravite	4,633	0,001	0,867	4,017	0,015	
Elbaite	4,614	0,001	0,867	4	0,017	-10,58
Elbaite	4,614	0,001	0,867	4,001	0,016	
Elbaite	4,615	0,001	0,867	4,002	0,016	
Dravite	4,633	0,001	0,867	4,018	0,018	-6,48
Dravite	4,633	0,001	0,867	4,017	0,019	
Dravite	4,633	0,001	0,867	4,018	0,019	
Elbaite	4,616	0,001	0,867	4,002	0,019	-10,35
Elbaite	4,615	0,001	0,867	4,002	0,022	
Elbaite	4,615	0,001	0,867	4,001	0,02	

m = measured; c = corrected

Online Appendix 3. Electron Microprobe analyses of tourmaline from tourmalinite, Ibaré ophiolite.

Spot	1	2	3	4	5	6	7	8	9	10	11	12	13	14	15	16	17	18	19	20	21	22	23	24	25	26	27	28	29	30
SiO2	36.99	36.88	37.22	36.99	37.08	36.97	37.13	37.03	36.92	36.80	36.94	36.74	37.50	36.78	36.89	37.08	36.39	37.22	37.20	36.86	36.44	37.14	36.61	36.64	36.97	37.30	36.88	36.85	37.26	36.37
TiO2	0.32	0.54	0.68	0.72	0.65	0.52	0.56	0.52	0.54	0.60	0.43	0.63	0.31	0.56	0.40	0.35	0.72	0.56	0.39	0.62	0.82	0.39	0.61	0.63	0.51	0.33	0.76	0.48	0.43	0.46
Al2O3	32.09	31.79	31.31	31.14	30.95	31.23	31.38	32.09	31.26	31.39	31.94	31.02	32.73	31.29	32.00	32.52	30.62	31.27	32.31	31.13	30.64	31.99	31.27	31.08	31.61	32.68	30.93	32.08	32.32	30.97
V2O3	0.00	0.03	0.10	0.02	0.01	0.03	0.02	0.03	0.00	0.05	0.05	0.05	0.02	0.03	0.01	0.02	0.05	0.04	0.05	0.03	0.02	0.06	0.02	0.04	0.04	0.00	0.00	0.01	0.00	0.01
Cr2O3	0.00	0.00	0.03	0.00	0.01	0.02	0.07	0.00	0.01	0.00	0.00	0.00	0.00	0.01	0.01	0.00	0.00	0.01	0.01	0.09	0.00	0.04	0.06	0.00	0.00	0.00	0.01	0.02	0.03	0.00
FeO	6.61	6.85	7.27	7.20	7.17	7.19	7.09	6.68	7.25	7.11	7.01	7.20	6.66	7.33	6.55	6.63	7.76	7.10	6.62	7.37	7.69	6.45	7.18	7.28	6.91	6.59	7.38	6.87	6.71	6.87
MgO	8.16	8.06	8.35	8.11	8.21	8.29	8.21	7.88	8.33	8.30	8.21	8.22	8.17	8.32	8.26	8.08	8.21	8.24	7.83	8.29	8.17	8.34	8.50	8.25	8.33	8.03	8.18	8.09	8.20	8.13
CaO	0.29	0.36	0.34	0.39	0.36	0.34	0.35	0.30	0.37	0.33	0.33	0.42	0.29	0.36	0.31	0.25	0.43	0.34	0.26	0.38	0.40	0.22	0.40	0.36	0.30	0.28	0.41	0.33	0.31	0.29
MnO	0.10	0.08	0.07	0.04	0.05	0.03	0.08	0.08	0.12	0.08	0.08	0.07	0.06	0.06	0.05	0.12	0.05	0.05	0.07	0.10	0.06	0.08	0.04	0.05	0.11	0.11	0.08	0.10	0.07	0.08
ZnO	0.06	0.05	0.05	0.00	0.04	0.04	0.00	0.00	0.06	0.00	0.00	0.00	0.02	0.03	0.00	0.04	0.04	0.02	0.00	0.07	0.00	0.06	0.01	0.00	0.05	0.05	0.02	0.04	0.05	0.00
Na2O	2.60	2.56	2.63	2.61	2.65	2.77	2.77	2.58	2.64	2.62	2.70	2.68	2.76	2.69	2.68	2.67	2.54	2.61	2.62	2.69	2.59	2.68	2.67	2.75	2.71	2.64	2.59	2.69	2.71	2.63
K2O	0.02	0.03	0.03	0.03	0.02	0.03	0.01	0.02	0.04	0.01	0.02	0.02	0.03	0.02	0.02	0.02	0.02	0.02	0.02	0.03	0.03	0.02	0.04	0.03	0.04	0.03	0.03	0.02	0.02	0.03
F	0.00	0.02	0.02	0.00	0.03	0.06	0.07	0.00	0.03	0.00	0.06	0.09	0.00	0.01	0.00	0.02	0.02	0.00	0.00	0.00	0.00	0.00	0.00	0.02	0.00	0.00	0.04	0.00	0.00	0.02
Cl	0.00	0.01	0.00	0.01	0.00	0.02	0.00	0.00	0.00	0.00	0.00	0.01	0.01	0.01	0.01	0.01	0.00	0.00	0.00	0.02	0.01	0.01	0.00	0.01	0.00	0.01	0.00	0.00	0.01	0.00
H2O*	3.72	3.70	3.73	3.70	3.69	3.68	3.69	3.72	3.69	3.70	3.70	3.65	3.78	3.70	3.71	3.73	3.66	3.72	3.73	3.70	3.67	3.73	3.70	3.68	3.72	3.75	3.68	3.72	3.75	3.64
B2O3*	10.78	10.76	10.82	10.74	10.73	10.75	10.79	10.79	10.75	10.74	10.80	10.70	10.95	10.74	10.77	10.85	10.63	10.78	10.82	10.75	10.64	10.81	10.73	10.69	10.78	10.89	10.72	10.79	10.88	10.58
Li2O*	0.04	0.05	0.01	0.07	0.07	0.04	0.08	0.11	0.00	0.00	0.03	0.05	0.09	0.00	0.05	0.05	0.00	0.05	0.12	0.00	0.00	0.04	0.00	0.03	0.02	0.08	0.03	0.05	0.07	0.03
Total	101.77	101.77	102.63	101.79	101.72	102.00	102.31	101.85	102.02	101.72	102.30	101.53	103.36	101.94	101.73	102.45	101.13	102.04	102.06	102.11	101.17	102.05	101.84	101.53	102.09	102.78	101.75	102.15	102.81	100.11
O=F	0.00	0.01	0.01	0.00	0.01	0.02	0.03	0.00	0.01	0.00	0.02	0.04	0.00	0.00	0.00	0.01	0.01	0.00	0.00	0.00	0.00	0.00	0.00	0.01	0.00	0.00	0.02	0.00	0.00	0.01
Total*	101.77	101.76	102.63	101.79	101.71	101.97	102.28	101.85	102.01	101.72	102.27	101.50	103.36	101.93	101.73	102.44	101.12	102.04	102.06	102.11	101.17	102.05	101.84	101.52	102.09	102.77	101.74	102.15	102.81	100.10
Formulas normalized on T + Y + Z = 15																														
B	3.00	3.00	3.00	3.00	3.00	3.00	3.00	3.00	3.00	3.00	3.00	3.00	3.00	3.00	3.00	3.00	3.00	3.00	3.00	3.00	3.00	3.00	3.00	3.00	3.00	3.00	3.00	3.00	3.00	3.00
Si	5.97	5.96	5.98	5.99	6.00	5.98	5.98	5.97	5.97	5.96	5.94	5.97	5.95	5.95	5.95	5.94	5.95	6.00	5.97	5.96	5.96	5.97	5.93	5.95	5.96	5.95	5.98	5.93	5.95	5.98
Al	0.03	0.04	0.02	0.01	0.00	0.02	0.02	0.03	0.03	0.04	0.06	0.03	0.05	0.05	0.05	0.06	0.05	0.00	0.03	0.04	0.04	0.03	0.07	0.05	0.04	0.05	0.02	0.07	0.05	0.02
Sum T	6.00	6.00	6.00	6.00	6.00	6.00	6.00	6.00	6.00	6.00	6.00	6.00	6.00	6.00	6.00	6.00	6.00	6.00	6.00	6.00	6.00	6.00	6.00	6.00	6.00	6.00	6.00	6.00	6.00	6.00
Al	0.06	0.01	0.00	0.00	0.00	0.00	0.00	0.06	0.00	0.00	0.00	0.00	0.08	0.00	0.04	0.08	0.00	0.00	0.09	0.00	0.00	0.03	0.00	0.00	0.00	0.10	0.00	0.02	0.04	0.00
Ti	0.04	0.06	0.08	0.09	0.08	0.06	0.07	0.06	0.07	0.07	0.05	0.08	0.04	0.07	0.05	0.04	0.09	0.07	0.05	0.08	0.10	0.05	0.07	0.08	0.06	0.04	0.09	0.06	0.05	0.06
V	0.00	0.00	0.01	0.00	0.00	0.00	0.00	0.00	0.00	0.01	0.01	0.01	0.00	0.00	0.00	0.00	0.01	0.01	0.01	0.00	0.00	0.01	0.00	0.01	0.01	0.00	0.00	0.00	0.00	0.00
Cr	0.00	0.00	0.00	0.00	0.00	0.00	0.01	0.00	0.00	0.00	0.00	0.00	0.00	0.00	0.00	0.00	0.00	0.00	0.00	0.01	0.00	0.01	0.01	0.00	0.00	0.00	0.00	0.00	0.00	0.00
Mg	1.96	1.94	1.90	1.88	1.89	1.92	1.91	1.89	1.93	1.95	1.97	1.90	1.93	1.93	1.99	1.93	1.86	1.92	1.88	1.89	1.85	2.00	1.95	1.90	1.97	1.91	1.87	1.94	1.95	1.97
Mn	0.01	0.01	0.01	0.01	0.01	0.00	0.01	0.01	0.02	0.01	0.01	0.01	0.01	0.01	0.01	0.02	0.01	0.01	0.01	0.01	0.01	0.01	0.01	0.01	0.01	0.01	0.01	0.01	0.01	0.01
Fe2+	0.89	0.93	0.98	0.97	0.97	0.97	0.96	0.90	0.98	0.96	0.94	0.98	0.88	0.99	0.88	0.89	1.06	0.96	0.89	1.00	1.05	0.87	0.97	0.99	0.93	0.88	1.00	0.92	0.90	0.94
Zn	0.01	0.01	0.01	0.00	0.01	0.01	0.00	0.00	0.01	0.00	0.00	0.00	0.00	0.00	0.00	0.00	0.01	0.00	0.00	0.01	0.00	0.01	0.00	0.00	0.01	0.01	0.00	0.00	0.01	0.00
Li*	0.02	0.04	0.01	0.05	0.05	0.03	0.05	0.07	0.00	0.00	0.02	0.03	0.06	0.00	0.04	0.03	0.00	0.03	0.08	0.00	0.00	0.02	0.00	0.02	0.01	0.05	0.02	0.03	0.04	0.02
Sum Y	3.00	3.00	3.00	3.00	3.00	3.00	3.00	3.00	3.01	3.00	3.00	3.00	3.00	3.01	3.00	3.00	3.02	3.00	3.00	3.00	3.01	3.00	3.01	3.00	3.00	3.00	3.00	3.00	3.00	3.00
Al	6.00	6.00	5.91	5.92	5.91	5.93	5.93	6.00	5.93	5.95	6.00	5.91	6.00	5.92	6.00	6.00	5.85	5.94	6.00	5.89	5.86	6.00	5.90	5.91	5.97	6.00	5.89	6.00	6.00	5.98
Mg	0.00	0.00	0.09	0.08	0.09	0.07	0.07	0.00	0.07	0.05	0.00	0.09	0.00	0.08	0.00	0.00	0.15	0.06	0.00	0.11	0.14	0.00	0.10	0.09	0.03	0.00	0.11	0.00	0.00	0.02
Sum Z	6.00	6.00	6.00	6.00	6.00	6.00	6.00	6.00	6.00	6.00	6.00	6.00	6.00	6.00	6.00	6.00	6.00	6.00	6.00	6.00	6.00	6.00	6.00	6.00	6.00	6.00	6.00	6.00	6.00	6.00
Ca	0.05	0.06	0.06	0.07	0.06	0.06	0.06	0.05	0.06	0.06	0.06	0.07	0.05	0.06	0.05	0.04	0.08	0.06	0.05	0.07	0.07	0.04	0.07	0.06	0.05	0.05	0.07	0.06	0.05	0.05
Na	0.81	0.80	0.82	0.82	0.83	0.87	0.86	0.81	0.83	0.82	0.84	0.84	0.85	0.84	0.84	0.83	0.80	0.82	0.82	0.84	0.82	0.84	0.84	0.87	0.85	0.82	0.82	0.84	0.84	0.84
K	0.00	0.01	0.01	0.01	0.00	0.01	0.00	0.00	0.01	0.00	0.00	0.00	0.01	0.00	0.00	0.00	0.00	0.00	0.00	0.01	0.01	0.00	0.01	0.01	0.01	0.01	0.01	0.00	0.00	0.01
Vacancy	0.13	0.13	0.12	0.11	0.10	0.07	0.07	0.14	0.10	0.12	0.09	0.08	0.09	0.09	0.10	0.12	0.12	0.12	0.13	0.09	0.10	0.12	0.08	0.06	0.09	0.13	0.11	0.10	0.11	0.10
Sum X	1.00	1.00	1.00	1.00	1.00	1.00	1.00	1.00	1.00	1.00	1.00	1.00	1.00	1.00	1.00	1.00	1.00	1.00	1.00	1.00	1.00	1.00	1.00	1.00	1.00	1.00	1.00	1.00	1.00	1.00

Composition in weight %, structural formula in atoms per formula unit.

* = calculated by stoichiometry. Structural formula based on 31 anions (O, OH, F)

31	32	33	34	35	36	37	38	39	40	41	42	43	44	45	46	47	48	49	50	51	52	53	54	55	56	57	58	59	60
36.60	36.83	37.12	36.72	37.20	36.96	37.00	37.10	36.79	37.06	37.04	37.17	37.13	36.86	36.85	36.84	36.73	36.89	37.03	36.96	37.21	36.83	37.26	36.72	36.85	36.79	36.70	36.96	37.01	36.52
0.51	0.63	0.72	0.58	0.32	0.37	0.37	0.24	0.69	0.65	0.68	0.50	0.30	0.56	0.71	0.41	0.66	0.31	0.51	0.63	0.45	0.68	0.52	0.72	0.52	0.52	0.61	0.47	0.65	0.69
31.25	31.53	31.19	31.25	32.06	31.77	31.78	33.00	30.58	31.38	31.05	31.58	32.08	31.28	31.01	31.93	31.27	32.14	31.26	31.30	31.73	31.36	31.43	31.03	31.67	31.11	31.22	31.76	31.35	33.02
0.01	0.04	0.04	0.01	0.04	0.04	0.03	0.00	0.02	0.04	0.03	0.00	0.03	0.06	0.00	0.00	0.03	0.04	0.09	0.00	0.01	0.04	0.03	0.02	0.04	0.03	0.03	0.01	0.04	0.09
0.04	0.00	0.00	0.00	0.01	0.00	0.04	0.05	0.07	0.06	0.03	0.00	0.00	0.00	0.00	0.00	0.01	0.00	0.00	0.00	0.00	0.00	0.01	0.03	0.00	0.00	0.04	0.07	0.00	0.05
6.90	6.98	7.13	7.25	6.60	6.46	6.33	6.50	7.52	7.19	7.26	7.10	6.25	7.14	7.62	6.78	7.40	6.83	7.18	7.27	6.84	7.33	7.37	7.28	7.26	7.06	7.11	6.91	7.26	6.83
8.17	8.42	8.47	8.21	8.02	8.31	8.64	7.89	8.15	8.39	8.19	8.10	8.30	8.26	8.25	8.04	8.21	8.06	8.32	8.31	8.03	8.29	8.27	8.30	8.16	8.37	8.16	8.33	8.22	7.16
0.41	0.37	0.38	0.28	0.23	0.24	0.24	0.26	0.39	0.37	0.35	0.37	0.24	0.34	0.38	0.34	0.44	0.27	0.35	0.27	0.35	0.32	0.31	0.49	0.33	0.34	0.35	0.26	0.42	0.34
0.10	0.06	0.05	0.08	0.08	0.07	0.05	0.06	0.03	0.06	0.04	0.08	0.07	0.01	0.06	0.09	0.04	0.07	0.07	0.02	0.06	0.09	0.07	0.06	0.05	0.07	0.04	0.07	0.04	0.09
0.01	0.05	0.00	0.03	0.00	0.00	0.00	0.03	0.04	0.00	0.00	0.05	0.00	0.02	0.03	0.00	0.04	0.02	0.00	0.00	0.02	0.04	0.02	0.00	0.02	0.00	0.04	0.02	0.02	0.03
2.65	2.70	2.76	2.63	2.70	2.70	2.79	2.62	2.71	2.67	2.71	2.70	2.80	2.66	2.72	2.62	2.59	2.66	2.78	2.76	2.65	2.74	2.68	2.61	2.64	2.65	2.65	2.67	2.69	2.66
0.03	0.02	0.02	0.04	0.02	0.04	0.02	0.03	0.04	0.04	0.02	0.02	0.03	0.02	0.03	0.03	0.02	0.04	0.04	0.03	0.04	0.06	0.03	0.02	0.04	0.03	0.03	0.03	0.03	0.03
0.00	0.02	0.00	0.02	0.00	0.00	0.02	0.05	0.00	0.00	0.01	0.05	0.07	0.00	0.08	0.00	0.04	0.00	0.00	0.06	0.00	0.00	0.00	0.13	0.07	0.00	0.00	0.06	0.03	0.06
0.01	0.01	0.00	0.00	0.01	0.00	0.01	0.02	0.01	0.00	0.00	0.00	0.00	0.01	0.00	0.01	0.00	0.01	0.03	0.01	0.01	0.02	0.01	0.01	0.01	0.00	0.00	0.01	0.01	0.00
3.68	3.71	3.73	3.68	3.72	3.71	3.71	3.73	3.68	3.73	3.70	3.70	3.69	3.70	3.67	3.71	3.68	3.72	3.71	3.68	3.72	3.71	3.73	3.63	3.68	3.69	3.69	3.69	3.71	3.70
10.67	10.78	10.81	10.70	10.80	10.75	10.78	10.87	10.67	10.80	10.75	10.80	10.80	10.73	10.74	10.75	10.73	10.77	10.77	10.76	10.79	10.77	10.81	10.71	10.77	10.70	10.70	10.78	10.78	10.82
0.05	0.01	0.04	0.00	0.10	0.06	0.02	0.08	0.05	0.02	0.07	0.08	0.10	0.02	0.00	0.07	0.00	0.04	0.04	0.02	0.11	0.00	0.01	0.03	0.01	0.00	0.04	0.00	0.06	0.20
101.10	102.15	102.46	101.47	101.93	101.45	101.82	102.52	101.44	102.45	101.90	102.30	101.89	101.66	102.14	101.60	101.88	101.86	102.19	102.08	102.01	102.27	102.55	101.77	102.11	101.34	101.38	102.10	102.30	102.28
0.00	0.01	0.00	0.01	0.00	0.00	0.01	0.02	0.00	0.00	0.00	0.02	0.03	0.00	0.03	0.00	0.02	0.00	0.00	0.03	0.00	0.00	0.00	0.05	0.03	0.00	0.00	0.02	0.01	0.03
101.10	102.15	102.46	101.46	101.93	101.45	101.81	102.51	101.44	102.45	101.90	102.28	101.86	101.66	102.11	101.60	101.86	101.86	102.19	102.06	102.01	102.27	102.55	101.71	102.08	101.34	101.38	102.07	102.29	102.26
3.00	3.00	3.00	3.00	3.00	3.00	3.00	3.00	3.00	3.00	3.00	3.00	3.00	3.00	3.00	3.00	3.00	3.00	3.00	3.00	3.00	3.00	3.00	3.00	3.00	3.00	3.00	3.00	3.00	3.00
5.96	5.94	5.97	5.96	5.99	5.98	5.96	5.93	5.99	5.96	5.99	5.98	5.97	5.97	5.96	5.96	5.95	5.95	5.97	5.97	5.99	5.94	5.99	5.96	5.95	5.98	5.96	5.96	5.96	5.87
0.04	0.06	0.03	0.04	0.01	0.02	0.04	0.07	0.01	0.04	0.01	0.02	0.03	0.03	0.04	0.04	0.05	0.05	0.03	0.03	0.01	0.06	0.01	0.04	0.05	0.02	0.04	0.04	0.04	0.13
6.00	6.00	6.00	6.00	6.00	6.00	6.00	6.00	6.00	6.00	6.00	6.00	6.00	6.00	6.00	6.00	6.00	6.00	6.00	6.00	6.00	6.00	6.00	6.00	6.00	6.00	6.00	6.00	6.00	6.00
0.00	0.00	0.00	0.00	0.07	0.03	0.00	0.15	0.00	0.00	0.00	0.00	0.06	0.00	0.00	0.04	0.00	0.06	0.00	0.00	0.01	0.00	0.00	0.00	0.00	0.00	0.00	0.00	0.00	0.12
0.06	0.08	0.09	0.07	0.04	0.04	0.04	0.03	0.08	0.08	0.08	0.06	0.04	0.07	0.09	0.05	0.08	0.04	0.06	0.08	0.05	0.08	0.06	0.09	0.06	0.06	0.07	0.06	0.08	0.08
0.00	0.00	0.01	0.00	0.01	0.00	0.00	0.00	0.00	0.01	0.00	0.00	0.00	0.01	0.00	0.00	0.00	0.00	0.01	0.00	0.00	0.00	0.00	0.00	0.01	0.00	0.00	0.00	0.00	0.01
0.00	0.00	0.00	0.00	0.00	0.00	0.00	0.01	0.01	0.01	0.00	0.00	0.00	0.00	0.00	0.00	0.00	0.00	0.00	0.00	0.00	0.00	0.00	0.00	0.00	0.00	0.01	0.01	0.00	0.01
1.94	1.96	1.91	1.93	1.92	2.00	2.07	1.88	1.84	1.92	1.88	1.92	1.99	1.94	1.87	1.94	1.90	1.94	1.92	1.93	1.93	1.90	1.92	1.89	1.94	1.96	1.92	1.99	1.89	1.72
0.01	0.01	0.01	0.01	0.01	0.01	0.01	0.01	0.00	0.01	0.01	0.01	0.01	0.00	0.01	0.01	0.01	0.01	0.01	0.00	0.01	0.01	0.01	0.01	0.01	0.01	0.01	0.01	0.01	0.01
0.94	0.94	0.96	0.99	0.89	0.87	0.85	0.87	1.02	0.97	0.98	0.96	0.84	0.97	1.03	0.92	1.00	0.92	0.97	0.98	0.92	0.99	0.99	0.99	0.98	0.96	0.97	0.93	0.98	0.92
0.00	0.01	0.00	0.00	0.00	0.00	0.00	0.00	0.00	0.00	0.00	0.01	0.00	0.00	0.00	0.00	0.00	0.00	0.00	0.00	0.00	0.00	0.00	0.00	0.00	0.00	0.00	0.00	0.00	0.00
0.04	0.01	0.03	0.00	0.07	0.04	0.01	0.05	0.03	0.01	0.04	0.05	0.06	0.01	0.00	0.04	0.00	0.02	0.03	0.01	0.07	0.00	0.01	0.02	0.01	0.00	0.02	0.00	0.04	0.13
3.00	3.00	3.00	3.01	3.00	3.00	3.00	3.00	3.00	3.00	3.00	3.00	3.00	3.00	3.00	3.00	3.00	3.00	3.00	3.00	3.00	3.00	3.00	3.00	3.00	3.00	3.00	3.00	3.00	3.00
5.96	5.93	5.88	5.95	6.00	6.00	6.00	6.00	5.86	5.91	5.91	5.97	6.00	5.94	5.88	6.00	5.92	6.00	5.92	5.93	6.00	5.91	5.94	5.89	5.97	5.94	5.94	5.99	5.92	6.00
0.04	0.07	0.12	0.05	0.00	0.00	0.00	0.00	0.14	0.09	0.09	0.03	0.00	0.06	0.12	0.00	0.08	0.00	0.08	0.07	0.00	0.09	0.06	0.11	0.03	0.06	0.06	0.01	0.08	0.00
6.00	6.00	6.00	6.00	6.00	6.00	6.00	6.00	6.00	6.00	6.00	6.00	6.00	6.00	6.00	6.00	6.00	6.00	6.00	6.00	6.00	6.00	6.00	6.00	6.00	6.00	6.00	6.00	6.00	6.00
0.07	0.06	0.07	0.05	0.04	0.04	0.04	0.04	0.07	0.06	0.06	0.06	0.04	0.06	0.07	0.06	0.08	0.05	0.06	0.05	0.06	0.05	0.05	0.08	0.06	0.06	0.06	0.04	0.07	0.06
0.84	0.84	0.86	0.83	0.84	0.85	0.87	0.81	0.85	0.83	0.85	0.84	0.87	0.83	0.85	0.82	0.81	0.83	0.87	0.87	0.83	0.86	0.83	0.82	0.83	0.83	0.83	0.83	0.84	0.83
0.01	0.00	0.00	0.01	0.00	0.01	0.00	0.01	0.01	0.01	0.00	0.00	0.01	0.00	0.01	0.01	0.00	0.01	0.01	0.01	0.01	0.01	0.01	0.00	0.01	0.01	0.01	0.01	0.01	0.01
0.09	0.09	0.07	0.12	0.11	0.10	0.08	0.14	0.07	0.10	0.09	0.09	0.08	0.10	0.08	0.11	0.11	0.11	0.06	0.08	0.10	0.08	0.11	0.09	0.11	0.10	0.10	0.11	0.08	0.11
1.00	1.00	1.00	1.00	1.00	1.00	1.00	1.00	1.00	1.00	1.00	1.00	1.00	1.00	1.00	1.00	1.00	1.00	1.00	1.00	1.00	1.00	1.00	1.00	1.00	1.00	1.00	1.00	1.00	1.00